# 55th ICFA Advanced Beam Dynamics Workshop on High Luminosity Circular $e^+e^-$ Colliders – Higgs Factory

## Topics

Parameters
Optics
Interaction region and machine-detector interface
Synchrotron radiation and shielding
Superconducting RF
Injectors and injection
Orbit stability and beam instability
Polarization
Instrumentation and control
"Green" Higgs factory

*October 9-12, 2014*
*Hotel Wanda Realm*
*Beijing, China*


*Http://hf2014.ihep.ac.cn*

*Email: hf2014@ihep.ac.cn*

*Registration Deadline: August 31, 2014*



# HF2014

ICFA EuCARD² XBEAM

***The 55th ICFA Advanced Beam Dynamics Workshop on***
***High Luminosity Circular $e^+e^-$ Colliders – Higgs Factory (HF2014)***
took place at Hotel Wanda Realm on October 9-12, 2014, Beijing, China.
It was hosted by the Institute of High Energy Physics (IHEP), Chinese Academy of Sciences (CAS).

Since the discovery of the Higgs particle in 2012 at CERN, there have been two new initiatives for a very large future circular collider, namely, the FCC in Europe and the CEPC-SppC in China. Both would serve as a Higgs factory in the first stage.

ICFA encouraged these initiatives and issued a statement that "ICFA supports studies of energy frontier circular colliders and encouraged global coordination." The HF2014 workshop focused on a circular $e^+e^-$ collider for a Higgs factory.

The topics include:
- Parameters
- Optics
- Interaction region and machine-detector interface
- Synchrotron radiation and shielding
- Superconducting RF
- Injectors and injection
- Orbit stability and beam instability
- Polarization
- Instrumentation and control
- "Green" Higgs factory

The workshop website is: http://hf2014.ihep.ac.cn

Weiren Chou, Qing Qin
Co-chairs of HF2014

## HF2014 International Organizing Committee (IOC)

| | | |
|---|---|---|
| Michael Benedikt | CERN | Switzerland |
| Marica Biagini | INFN-LNF | Italy |
| Alain Blodel | Univ. of Geneva | Switzerland |
| Alex Chao | SLAC | USA |
| Swapan Chattopadhyay | Cockcroft Institute | UK |
| Weiren Chou (Co-Chair) | Fermi Lab | USA |
| Jie Gao | IHEP | China |
| Stuart Henderson | Fermi Lab | USA |
| Andrew Hutton | JLab | USA |
| Eugene Levichev | BINP | Russia |
| Xinchou Lou | IHEP | China |
| Katsunobu Oide | KEK | Japan |
| Qing Qin (Co-Chair) | IHEP | China |
| Dave Rice | Cornell Univ. | USA |
| John Seeman | SLAC | USA |
| Chuanxiang Tang | Tsinghua Univ. | China |
| Jorg Wenninger | CERN | Switzerland |
| Frank Zimmermann | CERN | Switzerland |

## HF2014 Local Organizing Committee (LOC)

Tongzhou Xu (IHEP, Chair)
Huiping Geng (IHEP)
Yinghua Jia (IHEP)
Shuzhen Liu (IHEP)
Qian Pan (IHEP)
Shan Zeng (IHEP)
Ning Zhao (IHEP)

# Contents

# A NEW PARADIGM: ROLE OF ELECTRON-POSITRON AND HADRON COLLIDERS

Shou-hua Zhu
[1] Institute of Theoretical Physics & State Key Laboratory of Nuclear Physics and Technology, Peking University, Beijing 100871, China
[2] Collaborative Innovation Center of Quantum Matter, Beijing, China
[3] Center for High Energy Physics, Peking University, Beijing 100871, China

*Abstract*

In 2012, a light scalar boson (denoted as H(125) in this paper) was discovered at the LHC. We explore the possible correlation between the lightness of H(125) and the smallness of CP-violation based on the Lee model, namely the spontaneous CP-violation two-Higgs-doublet-model. It is a new way to understand why H(125) is light. Based on this we propose that it is the much heavier scalar bosons, instead of the H(125), which need to be understood. This opens a new paradigm that one tries to understand the electro-weak symmetry breaking and CP violation. For the new paradigm, similar to many other physics beyond the standard model, one need both electron-positron and higher energy hadron collider, as well as the low energy experiments, in order to pin down the whole picture.

## INTRODUCTION

The organizers of HF2014 invited me to give an overview on physics, especially the physics beyond the standard model (BSM), which can be investigated at Higgs Factories (HF). Since a new scalar (denoted as H(125) in this paper) was discovered in 2012, LHC is an obvious HF. For one hand, LHC can do much more in the future run, on the other hand, LHC precision is limited by its hadronic environment. Next generation electron-positron collider and higher energy hadron collider are under extensive discussion. One predominant example is the CEPC (circular electron and positron collider) with $\sqrt{s} = 240$ GeV or so, plus the possible update to super proton-proton collider (SPPC) with $\sqrt{s} = 50 - 100$ TeV or higher. It is quite natural to expect that CEPC can reach much higher precision that those of LHC, and SPPC can detect the much higher BSM scale than that of the LHC.

In principle, the whole BSM picture can usually be revealed via the combination efforts of LHC, CPEC/ILC, SPPC, FCC and other high energy colliders, as well as the low energy experiments which have certain unique opportunity, for example, CP violation and/or rare processes. There are numerous BSM, how to give the audience a relative global, objective and persuasive picture is a challenging task. In the end we decide to firstly give a brief overview on BSM motivations, then discuss a possible new paradigm as an example, which need high energy electron-positron and hadron colliders to pin down the whole picture.

## MOTIVATION FOR BSM

The discovery of H(125) is revolutionary. For the fist time in the history of particle physics, we have a complete theory to describe the electro-weak and strong interactions. If the H(125) is really the SM one, as many people believe, SM can be applicable to a very high scale, much higher than the weak scale. However we also have many reasons that BSM should exist. In this section, the motivations for BSM are categorized into 4 classes.

### *Motivation(I): Test New Types of Interactions*

In the SM, there are 3 types of interactions:

- Gauge interaction
- Yukwa interaction
- Higgs self interaction

Gauge interaction, which can describe the strong and electro-weak interactions excellently, is well-tested for most cases. The Yukawa interaction and Higgs self-interaction are new types of interactions, and which need to be checked in HF. In the SM Yukawa interaction is the origin of fermion mass, and induce the flavor changing processes. BSM can easily affect Yukawa interaction. For the Higgs self interaction in the SM, once Higgs boson mass is fixed, the triple $h^3$ and quartic $h^4$ interactions are also fixed. One motivation to measure the Higgs self couplings is related with electro-weak phase transition. In order to account for the matter dominant Universe, the Higgs self couplings are usually greatly altered. Another popular motivation is that Higgs potential might be more complicated than that in the SM. Therefore measuring the Higgs self interaction is the way to reconstruct the Higgs potential, though quite challenging.

### *Motivation (II): Account for Astrophysical Observations*

There are several astrophysical observations (dark matter (DM), baryon asymmetry, and inflation) which may be related to BSM at O(TeV). There is not suitable DM candidate in the SM. In order to keep DM stable or pseudo-stable, one usually introduces new symmetry, and one popular example is the supersymmetry (SUSY). SUSY can provide a natural SM candidate is thought as one of its successes. In order to construct a complete theory, one likely

ISBN 978-3-95450-172-4

introduces more Higgs fields, for example in the supersymmetric model we have to introduce at least two Higgs doublets.

SM can't account for baryon asymmetry in the Universe, though the 3 Saharov conditions are fulfilled. If one insists on the electro-weak baryon-genesis, the Higgs couplings must be altered, which can be tested in HF. Another possible connection between baryon asymmetry and HF is the CP violation. New CP violation other than CKM matrix may be revealed in HF.

### *Motivation (III): Theoretical Ones*

There are too many parameters in SM which could be reduced if we know what beneath the Higgs field(s). The introduction of scalar field brings some shortcomings to the theory, for example the naturalness issue. In order to make the theory natural, one has to introduce new strong interaction, new symmetry, or extra-dimension etc. There are many other theoretical issues, for example: what is the origin of P and CP violation, why are there 3 generations etc.

Last but not least, we don't include the gravity in the theory. HF may shed light on the nature of gravity, reveal hints for further knowledge on the space-time and quantum theory.

### *Motivation (IV): "Common Sense"*

For the fundamental science, exploring the unknown and discovering the unexpected phenomena are the primary driving force for the progress. We call this as "common sense" motivation. To pursue the higher energy and smaller distance is the obvious next goal.

As the second "common sense" motivation, H(125) is special. Since the discovery of H(125) we have this new physical object which need the experimentalists to measure its properties as precisely as possible and discover possible deviations from the SM predictions.

## SMALLNESS OF CP VIOLATION AND THE LIGHTNESS OF H(125)

### *A Story*

In 2006, officials of both PRC and US signed a document which indicated that a joint workshop would be held in June 2007, in order to explore the possibility of parity spontaneous breaking at electron-positron colliders. In January 2007, a mini-workshop was organized by Prof. K.T. Chao and Prof. Y.P. Kuang in order to prepare for the workshop. I was invited to give a theoretical and experimental review on left-right symmetric models. During that time, the popular parity restoration models is left-right symmetric models. My personal impression on this model is that the scale is too high to electron-positron colliders, even for LHC, because the low energy measurements like $K_0 - \bar{K}_0$ mixing and direct search from Tevatron have put very strict limits on right-handed gauge bosons. After the mini-workshop, I realized that other parity restoration approaches, like mirror models, might be tested at electron-positron collider and LHC [1]. In fact the parity of weak interaction is maximally violated, while CP is a quite good approximate symmetry. This is one of reasons why the left-right symmetric models suffering so severe constraints. During the June workshop, the honorary chair of which is T.D. Lee, my impression on this topic kept the same.

In July 2012, the new scalar H(125) was discovered by ATLAS and CMS of the LHC, which surprised many theorists including me. In the SM, the discovery is not strange. However in the BSM, the scalar mass tends to be the BSM scale. We were thinking possible new mechanism to account for the new discovery. In the end of 2012, just before the celebration of 80's birthday of Prof. Kuang, I wrote the paper on the possible connection between the spontaneous CP violation and the mass of the new scalar [2, 3]. Some people concerned on the viability of the model. After more than one year, after checking all important measurements, we found [4] the model does viable and can be tested in the future LHC and electron-positron colliders. Meanwhile we began to think the possible implication for understanding electro-weak symmetry breaking and origin of CP violation.

### *Smallness of CP Violation*

CP has been thought strict conserved after the discovery of P violation in 1957. However such situation did not last long, tiny CP violation was first discovered in neutral K-meson in 1964. Now all measured CP violated effects in neutral K- and B-meson, and charged B meson systems can be successfully accounted for by the CKM matrix, which is usually parameterized as the Wolfenstein formalism

$$V_{\rm CKM} = \begin{pmatrix} 1-\lambda^2/2 & \lambda & A\lambda^3(\rho-i\eta) \\ -\lambda & 1-\lambda^2/2 & A\lambda^2 \\ A\lambda^3(1-\rho-i\eta) & -A\lambda^2 & 1 \end{pmatrix} + \mathcal{O}(\lambda^4) \quad (1)$$

In order to measure magnitude of CP violation independent on basis, the Jarlskog invariant [5][6] was introduced as

$$J = A^2\lambda^6\eta = (2.96^{+0.20}_{-0.16}) \times 10^{-5}. \quad (2)$$

The smallness of $J$ means the smallness of CP-violation in the SM. In order to understand the smallness of CP violation, one has to go beyond the SM.

### *Lightness of H(125)*

BSM is well motivated as we have discussed in the last section. BSM scale is usually pushed to a much higher value than that of weak interaction, given the great success of the SM. In such circumstance, the 125 GeV scalar boson is unnatural, i.e. the lightness of the new scalar must link to certain mechanism. It should be emphasized that the issue of the lightness of H(125) differs in the SM and the BSM. In the SM, the mass of Higgs boson is only a free parameter, and $m_H = 125$ GeV simply implies that the interactions are in the weak regime. However in some BSM



ISBN 978-3-95450-172-4

models there exists a light scalar naturally. We enumerate several examples, (1) in the minimal super-symmetric model (MSSM), the lightest Higgs boson mass should be less than 140GeV after including higher-order corrections; (2) in the little higgs models, a Higgs boson which is treated as a pseudo-Nambu-Goldstone boson must be light due to classical global symmetry and it acquires mass through quantum effects only; (3) the anomalous in scale invariance models can also generate a light Higgs boson; (4) the lightness of Higgs boson can intimately connect with the spontaneous CP violation. While the first three approaches base on the *conjectured* symmetry, the last one utilizes the *observed* approximate CP symmetry. Historically Lee proposed the spontaneous CP violation in 1973 [7] as an alternative way to induce CP violation. For the fourth approach, Lee's idea is extended to account for the lightness of the observed Higgs boson.

### *Lee Model*

In order to analyze the connection between spontaneous CP violation and the Higgs boson mass, we begin with the description of Lee model [7] assuming that in the whole lagrangian there are no explicit CP-violated terms, which means all the CP-violated effects come from a complex vacuum.

For the Lee model, the interactions of scalar fields can be written as [7]

$$\mathcal{L} = (D_\mu\phi_1)(D^\mu\phi_1) + (D_\mu\phi_2)(D^\mu\phi_2) - V(\phi_1,\phi_2). \quad (3)$$

Here

$$\phi_1 = \begin{pmatrix} \phi_1^+ \\ \frac{v_1+R_1+iI_1}{\sqrt{2}} \end{pmatrix}, \qquad \phi_1 = \begin{pmatrix} \phi_2^+ \\ \frac{v_2 e^{i\xi}+R_2+iI_2}{\sqrt{2}} \end{pmatrix} \quad (4)$$

are the two Higgs doublets. We can see the $\xi$ is the only source of CP violation. Here there are two vacuum expectation values $v_1, v_2$ and $v = \sqrt{v_1^2+v_2^2} = 246$GeV as usual. Defining $R(I)_{ij}$ as the real(imaginary) part of $\phi_i^\dagger\phi_j$, we can write a general potential as

$$\begin{aligned} V &= V_2 + V_4 \\ &= \mu_1^2 R_{11} + \mu_2^2 R_{22} \\ &\quad + \lambda_1 R_{11}^2 + \lambda_2 R_{11}R_{12} + \lambda_3 R_{11}R_{22} \\ &\quad + \lambda_4 R_{12}^2 + \lambda_5 R_{12}R_{22} + \lambda_6 R_{22}^2 + \lambda_7 I_{12}^2. \end{aligned} \quad (5)$$

We can also write the general Yukawa couplings as

$$\begin{aligned} \mathcal{L}_y &= -\bar{Q}_{Li}(Y_{1d}\phi_1 + Y_{2d}\phi_2)_{ij} D_{Rj} \\ &\quad -\bar{Q}_{Li}(Y_{1u}\tilde{\phi}_1 + Y_{2u}\tilde{\phi}_2)_{ij} U_{Rj}, \end{aligned} \quad (6)$$

in which $\tilde{\phi}_i = \mathrm{i}\sigma_2\phi_i^*$ and all Yukawa couplings are real.

After rotating away Goldstone mode, we can expand the neutral Higgs boson mass matrix $\tilde{m}$ in series of $t_\beta(s_\xi)$ as

$$\tilde{m} = \tilde{m}_0 + (t_\beta s_\xi)\tilde{m}_1 + (t_\beta s_\xi)^2\tilde{m}_2 + \cdots \quad (7)$$

We found

$$\lim_{t_\beta s_\xi \to 0} \det(\tilde{m}) = \det(\tilde{m}_0) = 0 \quad (8)$$

which means a zero eigenvalue of $\tilde{m}_0$ thus there must be a light neutral scalar when $t_\beta s_\xi$ is small. To the leading order of $t_\beta s_\xi$, for the lightest scalar $h$, we have

$$\begin{aligned} m_h^2 &= \frac{v^2 t_\beta^2 s_\xi^2}{2}\left(\frac{(\tilde{m}_1)_{12}^2}{(\tilde{m}_0)_{22}} + \frac{(\tilde{m}_1)_{13}^2}{(\tilde{m}_0)_{33}} + (\tilde{m}_2)_{11}\right) \\ h &= I_2 + t_\beta s_\xi\left(\frac{(\tilde{m}_1)_{12}}{(\tilde{m}_0)_{22}}(c_\theta R_1 + s_\theta R_2)\right. \\ &\quad \left. + \frac{(\tilde{m}_1)_{13}}{(\tilde{m}_0)_{33}}(c_\theta R_2 - s_\theta R_1) - \frac{I_1}{t_\xi}\right), \end{aligned} \quad (9)$$

where $\theta = (1/2)\tan^{-1}(2\lambda_2/(4\lambda_1 - \lambda_4 + \lambda_7))$.

From the Yukawa couplings we will get the mass matrixes for fermions as

$$(M_U)_{ij} = \frac{v}{\sqrt{2}}(Y_{1u}c_\beta + Y_{2u}s_\beta e^{-i\xi})_{ij}, \quad (10)$$

$$(M_D)_{ij} = \frac{v}{\sqrt{2}}(Y_{1d}c_\beta + Y_{2d}s_\beta e^{i\xi})_{ij}. \quad (11)$$

We can always perform the diagonalization for $M_{U(D)}$ with matrixes $U(D)_L$ and $U(D)_R$ as

$$U_L M_U U_R^\dagger = diag\,(m_u, m_c, m_t)\,, \quad (12)$$

$$D_L M_D D_R^\dagger = diag\,(m_d, m_s, m_b)\,. \quad (13)$$

And $V_{\mathrm{CKM}} = U_L D_L^\dagger$ is the CKM matrix.

We choose all the nine free parameters as nine observables in Higgs sector: masses of four scalars $m_h, m_2, m_3$ and $m_{H^\pm}$; vacuum expected values $v_1, v_2, \xi$ and two mixing angles for neutral bosons. We choose them $c_1$ and $c_2$ defined as

$$\mathcal{L}_{h_i VV} = c_i h_i\left(\frac{2m_W^2}{v}W_\mu^+ W^{\mu-} + \frac{m_Z^2}{v}Z_\mu Z^\mu\right) \quad (14)$$

which just means the $h_i VV$ vertex strength comparing with that in SM. There is a sum rule $c_1^2 + c_2^2 + c_3^2 = 1$ due to spontaneous electro-weak symmetry broken, thus only two of the $c_i$ are free.

In the scalar sector, for non-degenerate neutral Higgs bosons, a quantity $K = c_1c_2c_3$ measures the CP violation effects [8][9], while in Yukawa sector, the Jarlskog invariant $J$ [6] measures that. In this scenario, to the leading order of $t_\beta s_\xi$, we have

$$K = c_1c_2c_3 = -s_\theta c_\theta(1+\eta_1)t_\beta s_\xi \propto t_\beta s_\xi \quad (15)$$

In order to calculate J, we define matrix $\hat{C}$ as

$$\hat{C} \equiv \left[M_U M_U^\dagger, M_D M_D^\dagger\right]. \quad (16)$$

We can always choose a basis in which the diagonal elements of $\hat{C}$ are zero. Thus

$$\begin{aligned} \hat{C} &= \begin{pmatrix} 0 & C_3 & -C_2 \\ -C_3 & 0 & C_1 \\ C_2 & -C_1 & 0 \end{pmatrix} + i\begin{pmatrix} 0 & C_3^* & C_2^* \\ C_3^* & 0 & C_1^* \\ C_2^* & C_1^* & 0 \end{pmatrix} \\ &= \left(\mathrm{Re}\hat{C} + i\mathrm{Im}\hat{C}\right) \end{aligned} \quad (17)$$

ISBN 978-3-95450-172-4

It can be proved that [4]

$$J = \frac{\prod C_i \sum (C_i^*/C_i)}{\prod \left(m_{U_i}^2 - m_{U_j}^2\right) \prod \left(m_{D_i}^2 - m_{D_j}^2\right)} \propto t_\beta s_\xi. \quad (18)$$

According to the equations (15), (18), and (9), we propose that the lightness of the Higgs boson and the smallness of CP-violation effects could be correlated through small $t_\beta s_\xi$ since both the Higgs mass $m_h$ and the quantities $K$ and $J$ to measure CP-violation effects are proportional to $t_\beta s_\xi$ at the small $t_\beta s_\xi$ limit.

## A NEW PARADIGM

In the last section, the connection between small CP violation and H(125) is explored in the simplest spontaneous CP violation Lee model. Based on the above discussion, a new paradigm emerges. In the past studies, one tried to account for the lightness of the H(125). In the new paradigm, the mass of H(125) is due to the approximate CP symmetry and the extra scalar bosons can be much heavier, e.g. at O(TeV) even in the strong-coupled regime. This opens a new approach to understand the electro-weak symmetry breaking and the origin of CP violation. The schematic diagram is shown in Fig. 1. For the optimistic case (from the point view of experimentalists), the extra new scalars can be not so heavy. For this case, LHC has the good opportunity to discover them.

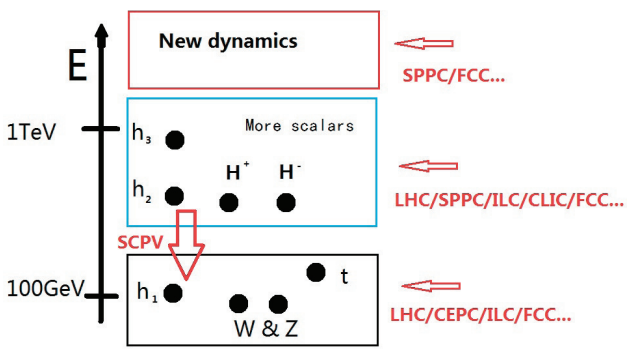


Figure 1: Schematic diagram for a new paradigm.

The generic feature of this new paradigm is summarized

- H(125) is not SM-like, instead H(125) is the CP mixing state
- There are other heavy neutral and charged Higgs bosons
- There are usually extra CP violation in scalar sector, besides CKM matrix, though they arise both from the complex vacuum
- The scale of the new mechanism for the complicated scalar sectors is higher.

## PHENOMENOLOGY: ROLE OF ELECTRON-POSITRON AND HADARON COLLIDERS

Based on studies of Ref. [4], the Lee model is still viable confronting the high and low energy experiments. The next natural question is how to confirm/exclude this model at future facilities.

We treat the H(125) as the lightest neutral Higgs boson. If Lee model is true, the extra neutral and charged Higgs bosons should be discovered at high energy colliders. As the general rules, the lighter the extra Higgs bosons, the easier they can be produced. In order to confirm the Lee model, another possible signal can be the FCNC decay of the neural Higgs bosons which are unobservable small in the SM. Furthermore the CP properties of the Higgs boson are essential measurements, though it is a very challenging task.

As we have pointed out [4] that there is no SM limit in this scenario, thus it is always testable at the future colliders, such as LHC with $\sqrt{s} = 14$TeV, CEPC, ILC, or TLEP with $\sqrt{s} = (240 \sim 250)$TeV, even before the discovery of other neutral Higgs bosons and charged Higgs boson. The coupling between H(125) and other particle (especially $W^\pm$ and $Z^0$) are usually suppressed by the factor of $\mathcal{O}(t_\beta s_\xi)$. In the $b\bar{b}$ decay channel or any VBF, VH associated production channel, a significant suppression can be the first sign of this scenario. On the contrary if the signals become even more SM-like, this scenario will be disfavored.

For future LHC with $\sqrt{s} = 14$TeV, the signal strengths will be measured with an uncertainty of about $10\%$ at the luminosity 300fb$^{-1}$ [10][11]. These measurements can be used to constrain $c_V$ ( which is $c_1$ in the last section). A Higgs boson with $c_V \geq (0.6 \sim 0.7)$ is hardly to be pseudoscalar dominant thus if $c_V \leq (0.6 \sim 0.7)$ is excluded, we can say this scenario is excluded. So we can test this scenario by fitting the signal strengths. We list the estimating results in Tab. 1. It should be noted that the true ability to test this scenario depends strongly on the real signal strengths from future experiments.

Table 1: Abilities to test the scenario at $\sqrt{s} = 14$TeV LHC. Lower limit for the allowed $c_V$ at $2\sigma$ and $3\sigma$ level are listed in the tables. For the up/down tables we assume all signal strengths are consistent with SM at $1\sigma/2\sigma$ level respectively.

| Excluded level | $2\sigma$ | $3\sigma$ |
|---|---|---|
| 300fb$^{-1}$ | 0.62 | 0.55 |
| 3000fb$^{-1}$ | 0.77 | 0.72 |
| Excluded level | $2\sigma$ | $3\sigma$ |
| 300fb$^{-1}$ | 0.53 | 0.45 |
| 3000fb$^{-1}$ | 0.7 | 0.65 |

At a HF with the $e^+e^-$ initial state at $\sqrt{s} = (240 \sim 250)$GeV, the dominant production process for a Higgs bo-



ISBN 978-3-95450-172-4

son is associated with a $Z^0$ boson. Another important production process is through VBF. In this scenario it is suppressed by a factor $c_1^2$ thus this scenario can be excluded if the total cross section favors SM. For the total cross section, a measurement with $\mathcal{O}(10\%)$ uncertainty is accurate enough to distinguish the scenario we discussed in this paper and SM at $3\sigma$ or even $5\sigma$ significance. Such accuracy can be easily achieved at CEPC/ILC/TLEP.

For this new paradigm, the role of the higher energy hadron collider (like SPPC) is to probe the new dynamics which is responsible for the electro-weak symmetry breaking, origin of CP and/or P violation etc.

## CONCLUSIONS AND DISCUSSIONS

In this paper, we explored the correlation between the lightness of Higgs boson and the smallness of CP-violation based on the Lee model, namely the spontaneous CP-violation two-Higgs-doublet-model. In this model, the mass of the lightest Higgs boson $m_h$ as well as the quantities $K$ and $J$ are $\propto t_\beta s_\xi$ in the limit $t_\beta s_\xi \to 0$, namely the CP conservation limit. Here $K$ and $J$ are the measures for CP-violation effects in scalar and Yukawa sectors respectively. It is a new way to understand why the Higgs boson discovered at the LHC is light. Based on this possible connection, we proposed that H(125) is due to the approximate CP symmetry and there are extra heavier scalars. This opens a new paradigm that one tries to understand the electro-weak symmetry breaking and CP violation. For this new paradigm, one needs both electron-positron and higher energy hadron collider, as well as the low energy experiments, to pin down the whole picture. We emphasize that this final conclusion is also applicable to many other BSM as well, and which is one of the most important motivations to pursue the next generation colliders.

## ACKNOWLEDGMENT

This work was supported in part by the Natural Science Foundation of China (Nos. 11135003 and 11375014).

## REFERENCES

[1] Wen-sheng Li, Peng-fei Yin, and Shou-hua Zhu, *Detecting $H->hh$ in the Mirror Model at the CERN Large Hadron Collider*, Phys.Rev. **D76** (2007), 095012.

[2] Shou-hua Zhu, *Complex Vacuum and Lightness of Higgs Boson*, arXiv:1211.2370.

[3] Yang Hu, You-Kai Wang, Peng-Fei Yin, and Shou-Hua Zhu, *On physics beyond standard model*, Front.Phys. **8** (2013), 516–539.

[4] Ying-nan Mao and Shou-hua Zhu, *Lightness of Higgs Boson and Spontaneous CP Violation in Lee Model*, arXiv:1409.6844.

[5] J. Beringer et. al. (Particle Data Group), Phys. Rev. D 86, 010001 (2012); K. A. Olive et al. (Particle Data Group), Chin. Phys. C 38, 090001 (2014 updated)

[6] C. Jarlskog, Phys. Rev. Lett. 55, 1039 (1985)

[7] T. D. Lee, Phys. Rev. D 8, 1226 (1973)

[8] G. C. Branco et. al. Phys. Rept. 516 (2012)

[9] A. Méndez and A. Pomaral, Phys. Lett. B 272, 313 (1991)

[10] CMS Collaboration, 1307.7135

[11] H. Okawa (on behalf of ATLAS and CMS Collaborations), http://moriond.in2p3.fr/QCD/2014/SundayAfternoon/Okawa.pdf

ISBN 978-3-95450-172-4

# FCC-*ee* OVERVIEW

F. Zimmermann, M. Benedikt, H. Burkhardt, F. Cerutti, A. Ferrari, J. Gutleber, B. Haerer, B. Holzer, E. Jensen, R. Kersevan, P. Lebrun, R. Martin, A. Mereghetti, J. Osborne, Y. Papaphilippou, D. Schulte, R. Tomas, J. Wenninger, CERN, Geneva, Switzerland; A. Blondel, M. Koratzinos, U. Geneva, Switzerland; M. Boscolo, INFN Frascati, Italy; L. Lari, ESS, Lund, Sweden; K. Furukawa, K. Ohmi, K. Oide, KEK, Tsukuba, Japan; S. White, ESRF, Grenoble, France; A. Bogomyagkov, I. Koop, E. Levichev, N. Muchnoi, S. Nikitin, D. Shatilov, BINP Novosibirsk, Russia; U. Wienands, SLAC, Stanford, USA; E. Gianfelice, FNAL, Batavia, USA; L. Medina, U. Guanajuato, Mexico

*Abstract*

The *FCC-ee* is a proposed circular $e^+e^-$ collider installed in a new 100 km tunnel delivering high luminosity to four experiments at centre-of-mass energies ranging from 91 GeV (Z pole) over 160 GeV (*W* threshold) and 240 GeV (*H* production) to 350 GeV (*t* physics). The *FCC-ee* design is pursued as part of the global Future Circular Collider (*FCC*) study, which regards the *FCC-ee* as a potential intermediate step towards a 100-TeV hadron collider, called *FCC-hh*, sharing the same tunnel infrastructure. We here report the *FCC-ee* design status.

## INTRODUCTION

Since 1960 about 30 ring colliders have been successfully built and operated. Many more $e^{\pm}$ storage-ring light sources have been constructed, with ever smaller transverse emittances. In short, storage rings and storage-ring colliders represent a well understood technology, typically exceeding their design performance within a few years. LEP was the highest energy lepton collider built so far. Its maximum c.m. energy reached 209 GeV, and its total synchrotron radiation power rose up to 23 MW. Figure 1 shows the evolution of the LEP-1/-2 peak-luminosity performance compared with the respective design values, and Figure 2 the vertical-to-horizontal emittance ratio towards the end of LEP-2. Both figures demonstrate better performance at higher beam energy (increasing over the years).

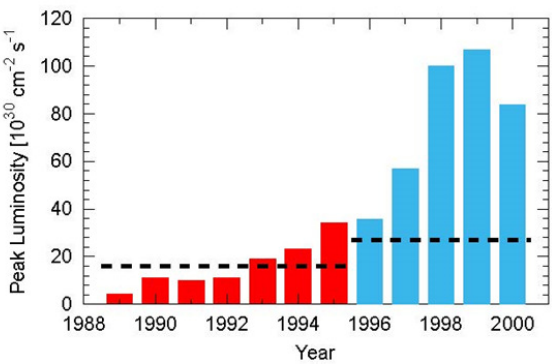


Figure 1: Peak luminosity of LEP-1 (red) and LEP-2 (blue) as a function of year, compared with the respective design values (dashed lines) [1].

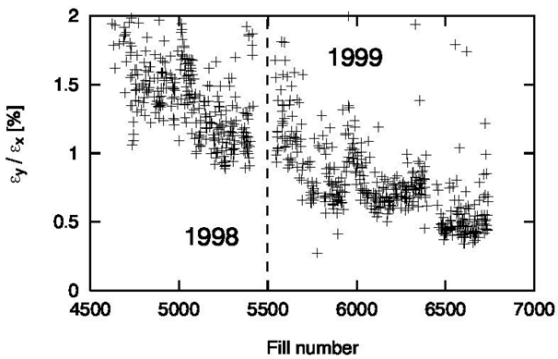


Figure 2: Vertical-to-horizontal emittance ratio at LEP in 1998 and 1999 [1]. The decrease reflects both changes in the damping partition numbers and improved steering [2].

In 1976, B. Richter foresightedly wrote that "An $e^+$-$e^-$ storage ring in the range of a few hundred GeV in the centre of mass can be built with present technology [and] ...would seem to be ... most useful project on the horizon" [3]. Figure 3, from the same reference, shows the cost-optimized circumference according to 1976 prices as a function of c.m. energy. For 300 GeV c.m. the cost optimum corresponds to a ring of about 90 km in size. This suggests that the 100 km tunnel for a 100-TeV hadron collider also is a good choice for hosting a circular $e^+e^-$ collider operating at up to 350-400 GeV.

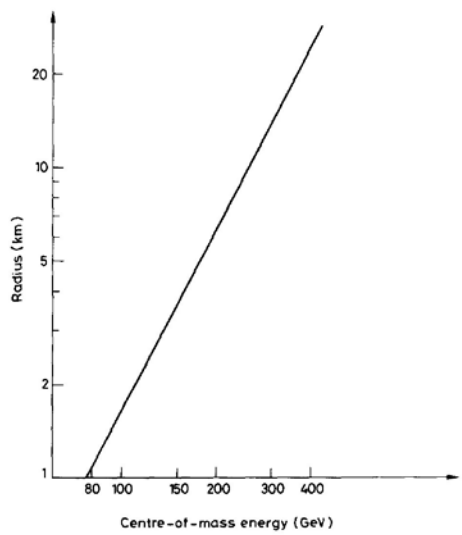


Figure 3: Cost-optimized circumference of a circular $e^+e^-$ collider versus centre-of-mass energy as of 1976 [3].



ISBN 978-3-95450-172-4

After first indications and later the confirmed discovery of a Higgs(-like) boson at the LHC, the years 2011 to 2013 have witnessed a revival of Burt Richter's idea, in the form of several new proposals for circular colliders at energies higher than LEP [4-11], such as LEP3 in the LHC tunnel, DLEP at twice the LEP/LHC size, and TLEP in an 80-100 km long tunnel, disucssed in a number of dedicated workshops [12-18].

The 2013 update of the European Strategy for Particle Physics requests CERN to "undertake design studies for accelerator projects in a global context, with emphasis on proton-proton and electron-positron high-energy frontier machines" [19]. This strategy update was formally adopted by the CERN Council.

## FCC STUDY

In response to the aforementioned request from the European Strategy, CERN has launched the Future Circular Collider (*FCC*) Study [20], with the mandate to complete a Conceptual Design Report (CDR) and cost review in time for the next European Strategy Update (2018). Presently an international collaboration is being formed with the goal to design a 100-TeV *pp*-collider (*FCC-hh*) together with an 80-100 km tunnel infrastructure in the Geneva area (Figure 4), as well as an $e^+e^-$ collider (*FCC-ee)* as a potential intermediate step, and to also study a *p-e* (*FCC-he*) collider option.

Dipole magnets with a field of about 16 T would allow 100-TeV *pp* collisions in a ring of 100 km circumference. These parameters represent the study baseline.

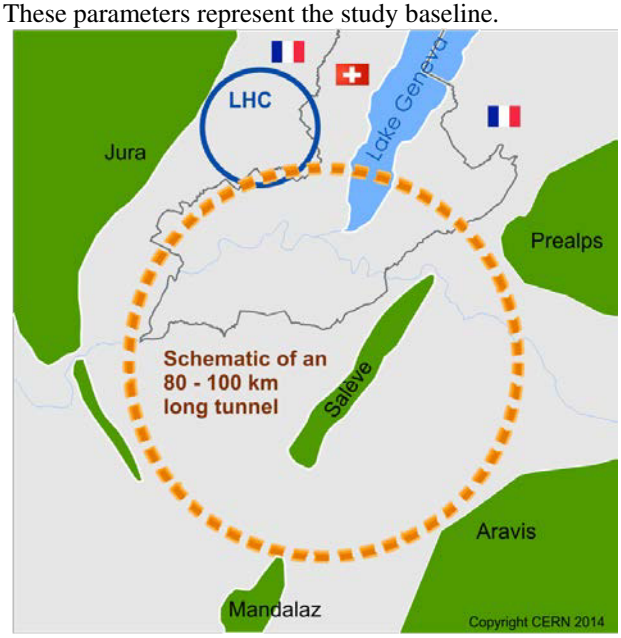


Figure 4: Schematic of an 80-100 km tunnel infrastructure in the Geneva basin.

An FCC kickoff meeting was organized at the University of Geneva on 12-15 February 2014 [21]. More than 340 participants from around the world reflected the widespread interest in the FCC concept and study.The kickoff meeting defined and endorsed the study structure shown in Figure 5. Collaboration Board and Study Coordination Group have been set up already.

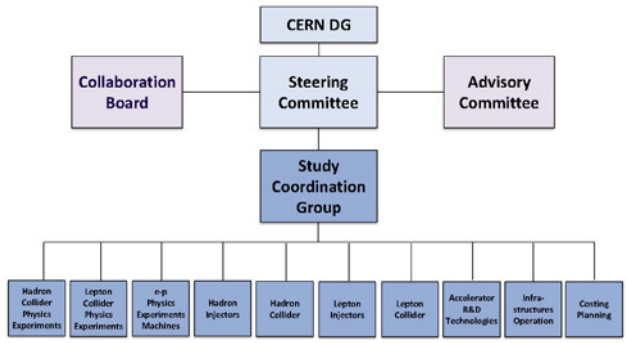


Figure 5: Organization structure of the FCC study.

A preparatory meeting of the collaboration board was held at CERN on 9 and 10 September 2014, with about 80 participants.. L. Rivkin (EPFL & PSI) was unanimously elected as interim Collaboration Board Chair by those institutes which had already formally joined the collaboration. Figure 6 shows the structure of the FCC Study Coordination Group.


Figure 6: The FCC Study Coordination Group.

## FCC-hh DESIGN

The physics requirements for *FCC-hh* include highest possible *pp* luminosity at 100 TeV. The present baseline foresees a luminosity of $L$=5x10$^{34}$ cm$^{-2}$s$^{-1}$ (as for *HL-LHC*). Higher luminosity appears possible, with implications for pile up, bunch spacing, shielding, cost, etc. In parallel heavy-ion collisions and ion-proton collisions are desired, as for the LHC. Replicating the LHC configuration, four experiments are foreseen, two of which with special purpose detectors. Though proton-beam polarization was successfully demonstrated at RHIC, it is an open question whether polarization can be preserved at the much higher energy of the *FCC*. The baseline beam parameters of *FCC-hh* are summarized in Table 1 [22]. Noteworthy are the figures for the event pile up (number of events per crossing) – which, at the same

ISBN 978-3-95450-172-4

luminosity of $5x10^{-34}$ $cm^{-2}s^{-1}$, exceeds the *HL-LHC* value because of a slightly higher cross section –, the total synchrotron radiation power of close to 5 MW (~500 times the LHC value) in a cold environment, and the longitudinal damping time of about 30 minutes (to be compared with half a day at the LHC).

Table 1: Baseline Parameters of *FCC-hh* Compared with *LHC* and *HL-LHC*

| parameter | *LHC* | *HL-LHC* | *FCC-hh* |
|---|---|---|---|
| c.m. energy [TeV] | 14 | | 100 |
| dipole field [T] | 8.33 | | 16 (20) |
| circumference [km] | 26.7 | | 100 (83) |
| luminosity [$10^{34}$ $cm^{-2}s^{-1}$] | 1 | 5 | 5 [→20?] |
| bunch spacing [ns] | 25 | | 25 {5} |
| events / bunch crossing | 27 | 135 | 170 {34} |
| bunch population [$10^{11}$] | 1.15 | 2.2 | 1 {0.2} |
| norm. transverse emitt. [mm] | 3.75 | 2.5 | 2.2 {0.44} |
| Interaction-Point (IP) beta function [m] | 0.55 | 0.15 | 1.1 |
| IP beam size [mm] | 16.7 | 7.1 | 6.8 {3} |
| synchrotron rad. [W/m/aperture] | 0.17 | 0.33 | 28 (44) |
| critical energy [keV] | 0.044 | | 4.3 (5.5) |
| total syn.rad. power [MW] | 0.007 | 0.0146 | 4.8 (5.8) |
| longitudinal damping time [h] | 12.9 | | 0.54 (0.32) |

## FCC-ee GOALS AND PARAMETERS

The physics requirements for *FCC-ee* comprise highest possible luminosity for a wide physics program ranging from the *Z* pole to the *t* production threshold, at beam energies between 45 and 175 GeV. The main physics programs are: (1) operation at 45.5 GeV beam energy for running at the *Z* pole as "TeraZ" factory and for high precision $M_Z$ and $\Gamma_Z$ measurements; (2) 80 GeV: *W* pair production threshold; (3) 120 GeV: *ZH* production (maximum rate of *H*'s); (4) 175 GeV: *t-tbar* threshold. Some measurable beam polarization is expected up to ≥80 GeV, which will allow for precise beam energy calibration at the *Z* pole and at the *W* -pair threshold. Key features are the small vertical beta function at the collision point, $\beta_y^*$, of only 1 mm, and a constant value of 100 MW for the synchrotron radiation (SR) power assumed at all energies. The power dissipation then defines the maximum beam current at each energy. Eventually a margin of a few percent may be required for losses in the straight sections.

Table 2 compares the baseline parameters of *FCC-ee* with those of LEP-2. For operation at the Z pole an alternative parameter set with almost ten times higher luminosity [24] is also included. The latter considers transversely smaller (lower emittance), but longer bunches (with reduced HOM losses as a welcome side-effect) colliding at 30-mrad crossing angle together with crab-waist sextupoles. Regardless of the collision scheme, the large number of bunches at the *Z*, *W* and *H* energies requires two separate rings, and the short beam lifetime, $\tau_{beam}$, limited by radiative Bhabha scattering at the high luminosity, calls for quasi-continuous injection (top-up).

Table 2: Baseline Parameters of *FCC-ee* [23] Compared with *LEP-2. For Z* Running an Alternative Scenario Based on Crab Waist Collisions is also Indicated

| parameter | LEP-2 | FCC-ee | | | | |
|---|---|---|---|---|---|---|
| | | Z | Z(c.w.) | W | H | t |
| $E_{beam}$ [GeV] | 104 | 45 | 45 | 80 | 120 | 175 |
| circum-ference [km] | 26.7 | 100 | 100 | 100 | 100 | 100 |
| current [mA] | 3.0 | 1450 | 1431 | 152 | 30 | 6.6 |
| $P_{SR,tot}$ [MW] | 22 | 100 | 100 | 100 | 100 | 100 |
| # bunches | 4 | 16700 | 29791 | 4490 | 1360 | 98 |
| $N_b$ [$10^{11}$] | 4.2 | 1.8 | 1.0 | 0.7 | 0.46 | 1.4 |
| $\varepsilon_x$ [nm] | 22 | 29 | 0.14 | 3.3 | 0.94 | 2 |
| $\varepsilon_y$ [pm] | 250 | 60 | 1 | 1 | 2 | 2 |
| $\beta^*_x$ [m] | 1.2 | 0.5 | 0.5 | 0.5 | 0.5 | 1.0 |
| $\beta^*_y$ [mm] | 50 | 1 | 1 | 1 | 1 | 1 |
| $\sigma^*_y$ [nm] | 3500 | 250 | 32 | 84 | 44 | 45 |
| $\sigma_{z,SR}$ mm] | 11.5 | 1.64 | 2.7 | 1.01 | 0.81 | 1.16 |
| $\sigma_{z,tot}$ [mm] (w BS) | 11.5 | 2.56 | 5.9 | 1.49 | 1.17 | 1.49 |
| hourglass factor $F_{hg}$ | 0.99 | 0.64 | 0.94 | 0.79 | 0.80 | 0.73 |
| beam-b. p. $\xi_y$ /IP | 0.06 | 0.03 | 0.175 | 0.06 | 0.093 | 0.092 |
| *L*/IP [$10^{34}$ $cm^{-2}s^{-1}$] | 0.01 | 28 | 212 | 12 | 6 | 1.7 |
| $\tau_{beam}$ [min] | 434 | 298 | 39 | 73 | 29 | 21 |

## DESIGN PROGRESS

For the layout of the FCC tunnel various shapes are considered within certain natural boundaries, as indicated in Figure 7. The geology in the Geneva basin is well suited to housing a circular machine. *FCC-ee* favours a planar design in order to allow for the smallest possible vertical emittance and to minimize depolarizing effects. The required compatibility with hadron collider imposes additional constraints [25], such as on the length of the various straights, the interaction-region (IR) geometry, length and shape of the dispersion suppressors, space needed for hadron collimation etc.

*FCC-ee* optics modules have been developed for arcs, dispersion suppressors, and various straight sections.



ISBN 978-3-95450-172-4

They can be assembled so as to adapt to the overall configuration, e.g. to a circular or racetrack shape of the tunnel. As an example, the arc-cell layout and optics for beam energies of 120 and 175 GeV is shown in Figures 8 and 9, respectively, with a FODO cell length of 50 m. Figure 10 illustrates an overall circular layout, with 12 straight sections. The dispersion function over 12 km of a circular 100 km ring is presented in Figure 11, with an arc length of 6.8 km and 1.5 km long straight sections. All of the straight sections accommodate superconducting radio-frequency (RF) systems. At the centre of each arc, a further straight may be inserted.

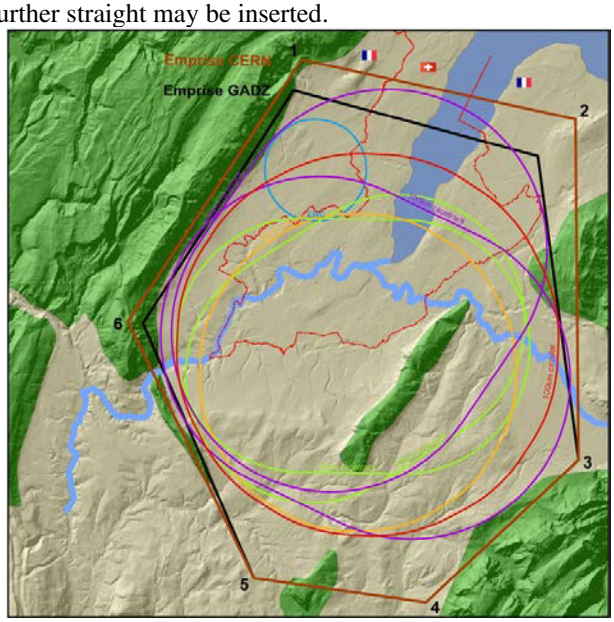


Figure 7: Schematic layouts and boundaries in the Geneva region [26].

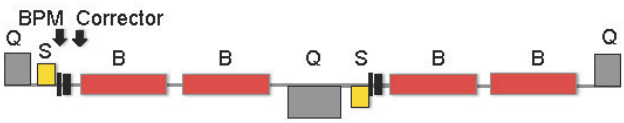


B = bending magnet, Q = quadrupole, S = sextupole

Figure 8: Arc-cell layout for 120 and 175 GeV [27].

At lower energies the arc cell length may need to be increased in order to maintain a reasonably large transverse emittance and acceptable beam-beam tune shifts. The phase advance per cell is another parameter affecting the emittance. Figure 12 displays possible changes in the optics configuration for operation at the *Z* pole. Increasing the cell length by a factor of six appears attractive. Likewise, for operation at the *W*-pair threshold an intermediate cell length of 100 m could be chosen. The corresponding ring optics, over 13 km, for either case are illustrated in Figure 13. The optics configurations are such that for all energies the horizontal equilibrium emittances due to synchrotron radiation are less than half the design value, leaving margin for the effect of errors and, possibly, high-intensity effects.

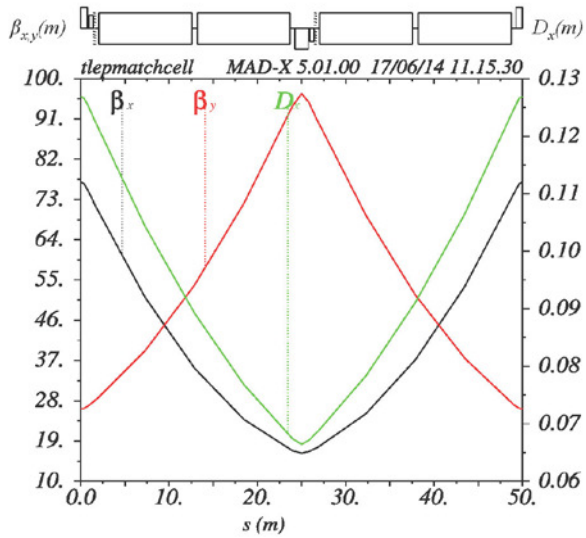


Figure 9: Arc-cell optics at 120 and 175 GeV [27].

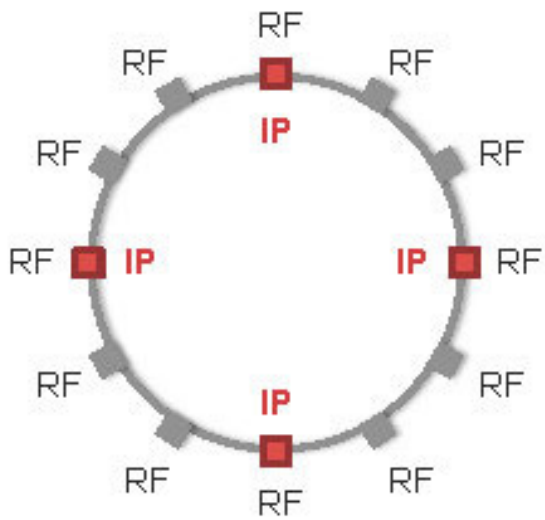


Figure 10: Circular layout with experimental insertions highlighted in red [27].

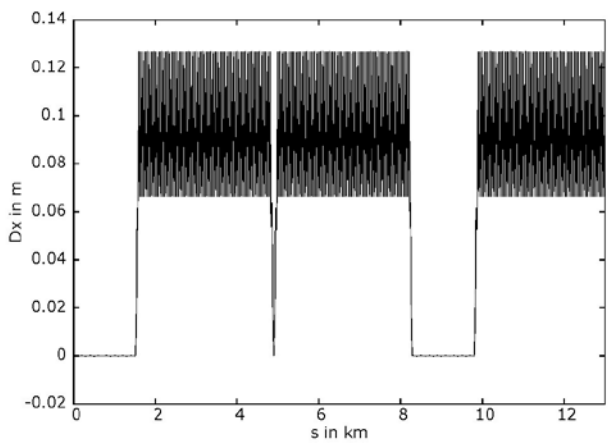


Figure 11: Dispersion function over 12 km including straight sections, for the circular layout of Figure 10 [28].



ISBN 978-3-95450-172-4

Figure 14 shows the SR energy loss per turn as a function of beam energy. For each collision energy this loss translates into a minimum RF voltage, determined by the overvoltage for a decent quantum lifetime and by the momentum acceptance needed with regard to beamstrahlung. At the t-tbar threshold this RF voltage amounts to about 11 GV, which is the maximum voltage considered for the *FCC-ee* design. Operation at 500 GeV c.m. would require a larger RF voltage of 35 GV.

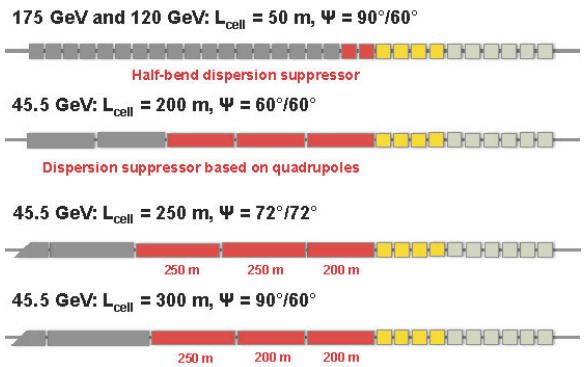


Figure 12: Possible optics configurations at 45.5 GeV compared with the high-energy case (on top). Dark grey color: arc cells; red: dispersion suppressor; yellow: straight matching sections (with RF); light grey: straight sections (with RF) [27].

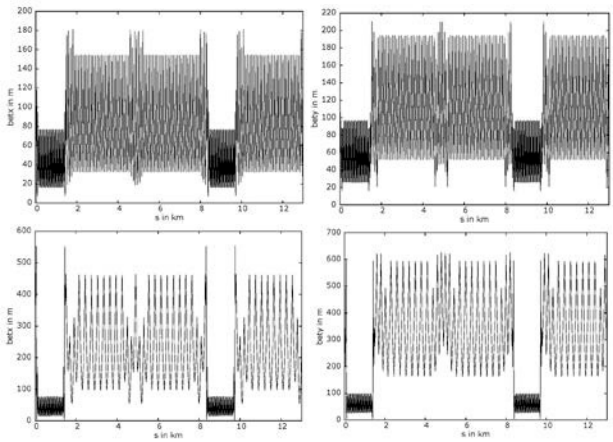

Figure 13: Optics (left: $\beta_x$, right: $\beta_y$) with 100 (top) and 300-m (bottom) arc cell length for operation at the *W*-pair threshold (80 GeV) and *Z* pole (45.5 GeV energy) [27].

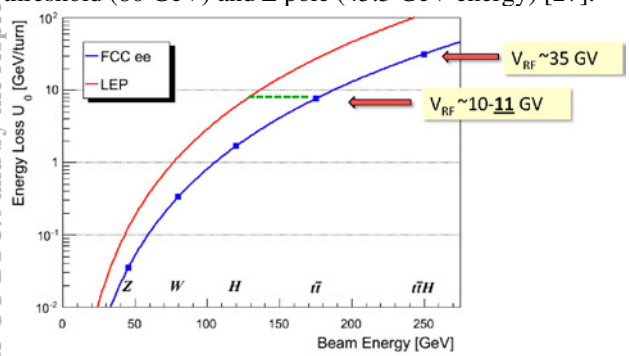


Figure 14: Energy loss per turn as a function of beam energy for *LEP* and for *FCC-ee*, translating into a minimum RF voltage required [29].

The RF system requirements are characterized by two regimes, namely operation at high gradient for *H* and *t* with up to ~11 GV total RF voltage, and high beam loading with currents of ~1.5 A at the *Z* pole. The RF system must be distributed over the ring in order to minimize energy excursions. At 175 GeV beam energy, the total energy loss amounts to about 4.5% per turn and optics errors driven by energy offsets may have a significant effect on the energy acceptance. The *FCC-ee* design aims at SC RF cavities with cw gradients of ~20 MV/m, and an RF frequency of 800 MHz (current baseline). The "nano-beam / crab waist" scheme [24] favors lower frequency, e.g. 400 MHz. The conversion efficiency of wall plug to RF power is critical. R&D is needed to push this efficiency far above 50% (a value achieved at LEP-2).

Concerning the synchrotron radiation it is noteworthy that SR heat per meter at the *FCC-ee* is lower than for many operating rings. For example, the *FCC-ee* SR heat load per meter is more than 10 times lower than for PEP-II or SPEAR (albeit with higher photon energies) [30]. The hard SR spectrum with a critical energy around 1 MeV calls for an efficient absorber and shielding system. A preliminary design is shown in Figure 15, together with results of pertinent FLUKA simulations in Figure 16.

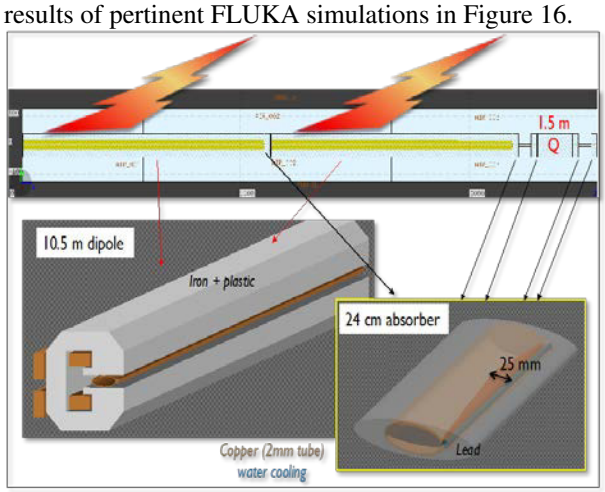


Figure 15: FLUKA geometry layout for half a FODO cell, showing dipole details with a preliminary absorber design including a 5-cm external *Pb* shield [31].

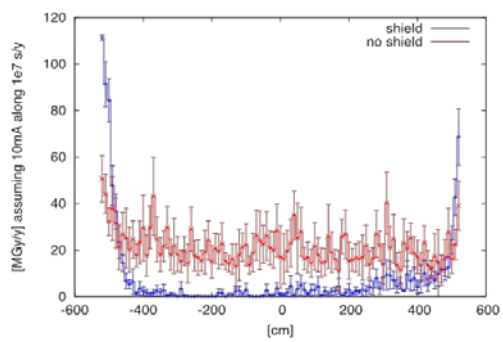


Figure 16: Simulated longitudinal peak-dose profile without (red) and with absorbers (blue) after operating with 10 mA beam current at 175 GeV over a time of $10^7$ s (116 days, or one "Snowmass year") [31].



ISBN 978-3-95450-172-4

The design luminosities are achieved with $\beta_y^* = 1$ mm, a value so small that it requires a local chromaticity correction. The corresponding IR design is inspired by linear collider final-focus systems. Unlike for the latter, here the beam does not pass the IR only once, and, therefore, the accumulated effect of optical aberrations, including in the non-IP betatron phase, become important. In addition, the local correction implies bending magnets close to the IP, with the associated SR fans. The distance between the IP and the front-face of the first quadrupole, $l^*$, is currently set to $l^* \geq 2$ m (for SuperKEKB it is ~1 m), with implications for the detector acceptance and luminosity measurement. The combination of the small $\beta_y^*$ and the required large energy acceptance is a challenge. Two preliminary IR designs [32,33] are shown in Figures 17 and 18, their dynamic apertures in Figure 19.

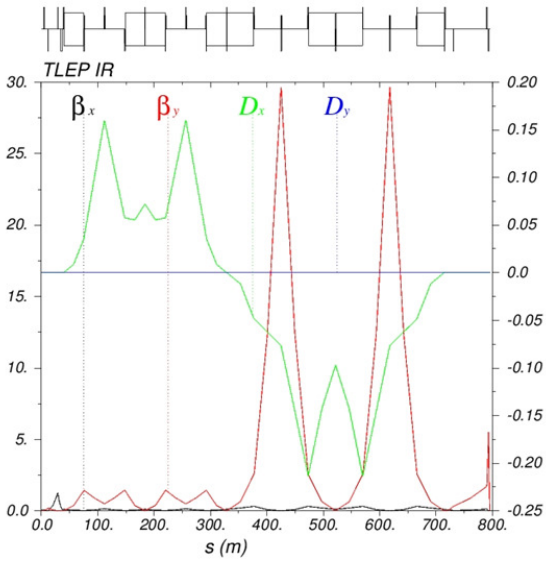


Figure 17: First modular IR design with dedicated chromatic correction sections [32].

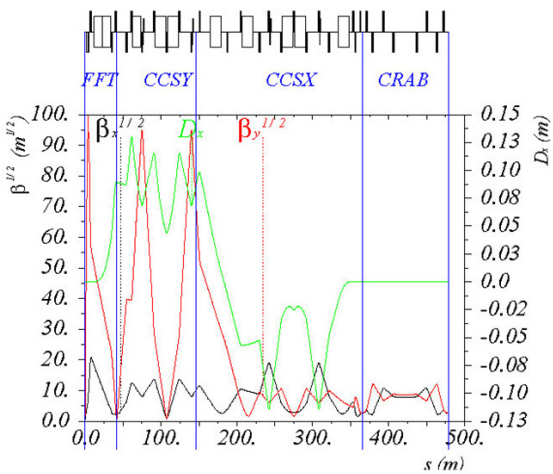


Figure 18: Second modular IR design also including a crab-waist [33].

The challenge for the machine-detector interface is to maximize performance (integrated luminosity) for the experiments with tolerable experimental conditions. This includes minimizing synchrotron radiation in the IR region, by choosing bends as weak as possible and as far as possible away from IP. The final quadrupoles, on the other hand, have to be strong and close to the IP. Their effect is mitigated by minimizing the beam offset from the quadrupole axis, and by controlling vertical halo/tails. The LEP IR, illustrated in Figure 20, is a good example of an optimized system, with about 100 collimators reducing the machine-induced background, and no direct or singly reflected photons reaching the experiment. A Monte-Carlo model for the synchrotron radiation was integrated into Geant4 [34]. Presently other generic tools are being developed for FCC IR studies [35].

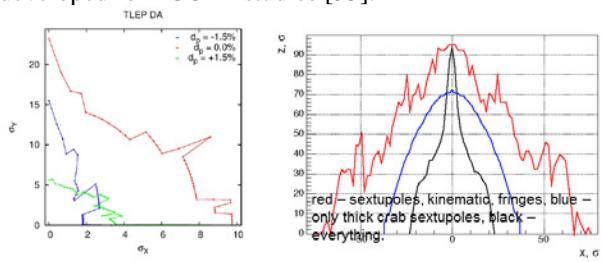


Figure 19: Dynamic aperture at different momentum offsets δ, simulated for the IR optics of Figure 17 (left) and on-momentum dynamic aperture including setupoles, kinematic terms, fringes, and crab sextupoles for the IR optics of Figure 18 (right) [32,33].

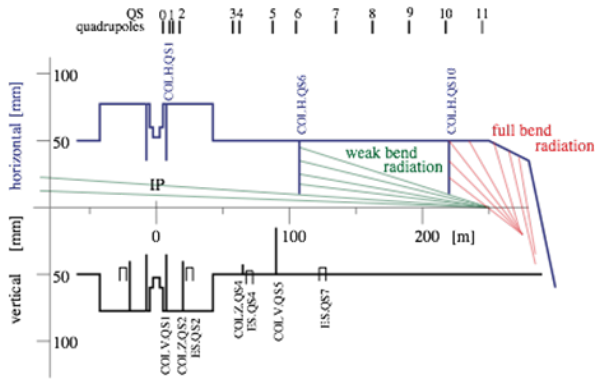


Figure 20: LEP IR design with weak bend and multiple masks [36].

The luminosity of the *FCC-ee* collider can be written as

$$L = \frac{f_{rev} n_b {N_b}^2}{4\pi\sigma_x\sigma_y} HF,$$

where $f_{rev}$ denotes the revolution frequency, $n_b$ the number of bunches per beam, $N_b$ the bunch population, $\sigma_x$ the horizontal rms IP spot size, $\sigma_y$ the vertical rms IP spot size, $H$ the luminosity reduction due to the hourglass effect, and $F$ the additional luminosity loss factor due to a crossing angle. The product $en_bN_bf_{rev}$ (with e the elementary charge) is equal to the beam current, which at constant SR power decreases as $1/E^4$. Another constraint comes from the nonlinear beam-beam interaction, the strength of which is characterized by the beam-beam parameter ξ. The vertical beam-beam parameter, roughly equal to the maximum beam-beam tune shift (per IP), is

$$\xi_y = \frac{{\beta_y}^* r_e N_b}{2\pi\gamma\sigma_y(\sigma_x + \sigma_y)} \sim \frac{{\beta_y}^* N_b}{E\sigma_y\sigma_x}$$

ISBN 978-3-95450-172-4

The beam-beam parameter is a measure of the tune spread in the beam. According to the experience at all past circular colliders the beam-beam parameter is limited to some maximum value, a fraction of an integer. Using the definition of $\xi_y$, introducing the limit from the SR power, and neglecting hourglass and crossing-angle effects, the luminosity scaling becomes

$$L \propto \frac{P_{SR}\xi_y}{E^3\beta_y^*}$$

Energy-dependent beam-beam parameter limits for 4 IPs can be scaled empirically from LEP data (Figure 21), using the inferred relation [37]

$$\xi_{y,max} \propto \frac{1}{\tau^{0.4}} \propto E^{1.2},$$

where τ refers to the radiation damping time. This scaling also is in reasonable agreement with beam-beam simulations for *FCC-ee* [33,38-40].

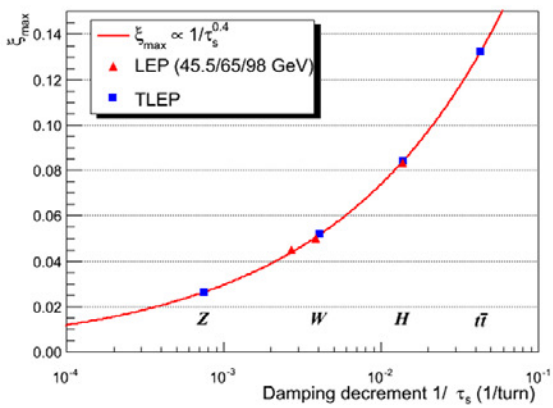


Figure 21: Maximum beam-beam tune shift as a function of damping decrement. Data from *LEP* (red triangles) are extrapolated to the *FCC-ee* (blue squares) according to a physical model [37].

Including the variation of the maximum beam-beam parameter with energy, we finally obtain

$$L \propto \frac{P_{SR}}{E^{1.8}\beta_y^*},$$

i.e. the loss in luminosity with energy is much less dramatic than a naïve look at the SR power might tend to suggest. In addition, the beam-beam limit may be raised significantly with crab-waist collision schemes [24,39,40]. The above scaling is valid as long as the strength of the interaction is dominated by the classical beam-beam interaction. At highest energies a different mechanism may constrain the beam parameters, namely beamstrahlung, i.e. the synchrotron radiation emitted during the collision in the field of the opposing bunch. The hard photon emission at the IPs can become a lifetime or performance limit for large bunch populations ($N_b$), small horizontal beam size ($\sigma_x$) and for short bunches ($\sigma_z$). The lifetime due to beamstrahlung depends on the bending radius ρ experienced during the collision,

$$\frac{1}{\rho} \approx \frac{N_b}{\gamma\sigma_x\sigma_z},$$

and on the relative energy acceptance η as [ 41,24]

$$\tau_{bs} \propto \frac{\rho^{3/2}\sqrt{\eta}}{\sigma_z\gamma^2}\exp(A\eta\rho/\gamma^2),$$

where $A$ is a constant.

To ensure an acceptable lifetime, ρ×η must be sufficiently large, which can be achieved by operating with flat beams (large $\sigma_x$), with long bunches, and with a large momentum acceptance of the lattice (about 1.5 – 2% is required; for comparison, LEP had an acceptance of less than 1%, and SuperKEKB is designed for η~1.5%).

The transition from the beam-beam dominated regime to the beamstrahlung-dominated regime depends on the momentum acceptance, as is illustrated in Figure 22, considering a vertical emittance of 2 pm and $\beta_y^*$=1 mm. Figure 23 highlights that the beamstrahlung lifetime is a steep function of the energy acceptance.

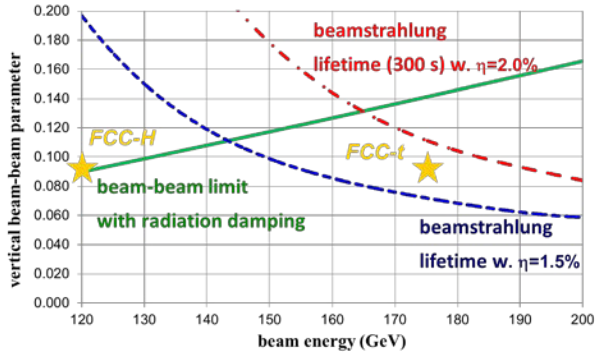


Figure 22: Limits due to classical beam-beam effect and due to beamstrahlung, with two different values for the energy acceptance, as a function of beam energy [42].

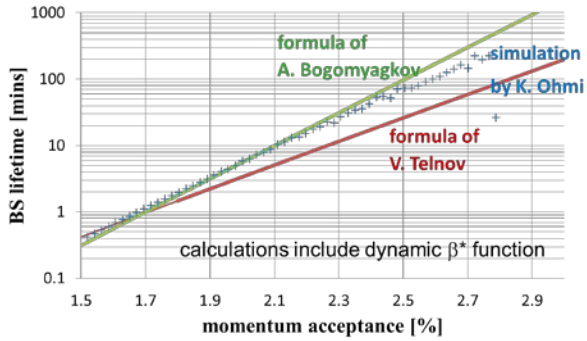


Figure 23: Beamstrahlung lifetime for *FCC-ee* at 350 GeV c.m. as a function of momentum acceptance η, comparing analytical expressions by V. Telnov [41] (red) and A. Bogomyagkov [24] (green) with simulation results from K. Ohmi (blue) [43]. The analytical calculations include the dynamic beta functions matching the simulations.

The $\beta_y^*$ evolution in $e^+e^-$ colliders since 1980 is illustrated in Figure 24, which also visualizes how SuperKEKB will pave the way for *FCC-ee*. Figure 25 displays the total *FCC-ee* luminosity (sum over 4 IPs) as a function of c.m. energy. Both the baseline [23] and the improved parameters [24] are shown. The expected high-luminosity values were confirmed in strong-strong and weak-strong beam-beam simulations including the effect of beamstrahlung [39]. For example, in Figure 26, the



ISBN 978-3-95450-172-4

luminosity for *FCC-ee* in Higgs production mode (240 GeV c.m.), simulated by the BBSS code, is $L \approx 7.5 \times 10^{34}$ $cm^{-2}s^{-1}$ per IP, or 25% above the design value. Also, according to BBWS, the luminosity at the Z pole (91 GeV c.m) is indeed much enhanced through the crab-waist scheme, by about a factor of 5, albeit for this case the simulated luminosity of $L \approx 1.5 \times 10^{36}$ $cm^{-2}s^{-1}$/IP still falls slightly short of the expectation [24].

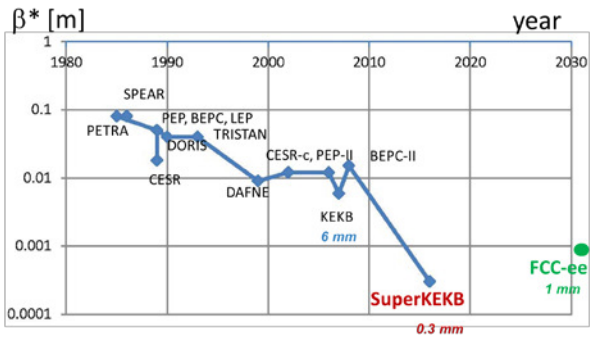


Figure 24: $\beta_y^*$ evolution over 5 decades.

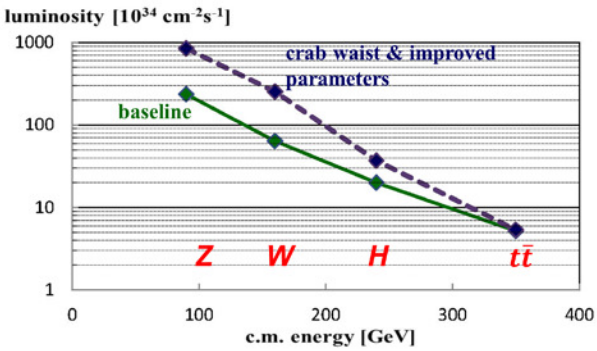


Figure 25: *FCC-ee* total luminosity (4 IPs) vs. c.m. energy – baseline parameters [23] (green solid curve) and crab-waist collision scheme [24] (blue dashed curve).

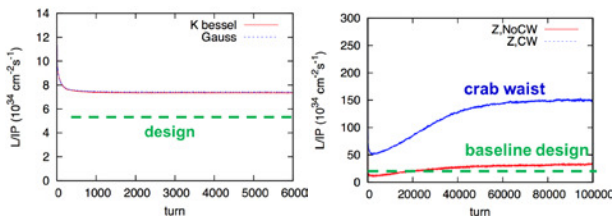


Figure 26: *FCC-ee* beam-beam performance validation including beamstrahlung [39] - BBSS strong-strong simulation at 240 GeV c.m. (left), and BBWS weak-strong simulation at 91 GeV with and without crab waist (bottom). Baseline design values are indicated by the dashed green lines.

SuperKEKB (Figure 27), with beam commissioning to start in 2015, will demonstrate several of the *FCC-ee* key concepts, such as top-up injection at high current; an extremely low $\beta_y^*$ of 300 μm (*FCC-ee*: 1 mm); an extremely low beam lifetime of 5 min (*FCC-ee*: ≥20 min); a small emittance coupling of $\varepsilon_y/\varepsilon_x$~0.25% (comparable to *FCC-ee*); a significant off momentum acceptance of ±1.5% (similar to the acceptance required for *FCC-ee*); a sufficiently high $e^+$ production rate of $2.5 \times 10^{12}$/s (*FCC-ee* needs less than $1.5 \times 10^{12}$/s for top-up operation, at all energies). SuperKEKB goes beyond the *FCC-ee* requirements for many of these parameters.

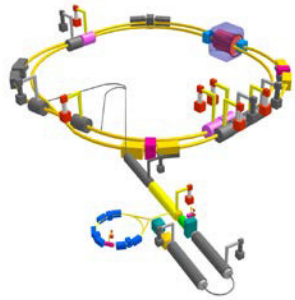

Figure 27: Schematic of SuperKEKB [44].

Beside the collider ring(s), a booster of the same size (same tunnel) must provide beams for top-up injection (Figure 28). The booster requires an RF system of the same size as the collider, but at low power (~ MW). The top up frequency is expected to be around ~0.1 Hz, and the booster injection energy 10-20 GeV. The booster ring should bypass the particle-physics experiments. Upstream of the booster a pre-injector complex for $e^+$ and $e^-$ beams of 10-20 GeV is required. The SuperKEKB injector appears to be almost suitable.

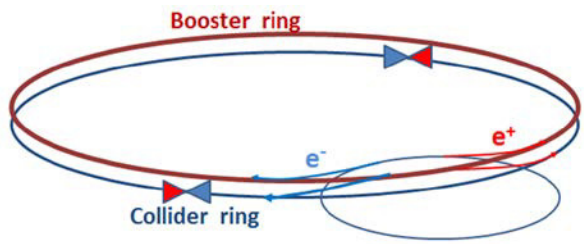


Figure 28: Schematic of booster and collider rings for fast top-up injection [4].

Polarized beams can be of interest for two reasons: (1) they allow for an accurate energy calibration using resonant depolarization, which will be a crucial advantage for measurements of $M_Z$, $\Gamma_Z$, and $M_W$, with expected precisions of order 0.1 MeV; and (2) they are necessary for any physics programme with longitudinally polarized beams, which would, however, also require that the transverse polarization be rotated into the longitudinal plane at the IP using spin rotators, e.g. as at HERA. Electron integer spin resonances are spaced by 440 MeV.

At LEP the polarization completely disappeared when the energy spread exceeded ~60 MeV (Figure 29). Noticing that the SR energy spread is proportional to $E^2/\sqrt{\varrho}$ (with $\varrho$ the bending radius), for *FCC-ee* a non-zero polarization is expected up to the *WW* threshold. However, for the same reason (large $\rho$) at the same beam energy the transverse polarization build-up (due to the Sokolov-Ternov effect) is about 40 times slower than at LEP, e.g. 190 h at the *Z* pole (assuming a $\varrho$ of 11 km); see Figure 30.



ISBN 978-3-95450-172-4

Adding wigglers may lower the polarization time $\tau_p$ to ~12 h, limited by the condition $\sigma_E \leq 60$ MeV and the SR power. Dedicated polarization wigglers were proposed and built for LEP [46]. In case of *FCC-ee*, due to the large SR power loss, such wigglers may only be used to pre-polarize some bunches (before the main injection). This will be sufficient for the purpose of energy calibration.

An alternative approach is to generate, accelerate and inject polarized bunches into the collider (requiring snakes in the booster ring, and a self-polarizing positron damping ring) with spins oriented in the horizontal plane [47]. Then the free spin precision frequency could be measured through laser Compton back scattering on the first ~10,000 turns after each injection, with subsequent Fourier analysis, and, thereby, the beam energy be determined. The feasibility of this scheme still needs to be demonstrated.

On the other hand, physics with longitudinally polarized electrons and positrons would require polarization levels of ≥ 40% for both beams, along with excellent resonance compensation. Such physics would also need spin rotators or snakes, and most likely only be possible at (much) lower intensity and luminosity.

Preliminary *FCC-ee* spin tracking simulations are being performed with the code SITROS [48].

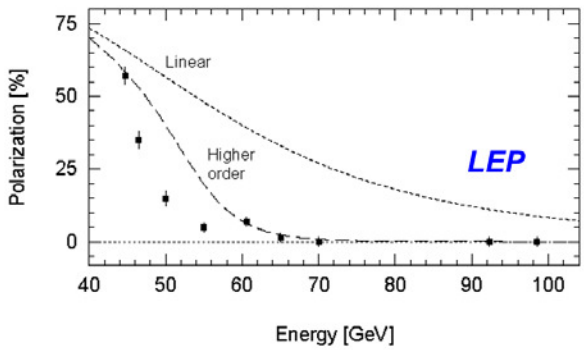


Figure 29: LEP polarization as a function of beam energy. Data points show the measured values. Solid and dashed lines correspond to model predictions [45].

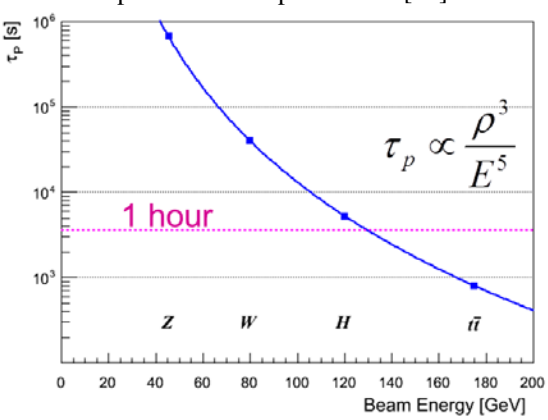


Figure 30: *FCC-ee* natural polarization time versus beam energy [29].

## CONCLUSIONS

Colliders and collider designs can look back at a long and successful history, with SuperKEKB set to be the next step. The *FCC* study plan matches the time scale of high-energy frontier physics sketched in Figure 31. After the kickoff meeting in February 2014, detailed work on the *FCC-ee* design has started. The wide scope of the *FCC* study leaves room for many interesting investigations. At present, the study emphasis is shifting towards parameter optimization and the choice between alternatives. Various technologies need dedicated design efforts, such as magnets, SRF, collimators, vacuum system, etc. The *FCC* study includes colleagues from around the world. The first annual FCC week will be organized in Washington DC, from 23 to 27 March 2015 [49].

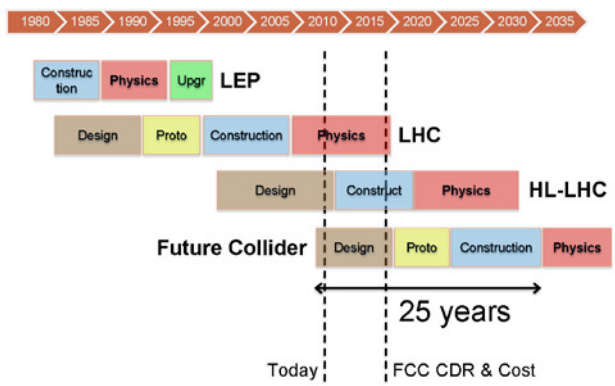


Figure 31: Time line of high-energy physics energy-frontier projects since 1980 with an extrapolation to the Future (Circular?) Collider.

## ACKNOWLEDGEMENTS

Our warm thanks go to Weiren Chou for organizing the HF2014 workshop, for inviting a presentation, and for diligently making sure, together with Ning Zhao, that this paper was written and submitted.

This work was partly funded by the European Commission under the FP7 Research Infrastructures project EuCARD-2, grant agreement no.312453.

## REFERENCES

[1] R. Assmann, "LEP Luminosity Revisited: Design and Reality," Proc. APAC'01 Beijing (2001).

[2] R. Assmann, P. Raimondi, G. Roy, J. Wenninger, "Emittance Optimization with Dispersion Free Steering at LEP," Phys.Rev.ST – Accel. Beams 3, 121001 (2000).

[3] B. Richter, "Very High Energy Electron-Positron Colliding Beams for the Study of Weak Interactions," NIM 136 (1976) 47.

[4] A. Blondel, F. Zimmermann, "A High Luminosity e+e- Collider in the LHC Tunnel to study the Higgs Boson," arXiv:1112.2518v1, 24.12.2011.



ISBN 978-3-95450-172-4

[5] K. Oide, "SuperTRISTAN - A Possibility of Ring Collider for Higgs Factory," KEK Seminar, 13 February 2012.
[6] A. Blondel et al, "LEP3: A High Luminosity e+e- Collider to study the Higgs Boson," arXiv: 1208.0504, submitted to ESPG Krakow.
[7] P. Azzi et al, "Prospective Studies for LEP3 with the CMS Detector," arXiv:1208.1662 (2012), submitted to ESPG Krakow.
[8] P. Janot, "A Circular e+e- Collider to study H(125)," PH Seminar, CERN, 30 October 2012 ICFA Higgs Factory Workshop: Linear vs Circular, FNAL, 14-16 Nov. '12.
[9] A. Blondel, F. Zimmermann, "Future Possibilities for Precise Studies of the X (125) Higgs candidate," CERN Colloquium, 22 Nov. 2012.
[10] M. Koratzinos et al., TLEP: A High-Performance Circular e+e− Collider to Study the Higgs Boson arXiv:1305.6498 [physics.acc-ph] (2013).
[11] M. Bicer et al., "First Look at the Physics Case of TLEP," JHEP 1401 (2014) 164.
[12] 1st EuCARD LEP3 workshop, CERN, 18 June 2012.
[13] 2nd EuCARD LEP3 WS, CERN, 23 October 2012.
[14] ICFA Workshop on Accelerators for a Higgs Factory: Linear vs. Circular ("HF2012"), FNAL, 14-16 November 2012.
[15] 3rd TLEP3 Day, CERN, 10 January 2013.
[16] 4th TLEP workshop, CERN, 4-5 April 2013.
[17] 5th TLEP workshop, 25-26 July 2013, Fermilab.
[18] 6th TLEP workshop, CERN, 16-18 October 2013, CERN.
[19] "The European Strategy for Particle Physics Update 2013," CERN-Council-S/0106, CERN ESC-E-106 http://cds.cern.ch/record/1567258/files/esc-e-106.pdf
[20] FCC site: http://cern.ch/fcc
[21] Kickoff site: http://indico.cern.ch/e/fcc-kickoff
[22] D. Schulte et al, "Specification: Future Circular Collider Study - Hadron Collider Parameters," EDMS No. 1342402, FCC-ACC-SPC-0001 v.1.0.
[23] J. Wenninger et al., "Specification: Future Circular Collider Study – Lepton Collider Parameters," EDMS No. 1346081, FCC-ACC-SPC-0003 v.2.0.
[24] A. Bogomyagkov, E. Levichev, and D. Shatilov, "Beam-beam effects investigation and parameters optimization for a circular e + e − collider at very high energies," Phys. Rev. ST Accel. Beams 17, 041004 (2014).
[25] B. Haerer, et al., "Constraints on the FCC-ee Lattice from the Compatibility with the FCC Hadron Collider," HF2014 Beijing, 9-12 October 2014.
[26] J. Osborne, "LHeC Civil Engineering," LHeC Advisory Committee Meeting, 26 June 2014.
[27] B. Haerer, B. Holzer, "Challenges and Status of the FCC-ee Lattice Design," HF2014 Beijing, 9-12 October 2014.
[28] B. Haerer, " FCC-ee lattices for Different Energies," FCC-ee Vidyo meeting 25 August 2014.
[29] J. Wenninger, "Lepton Collider Overview," FCC Kickoff, Geneva 13 February 2014.
[30] N. Kurita, "Synchrotron Radiation – Vacuum," HF2014 [13].
[31] L. Lari, F. Cerutti, A. Ferrari, A. Mereghetti, "Beam-machine Interaction at TLEP: First Evaluation and Mitigation of the Synchrotron Radiation Impact," IPAC'14 Dresden.
[32] H. Garcia et al., "FCC-ee Final Focus with Chromaticity Correction," IPAC'14 Dresden.
[33] A.V. Bogomyagkov, E.B. Levichev, P.A. Piminov "Interaction Region Lattice for FCC-ee (TLEP)," IPAC'14 Dresden; and "Update on IR Design," FCC-ee Vidyo meeting 23 June 2014.
[34] H. Burkhardt, "Monte Carlo Generation of the Energy Spectrum of Synchrotron Radiation CERN-OPEN-2007-018.
[35] M. Boscolo, H. Burkhardt, "Lost particles in the IR and Issues for Beam Induced Backgrounds in Higgs Factories," HF2014 Beijing, 9-12 October 2014.
[36] G. von Holtey et al., "Study of Beam-Induced Particle Backgrounds at the LEP Detectors," Nucl. Instrum. Methods Phys. Res., A 403 (1998) 205-246.
[37] R. Assmann, K. Cornelis, "The Beam-Beam Interaction in the Presence of Strong Radiation Damping," EPAC'2000 Vienna.
[38] S. White, and N. Mounet, " Beam-Beam Studies for TLEP (and Update on TMCI)," 6th TLEP WS [17].
[39] K. Ohmi, F. Zimmermann, "FCC-ee/CepC Beam-Beam Simulations with Beamstrahlung," IPAC'14.
[40] D. Shatilov, Beam-Beam Effects in High-energy Colliders: Crab Waist vs. Head-On," HF2014 Beijing, 9-12 October 2014.
[41] V. Telnov, "Restriction on the Energy and Luminosity of e+e− Storage Rings due to Beamstrahlung ," Phys.Rev.Lett. 110 (2013) 114801.
[42] M. Koratzinos, "Choice of Circumference, Minimum & Maximum Energy, Number of Collision Points, and Target Luminosity," HF2014 Beijing, 9-12 October 2014.
[43] K. Ohmi, "Beamstrahlung and Energy Acceptance," HF2014 Beijing, 9-12 October 2014.
[44] Y. Ohnishi et al., "Accelerator Design at SuperKEKB," Prog. Theor. Exp. Phys. 2013, 03A011.
[45] R. Assmann, "The Regimes of Polarization in a High Energy $e^+e^-$ Storage Ring," PAC'99 New York.
[46] A. Blondel and J.M. Jowett, "Dedicated Wigglers for Polarization," LEP Note 606 (1988).
[47] I. Koop, "Polarization Issues and Schemes for Energy Calibration," HF2014 Beijing, 9-12 October 2014.
[48] E. Gianfelice, "$e^{\pm}$ Collider – Polarization Considerations," HF2014 Beijing, 9-12 October 2014.
[49] FCC Week 2015, site http://cern.ch/fccw2015

ISBN 978-3-95450-172-4

# OVERVIEW OF THE CEPC ACCELERATOR

Q. Qin, S. Bai, J. Cheng, X.H. Cui, L. Dong, H.Y. Dong, Y.Y. Guo, J. Gao, H.P. Geng, D.P. Jin, W. Kang, S.P. Li, X.P. Li, G.P. Lin, Z.C. Liu, X.C. Lou, Z.J. Ma, G.X. Pei, H.M. Qu, Y. Sun, G. Xu, J.H. Yue, T. Yue, D. Wang, J.L. Wang, N. Wang, Y.F. Wang, Y.W. Wang, M. Xiao, J.Y. Zhai, C. Zhang, Y. Zhang, Z.S. Zhou, IHEP, 19B Yuquan Road, Shijingshan District, Beijing 100049, China
W. Chou, FNAL, Batavia, IL 60510, USA

*Abstract*

A circular electron positron collider (CEPC) was proposed in IHEP after the Higgs boson was discovered at LHC two years ago. In the meantime, some possible ring-based Higgs factories, were also proposed in different labs around the world. In these two years, studies focusing on the preliminary design of the ring, and the considerations on injectors, were carried out in IHEP. Some results on beam physics and hardware will be given in this paper.

## INTRODUCTION

Two years ago, CERN declared the discovery of the 126 GeV/$c^2$ Higgs boson, which is much less than expected before, causing the big possibility to build ring-based Higgs factory for further fine measurement of the new particle. Although muon collider, γ-γ collider, and linear collider were proposed to be the candidates of Higgs factory more than 10 years ago, some ring-based Higgs factories, such as LEP3 [1], TLEP [2], Super-Tristan [3], FNAL site-filter [4], etc., were suggested in different labs due to the relatively mature accelerator technology of circular machine. IHEP also proposed a circular $e^+e^-$ collider (CEPC) as a Higgs factory in September 2012 [5], which can be converted to a super proton-proton collider (SppC) in the future as a machine for new physics and discovery, shown as Figure 1 [6].

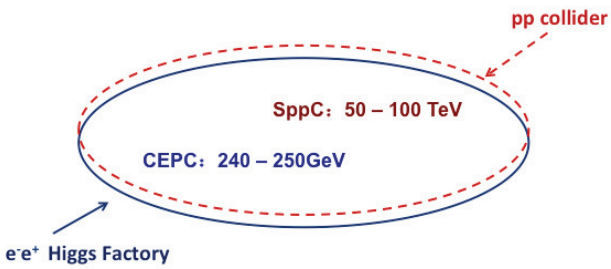


Figure 1: Schematic graph of the CEPC + SppC.

In the CEPC, the electron beam energy can be 120-125 GeV, and in the SppC, the proton beam energy can reach 25-50 TeV. The CEPC then can be thought as a natural extension of the BEPC, Beijing electron positron collider, which was built in 1980's and upgraded as BEPCII 10 years ago. From the BEPC and BEPCII, experiences on lepton machine's design, construction and operation are gradually accumulated. Accelerator technologies are also developed in IHEP, and other Chinese labs as well. Thus the CEPC becomes a very important direction in the field of high energy physics in China, and is the one we can do as a future high energy facility. In recent two years, we did some studies on the CEPC machine design, aiming on the pre-CDR to be finished by the end of 2014.

The current IHEP site is too small to accommodate the future CEPC and its auxiliary facilities. A candidate site for such a big machine is Funing of Qinhuangdao, a coast city northeast of Beijing and 300 km in between, shown in Figure 2.

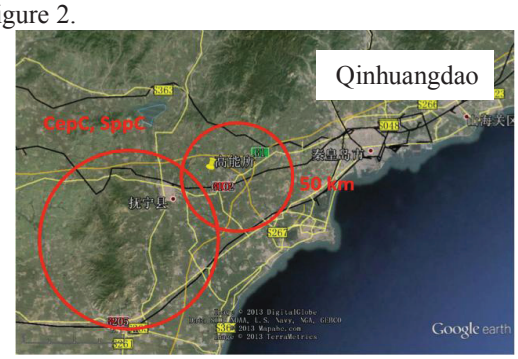


Figure 2: Possible location for future CEPC and SppC.

In this paper, the main studies on accelerator physics, such as main parameter determination, lattice design, final focus system, dynamic aperture simulation, beam-beam effect, injection chains, collective effects, etc., and some hardware system considerations of CEPC, are discussed. A preliminary overall time schedule will be given, and a summary of all studies is given at last.

## MAIN PARAMETERS AND LAYOUT

Since the energy loss due to synchrotron radiation is proportional to the fourth power of beam energy, a relatively low beam energy will save the RF power and make the ring more flexible. Beam energy of 120 GeV is thus chosen, because the cross-section of Higgs at that energy is similar as that of 125 GeV. The beam power compensated by the RF will be limited as 50 MW in a general design of such a big ring. Such a large amount synchrotron radiation also causes a strong beamstrahlung [7], which makes the bunch size at the interaction point (IP) diluted and the beam energy spread enlarged. Finally, it brings the beam lifetime to reduce dramatically, and the luminosity decrease as well. General speaking, if we keep the beam power unchanged, the bigger the ring, the more the beam current can be stored, and thus the higher the peak luminosity. Considering a possible p-p collider in the same tunnel of the CEPC in the future for much high energy of proton beams, at least 50 km is necessary for the circumference of the CEPC ring. As a Higgs factory, a peak luminosity of $1\times10^{34}cm^{-2}s^{-1}$ is the lower limit to fit the physics requirement of CEPC.



ISBN 978-3-95450-172-4

A linac is supposed to be the main injector of the CEPC. A booster is considered to be in the same tunnel of the main ring to save budget, and connect with transport lines to the ring and the linac, shown as Figure 3. For the time being, pretzel orbit scheme is applied in the main ring.

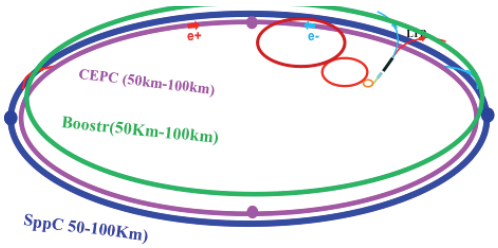


Figure 3: Accelerator chain of CEPC and future SppC.

In Figure 3, the SppC is also plotted as a future machine. The two small boosters inside the big rings are thought to be the boosters of SppC. So the design of the tunnel, the layout of the CEPC, and the interaction regions for all two machines, should be taken into account all together.

To design a high luminosity collider, the $\beta$ function at the IP in vertical, and beam-beam parameters are of an importance that we need to take them more seriously. Combining the existing machine experiences and the future one, we choose $\beta_y^*$=1.2mm, and vertical beam-beam parameter $\xi_y$ as large as 0.1. The accurate $\xi_y$ will be got from the beam-beam simulation. Accordingly, the horizontal $\beta$ at the IP is 0.8m. To get a high luminosity, the horizontal tune should be located very close to the half integer for each IP. So for 2 IPs, the horizontal tune of the whole ring is chosen to be just above the integer but very close to the integer.

Beamstrahlung effect should be carefully considered when other important parameters, such as beam current, emitance, momentum compaction, RF frequency, etc., are determined, as shown in [8] and [9].

Table 1 lists the main parameters of the CEPC ring, after the preliminary lattice design, which will be given in the following parts.

Table 1: Main Design Parameters of the CEPC Ring

| Para. | Unit | Value | Para. | Unit | Value |
|---|---|---|---|---|---|
| Energy | GeV | 120 | Circum. | km | 54.752 |
| $N_e$ | $10^{11}$ | 3.79 | $N_b$/beam | | 50 |
| Beam current | mA | 16.6 | SR power /beam | MW | 51.7 |
| $\varepsilon$ (x/y) | nm | 6.12/ 0.018 | Bending radius | km | 6.094 |
| $\beta_{IP}$ (x/y) | mm | 200/1 | $\sigma_x/\sigma_y$ (@IP) | μm | 70/0.15 |
| $\xi_{x,y}$ | | 0.118/ 0.083 | SR loss /turn | GeV | 3.11 |
| $\alpha_p$ | $10^{-4}$ | 0.336 | $\sigma_z$ | mm | 2.88 |
| $V_{rf}$ | GV | 6.87 | No. of IP | | 2 |
| $\nu_s$ | | 0.181 | $f_{rf}$ | GHz | 0.65 |
| $\delta_{SR}$ | | 0.0013 | Harm. No. | | 118712 |
| $\delta_{BS}$ | | 0.0008 | $\delta_{BS,\ tot}$ | | 0.00177 |
| $n_\gamma$ | | 0.23 | $\tau_{BS}$ | hr | 12.2 |
| $F_H$ | | 0.692 | $L$ /IP | /cm$^2$/s | $2.0\times10^{34}$ |

Since the beam loss due to synchrotron radiation is so large that RF cavities have to be distributed in nearly all the straight sections around the ring, compensating the energy saw-tooth effect. Figure 4 shows the IPs, straight sections, and RF sections all around the CEPC ring. In the figure, IP1 and IP3 are for the CEPC, while IP2 and IP4 are for the future SppC.

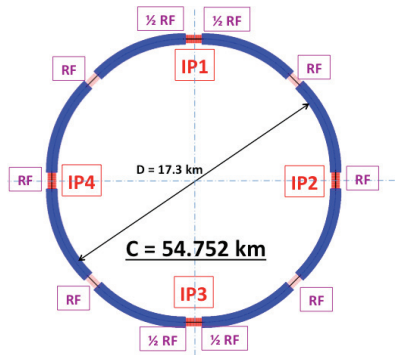


Figure 4: CEPC lattice and RF sections around the ring.

## ACCELERATOR PHYSICS

Accelerator physics design, consisting of lattice design, final focusing system (FFS), dynamic aperture study, beam-beam simulation, collective effect, etc., is the basic design of the whole machine.

### *Lattice Design*

The whole ring of the CEPC is divided into 8 arcs and 8 long straight sections (LSS). To be simple, a FODO cell is adopted in each arc, and the LSS as well. Both the horizontal and vertical phase advances in each cell are 60 degree. Figure 5 shows the Twiss functions in an arc.

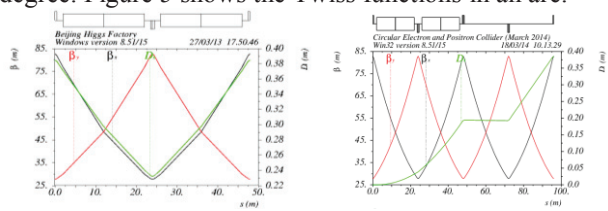

Figure 5: Twiss functions of a standard 60 degree cell (left) and a dispersion suppressor (right).

For more details of the lattice design, see [10].

### *FFS Design*

FFS plays an important rule in a collider, especially in the factory-like machine with very small vertical $\beta$ at the IP. It is the main source of the huge chromaticity, and need to be corrected by local chromaticity correction. The FFS is very critical to the machine-detector interface (MDI), and the background to the detector.

Some special lattice designs were developed for factory-like machine. Here, Cai's FFS design [11] was adopted. But different $L_0$ and other constraints made it to be optimized to fit the whole ring. In our design, $L^*$=1.5m. The total length of the FFS in one side of the IP is 341 m. Figure 6 shows the linear lattice of the FFS of CEPC.

ISBN 978-3-95450-172-4

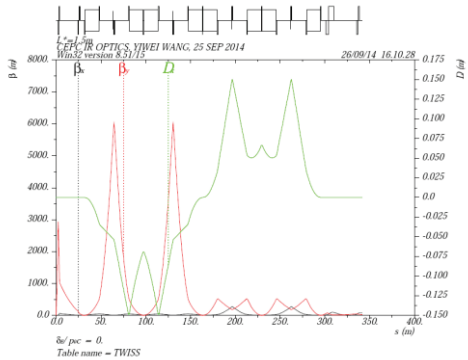

Figure 6: Twiss function of the FFS in the IR of CEPC.

How to design a good FFS is very critical to the dynamic aperture of the whole ring.

## *Dynamic Aperture*

In a big machine, such as the CEPC storage ring, both small $\beta$ function at IP and small emittance, will cause very large natural chromaticities in transverse directions. Furthermore, since the horizontal tune is very close to half integer for higher luminosity, natural chromaticity is very difficult to correct to be positive with a small anharmonicity. Strong non-linearity from FFS will cause the dynamic aperture to decrease dramatically. To correct the natural chromaticity globally, 2 sets of sextupole are used in the arcs. Other 4 sets of sextupole in the IR are devoted to correct chromaticity locally. MAD [12] and SAD [13] are used to do the dynamic aperture tracking. Figure 7 shows the tune and $\beta_{IP}$ variations as functions of particle momentum deviation. Figure 8 gives the results of dynamic aperture tracking for a damping time. More details of dynamic aperture study can be found in [14]. Magnetic error effect will be studied in the near future.

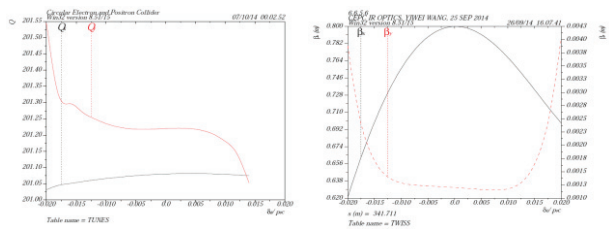

Figure 7: Tune and $\beta$ function at IP as functions of momentum deviation (left: tunes, right: $\beta$ function at IP).

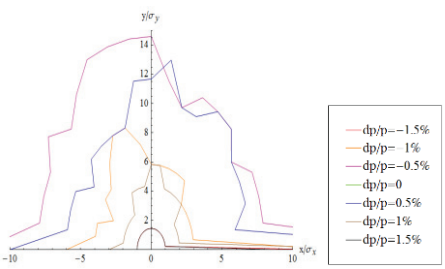

Figure 8: Dynamic aperture at different momentum deviations.

## *Beam-beam Simulation*

Beam-beam interaction is the most important issue to study in accelerator physics of a collider. Simulations with the codes of Y. Zhang in IHEP, and other codes of Ohmi and Shtatilov, give the results of tune scan with beamstrahlung effect, shown in Figure 9. The transverse tunes for better luminosity locate at [0.54, 0.61].

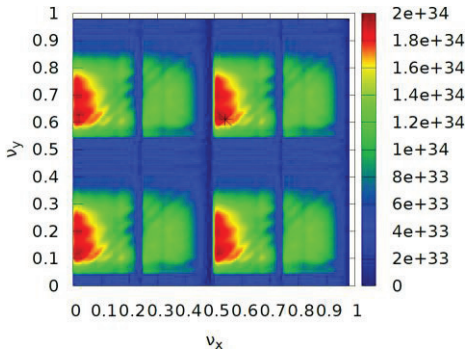

Figure 9: Beam-beam simulation for the tune scan.

Beam lifetime is also simulated with beamstrahlung effect. A quasi strong-strong model of beam-beam interaction gives the beam lifetime to be 1 to 3 hours with different simulation codes. More studies on beam-beam, such as luminosity as a function of bunch size, bunch current, and beam-beam parameters evaluated with equilibrium beam parameters, are also carried out [15].

## *Collective Effect*

Bunch lengthening is the main single bunch instability in lepton colliders. Multi-bunch instability also occurs when single bunch current or bunch spacing exceeds a threshold. These impedance-induced instabilities should be checked in the design. At current stage, since the hardware of the ring is far from fixed, especially the vacuum chamber and other vacuum parts, it is not easy to estimate the coupling impedance. Only the wake field and impedance of resistive wall and RF cavity around the ring are calculated, shown in Table 2.

Table 2: Impedance Estimation

| | $R$ (kΩ) | $L$(nH) | $k$(V/pC) | $\lvert Z_{//}/n\rvert_{eff}$(Ω) |
|---|---|---|---|---|
| Resistive wall (Al) | 9.5 | 124.4 | 301.3 | 0.0044 |
| RF cavity | 28.1 | - | 893.9 | - |
| Total | 37.6 | 124.4 | 1195.2 | 0.0044 |

The longitudinal wake is fitted with an analytical model of $W(s) = -Rc\lambda(s) - Lc^2\lambda'(s)$, where $R$ is the resistance of the ring, $L$ the inductance, $k$ the loss factor, and $|Z_{//}/n|_{eff}$ the low frequency effective impedance, to estimate the bunch lengthening.



ISBN 978-3-95450-172-4

If the bunch lengthening is estimated by scaling the SuperKEKB's geometric wake, the bunch length will increase at least ~10 %.

In addition, transverse mode coupling instability and coherent synchrotron radiation are not serious with the current impedance budget. Ion effects, such as electron cloud instability and ion trapping, are expected less affected due to the counter-rotating beam in the same ring. But the pretzel orbit the ions cannot be cleaned by positron beam, and will still have effect on electron beam.

The beam tilt due to transverse wake fields happens when beams pass through the vacuum chamber with a transverse offset, and the tail particles in a bunch will get a transverse kick, which causes a transverse displacement of the bunch tail at IP. It will reduce the luminosity in a big collider. In the CEPC case, closed orbit and additional pretzel orbit will make the beam tilt effect stronger.

More detailed calculations are given in [16].

### *Pretzel Scheme*

To save budget, one ring with pretzel orbits is adopted to the collision. Two sets of electrostatic separator are installed in each arc to separate two beams at the parasitic crossing points. Figure 10 shows the pretzel orbits produced with electrostatic separators and the phase advances between separators in the arcs. Some beam parameters are changed due to the pretzel orbits.

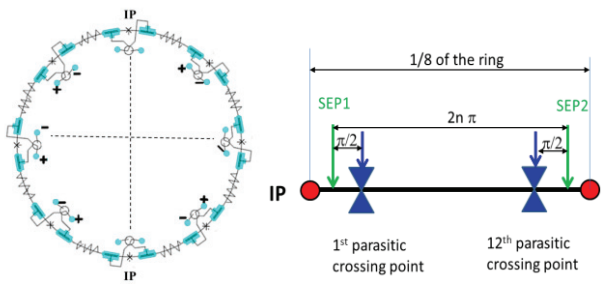


Figure 10: Pretzel orbit (left) and phase advance between two parasitic crossing points in one arc (right).

For the two IPs (IP2 and IP4 shown in Figure 4) of future possible SppC, we need to separate two beams to avoid collisions. More details on pretzel scheme study of CEPC are in [17].

Up to now, although we did some work on beam dynamics issues, we still have a lot of problems to be solved. Magnetic errors and their effects on beam, orbit correction, detailed impedance budget, synchrotron radiation heating, etc., need more studies.

## INJECTION

As shown in Figure 2, the whole injector of the CEPC contains a linac and a booster for the time being. In the current design, the booster is supposed to be in the same tunnel of the main ring.

### *Design of Booster*

The booster will be located in the same tunnel as the main ring of CEPC, and the future SppC ring as well. So one option to install the booster is up the main ring of CEPC, hanging on the roof of the tunnel. The layout and the circumference should be the same as those of the main ring of CEPC.

The booster is designed to supply beams to the collider with top-up injection rate of 0.1 Hz. The lattice functions of the cell and arc in the booster are shown in Figure 11. Table 3 gives the main parameters of the whole booster.

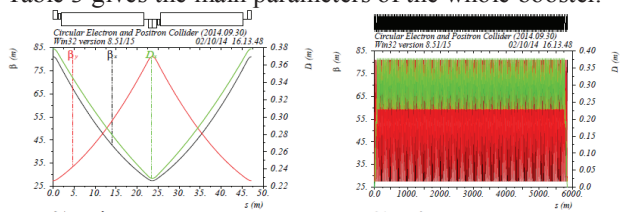

Figure 11: Twiss functions of a cell and an arc of the booster (left: FODO cell, right: arc).

Table 3: Main Parameters of the Booster

| | | |
|---|---|---|
| Circumference | km | 54.752 |
| Bending radius | km | 6.519 |
| Horizontal/vertical tunes | | 127.18/127.28 |
| No. of FODO structures | | 768 |
| FODO cell length | m | 71.665 |
| Phase advance/cell (H/V) | | 60°/60° |
| Maximum hori./verti. β | m | 123.84/122.97 |
| Maximum dispersion function | m | 0.879 |
| Length of bypass | m | 2×752.482 |
| Width of bypass | m | 13.0 |

The dipole field of the booster is 614 Gs at 120 GeV; but only 30.7 Gs at 6 GeV for injection. Such a low field makes the perturbation of the earth field be taken into account. One way to increase the bending field is to have another booster between the current booster and the linac. Test on the low field stability was done in IHEP with the BEPC dipole and a very small driven current to be given to the dipole. Detailed results of the test and other design studies can be found in [18].

Top-up injection is supposed to be used for the beam injection from the booster to the main ring. Injection calculations can be found in [19]. Simulation on injection is needed for further study.

### *Linac*

A normal conducting linac will be designed as the first injector of the CEPC. There are two scenarios for the linac with unpolarized beams. One is that both electron and positron beams are accelerated to 6 GeV, but the positron beam is produced or bombed the convertor with the 5 GeV electron beam. The positron beam is then transported back to the mid of linac and to be accelerated to 6 GeV, shown in Figure 12. Figure 13 shows another case of linac, but both two beams can be accelerated to 10 GeV. Polarized beam is also considered if physics requirement is proposed. But the polarized electron gun needs R&D.

ISBN 978-3-95450-172-4

More detailed design of linac will be given in the near future for the pre-CDR study.

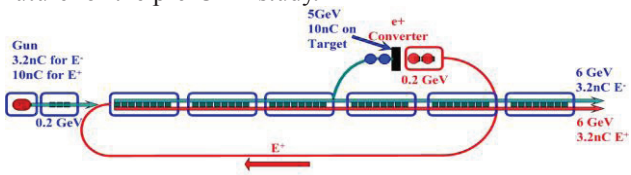


Figure 12: 6-GeV linac with unpolarized beams.

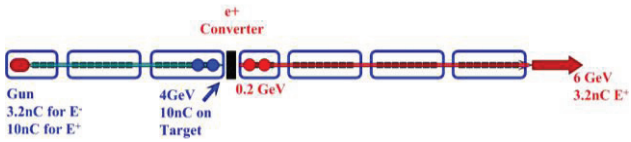


Figure 13: 10-GeV linac with unpolarized beams.

## TECHNICAL SYSTEM

Nearly all the technical systems have been looked at for the pre-CDR study. As the key technology and the most expensive system, superconducting RF system is more than concerned and will be seriously considered for its R&D.

RF system provides power to accelerator beams to the design energy and compensates the energy loss due to SR around the ring. Superconducting RF (SRF) system will have higher efficiency and lower the HOM loss due to cavity. But the cost of superconducting system and the necessary cryogenic system will be one of the major fractions of the whole machine. Table 4 lists the main parameters of the SRF of the CEPC and the booster.

Table 4: Main Parameters of the SRF System of CEPC

| | Main ring | Booster | LEP2 |
|---|---|---|---|
| Cavity Type | 650 MHz 5-cell Ni-doped Nb | 1.3 GHz 9-cell Ni-doped Nb | 352 MHz 4-cell Nb/Cu |
| Cavity number | 384 | 256 | 288 |
| $V_{cav}$ /$V_{RF}$ (MV/GV) | 18 MV / 6.87 GV | 20 MV / 5.04 GV | 12 MV / 3.46 GV |
| $E_{acc}$ (MV/m) | 15.5 | 19 | 6 ~ 7.5 |
| $Q_0$ | 2E10@2K | 2E10@ 2K | 3.2E9@ 4.2K |
| Cryo AC power(MW) | 25 | 2.5 (22% DF) | 6.1 |
| Cryomodule number | 96 (4 cav. / module) | 32 (8 cav. / module) | 72 (4 cav) |
| RF input power/ cav. (kW) | 260 | 20 | 125 |
| No. of RF source | 384(300 kW klys.) | 256 (25 kW SSA) | 36 (1.2 MW) |
| AC power (MW) | 200 | 2.4 (22% DF) | 85 |
| HOM damper power (W) | 10k ferrite +1k hook | 50 (hook+ ceramic) | 300 (hook) |

Although some kinds of SRF cavity, such as 1.3 GHz 9-cell cavity for ILC, 650 MHz β=0.82 5-cell cavity, and 500 MHz one-cell cavity with all cryomodule, coupler and other auxiliaries. Vertical and horizontal tests for 500 MHz cavity can be done in IHEP. But for high Q value with high acceleration gradient SRF cavity, we still need R&D in the near future. Some new techniques of coating at the inner surface of the cavity will be developed.

Other technical systems, like magnet, vacuum, beam instrumentation, mechanics, etc. needs R&D for their key parts of each system.

## PLAN IN THE NEAR FUTURE

The pre-CDR study of CEPC started from the end of 2012 in IHEP. The pre-CDR is expected to finish by the end of 2014. In the meantime, R&D items of some key technical systems are being put forward to, and are willing to be proposed as an R&D project in the period of 2016-2020. The technical design report (TDR) of CEPC will be hoped to finish during this 5 years if everything goes smoothly. The construction of the CEPC then will start from 2021 and will last for 8-10 years, if the government can approve the project.

When the CEPC is in its R&D and construction stages, the pre-study and R&D of the key technologies of SppC, are hopeful to carry on, and the similar R&D and other work to be done as that of CEPC as well.

## SUMMARY

The CEPC is the main high energy physics machine in the next decades around the world. Nearly all the aspects of the machine design have been touched. As the basis of the machine, accelerator physics studies of the CEPC main ring, is being carried on and getting progresses. But a lot of important issues of accelerator physics, the background to detector, machine detector interface, magnetic error effect, pretzel orbit induced physics or technical problems, etc., needs more studies in the near future. Thus, parameters of the main ring, booster, linac, etc., may be evolved or changed with the further study. The first stable version as a pre-CDR will be finished by the end of this year. Technical issues are being considered and some key technologies are proposed as the R&D project.

## REFERENCES

[1] A. Blondel & F. Zimmermann, "A High Luminosity $e^+e^-$ Collider in the LHC tunnel to study the Higgs Boson", arXiv: 1112.2518v1 [hep-ex], CERN-OPEN -2011-047,Jan. 2012.

[2] F. Zimmermann, "LEP3 and TLEP", talk given on the ICFA Beam Dynamics Workshop: Accelerators for a Higgs Factory: Linear vs. Circular (HF2012), Nov. 2012.

[3] K.Oide, "SuperTRISTAN: A possibility of ring collider for Higgs factory", KEK Seminar, February 2012.

[4] T. Sen, A $e^+e^-$ storage ring Higgs factory at Fermilab, talk given on the ICFA Beam Dynamics Workshop: Accelerators for a Higgs Factory: Linear vs. Circular (HF2012), Nov. 2012.



ISBN 978-3-95450-172-4

[5] Y.F. Wang, "A proposal on ring-based Higgs factory in China", 2nd Symposium on Accelerator-based HEP Strategy and Development in China, Sept. 2012.
[6] Q. Qin, "A Circular Higgs Factory", talk given on the ICFA Beam Dynamics Workshop: Accelerators for a Higgs Factory: Linear vs. Circular (HF2012), Nov. 2012.
[7] V.I. Telnov,"Restriction on the energy and luminosity of e+e- storage rings due to beamstrahlung", PRL 110, 114801 (2013).
[8] Q. Qin, et al, "Preliminary accelerator design of a circular Higgs factory in China", Proceedings of NaPAC'13, 2013.
[9] C. Zhang, "Optimizing beam intensity, number of bunches, bunch charge, and emittance", this proceedings, 2014.
[10] H.P. Geng, "Status of the CEPC lattice design", this proceedings, 2014.
[11] Y.H. Cai, "LBNL/SLAC Ring and Lattice Issues", talk given at the HF2012, FNAL, 2012.
[12] H. Grote, F.C. Iselin, "The MAD Program", CERN/ SL/90-13 (AP). 1990.
[13] SAD, "http://acc-physics.kek.jp/SAD/"
[14] Y.W. Wang, "CEPC IR optics", this proceedings, 2014.
[15] Y. Zhang, "Beam-beam effect in the CEPC", this proceedings, 2014.
[16] N. Wang, "Impedance and collective effects of CEPC", this proceedings, 2014.
[17] H.P. Geng, "Status of the CEPC lattice design", this proceedings, 2014.
[18] C. Zhang, "CEPC injector", this proceedings, 2014.
[19] X.H.Cui, "Beam lifetime and Injection consideration", this proceedings, 2014.

ISBN 978-3-95450-172-4

# CEPC DESIGN PERFORMANCE CONSIDERATIONS[1]

M. Koratzinos, University of Geneva and CERN, Geneva, Switzerland

*Abstract*

In this paper I will commend on the early CEPC design as of October 2014. In particular I will comment on the choice of circumference, minimum and maximum energy, number of collision points and target luminosity. I will finish with suggestions to increase performance with minimum incremental cost.

## CEPC DESIGN PHILOSOPHY

The design of the CEPC revolves around the philosophy of keeping costs low while achieving as much of the performance of an ultimate machine. For this reason the scope has been limited to primarily a Higgs factory, operating at a beam energy of 120GeV. Tunnel size has been kept to 54.8 kms, approximately twice as big as LEP. Two experiments are envisaged for $e^+e^-$ operation and a single beam pipe design has been chosen.

We will try to quantify the cost of these choices in terms of performance. In the late part of the paper we will also make suggestions to improve the performance of the baseline design.

## LUMINOSITY OF A CIRCULAR COLLIDER

The luminosity of a circular collider is given by

$$\mathcal{L} = \frac{3}{8\pi}\frac{e^4}{{r_e}^4}P_{tot}\ \frac{\rho}{{E_0}^3}\xi_y\frac{R_{hg}}{\beta_y^*} \qquad (1)$$

where $r_e$ and $e$ are the classical radius of the electron and its charge, $P_{tot}$ the total SR power dissipated by one beam, $\rho$ the bending radius, $E_0$ the beam energy, $\xi_y$ vertical beam-beam parameter, $\beta_y^*$ the vertical beta function at the interaction point and $R_{hg}$ the geometric hourglass factor.

The maximum achievable $\xi_y$ depends on if a specific machine is beam-beam or beamstrahlung dominated [1].

### *The Beam-beam Limit*

The beam-beam limit depends on the damping decrement $\lambda_d$, the amount of energy loss when electrons move from one IP to the next:

$$\lambda_d = \left(\frac{U_0}{E}\right)\frac{1}{n_{IP}} \qquad (2)$$

Where $U_0$ is the energy loss per electron in one turn. The LEP data has been used to derive this number following the formulation in [2]:

$$\xi_y{}^{max} \propto {\lambda_d}^{0.4} \qquad (3)$$

which when fitted to the maximum beam-beam parameters achieved at LEP yields the approximate formula

$$\xi_y{}^{max} \approx 0.86 \cdot {\lambda_d}^{0.4} \qquad (4)$$

We need to stress here that the above formulation is only based on a limited amount of LEP data and should be taken with a grain of salt. Beam-beam simulations and ultimately measurements on a real machine would provide a more accurate estimation, but for the purposes of this paper we consider the approach above adequate.

### *The Beamstrahlung Limit*

The beamstrahlung limit [3] is due to the fact that at high energies and luminosities beamstrahlung, the synchrotron radiation emitted by an incoming electron in the collective electromagnetic field of the opposite bunch at an interaction point, reduces beam lifetimes to values where the top-up injector cannot cope. The effect of beamstrahlung is very implementation specific and can be mitigated by small vertical emittance and large momentum acceptance.

Two analytical calculations exist for computing beam lifetimes due to beamstrahlung [3] [4] offering fast estimates of the effect. Analytical simulations assume Gaussian distributions (i.e. without non-Gaussian tails) and have other approximations. Therefore it is important to be checked against a complete simulation such as the one by K. Ohmi [5]. The comparison between the two analytical calculations and the simulation for two different energies (where beamstrahlung plays a crucial role in defining the beam lifetime) and for the specific implementation of FCC-ee [6] is shown in Figure 1 and Figure 2. Care is taken to use the effective $\beta_x^*$ coming out of the simulation, rather than the design value.

Both analytical calculations show reasonable agreement for momentum acceptances of interest here (between 1.5% and 2%) at beam energies of both 120GeV and 175GeV. This justifies the use of the analytic formulas instead of the much more accurate but time-consuming simulation for the purposes of this work.

The two regimes (the beam-beam dominated and the beamstrahlung dominated one), for the specific implementation of FCC in [6], can be seen in **Figure 3**. Such a machine would be beamstrahlung dominated at

[1] Talk title: Choice of circumference, minimum & maxim energy, number of collision points, and target luminosity



ISBN 978-3-95450-172-4

175GeV, but at lower energies will be beam-beam dominated.

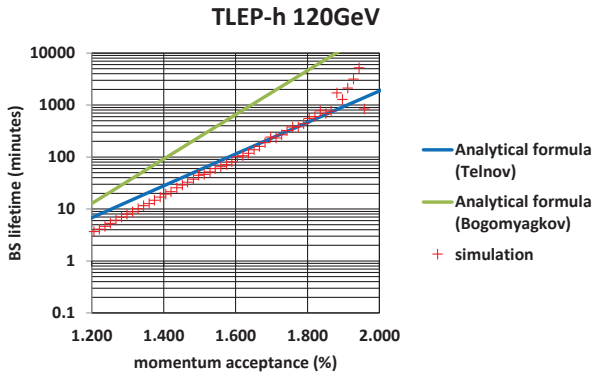


Figure 1: Beamstrahlung lifetimes for FCC-ee at 120GeV: comparison between the two analytical formulas and simulation.

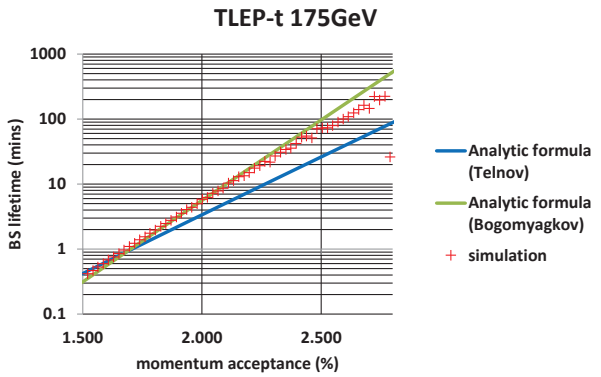


Figure 2: Beamstrahlung lifetimes for FCC-ee at 175GeV: comparison between the two analytical formulas and simulation.

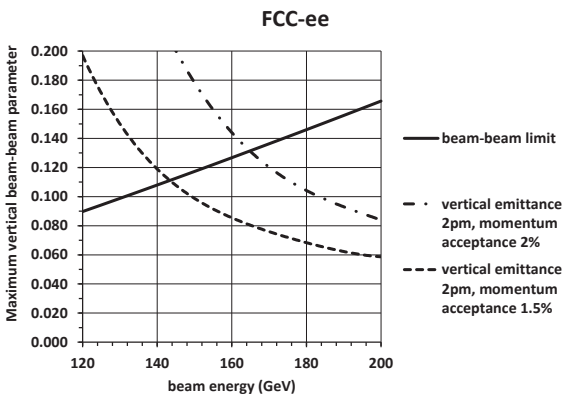


Figure 3: The beam-beam (solid line) and beamstrahlung limits for FCC-ee **[6]**. The beamstrahlung curves have been obtained assuming a beam lifetime of 300 seconds and two different momentum acceptance values using to the analytical formula in **[3]**. The machine is beamstrahlung dominated above approximately 165 GeV if the momentum acceptance is 2%.

The CEPC has different parameters, therefore the beamstrahlung curves are different. Regarding the beam-beam curve, the smaller diameter of the CEPC makes damping stronger and therefore a higher beam-beam parameter should be achievable in theory, however the CEPC approach uses a more conservative extrapolation of the maximum beam-beam parameter. As in the FCC-ee case, the machine is beam-beam limited at 120 GeV. The two regime plot of the CEPC can be seen in **Figure 4**.

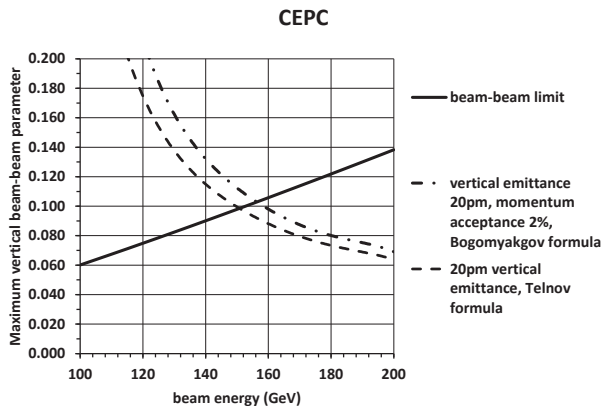


Figure 4: The beam-beam (solid line) and beamstrahlung limits for a collider with parameters of the CEPC. The beamstrahlung curves have been obtained assuming a beam lifetime of 300 seconds and a momentum acceptance and 2% for both analytical formulas in [4] and [3]. The machine is beamstrahlung dominated above approximately 155 GeV.

## RING CIRCUMFERENCE

As seen from eqn. (1), going to larger ring sizes increases the luminosity due to the increase in bending radius (linearly) but decreases it due to a smaller damping decrement (to the power 0.4, if we follow the parameterisation in [2]). The overall effect is an increase of luminosity with the ring circumference to the power 0.6. Therefore increasing the ring circumference to 70km ring increases luminosity by 20%. Going to a 100 km ring increases luminosity by 45%.

Table 1: Comparison of maximum luminosity for the CEPC design with the baseline tunnel circumference (53.6kms) and a larger ring (70kms). The beam-beam parameter decreases due to less damping for the bigger ring. Parameters affecting the bunch length $\sigma_z$ have been kept the same.

| Ring size | $\xi_y$ | $\sigma_z$ (mm) | Luminosity ($10^{34}$) |
|---|---|---|---|
| 53600m | .075 | 2.7 | 1.8 |
| 70000m | .067 | 2.7 | 2.2 |

The gain is modest, so the choice of tunnel size will also depend on other parameters, for example the desire to run at 175 GeV, which becomes easier with a larger ring, and

ISBN 978-3-95450-172-4

the pp option later on, whose energy reach again benefits from a larger ring.

## NUMBER OF EXPERIMENTS

The CEPC design foresees two experiments. If four experiments were available, then the damping decrement between IPs would decrease by a factor of 2, and the maximum beam-beam parameter, following always the parameterisation in [2], would decrease by about 30%, as would the luminosity per experiment since we are at the beam-beam regime. Therefore having twice as many experiments would finally increase the luminosity yield per year by around 50%.

Table 2: Comparison of luminosity delivered to experiments as a function of the number of installed experiments. Damping decreases going from two to four experiments and therefore so does the corresponding maximum beam-beam parameter.

| Energy | IPs | $\xi_y$ | Luminosity per IP ($10^{34}$) | Lumi*$N_{IP}$ ($10^{34}$) |
|---|---|---|---|---|
| 120GeV | 2 | 0.075 | 1.84 | 3.68 |
| 120GeV | 4 | 0.057 | 1.40 | 5.60 |

## RUNNING AT 45 GEV

45 GeV running is a highlight of the FCC-ee programme, as very high luminosities can be achieved. This comes at the expense of having many - O(10,000) - bunches circulating. Since the machine is beam-beam dominated at low energies, increasing the emittance in both planes decreases the number of bunches in the machine without affecting overall performance. In the case of FCC-ee emittances are increased by a factor 15 compared to 120GeV running. The CEPC design with a single beam-pipe and the pretzel scheme for bunch separation would not be able to run with more than O(100) bunches per species. This will severely limit the luminosity of the CEPC at the Z peak, but will also limit the synchrotron radiation power loss. The maximum beam-beam parameters can here be predicted with some confidence as the CEPC with two experiments and twice the size has the same damping decrement as LEP (=0.045). $\beta_x$ was adjusted to 0.4 m to give equal beam-beam parameters in x and y. Table 3 shows the essential parameters of the CEPC running at 45 GeV. The first row is simply extrapolating from the 120GeV design keeping emittances the same, the second is the result of increasing emittances by a factor of 20 in an attempt to limit the number of bunches and the third is limiting also the power to 20% of the initial power. The resulting number of bunches – 160 – might just be manageable with a single beam-pipe and the delivered luminosity would be a factor of 14 smaller than the advertised performance of FCC-ee at 45GeV and four experiments. Finding a way to accommodate more bunches would increase the performance at 45 GeV dramatically.

Table 3: Synchrotron radiation power per beam, number of bunches and expected luminosity for different schemes for CEPC 45GeV running.

| Scheme | Power (MW) | No. of bunches | Lumi ($10^{34}$) |
|---|---|---|---|
| **Extrapolating from 120GeV** | 50 | 15500 | 27 |
| Increasing emittances by 20 | 50 | 780 | 21 |
| **Reducing power by 5** | 10 | 160 | 4 |

## RUNNING AT 175 GEV

Running above the $t\bar{t}$ threshold is considered an important part of the physics programme of FCC-ee but is not a high priority for the CEPC. The smaller ring diameter would make the energy loss per turn due to synchrotron radiation higher, needing more RF voltage. Both the CEPC and FCC-ee would be running in a beamstrahlung-dominated regime at this energy. The energy loss per turn for the CEPC is 13.6GeV. This necessitates an RF system twice as big as that of FCC-ee, with around 1200m of RF cavities. The performance of both machines can be compared in Table 4. There is a performance loss of a factor 5 compared to the parameters of FCC-ee.

Table 4: Energy loss per turn, emittances, number of bunches and projected luminosities for 175GeV running for the CEPC and FCC-ee circular colliders.

| Ring | E_loss (GeV) | $\epsilon_x/\epsilon_y$ (nm/pm) | No. bunches | Luminosity ($10^{34}$) |
|---|---|---|---|---|
| CEPC | 13.6 | 7/10 | 7 | 0.8 |
| FCC-ee | 7.6 | 2/2 | 98 | 1.8 |

## SUGGESTIONS FOR IMPROVED PERFORMANCE

Here we examine if there are avenues to pursue to increase the performance of the CEPC while sticking on the strategic choices of ring diameter, number of experiments and single beam-pipe design.

Effectively, the largest limitation comes from the constrained number of bunches due to the single beam-pipe design. The disadvantage becomes more pronounced if one is to run at lower energies and more specifically at 45GeV, which adds an extra dimension to the physics case of the machine. Another disadvantage is that a crab waist scheme that looks promising for the FCC-ee (admittedly for energies lower than 120GeV) cannot be implemented at the CEPC with the single beam-pipe option.

There is a way, however, to mostly keep the single beam-pipe design philosophy and at the same time allow for more bunches: the introduction of a double beam pipe in two or four straight sections and the introduction of a bunch train



ISBN 978-3-95450-172-4

scheme. Electrostatic separators can be used to separate the beams at the edges of the relevant straight sections initially and magnetic elements can take over after the beams are separated sufficiently. In such a scheme, one or two bunch trains of electrons and positrons can circulate with no parasitic collisions, provided that the total length of the bunch trains is less than the length of the double-pipe straight sections. In this scheme and with a total length of the double pipe straight sections of 4 kms, 2000 electron and positron bunches can be accommodated with a 2 m (7 nsec) separation. The increase in cost is modest, as less than 10% of the machine is equipped with a double beam pipe. The arcs keep the single beam-pipe design. Such a design can naturally accommodate a crab waist collision scheme.

Another weakness of the design is the inconsistent bunch length compared to the $\beta_y^*$ value (2.7mm compared to 1.2mm). $\beta_y^*$ has correctly been set to a low value, as it directly affects luminosity. Here the value chosen is 20% larger than that of the FCC-ee design. However, the fact that the bunch length is 2.3 times the $\beta_y^*$ value introduces a large geometrical loss factor (hourglass value of 0.68) and, more importantly, gives rise to beam instabilities that result in lower luminosities. On the other hand, the large bunch length masks the fact that the design is in reality beamstrahlung limited, had the bunch length been as short as in the FCC-ee design – indeed, in such a case the beam lifetime drops to a bit more than a minute.

Looking closely at the parameters, one realises that the CEPC design has a factor of 7/10 larger horizontal/ vertical emittance compared to the FCC-ee design. The emittance ratio of 330 used in the CEPC design is a realistic number and close to what was achieved at LEP (250) – the FCC-ee design pushes this number to 500 or even 1000 for the $t\bar{t}$ running. However, the horizontal emittance of the CEPC design is too large when seen in context of what the FCC-ee design expects to achieve. The ways to reduce the horizontal (and, therefore vertical) emittance include:

- The introduction of stronger focusing by adopting $90^o$ FODO optics instead of the current $60^o$ CEPC design for the horizontal plane. Theoretically, going from $60^o$ to $90^o$ optics reduces the emittance by a factor 3.
- Adopt a shorter FODO cell. The bending angle of the CEPC is twice as big as the FCC-ee one per unit length, and the emittance depends on the third power of the bending angle. Going to a FODO length of 38 m from the current 47.2 m would give a factor of 2 lower emittance.

LEP run in various configurations, but 90/60 optics worked well.

It should be mentioned here that above mentioned solutions have repercussions regarding the cost of the magnet system of the machine.

The momentum compaction factor could also be reduced (the FCC-ee design has a momentum compaction factor which is a factor of 7 smaller) and at least a factor of 2 reduction will be necessary to avoid having a bunch length much larger than $\beta_y^*$. Moving from a phase advance of $60^o$ to $90^o$ would reduce the momentum compaction factor by a factor 2. Reducing the FODO length to 38 m would give another factor 1.5, for a total factor 3 reduction.

This suggestion for the parameter set of CEPC can be seen in Table 5 (modifications in bold typeface). Essentially the horizontal and vertical emittances have been reduced by a factor 3 (this should be achievable by only going to a $90^o$ optics without any shortening of the FODO length). The momentum compaction factor has also been reduced by 3. This can be achieved by a combination of $90^o$ optics and shorter FODO length. The CEPC philosophy of a higher beam-beam parameter in the horizontal plane has been followed, although the CERN design uses similar beam-beam parameters in both planes. Due to the lower momentum compaction number the bunch length is now reduced to acceptable values (the equilibrium bunch length is calculated to be 1.55mm). Since the horizontal and vertical beam size is now reduced due to the smaller emittances and the bunch length is also reduced, less charge per bunch is called for to avoid beamstrahlung lifetime problems. This increases the total number of bunches to 120. This is still possible (but marginal perhaps) with the pretzel (single beam-pipe) scheme, but is a non-issue in the bunch separation scheme proposed above. The luminosity shows a healthy increase to above $3\times10^{34}\text{cm}^{-2}\text{s}^{-1}$.

## ACKNOWLEDGMENTS

This paper would not be possible without the valuable input of many colleagues, I would like to single out Dmitry Shatilov for his helpful insight to the problems discussed here.

## REFERENCES

[1] M. Koratzinos, Performance limitations of circular colliders: head-on collisions, *CERN-ACC-NOTE-2014-0066.*

[2] R. Assmann and K. Cornelis, The beam-beam limit in the presence of strong synchrotron radiation damping, *CERN-SL-2000_046 OP.*

[3] A. Bogomyagkov et al., Beam-beam effects investigation and parameters optimization for a circular e + e − collider at very high energies, *Phys.Rev.ST Accel.Beams 17 (2014) 041004.*

[4] V. Telnov, Restriction on the energy and luminosity of e+e- storage rings due to beamstrahlung, *Phys. Rev. Letters 110, 114801 (2013) arXiv:1203.6563.*

[5] K. Ohmi, F. Zimmermann, FCC-ee/CepC Beam-Beam Simulations with Beamstrahlung, *Proceedings of IPAC2014, Dresden, Germany*, 2014.

[6] Wenninger, J. et al., Future Circular Collider Study Lepton Collider Parameters, *CERN EDMS no. 1346082,* 2014.



ISBN 978-3-95450-172-4

Table 5: The CEPC Parameter Set as was Presented on 10 October 2014 and as Suggested in This Paper

| Parameter | Unit | Value 10/10/2014 | Value – this suggestion |
|---|---|---|---|
| Beam energy [E] | GeV | 120 | 120 |
| Circumference [C] | m | 54752 | 54752 |
| Number of IPs[$N_{IP}$] | | 2 | 2 |
| SR loss/turn [$U_0$] | GeV | 3.11 | 3.11 |
| Bunch number/beam[$n_B$] | | 50 | **120** |
| Bunch population [$N_e$] | | 3.79E+11 | **1.5E+11** |
| SR power/beam [P] | MW | 51.7 | **50** |
| Beam current [I] | mA | 16.6 | 16.6 |
| Bending radius [ρ] | m | 6094 | 6094 |
| momentum compaction factor [$\alpha_p$] | | 3.36E-05 | **1.1E-05** |
| Revolution period [$T_0$] | s | 1.83E-04 | 1.83E-04 |
| Revolution frequency [$f_0$] | Hz | 5475.46 | 5475.46 |
| emittance (x/y) | nm | 6.12/0.018 | **2/0.006** |
| $\beta^*$(x/y) | mm | 800/1.2 | 800/1.2 |
| Transverse beam size (x/y) | μm | 69.97/0.15 | **40/0.085** |
| $\xi_x/\xi_y$ per IP | | 0.118/0.083 | **0.146/0.104** |
| Bunch length SR [$\sigma_{s.SR}$] | mm | 2.14 | **1.24** |
| Bunch length total [$\sigma_{s.tot}$] | mm | 2.65 | **1.55** |
| Lifetime due to Beamstrahlung | min | 47(simulation) | **68/360 (analytical)** |
| lifetime radiative Bhabha scattering [$\tau_L$] | min | 51 | **34** |
| RF voltage [$V_{rf}$] | GV | 6.87 | 6.87 |
| RF frequency [$f_{rf}$] | MHz | 650 | 650 |
| Harmonic number [h] | | 118800 | 118800 |
| Synchrotron oscillation tune [$\nu_s$] | | 0.18 | **0.10** |
| Damping partition number [Jε] | | 2 | 2 |
| Energy spread SR [$\sigma_{\delta.SR}$] | % | 0.132 | 0.132 |
| Energy spread BS [$\sigma_{\delta.BS}$] | % | 0.096 | **0.099** |
| Energy spread total [$\sigma_{\delta.tot}$] | % | 0.163 | **0.165** |
| $n_\gamma$ | | 0.23 | **0.17** |
| Transverse damping time [$n_x$] | turns | 78 | 78 |
| Longitudinal damping time [$n_\varepsilon$] | turns | 39 | 39 |
| Hourglass factor | | 0.68 | **0.81** |
| Luminosity /IP | $cm^{-2}s^{-1}$ | 2.04E+34 | **3.07E+34** |
| FODO length | m | 48 | **38** |
| FODO phase advance (horiz./vertical) | degrees | 60/60 | **90**/60 |



ISBN 978-3-95450-172-4

# RING CIRCUMFERENCE AND TWO RINGS VS ONE RING

Richard Talman
Laboratory of Elementary-Particle Physics,
Cornell University

*Abstract*

The natural next future circular collider is a circular e+e- Higgs Factory and, after that, a post-LHC p,p collider in the same tunnel. The main Higgs factory cost-driving parameter choices include: tunnel circumference $C$, whether there is to be one ring or two, what is the installed power, and what is the "Physics" for which the luminosity deserves to be maximized. This paper discusses some of the trade-offs among these choices, and attempts to show that the optimization goals for the Higgs factory and the later p,p collider are consistent.

## GENERAL COMMENTS

The quite low Higgs mass (125 GeV) makes a circular e+e- collider (FCC-ep) ideal for producing background-free Higgs particles. There is also ample physics motivation for planning for a next-generation proton-proton collider with center of mass energy approaching 100 TeV. This suggests a two-step plan: first build a circular e+e- Higgs factory; later replace it with a 100 TeV pp collider (or, at least, center of mass energy much greater than LHC). This paper is devoted almost entirely to the circular Higgs factory step, but keeping in mind the importance of preserving the p,p collider potential.

The main Higgs factory cost-driving parameter choices include: tunnel circumference $C$, whether there is to be one ring or two, what is the installed power, and what are the physics priorities. From the outset I confess my prejudice towards a single LEP-like ring, optimized for Higgs production at $E = 120$ Gev, with minimum *initial* cost, and highest possible eventual p,p energy. This paper discusses some of the trade-offs among these choices, and attempts to show that electron/positron and proton/proton optimization goals are consistent.

Both Higgs factory power considerations and eventual p,p collider favor a tunnel of the largest possible radius $R$. Obviously one ring is cheaper than two rings. For 120 GeV Higgs factory operation (and higher energies) it will be shown that one ring is both satisfactory and cheaper than two. But higher luminosity (by a factor of five or so) at the (45.6 GeV) $Z_0$ energy, requires two rings.

Unlike the $Z_0$, there is no unique "Higgs Factory energy". Rather there is the threshold turn-on of the cross section shown, for example, in Figure 1 of my WG 2 paper "Single Ring Multibunch Operation and Beam Separation".

We arbitrarily choose 120 GeV per beam as the Higgs particle operating point and identify the single beam energy this way in subsequent tables. Similarly identified are the $Z_0$ energy (45.6 GeV), the W-pair energy of 80 GeV, the LEP energy (arbitrarily taken to be 100 GeV) and the $t\bar{t}$ energy of 175 GeV to represent high energy performance.

## SCALING UP FROM LEP TO HIGGS FACTORY

### *Scaling Radius and Power Inversely Conserves Luminosity*

Most of the conclusions in this paper are based on scaling laws, either with respect to bending radius $R$ or with respect to beam energy $E$. Scaling with bend radius $R$ is equivalent to scaling with circumference $C$. (Because of limited "fill factor", RF, straight sections, etc., $R \approx C/10$.)

Higgs production was just barely beyond the reach of LEP's top energy, by the ratio 125 GeV/105 GeV = 1.19. This should make the extrapolation from LEP to Higgs factory quite reliable. In such an extrapolation it is increased radius more than increased beam energy that is mainly required.

One can note that, for a ring three times the size of LEP, the ratio of $E^4/R$ (synchrotron energy loss per turn) is $1.19^4/3 = 0.67$—i.e. *less than final LEP operation*. Also, for a given RF power $P_{\rm rf}$, the total number of stored particles is proportional to $R^2$—doubling the ring radius cuts in half the energy loss per turn and doubles the time interval over which the loss occurs. These comments deflate a long-held perception that LEP had the highest practical energy for an electron storage ring.

There are three distinct upper limit constraints on the luminosity. Maximum luminosity results when the parameters have been optimized so the three constraints yield the same upper limit for the luminosity. For now we concentrate on just the simplest luminosity constraint $\mathcal{L}^{\rm RF}_{\rm pow}$, the maximum luminosity for given RF power $P_{\rm rf}$. With $n_1$ being number of stored particles per MW; $f$ the revolution frequency; $N_b$ the number of bunches, which is proportional to $R$; $\sigma^*_y$ the beam height at the collision point; and aspect ratio $\sigma^*_x/\sigma^*_y$ fixed (at a large value such as 15);

$$\mathcal{L}^{\rm RF}_{\rm pow} \propto \frac{f}{N_b}\left(\frac{n_1 P_{\rm rf}[\rm MW]}{\sigma^*_y}\right)^2. \qquad (1)$$

Consider variations for which

$$P_{\rm rf} \propto \frac{1}{R}. \qquad (2)$$

Dropping "constant" factors, the dependencies on $R$ are, $N_b \propto R$, $f \propto 1/R$, and $n_1 \propto R^2$. With the $P_{\rm rf} \propto 1/R$ scaling of Eq. (2), $\mathcal{L}$ is independent of $R$. In other words, the luminosity depends on $R$ and $P_{\rm rf}$ only through their product

ISBN 978-3-95450-172-4

$RP_{\rm rf}$. Note though, that this scaling relation *does not* imply that $\mathcal{L} \propto P_{\rm rf}^2$ at fixed $R$.

This radius/power scaling formula can be checked numerically by comparing Tables 5 and 6 in the present paper, which assume 100 km circumference, 25 MW/beam, with the corresponding tables in my "Single Ring Multibunch Operation and Beam Separation" paper which assume 50 km circumference, 50 MW/beam. The comparison is only approximate since other parameters and the scalings from LEP are not exactly the same in the two cases.

### *Parameter Scaling with Radius*

For simplicity, even if it is not necessarily optimal, let us assume the Higgs factory arc optics can be scaled directly from LEP values, which are: phase advance per cell $\mu_x = \pi/2$, full cell length $L_c = 79$ m. (The subscript "c" distinguishes the Higgs factory collider lattice cell length from injector lattice cell length $L_i$.)

Constant dispersion scaling formulas are given in Table 1. These formulas are derived in my WG 6 paper "Lattice Optimization for Top-Off Injection", at this meeting. These formulas are then applied to extrapolate from LEP to find the lattice parameters for Higgs factories of circumference 50 km and 100 km, shown in Table 4.

Table 1: Constant Dispersion (see shaded row) Scaling with R of Various Lattice and Beam Parameters

| Parameter | Symbol | Proportionality | Scaling |
|---|---|---|---|
| phase advance per cell | $\mu$ | | 1 |
| collider cell length | $L_c$ | | $R^{1/2}$ |
| bend angle per cell | $\phi$ | $= L_c/R$ | $R^{-1/2}$ |
| quad strength $(1/f)$ | $q$ | $1/L_c$ | $R^{-1/2}$ |
| dispersion | $D$ | $\phi L_c$ | 1 |
| beta | $\beta$ | $L_c$ | $R^{1/2}$ |
| tunes | $Q_x, Q_y$ | $R/\beta$ | $R^{1/2}$ |
| Sands's "curly H" | $\mathcal{H}$ | $= D^2/\beta$ | $R^{-1/2}$ |
| partition numbers | $J_x/J_y/J_\epsilon$ | = 1/1/2 | 1 |
| horizontal emittance | $\epsilon_x$ | $\mathcal{H}/(J_x R)$ | $R^{-3/2}$ |
| fract. momentum spread | $\sigma_\delta$ | $\sqrt{B}$ | $R^{-1/2}$ |
| arc beam width-betatron | $\sigma_{x,\beta}$ | $\sqrt{\beta\epsilon_x}$ | $R^{-1/2}$ |
| -synchrotron | $\sigma_{x,synch.}$ | $D\sigma_\delta$ | $R^{-1/2}$ |
| sextupole strength | $S$ | $q/D$ | $R^{-1/2}$ |
| dynamic aperture | $x^{\max}$ | $q/S$ | 1 |
| relative dyn. aperture | $x^{\max}/\sigma_x$ | | $R^{1/2}$ |
| pretzel amplitude | $x_p$ | $\sigma_x$ | $R^{-1/2}$ |

## STAGED OPTIMIZATION

### *A Cost Model*

To maximize both the likelihood of initial approval and the eventual p,p performance, the cost of the first step has to be minimized and the tunnel circumference maximized. Surprisingly, these requirements are quite consistent. Consider optimization principles for three FCC stages:

- **Stage I, e+e-:** Starting configuration. Minimize cost at "respectable" luminosity, e.g. $10^{34}$. Constrain the number of rings to 1, and the number of IP's to $N^* = 2$.
- **Stage II, e+e-:** Maximize luminosity/cost for production Higgs (etc.) running. Upgrade the luminosity by some combination of: $P_{\rm rf} \rightarrow 2P_{\rm rf}$ or $4P_{\rm rf}$, one ring $\rightarrow$ two rings, increasing $N^*$ from 2 to 4, or decreasing $\beta_y^*$.
- **Stage III, pp:** Maximize the ultimate physics reach, i.e. center of mass energy, i.e. maximize tunnel circumference.

### *Cost Optimization*

Treating the cost of the 2 detectors as fixed, and letting $C$ be the cost exclusive of detectors, the cost can be expressed as a sum of a term proportional to size and a term proportional to power;

$$C = C_R + C_P \equiv c_R R + c_P P_{\rm rf} \tag{3}$$

where $c_R$ and $c_P$ are unit cost coefficients. As given by Eq. (2), for constant luminosity, the RF power, luminosity, and ring radius, for small variations, are related by

$$P_{\rm rf} = \frac{\mathcal{L}}{k_1 R}. \tag{4}$$

Minimizing $C$ at fixed $\mathcal{L}$ leads to

$$R_{\rm opt} = \sqrt{\frac{1}{k_1}\frac{c_P}{c_R}}\,\mathcal{L}. \tag{5}$$

Conventional thinking has it that $c_P$ is universal world wide but, at the moment, $c_R$ is thought to be somewhat cheaper in China than elsewhere. If so, the optimal radius should be somewhat greater in China than elsewhere. Exploiting $P_{\rm rf} \propto \mathcal{L}/R$, some estimated costs (in arbitrary cost units) and luminosities for Stage I and (Higgs Factory)Stage-II are given in Table 2. The luminosity estimates are from Table 6 and are explained in later sections and in my WG 6 paper, "Lattice Optimization for Top-Off Injection".

Table 2: Estimated costs, one ring in the upper table, two in the lower. *A crude LEP spread sheet shows that doubling the radius and halving the power leaves the accelerator cost not very much changed. Also bending magnet costs are assumed to be proportional to stored magnetic energy.

| | $R$ km | $P_{\rm rf}$ MW | $C_{\rm tun}$ arb. | $C_{\rm acc}$ arb. | Phase-I cost arb. | $\mathcal{L}^I$ (Higgs) $10^{34}$ | $\mathcal{L}^I$ $(Z_0)$ $10^{34}$ | $\mathcal{L}^{II}$ (Higgs) $10^{34}$ |
|---|---|---|---|---|---|---|---|---|
| 1 | 5 | 50 | 0.5 | 2.5 | 3.0 | 1.2 | 2.6 | 2 |
| | 10 | 25 | 1.0 | 2.5* | **3.5** | 1.2 | 5.2 | **5** |
| | 10 | 50 | 1.0 | 4.0 | 5.0 | 2.3 | 10.4 | 5 |
| 2 | 5 | 50 | 0.5 | 4.5 | 5.0 | 1.2 | 21 | 2 |
| | 10 | 25 | 1.0 | 4.5* | 5.5 | 1.2 | 21 | 5 |
| | 10 | 50 | 1.0 | 7.0 | 8.0 | 2.3 | 42 | 5 |

Note that doubling the radius, while cutting the power in half, increases the cost only modestly, while leaving generous options for upgrading to maximize Higgs luminosity, as well as maximizing the potential p,p physics reach. The shaded row in Table 2 seems like the best deal. Both Higgs factory and, later, p,p luminosities are maximized, and the initial cost is (almost) minimized. Of course this optimization has been restricted to a simple choice between 50 km and 100 km circumference.



ISBN 978-3-95450-172-4

## LUMINOSITY LIMITING PHENOMENA

### *Saturated Tune Shift*

My electron/positron beam-beam simulation [2] dead reckons the saturation tune shift $\xi_{\max}$ which is closely connected to the maximum luminosity. For an assumed $R \propto E^{5/4}$ scaling, $\xi_{\max}$ is plotted as a function of machine energy $E$ in Figure 1. This plot assumes that the r.m.s. bunch-length $\sigma_z$ is equal to $\beta_y^*$, the vertical beta function at the intersection point (IP).

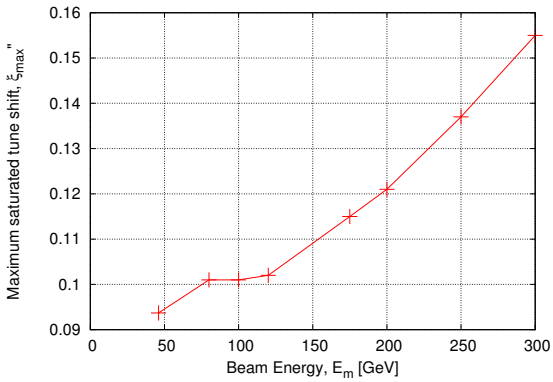


Figure 1: Plot of maximum tune shift $\xi_{\max}$ as a function of maximum beam energy for rings such that $E \propto R^{5/4}$. The non-smoothness has to be blamed on statistical fluctuations in the Monte Carlo program calculation. The maximum achieved tune shift parameter 0.09 at 100 GeV at LEP was less than shown, but their torturous injection and energy ramping seriously constrained their operations.

The physics of the simulation assumes there is an equilibrium established between beam-beam heating versus radiation cooling of vertical betatron oscillations. Under ideal single beam conditions the beam height would be $\sigma_y \approx 0$. This would give infinite luminosity in colliding beam operation —*this is unphysical*. In fact beam-beam forces cause the beam height to grow into a new equilibrium with normal radiation damping. It is parametric modulation of the vertical beam-beam force by horizontal betatron and longitudinal synchrotron oscillation that modulates the vertical force and increases the beam height. The resonance driving strength for this class of resonance is proportional to $1/\sigma_y$ and would be infinite if $\sigma_y$=0—*which is also unphysical*. Nature, "abhoring" both zero and infinity, plays off beam-beam emittance growth against radiation dampling. However amplitude-dependent detuning limits the growth, so there is only vertical beam growth but no particle loss (at least from this mechanism). In equilibrium the beam height is proportional to the bunch charge. The simulation automatically accounts for whatever resonances are nearby.

To estimate Higgs factory luminosity the tune plane is scanned for various vertical beta function values and bunch lengths, as well as other, less influential, parameters. The resulting ratio $(\xi^{\text{sat}}/\beta_y^*)$ is plotted in Figure 2. The ratio $\xi^{\text{sat.}}/\beta_y^*$ determines the beam area $A_{\beta_y}$ just sufficient for

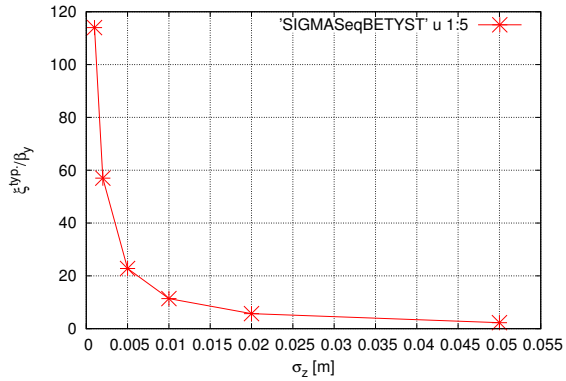


Figure 2: Plot of $\xi^{\text{sat.}}/\beta_y$ as a function of $\sigma_z$, with $\beta_y^* = \sigma_z$, $\delta = 0.00764$, and synchrotron tune advance between collisions $Q_s = 0.0075$.

vertical saturation according to the formula,

$$A_{\beta_y} = \pi\sigma_x\sigma_y = \frac{N_p r_e}{2\gamma}\frac{1}{(\xi^{\text{sat.}}/\beta_y)}. \qquad (6)$$

This fixes the tune-shift-saturated charge density (per unit transverse area). It is only the product $\sigma_x\sigma_y$ that is fixed but there is a broad optimum in luminosity for aspect ratio $a_{xy} = \sigma_x/\sigma_y \approx 15$. To within this ambiguity all transverse betatron parameters are then fixed. $\beta_x^*$ is adjusted to make horizontal and vertical beam-beam tune shifts approximately equal. The lattice optics is adjusted so that the (arc-dominated) emittance $\epsilon_x$ gives the intended aspect ratio $a_{xy}$; $\epsilon_x = \sigma_x^2/\beta_x^*$.

(Incidentally, it will not necessarily be easy to optimize $\epsilon_x$ for each beam energy. My W6 paper "Lattice Optimization for Top-Off Injection" discusses tailoring cell length $L_c$ to adjust $\epsilon_x$. Unfortunately other considerations influence the choice of $L_c$ and, in any case, once optimized for one energy, $L_c$ remains fixed at all energies.)

### *Beamstrahlung*

"Beamstrahlung" is the same as synchrotron radiation, except that it occurs when a particle in one beam is deflected by the electric and magnetic fields of the other beam. Emission of the occasional single *hard* x-ray is inevitable and the lost energy has to be paid for. Much worse is the possibility that the reduction in momentum causes the particle itself to be lost, greatly magnifying the energy loss. It is this process that makes beamstrahlung so damaging. The damage is quantified by the beamstrahlung-dominated beam lifetime $\tau_{\text{bs}}$. The important parameter governing beamstrahlung is the "critical energy" $u_c^*$ which is proportional to 1/bunch-length $\sigma_z$; beamstrahlung particle loss increases exponentially with $u_c^*$. To decrease beamstrahlung by increasing $\sigma_z$ also entails increasing $\beta_y^*$ which reduces luminosity. A favorable compromise can be to increase charge per bunch along with $\beta_y^*$.

ISBN 978-3-95450-172-4

*Reconciling the Luminosity Limits*

The number of electrons per bunch $N_p$ itself is fixed by the available RF power and the number of bunches $N_b$. For increasing the luminosity $N_b$ wants to be *reduced*. To keep beamstrahlung acceptably small $N_b$ wants to be *increased*. The maximum achievable luminosity is determined by this compromise between beamstrahlung and available power.

Three luminosities can be defined: $\mathcal{L}^{\rm RF}_{\rm pow}$ is the RF power limited luminosity (introduced earlier to analyse constant luminosity scaling); $\mathcal{L}^{\rm bb}_{\rm sat}$ is the beam-beam saturated luminosity; $\mathcal{L}^{\rm bs}_{\rm trans}$ is the beamstrahlung-limited luminosity. Single beam dynamics gives $\sigma_y = 0$ which implies $\mathcal{L}^{\rm RF}_{\rm pow} = \infty$? Nonsense. Recalling the earlier discussion, the resonance driving force, being proportional to $1/\sigma_y$ would also be infinite. As a result the beam-beam force expands $\sigma_y = 0$ as necessary. *Saturation is automatic* (unless the single beam emittance is already too great for the beam-beam force to take control—it seems this condition was just barely satisfied in highest energy LEP operation). Formulas for the luminosity limits are:

$$\mathcal{L}^{\rm RF}_{\rm pow} = \frac{1}{N_b}\, H(r_{yz})\, \frac{1}{a_{xy}}\, \frac{f}{4\pi} \left(\frac{n_1 P_{\rm rf}[\rm MW]}{\sigma_y}\right)^2, \qquad (7)$$

$$\mathcal{L}^{\rm bb}_{\rm sat} = N_{\rm tot.} H(r_{yz})\, f\, \frac{\gamma}{2r_e}\, (\xi^{\rm sat.}/\beta_y), \qquad (8)$$

$$\mathcal{L}^{\rm bs}_{\rm trans} = N_b H(r_{yz})\, a_{xy} \sigma_z^2\, f \left(\frac{\sqrt{\pi}\ 1.96\times 10^5}{28.0\,\rm m\ \sqrt{2/\pi}}\right)^2 \times \times \frac{1}{r_e^2 \widetilde{E}^2} \left(\frac{91\eta}{\ln\left(\frac{1/\tau_{\rm bs}}{f\, n^*_{\gamma,1}\, \mathcal{R}^{\rm Gauss}_{\rm unif.}}\right)}\right)^2. \qquad (9)$$

Here $H(r_{yz})$ is the hourglass reduction factor. If $\mathcal{L}^{\rm bs}_{\rm trans} < \mathcal{L}^{\rm bb}_{\rm sat}$ we must increase $N_b$. But $\mathcal{L}^{\rm bs}_{\rm trans} \propto N_b$, and $\mathcal{L}^{\rm RF}_{\rm pow} \propto 1/N_b$. We accept the compromise $N_{\rm b,new}/N_{\rm b,old} = \mathcal{L}^{\rm bb}_{\rm sat}/\mathcal{L}^{\rm bs}_{\rm trans}$ as good enough.

Parameter tables, scaled up from LEP, are given for 100 km circumference Higgs factories in Tables 5 and 6. The former of these tables assume the number of bunches $N_b$ is unlimited. The latter table derates the luminosity under the assumtion that $N_b$ cannot exceed 200. Discussion of the one ring vs two rings issue can therefore be based on Table 6.

Some parameters not given in tables are: Optimistic=1.5 (a shameless excuse for actual optimatization), $\eta_{\rm Telnov}$=0.01 (lattice fractional energy acceptance), $\tau_{\rm bs}$=600 s, $R_{\rm GauUnif}$= 0.300, $P_{rf}$ = 25 MW, Over Voltage=20 GeV, aspect ratio $a_{xy}$=15, $r_{yz} = \beta^*_y/\sigma_z$=1, and $\beta_{\rm arc\ max}$=198.2 m.

With the exception of the final table, which is specific to the single ring option, the following tables apply equally to single ring or dual ring Higgs factories. The exception relates to $N_b$, the number of bunches in each beam. With $N_b$ unlimited (as would be the case with two rings) all parameters are the same for one or two rings (at least according to the formulas in this paper).

## ONE RING OR TWO RINGS?

With one ring, the maximum number of bunches is limited to approximately ≤ 200. (I have not studied crossing angle schemes which may permit this number to be increased.) For $N_b > 200$ the luminosity $\mathcal{L}$ has to be de-rated accordingly; $\mathcal{L} \to \mathcal{L}_{\rm actual} = \mathcal{L} \times 200/N_b$. This correction is applied in Table 6. This table, whose entries are simply drawn from Table 5, makes it easy to choose between one and two rings. Entries in this table have been copied into the earlier Table 2. When the optimal number of bunches is less than (roughly) 200, single ring operation is satisfactory, and hence favored. When the optimal number of bunches is much greater than 200, for example at the $Z_0$ energy, two rings are better.

Note though, that the $Z_0$ single ring luminosities are still very healthy. In fact, with $\beta^*_y$=10 mm, which is a more conservative estimate than most others in this paper and in other FCC reports, the $Z_0$ single ring penalty is substantially less.

Luminosities and optimal numbers of bunches in Phase II Higgs factory running are shown in Figure 3.

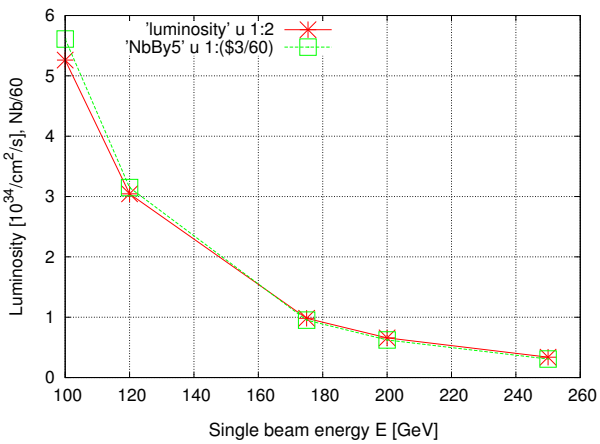


Figure 3: Dependence of luminosity on single beam energy (after upgrade to Stage II luminosity). The number of bunches (axis label to be read as $N_b/60$) is also shown, confirming that (as long as the optimal value of $N_b$ is 1 or greater) the luminosity is proportional to the number of bunches. There is useful luminosity up to $E$ = 500 GeV CM energy.

## REFERENCES

[1] J. Jowett, *Beam Dynamics at LEP,* CERN SL/98-029 (AP), 1998

[2] R. Talman, *Specific Luminosity Limit of e+/e- Colliding Rings,* Phys. Rev. ST-AB, 2002



ISBN 978-3-95450-172-4

Table 3: Single beam parameters, assuming 100 km circumference. The second last column (†) lists the value of $\epsilon_x$ appropriate only for $\beta_y^* = 5$ mm. Though determined by arc optics, $\epsilon_x$ has to be adjusted, according to the value of $\beta_y^*$, to optimize the beam shape at the IP. Other cases can be calculated from entries in other tables. $U_1$ is the energy loss per turn per particle. $u_c$ is the critical energy for bending element synchrotron radiation. $\delta$ is the synchrotron radiation damping decrement.

| name | $E$ GeV | $C$ km | $R$ km | $f$ KHz | $U_1$ GeV | $eV_{\mathrm{excess}}$ GeV | $n_1$ elec./MW | $\delta = \alpha_2$ | $u_c$ GeV | $\epsilon_x$† nm | $\sigma_x^{\mathrm{arc}}$ mm |
|---|---|---|---|---|---|---|---|---|---|---|---|
| Z | 46 | 100 | 10.6 | 3.00 | 0.04 | 20 | 5.81e+13 | 0.00020 | 0.00002 | 0.573 | 2 |
| W | 80 | 100 | 10.6 | 3.00 | 0.34 | 20 | 6.08e+12 | 0.00107 | 0.00011 | 1.771 | 1.19 |
| LEP | 100 | 100 | 10.6 | 3.00 | 0.83 | 19 | 2.49e+12 | 0.00209 | 0.00021 | 2.767 | 0.972 |
| H | 120 | 100 | 10.6 | 3.00 | 1.73 | 18 | 1.20e+12 | 0.00361 | 0.00036 | 3.984 | 0.824 |
| tt | 175 | 100 | 10.6 | 3.00 | 7.83 | 12 | 2.66e+11 | 0.01119 | 0.00112 | 8.473 | 0.585 |

Table 4: Higgs factory parameter values for 50 km and 100 km options. The entries are mainly extrapolated from Jowett's, 45.6 Gev report [1], and educated guesses. "N/Sc." indicates (important) parameters too complicated to be estimated by scaling. Duplicate entries in the third column, such as 45.6/91.5 are from Jowett [1]; subsequent scalings are based on the 45.6 Gev values.

| Parameter | Symbol | Value | Unit | Energy-scaled | Radius- | scaled |
|---|---|---|---|---|---|---|
| Mean bend radius | $R$ | **3026** | m | **3026** | **5675** | **11350** |
| | $R/3026$ | | | 1 | 1.875 | 3.751 |
| Beam Energy | $E$ | **45.6**/91.5 | GeV | **120** | **120** | **120** |
| Circumference | $C$ | 26.66 | km | 26.66 | 50 | 100 |
| Cell length | $L_c$ | | m | 79 | 108 | 153 |
| Momentum compaction | $\alpha_c$ | 1.85e-4 | | 1.85e-4 | 0.99e-4 | 0.49e-4 |
| Tunes | $Q_x$ | 90.26 | | 90.26 | 123.26 | 174.26 |
| | $Q_y$ | 76.19 | | 76.19 | 104.19 | 147.19 |
| Partition numbers | $J_x/J_y/J_\epsilon$ | 1/1/2 | | 1/1.6/1.4 ! | 1/1/2 | 1/1/2 |
| Main bend field | $B_0$ | 0.05/0.101 | T | 0.1316 | 0.0702 | 0.0351 |
| Energy loss per turn | $U_0$ | 0.134/2.05 | GeV | 6.49 | 3.46 | 1.73 |
| Radial damping time | $\tau_x$ | 0.06/0.005 | s | 0.0033 | 0.0061 | 0.0124 |
| | $\tau_x/T_0$ | 679/56 | turns | 37 | 69 | 139 |
| Fractional energy spread | $\sigma_\delta$ | 0.946e-3/1.72e-3 | | 0.0025 | 0.0018 | 0.0013 |
| Emittances (no BB), $x$ | $\epsilon_x$ | 22.5/30 | nm | 21.1 | 8.2 | 2.9 |
| $y$ | $\epsilon_y$ | 0.29/0.26 | nm | 1.0 | 0.4 | 0.14 |
| Max. arc beta functs | $\beta_x^{\max}$ | 125 | m | 125 | 171 | 242 |
| Max. arc dispersion | $D^{\max}$ | 0.5 | m | 0.5 | 0.5 | 0.5 |
| Beta functions at IP | $\beta_x^*, \beta_y^*$ | 2.0,0.05 | m | 1.25/0.04 | N/Sc. | N/Sc. |
| Beam sizes at IP | $\sigma_x^*, \sigma_y^*$ | 211, 3.8 | $\mu$m | 178/11 | N/Sc. | N/Sc. |
| Beam-beam parameters | $\xi_x, \xi_y$ | 0.037,0.042 | | 0.06/0.083 | N/Sc. | N/Sc. |
| Number of bunches | $N_b$ | 8 | | 4 | N/Sc. | N/Sc. |
| Luminosity | $\mathcal{L}$ | 2e31 | $\mathrm{cm}^{-2}\mathrm{s}^{-1}$ | 1.0e32 | N/Sc. | N/Sc. |
| Peak RF voltage | $V_{\mathrm{RF}}$ | 380 | MV | 3500 | N/Sc. | N/Sc. |
| Synchrotron tune | $Q_s$ | 0.085/0.107 | | 0.15 | N/Sc. | N/Sc. |
| Low curr. bunch length | $\sigma_z$ | 0.88 | cm | $\frac{\alpha_c R \sigma_e}{Q_s E}$ | N/Sc. | N/Sc. |



ISBN 978-3-95450-172-4

Table 5: The major factors influencing luminosity, assuming 100 km circumference and 25 MW/beam RF power. The predicted luminosity is the smallest of the three luminosities, $\mathcal{L}^{\mathrm{RF}}$, $\mathcal{L}^{\mathrm{bs}}_{\mathrm{trans}}$, and $\mathcal{L}^{\mathrm{bb}}$. All entries in this table apply to either one ring or two rings, except where the number of bunches $N_b$ is too great for a single ring.

| name | $E$ | $\epsilon_x$ | $\beta^*_y$ | $\epsilon_y$ | $\xi_{\mathrm{sat}}$ | $N_{\mathrm{tot}}$ | $\sigma_y$ | $\sigma_x$ | $u^*_c$ | $n^*_{\gamma,1}$ | $\mathcal{L}^{\mathrm{RF}}$ | $\mathcal{L}^{\mathrm{bs}}_{\mathrm{trans}}$ | $\mathcal{L}^{\mathrm{bb}}$ | $N_b$ | $\beta^*_x$ | $P_{\mathrm{rf}}$ |
|---|---|---|---|---|---|---|---|---|---|---|---|---|---|---|---|---|
| | GeV | nm | mm | pm | | $10^{12}$ | $\mu$m | $\mu$m | GeV | | $10^{34}$ | $10^{34}$ | $10^{34}$ | | m | MW |
| Z | 46 | 0.949 | 2 | 63.3 | 0.094 | 1500 | 0.356 | 5.34 | 0.000 | 2.01 | 52.5 | 103 | 52.5 | 65243 | 0.03 | 25 |
| W | 80 | 0.336 | 2 | 22.4 | 0.101 | 150 | 0.212 | 3.17 | 0.001 | 2.10 | 9.66 | 17.2 | 9.6 | 10980 | 0.03 | 25 |
| LEP | 100 | 0.223 | 2 | 14.9 | 0.101 | 62 | 0.172 | 2.59 | 0.002 | 2.13 | 4.95 | 8.46 | 4.94 | 5421 | 0.03 | 25 |
| H | 120 | 0.159 | 2 | 10.6 | 0.102 | 30 | 0.146 | 2.19 | 0.003 | 2.17 | 2.86 | 4.74 | 2.86 | 3044 | 0.03 | 25 |
| tt | 175 | 0.078 | 2 | 5.33 | 0.118 | 6.6 | 0.103 | 1.55 | 0.006 | 2.24 | 0.923 | 1.43 | 0.92 | 920 | 0.03 | 25 |
| Z | 46 | 17.2 | 5 | 1140 | 0.094 | 1500 | 2.39 | 35.89 | 0.001 | 2.16 | 21 | 35.1 | 21. | 3605 | 0.075 | 25 |
| W | 80 | 6.11 | 5 | 408 | 0.101 | 150 | 1.43 | 21.42 | 0.003 | 2.26 | 3.86 | 5.83 | 3.86 | 602 | 0.075 | 25 |
| LEP | 100 | 4.07 | 5 | 271 | 0.101 | 62 | 1.16 | 17.47 | 0.005 | 2.31 | 1.98 | 2.86 | 1.97 | 296 | 0.075 | 25 |
| H | 120 | 2.92 | 5 | 195 | 0.102 | 30 | 0.987 | 14.80 | 0.008 | 2.35 | 1.15 | 1.6 | 1.14 | 166 | 0.075 | 25 |
| tt | 175 | 1.47 | 5 | 98.1 | 0.118 | 6.6 | 0.7 | 10.51 | 0.017 | 2.43 | 0.369 | 0.479 | 0.37 | 49 | 0.075 | 25 |
| Z | 46 | 155 | 10 | 10300 | 0.094 | 1500 | 10.2 | 152.3 | 0.002 | 2.29 | 10.5 | 15.5 | 10.5 | 400 | 0.15 | 25 |
| W | 80 | 55.4 | 10 | 3690 | 0.101 | 150 | 6.08 | 91.17 | 0.007 | 2.41 | 1.93 | 2.55 | 1.93 | 66 | 0.15 | 25 |
| LEP | 100 | 37.0 | 10 | 2470 | 0.101 | 62 | 4.97 | 74.48 | 0.011 | 2.46 | 0.989 | 1.25 | 0.99 | 32 | 0.15 | 25 |
| H | 120 | 26.6 | 10 | 1770 | 0.102 | 30 | 4.21 | 63.15 | 0.016 | 2.50 | 0.573 | 0.696 | 0.57 | 18.3 | 0.15 | 25 |
| tt | 175 | 13.5 | 10 | 898 | 0.118 | 6.6 | 3.0 | 44.94 | 0.036 | 2.60 | 0.185 | 0.207 | 0.19 | 5.5 | 0.15 | 25 |

Table 6: Luminosites achievable with a single ring for which the number of bunches $N_b$ is limited to 200, assuming 100 km circumference and 25 MW/beam RF power. Entries in this table have been distilled down to include only the most important entries in Table 5, as corrected for the restricted number of bunches. The luminosity entries in Table 2 have been obtained from this table.

| $E$ | $\beta^*_y$ | $\xi_{\mathrm{sat}}$ | $\mathcal{L}_{\mathrm{actual}}$ | $N_{\mathrm{actual}}$ | $P_{\mathrm{rf}}$ |
|---|---|---|---|---|---|
| GeV | m | | $10^{34}$ | | MW/beam |
| 46 | 0.002 | 0.094 | 0.161 | 200 | 25 |
| 80 | 0.002 | 0.1 | 0.176 | 200 | 25 |
| 100 | 0.002 | 0.1 | 0.182 | 200 | 25 |
| 120 | 0.002 | 0.1 | 0.188 | 200 | 25 |
| 175 | 0.002 | 0.12 | 0.200 | 200 | 25 |
| 46 | 0.005 | 0.094 | 1.165 | 200 | 25 |
| 80 | 0.005 | 0.1 | 1.282 | 200 | 25 |
| 100 | 0.005 | 0.1 | 1.334 | 200 | 25 |
| 120 | 0.005 | 0.1 | 1.145 | 166 | 25 |
| 175 | 0.005 | 0.12 | 0.369 | 50 | 25 |
| 46 | 0.010 | 0.094 | 5.247 | 200 | 25 |
| 80 | 0.010 | 0.1 | 1.932 | 66.5 | 25 |
| 100 | 0.010 | 0.1 | 0.989 | 32.7 | 25 |
| 120 | 0.010 | 0.1 | 0.573 | 18.3 | 25 |
| 175 | 0.010 | 0.12 | 0.185 | 5.5 | 25 |



ISBN 978-3-95450-172-4

# SINGLE RING MULTIBUNCH OPERATION AND BEAM SEPARATION

Richard Talman
Laboratory of Elementary-Particle Physics,
Cornell University

*Abstract*

The counter-circulating electrons and positrons in a circular Higgs Factory have to be separated everywhere except at the $N^*$ intersection points (IP). The separation has to be electric and, to avoid unwanted increase of vertical emittance $\epsilon_y$, the separation has to be horizontal. This paper considers only head-on collisions at $N^* = 2$ IP's, with the beams separated everywhere else (but with nodes at RF cavities) by closed electric bumps.

## ELECTRIC BUMP BUNCH SEPARATION

### *Operating Energies*

Typical energies for "Higgs Factory" operation are established by the cross sections shown in Figure 1. We arbitrarily choose 120 GeV per beam as the Higgs particle operating point and identify the single beam energy this way in subsequent tables. Similarly identified are the $Z_0$ energy (45.6 GeV), the W-pair energy of 80 GeV, the LEP energy (arbitrarily taken to be 100 GeV) and the $t\bar{t}$ energy of 175 GeV to represent high energy performance.

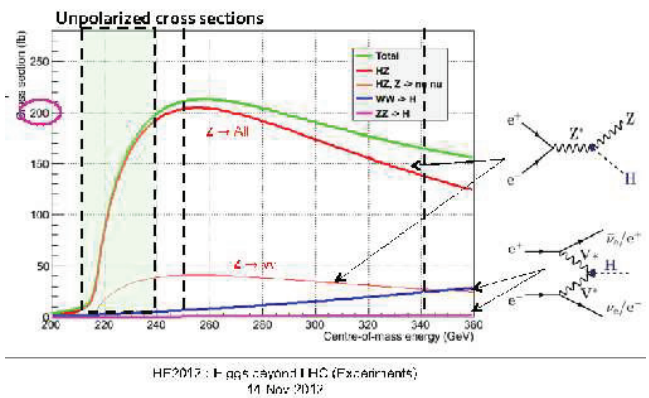


Figure 1: Higgs particle cross sections up to $\sqrt{s} = 0.3$ TeV (copied from Patrick Janot); $\mathcal{L} \geq 2 \times 10^{34}/\text{cm}^2/\text{s}$, will produce 400 Higgs per day in this range.

### *Bunch Separation at LEP*

Much of the material in this section has been drawn from John Jowett's article "Beam Dynamics at LEP" [1]. When LEP was first commissioned for four bunches ($N_b$=4) and four IPs ($N^*$=4) operation, bunch collisions at the 45 degree points were avoided by vertical electric separation bumps. It was later realized that vertical bumps are inadvisable because of their undesirable effect on vertical emittance $\epsilon_y$, which needs to be minimized. We therefore consider only horizontal separation schemes.

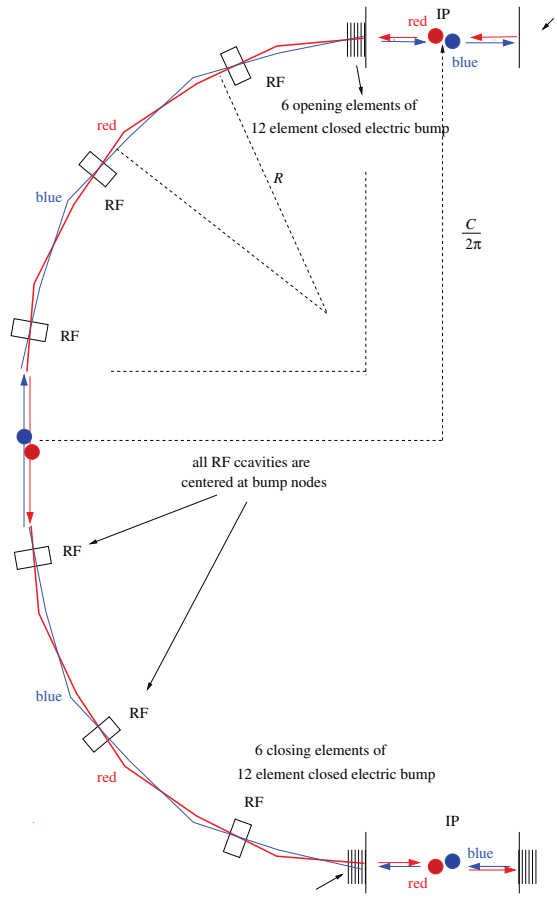


Figure 2: Cartoon illustrating beam separation in one arc of a Higgs factory. There are $N_b$=4 bunches in each beam and $N^*$=2 interaction points (IP). The bend radius $R$ is significantly less than the average radius $C/(2\pi)$; roughly $C = 3\pi R$. For scaling purposes $R$ and $C$ are taken to be strictly proportional. Far more separation loops and crossovers are actually needed than are shown.

Various horizontal pretzel separation schemes were tried at LEP. They were constrained by the need to be superimposed on an existing lattice. LEP investigations in the early 1990's mainly concentrated on what now would be called quite low energies, especially the $Z_0$ energy, $E = 45.6$ GeV. For a Higgs factory we need to plan for energies four or five times higher. The required product of separator length multiplied by electric separator field has to be greater by the same factor to obtain the same angular separation. Actually the factor may have to be somewhat greater than this because of the larger bunch separation needed with increased ring circumference.

ISBN 978-3-95450-172-4

Before continuing, allow me a brief digression concerning the etymology of the technical and metaphorical term "pretzel". The term was coined by Raphael Littauer, the inventor of pretzel beam separation. Raphael's language skills, even not in his mother tongue, rivaled his physics skills, which is a very high standard indeed. The pretzel "idea" first came to Boyce "Mac" McDaniel, director of the Cornell Laboratory of Nuclear Studies at the time. But it was Raphael that fleshed out the idea and led its successful implementation.

Separating the beam in a pre-existing ring is significantly more difficult than designing beam separation during the planning stage, as was done, for example, for the 45 degree separation points in the initial LEP ring. Obviously the separators have to be electric and therefore probably quite long. At CESR there was no free space long enough, so an existing magnet had to be made shorter and stronger to free up space for an electric separator. Even so, the required electric field was uncomfortably large.

With $N_b$ equally-spaced bunches in each of the counter-rotating beams the beams need to be separated at the $2N_b - N^*$ "parasitic" crossing points. Standard closed bumps are typically $\pi$-bumps or $2\pi$ bumps. But, with 4 deflectors, two at each end of a sector, bumps can easily be designed to be $n\pi$ bumps, where $n$ is an arbitrary integer matched to the desired number of separation points.

As first realized by McDaniel, instead of having closed bumps one can make do with a single separator. The effect of a single electric deflection is to make the closed orbits of the counter-circulating beams different *everywhere*. Even in this case there are periodic "nodes" at which the distorted orbits cross. To achieve the desired beam separation, one has only to arrange for the desired crossing points to be at nodes and the parasitic crossing points to be at "loops" of the respective closed orbits.

Littauer introduced the picturesque term "pretzel" to distill the entire discussion of the previous four paragraphs into a single word. I have reviewed this history as reaction against the recent indiscriminate use of the term pretzel to describe separation schemes irrespective of whether or not they match the metaphor. This may be overly pedantic, but a name such as "multibump" or, to preserve the chronology, "closed pretzel" would more accurately describe the beam separation scheme I propose. When designing a collider from scratch it seems to me unlikely that a pretzel, as the term was originally understood, will ever be optimal.

This discussion is illustrated pictorially in Figure 3 using a space-time plot introduced (in this context) by John Jowett. The beams are plotted as "world trajectories", whose crossings in space do not, in general, coincide with their crossings in time. Separated points with the same label correspond to the same point at different times.

In the figure, associating point 4 with point 1 would correspond to the original pretzel scheme in which the counter-circulating orbits are different everywhere in the ring. With the proposed "closed pretzels" there is no such association. The separated beams are smoothly merged onto common orbits at both ends.

It is important to distinguish transverse bump displacement from the time axis in the space-time diagram. A head-on collision occurs when two populated bunches pass through the same space-time point. To avoid parasitic crossings the minimum bunch separation distance is therefore twice the closed bump period.

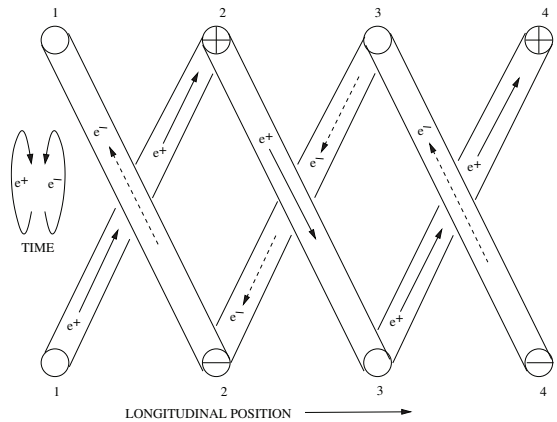


Figure 3: A minimal and modified "Jowett Toroidal Space-Time Beam Separation Plot" illustrating the separation of counter-circulating beams. Points with the same label at the top and the bottom of the plot are the same points (at different times). Though drawn to suggest a toroid the plot is purely two dimensional. The original Littauer pretzel encompassed the whole ring—that is, in this figure, points 1 and 4 would also be identified. But this identification is not essential.

Another separation scheme tried at LEP was local electric bumps close to the 4 IP's and angle crossing to permit "trains" with more than one bunch per train. This permitted as many as 4 bunches per train though, in practice, more than 3 were never used. For lack of time this option is not considered in this paper.

The primary horizontal separation scheme at LEP is illustrated in Jowett's clear, but complicated, Figure 3 [1,2]. The scheme used 8 primary separators and 2 trim separators with the separation bumps continuing through the 4 IP's, and with the physics detectors centered on pretzel nodes to enable collisions there. Starting from scratch in a circular collider that is still on the drawing board, one hopes for a simpler separation scheme.

## *Separated Beams and RF Cavities*

By introducing slightly shortened, slightly strengthened, special purpose bending magnets to make space for electric separators, multi-element electric bumps can be located arbitrarily without seriously perturbing any existing lattice design. But there is an issue with separated orbits and RF cavities. Probably both beams should pass through the centers of the RF cavities. But it seems safe to assume that the closed orbit angles through the RF can be (symmetrically)



ISBN 978-3-95450-172-4

different from zero. Otherwise, far more electric separators will be required, and far fewer bunches would be possible. RF cavities are therefore to be placed at beam separation nodes. (This may complicate betatron tune tunability?)

"Topping-off" injection is essential; especially to permit large beam-beam tune shifts. As long as the beam current is constant the beam-beam deflection is equivalent to an ideal lens, focusing in both planes, though with strong octupole superimposed. The linear focusing part can be incorporated into the (linear) lattice optics. And the superimposed octupole is not necessarily very damaging. Strong damping makes bump-free, kicker-free, bunch-by-bunch, high-efficiency, vertical injection possible. Then steady-state, continuous operation without fill cycling may be possible.

Somewhat reduced beam separation at bump ends is assumed to be acceptable. With crossing angle the number of bunches may later be increased.

## 6 + 6 ELEMENT CLOSED ELECTRIC BUMP

Bunches must not collide in arcs. They should be separated by at least 10 beam width sigmas when they pass. With both beams passing through the same RF, the path lengths between RF cavities probably have to be equal. A single ring is as good as dual rings if the total number of bunches can be limited to, say, less than 200. Here it is proposed to support only head-on collisions at each of the two IP's. The minimum bunch spacing will then be slightly greater than the total length of the intersection region (IR).

The half ring shown in Figure 2 shows a closed electric bump in the west arc. Orbits are common only in the two IR's. On the exit from each IR an electric bump is started and the bump is closed just before the next IR. These "bumps" are very long, almost half the circumference. As already explained, this is not "pretzel" beam separation, as that term was initially understood. Other than being horizontal rather than vertical and having multiple avoided parasitic collisions, these are much like the four separation bumps in the original LEP design.

Closed bumps require at least 3, or for symmetry, 4 controllable deflectors. Here a 12-bump scheme is described, with 6 electrostatic separators at the bump start and 6 at the bump stop. This scheme could be needed if the lattice cell lengths are too short to contain sufficiently strong electric separators. In my WG6 paper I show that the optimal collider cell length $L_i$ is significantly longer than was assumed when this separation scheme was designed. With longer cells a simpler 4 or 6 kicker bump may be adequate.

The design orbit spirals in significantly; this requires the RF acceleration to be distributed quite uniformly. Basically the ring is a "curved linac". The only betatron tune tunability is in the arcs. As the arc phase advances are changed (by a percent or so) the bumps have to be closed (very accurately) by tuning phase advance per cell and electric separators. As with beam separation in LEP, trim separators may be required.

Sketches and design formulas for a multi-element electric bump are shown in Figure 4. Figure 5 exhibits the separation of up to 112 bunches in a 50 km ring. Notice that, to avoid head-on parasitic collisions, the bunch separations are equal to two wavelengths of the electric bump pattern.

## BUNCH SEPARATION PARTITION NUMBER SHIFT

(Mangling Jowett's careful formulation [1] for brevity) the longitudinal partition number $J_\epsilon$ depends on focusing function $K_1$, dispersion $D$, and on fractional momentum offset, $\delta = \bar{\delta} + \delta_{s.o.}$ (where "s.o." stands for synchrotron oscillation) and separator displacement $x_p(s)$;

$$J_\epsilon(\delta, x_p) = 2 + \frac{2\oint K_1^2 D^2 ds}{\oint (1/R^2) ds}(\bar{\delta} + \delta_{s.o.}) + \\ + \frac{2\oint K_1^2 (D(s) - D_0(s)) x_p(s) ds}{\oint (1/R^2) ds}; \quad (1)$$

here $D/D_0$ are the separator-on/separator-off horizontal dispersion functions. The middle term here can be used to shift $J_\epsilon$ away from 2, as proved useful at LEP, but it does not depend on $x_p$; it is shown only as protection against confusing it with the final term.

Setting $\bar{\delta} + \delta_{s.o.}$=0, and averaging, the separator-displaced partition number is

$$J_\epsilon(|x_p|) = 2 + \frac{2 < K_1^2 (D - D_0) x_p >}{< 1/R^2 >}. \quad (2)$$

In spite of $x_p$ averaging to zero, there is a non-vanishing shift of $J_\epsilon(|x_p|)$ because $K_1$, $D$, and $x_p$ are correlated. At LEP this shift was observed to be significanly damaging and to be dominated by sextupoles. The factors in Eq. (2) scale as

$$x_p \propto \sigma_x \propto \frac{1}{R^{1/2}}, \quad K_1 = \frac{q}{l_q} \propto \frac{1/R^{1/2}}{R^{1/2}} \propto \frac{1}{R}, \\ D - D_0 \propto S \propto \frac{1}{R^{1/2}}, \quad \Delta J_\epsilon(|x_p|) \propto \frac{1}{R}. \quad (3)$$

These scaling formulas (derived in my WG 6 report) indicate that the seriousness of this partition number shift actually decreases with increasing $R$. Even if this were not true, should the partition number shift be unacceptably large, it can be reduced by increasing the quadrupole length $l_q$ to decrease $K_1$. The partition number shift is due to excess radiation in the quadrupoles. Since this radiation intensity is proportional to the square of the magnetic field, doubling the quadrupole length halves the radiation and the partition number shift.

## BEAM SEPARATION IN INJECTION-OPTIMIZED COLLIDER LATTICE

The beam separation scheme shown so far has used a very short collider cell length $L_c$ = 60 m. Table 1 (which is

ISBN 978-3-95450-172-4

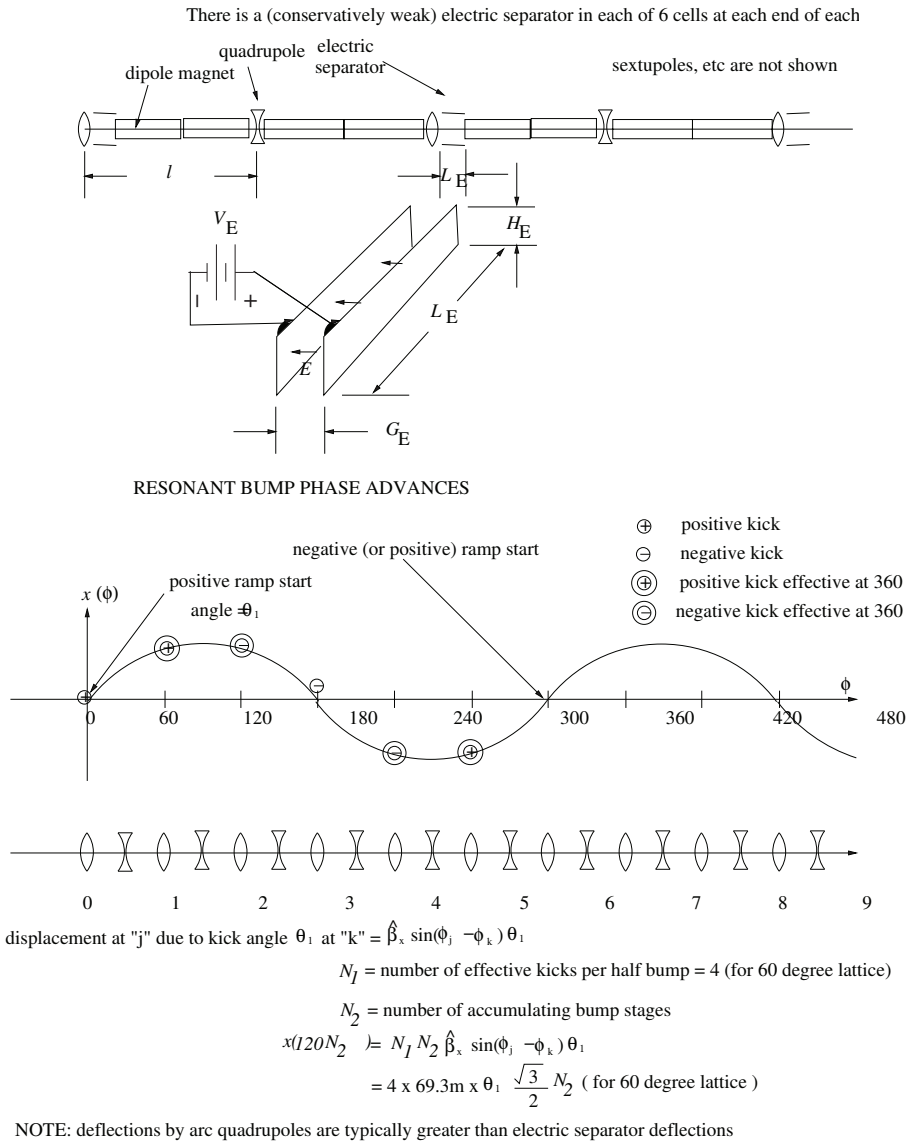


Figure 4: Sketches and design formulas for a multi-element electric bump.

explained in my W6 paper) describes the scaling of lattice parameters obtained after redesigning both injector and collider for efficient injection. The resulting collider cell length is $L_c = 213$ m. Because the cells are so long, there may be no need for multiple electrostatic separators. Instead one may use, for example, two or three electric kickers to launch each electric bump, with two or three matched kickers to terminate it. A large increase in cell length will surely also require a corresponding increase in longitudinal separation of circulating bunches. The single beam luminosity will be correspondingly reduced if the luminosity is already limited by the maximum number of bunches, as in the case of $Z_0$ production. The luminosity reduction should be little affected at the Higgs energy and above.

Irrespective of bunch separation schemes, the minimum bunch separation will still be at least equal to the length of the intersection region. For single ring operation this will probably be less restrictive than the bunch separation required for the separation scheme.

## PREDICTED LUMINOSITIES

With one 100 km circumference ring, the maximum number of bunches is limited to about 200. For $N_b < 200$ the luminosity $\mathcal{L}$ has to be reduced proportionally. $\mathcal{L} \rightarrow \mathcal{L}_{\rm actual} = \mathcal{L} \times N_b/200$. Luminosities in the 100 $km$, 25 MW case are given in my WG2 report "Ring Circumference and Two Rinfs vs One Ring". Here, for comparison, and to more nearly match the separation scheme shown in Figure 5, the circumference is assumed to be $C$=50 km, the RF power 50 MW per beam, and the number of bunches $N_b$=112. The results are shown in Table 3 (unlimited $N_b$) and Table 4 (with $N_b$=112); saturation tune shifts from reference [3].



ISBN 978-3-95450-172-4

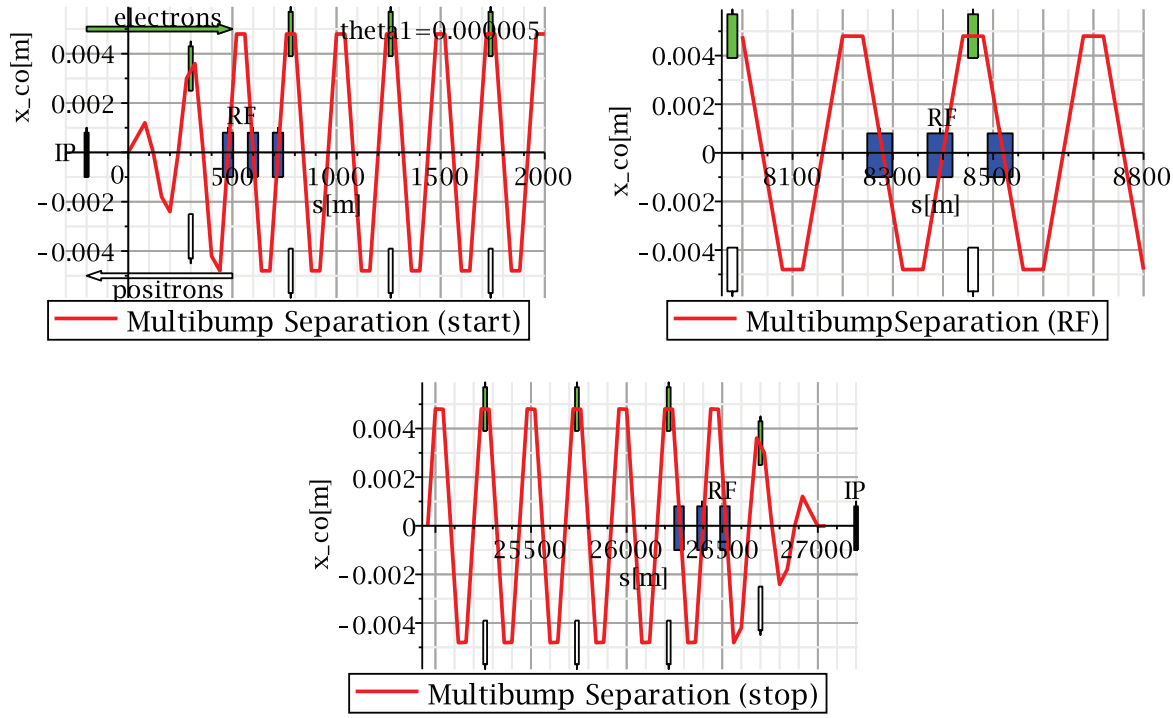


Figure 5: Short partial sections of the multibump beam separation are shown: one at the beginning, one at an RF location in the interior, and one at the far end of a long arc in Figure 2. The bunch separations are 480 m in a 50 km ring with cell length $L_c$ = 60 m. IP's are indicated by vertical black bars, RF cavities by blue rectangles, electron bunches are green rectangles moving left to right, positron bunches are open rectangles moving from right to left. Counter-circulating bunches are separated at closed bump loop locations, and they must not pass through the nodes at the same time.

The values of parameters not shown in the tables are $\eta_{\text{Telnov}}$=0.01, $\beta_y^*$ =5 mm, $xi^{\text{typ.}}/\beta_y^*$=22.8, $\tau_{\text{bs}}$=600 s, Optimistic= 1.5, $R_{\text{Gau-unif}}$=0.30, $eV_{\text{rf}}$=20 GeV, $OV_{\text{req.}}$=20 GV, $a_{xy}$=15, $r_{yz}$=1, $\beta_{x,\text{arcmax}}$=120 m.

## REFERENCES

[1] J. Jowett, *Beam Dynamics at LEP,*CERN SL/98-029 (AP), 1998

[2] J. Jowett, *More Bunches with Pretzel,* Private communication "pzl6.dvi".

[3] R. Talman, *Specific Luminosity Limit of e+/e- Colliding Rings,*Phys. Rev. ST-AB, 2002

ISBN 978-3-95450-172-4

Table 1: Scaling of Collider Lattice Parameters for Improved Injection Efficiency Collider

| Parameter | Symbol | Proportionality | $L \propto R^{3/4}$ collider | Values $C$=100 km |
|---|---|---|---|---|
| phase advance per cell | $\mu_x$ | | 90° | |
| cell length | $L$ | | $R^{3/4}$ | 213 m |
| bend angle per cell | $\phi$ | $= L/R$ | $R^{-1/4}$ | |
| quad strength $(1/f)$ | $q$ | $1/L$ | $R^{-3/4}$ | |
| dispersion | $D$ | $\phi L$ | $R^{1/2}$ | |
| beta | $\beta$ | $L$ | $R^{3/4}$ | |
| tune | $Q_x$ | $R/\beta$ | $R^{1/4}$ | 125.26 |
| tune | $Q_y$ | $R/\beta$ | $R^{1/4}$ | 105.19 |
| Sands's "curly H" | $\mathcal{H}$ | $= D^2/\beta$ | $R^{1/4}$ | |
| partition numbers | $J_x/J_y/J_\epsilon$ | 1/1/2 | 1/1/2 | |
| horizontal emittance | $\epsilon_x$ | $\mathcal{H}/(J_x R)$ | $R^{-3/4}$ | |
| fractional energy spread | $\sigma_\delta$ | $\sqrt{B}$ | $R^{-1/2}$ | |
| arc beam width-betatron | $\sigma_{x,\beta}$ | $= \sqrt{\beta\epsilon_x}$ | 1 | |
| -synchrotron | $\sigma_{x,synch.}$ | $= D\sigma_\delta$ | 1 | |
| sextupole strength | $S$ | $q/D$ | $R^{-5/4}$ | |
| dynamic aperture | $x^{\max}$ | $q/S$ | $R^{1/2}$ | |
| relative dyn. aperture | $x^{\max}/\sigma_x$ | | $R^{1/2}$ | |
| separator amplitude | $x_p$ | $\sigma_x$ | 1 | |

Table 2: Parameters Values Scaled from LEP

| Parameter | Symbol | LEP-extrapolated | Unit | Collider | |
|---|---|---|---|---|---|
| mean bend radius | $R$ | **3026** | m | **5675** | **11350** |
| beam energy | | 120 | GeV | 120 | 120 |
| circumference | $C$ | 26.7 | km | 50 | 100 |
| cell length | $L$ | 79 | m | 127 | 213 |
| momentum compaction | $\alpha_c$ | 1.85e-4 | m | 1.35e-4 | 0.96e-4 |
| tunes | $Q_x$ | 90.26 | | 105.26 | 125.26 |
| | $Q_y$ | 76.19 | | 89.19 | 105.19 |
| partition numbers | $J_x/J_y/J_\epsilon$ | 1/1.6/1.4 | | 1/1/2 | 1/1/2 |
| main bend field | $B_0$ | 0.1316 | T | 0.0702 | 0.0351 |
| energy loss per turn | $U_0$ | 6.49 | GeV | 3.46 | 1.73 |
| radial damping time | $\tau_x$ | 0.0033 | s | 0.0061 | 0.0124 |
| | $\tau_x/T_0$ | 37 | turns | 69 | 139 |
| fractional energy spread | $\sigma_\delta$ | 0.0025 | | 0.0013 | 0.0009 |
| emittances (no BB), $x$ | $\epsilon_x$ | **21.1** | nm | **13.2** | **7.82** |
| $y$ | $\epsilon_y$ | 1.0 | nm | 0.66 | 0.39 |
| max. arc beta functs | $\beta_x^{\max}$ | 125 | m | 200 | 337 |
| max. arc dispersion | $D^{\max}$ | 0.5 | m | 0.68 | 0.97 |
| quadrupole strength | $q \approx \pm 2.5/L_p$ | 0.0316 | 1/m | 0.0197 | 0.0117 |
| max. beam width (arc) | $\sigma_x = \sqrt{\beta_x^{\max}\epsilon_x}$ | 1.6 | mm | 1.625 | 1.558 |
| (ref) sextupole strength | $S = q/D$ | 0.0632 | $1/m^2$ | 0.0290 | 0.0121 |
| (ref) dynamic aperture | $x^{da} \sim q/S$ | ~0.5 | m | ~0.679 | ~0.967 |
| (rel-ref) dyn.ap. | $x^{da}/\sigma_x$ | ~0.313 | | ~0.417 | ~0.621 |
| separator amplitude | $\pm 5\sigma_x$ | ±8.0 | mm | ±8.1 | ±7.8 |



ISBN 978-3-95450-172-4

Table 3: Luminosity influencing parameters and luminosities with unlimited number of bunches $N_b$, assuming 50 km circumference ring and 50 MW per beam RF power.

| name | $E$ | $\epsilon_x$ | $\beta^*_y$ | $\epsilon_y$ | $\xi_{\mathrm{sat}}$ | $N_{\mathrm{tot}}$ | $\sigma_y$ | $\sigma_x$ | $u^*_c$ | $n^*_{\gamma,1}$ | $\mathcal{L}^{\mathrm{RF}}$ | $\mathcal{L}^{\mathrm{bs}}_{\mathrm{trans}}$ | $\mathcal{L}^{\mathrm{bb}}$ | $N_b$ | $\beta^*_x$ | $P_{\mathrm{rf}}$ |
|---|---|---|---|---|---|---|---|---|---|---|---|---|---|---|---|---|
| | GeV | nm | mm | pm | | | $\mu$m | $\mu$m | GeV | | $10^{34}$ | $10^{34}$ | $10^{34}$ | | m | MW |
| Z | 46 | 0.916 | 2 | 61.1 | 0.094 | 7.3e+14 | 0.35 | 5.24 | 0.000 | 1.97 | 52.5 | 96.8 | 52.513 | 33795 | 0.03 | 50 |
| W | 80 | 0.323 | 2 | 21.6 | 0.101 | 7.6e+13 | 0.208 | 3.12 | 0.001 | 2.06 | 9.66 | 16.2 | 9.661 | 5696 | 0.03 | 50 |
| LEP | 100 | 0.215 | 2 | 14.3 | 0.101 | 3.1e+13 | 0.169 | 2.54 | 0.002 | 2.10 | 4.95 | 8 | 4.947 | 2814 | 0.03 | 50 |
| H | 120 | 0.153 | 2 | 10.2 | 0.102 | 1.5e+13 | 0.143 | 2.15 | 0.003 | 2.13 | 2.86 | 4.48 | 2.863 | 1581 | 0.03 | 50 |
| tt | 175 | 0.077 | 2 | 5.12 | 0.118 | 3.3e+12 | 0.101 | 1.52 | 0.006 | 2.19 | 0.923 | 1.35 | 0.923 | 478 | 0.03 | 50 |
| Z | 46 | 16.5 | 5 | 1100 | 0.094 | 7.3e+14 | 2.35 | 35.21 | 0.001 | 2.12 | 21 | 33.2 | 21.005 | 1872 | 0.075 | 50 |
| W | 80 | 5.88 | 5 | 392 | 0.101 | 7.6e+13 | 1.4 | 20.99 | 0.003 | 2.22 | 3.86 | 5.52 | 3.864 | 313 | 0.075 | 50 |
| LEP | 100 | 3.91 | 5 | 261 | 0.101 | 3.1e+13 | 1.14 | 17.12 | 0.005 | 2.26 | 1.98 | 2.71 | 1.979 | 154 | 0.075 | 50 |
| H | 120 | 2.80 | 5 | 187 | 0.102 | 1.5e+13 | 0.966 | 14.50 | 0.007 | 2.30 | 1.15 | 1.52 | 1.145 | 86 | 0.075 | 50 |
| tt | 175 | 1.41 | 5 | 94 | 0.118 | 3.3e+12 | 0.686 | 10.28 | 0.016 | 2.38 | 0.369 | 0.455 | 0.369 | 26 | 0.075 | 50 |
| Z | 46 | 149 | 10 | 9900 | 0.094 | 7.3e+14 | 9.95 | 149.28 | 0.002 | 2.24 | 10.5 | 14.7 | 10.503 | 208 | 0.15 | 50 |
| W | 80 | 53.1 | 10 | 3540 | 0.101 | 7.6e+13 | 5.95 | 89.26 | 0.007 | 2.36 | 1.93 | 2.42 | 1.932 | 34 | 0.15 | 50 |
| LEP | 100 | 35.4 | 10 | 2360 | 0.101 | 3.1e+13 | 4.86 | 72.88 | 0.011 | 2.41 | 0.989 | 1.19 | 0.989 | 17 | 0.15 | 50 |
| H | 120 | 25.4 | 10 | 1700 | 0.102 | 1.5e+13 | 4.12 | 61.78 | 0.016 | 2.45 | 0.573 | 0.663 | 0.573 | 9.5 | 0.15 | 50 |
| tt | 175 | 12.9 | 10 | 857 | 0.118 | 3.3e+12 | 2.93 | 43.92 | 0.035 | 2.54 | 0.185 | 0.198 | 0.185 | 2.9 | 0.15 | 50 |

Table 4: Luminosity influencing parameters and luminosities with the number of bunches limited to $N_b = 112$, assuming 50 km circumference ring and 50 MW per beam RF power.

| $E$ | $\beta^*_y$ | $\xi_{\mathrm{sat}}$ | $\mathcal{L}_{\mathrm{actual}}$ | $N_{\mathrm{actual}}$ | $P_{\mathrm{rf}}$ |
|---|---|---|---|---|---|
| GeV | m | | $10^{34}$ | | MW |
| 46 | 0.002 | 0.094 | 0.174 | 112 | 50 |
| 80 | 0.002 | 0.1 | 0.190 | 112 | 50 |
| 100 | 0.002 | 0.1 | 0.197 | 112 | 50 |
| 120 | 0.002 | 0.1 | 0.203 | 112 | 50 |
| 175 | 0.002 | 0.12 | 0.216 | 112 | 50 |
| 46 | 0.005 | 0.094 | 1.256 | 112 | 50 |
| 80 | 0.005 | 0.1 | 1.380 | 112 | 50 |
| 100 | 0.005 | 0.1 | 1.434 | 112 | 50 |
| 120 | 0.005 | 0.1 | 1.145 | 86.6 | 50 |
| 175 | 0.005 | 0.12 | 0.369 | 26.1 | 50 |
| 46 | 0.010 | 0.094 | 5.644 | 112.0 | 50 |
| 80 | 0.010 | 0.1 | 1.932 | 34.7 | 50 |
| 100 | 0.010 | 0.1 | 0.989 | 17.1 | 50 |
| 120 | 0.010 | 0.1 | 0.573 | 9.5 | 50 |
| 175 | 0.010 | 0.12 | 0.185 | 2.9 | 50 |



ISBN 978-3-95450-172-4

# CHALLENGES AND STATUS OF THE FCC-*ee* LATTICE DESIGN

B. Haerer*, CERN, Geneva, Switzerland, KIT, Karlsruhe, Germany,
B. J. Holzer, CERN, Geneva, Switzerland

*Abstract*

Following the recommendations of the European Strategy Group for High Energy Physics, CERN started the Future Circular Collider Study (FCC), a design study for possible future circular collider projects to investigate their feasibility for high energy physics research. One part of this study is FCC-ee, an e+e- collider with a circumference of 100 km. Challenges for the lattice design result from operation at four different beam energies ranging from 45.5 GeV to 175 GeV. Very high beamstrahlung effects at high energies and the beam-beam limit at low energies request emittance parameters that rise with decreasing beam energy. This paper will present the status of the lattice design and the lattice modifications needed to achieve the requested emittance parameters.

## INTRODUCTION

The Large Electron Positron Collider (LEP) was the most powerful lepton machine that was ever build. Its maximum beam energy was limited by the available power of the RF cavities that fed back the high amount of energy lost by synchrotron radiation. When LEP finished operations in 1995 investigations of lepton machines with even higher beam energy moved to linear accelerators (e.g. CLIC, ILC). After nearly 20 years CERN launched a design study for the feasibility of circular colliders for future high energy physics research, called FCC. One part of the study, FCC-hh, is a possible proton discovery machine with 100 TeV center of mass energy. The circumference would be about 80 km-100 km based on $Nb_3Sn$ technology with magnetic fields of 16 T-20 T [1]. Given the technical infrastructure and the large bending radius of 10.6 km a future circular lepton collider for precision studies in the energy range of 90 GeV to 350 GeV could still be operated with an acceptable amount of synchrotron radiation loss. This part of the study, which could bring the come back of circular high energy lepton colliders, is called FCC-ee. As a third part, a proton electron option called FCC-he is considered. Deep inelastic scattering could basically be studied in two options: a LHeC like linac-ring option and a ring-ring option. In this paper the status of the FCC-ee lattice design and its modifications in order to achieve the requested emittance parameters are discussed in detail.

### *Physics Goals*

FCC-ee is designed to provide highest possible luminosity for precision studies of a wide physics program. This covers four different center of mass energies: 91 GeV for measurements of the Z pole, 160 , which is the W pair production threshold, 240 GeV for H production and the $t\bar{t}$ threshold at 350 GeV. To reach the goal of highest possible luminosity, for each of the physics programs a set of baseline parameters was assembled shown in Table 1.

## CHALLENGES

The limit of luminosity performance in a lepton storage ring strongly depends on the energy of the colliding beams. Thus the machine has to be designed and optimized for each of the four energies separately while using the same hardware. At high energies the luminosity lifetime is limited to 15-20 min by beamstrahlung [2]. This requires on the one hand top up injection from a full energy booster and on the other hand a very high momentum acceptance of 1-2 %. At low energies the luminosity is limited by the beam-beam effect, which creates a tuneshift of the working point. Assuming two equal beams sizes the beam-beam parameter is given by [3]

$$\xi_q = \frac{N r_e}{\gamma} \frac{\beta_q^*}{2\pi\sigma_q(\sigma_x + \sigma_y)}, \qquad (1)$$

where $q$ stands for $x$ or $y$ and $N$ is the bunch population. To keep the tuneshift small, the beam size $\sigma$ must be increased by a larger emittance. However in electron storage rings the horizontal equilibrium emittance is proportional to $\gamma^2$ [4], so the emittance is decreasing with lower energy. Consequently the lattice needs to be modified between operation at different energies. At the same time a very small ration of vertical and horizontal emittance of 0.1 % must be achieved for highest luminosity. The vertical emittance of 1 pm corresponds to performances of synchrotron light sources and sets serious constraints on the alignment requirements of the machine.

At 175 GeV beam energy very high synchrotron radiation losses of 7.5 GeV per turn will require a sophisticated absorber design to protect the vacuum chamber. Furthermore equally distributed RF sections will be needed to keep the energy sawtooth effect on a reasonable level. At 45.5 GeV beam energy the high beam current and the large number of bunches make it mandatory to use two separated vacuum chambers instead of a common one and a crossing angle in the interaction region to avoid multiple bunch crossings inside the detector. A further challenge for the interaction region design is the very small vertical beta function at the interaction point $\beta^* = 1$ mm. Very strong focusing is required, which creates high chromaticity. Therefore a local chromaticity correction scheme is foreseen before entering the arcs [5]. Still the strong sextupoles must provide sufficient dynamic aperture for momentum deviations of up to 2 % created by the beamstrahlung.

* bastian.harer@cern.ch



ISBN 978-3-95450-172-4

Table 1: Compendium of Baseline Parameters for the Different Physics Programs of FCC-ee [2]

| | FCC-ee Z | FCC-ee W | FCC-ee H | FCC-ee tt |
|---|---|---|---|---|
| Beam energy (GeV) | 45.5 | 80 | 120 | 175 |
| Beam current (mA) | 1450 | 152 | 30 | 6.6 |
| Bunches/beam | 16700 | 4490 | 1330 | 160 |
| Transverse emittance $\epsilon$ (nm) | | | | |
| - Horizontal | 29.2 | 3.3 | 0.94 | 2 |
| - Vertical | 0.06 | 0.007 | 0.0019 | 0.002 |
| Betatron function at IP $\beta^*$ (m) | | | | |
| - Horizontal | 0.5 | 0.5 | 0.5 | 1 |
| - Vertical | 0.001 | 0.001 | 0.001 | 0.001 |
| Energy loss/turn (GeV) | 0.03 | 0.33 | 1.67 | 7.55 |
| Total RF voltage (GV) | 2.5 | 4 | 5.5 | 11 |
| Peak luminosity ($10^{34}$ cm$^{-2}$s$^{-1}$) | 28.0 | 12.0 | 5.9 | 1.2 |

## THE FCC-EE LAYOUT

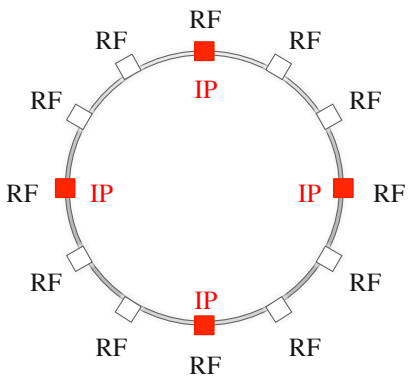


Figure 1: The layout of the FCC-ee lattice. Twelve dispersion free straight sections are equally distributed around the ring. The ones housing RF are marked in white, the ones that also include an interaction point (IP) in red.

The FCC-ee layout illustrated in figure 1 has a circular shape with the circumference of 100 km. Twelve dispersion free straight sections with the length of 1.5 km each are equally distributed to house RF installation. Four of them additionally contain mini-beta insertions for the experiments in a 4-fold symmetry. The final length of the straight sections for injection, beam dump, collimation and RF is determined by the requirements of the FCC hadron machine. The straight sections including experiments need to provide enough space for the interaction region of FCC-ee, which probably will be broader and longer than the one of FCC-hh due to the chromaticity correction scheme [1]. The twelve arcs in-between the straight sections have a length of 6.8 km including half-bend dispersion suppressors at the beginning and at the end. Currently they still consist of two sub-arcs, divided by a dispersion suppressor. To store a high number of bunches, two separate beam pipes are foreseen, which are placed side-by-side to conserve polarization and avoid vertical dispersion. However in this early design stage one single ring is implemented. For the calculations presented in this paper, the straight sections including mini-beta insertions were replaced by regular straight sections. This has no influence on the equilibrium emittance as the emittance is defined by the parts of the lattice with non-zero dispersion.

## THE FCC-EE FODO CELL

The regular FCC-ee arc FODO cell is designed for 175 GeV beam energy and is the basis for the High Energy Lattice. A non-scale sketch is provided in figure 2. The cell is 50 m long and contains four bending magnets with the length of 10.5 m each. According to calculations of the CERN vacuum group after this length an absorber must be installed to protect the vacuum chamber from the synchrotron light fan. In addition lumped absorbers will be placed inside the vacuum chamber in the middle of each bending magnet [6]. Both focusing and defocussing quadrupoles have the length of 1.5 m and divide the cell into two parts with equal length. After each quadrupole a sextupole, a beam position monitor and a corrector magnet for the respective plane are placed. The current FCC-ee FODO cell layout already considers drift spaces for absorbers, flanges and bellows. In the straight sections the bending magnets are replaced by RF cavities.

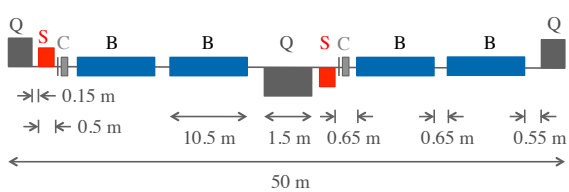


Figure 2: Non-scale sketch of the FCC-ee FODO cell. Bending magnets are labeled with B, quadrupoles with Q and sextupoles with S. C stands for a collective of beam position monitor and a corrector.

### *Optical Functions*

Following LEP experience a phase advance of 90 ° per cell in the horizontal plane and 60 ° in the vertical plane

ISBN 978-3-95450-172-4

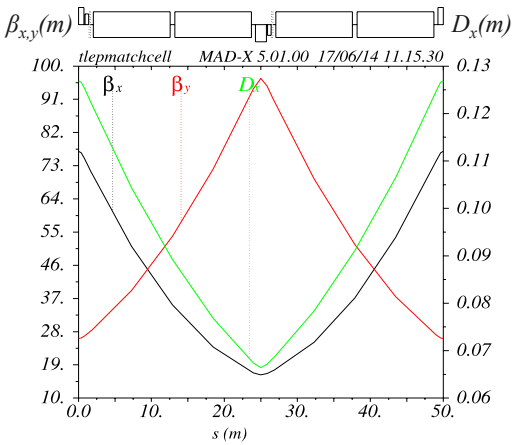


Figure 3: Beta functions and horizontal dispersion of the FCC-ee FODO cell.

were chosen. The beta functions and the dispersion function calculated with MAD-X are shown in figure 3. With a maximum of 12.7 cm the dispersion function is by one order of magnitude smaller compared to LEP (2.2 m) [7].

### *Horizontal Emittances of the High Energy Lattice*

The horizontal equilibrium emittance of a beam in an electron storage ring can approximately be written as [4]

$$\epsilon_x = \frac{C_g}{J_x}\gamma^2\theta^3 F. \tag{2}$$

$C_g = 3.832 \times 10^{-13}$ is a constant, $J_x$ is the horizontal damping partition number, $\gamma$ is the Lorentz factor and $\theta$ is the bending angle of the dipole magnets in a half cell. $F$ is a numerical factor, that depends on the lattice design. In case of a FODO cell lattice it is given by

$$F = \frac{1}{2\sin\psi}\frac{5+3\cos\psi}{1-\cos\psi}\frac{L}{l_b}, \tag{3}$$

where $L$ is the cell length, $\psi$ is the phase advance per cell and $l_b$ the total length of the bending magnets. According to equation (2) the equilibrium emittance $\epsilon_x$ of an 175 GeV electron beam in the FCC-ee lattice should be in the order of 1.04 nm rad. The emittance calculation with MAD-X had the result $\epsilon = 1.00$ nm rad, which agrees nicely with the analytical result and is exactly the half of the baseline parameter. As the emittance probably will increase as soon as coupling, misalignments and non-linear effects like the beam-beam effect are considered, this factor of two for now will be kept to leave a margin.

Changing the beam energy while not modifying the lattice will have an impact on the emittance proportional to $\gamma^2$. For 120 GeV beam energy the analytically calculated emittance is 0.49 nm rad, which was confirmed by calculation with MAD-X. Also taking the margin of factor two into account, this is a deviation from the baseline parameter 0.47 nm rad of just 3.8 %. Fine tuning with wigglers will be applied using the same lattice. For 80 GeV beam energy the emittance however would shrink to 0.218 nm rad, for 45.5 GeV even to 0.071 nm rad. To disarm the beam-beam effect the emittance must be increased by one order of magnitude in case of 80 GeV beam energy and three in case of 45.5 GeV. With wigglers this is not possible both from technical and economical point of view. As a consequence the lattice itself must be modified.

## POSSIBILITIES TO INCREASE THE EMITTANCE

The equilibrium emittance is generally given by [8]

$$\epsilon = \left(\frac{\delta p}{p}\right)^2 \left(\gamma D^2 + 2\alpha DD' + \beta D'^2\right), \tag{4}$$

so the key to increase the emittance is a larger dispersion. The maximum dispersion in a FODO lattice can be derived as [9]

$$\hat{D} = \frac{L^2}{\rho}\cdot\left(1+\frac{1}{2}\sin\left(\frac{\psi}{2}\right)\right)/\sin^2\left(\frac{\psi}{2}\right), \tag{5}$$

which allows two possibilities to modify the emittance: changing the cell length and changing the phase advance.

### *Changing of the Cell Length*

According to equation (5) the dispersion function depends on the cell length squared. Thus to obtain a larger dispersion the FODO cell must be increased. However changing the cell length is not possible in any arbitrary way because of the fixed the position of the quadrupole magnets. Thus it is just possible to increase the cell length by multiples of the High Energy FODO cell length, which is 50 m. An example of a possible scenario is illustrated in figure 4: by switching off all the defocussing quadrupoles and inverting the polarity of every second focusing quadrupole the cell length is doubled. Even longer cells can be achieved, when more quadrupoles are switched off. To guarantee smooth operation the relevant quadrupoles need to be equipped with switches, that should be included in the technical design from the beginning. This was already done for the sextupoles at HERA.

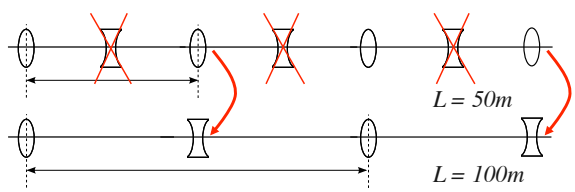


Figure 4: Approach of changing the cell length with fixed element positions. To double the cell length every defocussing quadrupole is switched off and the polarity of every second focusing is inverted.



ISBN 978-3-95450-172-4

*Tuning the Phase Advance*

A second way to modify the dispersion without changing the lattice itself is tuning the horizontal phase advance by modifying gradient of the quadrupoles. Figure 5 shows the dispersion of the FCC-ee FODO cell as a function of the phase advance. To obtain a larger dispersion, the phase advance must be decreased. However the singularity for $\psi \rightarrow 0$ in equation (5) causes a very fast increase of the dispersion. At operation with phase advances smaller than 40 ° the beam emittance will be very sensitive tune shifts and optics tolerances. For stability reasons it is therefore recommended to choose a larger phase advance.

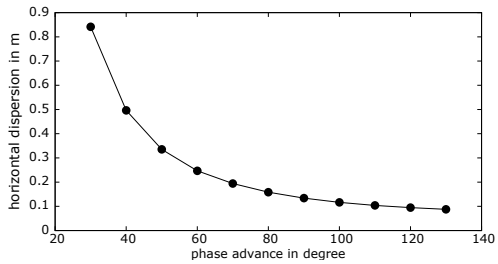


Figure 5: The maximum horizontal dispersion of an FCC-ee FODO cell as a function of the phase advance.

The strongest constraint on the choice of the phase advance is given by the necessity of a sophisticated sextupole scheme. For higher order chromaticity correction the phase advance between two sextupoles must be an integer divider of 360 ° like for example 60 °, 72 ° or 90 °.

## OBJECTIVES FOR LATTICE CHANGES

The key to increase the emittance is the modification of the arc FODO cells. Feasible changes feature two characteristics: the cell length is a multiple of 50 m and the ratio of 360 ° and the phase advance is an integer value. Combinations of cell length and phase advance that approximately result in the desired emittance values are listed in Table 2. For 80 GeV there are two alternatives: $L = 100$ m with $\psi = 90$ ° and $L = 50$ m with $\psi = 45$ °, while for 45.5 GeV three options are possible: $L = 200$ m, $\psi = 60$ °, $L = 250$ m, $\psi = 72$ ° and $L = 300$ m, $\psi = 90$ °.

Table 2: Feasible FODO Cell Layouts for 80 GeV and 45.5 GeV Beam Energy and Their Design Emittances according to Equation (2)

| $E$ (GeV) | $L$ (m) | $\psi$ (°) | $\epsilon_x$ (nm rad) |
|---|---|---|---|
| 80 | 100 | 90 | 1.74 |
| | 50 | 45 | 1.50 |
| 45.5 | 200 | 60 | 13.56 |
| | 250 | 72 | 15.91 |
| | 300 | 90 | 15.24 |

However both changing the cell length and tuning the phase advance result in a dysfunction of the dispersion suppressors. In order to keep the same geometry the strength of the bending magnets must not be changed. Instead quadrupoles of the arc are needed to re-establish the correct function of the dispersion suppressors. The lattice in the straight sections will not be changed, to keep the same optics conditions for the injection scheme, interaction regions etc.

## LATTICES FOR 80 GEV AND 45.5 GEV BEAM ENERGY

For each FODO cell option listed in Table 2 a lattice was set up and evaluated with MAD-X. An overview of the optics parameters is given in Table 3. The emittance values calculated by MAD-X are in nice agreement with the analytical calculation. Figure 6 shows the horizontal beta functions of the two lattices for 80 GeV beam energy. The FODO cell modifications have different impact on the betafunctions. In both lattices four additional quadrupoles from the arcs are supporting the dispersion suppressors. This of course has an impact on the beta functions and creates the peaks, that can be seen in both plots. The horizontal

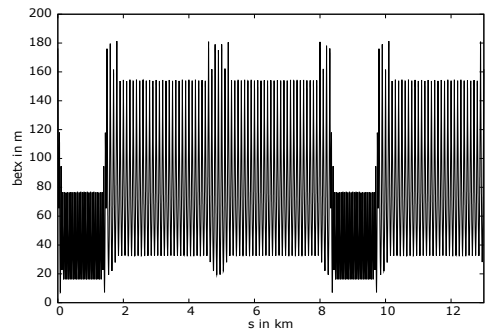


a)

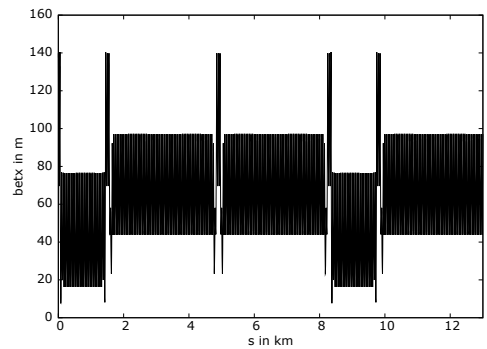


b)

Figure 6: The horizontal beta functions for the lattices for 80 GeV beam energy. Plot a) shows the first 13 km of the lattice with 100 m, $\psi = 90$ ° FODO cells, b) the one with 50 m, $\psi = 45$ ° FODO cells beginning with a straight section.

beta function for the 300 m FODO cell lattice intended for 45.5 GeV beam energy is displayed in figure 7. The beta function in the dispersion suppressors reaches up to 550 m. As the closed orbit depends on the absolute value of the beta function alignment becomes an issue. Independent of the lattice at 45.5 GeV beam energy the energy loss per

ISBN 978-3-95450-172-4

Table 3: Comparison of the parameters of the lattices based on different FODO cell layouts and the design parameters. The listed parameters are the cell length $L$, the phase advance $\psi_x$, the equilibrium emittance $\epsilon_x$, the energy loss per turn $U_0$, the momentum compaction factor $\alpha_p$, the maximum values of horizontal and vertical beta functions $\hat{\beta}_x$ and $\hat{\beta}_x$ as well as the maximum horizontal dispersion $\hat{D}_x$.

| | 80 GeV | | Design parameter | 45.5 GeV | | | Design parameter |
|---|---|---|---|---|---|---|---|
| $L$ (m) | 100 | 50 | - | 200 | 250 | 300 | - |
| $\psi_x$ (°) | 90 | 45 | - | 60 | 72 | 90 | - |
| $\epsilon_x$ (nm rad) | 1.70 | 1.47 | $2 \times 1.65$ | 12.5 | 14.5 | 14.2 | $2 \times 14.6$ |
| $U_0$ (MeV/turn) | 337.03 | 337.03 | 330 | 35.3 | 35.3 | 35.3 | 30 |
| $\alpha_p$ ($10^{-5}$) | 2.22 | 1.99 | 2 | 1.69 | 1.86 | 1.81 | 1.8 |
| $\hat{\beta}_x$ (m) | 181.54 | 141.47 | - | 366.5 | 465.71 | 554.0 | - |
| $\hat{\beta}_y$ (m) | 211.05 | 141.68 | - | 407.92 | 477.70 | 626.43 | - |
| $\hat{D}_x$ (m) | 0.58 | 0.41 | - | 4.02 | 4.87 | 4.56 | - |

turn is 15 % higher than estimated in the baseline parameter list. This will have an influence on the maximum bunch number and bunch population, which are compatible with the maximum power consumption of 50 MW.

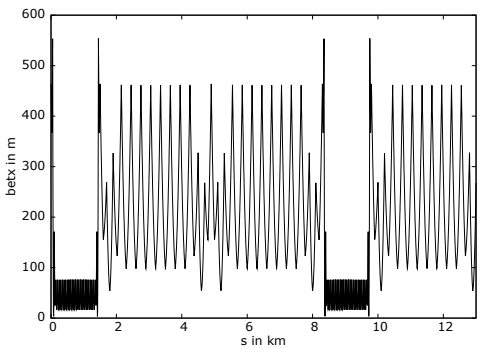


Figure 7: Horizontal beta function for a FODO cell with a 300 m length and a phase advance 90 ° at the first 13 km of the lattice beginning with a straight section.

## NEXT STEPS

In following calculations misalignments will be introduced in order to analyze the vertical emittance and closed orbit corrections. To finalize the lattice design an advanced sextupole scheme including higher order chromaticity corrections will be added before investigating the impact of the beam-beam effect.

## CONCLUSION

The design of the future FCC high energy electron positron collider has to face a variety of challenges: the lattice has to be designed and optimized for the requirements of four different center of mass energies in the range of 90-350 GeV. At high energies the luminosity is limited by beamstrahlung creating momentum deviations up to 2 %. At low energies the beam-beam effect demands an emittance increase of three orders of magnitude to avoid large tune shifts. The very strong focusing in the final focus system required to achieve a vertical $\beta^*$ of 1 mm creates very high chromaticity, that has to be corrected in a local correction scheme while still providing sufficient dynamic aperture.

Starting at the highest beam energy of 175 GeV with a lattice consisting of 50 m FODO cells with 90/60 ° phase advance, first lattice layouts that achieve the emittance parameters for the low energy beams were developed. For 120 GeV beam energy the same lattice can be used, but for 80 GeV and 45.5 GeV the lattice has to be changed by increasing the cell length up to 300 m and tuning the phase advance. Still some fine tuning with wigglers is required, but the baseline parameters could approximately be achieved leaving a margin of a factor two for emittance increase caused by coupling, misalignments and non-linear effects like the beam-beam effect. The lattices described in this paper provide the basis for further development like a state-of-the-art chromaticity correction scheme. The final choice of the lattice will also depend on the results of those investigations.

## ACKNOWLEDGMENT

This work is supported by the German Bundesministerium für Bildung und Forschung (BMBF).

## REFERENCES

[1] B. Haerer et al., "Constraints on the FCC-ee Lattice from the compatibility with the FCC Hadron Collider", *These Proceedings*, HF2014, Beijing, China (2014)

[2] Future Circular Collider Study, "Lepton Collider Parameters", FCC-1401201640, CERN, 2014

[3] A.W. Chao et al., *Handbook of Accelerator Physics and Engineering*, World Scientific, Singapore, 2013

[4] L.C. Teng, "Minimizing the Emittance in Designing the Lattice of an Electron Storage Ring", Fermilab/TM-1269, June 1984

[5] R. Martin et al., "Status of the FCC-ee Interaction Region Design", *These Proceedings*, HF2014, Beijing, China (2014)

[6] R. Kersevan, Internal communication

[7] *LEP Design Report*, (Geneva: CERN, 1984)

[8] M. Sands, *The Physics of Electron Storage Rings. An Introduction*, SLAC-121, 1970

[9] "CERN Accelerator School: 5th General Accelerator Physics Course", *Proceedings*, CERN-1994-2, CERN, Geneva, 1994



ISBN 978-3-95450-172-4

# STATUS OF CEPC LATTICE DESIGN

H. Geng*, G. Xu, W. Chou, Y. Guo, N. Wang, Y. Peng, X. Cui, Y. Zhang, T. Yue, Z. Duan, Y. Wang, D. Wang, S. Bai, Q. Qin, J. Gao, F. Su, M. Xiao
Institute of High Energy Physics, CAS, Beijing, China

*Abstract*

IHEP has proposed a circular electron and positron collider (CEPC) to study the properties of the Higgs boson. In the baseline design, the circumference of CEPC will be taken as 50km, and a sing ring scheme will be adopted, e.g., the electron and positron beam will share the beam pipes. This paper will show the latest design of the CEPC lattice, including the design of the main ring lattice and the pretzel scheme. Some critical issues that we encountered when designing the lattice will also be discussed.

## INTRODUCTION

After the discovery of Higgs-like boson at CERN [1-3], many proposals have been raised to build a Higgs factory to explicitly study the properties of the particle. One of the most attractive proposals is the Circular Electron and Positron Collider (CEPC) project in China [4,5].

CEPC is a ring with a circumference of 50-70 km, which will be used as electron and positron collider at phase-I and will be upgraded to a Super proton-proton Collider (SppC) at phase-II. The designed beam energy for CEPC is 120 GeV, the main constraints in the design is the synchrotron radiation power, which should be limited to 50 MW, the target luminosity is ~$10^{34}cm^{-2}s^{-1}$.

As beam energy is high, CEPC favors more arcs which enables RF cavities to compensate the energy loss in the straight section, thus can reduce energy variation from synchrotron radiation. SppC needs long straight sections for collimators etc. To compromise between CEPC and SppC, the ring is decided to have 8 arcs and 8 straight sections, RF cavities will be distributed in each straight section.

In this paper, we will show the latest design of the CEPC lattice, including the design of the main ring lattice and the pretzel scheme. Some critical issues that we encountered when designing the lattice will also be discussed.

## LATTICE DESIGN OF THE RING

The circumference of the ring is 54km with 8 arcs and 8 straight sections. The layout of the ring is shown in Fig. 1. There are four IPs in the ring, IP1 and IP3 will be used for CEPC, while IP2 and IP4 will be used for SPPC. The RF sections are distributed in each straight section. At the IP section, the RF cavities will be symmetrically placed at the two ends of the section, at the other straight sections, the RF cavities can be located together at the middle of each straight section.

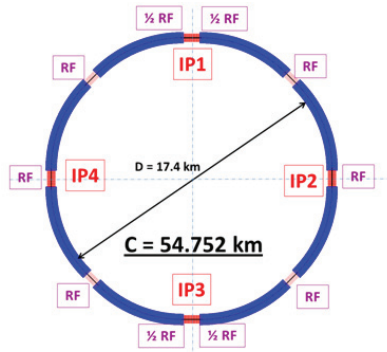


Figure 1: Layout of the CEPC ring.

### *FODO Cells*

The lattice for CEPC ring has been chosen to use the standard FODO cells with 60 degrees phase advances in both transverse planes. The FODO cell structure is chosen to have a maximum filling factor. The 60 degrees phase advance is chosen to have a relatively large beam emittance, so that a relatively longer beamstrahlung beam lifetime, than the 90 degrees phase advance lattice cells.

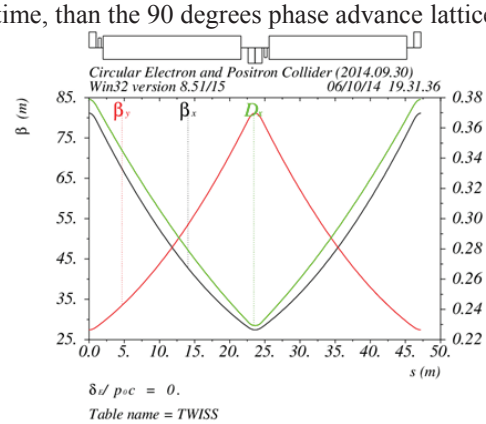


Figure 2: Beta functions and dispersion function of a standard FODO cell with 60/60 degrees phase advance in CEPC ring.

A standard FODO cell with 60 degrees phase advance is shown in Fig.2. The length of each bend is 19.6m, the length of each quadrupole is 2.0m. There is one sextupole, with a length of 0.4 m, next to each quadrupole for chromatic corrections. The distance between the sectupole and the adjacent magnet is 0.3 m, while the distance between each quadrupole and the adjacent bending magnet is 1.0 m. The total length of each cell is 47.2 m.

*genghp@ihep.ac.cn

ISBN 978-3-95450-172-4

### *Dispersion Suppressors*

The dispersion suppressors are formed by pulling out the bending magnets in the second last FODO cell on each side of every arc section in CEPC ring. The beta functions and dispersion function of one dispersion suppressor is shown in Fig. 3.

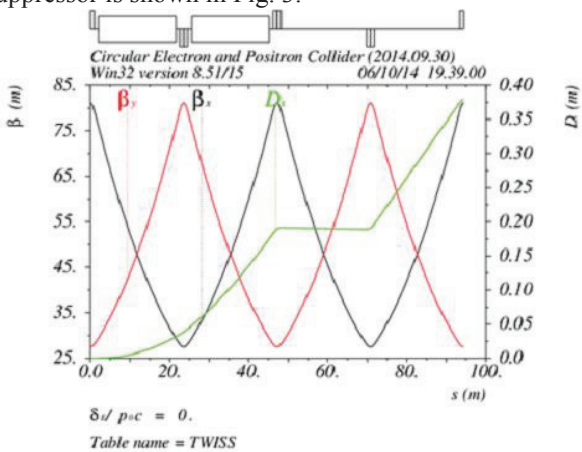


Figure 3: The beta functions and dispersion function of a dispersion suppressor in CEPC ring.

### *Straight Sections*

The straight sections have two different lengths, the four straight sections which have the IPs have a length of 1132.8 m, and the other straight sections have a length of 849.6 m. The first four FODO cells at each end of every straight sections are used for matching and working point adjustment. The beta functions and dispersion function of a short straight section in CEPC ring is shown in Fig. 4.

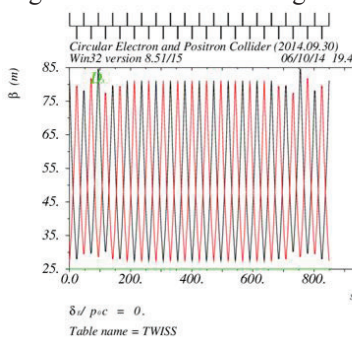


Figure 4: The beta functions and dispersion function of a short straight section in CEPC ring.

### *Dynamic Aperture*

We use the code SAD to track the dynamic aperture of the ring. Three transverse damping times were tracked to characterize the dynamic aperture size. Momentum spread from +2% to -2% were tracked. The tracking result is shown in Fig. 5. The dynamic aperture shown in Fig. 5 has been normalized to transverse beam sizes. No coupling and full coupling has been assumed to calculate the horizontal and vertical beam sizes. From Fig. 5 we can that the dynamic aperture is ~60 times beam sizes in both horizontal and vertical planes.

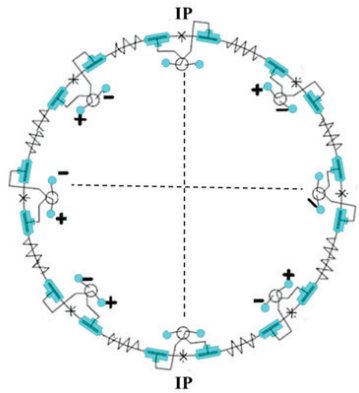


Figure 5: The beta functions and dispersion function of a short straight section in CEPC ring.

### *Pretzel Orbit*

In order to allow both electron and positron travel in the same beam pipe, the two beams have to be properly separated at the parasitic crossing points. A so called pretzel orbit is the normal way to separate the two beams.

For CEPC, there are 50 bunches for each beam , thus there are 100 crossing or collision points. The two beams have to be separated at all the crossing points except for IP1 and IP3.

We use one pair of electrostatic separators to separate the beams at each arc section. One separator will be placed π/2 phase advance before the first crossing point in the arc section, the other separator will be placed π/2 phase advance after the last crossing point in this arc section. With these 8 pairs of separators, all the crossing points in the arc section can be well separated. At IP2 and IP4, we need extra pairs of electrostatic separators to avoid beam collision. Two more pairs of separators will be placed π/2 phase advance before and after IP2 and IP4 to separate the beams in these two collision points. In total, ten pairs of electrostatic separators will be used in CEPC ring to avoid all the parasitic crossing points. The layout of the electrostatic separators and its orbit is shown inFig.6.

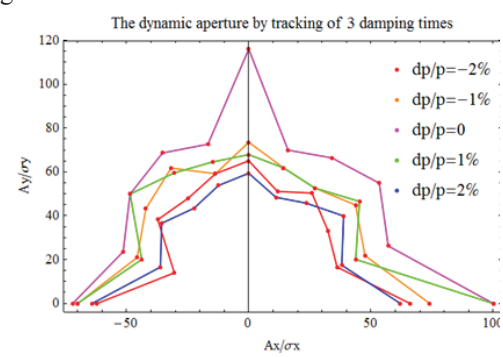


Figure 6: The beta functions and dispersion function of a short straight section in CEPC ring.

Beams can be separated in either horizontal or vertical plane. With horizontal separation, the separation distance is bigger as the beam size is bigger than vertical. With vertical separation, the separation distance is smaller, but



ISBN 978-3-95450-172-4

it can easily induce big coupling between horizontal and vertical planes. As the coupling factor in CEPC is strictly limited to a small value to have a big luminosity, thus we choose horizontal separation scheme for CEPC.

The maximum separation distance between the two beams has a big effect on the beam lifetime. To allow for a reasonable beam lifetime, a maximum separation distance of $5\sigma_x$ is considered for CEPC. The resulted pretzel orbit in one arc section is shown in Fig. 7.

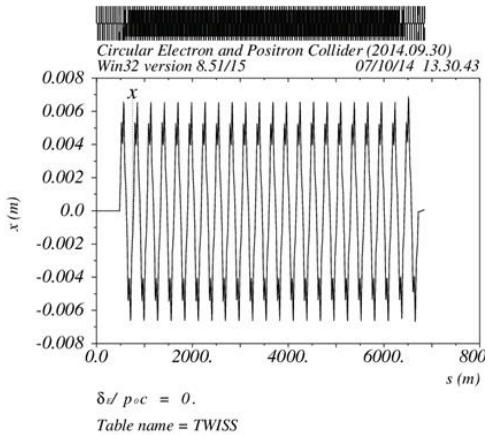


Figure 7: Pretzel orbit of electron beam in one arc section of CEPC ring.

### *Saw Tooth Orbit*

The beam energy of CEPC is very high, 120 GeV. At this beam energy, the synchrotron radiation effect is very strong. For CEPC, the synchrotron radiation loss per turn is 3 GeV for both beams, which means the energy difference at the entrance and exit of one arc section is

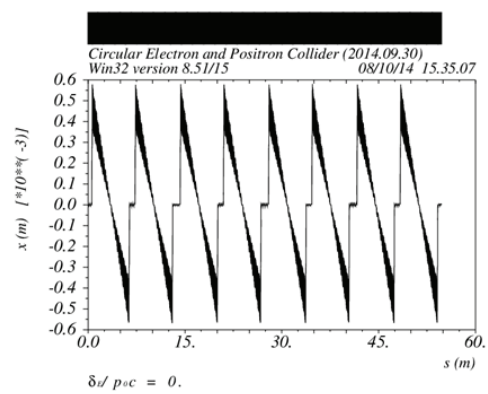


Figure 8: Saw tooth orbit in CEPC ring.

~0.3%, and at the following straight section, the energy loss will be compensated by RF cavities, and then the beam will loss energy from synchrotron radiation when entering the next arc section. Looking at the whole ring, the beam energy has a saw tooth structure. This energy saw tooth from the synchrotron radiation effect will in turn result in a beam orbit saw tooth because of the change of the beam centre energy.

In CEPC, the saw tooth orbit is calculated with MAD and is shown in Fig. 8.

We can see from Fig. 8 that the maximum sawtooth orbit is ~0.6 mm, which is one order smaller than the maximum pretzel orbit.

## DISCUSSIONS

When designing the CEPC lattice, we found two issues which is very critical. First, the pretzel orbit has a big distortion on the original beta functions and dispersion functions, which in turn will result in change of tune and beam emittance. The distortion comes from the extra field seen by the beam when it is not on axis. The beam sees a dispole field in quadrupoles, the maximum strength of the dipole field is only slightly weaker than the field in the main bending magnets. At sextupoles, the beam sees both dipole and quadrupole field, but the strength is one order smaller than the nominal dipole and quadrupole field in the ring. The total effect from the off axis field from the quadrupole and sextupole distorts the periodicity of beta functions and dispersion functions, which have a significant effect on dynamic aperture reduction.

Another effect from the pretzel orbit is it enables the coupling of sextupole strength and the working point. This makes the chromatic correction and the working point adjustment inseparable.

The saw tooth orbit is a common behaviour at all rings at such a high energy. It has been proved the feasibility to correct the saw tooth orbit at double rings [6]. But, for CEPC, it is a single ring machine, both electron and positron beams share the same vacuum pipe, the correction method used in double rings could not be applied here. It seems that this orbit is uncorrectable at CEPC, if it is tolerable or not shall be clarified later.

## SUMMARY

We have introduced the status of CEPC lattice design. The detailed lattice design principle and results have been showed. As the CEPC ring is a single ring machine, we also described our pretzel orbit design method and results. The critical issues such as distortion effect on beta functions and dispersion from pretzel orbit and the saw tooth effect has also been introduced.

The main topics in CEPC lattice design have been investigated, but the lattice distortion from pretzel orbit and the correction scheme of saw tooth orbit has not been fully solved. More work need to be done for CEPC lattice design.

## ACKNOWLEDEMENT

The authors would like to thank th Yunhai Cai, Richard Talman, Dave Rice, Yoshihiro Funakoshi, Dmitry Shatilov , Kazuhito Ohmi , Yuhong Zhang, and those who are not mentioned here, for their help and useful discussions.



ISBN 978-3-95450-172-4

## REFERENCES

[1] Adrian Cho, "Higgs Boson Makes Its Debut After Decades-Long Search", Science 337 (6091): 141–143.
[2] "Observation of a New Particle with a Mass of 125 GeV", http://cms.web.cern.ch/news/observation-new-particle-mass-125-Gev.
[3] CMS collaboration, "Observation of a new boson at a mass of 125 GeV with the CMS experiment at the LHC"， Physics Letters B, 716(1):30-61.
[4] "Accelerators for a Higgs Factory: Linear vs. Circular (HF2012)", Fermi National Laboratory, 14-16 November, 2012 .
[5] S. Henderson. "Accelerators for a Higgs Factory", Report at HF2012, Fermi Lab, 14-16 November, 2012 .
[6] K. Oide, "Supertristan, a possibility of ring collider for Higgs factory", Presentation at HF2014, Fermi National Laboratory, 14-16 November, 2012 .



ISBN 978-3-95450-172-4

# A GREEN CEPC USING THE POWER OF NUCLEAR WASTE

Z.C. Liu#, J. Gao, IHEP, Beijing, 100049, China

*Abstract*

China is proposing to build an efficient Higgs factory, CEPC, a 52 km ring under the ground, to search the mysteries of the particle physics. This large circular collider would allow the Higgs boson to be studied with greater precision than at the much smaller Large Hadron Collider (LHC) at CERN. However, several hundreds of MW wall power is needed to run such a huge machine. With the development of China's nuclear power, a huge amount of long-lived nuclear waste needs to be safe disposed. The nuclear waste can be safely disposed by Accelerator Driven Sub-critical System (ADS) and provide electric power at the same time. Both CEPC and ADS are based on the superconducting accelerator technology and the power of the CEPC can be fully covered by the ADS. A green CEPC running in China is possible in the future.

## INTRODUCTION

The Standard Model (SM) of particle physics can describe the strong, weak and electromagnetic interactions under the framework of quantum gauge field theory. The theoretical predictions of SM are in excellent agreement with the past experimental measurements. After the discovery of the Higgs particle, it is natural to measure its properties as precise as possible, including mass, spin, CP nature, couplings, and etc., at the current running Large Hadron Collider (LHC) and future electron positron colliders, e.g. the International Linear Collider (ILC). The low Higgs mass of ~125 GeV makes possible a Circular Electron Positron Collider (CEPC) as a Higgs Factory, which has the advantage of higher luminosity to cost ratio and the potential to be upgraded to a proton-proton collider to reach unprecedented high energy and discover New Physics. CEPC is the development in energy frontier of particle physics, and the next step of BEPC and BEPCII. As the energy is about 125GeV for the circular machine, it is a huge machine that ever built in china in fundamental research. The machine will be in a ~50km tunnel underground to keep electron and positron colliding. As the project is only for the fundamental research, it is a large non-profit and high operation cost machine. The construction cost will be much larger than the BEPCII. Huge energy consuming is a problem must be in concern as the machine will consume several hundred MW wall power in operation.

## CEPC POWER CONSUMING

The CEPC is large circular collider with ~50km ring. Figure 1 shows the schematic layout of CEPC. The booster, CEPC and SppC will share the same tunnel. Table 1 shows the main parameters of the CEPC. The beam SR loss will be 51.7MW/turn. As there will be two beams in the ring, about 100MW/turn beam power will be lost. Considering the RF power source, cryogenic system and so on, the total power consuming will be about 300MW. Comparing will LHC and ILC, it is about two times of the LHC power consuming and about the same as ILC [1].

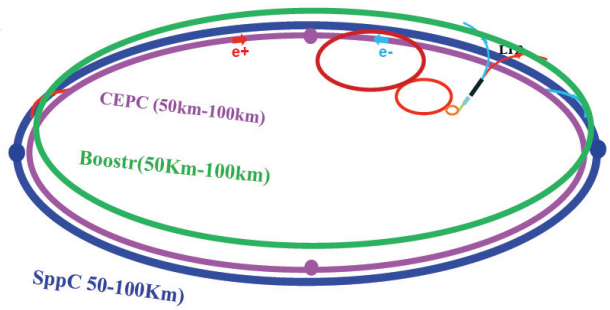


Figure 1: The road map of ADS linac project.

## ENERGY PROBLEM IN CHINA

China has a population of about 1.3 billion. Now the average energy consumption per person is less than one half of the world level and less than one tenth of the developed country's level. However, the fast development of economy at annual rate of 7-10% has been kept for more than 20 years, and it will last for much more years. China will keep the fast development country for a long time. China has been the second largest energy producing and consumption country [2]. The population of China will be 1.5 billion at 2050, conservatively predicted capacity of electricity will be 1200~1500GWe. China will probably be the first largest $CO_2$ producer at 2025 [2]. And in the near future, China will become the first largest energy producing and consumption country. Therefore, China faces serious pollution and energy shortage in the future. Renewable energy, sustainable energy and nuclear energy must be considered to solve the pollution problem and energy shortage. Now China has made great effort to develop renewable energy, sustainable energy and nuclear energy. Figure 2 shows the renewable and sustainable energy that mainly used in China.


Figure 2: Renewable and sustainable energy in China.

#zcliu @ihep.ac.cn

ISBN 978-3-95450-172-4

Table 1: CEPC Main Parameters

| Parameter | Unit | Value | Parameter | Unit | Value |
|---|---|---|---|---|---|
| Beam energy [E] | GeV | 120 | Circumference [C] | m | 54752 |
| Number of IP[$N_{IP}$] | | 2 | SR loss/turn [$U_0$] | GeV | 3.11 |
| Bunch number/beam[$n_B$] | | 50 | Bunch population [Ne] | | 3.79E+11 |
| SR power/beam [P] | MW | 51.7 | Beam current [I] | mA | 16.6 |
| Bending radius [r] | m | 6094 | momentum compaction factor [$a_p$] | | 3.36E-05 |
| Revolution period [$T_0$] | s | 1.83E-04 | Revolution frequency [$f_0$] | Hz | 5475.46 |
| emittance (x/y) | nm | 6.12/0.018 | $b_{IP}$(x/y) | mm | 800/1.2 |
| Transverse size (x/y) | mm | 69.97/0.15 | $x_{x,y}$/IP | | 0.118/0.083 |
| Beam length SR [$s_{s.SR}$] | mm | 2.14 | Beam length total [$s_{s.tot}$] | mm | 2.65 |
| Lifetime due to Beamstrahlung (simulation) | min | 47 | lifetime due to radiative Bhabha scattering [$t_L$] | min | 52 |
| RF voltage [$V_{rf}$] | GV | 6.87 | RF frequency [$f_{rf}$] | MHz | 650 |
| Harmonic number [h] | | 118800 | Synchrotron oscillation tune [$n_s$] | | 0.18 |
| Energy acceptance RF [h] | % | 5.99 | Damping partition number [Je] | | 2 |
| Energy spread SR [$s_{d.SR}$] | % | 0.132 | Energy spread BS [$s_{d.BS}$] | % | 0.119 |
| Energy spread total [$s_{d.tot}$] | % | 0.163 | $n_g$ | | 0.23 |
| Transverse damping time [$n_x$] | turns | 78 | Longitudinal damping time [$n_e$] | turns | 39 |
| Hourglass factor | Fh | 0.658 | Luminosity /IP[L] | $cm^{-2}s^{-1}$ | 2.04E+34 |

By the end of 2012, China has the total installed power generation capacity of 1144910MW, including hydropower 248900MW, thermal power 819170MW (71.5%), nuclear power 12570MW, wind power 60830MW and solar power 3280MW. By the end of August 2013, China has wind power 68450MW, solar power 8980MW, nuclear power 14780MW and biomass energy 8000MW [3]. That is 8.5% of the total.

And in 2015, the renewable and sustainable energy will be hydropower 2900000MW, wind power 100000MW, nuclear power 40000MW, solar power 35000MW, biomass power 13000MW [3]. That is about 32% of the total electricity power.

China still keep very high investment on renewable energy. In 2013, China invested 56 billion U.S. dollar on renewable energy, for the first time more than Europe. Europe invested 48 billion U.S. dollar, on the second place. The third is USA with 36 billion U.S. dollar. India and Brazil also invested 6 and 3 billion U.S. dollar separately.

By the end of August 2013, the electric energy production is 14780MW. That is 1.23% of total electric energy production(~1200000MW). Before the Fukushima Daiichi accident, there are 15 operational reactors, 26 under construction reactors and 18 planed reactors. Figure 3 shows the reactors location in China [2]. Now China has 21 operational reactors and on the sixth place of the world nuclear power country. There are 27 reactors under construction in China by the end of September 2014. Figure 4 shows the number of reactors in operation of the countries worldwide [4]. Figure 5 shows the number of reactors under construction of the countries worldwide [5].

In 2020, there will be 58GW reactors in operation which is 4% of total electricity capacity and 30GW reactors under construction. It means that about 7 new units need to be constructed per year from now to 2020. In about 2050, there will be 240GW nuclear power in China [2].

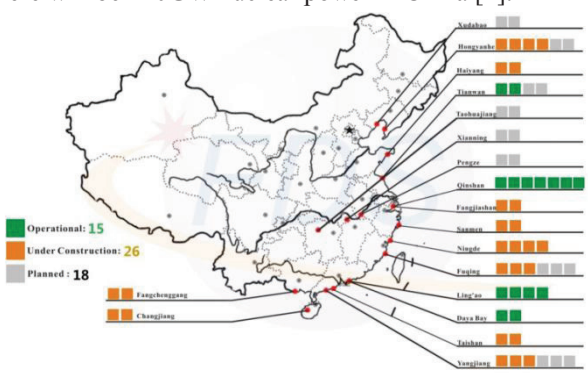


Figure 3: China's nuclear power reactors before Fukushima Daiichi accident [2].

However, the nuclear power plant will produce large amount of nuclear waste. For 1000MW nuclear power plant, there will be 10s of tons nuclear waste per year. After processing, it becomes $4m^3$ high radiation nuclear waste, $20m^3$ medium radiation nuclear waste, $140m^3$ low radiation nuclear waste and $200m^3$ non-radiation nuclear waste.

There are 150 tons of high radiation nuclear waste per year in China (2008 data). And there will be 3200 tons per year in 2030. Nuclear waste is a serious problem and must be solved in the future. It is a bottle neck for nuclear power development in China.



ISBN 978-3-95450-172-4

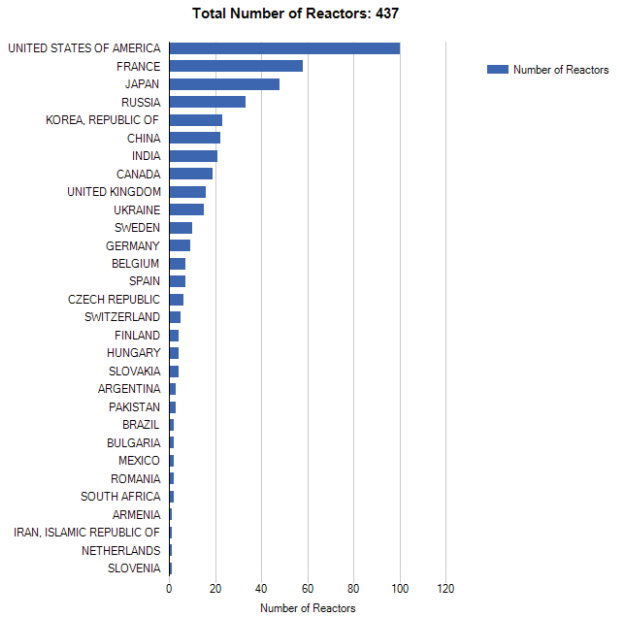


Figure 4: Number of reactors in operation.

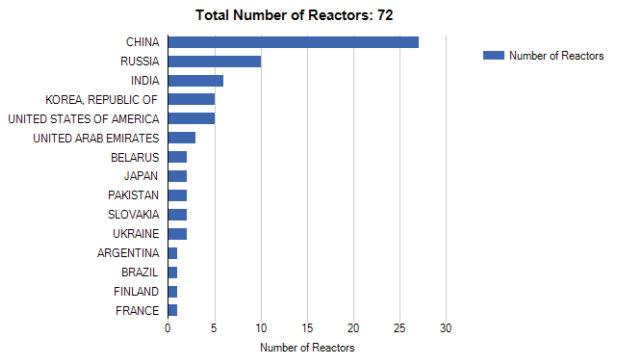


Figure 5: Number of reactors under construction.

## ADS PROGRAM

China is developing the Accelerator Driven Sub-critical System (ADS) which is composed of a nuclear reactor operating in subcritical mode and a main linac providing the required complement neutrons. The aim of the ADS project is to dispose the nuclear waste. And the ADS is also a good choice of solving future energy shortage by safe utilization of nuclear power. Figure 6 shows the schematic of the ADS proton linac project.

The ADS program launched in 2011 and plan to construct demonstration ADS transmutation system at ~2030s through three stages. The first stage is to built a 10MW research facility at ~2023 to solve the key technology. There will be a 10MeV injector in operation by the end of 2016. The second stage is to built a 100MW experimental facility by the end of ~2030. The third stage is to built a 1000MW demo facility at ~2040. Therefore, the CEPC power can be partially or fully supplied by ADS.

ADS has been recognized as a good option for nuclear waste transmutation. And now it has been supported by CAS as a long-term program. ADS can provide electric power to the society as a nuclear plant. The fuel can be nuclear waste or thorium (Th-232) since it is three times as abundant in the earth's crust as uranium. Figure 7 shows the principle of the ADS. The proton accelerator using superconducting cavity will accelerate the proton beam to 1.5GeV and then the beam hit the liquid metal target in the reactor to produce enough neutron to start the subcritical transmutation in the reactor cooled by PbBi. The heat of the reaction will be conducted out and transferred to electricity to power the ADS self-system and provide to the society.


Figure 6: The road map of ADS linac project.

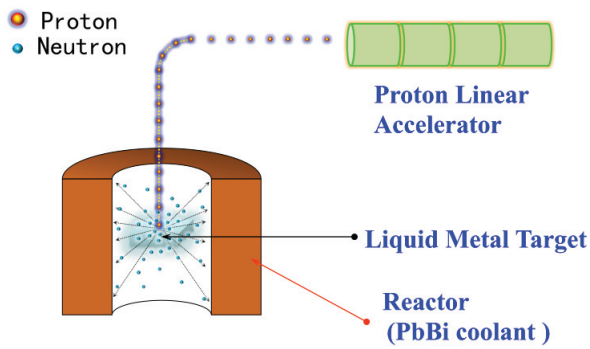


Figure 7: Principle of ADS.

Many accelerator technologies have been developed by the ADS R&D, such as superconducting technology, RF power source, cryomodule and 2K helium system. Table 2 shows the technology that can be shared by CEPC and ADS. Figure 8 -12 show the equipment of ADS that can be shared by CEPC.

Table 2: Technology Shared by CEPC and ADS

| Shared Tech. | CEPC | ADS |
|---|---|---|
| Superconducting technology | ✓ | ✓ |
| RF system | ✓ | ✓ |
| Power source | ✓ | ✓ |
| Cryogenic system | ✓ | ✓ |
| SC Magnet | ✓ | ✓ |
| Vacuum | ✓ | ✓ |

ISBN 978-3-95450-172-4

Figure 8: Superconducting spoke cavity power source (left), superconducting magnet power source (middle), RFQ cavity power source (right).

Figure 9: Superconducting spoke021 cavity.

Figure 10: Superconducting spoke021 cavity (up) and 650MHz elliptical 082 cavity (down).


Figure 11: 12 meters long cryomodule for Euro-XFEL .

Figure 13 shows the schematic layout of the green CEPC in the future. The nuclear waste from the traditional nuclear power plant will be used in the ADS system and provide electric power to the national smart grid. Part of the electric power will be send to the society and the other part will be send to the CEPC to keep the facility on operation. Both CEPC and ADS share the same technology.

Figure 12: 2K cryogenic LHe system.


Figure 13: Green CEPC in the future.

## SUMMARY

CEPC is a large machine and need huge power of about 300MW. That is about two times of LHC. Huge power consumption and high operation cost must be in consideration. For the future large accelerator project, the world scientist promote using clean energy and keep the accelerator running at a green mode. Now China is developing nuclear power, but the bottle neck of nuclear power development is the nuclear waste. However, ADS can safely solve this problem and provide electric power. CEPC and ADS based on a lot of same technology, such as superconducting technology and so on. The CEPC construction can be motivated by the ADS technology improvement and run in a green mode.

## REFERENCES

[1] Denis Perret-Gallix, The Green ILC, LCWS, Tokyo Univ. Nov. 2013.

[2] Yican Wu, Accelerator Driven System (ADS) : A Nuclear Technology Bridge between Fission and Fusion Energy in China, ICENES-16, Madrid, Spain, (2013).



ISBN 978-3-95450-172-4

[3] 全国人大常委会执法检查组在关于检查 《中华人民共和国可再生能源法》实施情况报告.
[4] http://www.iaea.org/PRIS/WorldStatistics/Operation-alReactorsByCountry.aspx.
[5] http://www.iaea.org/PRIS/WorldStatistics/UnderCon-structionReactorsByCountry.aspx.



ISBN 978-3-95450-172-4

# GREENING FOR BOSONS

T. Parker, European Spallation Source, Lund, Sweden
P.Peck, IIIEE, Lund University, Sweden

*Abstract*

Throughout history, scientific advancement has been dependent upon advances in the technologies of research. However, branches of research that today rely on Research Infrastructures (RIs) such as accelerators require technological investments so large that multi-nation collaborations are required to fund them. Modern accelerator science also has massive (and increasing) energy needs, yet the very provision of secure, equitable, clean and cost effective energy is one of the greatest sustainability challenges facing society. Modern energy provision systems are fundamental to development, yet also constitute one of the greatest threats to sustainability via their contribution to environmental degradation and climate change. This paper works from a premise that any new proposal for investment in an RI should credibly demonstrate that it would deliver more value than cost to society. As our understanding of the negative impacts of energy use grows, the demonstration of overall value creation has become more complex; it must now include consideration of an RI's 'energy system footprint'. Programs to reduce the energy footprint can help address this delicate balance. This paper uses experiences in the development of the European Spallation Source (ESS) in Sweden to demonstrate how credible programs to improve the energy performance of an RI can take form.

## THE REASON FOR GREENING

### *Research Infrastructure*

We use the term "Research Infrastructure" (RI) to denote scientific facilities of such magnitude that they are comparable to other infrastructure such as airports, bridges or tunnels. Many of these facilities are based on accelerators, but there are also telescopes, supercomputers, reactors, wind tunnels, and more.

The funding of scientific RIs is also an issue that can be compared with that of bridges and airports. Such investments are often necessarily financed by governments, but are motivated by explicit expectations that the benefits they provide to society, both in the medium and long-term, far outweigh their costs. There is thus, a strong social element in the argument for investments in RIs such as particle accelerators. This social argument element includes the societal value of knowledge as a goal in itself.

### *Costs and Benefits of RIs*

Just as each breakthrough in the crafting of lenses has paved the way for new scientific discovery with telescopes and microscopes that can see further, or 'smaller', each generation of accelerator-based RI required for the next level of knowledge needs to be more powerful. While technological improvements help ameliorate the situation, for the most part, each RI generation with increased performance also needs increased energy input – and the overall energy consumption (and operational cost) increases.

In order to attract governments to join the financing of new RIs, scientists and other proponents must successfully argue that benefits continue to (significantly) outweigh the costs. Cost/benefit assessments however, are complex; both the benefits and the costs are likely to contain a large proportion of intangible or contingent items. As positives, these can include the effects of creativity and innovation; as negatives, there may be fear of (potential) accidents, concern about radiation or simply NIMBYism. It can therefore be a difficult task to demonstrate net benefit. It is perilous to disregard stakeholder concerns however. Proponents of scientific infrastructure, often themselves scientists, may tend to undervalue risk vectors that seem irrational, or factually unfounded, such as the concerns of neighbours of the potential dangers of the research to be conducted (e.g. the 'creation of a black hole', the potential of a meltdown, etc.). Even if concerns are unfounded, they can still be real, both in the minds of neighbours, and even in law. In Swedish environmental legislation, as one example, the concerns of neighbours are considered as an 'environmental impact' and must be managed; just as emissions are.

## SUSTAINABILITY

Humankind places an increasing burden on the planet. Despite our gains in efficiency, the effects of population growth and economic growth consume increasing amounts of resources [1], [2]. Scarcity of resources leads to price volatility – and to 'security of supply' challenges that are most serious for those most sensitive to price. Food, water and energy can always be produced and distributed to those who can afford them. This is not the central challenge for sustainability. A very important challenge however, is to do so for the world's poor.

Science can substantially contribute to both the knowledge needed to lower the cost of supplying life essentials, and to the growth needed for the poorest to access them. This is an important argument for investment in science. However, it is also important to recognise that an initial investment of resources to create large RIs places additional stress on supply systems. It can contribute to energy poverty by raising prices, and also competes directly for potentially scarce energy with such sectors as food production.

In addition to its highly publicized links to climate change [3], energy also plays important roles in the



ISBN 978-3-95450-172-4

supply of food. World food production is dependent on energy carriers to produce and distribute chemical fertilizer, and to produce and distribute the food.. Conversely, agriculture can be used to produce useful energy forms, such as biomass and biofuel. In doing so, energy supply competes directly for land with food production.

The concept of Sustainable Development is commonly represented using three pillars: environment, economy and society. These may also be useful to understand and discuss the impact of accelerator projects both inside and outside the facility boundary. Energy is not only an environmental issue; it is most certainly a critical economic issue for the facility, as energy use is a substantial part of operating costs, and price fluctuations pose a serious threat to the planned scope of operations.

The establishment of new research infrastructure can also tangibly affect local resource markets and distribution. On the margin, use of resources for research infrastructure competes with other uses; in some areas (such as rare earths) even globally.

## CASE ESS

The European Spallation Source, the world's 'brightest' neutron source is now being built in Lund, Sweden. The first cornerstone is being laid on October 9, 2014. The first neutrons are to be delivered by the end of 2019. Ramp up to full power will then continue to 2025, after which the planned lifetime is 40 years. A 5MW linear accelerator will propel bunches of 10E12 protons into a rotating tungsten target, where neutrons will be spalled from tungsten nuclei, each proton liberating around 30 neutrons [4].

The justification for a new neutron source is that neutrons are especially useful for investigating inside materials in a way that complements more common X-ray methodologies. Neutrons, by virtue of their mass, are especially sensitive to the nuclei of light atoms, such as those of organic compounds found in life sciences, and also in the energy field. Within the field of energy applications, neutrons can facilitate investigation of in many areas. Combustion processes are one example: where engines can be examined while running, and additives tested to improve efficiency. As another example, lithium ion batteries can be examined with both neutrons and X-rays. This gives a more comprehensive understanding of how ion structures change in the batteries. Similarly, neutrons are useful for fuel cell research, to understand the details of how ions interact with membranes; for hydrogen storage in metals; for the study of carbon capture and storage mechanisms; and for material structural investigations needed for photovoltaics development. Extreme materials research is yet another area: extremely heat-resistant materials can be tested for application in more efficient power plants – and neutrons can also be used to investigate the structural integrity of existing power plants. [5]

These are just a few of the possible uses of ESS in the energy arena. There are many more in life sciences, and other important research fields, such as the development of new materials. Viewed from this perspective ESS can be considered to be somewhat of a 'Swiss army knife', with many uses. It is 'workhorse' facility, applicable on technology close to market (even post market). The practical usefulness of ESS combined with its special importance for life science and energy have made it relatively easy to formulate and evaluate the 'sustainable science' case for the facility. "Science for Society" has been used as a motto throughout the history of the project.

### *Responsible, Renewable, Recyclable*

As an energy-intensive facility in an increasingly 'resource constrained world', the ESS is committed to implementing its self-developed energy program "Responsible, Renewable, Recyclable". This requires that the facility must be energy efficient, use only renewable energy sources and will recycle its waste heat. The ESS board of directors has set firm goals for each pillar of the program.

### *Energy Inventory*

Twice per year, ESS performs an Energy inventory to calculate the energy use in the future operations. The inventory serves the dual purposes of assessing performance in relation to baseline goals for consumption, and focusing attention on energy efficiency.

At the launch of the ESS project, there was insufficient data to perform an inventory based on the ESS design. Therefore, the first energy inventories for ESS were performed at the Spallation Neutron Source (SNS) at Oak Ridge National Laboratory in the USA, with scaling and adjustment according to known differences. These studies were vital to the early implementation of the ESS energy strategy and are a good example of the power of collaboration between facilities.

The original plans for ESS, based on a 2002 design proposal, called for an annual energy consumption of 610 GWh for a MW accelerator facility [6]. The Scandinavian bid to host ESS was based on a slimmer single-purpose version (long-pulse) and greatly increased use of superconduction; this yielding a much reduced overall demand.

### *Heat Recovery*

To facilitate recovery and reuse of heat ejected in cooling cycles, ESS has signed an agreement with the local district heating provider (Kraftringen) that has three parts. First, ESS will be connected to the district-heating grid, an investment of 5 M€. Second, ESS will sell surplus heat to Kraftringen at a market-based rate, varying over the year. Recycling of the entire surplus heat (using heat pumps) would generate a revenue of 5M€ per year to ESS (but also involves additional power use, and costs for running heat pumps). Third, ESS will purchase heat from the grid for pre-operations and as back-up in the event of failure in internal heat supply.

The technical conditions within the agreement also concretise requirements for a significant design change

ISBN 978-3-95450-172-4

for an accelerator RI. High-temperature cooling cycles are a pre-requisite, in that the district heating system requires 80°C as a supply temperature to function. This is also linked to important developments on the heat-grid side, as historic temperature requirements have been significantly higher than 80°C, especially in winter. The return temperature, which corresponds to the cooling temperature available for ESS, is around 50°C. With this design configuration, any equipment or system that generates less than 80°C, or must be cooled to below 50°C, necessitates the use of heat pumps. The greater the temperature gap, the greater is the electricity demand for the heat pumps. However, while heat pumping to facilitate recycling of low-grade heat (down to 10°C) for delivery to 80° district heating is technically feasible, under many conditions it may be economically and environmentally questionable. Therefore alternative technical pathways are worthy of examination.

In this light, heat at 40°C and below can be used in other areas such as space heating, for greenhouses, drying of biofuels, and for heating of bio-digesters or aquaculture ponds. For the ESS, a 'hybrid-cooling regime' supporting a food production cooling chain has been proposed. It encompasses greenhouses, fish farming and fish fodder production with yeast. A guiding principle for this is to put together a cooling chain of declining temperatures so that the heat is used efficiently. An important point is that these processes also form a nutrient loop. Hydroponic greenhouse farming can use the fish excrements as fertilizer, eliminating a major energy consumer in agricultural processes. Fish can be fed with fodder made from yeast, which can be produced on a substrate of organic waste. Thus waste heat combines with organic waste to produce new, high quality, locally produced food. A schematic of the envisioned cooling and nutrient chains is shown in Figure 1.

For ESS, the result would be similar revenue to a solution where the facility upgrades waste heat to 80°C with heat pumps, however, it involves lower costs, lower energy use and a suite of ancillary socio-economic benefits. Among other things, this system can deliver increased food security and quality, improved land and marine environment, and local economic activity.

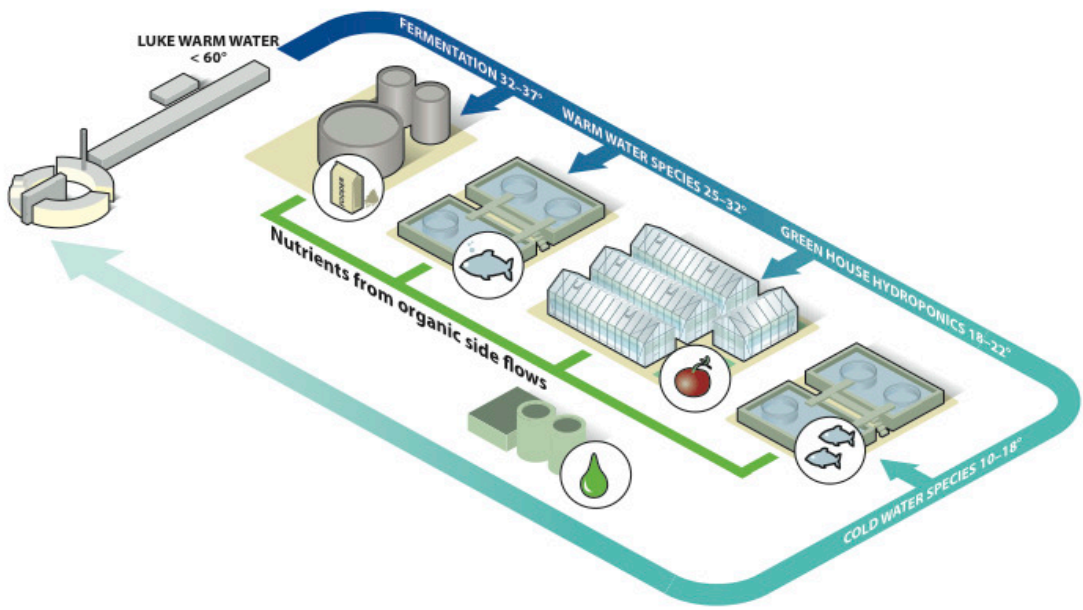


Figure 1: A 'hybrid cooling regime' proposed for ESS. A cooling chain of declining temperatures is paired with a nutrient loop from agricultural and food waste.

## *Remarkable and Replicable*

The 'Responsible, Renewable and Recyclable' strategy was born out of the competition to host ESS. In order to work as a unique selling point, it was necessary to adopt a strategy that would be perceived as well beyond current best practice. In the spirit of the RRR-slogan, the solution also needed to be 'Remarkable'.



ISBN 978-3-95450-172-4

However, it must be recognized that the 'Renewable' and 'Recyclable' parts of the ESS energy strategy build on local opportunities that may not be available elsewhere. The ESS site happens to also host a wind turbine already – and even more importantly, the structure of the energy market is such that power can be traded, throughout the Nordic grid, with limited transaction costs. This helps by broadening siting options for renewable energy from the immediate surrounds, to the entire grid region. For 'Recyclable', a vital enabling factor is the existence of district heating system that already delivers a TWh/yr of heat to Lund and neighbouring areas. More broadly, ESS benefits from an environment where there is a significant demand for space heating due to a cool-temperate climate with average mid-winter daytime temperatures at approximately 0°C.

Although ESS benefits from some opportunities that are unusual in the accelerator community, there is nothing in these boundary conditions that is not equally applicable for many types of energy intensive industry in the region, of which there are a number. The ESS solutions can readily be applied in industry, i.e. the strategy is also 'Replicable'. This is an important societal benefit, delivering a significant leverage to society's investment in this RI.

The strategy as originally formulated reflected emerging social expectations for energy, that at the time were perceived as the main sustainability issue for the facility. However, as the implementation of the strategy has evolved, other sustainability issues, such as food, water, land-use and transportation have gained greater recognition, and are now explicitly included in discussions and in concrete planning.

The sustainability challenges facing ESS reflect a growing global imperative that we adjust consumption and production systems to align with a carbon and resource constrained future. These are issues that are being experienced, and increasingly addressed, by businesses worldwide [7].

## COLLABORATION

Reflecting the broader applicability of a 'Responsible' energy culture throughout the RI field, the ESS, CERN and ERF (the European Association of National Research Facilities) together hosted an *Energy for Sustainable Science* workshop in Lund in October 2011. All the national laboratories of Europe, along with a number of international labs attended. The event became somewhat of a 'kick-off' for a movement focused on energy issues at large-scale research laboratories – now often referred to as 'The Grand Energy Challenge'. The ensuing network has already spawned a number of collaborative and individual efforts, many of which were presented at the second workshop, held at CERN in October 2013. The motivation underlying such activities is captured in the content of the executive summary of the 2011 gathering, where the organizing committee discusses the "*Energy Grand Challenge"* and strongly argues for an RI role in process of meeting this sustainability challenge. There were several points to this argument. A first was that RIs can be a focal point for innovation; they can both deliver groundbreaking research and provide a nurturing innovative environment. A second is that RIs, although industrial in scale, differ from industry in that they share and disseminate results, scientific advances and technological improvements, thus leveraging improvements for society. The combination of industrial scale, free(er) information dissemination and international networking also make RIs an excellent training ground for young researchers and engineers for future opportunities in industry. As a third point, RIs are often required to innovate in order to deliver the science expected of them; as such, they are natural test beds for innovative schemes of energy management [8].

Another on going European collaboration, conceived in parallel with the abovementioned workshops, is the energy efficiency work package in the EU accelerator development project 'EuCARD2'. This collaboration encompasses energy recovery, accelerator efficiency and other issues. It is especially significant because energy issues are discussed in the context of the pinnacle of accelerator development [9].

## CONCLUSION

At the ESS, an energy program within this RI is now seen as a fundamental item – an 'expectation' rather than a option. Importantly, there is also evidence that this 'expectation', or 'norm' is spreading in the RI community. While we would argue that the ESS "Responsible, Renewable, Recyclable" concept is neither perfect nor universal, it provides a benchmark for future development – and is certainly useful to showcase how an energy culture both complements the traditional expectations of an RI, and prepares it for escalating stakeholder expectations in areas such as resource efficiency, and for more volatile resource markets.

As the total efficiency of accelerator systems is generally unimpressive, energy efficiency must be the primary objective of such work – and the earlier efficiency efforts are made, the greater their potential benefit. While it will likely be possible to make incremental improvements all through an RI life cycle, major improvements can usually only be made before the facility is built – utilizing the combined strength of design flexibility and buying power to define better systemic performance from the outset.

This sentence helps define our first rule of heat recycling at ESS – don't! Use efficiency efforts to avoid energy consumption and the ensuing heat creation. Then, where waste heat cannot be avoided seek to 'reuse' heat. Where options exist, deliver immediately 're-usable' heat streams – for example via high temperature cooling in a

ISBN 978-3-95450-172-4

facility. As a third step examine options for the use of low-grade heat.

As the driving forces underlying a mandate for energy efficiency, low carbon energy systems, and energy price stability for RIs continue to escalate; a foundation for action now exists in the international RI community. Continued and intensified interactions between RI laboratories and projects, both in dedicated fora like the "Energy for Sustainable Science" workshop series, and in conjunction with other interactions such as this "*The 55th ICFA Advanced Beam Dynamics Workshop on High Luminosity Circular e+e- Colliders – Higgs Factory*". conference are important to continue such work. As immediate actions, it will be useful to develop clear performance indicators (and benchmarks) for parameters such as *energy delivered/energy used* to map and track progress in accelerator utilization or design, or both. Further, worldwide collaboration on accelerator efficiency can increase leverage for actors such as designers, suppliers, constructors and managers to deliver technical solutions to meet our *Grand Energy Challenge*.

Showcasing of successful projects in laboratories across the world will be an important part of helping the Science community to both understand and rise to meet such challenges.[10]

## REFERENCES


[1] P. Gerland, A. E. Raftery, H. Ševčíková, N. Li, D. Gu, T. Spoorenberg, L. Alkema, B. K. Fosdick, J. Chunn, N. Lalic, G. Bay, T. Buettner, G. K. Heilig, and J. Wilmoth, "World population stabilization unlikely this century," *Science*, Sep. 2014.

[2] IPCC, "Summary for Policymakers," in *Climate Change 2014: Impacts, Adaptation, and Vulnerability. Part A: Global and Sectoral Aspects. Contribution of Working Group II to the Fifth Assessment Report of the Intergovernmental Panel on Climate Change*, C. B. Field, V. R. Barros, D. J. Dokken, K. J. Mach, M. D. Mastrandrea, T. E. Bilir, M. Chatterjee, K. L. Ebi, Y. O. Estrada, R. C. Genova, B. Girma, E. S. Kissel, A. N. Levy, S. MacCracken, P. R. Mastrandrea, and L. L. White, Eds. Cambridge, United Kingdom, and New York, NY, USA: Cambridge University Press, 2014, pp. 1–32.

[3] S.Chu and A. Majumdar, "Opportunities and challenges for a sustainable energy future," *Nature*, vol. 488, no. 7411, pp. 294–303, Aug. 2012.

[4] Steve Peggs, Ed., *ESS Technical Design Report*. European Spallation Source, 2013.

[5] *Neutrons for Global Energy Solutions 2010 Book of Abstracts*. Forschungszentrum Jülich GmbH, 2010.

[6] G. S. Bauer, F. H. Bohn, K. Bongardt, F. Carsughi, A. Claver, K. N. Clausen, I. S. K. Gardner, C. Hake, H. Tietze-Jaensch, and H. Ullmaier, Eds., *The ESS Project Volume III Technical Report*. ESS Council.

[7] WBCSD, "WATER, FOOD AND ENERGY NEXUS CHALLENGES," World Business Council for Sustainable Development, Paris, 2014.

[8] F. Bordry, T. Parker, and C. Rizzuto, "Main findings of the first joint workshop on Energy management for large-scale research infrastructures," presented at the Energy for Sustainable Science workshop, Lund, Sweden, 2011.

[9] J. Stadlmann, R. Gehring, E. Jensen, T. Parker, and P. Seidel, "Energy efficiency of particle accelerators - A networking effort within the EuCard2 program," presented at the 5th International Particle Accelerator Conference, Dresden, Germany, 2014, pp. 4016–4018.

[10] T. Parker, "Sustainable energy: Cutting science's electricity bill," *Nature*, vol. 480, no. 7377, p. 315, Dec. 2011.




ISBN 978-3-95450-172-4

# PARAMETER OPTIMIZATION IN HIGGS FACTORY DESIGN

C. Zhang, IHEP, CAS, P.O.Box 918, Beijing 100049, China

*Abstract*

In this paper, parameter optimization of Higgs factories is discussed focusing on the designs of CEPC and FCCee. The total beam current in Higgs factories is limited by synchrotron radiation power, and then the machine size and cost; maximum linear tune shift is limited by beam-beam interaction; reduction of beta-function at interaction point is restricted by the distance of the final focusing quadrupole to the interaction point, bunch length, "hour glass" effect and dynamic aperture. Beamstrahlung effects beam energy spread and lifetime in the colliders, limiting luminosity reach. High luminosity in the Higgs factories requires optimization of parameters.

## LUMINOSITY

Discovery of Higgs boson of 125 GeV, shown in Fig.1, not far from the LEPII reached energy, makes it feasible to build circular $e^+e^-$ colliders of 120 GeV and neighbouring energies as Higgs factories with high luminosity.

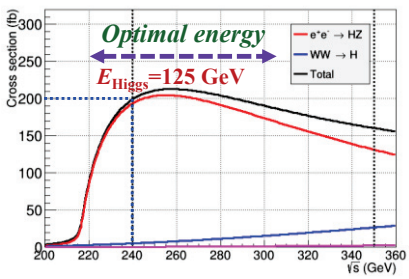


Figure 1: Energy of Higgs boson and Higgs factories.

The luminosity in circular collider is given in Eq. (1) assuming beam aspect ratio $r=\sigma_y/\sigma_x<<1$, $\sigma_x$ and $\sigma_y$ being horizontal and vertical beam size at interaction point (IP).

$$L = \frac{1}{2e \cdot r_e E_0} \cdot \xi_y \frac{E \cdot k_b I_b}{\beta_y^*} H_g \qquad (1)$$

Where $e$ is electron charge, $r_e$ is classical radius of electron, $E_0$ is rest energy of electron, $E$ is colliding beam energy, $k_b$ and $I_b$ are bunch number and current respectively, $\xi_y$ is vertical beam-beam parameter, $\beta_y^*$ is beta function at IP and $H_g$ is hour glass factor expressed as:

$$H_g = \frac{L}{L_0} = \frac{\beta_y^*}{\sqrt{\pi}\sigma_z} \exp\left(\frac{\beta_y^{*2}}{2\sigma_z^2}\right) K_0\left(\frac{\beta_y^{*2}}{2\sigma_z^2}\right) \qquad (2)$$

Here $\sigma_z$ is bunch length. The formula is applies to the zero crossing angle case.

It can be seen in Eq. (1) that the luminosity is closely related to total beam current, beta function at IP, maximum beam-beam parameter, hour glass factor which always less than 1. And all parameters are correlated. The correlation of the parameters are illustrated in Figure 2.

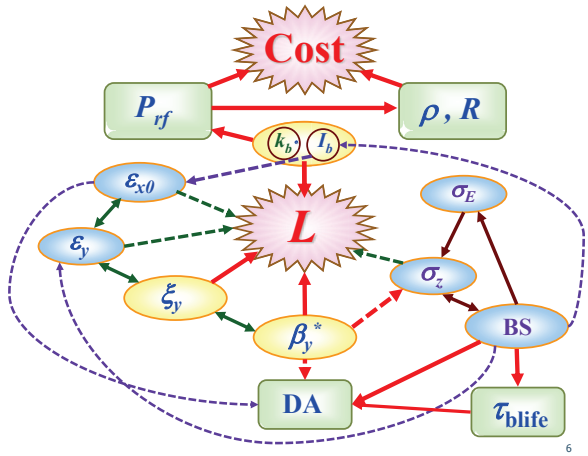


Figure 2: Correlation of parameters in colliders.

As shown in Fig. 2, luminosity is in the centre of the correlation net while the cost of the collider is the top concern especially for such a high energy $e^+e^-$ collider like Higgs factories. In following sections optimization of the parameters related to luminosity and cost are discussed based on the designs of CEPC [1] and FCCee [2].

## BEAM-BEAM PARAMETER

Beam-beam parameter, or linear beam-beam tune shift, characterizes the strength of the beam-beam force [3]:

$$\xi_{x,y} = \frac{r_e}{2\pi e} \frac{I_b \beta_{x,y}^*}{\gamma \cdot f_0 \sigma_{x,y} (\sigma_x + \sigma_y)} \qquad (3)$$

here $\gamma$ is relativistic energy and $f_0$ is revolution frequency. The larger the beam-beam parameters, the higher the luminosity will be reached. The maximum achievable beam-beam parameter strongly depends on the radiation damping in storage rings. The LEP beam-beam performance gives the following scaling law [4]:

$$\xi_y^{\max} = 0.5\tau_E^{-0.4} \qquad (4)$$

Taking advantage of the LEP scaling law of Eq. (3), the maximum vertical beam-beam parameters for CEPC and FCCee are calculated in comparison with their designed values in Table 1 and Fig. 3.

Table 1: Calculated and Designed Maximum Vertical Beam-beam Parameters for CEPC and FCCee

| Parameter | | CEPC | FCCee | | | |
|---|---|---|---|---|---|---|
| $E$ (GeV) | | 120 | 45.5 | 80 | 120 | 175 |
| $\tau_E$ (turns) | | 39 | 1320 | 243 | 72 | 23 |
| $\xi_y^{\max}$ | Cal. | 0.15 | 0.028 | 0.056 | 0.090 | 0.143 |
| | Des. | 0.083 | 0.03 | 0.059 | 0.093 | 0.092 |

ISBN 978-3-95450-172-4

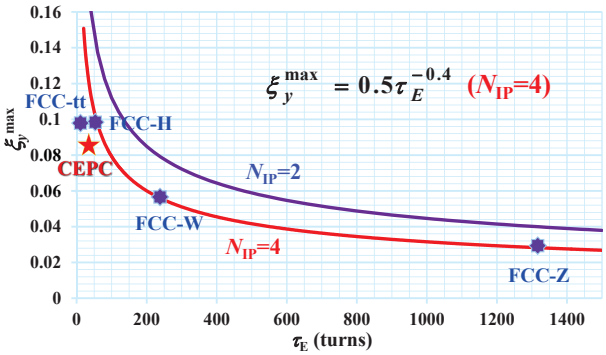


Figure 3: Designed $\xi_y^{max}$ for CEPC and FCCee in comparison with LEP scaling curve.

It can be found in Fig. 3 that the designed $\xi_y^{max}$ values of FCC-H, FCC-W and FCC-Z are well on the LEP scaling curve, while the $\xi_y^{max}$ values of FCC-tt and CEPC are below the curve. The reason for FCC-tt may trace to the limitation of total beam current, while the lower $\xi_y^{max}$ of CEPC design, which is also suggested by beam-beam simulation, may come from other parameters not taken into account in the scaling law especially bunch length.

## BEAM INTENSITY

It is well known that the beam intensity in high energy $e^+e^-$ collider is limited by total synchrotron radiation (SR) power:

$$P_{sr} = U_0 \cdot k_b I_b = C_\gamma \frac{E^4}{\rho} k_b I_b \qquad (5)$$

Here $\rho$ is bending radius, $U_0$ is SR loss per revolution and $C_\gamma = 8.846\times10^{-5}$ m/(GeV)$^3$ is SR constant for electron. As shown in Eq. (5) that the total beam current $k_b \cdot I_b$ is limited by the SR power loss $P_{SR}$. The luminosity is related to the RF power and bending radius as:

$$L_0 = \frac{3(m_e c^2)^2}{8\pi r_e^2} \frac{\xi_y}{\beta_y^*} \cdot \frac{P_{rf}\rho}{E^3} = 2.45\times10^{39} \frac{\xi_y}{\beta_y^*(\text{mm})} \cdot \frac{P_{rf}(\text{MW})\rho(\text{km})}{E^3(\text{GeV}^3)} \qquad (6)$$

Figure 4 gives luminosity vs. beam energy for $\rho$=6.1 km (CEPC), 11km (FCC) and $P_{SR}$=50 MW (CEPC & FCC).

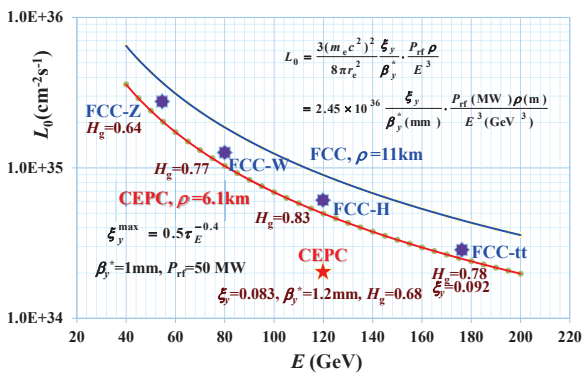


Figure 4: Luminosity vs. beam energy in CEPC & FCC.

It can be seen in Fig.4 that the designed luminosity for both CEPC and FCCee is below the luminosity curve for $\beta_y^*$ =1mm and $P_{SR}$=50MW. This is because of the hour glass effect of $H_g = L/L_0 < 1$. Another reason for CEPC is the design $\beta_y^*$=1.2 mm, 20% larger than 1mm calculated for the luminosity curve.

## $\beta_y^*$ AND BUNCH LENGTH

It is shown in Eq. (3) and Eq. (1) that the smaller the beta function at IP and the smaller the beam-beam tune shift, the higher the initial luminosity $L_0$ will be. However, the beta-function at the final focusing quadrupole (FFQ) is inversely proportional to $\beta_y^*$ such that $\beta_y^{FFQ} = L^{*2}/\beta_y^*$, where the $L^*$ is distance from FFQ to IP, which is restricted by the geometry of the detector. Large $\beta_y^{FFQ}$ requires large aperture of FFQ and also increases chromaticity $\Delta\xi_y = (\beta_y \cdot kl)_{FFQ}/4\pi$, causing dynamic aperture problem. This is why the $\beta_y^*$ is chosen as ~1mm instead of further smaller in Higgs factory design (1.2 mm for CEPC, and 1mm for FFC).

However, the hour glass effect prevents the luminosity reaching to $L_0$. Figure 5 exhibits the hour glass factor $H_g = L/L_0$ as a function of $\sigma_z/\beta_y^*$.

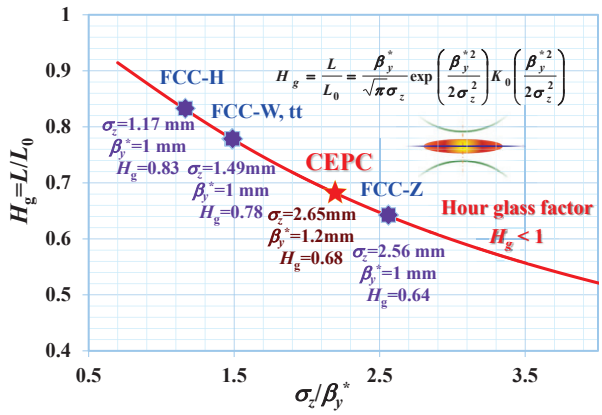


Figure 5: Hour glass factors for CEPC & FCC.

As shown in Fig. 5 that the hour glass factors in Higgs factory designs are 0.83, 0.78, 0.78, 0.68 and 0.64 for FCC-H, FCC-W, FCC-tt, CEPC and FCC-Z respectively. It is realized that the $Hg$=0.6~0.7 is too small and one needs to further optimize the collider parameters.

The key parameter in the hour glass formula Eq.(2) is the ratio of $\sigma_z/\beta_y^*$. Bunch length $\sigma_z$ should be short enough comparing to $\beta_y^*$ in order to restore the initial luminosity $L_0$ as fully as possible. It is worth to mention that the large $\sigma_z/\beta_y^*$ may also cause beam-beam synchro-betatron oscillation and other nonlinear effects.

Bunch length in electron storage rings is determined by synchrotron radiation and collective bunch lengthening effects. The natural bunch length in storage ring $\sigma_{z0}$ is expressed as:

$$\sigma_{z0} = \frac{R\alpha_p}{\nu_s}\sigma_{E0} = \frac{R\alpha_p}{\nu_s}\gamma\sqrt{\frac{C_q}{J_E\rho}} \qquad (7)$$



ISBN 978-3-95450-172-4

Where $R$ is the ring radius, $\alpha_p$ is momentum compaction factor, $\nu_s$ is synchrotron tune, $\sigma_{E0}$ is natural beam energy spread, $J_E \approx 2$ is longitudinal damping partition number and $C_q = 3.832\times10^{-13}$ m is quantum constant.

Small $\alpha_p$ and high $V_{rf}$ (this is a case in Higgs factories) result large $\nu_s$ and short bunch, which may help to relax hour class effect. On the other hand, potential and microwave instability, as well as beamstrahlung effects may cause bunch lengthening, and beamstrahlung fractional energy spread $\delta_{bs} \propto \sigma_z^{-2}$. This suggests suitable compromising choice of bunch length. The typical value of $\sigma_{z0}$ in Higgs factories is 1-2 mm.

## BEAMSTRAHLUNG

Beamstrahlung is the radiation from one beam of charged particles in colliders caused by its interaction with the electromagnetic field of an opposite beam.

Beamstrahlung adds energy spread to beam [5]:

$$\Delta\sigma_{\delta,B} = \frac{1}{2}\sqrt{\frac{\tau_E n_{IP}}{T_0}}\sigma_{\delta,B} \qquad (8)$$

where $n_{IP}$ is number of IP's in the collider, $T_0$ is revolution period and $\sigma_{\delta,B}$ is standard deviation of the energy loss expressed as:

$$\sigma_{\delta,B} = 1.24\left(0.333 + \frac{4.583}{n_\gamma}\right)^{1/2}\left[\frac{\alpha\sigma_z}{\bar{\lambda}_c\gamma}\frac{\Upsilon^2}{(1+(1.5\Upsilon)^{2/3})^2}\right] \qquad (9)$$

Average emitted photon number per collision is given by:

$$n_\gamma = 2.45\left[\frac{\alpha\sigma_z}{\bar{\lambda}_c\gamma}\frac{\Upsilon}{(1+\Upsilon^{2/3})^{1/2}}\right] \qquad (10)$$

Where $\alpha$=1/137 is fine structure constant, $\bar{\lambda}_c$ is the electron Compton wavelength divided by $2\pi$, $\bar{\lambda}_c = r_e/\alpha$, and $\Upsilon$ is the beamstrahlung strength is the following:

$$\Upsilon = \frac{5}{6}\frac{r_e^2\gamma\cdot N_e}{\alpha\sigma_z(\sigma_x+\sigma_y)} \qquad (11)$$

Beamstrahlung effects beam energy spread and lifetime in circular colliders, the beamstrahlung caused lifetime is expressed as [6]:

$$\tau_{BS} = \frac{20\sqrt{6\pi}r_e\gamma\cdot u^{2/3}e^u}{\alpha^2\sigma_e\sigma_z}T_0 \qquad (12)$$

with

$$u = \frac{\eta_e E}{E_{cb}} = \frac{\alpha\eta_e\sigma_x\sigma_z}{3\gamma\cdot r_e^2 N_e} \qquad (13)$$

Beamstrahlung caused beam energy spread and bunch length are calculated using Eq. (8) – (11) and lifetime is estimated with Eq. (12)-Eq. (13), giving in Table 2.

Table 2: Beamstrahlung Caused Beam Energy Spread and Lifetime Calculated for CEPC and FCCee

| Param | Unit | CEPC | FCC | | | |
|---|---|---|---|---|---|---|
| $E$ | GeV | 120 | 45.5 | 80 | 120 | 175 |
| $\xi_y$ | | 0.083 | 0.03 | 0.059 | 0.093 | 0.092 |
| $N_e$ | $10^{11}$ | 3.79 | 1 | 0.7 | 0.46 | 1.4 |
| $r=\varepsilon_y/\varepsilon_x$ | | 0.003 | 0.002 | 0.002 | 0.001 | 0.001 |
| $\sigma_z$ | mm | 2.65 | 1.64 | 1.01 | 0.81 | 1.16 |
| $\sigma_{\delta,BS}$ | % | 0.096 | 0.044 | 0.071 | 0.10 | 0.12 |
| $\sigma_{\delta,total}$ | % | 0. 16 | 0.060 | 0.10 | 0.14 | 0.18 |
| $\tau_{BS}$ | min. | 47 * | 298 | 73 | 29 | 21 |

* Obtained by beam-beam-simulation

It can be seen from Table 2 that beamstrahlung significantly effects on beam energy spread and lifetime, limiting luminosity reach in CEPC and FCCee. Several measures are taken to mitigate the beamstrahlung effects in Higgs factory design, including to use very flat colliding beams ($r=\sigma_y/\sigma_x<<1\%$), to provide large energy acceptance (1.5%-2%) and to optimize bunch length together with hour glass effect. The top-up injection should be applied to keep peak beam current.

## BUNCH NUMBER, POPULATION AND EMITTANCE

Total beam current $k_b\cdot I_b$ is limited by RF power. The bunch number $k_b$ and population $N_e=I_b/(e\cdot f_0)$ need to be optimized to make best use of the expensive current.

As shown in Eq. (11) the beamstrahlung strength Y is proportional to bunch population $N_e$, so smaller $I_b$ and larger $k_b$ are preferred for reducing the beamstrahlung effects. In CEPC, the single ring structure prevents a large bunch number, so $k_b$=50 is chosen and bunch population is $3.79\times10^{11}$. Taking advantage of double ring structure, more bunches can be operated in FCC. The bunch numbers get to 1360 (FCC-H), 16700 (FCC-Z), 4490 (FCC-W) and 98 (FCC-tt) with populations of $1.0\times10^{11}$, $0.7\times10^{11}$, $0.46\times10^{11}$ and $1.4\times10^{11}$ respectively.

Beam emittance is closely related the maximum bunch population allowed in collisions, shown in Eq.(3). In the case of optimum coupling when the coupling coefficient $\kappa=\varepsilon_y/\varepsilon_x=\beta_y^*/\beta_x^*=\sigma_y/\sigma_x$, Eq. (3) can be written as:

$$\xi_x = \xi_y = \frac{r_e}{2\pi\gamma}\frac{N_e}{\varepsilon_{x0}} \qquad (14)$$

It is shown in Eq.(14) that horizontal emittance $\varepsilon_{x0}$ should be low enough to reach $\xi_y^{max}$ for the small bunch population. The vertical emittance $\varepsilon_y$ should be further smaller to reduce the beamstrahlung caused energy spread. The typical value of coupling coefficient $\kappa$ is 0.001-0.002.

To sum up, the luminosity related parameters of CEPC [1] and FCCee [2] are given in Table 3.

ISBN 978-3-95450-172-4

Table3: Luminosity Related Parameters of CEPC and FCCee

| Parameter | CEPC | FCC | | | |
|---|---|---|---|---|---|
| | | Z | W | H | tt |
| $E$ (GeV) | 120 | 45.5 | 80 | 120 | 175 |
| $C$ (km) | 54.8 | 100 | | | |
| $\rho$ (km) | 6.1 | 11 | | | |
| $N_{IP}$ | 2 | 4 | | | |
| $k_b$ | 50 | 16700 | 4490 | 1360 | 98 |
| $N_e$ ($10^{11}$) | 3.79 | 1.0 | 0.7 | 0.46 | 1.4 |
| $\varepsilon_x$ (nm·rad) | 6.12 | 29.2 | 3.3 | 0.94 | 2.0 |
| $\varepsilon_y$ (pm·rad) | 18.4 | 60 | 7 | 1.0 | 2 |
| $\sigma_{E,SR}$ (%) | 0.13 | 0.04 | 0.07 | 0.10 | 0.14 |
| $\sigma_{E,total}$ (%) | 0.16 | 0.06 | 0.09 | 0.14 | 0.19 |
| $\sigma_{z,SR}$ (mm) | 2.14 | 1.64 | 1.01 | 0.81 | 1.16 |
| $\sigma_{z,total}$ (mm) | 2.65 | 2.56 | 1.49 | 1.17 | 1.49 |
| $\beta_x^*$ (m) | 0.8 | 0.5 | 0.5 | 0.5 | 1.0 |
| $\beta_y^*$ (mm) | 1.2 | 1.0 | 1.0 | 1.0 | 1.0 |
| $U_0$ (GeV) | 3.11 | 0.03 | 0.33 | 1.67 | 7.55 |
| $P_{SR}$ (MW) | 50 | 50 | | | |
| $V_{RF}$ (GV) | 6.9 | 2.5 | 4 | 5.5 | 11 |
| $f_{RF}$ (MHz) | 650 | 800 | | | |
| $\tau_E$ (turns) | 39 | 1320 | 243 | 72 | 23 |
| $A_E$ (%) | 6.0 | 2.7 | 7.2 | 11.2 | 7.1 |
| $f_s$ | 0.18 | 0.65 | 0.21 | 0.096 | 0.10 |
| $H_g$ | 0.68 | 0.64 | 0.77 | 0.83 | 0.78 |
| $L$ ($10^{34}$cm$^{-2}$s$^{-1}$) | 2.0 | 28.0 | 12.0 | 6.0 | 1.8 |
| $\xi_x$ | 0.118 | 0.031 | 0.06 | 0.093 | 0.092 |
| $\xi_y$ | 0.83 | 0.030 | 0.059 | 0.093 | 0.092 |
| $\tau_{lum}$ (min) | 48 | 298 | 73 | 29 | 21 |

## CONCLUSION

Low Higgs mass makes it feasible to build circular electron-positron colliders as a Higgs factories with high luminosity. High luminosity in Higgs factories calls for large rings with high RF power, large maximum beam-beam parameters, large dynamic aperture, small beam aspect ratio $r=\sigma_y/\sigma_x$ and optimized beta-function at IP, bunch length, beam emittance and other parameters. $\xi_y^{max}$ is chosen based on the LEP data and beam-beam simulation; 1 mm scale $\beta_y^*$ can be obtained with optimized $L^*$, $\sigma_z$, dynamic aperture, but remains very challenging; Beamstrahlung limiting beam lifetime prefers smaller bunch population, more bunches and lower beam emittance. Design of proposed Higgs factories is in an active progress, and their parameters have been being optimized.

## ACKNOWLEDGMENT

The author acknowledges Dr. F. Zimmermann of CERN for providing updated material on FCC design. He also wish to thank all the members of the CEPC team for stimulating daily discussion.

## REFERENCES

[1] Q.Qin, Overview of the CEPC Accelerators,THP3H2, HF2014 Proceedings.

[2] FCC team, Future Circular Collider Study Lepton Collider Parameters, FCC-ACC-SPC-0003 (2014).

[3] A. Chao, Beam-beam instability, Physics of High Energy Particle Accelerators, AIP Conf. Proc. 127, (1983).

[4] R. Assmann and K. Cornelis, The Beam-Beam Interaction in the Presence of strong Radiation Damping, Proc. EPAC2000, 1187-1189 (2000).

[5] K. Yokoya, Quantum Correction To Beamstrahlung due to the Finite Number of Photons, NIM A251 (1986).

[6] V. I. Telnov, Restriction on the Energy and Luminosity of $e^+e^-$ Storage Rings due to Beamstrahlung, Phys. Rev. Letters 110, 114801 (2013).



ISBN 978-3-95450-172-4

# POLARIZATION ISSUES IN THE $e\pm$ FCC

E. Gianfelice-Wendt (Fermilab*, Batavia)

*Abstract*

After the Higgs boson discovery at LHC, the international physics community is considering the next energy frontier circular collider (FCC). A *pp* collider of 100 km with a center of mass energy of about 100 TeV is believed to have the necessary discovery potential. The same tunnel could host first a $e^+e^-$ collider with beam energy ranging between 45 and 175 GeV. In this paper preliminary considerations on the possibility of self-polarization for the $e^\pm$ beams are presented.

## INTRODUCTION

$e^\pm$ beams in a ring accelerator may become vertically polarized through the Sokolov-Ternov effect [1]. A small part of the radiation emitted by particles moving in a constant homogeneous field is accompanied by spin flip wrt the field direction. The probability of spin flip in the direction parallel to anti-parallel and from anti-paralle to parallel to the field are slightly different and this results in a polarization of 92.4 %, independently of energy. The polarization rate is given by

$$\frac{1}{\tau_{ST}} = \frac{5\sqrt{3}}{8}\frac{r_0 h}{2\pi m_0}\frac{\gamma^5}{|\rho|^3}$$

which strongly depends upon energy and radius. In actual ring accelerators there are not only dipoles. Quadrupoles for instance are needed for beam focusing. When a particle emits a photon it starts to perform synchro-betatron oscillations around the machine actual closed orbit experiencing extra possibly non vertical fields. The expectation value $\vec{S}$ of the spin operator moves according to the Thomas-Bargmann-Michel-Telegdi (Thomas-BMT) equation [2] [3]

$$\frac{d\vec{S}}{dt} = \vec{\Omega}\times\vec{S}$$

$\vec{\Omega}$ depends on machine azimuth and phase space position, $\vec{u}$. In the laboratory frame and MKS units it is given by

$$\vec{\Omega}(\vec{u};s) = -\frac{e}{m_0}\left[\left(a+\frac{1}{\gamma}\right)\vec{B} - \frac{a\gamma}{\gamma+1}\vec{\beta}\cdot\vec{B}\vec{\beta} - \left(a+\frac{1}{\gamma+1}\right)\vec{\beta}\times\vec{E}\right]$$

with $\vec{\beta} \equiv \vec{v}/c$ and $a = (g-2)/2$=0.0011597 ($e^\pm$). The T-BMT equation describes a precession of $\vec{S}$ around $\vec{\Omega}$. In a planar machine the *periodic* solution, $\hat{n}_0$, is vertical. The number of precessions per turn, the "naive" spin tune, in the rotating frame is $a\gamma$. Photon emission results in a randomization of the particle spin directions (*spin diffusion*). Polarization will be therefore the result of the competing process, the Sokolov-Ternov effect and the spin diffusion caused by stochastic photon emission. The problem has been studied and solved in a semiclassical approximation by Derbenev and Kondratenko [4]. They found that the polarization is oriented along the *periodic* solution, $\hat{n}_0$, of the Thomas-BMT equation along the *closed orbit* and its value is

$$P_{DK} = P_{ST}\frac{\oint ds < \frac{1}{|\rho|^3}\hat{b}\cdot(\hat{n} - \frac{\partial\hat{n}}{\partial\delta}) >}{\oint ds < \frac{1}{|\rho|^3}\left[1 - \frac{2}{9}(\hat{n}\cdot\hat{s})^2 + \frac{11}{18}(\frac{\partial\hat{n}}{\partial\delta})^2\right] >}$$

with

$$\hat{b} \equiv \vec{v}\times\dot{\vec{v}}/|\vec{v}\times\dot{\vec{v}}|$$

The <> brackets indicate averages over the phase space. The term $\partial\hat{n}/\partial\delta$, with $\delta \equiv \delta E/E$ quantifies the depolarizing effects resulting from the trajectory perturbations due to photon emission.

The corresponding polarization rate is

$$\tau_{DK}^{-1} = P_{ST}\frac{r_e\gamma^5\hbar}{m_0 C}\oint < \frac{1}{|\rho|^3}\left[1 - \frac{2}{9}(\hat{n}\cdot\hat{s})^2 + \frac{11}{18}(\frac{\partial\hat{n}}{\partial\gamma})^2\right] >$$

In a perfectly planar machine $\partial\hat{n}/\partial\delta$=0. In presence of quadrupole vertical misalignments (and/or spin rotator) $\partial\hat{n}/\partial\delta \neq$0 and large when

$$\nu_{spin} \pm mQ_x \pm nQ_y \pm pQ_s = \text{integer}$$

Polarization in an actual ring accelerator has been observed for the first time at ACO in Orsay in 1968. The self polarization mechanism has been exploited more recently in large accelerators, namely HERA-e and LEP. While in LEP beam polarization was used for precise energy measurement through RF resonant depolarization, at HERA the provision of beam polarization was an integral part of the physics program and 3 pairs of spin rotators were build-in for turning the direction of polarization of the lepton beams from vertical to longitudinal at the HERMES, H1 and ZEUS experiments. HERA-e was operating at 27.5 GeV and the dipole bending radius was about 600 m, corresponding to a polarization time of the order of 30 minutes. The maximum transverse polarization achieved at HERA-e was about 75%. LEP dipole bending radius was about 3000 m and energy ranged between 40 and 100 GeV. The polarization level strongly decreased with energy and above 65 GeV no polarization was detected [5]. Qualitatively this can be explained by the increasing of spin diffusion with energy.

Both at HERA-e and LEP the high level of polarization was obtained through

- Optimization of energy;
- Choice of orbital tunes: small values of the fractional part result in a larger region free from low order resonances;

* operated by Fermi Research Alliance, LLC under Contract No. DE-AC02-07CH11359 with the United States Department of Energy.

ISBN 978-3-95450-172-4

- Careful correction of the (vertical) closed orbit;
- Dedicated correction of the nominal $\hat{n}_0$ distortion, $\delta\hat{n}_0$, due to magnet misalignments.

## FCC SCENARIO

For the FCC $e^-e^+$ collider precise energy measurement are required for $Z$ and $WW$ resonances at 45 and 80 GeV respectively.

Giving that the geometry is fixed by the maximum field, $B_{max}$, attainable for bending the 50 TeV protons and assuming $B_{max}$=16 T, the bending radius is $\rho_b = p/(eB)$=10423.6 m. The total length of the dipoles is $L_{bends} = 2\pi\rho_b$=65493.5 m which, for $L_{tot}$=100 km, gives a filling factor of $L_{bends}/L_{tot}$=0.655.

Chromaticity correction limits the minimum value of the dispersion in the arcs. In a FODO cell, for instance, the maximum dispersion is given by

$$\hat{D} = \frac{L_{cell}\phi_b}{2}\frac{1+0.5\sin\mu/2}{\sin^2\mu/2}$$

$\phi_b$ and thus $\ell_b$ [1] should be large for avoiding too small dispersion.

For the following computations a "toy" machine made out of FODO cells has been used with 30 m long bending dipoles and $\phi_b = \ell_b/\rho_b$=2.878 mrad bending angle and $\mu = 60^o$ phase advance in both planes. The resulting FODO optics is shown in Figure 1.The momentum compaction is 3.2e-5.

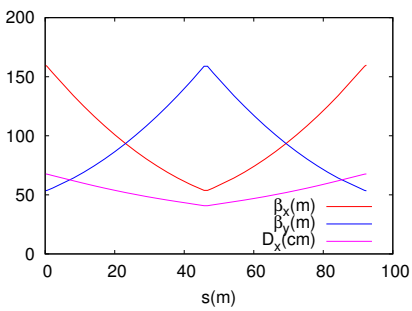


Figure 1: FODO Twiss functions (m) and dispersion (cm).

The large bending radius is may be appealing for some beam parameters (small energy loss and equilibrium emittance) but increases the damping time and the Sokolov-Ternov polarization time.

In Table 1 are shown the relevant beam parameters for a 100 km long machine with $\rho_b$=10423.6 m.

[1] $L_{cell} = 0.655 L_{bends}/2\pi/\phi_b$

Table 1

| $E$ (GeV) | $U_0$ (MeV) | $\Delta E/E$ (%) | $\epsilon_x$ ($\mu$m) | $\tau_x$ (ms) | $\tau_{pol}$ (h) |
|---|---|---|---|---|---|
| 45 | 35 | 0.038 | 0.85e-3 | 868 | 256 |
| 80 | 349 | 0.067 | 0.27e-2 | 218 | 14 |

## POLARIZATION WITH WIGGLER MAGNETS

For decreasing the polarization time the obvious recipe is increasing synchrotron radiation emission by introducing *wiggler* magnets.

The polarization rate in a perfect planar machine, with vertical fields possibly pointing in opposite directions is given by

$$\tau_p^{-1} = \frac{5\sqrt{3}}{8}\frac{r_e\gamma^5\hbar}{m_0 C}\oint\frac{ds}{|\rho|^3} = F\Big[\int_{dip}\frac{ds}{|\rho_d|^3} + \int_{wig}\frac{ds}{|\rho_w|^3}\Big]$$

with $F \equiv 5\sqrt{3}r_e\gamma^5\hbar/8m_0C$. Therefore *any* wiggler decreases $\tau_p$. The polarization is given by

$$\vec{P} = \hat{n}_0\, P_{ST}\frac{\oint ds\frac{\hat{B}\cdot\hat{n}_0}{|\rho|^3}}{\oint ds\frac{1}{|\rho|^3}}$$

that is

$$P \propto \tau_p \oint ds\,\frac{\hat{B}\cdot\hat{n}_0}{|\rho|^3}$$

Lowering the polarization time may lower the polarization level. We can separate the contribution of guiding dipoles and wigglers

$$\oint ds\,\frac{\hat{B}\cdot\hat{n}_0}{|\rho|^3} = \int_{dip} ds\,\frac{\hat{B}_d\cdot\hat{n}_0}{|\rho_d|^3} + \int_{wig} ds\,\frac{\hat{B}_w\cdot\hat{n}_0}{|\rho_w|^3}$$

The wiggler does not change $\hat{n}_0$ which in a perfectly planar ring is vertical; therefore

$$\int_{wig} ds\,\frac{\hat{B}_w\cdot\hat{n}_0}{|\rho_w|^3} = \frac{1}{ep}\int_{wig} ds\, B_w^3$$

This term must be large, and should have the same sign as the guiding field contribution, in order to maximize the level of polarization. For instance, an antisymmetric wiggler, $B(s) = -B(-s)$, would results in very small polarization.

The condition on $\int_{wig} ds\, B_w^3$ must be added to the usual constraint that the orbit outside the wiggler region should be unperturbed which translates in the conditions

$$\int_{wig} ds\, B_w = 0 \Rightarrow x' = 0 \quad \text{outside wiggler}$$

$$\int_{wig} ds\, sB_w = 0 \Rightarrow x = 0 \quad \text{outside wiggler}$$



ISBN 978-3-95450-172-4

A symmetric wiggler automatically fulfills the condition for $x = 0$. If in addition the field integral vanishes thus also $x' = 0$. A similar field arrangement as proposed for the LEP polarization wigglers [6] has been here considered (see Figure 2) with $B_+/B_-$=6.

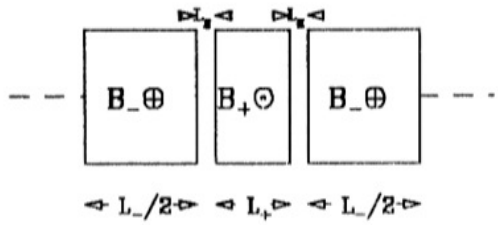


Figure 2: LEP polarization wiggler (figure from [6]).

Four dispersion free sections have been inserted in the "toy" machine for accommodating 4 of such wigglers with $L_+$= 8 m. The optics is almost unperturbed (see Figure 3)

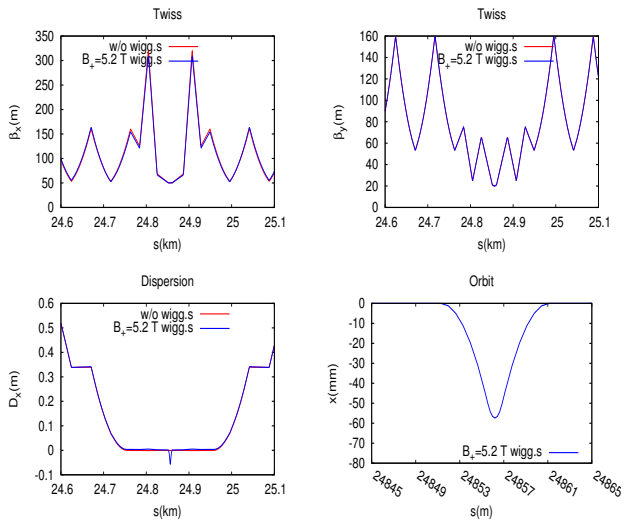


Figure 3: Twiss functions (up), horizontal dispersion and orbit (bottom) at the wiggler location with $B_+$=5.2 T.

Relevant beam parameters in presence of wigglers [2] are quoted in Table 2

Table 2

| $B_+$ (T) | $U_0$ (MeV) | $\Delta E/E$ (%) | $\epsilon_x$ ($\mu$m) | $\tau_x$ (s) | $P$ (%) | $\tau_{pol}$ (min) |
|---|---|---|---|---|---|---|
| 0 | 37 | .04 | .8e-3 | .82 | 92.4 | 14e3 |
| 1.3 | 64 | .22 | .5e-2 | .48 | 87.6 | 247 |
| 2.6 | 144 | .41 | .070 | .21 | 87.6 | 31 |
| 3.9 | 278 | .55 | .274 | .11 | 87.6 | 9 |
| 5.2 | 466 | .65 | .691 | .06 | 87.6 | 4 |

The increase of the energy spread is potentially harmful for polarization. As a comparison the beam relative energy spread was ~0.1% in HERA-e and ~0.16% in LEP at 100 GeV.

Distance between *imperfection* (or zeroth) order resonances is $\Delta E$= 440 MeV independently of energy. How well must be corrected the closed orbit and $\delta n_0$ in order to achieve a minimum useful level of polarization for energy measurement (~ 5-10%) must be investigated by accurate simulations.

## PRELIMINARY SIMULATIONS

In [7] a detailed description of available codes for evaluating radiative polarization may be found.

In Figure 4 and Figure 5 polarization and $\delta\hat{n}_0$ vs.energy computed by SLIM [8] (*linear* orbital and spin motion) for the FCC "toy" ring w/o and with 4 wigglers ($B_+$=5.2 T) respectively and in presence of random quadrupole vertical misalignment is shown. The rms value of the misalignment is 150$\mu$m and the resulting rms vertical closed orbit is 5.4 mm. No corrections have been applied. The orbital tunes are $Q_x$=181.185, $Q_x$=183.227 and $Q_s$=0.09. The red line indicates the polarization in the ideal machine. The curves labeled as $P_z$ (with $z$=$x, y, s$) are the polarization levels related to the three degrees of freedom separately.

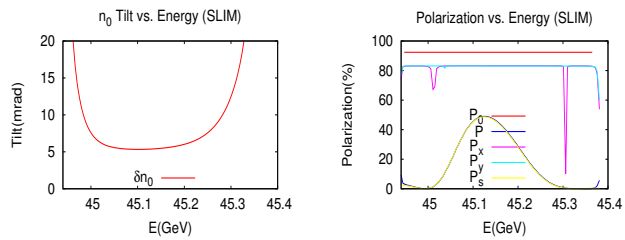


Figure 4: $\delta\hat{n}_0$ (left) and polarization(right) vs. energy w/o wigglers with $\delta_y^Q$=150 $\mu$m.

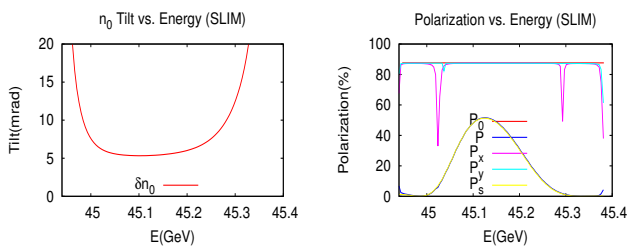


Figure 5: $\delta\hat{n}_0$ (left) and polarization(right) vs. energy with 4 wigglers ($B_+$=5.2 T) with $\delta_y^Q$=150 $\mu$m.

In presence of errors first order resonances appear, the strongest being the $\nu_s$=$integer \pm Q_s$ ones. Taking into account that no corrections have been applied, the situation seems at a first sight not hopeless.

[2] Implications on luminosity, beam-beam etc not investigated!

ISBN 978-3-95450-172-4

Actually the spin motion is *not* linear and non-linear calculations are mandatory. Codes treating non-linearized spin motion in a semi-analytical approach have either convergence problems at high energy or requires very large computing power. Two tracking codes are available, SITROS [9] and SLICKTRACK [10]. The first one, the only currently at hand to the author, has been used here.

In Figure 6 and 7 the SITROS calculations for the machine with random errors and w/o wigglers are shown for $\delta_y^Q$=10 and 50 $\mu$m respectively. No corrections have been applied. The orbital tunes are $Q_x$=181.124, $Q_x$=183.207 and $Q_s$=0.1.

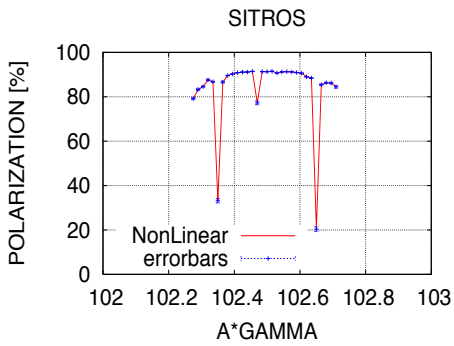


Figure 6: Polarization vs. spin tune w/o wigglers with $\delta_y^Q$=10 $\mu$m.

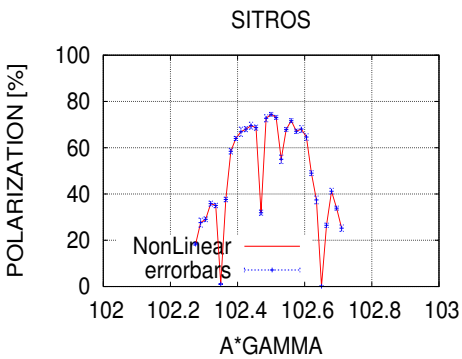


Figure 7: Polarization vs. spin tune w/o wigglers with $\delta_y^Q$=50 $\mu$m. The corresponding rms vertical orbit is 2 mm.

Much needed computations in the presence of wigglers are going on.

## SUMMARY

A preliminary study of polarization in the FCC $e^{\pm}$ ring at the $Z$ resonance energy (45 GeV) has been presented. It has been shown that owing to the unfavorable dimension of the machine the polarization time can be reduced to reasonable values only by inserting wigglers. The resulting large energy spread is expected to lead to depolarization in presence of magnet misalignments, in particular the vertical ones. The sensitivity of orbit and $\delta\hat{n}_0$ to errors increases with the strengths of the quadrupoles, the Twiss functions at their location and their *absolute* number.

At 80 GeV weaker wigglers will be needed; however the natural energy spread will be higher too so that the same issues as for the 45 GeV case will be likely encountered.

Finally it is worth noting that in [11] a resurrection of polarization is predicted at high energy (or in presence of a large energy spread) when the condition

$$\frac{\nu_{spin} T_{rev}}{\tau_p Q_s^3} \ll 1$$

is satisfied. This means that, unlike the case when the energy spread is small, large values of the synchrotron tune are preferable. This prediction should be tested by simulations.

## REFERENCES

[1] A. A. Sokolov and I. M. Ternov, Sov. Phys. Dokl. 8 (12) 1203 (1964).
[2] L. Thomas, Phil. Mag., Vol. 3 (1927).
[3] V. Bargmann, L. Michel and V. L. Telegdi, Phys. Rev. Lett., vol.2, p.435, (1959).
[4] Ya. S. Derbenev and A. M. Kondratenko, Sov. Phys. JETP, 37, 968 (1973).
[5] R. Assmann et al., in proceedings of SPIN 2000, Osaka, Japan, October 2000.
[6] A. Blondel and J. M. Jowett, in proceedings of Polarization at LEP, vol. 2, 216-232 (1987).
[7] D. P. Barber and G. Ripken, in Handbook of Acc. Phys. and Engineering, World Scientific (1999).
[8] A. W. Chao, NIM, 180, 29 (1981).
[9] J. Kewisch, DESY 85-109 (1985).
[10] D. P. Barber, unpublished.
[11] Ya. S. Derbenev, A. M. Kondratenko and A. N. Skrinsky, Part.



ISBN 978-3-95450-172-4

# ANALYSIS OF BEAM DYNAMICS IN A CIRCULAR HIGGS FACTORY*

Yunhai Cai†, SLAC National Accelerator Laboratory, Menlo Park, CA 74024, USA

*Abstract*

We design a circular Higgs factory with a center-of-mass energy of 240 GeV residing in a 50-km tunnel. Aside from two strong focusing systems and a low-emittance lattice in arcs that are required to achieve a factory luminosity of $1.0 \times 10^{34}\text{cm}^{-2}\text{s}^{-1}$, a large momentum aperture of 2% is absolutely necessary to mitigate the effect of beamstrahlung and retain an adequate beam lifetime. This turns out to be the most challenging aspect in the design. We comprehensively study the single-particle dynamics and identity many nonlinear aberrations that limit the performance of the optics.

## INTRODUCTION

Since the discovery of the Higgs particle at LHC, the recent results for ATLAS and CMS have shown that the discovered particle resembles the Higgs boson in the standard model of elementary particles. Because of this remarkable discovery, it becomes increasingly important to precisely measure the property of the particle that gives the mass to all and to study the nature of the spontaneous symmetry breaking in the standard model.

The relatively low mass of the Higgs boson provides an opportunity to build an $e^+$ and $e^-$ collider to efficiently and precisely measure its properties. In the production channel of $e^+e^- \rightarrow HZ$, the beam energy required for such a collider is about 120 GeV, which is only 15% higher than the energy reached about two decades ago at LEP2. Can we design and build a circular Higgs factory (CHF) within a decade? What are the major challenges in the design? In this paper, we will address these questions.

## LUMINOSITY

In a collider, aside from its energy, its luminosity is the most important design parameter. For Gaussian beams, we can write the bunch luminosity as

$$\mathcal{L}_b = f_0 \frac{N_b^2}{4\pi\sigma_x\sigma_y} R_h, \tag{1}$$

where $f_0$ is the revolution frequency, $N_b$ the bunch population, $\sigma_{x,y}$ transverse beam sizes, and $R_h$ is a factor of geometrical reduction due to a finite bunch length $\sigma_z$ and is given by

$$R_h = \sqrt{\frac{2}{\pi}} a e^{a^2} K_0(a^2), \tag{2}$$

$a = \beta_y^*/(\sqrt{2}\sigma_z)$, $\beta_y^*$ is the vertical beta function at the interaction point (IP), and $K_0$ the modified Bessel function. In order to avoid $R_h$ becoming too small, we shall require $\sigma_z \approx \beta_y^*$. Obviously, for a number of $n_b$ bunches, the total luminosity is $\mathcal{L} = n_b \mathcal{L}_b$.

In general, the beam sizes in the luminosity formula are not static variables. They are subject to the influence of the electromagnetic interaction during the collision. Typically, for flat beams, the vertical beam size will be blown up by the beam-beam force. To take this effect into account, we introduce the beam-beam parameter as [1]

$$\xi_y = \frac{r_e N_b \beta_y^*}{2\pi\gamma\sigma_y(\sigma_x + \sigma_y)}, \tag{3}$$

where $\gamma$ is the Lorentz factor and $r_e$ the classical electron radius. Using this formula for $\xi_y$, we can rewrite the luminosity as [2]

$$\mathcal{L} = \frac{cI\gamma\xi_y}{2r_e^2 I_A \beta_y^*} R_h, \tag{4}$$

where $I$ is the beam current and $I_A = ec/r_e \approx 17045$ A, the Alfven current. Since $\xi_y$ is limited below 0.1 in most colliders, this formula is often used for estimating an upper bound of the luminosity.

Table 1: Main Parameters of a Circular Higgs Factory

| Parameter | LEP2 | CHF |
|---|---|---|
| Beam energy, $E_0$ [GeV] | 104.5 | 120.0 |
| Circumference, $C$ [km] | 26.7 | 47.5 |
| Beam current, $I$ [mA] | 4 | 14.4 |
| SR power, $P_{SR}$ [MW] | 11 | 50 |
| Beta function at IP, $\beta_y^*$ [mm] | 50 | 2 |
| Bunch length, $\sigma_z$ [mm] | 16.1 | 1.5 |
| Hourglass factor, $R_h$ | 0.98 | 0.76 |
| Beam-beam parameter, $\xi_y$ | 0.07 | 0.07 |
| Luminosity/IR, $\mathcal{L}$ [$10^{34}\text{cm}^{-2}\text{s}^{-1}$] | 0.0125 | 1.01 |

In Table 1, we tabulated a set of consistent parameters for a CHF. In contrast to the B-factories [3,4], the beam current is severely limited by the power of synchrotron radiation at very high energy. To reach the factory luminosity, we need to have very strong final focusing systems and a very low emittance lattice. This combination makes the design of optics much more difficult compared with that of the B-factories.

## SYNCHROTRON RADIATION

When an electron is in circular motion with a bending radius $\rho$, its energy loss per turn to synchrotron radiation is given by

$$U_0 = \frac{4\pi r_e m c^2 \gamma^4}{3\rho}. \tag{5}$$

* Work supported by the Department of Energy under Contract Number: DE-AC02-76SF00515.

† yunhai@slac.stanford.edu

ISBN 978-3-95450-172-4

This loss has to be compensated by an RF system. The required RF power per ring is

$$P_{SR} = U_0 I/e. \tag{6}$$

For the beam parameters in Table 1 and $\rho = 5.2$ km, we have $U_0 = 3.6$ GeV, which means that electron loses about 2.5% of its energy every turn. Assuming $P_{SR}$ has to be less than 50 MW, the beam current is limited to 14.4mA in the ring. Applying the expression of $P_{SR}$ to the luminosity formula, we obtain

$$\mathcal{L} = \frac{3c\xi_y \rho P_{SR}}{8\pi r_e^3 \gamma^3 \beta_y^* P_A} R_h, \tag{7}$$

where $P_A = mc^2 I_A/e \approx 8.7$ GW. This scaling property of luminosity in $e^+e^-$ colliders at extremely high energy was first given by Richter [5].

For a CHF with beam energy larger than 120 GeV, its beam current will be severely capped by the electrical power consumed by the RF system and therefore a smaller $\beta_y^*$ seems the only option to reach the required factory luminosity.

## BEAMSTRAHLUNG

Another important aspect of very high energy colliding beams is the emission of photons during collision. In general, this phenomenon is well known and called beamstrahlung. Recently, Telnov found [6] that the most limiting effects to a CHF is an event when a high-energy photon is emitted by an electron in the beamstrahlung process. The electron energy loss can be so large that it falls outside of the momentum aperture $\eta$ in the colliding ring. For a typical CHF, is was suggested that the following,

$$\frac{N_b}{\sigma_x \sigma_z} < \frac{0.1\eta\alpha}{3\gamma r_e^2}, \tag{8}$$

has to be satisfied to achieve 30 minutes of beam lifetime. Here $\alpha \approx 1/137$ is the fine structure constant. If we introduce aspect ratios of beta functions at the IP and emittances in the ring, namely $\kappa_\beta = \beta_y^*/\beta_x^*$ and $\kappa_e = \epsilon_y/\epsilon_x$, this criteria can be rewritten as

$$\frac{N_b}{\sqrt{\epsilon_x}} < \frac{0.1\eta\alpha\sigma_z}{3\gamma r_e^2}\sqrt{\frac{\beta_y^*}{\kappa_\beta}} \tag{9}$$

.

On the other hand, to achieve the beam-beam parameter $\xi_y$, we need

$$\frac{N_b}{\epsilon_x} = \frac{2\pi\gamma\xi_y}{r_e}\sqrt{\frac{\kappa_e}{\kappa_\beta}}. \tag{10}$$

Combining this equation with Eq. (9), we have

$$\epsilon_x < \frac{\beta_y^*}{\kappa_e}\left(\frac{0.1\eta\alpha\sigma_z}{6\pi\gamma^2\xi_y r_e}\right)^2. \tag{11}$$

Since the quantities like $\xi_y$, $\beta_y^*$, and $\sigma_z$ are largely determined by the required luminosity and $\gamma$ by the particle to be studied, this inequality specifies a low-emittance lattice that is required to achieve 30 minutes of beam lifetime. Normally, the natural emittance scales as $\gamma^2$. Here it requires a scaling of $\gamma^{-4}$, indicating another difficulty in designing a factory with much higher energy beyond 120 GeV.

Table 2: Additional parameters selected to mitigate the beamstrahlung effects and reach 30 minutes in beamstrahlung beam lifetime.

| Parameter | LEP2 | CHF |
|---|---|---|
| Beam energy, $E_0$ [GeV] | 104.5 | 120.0 |
| Circumference, $C$ [km] | 26.7 | 47.5 |
| Horizontal emittance, $\epsilon_x$ [nm] | 48 | 1.7 |
| Vertical emittance, $\epsilon_y$ [nm] | 0.25 | 0.0043 |
| Momentum acceptance, $\eta$ [%] | 1.0 | 2.0 |
| Momentum compaction, $\alpha_p$ [$10^{-5}$] | 18.5 | 1.43 |

As shown in Table 2, we need to design a lattice with much smaller emittance than the one in LEP2 to mitigate the beamstrahlung effect. Typically, a low emittance lattice requires smaller dispersion and stronger focusing. Both will lead to an increase in the strength of the sextupole therefore dramatically reduce the dynamic aperture of the storage ring.

In the choice of the main design parameters, we want a factor of 100 increase in luminosity from LEP2. Because of the limit of the electric power, the increase of luminosity is largely achieved by a combination of very small beta functions at the IP and low emittance lattice. In summary, the lattice of a CHF has following main challenges:

- Low emittance lattice at high energy
- High packing factor of magnets
- Strong final focusing
- Large momentum acceptance
- Short bunches

A high packing factor is required to reduce synchrotron radiation in the bending magnets and not increase the circumference of the ring. We will proceed to a specific design to assess how difficult it is to meet these challenges.

## ARC

For an electron ring, the horizontal emittnace is given by

$$\epsilon_x = F\frac{C_q\gamma^2}{J_{xd}}\theta^3, \tag{12}$$

where $C_q$ is a constant,

$$C_q = \frac{55}{32\sqrt{3}}\frac{\hbar}{mc}, \tag{13}$$

and $\theta$ is the bending angle of the dipole. Here $J_{xd}$ is the damping partition number and typically equals one. $F$ is a factor that depends on the type of cell. For FODO cells, it



ISBN 978-3-95450-172-4

is at an order of one. In general, the stronger focusing of a cell, the smaller its $F$. Clearly, as seen in Eq. (12), the most effective way to reduce the emittance is to make the bending angle in a cell small. That implies that we use more cells.

In the arcs, we choose FODO cells because of their high packing factor and use many cells to reach the required emittance. the $60^0$ phase advance is selected due to its property of resonance cancellation that we will explain later. The optics of the cell is illustrated in Fig. 1. Every six cells makes a unit transformation of betatron oscillation. In our design, each arc consists of 32 units and ends with dispersion suppressors. Similar to LEP2, we have eight arcs and eight straight sections to complete a ring with parameters shown in Table 2.

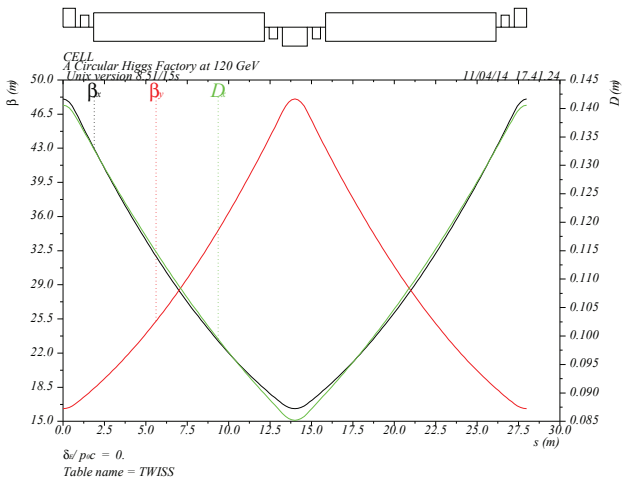


Figure 1: Lattice functions in a $60^0$ FODO cell.

Table 3: The nonlinear chromaticities and tune shifts due to betatron amplitudes in the lattice that consists of arcs and simple straight sections.

| Derivatives of tunes | Values |
|---|---|
| $\partial\nu_{x,y}/\partial\delta$ | $0, 0$ |
| $\partial^2\nu_{x,y}/\partial\delta^2$ | $-102, +128$ |
| $\partial^3\nu_{x,y}/\partial\delta^3$ | $+666, +557$ |
| $\partial\nu_x/\partial J_x\ [m^{-1}]$ | $-3.08\times10^5$ |
| $\partial\nu_{x,y}/\partial J_{y,x}\ [m^{-1}]$ | $-1.02\times10^6$ |
| $\partial\nu_y/\partial J_y\ [m^{-1}]$ | $-2.70\times10^5$ |

In this study, we set two families of sextupoles to make the linear chromaticity zero in the ring. For the third-order resonances, the contribution of sextupoles to all driving terms along the storage ring are computed [7] using the Lie method and plotted in Fig. 2. As one can see from the figure, they are all canceled out within one betatron unit (made with six cells), as predicted by theorem [8].

For the fourth-order resonances, we find similar cancelations [7] as shown in Fig. 3 except for one resonance:

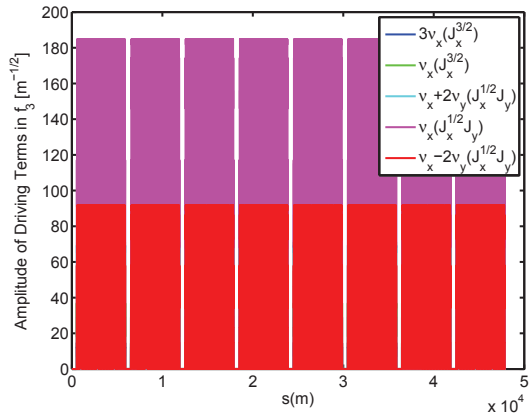


Figure 2: All third-order resonances driven by sextupoles.

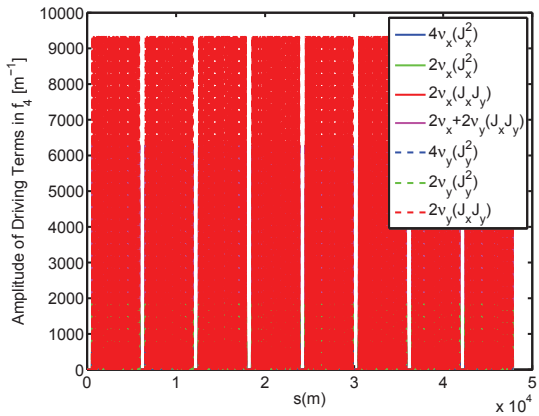


Figure 3: Fourth-order resonances driven by sextupoles.

$2\nu_x - 2\nu_y = 0$. Since this resonance overlaps the same the line as the linear coupling resonance in the betatron tune space, we can ignore it because the ring cannot operate near the linear resonance anyway.

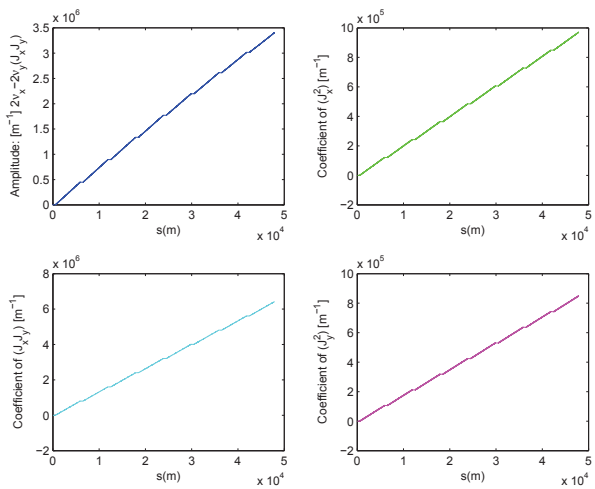


Figure 4: The four residual 4th-order terms in the Lie operator: $f_4$.



ISBN 978-3-95450-172-4

It is also worth noting that there are three more terms of geometric aberrations in $f_4$. They do not drive any resonances but shifts of betatron tunes. All four residual geometric terms in $f_4$ are shown in Fig. 4 as they are accumulated along in the ring. As we can see, they are continually increasing and reach very large values. To quantify their effects on the beam, we compute the tune shifts along with the high-order chromaticities using the normal form analysis [9] and tabulate the result in Table 3. Comparing with the existing storage rings, these tune shifts are too large at least by an order of two in magnitude.

## FINAL FOCUSING SYSTEM

Note that the beam lifetime condition in Eq. (11) does not depend on $\kappa_\beta$. Therefore, according to Eq. (10), $\kappa_\beta$ (or $\beta_x^*$) can be used to adjust the bunch population $N_b$ or equivalently the number of bunches $n_b$ when the total current is limited by the electrical power. Here we would like to choose a large $\beta_x^*$, leading to a smaller $n_b$. Our choice of the parameters in the interaction region are tabulated in Table 4.

Table 4: Other parameters determined by a specific design of final focusing system.

| Parameter | LEP2 | CHF |
|---|---|---|
| Beam energy, $E_0$ [GeV] | 104.5 | 120.0 |
| Circumference, $C$ [km] | 26.7 | 47.5 |
| $\beta_x^*$ [mm] | 1500 | 200 |
| $\beta_y^*$ [mm] | 50 | 2 |
| Bunch population, $N_b$ [$10^{10}$] | 57.5 | 32.0 |
| Number of bunches, $n_b$ | 4 | 25 |

It is always challenging to design a final focusing system (FFS) in a circular collider. In the CHF, it becomes even more so because of a smaller $\beta_y^*$ (2 mm) and a longer distance $L^*$ (2 meter) which is the distance between the IP and the first focusing quadrupole.

Here we adopt an optics similar to the design of a linear collider. The optics of the FFS is shown in Fig. 5. The FFS starts with a final transformer (FT), continues with a chromatic correction in the vertical (CCY) and then the horizontal plane (CCX), and ends with a matching section. The entire FFS has three imaging points and fits in a 175-meter long straight section.

The FT contains only two quadrupoles which serve as the final focusing doublet. The betatron phase advances are nearly $180^0$ in both planes. At the end of the FT, we have the first imaging point where the beta functions remain very small. In our study, we have reduced the number of quadrupoles in this section to maximize the momentum aperture in the FFS. A drawback of this approach is that the beta functions at the end of the FT cannot be adjusted.

The CCY consists of four $90^0$ FODO cells and make a unit of betatron transformer. The module starts at the middle of the defocusing quadrupole to enhance the peak of the vertical beta function at the positions of a pair of sextupoles separated by "-I" transformation. Two pairs of dipoles create two dispersion bumps, providing the dispersions at the location of the sextupole. At the end of the CCY, we have the second imaging point at which the lattice functions are identical to those at the first one.

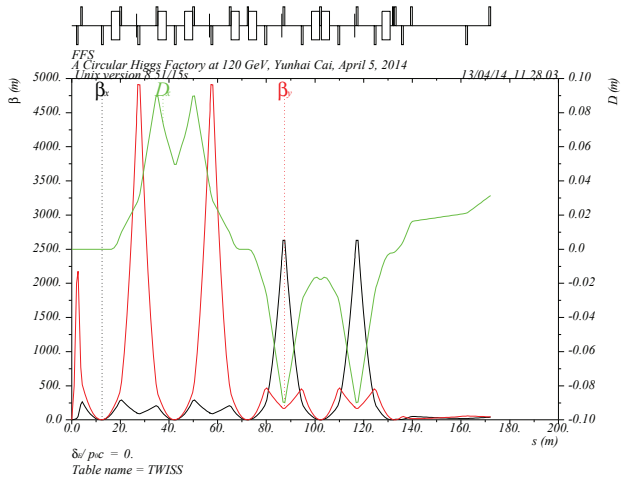


Figure 5: Lattice functions in a final focusing system with local chromatic compensation section.

Similarly, we construct the CCX, but starting at the middle of the focusing quadrupole. And at the end of the CCX, we have the third image point. Here, we have essentially compensated the local chromaticity as shown in Fig. 6 and transport the very small beta functions at the IP to the end of the CCX. In the matching module, we can place the quadrupoles near the third imaging point without the worry of $L^*$ and match easily the FFS to the dispersion suppressor.

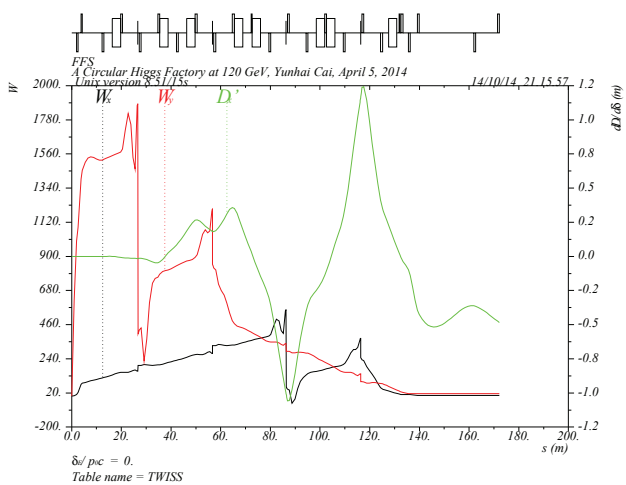


Figure 6: W function in the final focusing system with the local chromatic compensation.

Finally, we use the longitudinal cyclical symmetry in the CCY and CCX to adjust the betatron phase between the final



ISBN 978-3-95450-172-4

doublet and the sextupole pairs to optimize the second order chromaticity in the FFS. We should note that the second order dispersion leaks out of the FFS as shown in Fig. 6.

Aside from those chromatic aberrations, there are many large geometric and chromatic aberrations in the FFS. As shown in Fig. 7, a fifth-order aberration, $p_x p_y^2 \delta^2$, increases in large steps at the position of the sextupoles in the FFS. It was pointed out by Oide [10] that this aberration can be compensated by a proper setting of asymmetric dispersions at the positions of the pair of sextupoles.

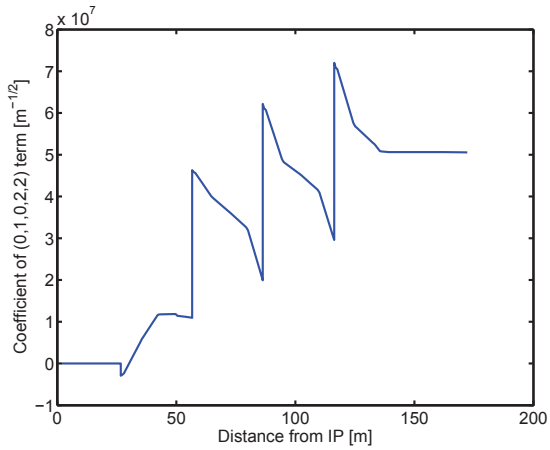


Figure 7: A fifth order aberration in the single-Lie operator in the normalized coordinates.

From the analysis, we find also that the largest aberration in fifth-order is $p_y^4 \delta$ as shown in Fig. 8. The source of this aberration is the kinematic term but enhanced by the strong sextupoles. This huge aberration may well be the bottleneck of the FFS. It can significantly degrade the off-momentum aperture of the collider.

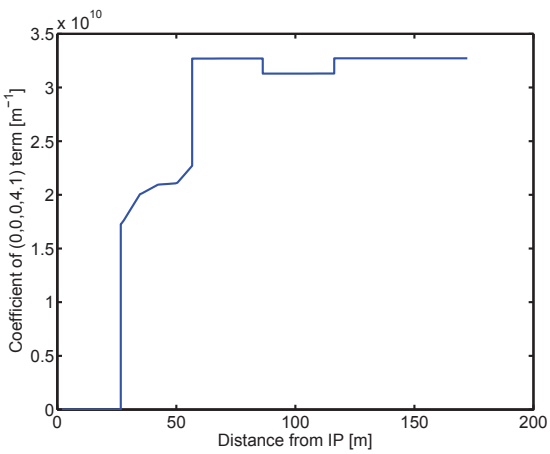


Figure 8: The largest fifth order aberration in the single-Lie operator in the normalized coordinates.

## COLLIDER

Replacing two interaction regions with two simple straights in the arc lattice, we build a collider lattice shown in Fig. 9.

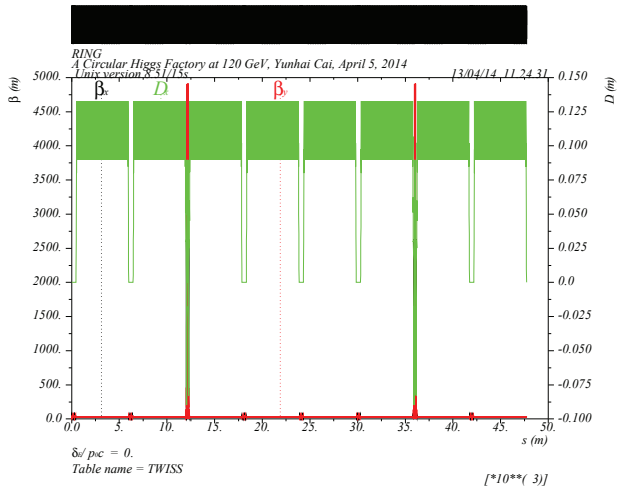


Figure 9: Lattice functions in the CHF that includes two interaction regions.

We readjust the settings of two families of the sextupoles in the arcs for a few units of positive chromaticity and obtain the bandwidth of momentum deviation of ±2% as shown in Fig. 10.

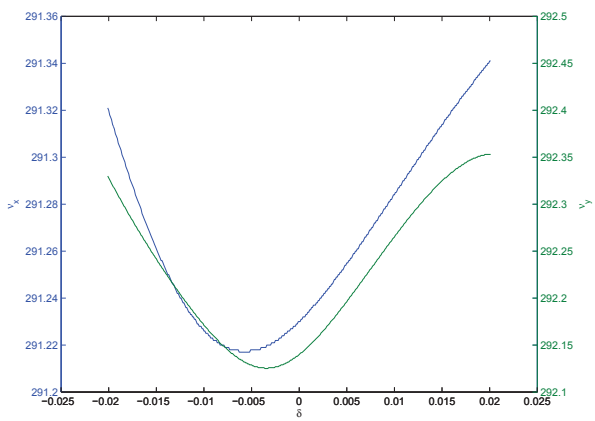


Figure 10: Betatron tunes of the collider ring as a function of relative momentum.

Since the strongest quadrupoles and sextupoles are positioned at the highest beta functions in the FFS, naturally the IR contains many high-order aberrations. We compute the third-order and fourth-order driving terms in the collider. The cancellation of the resonances at third-order remains intact. But the fourth-order resonance driving terms become much larger as shown in Fig. 11. Clearly, the aberrations in the IR are dominant in the entire ring. The source of

ISBN 978-3-95450-172-4

the fourth-order aberration are the kinematic terms from the perturbation expansion of the Hamiltonian.

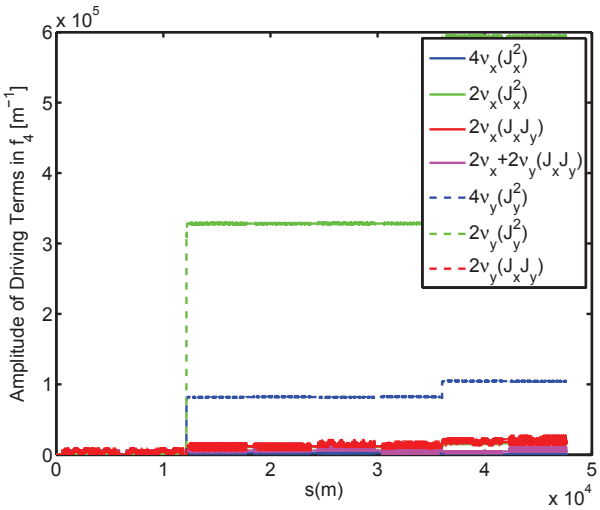


Figure 11: Fourth-order resonances driving terms in the lattice with two interaction regions.

To confirm their effects in the collider, we compute the tune shifts, the high-order chromaticities, and geometric and chromatic tune shifts using the normal form analysis and tabulate the result in Table 5. Indeed, the table shows that the geometric and chromatic tune shifts are much larger at $\delta = 0.01$ than the geometric tune shifts, which themselves are already two order of magnitudes too large as mentioned previously.

Table 5: The nonlinear chromaticities and tune shifts due to betatron amplitudes in the collider that contains two interaction regions.

| Derivatives of tunes | Values |
|---|---|
| $\partial\nu_{x,y}/\partial\delta$ | $0, 0$ |
| $\partial^2\nu_{x,y}/\partial\delta^2$ | $+496, +1750$ |
| $\partial^3\nu_{x,y}/\partial\delta^3$ | $-74400, -345000$ |
| $\partial\nu_x/\partial J_x\ [m^{-1}]$ | $-2.94\times10^5$ |
| $\partial\nu_{x,y}/\partial J_{y,x}\ [m^{-1}]$ | $-9.91\times10^5$ |
| $\partial\nu_y/\partial J_y\ [m^{-1}]$ | $-1.07\times10^5$ |
| $\partial^2\nu_x/\partial\delta\partial J_x\ [m^{-1}]$ | $-1.11\times10^9$ |
| $\partial^2\nu_{x,y}/\partial\delta\partial J_{y,x}\ [m^{-1}]$ | $-1.75\times10^9$ |
| $\partial^2\nu_y/\partial\delta\partial J_y\ [m^{-1}]$ | $-1.56\times10^{10}$ |

## CONCLUSION

Despite much progress being made since the last Higgs workshop two years ago, we have not yet solved the problem of the off-momentum dynamic aperture in the collider. From our systematic analysis, we find the following design issues:

- Tune shifts vs. amplitudes are very large due to interlaced sextupoles in the arcs
- The second-order dispersion in the interaction region leads out to the arcs
- Second- and third- order chromaticity are too large in the collider
- Huge geometric-chromatic aberration seen in 5th-order Lie operators in the final focusing system

As shown in our study, the CHF requires not only a final focusing system with an ultra-low beta at the interaction point but also a very low-emittance lattice at very high energy. Such optics in a storage ring with a larger momentum aperture will be the ultimate challenge for our accelerator community in the next decade.

## ACKNOWLEDGMENT

I would like to thank Alex Chao, Yuri Nosochkov, Richard Talman, Uli Wienands, and Frank Zimmermann for many stimulating discussions.

## REFERENCES

[1] F. Amman and D. Ritson, "Design of electron-positron colliding beam rings," 1961 Inernat. Conf. on High Energy Accelerators, Brookhaven, p471, (1961).

[2] J.T. Seeman, "Beam-beam interaction: luminosity, tails and noise," SLAC-PUB-3182, July (1983).

[3] "PEP-II: An Asymmetric B Factory", Conceptual Design Report, SLAC-418, June 1993.

[4] "KEKB B-factory Design Report", KEK-Report-95-7, (1995).

[5] B. Richter, "Very high electron-positron colliding beams for the study of weak interactions," Nucl. Instr. Meth. **136** p47 (1976).

[6] V.I. Telnov, "Restriction on the energy and luminosity of $e^+e^-$ storage rings due to beamstrahlung," Phys. Rev. Lett. **110**, 114801 (2013).

[7] Y. Cai, "Single-particle dynamics in electron storage rings with extremely low emittance", Nucl. Instr. Meth. **A645**, p168 (2011).

[8] K.L. Brown and R.V. Servranckx, "Optics modules for circular accelerator design," Nucl. Instr. Meth., **A258**, p480 (1987).

[9] E. Forest, M. Berz, and J. Irwin, "Normal form methods for complicated periodic systems: a complete solution using differential algebra and Lie operators," Part. Accel. **24** 91 (1989).

[10] K. Oide, "Final focus system with odd-dispersion scheme," KEK Preprint 92-58, July (1992).



ISBN 978-3-95450-172-4

# DYNAMIC APERTURE OPTIMIZATION IN SuperKEKB

Y. Ohnishi*, H. Koiso, A. Morita, K. Ohmi, K. Oide, H. Sugimoto, D. Zhou,
KEK, Tsukuba, Japan

*Abstract*

Colliders squeeze a beam spot at an interaction point(IP) to obtain higher luminosity. Large natural chromaticity generated in a final focus system should be corrected by strong sextupole magnets. Nonlinear effects in the sextupole field and the final focusing magnets decreases the dynamic aperture significantly. Optimization of the dynamic aperture is based on a numerical particle-tracking simulations since aberrations of particle motions due to nonlinear and higher-order effects are treated. In particular, low emittance and low beta functions at IP in SuperKEKB, the dynamic aperture is one of the important issues for both Touschek lifetime and injection efficiency. We present an optimization procedure of the dynamic aperture in SuperKEKB.

## INTRODUCTION

The target luminosity of SuperKEKB is $8\times10^{35}$ $\mathrm{cm}^{-2}\mathrm{s}^{-1}$ which is 40 times higher than the peak luminosity of KEKB. In order to achieve the target luminosity, the vertical beta function at the interaction point (IP) is necessary to be squeezed down to about 300 $\mu$m and the beam current needs to be increased 3.6 A in LER with keeping the same beam-beam parameter in the vertical direction, $\sim$0.09 as KEKB.

A bunch length is 5$\sim$6 mm which is much longer than the vertical beta function to suppress coherent synchrotron radiation (CSR). "Nano-beam scheme" proposed by P. Raimondi[1] is adopted to avoid a luminosity degradation due to an hourglass effect. A large Piwinski angle is introduced in the nano-beam scheme. The crossing-angle is 83 mrad in the horizontal direction between a positron low energy ring (4 GeV, LER) and an electron high energy ring (7 GeV, HER). The horizontal emittance is reduced to 3.2$\sim$4.6 nm and the horizontal beta function is also squeezed to 25$\sim$32 mm to realized the nano-beam scheme. A small vertical emittance is necessary to obtain a higher luminosity in the nano-beam scheme. The ratio of the vertical emittance to the horizontal emittance is required to be less than $\sim$0.27 % under an influence of the beam-beam interaction as well as including machine error. The machine parameters will be found in elsewhere[2].

Touschek lifetime will be expected to be very short and the linac injector will need to be improved to provide enough injection beams to compensate short lifetime. A dynamic aperture is one of important issues at SuperKEKB because the dynamic aperture will affect both of the lifetime and the injection efficiency.

* Email: yukiyoshi.onishi@kek.jp

## LATTICE DESIGN

The linear chromaticity of focusing magnets in a ring is written by

$$\xi_{x,y} = \frac{\partial \nu_{x,y}}{\partial \delta} = -\frac{1}{4\pi}\int K(s)\beta_{x,y}(s)ds, \qquad (1)$$

where $\nu_{x,y}$ is betatron tune and $\delta = \Delta p/p_0$ the momentum deviation from the design momentum $p_0$, $K(s)$ the focusing strength, $\beta_{x,y}(s)$ the beta function as a function of location $s$. The linear chromaticity is $\xi_x = -105$ and $\xi_y = -776$ in the LER and $\xi_x = -171$ and $\xi_y = -1081$ in the HER, respectively. The linear chromaticity is corrected with noninterleaved sextupoles at SuperKEKB. The noninterleaved chromaticity corrections in the arc section are shown in Figures 1 and 2.There are 50 pairs of sextupole

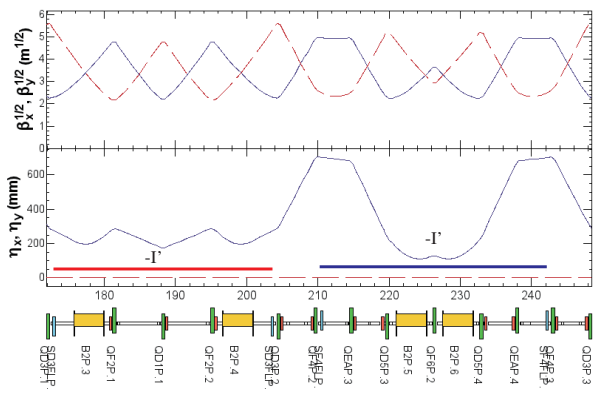


Figure 1: Arc cell in LER.

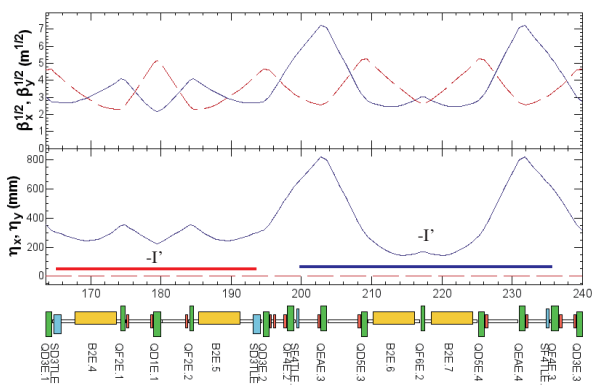


Figure 2: Arc cell in HER.

magnets in the arc section and 4 pairs in the interaction region (IR). The transfer matrix between two identical sextuple magnets is $-I'$ to compensate a nonlinear kick due

ISBN 978-3-95450-172-4

to strong field of the sextupoles. The phase advance between two sextupoles is $\pi$ in the horizontal and the vertical direction. The configuration of the focusing and the defocusing sextupoles are noninterleaved. A nonlinear kick due to one of the sextupole pair can be canceled by the other sextupole magnet for an on-momentum particle, however, the chromaticity can be corrected properly.

The final focus (FF) is designed to achieve extremely low beta functions at IP. In order to squeeze the beta functions, doublets of a vertical focusing (QC1) and a horizontal focusing quadrupole magnet (QC2) are adopted. The magnet system consists of superconducting magnets to make strong focusing strength. The magnitude of $\xi_{x,y}$ in Eq. (1) is determined by a linear optics and becomes large as increasing the focusing strength. Since approximately 80 % of the linear chromaticity in the vertical direction is induced in the FF, a local chromaticity correction (LCC) is adopted to correct the large chromaticity near the FF. There are 2 pairs for the vertical direction (Y-LCC) and another 2 pairs of sextupoles for the horizontal direction (X-LCC) in the IR. The phase advance between QC1 and the Y-LCC is $\pi$ in the vertical direction and between QC2 and X-LCC is $2\pi$ in the horizontal direction for each side of IP. Horizontal dispersions are created at the LCC by using several dipole magnets. Figures 3 and 4 show the lattice design of the LCC region.

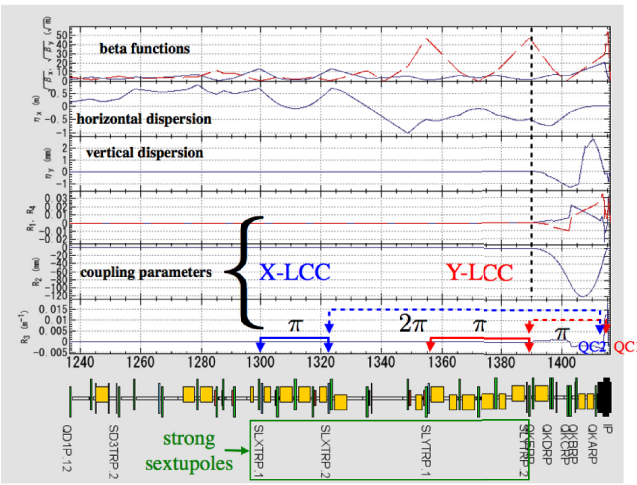


Figure 3: Local chromaticity correction in LER.

The nonlinear effect in the final focus system decreases the dynamic aperture significantly. In addition to the nonlinear magnetic field, the drift space is not linear system as shown in a Hamiltonian. Especially, when the beta function is squeezed in the vicinity of IP and decreased with distance from IP, the effect cannot be ignored. The aperture of the motion can be described by a simple one-dimensional Hamiltonian[3]. The aperture for the initial action, $J_0$ is expressed by

$$J_{y0} = \frac{\beta_y^{*2}}{\left(1 + \frac{2}{3} \mid K \mid L^{*2}\right) L^*} A(\mu_y), \qquad (2)$$

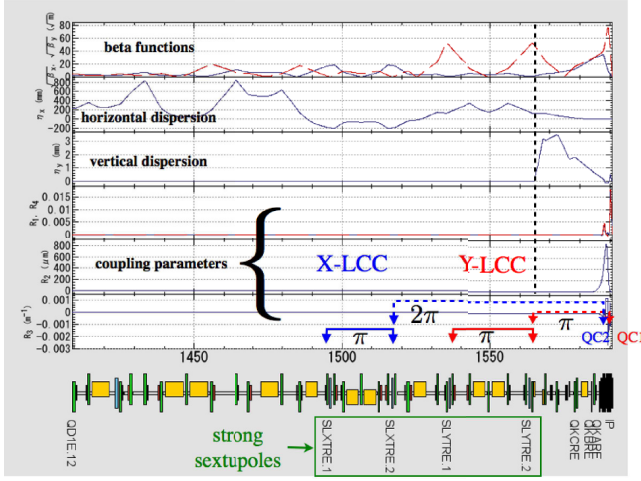


Figure 4: Local chromaticity correction in HER.

where $K = B'/B\rho$ is the focusing strength of the final focusing quadrupole in the vertical direction, $L^*$ the distance from IP to the final focusing quadrupole, $A(\mu_y)$ a universal function determined by the one-dimensional model. Table 1 shows the parameters to evaluate the dynamic aperture in SuperKEKB.

Table 1: Estimation of the Dynamic Aperture

| | LER | HER | Unit |
|---|---|---|---|
| $\beta_y^*$ | 270 | 300 | $\mu$m |
| $K$ | -5.1 | -3.1 | 1/m$^2$ |
| $L^*$ | 0.76 | 1.22 | m |
| $J_{y0}/A(\mu_y)$ | 0.032 | 0.018 | $\mu$m |

## OPTIMIZATION OF DYNAMIC APERTURE

It is difficult to apply either an analytic approach or a perturbative method to an evaluation of the dynamic aperture since there is the final focus system as described above and the sextupole magnets to correct the large chromaticity causes strong nonlinear effects. Therefore, the dynamic aperture is estimated by using SAD[4]. Six canonical variables, $x$, $p_x$, $y$, $p_y$, $z$, and $\delta$ are used to describe the motion of a particle, while $p_x$ and $p_y$ are transverse canonical momenta normalized by the design momentum, and $\delta$ is the relative momentum deviation from $p_0$. A synchrotron oscillation is included while a synchrotron radiation and a quantum excitation are turned off during tracking simulations. The FF region within $\pm$ 4 m from IP, the magnetic field of Belle II and the anti-solenoids and QCS(QC1 and QC2) along the longitudinal direction on the beam line is sliced by thickness of 10 mm of constant $B_z$ or $K_1 = B'L/B\rho$ to make the lattice model. Higher order multipole fields up to 44-poles for normal and skew fields are included in the slices[5]. The three-dimensional



ISBN 978-3-95450-172-4

solenoid field is calculated by using ANSYS[6] which is a electromagnetic field simulation code. The behavior of the solenoid field is also implemented by slices in the model[7]. The fringe field of the solenoid field and higher order multipole fields of the final focusing magnets affect the dynamic aperture significantly.

The beam lifetime should be long enough to store the beam currents stably. Touschek lifetime contributes the total lifetime significantly because of the low emittance in SuperKEKB. The target of Touschek lifetime is 600 sec for the nominal machine parameters in SuperKEKB. Touschek lifetime depends on the dynamic aperture and the density of particles in a bunch. The larger dynamic aperture is obtained by optimizing 54 families of sextupoles and 12 (LER) or 10 (HER) families of skew sextupoles in both and the LCC, and 3 (LER) or 2 (HER) octupole coils in QCs. The optimization utilizes an off-momentum matching and a down-hill simplex method as a function of an area of the dynamic aperture. The octupole magnets make the transverse dynamic aperture larger by deforming the phase space at the large amplitude to fit the physical aperture. The skew sextupole magnets correct chromatic X-Y coupling. The skew sextupole filed is induced by rotating the normal sextupole in the LER. In the HER, the skew sextupole magnets are placed in the vicinity of the sextupole magnets in the arc cell.

The dynamic aperture is estimated by a particle tracking in the LER and the HER, respectively. The particle tracking is performed for 1000 turns to define a stable region with synchrotron oscillations. The dynamic aperture is important for keeping enough Touschek lifetime as well as an injection aperture. Figures 5 and 6 show the dynamic aperture in the LER and the HER, respectively. The area of the dynamic aperture is fitted by an ellipse to estimate Touschek lifetime. Two initial betatron phases of $(0, 0)$ and $(\pi/2, \pi/2)$ in the horizontal and vertical plane are calculated in the dynamic aperture survey. Touschek lifetime is defined by average of two cases since the larger betatron amplitude becomes a nonlinear region and a Poincare plot differs from a circle. The requirement of Touschek lifetime is almost satisfied in the ideal lattice and the optimization has been still continued. The transverse dynamic aperture in the plane of betatron tunes for the case that the initial vertical amplitude is zero with the on-momentum particle is shown in Figure 7.The nominal betatron tune is $(\nu_x, \nu_y) = (44.53, 46.57)$ in the LER and $(\nu_x, \nu_y) = (45.53, 43.57)$ in the HER, respectively.

## DYNAMIC APERTURE UNDER INFLUENCE OF BEAM-BEAM EFFECT

The dynamic aperture will be reduced under the influence of beam-beam effects in the nano-beam scheme. A particle with a horizontal amplitude collides at a location different from IP in the longitudinal direction due to the crossing angle of 83 mrad between two beam lines in the horizontal plane. The deviation along the beam axis is written by

$$\Delta z = \frac{\Delta x}{2\phi_x}, \tag{3}$$

where $\Delta x$ is the horizontal amplitude and $\phi_x$ the half crossing angle. The beta function is written by a function of the

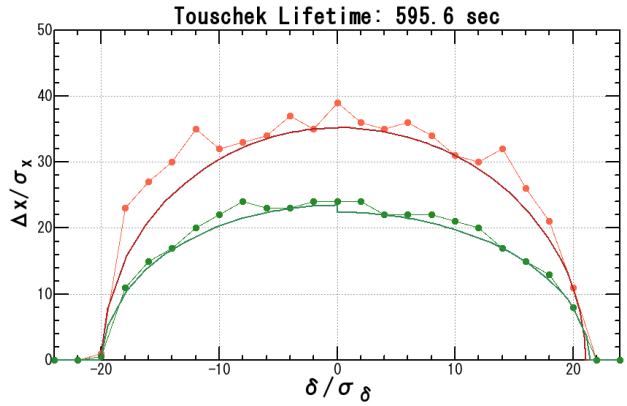


Figure 5: Dynamic aperture and Touschek lifetime in LER.

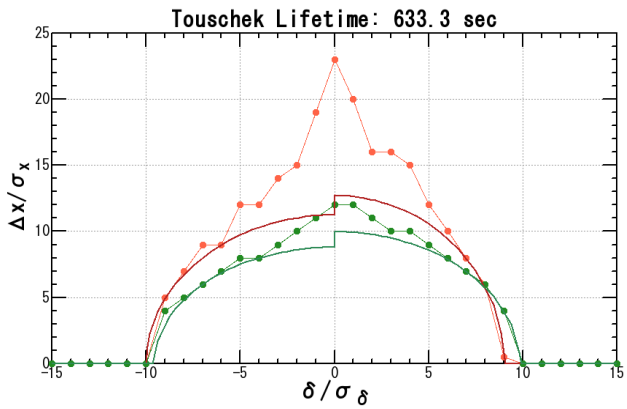


Figure 6: Dynamic aperture and Touschek lifetime in HER.

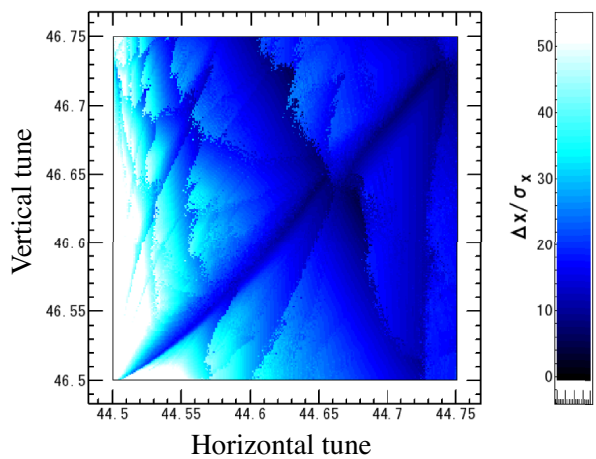


Figure 7: Tune scan for transverse aperture in LER.

ISBN 978-3-95450-172-4

distance from IP:

$$\beta_y(\Delta z) = \beta_y^* + \frac{\Delta z^2}{\beta_y^*}. \quad (4)$$

Therefore, the particle with a horizontal amplitude is kicked at a large vertical beta function and the vertical amplitude will increase due to the beam-beam interactions for an initial non-zero vertical amplitude. This behavior is a kind of an hourglass effect. The vertical amplitude given by the beam-beam kick is

$$\Delta y \propto \theta_{bb,y}\sqrt{\beta_y(\Delta z)}. \quad (5)$$

The particle is lost if the vertical amplitude increases and is out of a stable region. In the case of a particle with the horizontal amplitude of $30\sigma_x$ in the LER, the deviation from IP becomes 3.6 mm in the longitudinal direction where the vertical beta function is 48 mm. The vertical beta function becomes 180 times of the nominal beta function at IP.

Touschek lifetime in the HER reduces about 10 % due to the beam-beam effect, however, the impact in the LER is much larger than the HER. Figure 8 shows the dynamic aperture in the vertical and the horizontal plane under the influence of the beam-beam effect. The initial momentum deviation is zero in the figure. The transverse aperture is reduced significantly compared with the dynamic aperture without the beam-beam effect. The particle with the horizontal amplitude larger than $10\sigma_x$ is lost due to the vertical oscillation even though the initial amplitude is zero in the vertical direction because of the vertical amplitude is induced by nonlinearities such as X-Y coupling originate from the IR.

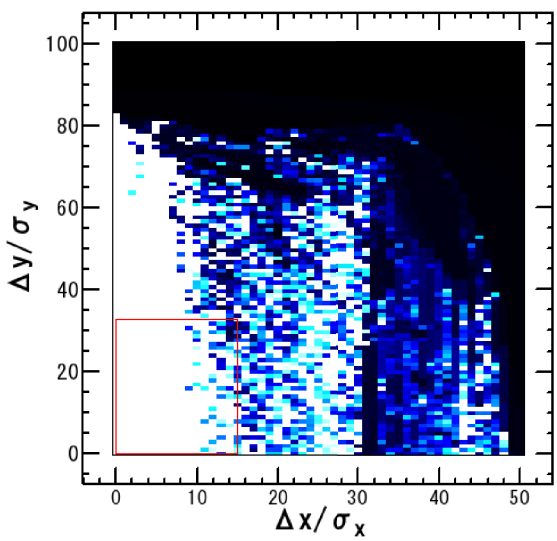


Figure 8: Dynamic aperture in the transverse plane when the initial momentum deviation is zero in LER. White color indicates a stable and black color indicates an unstable region. Rectangle (red) shows the necessary injection acceptance.

Touschek lifetime in the LER will be about 100 sec under the influence of the beam-beam effect without any optimization procedures. If we change the working point from the nominal betatron tunes to ($\nu_x$,$\nu_y$)=(44.53,46.54), Touschek lifetime will be improved to be 230 sec with re-optimization of the sextupoles and so on.

## CRAB-WAIST SCHEME

Another approach to compensate the beam-beam effect for the large horizontal amplitude is "Crab-waist scheme"[8]. Hamiltonian of the crab-waist term is

$$H_{cw} = \frac{\lambda}{2} x p_y^2, \quad (6)$$

where

$$\lambda = \frac{1}{\tan 2\phi_x}. \quad (7)$$

If we consider the ideal case of the crab-waist scheme, the map of the beam-beam interaction is replaced with

$$f_{BB} \rightarrow f_{cw}(+\lambda) \cdot f_{BB} \cdot f_{cw}(-\lambda), \quad (8)$$

where the map of the crab-waist is

$$f_{cw}(\lambda) : p_x \rightarrow p_x + \frac{\lambda}{2} p_y^2 \quad (9)$$

$$y \rightarrow y - \lambda x p_y. \quad (10)$$

A feasibility of the ideal crab-waist scheme has been studied by using tracking simulations. The dynamic aperture is almost recovered by the ideal crab-waist which is compared with Figure 8. In order to accomplish the crab-waist in the realistic lattice, two sextupole magnets are utilized. In the case of the realistic lattice, the $x^3$ term comes from the sextupole is added to the crab-waist term in the Hamiltonian. However, it can be ignored by choosing a large ratio of the vertical beta function to the horizontal at the sextupole magnet.

Two sextupole magnets are placed for each side of IP and shift a waist of colliding particles having a horizontal amplitude to cancel the deviation from the waist. The betatron phase advance between a crab-waist sextupole and IP is adjusted to be $m\pi$ in the horizontal direction and $(n+1/2)\pi$ in the vertical direction, where $m$ and $n$ are arbitrary integers. The strength of the crab-waist sextupoles are

$$| K_2 | = \frac{1}{\tan 2\phi_x \beta_y^* \beta_{y,s}} \sqrt{\frac{\beta_x^*}{\beta_{x,s}}}, \quad (11)$$

where $\beta_{x,s}$ and $\beta_{y,s}$ are the horizontal and the vertical beta function at the sextupoles, respectively. The sign of $K_2$ is chosen so as to shift the waist at IP properly and cancel a nonlinear kick between a pair of the crab-waist sextupoles. The lattice design for the crab-waist scheme in the LER is shown in Figure 9.The crab-waist sextupole is assumed to be a thin lens to make the model simple in this report. The



ISBN 978-3-95450-172-4

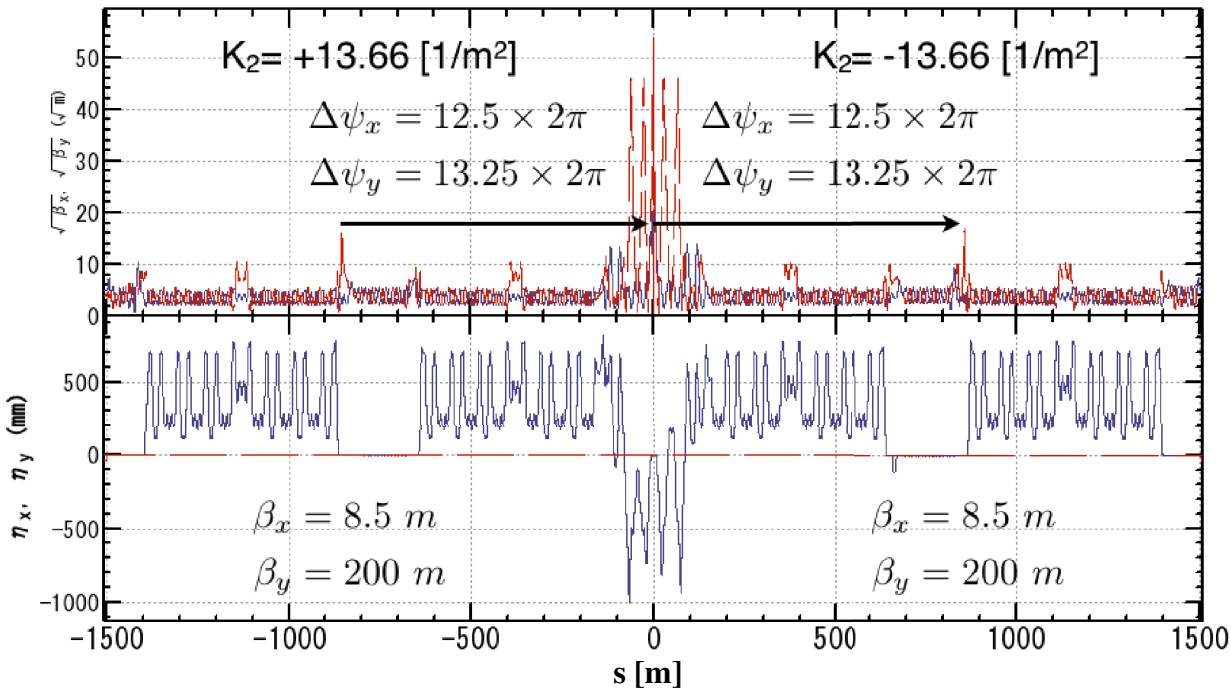


Figure 9: Lattice candidate for the crab-waist scheme at SuperKEKB.

Table 2: Machine Parameters for the Crab-waist Scheme in the LER

| | Symbol | LER | Unit |
|---|---|---|---|
| Horizontal beta at IP | $\beta_x^*$ | 32 | mm |
| Vertical beta at IP | $\beta_y^*$ | 270 | $\mu$m |
| Half crossing angle | $\phi_x$ | 41.5 | mrad |
| Horizontal beta at sextupole | $\beta_{x,s}$ | 8.5 | m |
| Vertical beta at sextupole | $\beta_{y,s}$ | 200 | m |
| Horizontal phase advance | $\Delta\psi_x$ | $25\pi$ | rad |
| Vertical phase advance | $\Delta\psi_y$ | $26.5\pi$ | rad |
| Nominal field of sextupole | $\mid K_2 \mid$ | 13.66 | $1/m^2$ |

machine parameters for the crab-waist scheme in the LER are shown in Table 2.

Figure 10 shows transverse dynamic aperture in the LER as a function of $K_2$ for the crab-waist sextupoles. The initial momentum deviation and the vertical amplitude are zero in the simulations. The dynamic aperture decreases as increasing the strength of the sextupoles. The beam-beam effect is turned off in the simulation. The nonlinear kick due to the crab-waist sextupole can be canceled by another sextupole for the reference particle, however, it cannot be canceled for a particle with a large initial amplitude. The transfer map between two sextupoles which includes the IR with the final focus is no longer the linear map. The term of $\Delta p_y = K_2 xy$ will increase the vertical amplitude, then the particle will be lost and the dynamic aperture will be reduced.

Figure 11 shows the transverse dynamic aperture in the

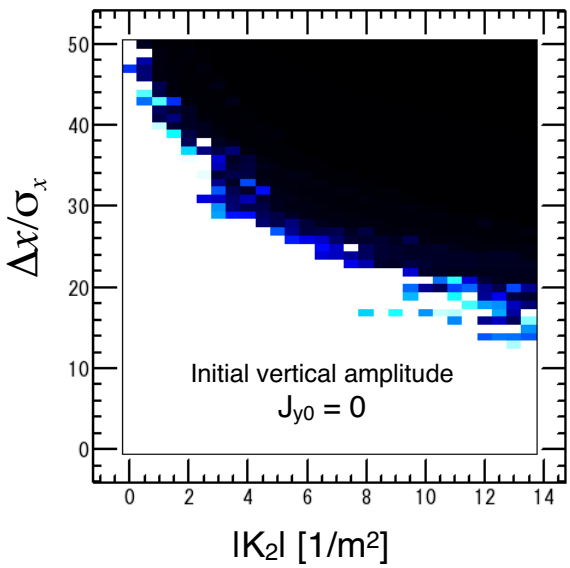


Figure 10: Dynamic aperture in the transverse plan for the crab-waist lattice without beam-beam effects.

LER which is similar to Figure 10, but the beam-beam effect is turned on. The dynamic aperture is indeed recovered by the crab-waist sextupoles as increasing the field strength until the nonlinear kick from the sextupoles restricts the dynamic aperture. Therefore, it implies the difficulty comes from the cancellation of the nonlinear kick by a pair of crab-waist sextupoles for the large horizontal amplitude of a particle without the beam-beam effect.

ISBN 978-3-95450-172-4

Fourier analysis for the crab-waist on and off is performed to investigate what frequency is a dominant source for the amplitude growth. The frequency spectrum for the vertical action is shown in Figure 12.The initial horizontal amplitude increases from 1 to 15 sigmas with keeping the initial vertical amplitude zero and the vertical amplitudes for the frequency are plotted. In the case that the crab-waist turned on, the strength of the crab-waist sextupole is $K_2$ =11 m$^{-2}$ which is 80 % of the nominal value. When the spectrum is compared for each other, the spectrum for the crab-waist on is almost similar to that of turned off except for the component of the vertical tune. The vertical amplitude corresponds to the vertical tune increases as increasing the initial horizontal amplitude significantly for the crab-waist on.

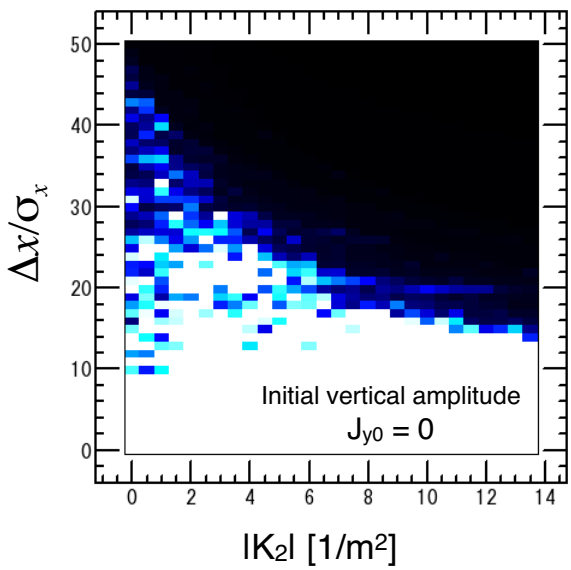


Figure 11: Dynamic aperture in the transverse plan for the crab-waist lattice with beam-beam effects.

## SUMMARY

We present the issues of the dynamic aperture in SuperKEKB. The dynamic aperture is optimized for the both of LER and HER. The Touschek lifetime of 600 sec has been accomplished without machine error and beam-beam interactions. The variables to optimize the dynamic aperture are sextupoles, skew sextupoles, and octupoles which are more than 50 variables. The optimization is based on the chromaticity corrections for the off-momentum optics and the down-hill simplex method by using tracking simulations.

The dynamic aperture under the influence of the beam-beam interactions will be reduced in the nano-beam scheme. Especially, a particle with a large horizontal amplitude will receive a large beam-beam kick in the vertical plane. The Touschek lifetime in the LER is ∼200 sec so far with the beam-beam effects after choosing better working

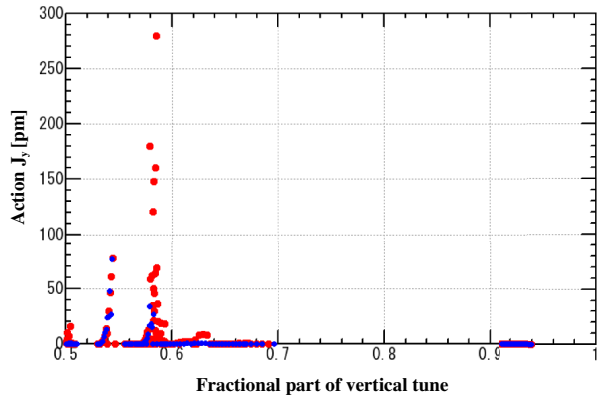


Figure 12: Action as a function of fractional part of tune in the vertical direction in LER. Blue plots show crab-waist turned off and red plots show crab-waist turned on. The field strength of the sextupole, $K_2$, is 11 m$^{-2}$ for the crab-waist on.

point and re-optimization. The crab-waist scheme is one of solutions to cure the beam-beam effect. However, the crab-waist has a big issue which comes from nonlinear terms between two crab-waist sextupoles without the beam-beam effect. No solution is found to alleviate the nonlinear kick due to the sextupoles in the crab-waist scheme since the transfer map between sextupoles includes strong nonlinear components such as the final focus system.

## REFERENCES

[1] "SuperB Conceptual Design Report", INFN/AE-07/2, SLAC-R-856, LAL 07-15, March 2007.

[2] Y. Ohnishi et al., Prog. Theor. Exp. Phys. 2013 03A011 (2013).

[3] K. Oide and H. Koiso, Phys. Rev. **E 47** (1993) 2010.

[4] *Strategic Accelerator Design*, http://acc-physics.kek.jp/SAD

[5] A. Morita et al., Proc. of IPAC'11, THPZ005, September 2011.
A. Motita et al., Proc. of IPAC'12, TUPPC018, May 2012.

[6] http://www.ansys.com

[7] H. Yamaoka et al., Proc. of IPAC'12, THPPD023, May 2012.

[8] P. Raimondi et al., LNF-07-003-IR, February 2007.



ISBN 978-3-95450-172-4

# THE EFFECT OF IR IMPERFECTION ON DYNAMIC APERTURE IN SUPERKEKB/ DYNAMIC APERTURE STUDY OF CEPC

H. Sugimoto, KEK, Tsukuba, Japan

*Abstract*

Interaction region (IR) is the most critical part of colliders to optimize the dynamic aperture because a detector solenoid and strong final focus magnets give rise to complicated nonlinear beam dynamics. Design of the SuperKEKB IR has been carried out with considering the effect of a possible IR imperfection on the machine performance. In this paper, degradation of dynamic aperture due to error fields from the final focus magnets is discussed. We also present a preliminary study of dynamic aperture of CEPC based on the experience of the SuperKEKB lattice design.

## INTRODUCTION

The KEKB accelerator [1] is being upgraded to a SuperB accelerator named SuperKEKB [2]. SuperKEKB consists of 7 GeV electron (HER) and 4 GeV positron (LER) storage rings with a injector linac and a positron damping ring. The target luminosity of $8 \times 10^{35}\mathrm{cm}^{-2}\mathrm{s}^{-1}$ is obtained by 2 times higher beam current (3.6 A for $e^+$ and 2.6 A for $e^-$), 1/20 times smaller vertical beta function $\beta_y^*$ (0.3 mm), and larger crossing angle of 83 mrad. This approach also requires the low emittance optics to realize the nano-beam collision. The Touschek effect is enhanced in such a low emittance beam and restricts the beam lifetime. Meanwhile squeezing the beta function at the interaction point (IP) results the huge natural chromaticity and makes the chromaticity correction difficult. Furthermore the huge beta function enhances the undesired nonlinear effects in IR likely restricts the beam stability. Therefore the optimization of the dynamic aperture is one of the most challenging topic of the SuperKEKB lattice design.

A large number of feedback procedures between hardware and optics group have been repeated with consideration on detailed hardware specifications to obtain the sufficiently wide dynamic aperture. Overview of the lattice design and effects of the error fields due to the IR imperfection are reported in this paper.

Optimization of the dynamic aperture is a common issue on future high energy circular colliders. Sufficiently wide momentum acceptance is especially important requirement because the beamstrahlung is critical in such a high energy collider. We recently started the optimization of the dynamic aperture for the CEPC project proposed in China. In this paper, a preliminary study of the dynamic aperture of the CEPC lattice is also presented.

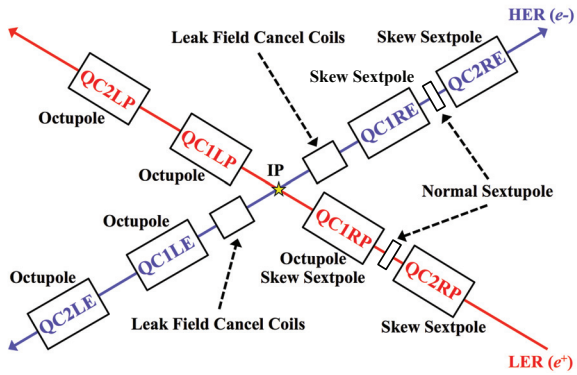


Figure 1: IR schematic view and arrangement of higher-order corrector coils. All magnets have superconducting corrector coils of a dipole, a skew dipole and a skew quadrupole.

## SUPERKEKB IR DESIGN OVERVIEW

Figure 1 shows schematic view of the SuperKEKB IR [3]. Each storage ring has 4 superconducting magnets to squeeze the beam size at IP. All quadrupole magnets except for QC1Ps have iron or permendur yoke for preventing leakage fields to the opposite beam line. The HER beam line has cancel coils of sextuple, octupole, decapole and dodecapole in order to compensate the leakage filed from QC1Ps of the LER beam line.

The SuperKEKB IR has a detector solenoid of 1.5 T, and this solenoid field is troublesome in the design of the beam optics and optimization of the dynamic aperture. For example, the finite crossing angle between the beam line and the solenoid axis generates the vertical emittace due to the solenoid fringe field. Therefore, the angle between solenoid axis and two beam lines should be chosen by compromising the vertical emittance generation in HER and LER. In the SuperKEKB IR design, this angle is chosen to be half of the crossing angle. Compensation solenoids are installed in order to suppress the effect of the solenoid field on the beam optics as much as possible. The field distribution is optimized so that the solenoid field integral from IP to each side of IR vanishes, $\int B_z(s)\,ds = 0$ for coupling matching, and reduce the peak of $\partial B_z/\partial s$ for vertical emittance suppression.

All quadrupole magnets have superconducting corrector coils of a dipole, a skew dipole and a skew quadrupole. Horizontal or vertical offset of the quadrupole magnets from the beam line is adopted to reduce required field strength of the dipole corrector in orbit matching. In addition to these

ISBN 978-3-95450-172-4

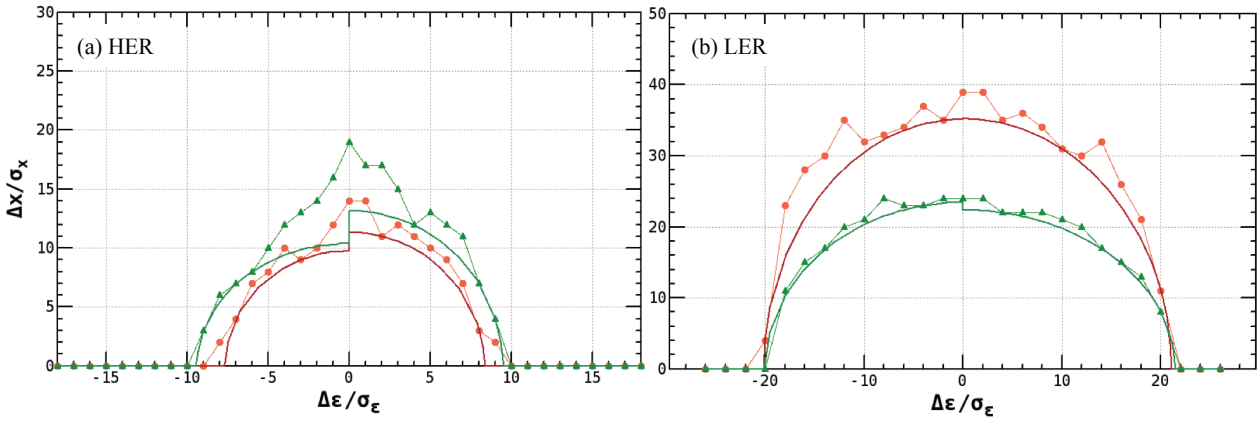


Figure 2: Dynamic aperture of (a) HER and (b) LER. Horizontal and vertical axes represent horizontal and momentum space in unit of their equilibrium values, respectively. The initial vertical amplitude of the tracking particle is chosen to be 0.27% of the initial horizontal amplitude. The initial horizontal and vertical betatron phases $(\phi_{x0}, \phi_{y0})$ are $(0,0)$ (dots) and $(\pi/2, \pi/2)$ (triangles).

low order correctors, sextupole and octupole coils are installed to optimize the dynamic aperture. The arrangement of sextuple and octupole coils is determined by tolerance of QCS imperfections. Rotations of the quadrupole magnets are also introduced in LER to help the optics matching. Huge chromaticity originated in the extremely strong focusing in IR is compensated by the local chromaticity correction (LCC) scheme with sextupole magnets installed near IR.

The dynamic aperture is evaluated by particle tracking simulation using accelerator modeling code SAD [4]. Accurate modeling of IR is essential for reliable numerical simulation. In our approach, the full three-dimensional (3D) magnetic field is modeled by series of multiple slices. The multipole strengths are evaluated from multipole filed expansion of 3D field calculated by ANSYS code [5]. The multipole fields up to 44 poles are take into account, and the thickness of the multipole slice is chosen to be 1 cm. Figure 2 shows the dynamic aperture of LER and HER, wherethe dynamic aperture is evaluated through 1000-turn particle tracking simulation without beam-beam force, synchrotron radiation and quantum excitation.

We re-optimize the linear optics and dynamic aperture every time the IR hardware design is updated. Typical procedure for the re-optimization is briefly described as follows. We first evaluate the 3D field distribution using ANSYS code taking into account hardware design changes, then the IR model is updated by the multipole filed expansion of the 3D field data. After updating the IR model, orbit and linear optics matching is performed. Finally the dynamic aperture is optimized by the Down-hill simplex algorithm. Available knobs are 54 sextupole pairs along the ring and octupole correctors (3/LER, 2/HER) installed in IR. Finite amplitude matching and off-momentum optics matching are employed to find the initial set of the knob parameters as needed.

## QCS IMPERFECTION

Field measurement of the QC1P prototype shows unexpected normal and skew sextupole field, and their field strength is ~0.1 % of the main quadrupole field. These error fields are likely due to misalignment of the main coils of a few tens of $\mu$m. Numerical simulation study is conducted to investigate its effect on the dynamic aperture.

Figure 3 shows degradation of the LER dynamic aperture due to the error field, where Touschek lifetime evaluated by the dynamic aperture as a function of the amplitude of skew sextupole error field is plotted. For simplicity, the error field is modeled by thin sextupole lens attached to the beam line.In this simulation. We assume that only QC1LP and QC1RP magnets has error field, and their magnitudes are identical. All 4 possible combinations of signs of the sextupole field are evaluated in Fig. 3. The sextupole field

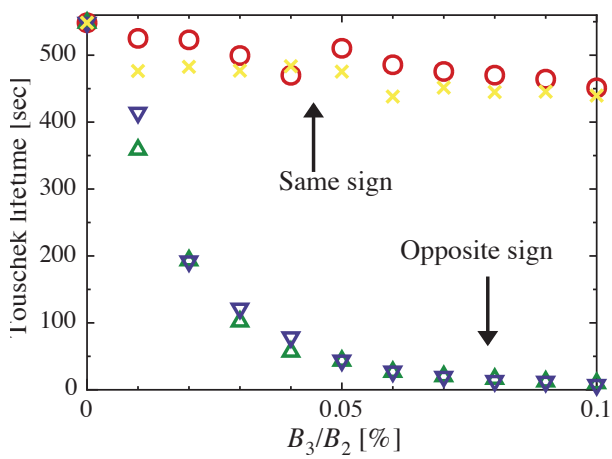


Figure 3: Touschek lifetime of LER as a function of the amplitude of skew sextupole error field, where horizontal axis indicates the ratio of skew sextupole field $B_3$ to quadrupole field $B_2$.



ISBN 978-3-95450-172-4

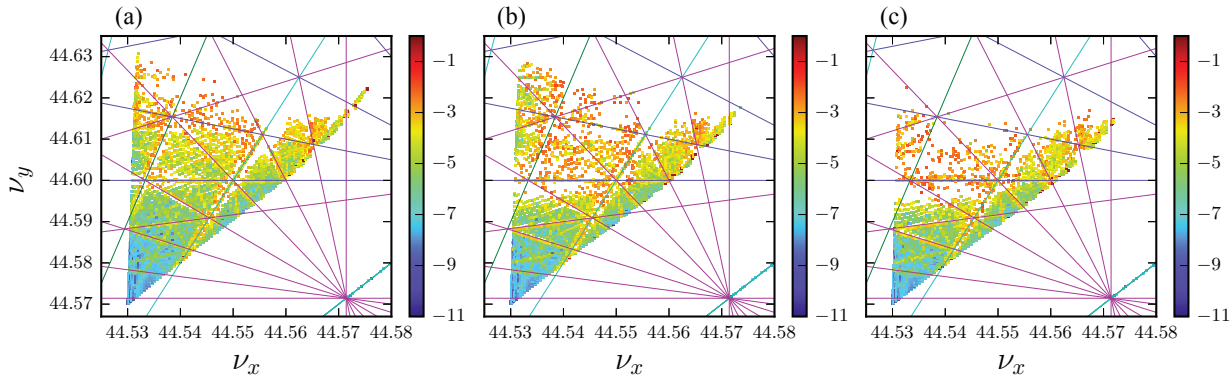


Figure 4: Footprints of LER with (a) $B_3/B_2 = 0$, (b) $5 \times 10^{-3}$%, and (c) $1 \times 10^{-2}$%.

reduces the dynamic aperture even though the error field is order of 0.01 % of the quadrupole field, $B_2$. Since the betatron phase advance between QC1RP and QC1LP are almost $\pi$, the degradation of the dynamic aperture is less serious when their signs are same.

In order to reveal the effect of the error field in view point of the resonance instability, frequency map analysis [6] is applied. An illustrative result is shown in Fig. 4, where the so-called footprint of LER with three different error amplitude is plotted. The color indicates the tune diffusion rate defined by $\log_{10}\sqrt{(\nu_{x1}-\nu_{x2})^2+(\nu_{y1}-\nu_{y2})^2}$, where $\nu_{x1}$ and $\nu_{y1}$ respectively denote the horizontal and vertical tunes calculated by the tracking data of first 1000 turns, $\nu_{x2}$ and $\nu_{y2}$ are those for the following 1000 turns. The NAFF algorithm [6], which is a more accurate technique compared to the fast Fourier transform is applied in the tune calculation. The tracking simulation is done for on-momentum particle without the synchrotron motion. We found that the sextupole error field excite the 5-th order resonances around $\nu_y = 44.6$. Taking these results, we decided to install the sextupole and skew sextupole coils to the final focus system (QCS) as show in Fig. 1.

Similar numerical simulations for higher order multipole error fields are also carried out to estimate the tolerance of the field quality of the QCS magnets. The simulation results are summarized in Fig. 5, where multipole error fields of $n = 4 \sim 10$ are evaluated individually. The multipole field of $n = 4$ here means decapole field. In the simulation, the thin lens multipoles are inserted to the all QCS magnets, and their magnitudes are identical. The worst case among the all 16 possible combinations of signs of the error field are plotted in Fig. 5. As expected, reduction of the dynamic aperture becomes smaller when $n$ becomes larger. In the case of HER, the multipole of $n = 10$ is almost negligible at least in this parameter range. On the other hand, the multipole of $n = 10$ significantly reduces the dynamic aperture of LER even when $B_n/B_2$ is less than 0.01 %. In other word, LER is more sensitive to the nonlinear distortion compared with HER. Touschek effect is stronger in the LER owing to the lower beam energy. Thus, as shown in Fig. 2, the particle with larger amplitude has to be stable in order to obtain the same Touschek lifetime as HER. These numerical results are now considered as the tolerance of the field quality of the QCS magnets.

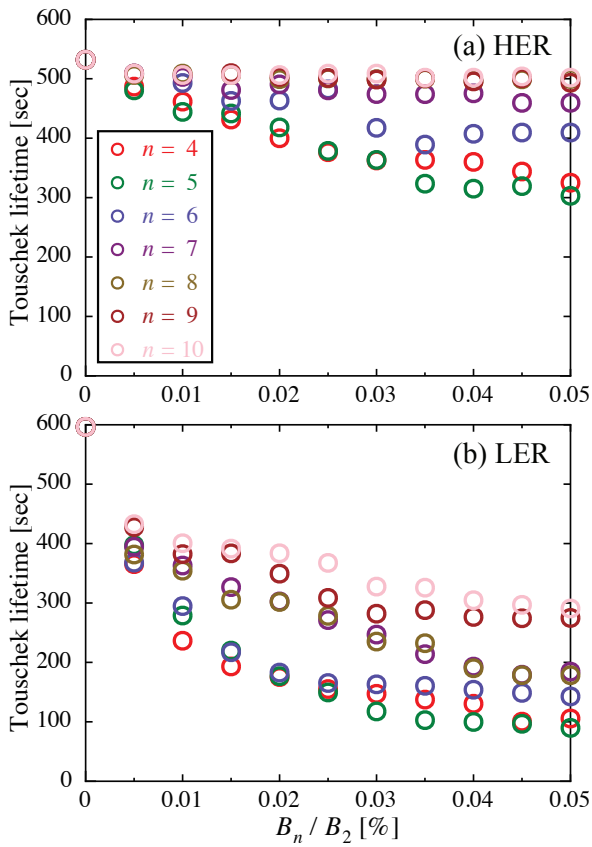


Figure 5: Touschek lifetime of (a) LER and (b) LER as a function of the amplitude of higher order multipole error fields.

ISBN 978-3-95450-172-4

## CEPC LATTICE AND DYNAMIC APERTURE

CEPC is a large $e^+$-$e^-$ collider for a Higgs factory. The project is now under study to complete a preliminary conceptual design report (Pre-CDR) by the end of 2014. We recently started the study of the dynamic aperture of the CEPC lattice. The one of most challenging beam optics issue is the sufficiently wide momentum acceptance of ±2% for strong beamstrahlung effects. In the following parts of this paper, We present the first survey on the CEPC lattice and very preliminary study on the dynamic aperture based on the experience of the SuperKEKB lattice design.

### *Optics*

Optical function in the arc lattice is shown in Fig. 6. The arc cell is based on a 60 degrees FODO cell. The sextupole magnets are installed next to each quadrupole for the chromaticity correction. Although the FODO cell is better for high packing factor, KEKB-type arc cell, a cell with non-interleaved sextupole pairs [7], is probably preferable in terms of optimization of the dynamic aperture since the required momentum acceptance of ±2% is very challenging. Possibility of applying other type of cell should be investigated in near future.

Figure. 7 shows the optical function in the final focus system (FFS). FFS is composed of the sections for horizontal and vertical local chromaticity corrections (X-LCC and Y-LCC) with $-\boldsymbol{I}$ sextupole pairs. The betatron phase advance between sextupole is $\pi$ to cancel the undesired nonlinear kick from the sextupoles. The vertical phase advance between final defocusing quadrupole (Q1FFS) and Y-LCC is $\pi$. On the other hand, the horizontal phase advance between the final focusing quadrupole (Q2FFS) and X-LCC is $3\pi$. Changing this horizontal phase advance from $3\pi$ to $2\pi$ may improve the performance of the X-LCC, and it should be studied in near future.

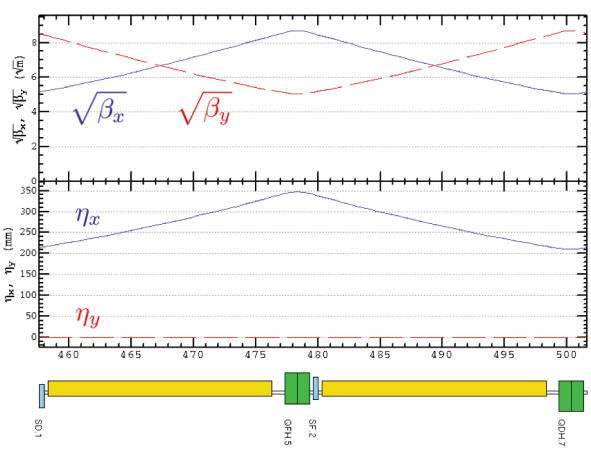


Figure 6: Optical functions of the CEPC arc cell.

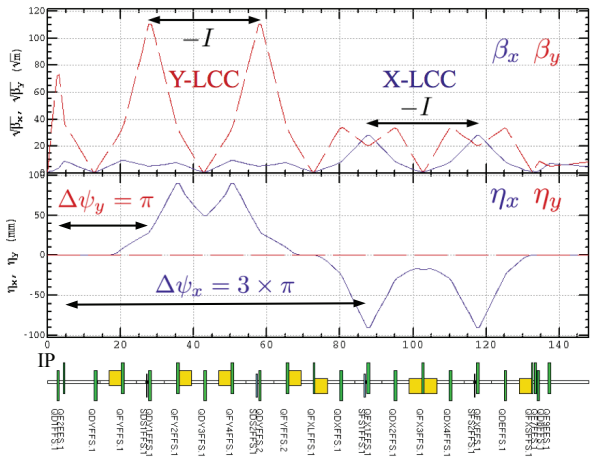


Figure 7: Optical functions in FFS.

Table 1: Natural Chromaticity $(\xi_x, \xi_y)$

| | SuperKEKB HER | SuperKEKB LER | CEPC |
|---|---|---|---|
| FFS | (-108, -1022) | (-54, -721) | (-108, -2404) |
| Arc | (-38, -29) | (-31, -33) | (-182, -188) |
| Others | (-23, -19) | (-19, -35) | (-31, -25) |
| Total | (-169, -1070) | (-104, -789) | (-321, -2617) |

### *Lattice Nonlinearity*

The natural chromaticity of CECP lattice is shown in Table 1 with comparison to that of SuperKEKB. As usual, FFS is the most dominant source of the natural chromaticity. Total natural chromaticity is more than twice as large as that of SuperKEKB. The essential difference between SuperKEKB and CEPC is number of IPs. The CEPC lattice has 2 IPs. The chromaticity correction, therefore, is probably more difficult than SuperKEKB.

It is well known that the nonlinearity around IP restricts the dynamic aperture. The dynamic aperture associated to the both the kinematic term and nonlinear fringe of the final focus magnet is given by [7],

$$J_{y0} = \frac{\beta_y^{*2}}{(1 - 2k_1 l^{*2}/3)\, l^*} A(\mu_y), \qquad (1)$$

where $J_{y0}$ is aperture for the original action, the $\beta_y^*$ is the vertical beta function at IP, $l^*$ is the distance between IP and the quadrupole face, and $k_1$ is the focusing strength. The function $A(\mu_y)$ is a universal function which depends only on the fractional part of the vertical tune [4], thus the ratio between $J_{y0}/A(\mu_y)$ gives us an index of the dynamic aperture associated to the nonlinear terms around IP. Table 2 shows theses parameters of CEPC lattice with comparison to those of KEKB and SuperKEKB. The ratio $J_{y0}/A(\mu_y)$ of CEPC is similar order of magnitude to that of SuperKEKB.



ISBN 978-3-95450-172-4

Table 2: Nonlinear Terms Around IP

| | KEKB | SuperKEKB HER | SuperKEKB LER | CEPC | Units |
|---|---|---|---|---|---|
| $\beta_y^*$ | 5900 | 300 | 270 | 1200 | $\mu$m |
| $k_1$ | -1778 | -3.0539 | -5.104 | -1.2881 | $1/m^2$ |
| $l^*$ | 1.762 | 1.221 | 0.766 | 2.5 | m |
| $J_{y0}/A(\mu_y)$ | 4.22 | 0.0183 | 0.0317 | 0.0904 | $\mu$m |

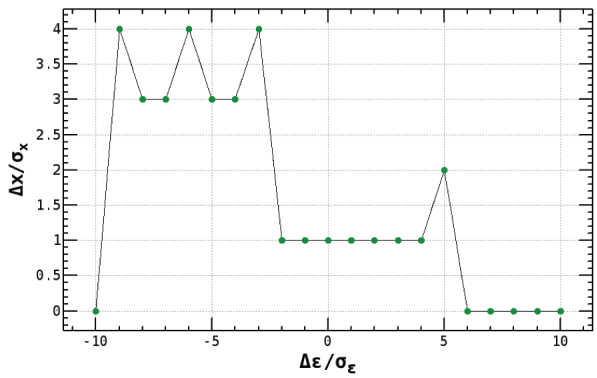


Figure 8: Dynamic aperture of the presented CEPC lattice. Horizontal and vertical axes represent horizontal and momentum space in unit of their equilibrium values, respectively. The initial vertical amplitude of the tracking particle is chosen to be 0.3% of the initial horizontal amplitude. The initial horizontal and vertical betatron phases $(\phi_{x0}, \phi_{y0})$ are $(0,0)$.

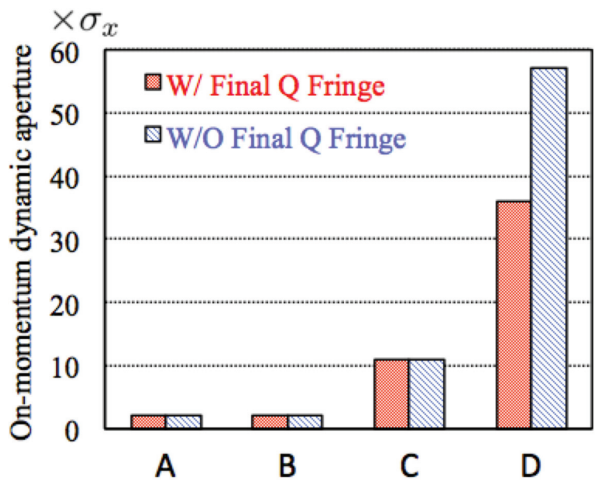


Figure 9: On-momentum dynamic aperture of the CEPC lattice with four different sextupole conditions. The sextupole conditions are listed in Table 3.

### *Dynamic Aperture*

The dynamic aperture of the presented CEPC lattice is shown in Fig. 8. The dynamic aperture is evaluated through 1000-turn particle tracking simulation. Even for on-momentum, dynamic aperture is far from the target values of $40\sigma_x$.

In order to investigate the dominant cause of the restriction of on-momentum dynamic aperture, we calculate on-momentum dynamic aperture with four different sextupole conditions. The sextupole conditions are listed in Table 3. In the all simulation, the synchrotron motion is frozen out to focus on the on-momentum beam dynamics. Simulation results are summarized Fig. 9(red bar). The result of case B shows the dynamic aperture is not improved by turning off the arc sextupole. The dynamic aperture is improved in some degree by turning off the sextuples used in the LCC section (case C). According to these numerical results, we conclude that the geometric terms originated from the sextupole magnets seem to be too large in the presented CEPC lattice.

In addition to these simulation, we tried analogous simulations by turning off the fringe field of the final quadrupole magnets (blue bar). We notice that the fringe effect is not visible in case A, B, and C, while the dynamic aperture is remarkably improved in case D. The result indicates that the fringe effect will be important once the geometric term of the sextupole is minimized. In such cases some octuple correctors can be used to compensate the fringe effect because a quadrupole fringe field induces an octupole-like transverse kick.

Table 3: Sextupole Conditions Assumed in Fig. 9

| Case | Arc Sextupole | LCC Sextupole |
|---|---|---|
| A | On | On |
| B | Off | On |
| C | On | Off |
| D | Off | Off |

On-momentum dynamic aperture as a function of the LCC sextupole strength is shown in Fig. 10. Figure. 10 says that the sextupole field is too strong for the required dynamic aperture of $40\sigma_x$. The Y-LCC sextupole should be reduced by about one-tenth. In order to reduce the sextupole strength, the horizontal dispersion function at the LCC sextupole magnets should be increased. However, the large the dispersion function involves emittance generation and detector background due to the synchrotron radiation. Further study is, therefore, needed to optimize the FFS optics.

ISBN 978-3-95450-172-4

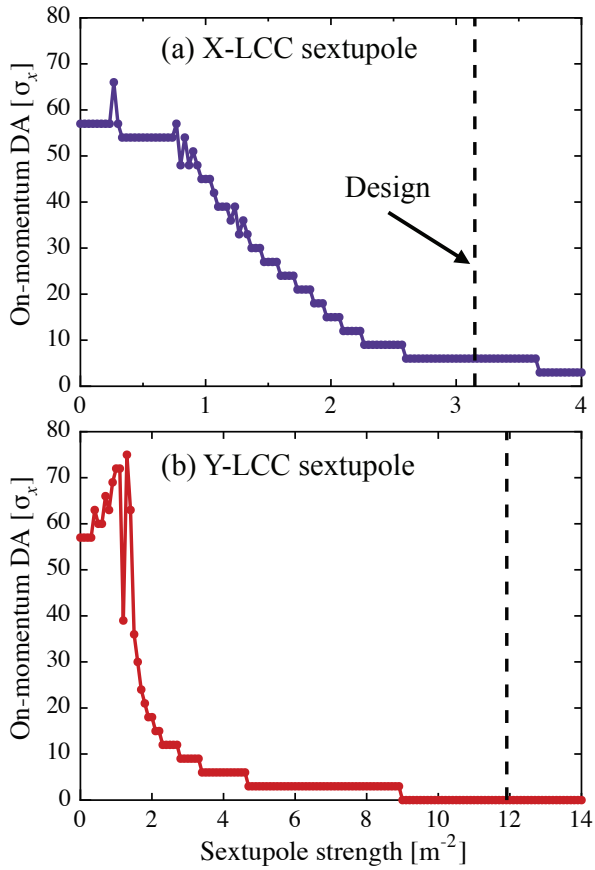


Figure 10: On-momentum dynamic aperture as a function of the (a) X-LCC sextupole and (b) Y-LCC sextupole strengths.

## SUMMARY

The overview of the SuperKEKB IR design is presented. The effects of sextupole error field from QCS on the dynamic aperture is evaluated, and we decided to install normal and skew corrector coils to IR. We also present the tolerance of field quality of the final focus magnets by evaluating the effects of higher order multipole error field on the dynamic aperture.

A preliminary study on the dynamic aperture of the CEPC lattice is also reported. The dominant cause of the restriction of the dynamic aperture is the huge geometric terms originated from the LCC sextupole magnets. In order to decrease the sextupole strength, the horizontal dispersion at the LCC sextupole magnets should be increased. Further systematic study on the FFS optics is needed to improve the dynamic aperture.

## ACKNOWLEDGEMENTS

The presented design study of the SuperKEKB IR is carried out by the SuperKEKB optics group. The author would like to thank the IHEP beam optics group for proving the information of CEPC lattice. The author also thanks A. Morita and Y. Ohnishi for useful comments on the dynamic aperture study of CEPC.

## REFERENCES

[1] "KEKB B-Factory Design Report", KEK Report 95-7 (1995).

[2] Y. Ohnishi *et al.*, Prog. Theor. Exp. Phys. 2013 03A011 (2013).

[3] N. Ohuchi *et al.*, Proc. of PAC2013, Pasadena, USA, WEODA1, p.761 (2013).

[4] K. Oide, Nucl. Inst. Meth. A **276**, 427 (1989). `http://acc-physics.kek.jp/SAD/`

[5] ANSYS, `http://www.ansys.com`

[6] L. Nadolski and J. Laskar, Phys. Rev. ST Accel. Beams **6**, 114801 (2003).

[7] K. Oide and H. Koiso, Phys. Rev. E **47**, 2010 (1993).



ISBN 978-3-95450-172-4

# LIFE TIME AND INJECTION CONSIDERATIONS FOR CEPC

Cui Xiaohao, Xu Gang, Geng Huiping, Guo Yuanyuan, IHEP, Beijing, China

*Abstract*

To make a precise study on the Higgs bosons, CEPC ,a circular storage ring collider is being proposed in China. The beam lifetime calculation results in CEPC are shown in this paper. Due to the fact of short lifetime, a top-up injection scheme is needed and some considerations on the injection design is presented.

## INTRODUCTION

After the discovery of Higgs bosons at LHC, e+e- collider working as a Higgs factory for further studies has been in consideration throughout the world. CEPC is such a circular e+e- collider proposed in China. The electron and positron energy are chosen to be 120 GeV, which is optimized for a Higgs research. This Collider has a circumference of 50 km, which is about twice the size of LHC, the existing world largest circular collider. Synchrotron radiation energy loss power is 50 MW, and the budget should be more than 20B CNY. The main parameters are listed below in Table 1.

Table 1: Main Parameters of CEPC

| **Beam Energy** | **120 GeV** |
|---|---|
| Circumference | 54.75 km |
| Luminosity | 2.0E34 cm-2s-1 |
| SR power/beam | 50 MW |
| Number of IPs | 2 |
| Number of Bunches/beam | 50 |
| Momentum compaction factor | 3.39E-5 |
| Energy acceptance | 0.01 |
| Beam current | 16.6 mA |
| Horizontal emittance | 6.12E-9 m.rad |
| Bunch length | 0.00253 m |
| Beam-Beam parameters(x/y) | 0.116/0.082 |
| Emittance coupling | 0.003 |

## BEAM LIFETIME

Beam lifetime in a storage ring is a parameter to describe the losing rate of particles, it is defined to be [1]:

$$\frac{1}{\tau} = -\frac{1}{N}\frac{dN}{dt}. \qquad (1)$$

In storage rings many effects could reduce the beam intensity, so that the beam life time should include many parts, the total lifetime and the lifetime due to a single beam loss mechanism have a relation as:

$$\frac{1}{\tau_{total}} = \sum \frac{1}{\tau_i} \qquad (2)$$

For the CEPC lifetime study lifetime from these effects are taken into account [2]:

(i) Beam-Gas scattering
(ii) Quantum fluctuation of radiation
(iii) Touschek effects
(iv) Radiative BaBar
(v) Beamstrahlung effect

The beam lifetime of CEPC is shown in Table 2, in the calculation a gas consists of 80% H2 and 20% CO with a vacuum pressure of 1E-8 Torr, and a 1.5 cm vacuum chamber radius is assumed.

Table 2: Lifetime of CEPC Due to Different Effects

| | **Lifetime** | **Unit** |
|---|---|---|
| Elastic H2 scattering | 189 | Hours |
| Elastic CO scattering | 15 | Hours |
| Inelastic H2 scattering | 149 | Hours |
| Inelastic CO scattering | 14 | Hours |
| Transverse quantum | 2218 | Hours |
| Longitudinal quantum | Infinity | Hours |
| Touschek | 530 | Hours |
| Radiative BhaBha | 51 | Min |
| Beamstrahlung | 80 | Min |
| Total lifetime | 30 | Min |

## INJECTION DESIGN

The current baseline design of CEPC injection is chosen to use a ramping booster as the main injector. The system consists of one Linac which accelerates the electrons and positrons to 6 GeV, a booster ring which ramps from 6GeV up to high energy of 120 GeV. A sketch of the system is shown in Figure 1.

ISBN 978-3-95450-172-4

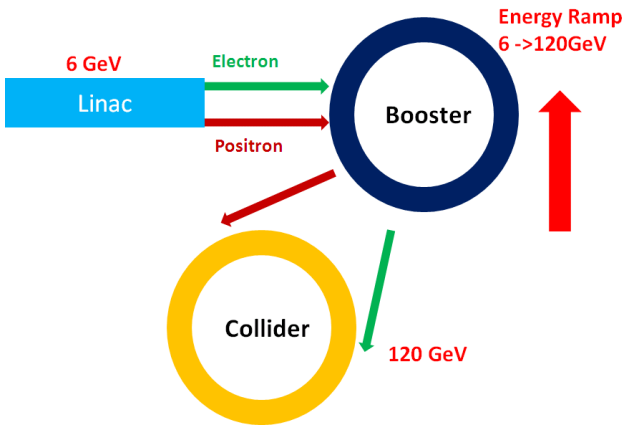


Figure 1: A schematic diagram of CEPC system configuration.

The main collider is designed to be 8-fold symmetric, it has 8 arc sections and 8 long straight sections, as shown in Figure 2. IP1 and IP2 are sections for the real IPs, IP3 and IP4 are preserved for the IPs of SPPC, so the injection of electrons and positrons are put in the straight sections right next to the IP1, separately. The booster is installed in the same tunnel with the main colliders, it is with the same circumference and stays right up-side with the collider. Due to the short beam lifetime, top-up injection is needed, and in a injection process the injection time length is mainly determined by the ramping time of the booster. To reduce the injection time, 50 bunches are injected from the booster in one ramping cycle. 50 bunches in the booster are designed to have the same time structure with that in the main collider, the kickers in the booster and collider are turned on before a bunch comes and turned off after, thus 50 bunches are injected into the main collider one by one.

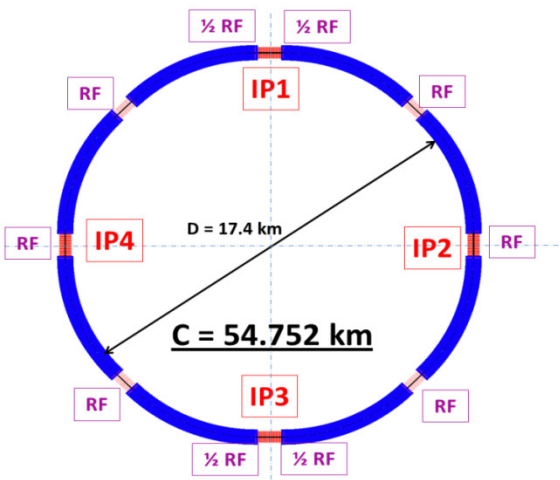


Figure 2: The layout of the CEPC main collider.

The top-up injection period is determined by the lifetime, the luminosity drop and the positron production rate. For a 30 min lifetime in CEPC, 10% luminosity drop needs to fill the bunch every 90 seconds, and the bunch charge in the booster need to be 2.8 nC. When the current in the main collider is dumped, we need to inject with a frequency higher than the top-up mode. Assuming the injection period is 60 seconds , 30 min is needed to reach the peak current.

For a baseline design of the injection mode, betatron injection is chosen , and three kickers are used to bump the circulating beam near the injected beam. The Twiss function at the injection section is shown in Figure 3.

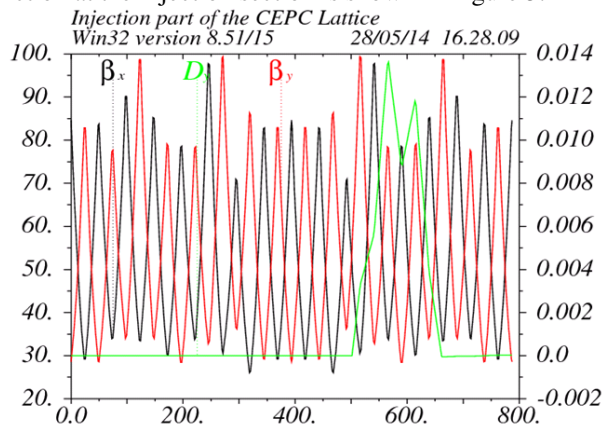


Figure 3: The Twiss functions in the injection straight section.

The bump height and the machine acceptance is determined from the injection phase space [3]:

$$\text{Acceptance length} > 5\sigma_e + 10\sigma_i + S \quad (3)$$

$$\text{Bump height} > 10\sigma_i + S \quad (4)$$

Where, $\sigma_{xc}$ is the beam size of the circulating beam, $\sigma_{xi}$ is the beam size of the injected beam, S is the thickness of the septum board. For our design, the kicker gives a 20 mm bump and the acceptance should be larger than 15mm.

## CONCLUSION

In this paper, a primer baseline design of the injection system is given. Still, there are many works to be done. Detector protection should be considered in top-up injection, beam instabilities with pretzel orbit is a serious problem, and effects of imperfections should be included. These will be done in our future work.

## ACKNOWLEDGEMENT

This work is supported by the National Natural Science Foundation of China(Y3118D005C).

## REFERENCES

[1] S.Y. Lee, Accelerator Physics, (World Scientific Publishing, 2004), 456.
[2] A. Hofmann, Proceedings, General accelerator physics, vol. 1. CERN Geneva—CERN-94-01.
[3] J.T. Seeman, Injection Issues of Electron-Positron Storage Rings, SLAC-PUB-5933.



ISBN 978-3-95450-172-4

# CONSTRAINTS ON THE FCC-*ee* LATTICE FROM THE COMPATIBILITY WITH THE FCC HADRON COLLIDER

B. Haerer*, CERN, Geneva, Switzerland, KIT, Karlsruhe, Germany,
W. Bartmann, M. Benedikt, B. J. Holzer, J. A. Osborne, D. Schulte, R. Tomas,
J. Wenninger, F. Zimmermann, CERN, Geneva, Switzerland
M. J. Syphers, MSU, East Lansing, Michigan, USA
U. Wienands, SLAC, Menlo Park, California, USA

*Abstract*

Following the recommendations of the European Strategy Group for High Energy Physics, CERN launched the Future Circular Collider Study (FCC), a design study for possible future circular collider projects to investigate their feasibility for high energy physics research. The FCC Study covers three different machines with a circumference of 100 km: an electron positron collider with collision energies in the range of 90 GeV to 350 GeV (FCC- ee), a proton proton collider with a maximum energy of 100 TeV (FCC-hh) and an electron proton option (FCC-he). This paper will present the constraints on the design of the FCC-ee lattice and optics from geometry and lattice considerations of the hadron machine.

## INTRODUCTION

With the discovery of a Higgs boson all particles of the standard model of particle physics have been found. In order to discover new physics CERN started to study a future discovery machine called FCC-hh with proton proton collisions at 100 TeV center of mass energy. Considerations presented in this paper will show that such a machine will need to have a circumference of 80 km-100 km given by the achievable technology. Having this tunnel available it is obvious to think about an electron positron collider for precision measurements as well [1]. The large circumference allows operation with an acceptable amount of synchrotron radiation losses and the costs for a second machine decrease drastically, as no extra tunnel has to be built. However straight sections for RF installation have to be provided to deal with the synchrotron radiation loss in such a storage ring. This part of the design study, earlier known as TLEP, is called FCC-ee. The third part of the study, FCC-he, covers the investigation of future electron proton collisions in order to study deep inelastic scattering. This comprises two options: a LHeC like linac-ring option and, in case FCC-hh and FCC-ee can be hosted and operated in the tunnel at the same time, a ring-ring option. Each machine of the FCC study has special requirements, that have to be considered in the design phase. This paper focuses on the constraints on the FCC-ee lattice design from the compatibility with FCC-hh. Contrary to FCC-ee, for a beam energy of 50 TeV in the hadron machine a new magnet technology has to be developed. The maximum bending radius in the arcs and consequently the circumference of the machine directly depends on the achievable magnetic field. The length of the long straight sections needed for insertions also contributes to the circumference. They must provide enough space to house RF installation, collimators, kickers for injection and beam dump and the detectors. If LHC is used as an injector, the circumference and harmonic number of FCC should be rational multiples of the LHC's to allow bunch to bucket transfer. Furthermore the FCC-hh and LHC tunnels should be close to each other to guarantee a reasonable length of the transfer lines. For locating a 100 km circular collider also geologic aspects play a major role. The constraints arising from the requirement of hosting both machines in the tunnel at the same time and from the compatibility with FCC-he are not covered in this paper.

* bastian.harer@cern.ch

## BENDING RADIUS AND CIRCUMFERENCE

The beam rigidity of a 50 TeV proton beam is

$$B\rho = p/e \approx 1.67 \times 10^5 \text{ Tm}. \quad (1)$$

To bend such a stiff beam in a reasonable radius a new technology of superconducting magnets needs to be developed. A prototype dipole based on $Nb_3Sn$ technology could reach a magnetic field of $B$ =16 T [2]. Such a magnet would define a bending radius of $\rho$ = 10.7 km. If even higher magnetic fields of $B$ =20 T could be achieved, the bending radius could be reduced to $\rho$ =8.5 km. Assuming 16 T magnets and 67 % of the whole circumference including long straight section being occupied by bending magnets the circumference $C$ would approximately be 100 km. As mentioned before, if LHC is used as an injector, the circumference of FCC should be a multiple of the LHC circumference, which is 26.66 km [3]. For 16 T magnets approximately 106.64 km should be taken as circumference and 79.98 km for the 20 T version. Both possibilities are studied, the final choice will depend on the technical progress in magnet technology.

Table 1: Circumference and Ending Radius for Different Magnetic Felds of the Bending Magents

| $B$ in T | $\rho$ in km | $C$ in km |
|---|---|---|
| 16 | 10.7 | 106.64 |
| 20 | 8.5 | 79.98 |

ISBN 978-3-95450-172-4

## LAYOUT OBJECTIVES AND SHAPE OF THE MACHINE

The maximum momentum of the particle beam in a hadron machine is limited by the bending radius of the dipoles. Therefore the design aims to maximize the integral magnetic dipole field around the machine

$$\oint B(s)\,\mathrm{ds}. \tag{2}$$

Practically that means highest possible dipole fill factor and avoiding sections without full strength bending magnets as far as possible. This includes straight sections but missing bend or half-bend dispersion suppressors as well. The energy in a lepton machine on the contrary is limited by synchrotron radiation. The energy loss per turn is given by [4]

$$U_0 = \frac{4\pi}{3}\alpha\hbar c\frac{\gamma^4}{\rho}. \tag{3}$$

The lost energy needs to be fed back to the beam in straight sections with RF installation. Those cavities must be positioned in dispersion free sections to avoid coupling between the longitudinal and transversal planes. The design for a lepton machine not only aims for maximum dipole fill factor in order to maximize the bending radius and minimize the radiation power, but contrary to a hadron machine also for a high number of straight RF sections to narrow down the energy sawtooth of the orbit. This is important because particles with large energy deviations will move on dispersion orbits with large amplitude and cross strong non-linear fields or even get lost while hitting the geometric aperture. Those layout requests end up in different shapes of the machine: in case of a hadron machine, the minimal number of dispersion suppressors is given by a racetrack design, where all infrastructure like injection, ejection, RF and interaction regions is concentrated in two very long straight sections which are connected by two arcs. In case of a lepton machine a circular design with equally distributed straight RF sections is preferred. The more dispersion free RF sections are provided the smaller is the energy sawtooth.

In general it is useful to ensure a phase advance of $(n + 1/2)\pi$ with $n$ being an integer between two interaction points to correct higher order chromaticity. In a racetrack like geometry with clustered interaction regions the preservation of the phase advance is easier than in a circular layout because of the smaller distance between those points (e. g. SSC design [5]). Still measurements at LHC have shown, that the phase advance can be kept stable between the two high-luminosity experiments ATLAS and CMS, which have a distance of ca. 13.3 km. So clustering the interaction points is not a compulsory requirement from an optics point of view.

## LOCATION OF THE FCC TUNNEL

A variety of boundary conditions has to be considered in context of a possible location of FCC.

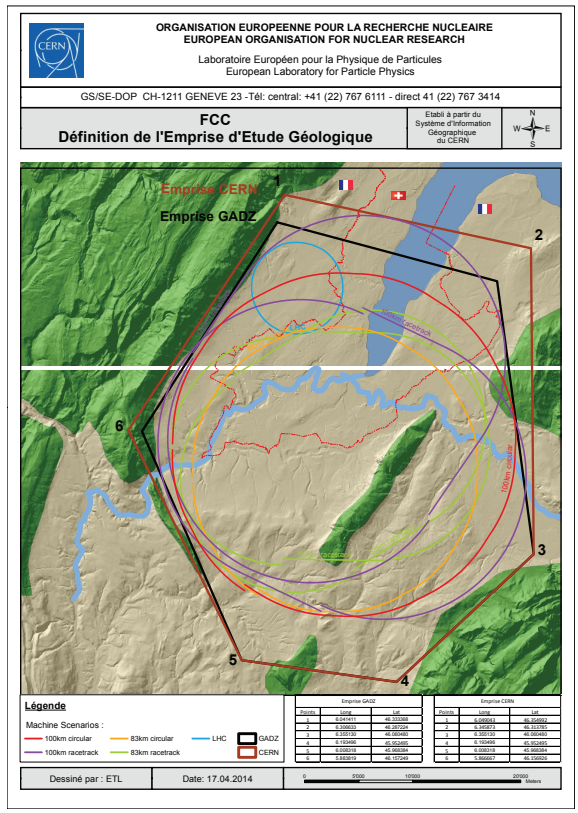


Figure 1: The geological study area with some proposals for the location for both circular and racetrack shaped machines with the circumference 80 km and 100 km (Defined by the FCC Civil Engineering Group chaired by J. Osborne).

### *Geology*

Building a tunnel with the length of 100 km is a civil engineering challenge. The geology of the area plays a major role and must be studied carefully before deciding the exact location. The geological study area defined by the FCC Civil Engineering Group is shown in figure 1. Its borders are defined by the surrounding area: the Pre-Alps in the East and South-East, the Jura Mountains in the West, Mount Vuache in the South and Lake Geneva to the North. The mountains consist mostly of Limestone, with some Karstic features, making the risk of encountering water very high. Tunnel excavation in this type of rock can be complicated and expensive due to stored water in the rocks. The depth of the access shafts needs to be minimized to facilitate the installation of services and optimize the safety paths. As far as possible, the tunnel should be housed in the Molasse Rock, a sedimentary rock made up of sandstone and marls.

### *Tilting the Tunnel*

For finding an appropriate location for the future FCC tunnel it is considered to tilt the tunnel plane. This was already done when the LHC tunnel was built for LEP. The median plane was tilted with respect to the horizontal by 1.42 % [6] to maximize the tunnel extent in Molasse Rock environment and to minimize the depth of the access shafts.



ISBN 978-3-95450-172-4

In case of FCC such a tilt could allow passing Lake Geneva further in the North without increasing the depth of the access shafts to the Southern part of the machine.

### *Location Relative to LHC*

With the LHC, CERN already has a high energy hadron machine available that could be used as injector for FCC-hh. Below 3.5 TeV the power converters and the cooling system allow to ramp the LHC bending magnets with up to 50 A/s. Combined with its double ring layout LHC would be a very efficient injector delivering up to 2800 bunches per beam. To keep the transfer lines reasonably short the FCC tunnel should overlap or cross one LHC straight section. Nevertheless there is a minimum horizontal distance between the LHC extraction point and a possible FCC injection point, which is necessary to overcome the difference in depth. Due to maintenance and engineering reasons the slope of the transfer line tunnel should not be larger than 5 %. Thus the required distance depends on the beam energy, the magnet technology used and the difference in depth. Figure 2 shows this dependency for a beam energy 3.5 TeV and a dipole filling factor of 0.75, which leaves enough space for machine protection elements. The different lines correspond to different vertical distance between the LHC and the FCC tunnels, which is labeled on the right. Obviously the transfer line must be longer, if the vertical distance of the tunnels is larger or the magnetic field of the dipoles is smaller. So choosing normal conducting magnets will elongate the transfer line. Assuming a difference of depth of less than 200 m and reasonable dipole fields the LHC extraction point and FCC injection point need to have a distance between about 0.5 km and 1.5 km.

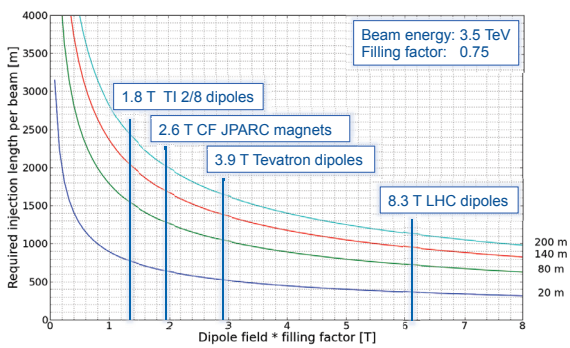


Figure 2: The plot shows the required horizontal distance between the extraction point at LHC and a future injection point at FCC-hh ring as a function of the magnetic field of the used bending magnets. Each line stands for a certain vertical distance of the two tunnels, which is labeled on the bottom right of the plot.

## LENGTH OF LONG STRAIGHT SECTIONS

Long straight sections are used for various purposes: RF installation, injection, beam dump, collimation and mini-beta insertions for the experiments. For the injection of pre-accelerated beams from the arriving transfer line to the main ring, septum magnets are used followed by kicker magnets. Additionally machine protection elements will be needed to prevent damage in case of failure. For the injection of a 3.3 TeV proton beam into FCC-hh these group of elements will require space with the length of 600 m, corresponding to about three FODO cells, that will have to be modified. The extraction to the beam dump line uses the same scheme, but it has to be laid out for up to 50 TeV beam energy. Though longer kicker rise times can be accepted, more space will be necessary. First estimates predict a length between 800 m and 1000 m. For the collimation system two 2.8 km long straight sections are foreseen.

## INTERACTION REGION

The biggest experiment at LHC is the ATLAS detector with about 45 m length and 25 m height. However for particle detection at 100 TeV center of mass energy even larger detectors are needed, because the particle jets penetrate deeper before the particles are absorbed in the calorimeter. The current FCC-hh interaction region design therefore assumes an $L^*$ of 46 m, which corresponds to a 92 m long drift space for the detector. The length of the complete FCC-hh interaction region including matching sections and dispersion suppressors is approximately 1100 m long. The interaction region layout for FCC-ee is completely different: In the FCC-hh final focus system a very tiny crossing angle of ca. 70 µrad is used. In the FCC-ee design the ambitious request for the vertical beta function at the interaction point $\beta^* = 1$ mm needs to be combined with a small $L^*$ of 2 m to prevent the beta function from growing to unreasonable size. To minimize synchrotron radiation the two beams must be focused by separated quadrupoles, thus the crossing angle is defined by the quadrupole's aperture and the size of the coils. The CERN interaction region design is based on a crossing angle of 11 mrad, while the final focus system designed by the Budker Institute of Nuclear Physics (BINP) is based upon 30 mrad [7]. In combination with a local chromaticity correction scheme this leads to different geometries of the interaction regions, that are shown in figure 3. While in the FCC-hh design the two beams are separated by 40 cm in the matching sections, the ones for FCC-ee have a distance up to 2 m. Including matching sections and dispersion suppressors the FCC-ee interaction region will probably be longer than the one for FCC-hh. So the dimensions of the straight sections next to the experiments will be defined by the requests of FCC-ee.

## CONCLUSION

The compatibility of the FCC-ee lattice with FCC-hh requires the same layout and geometry given by the tunnel. While the magnetic fields for FCC-ee can easily be obtained (see Table 2), the circumference and the bending angle for the FCC-hh machine are defined by the achievable magnetic fields. The length of the straight sections depends on the re-

ISBN 978-3-95450-172-4

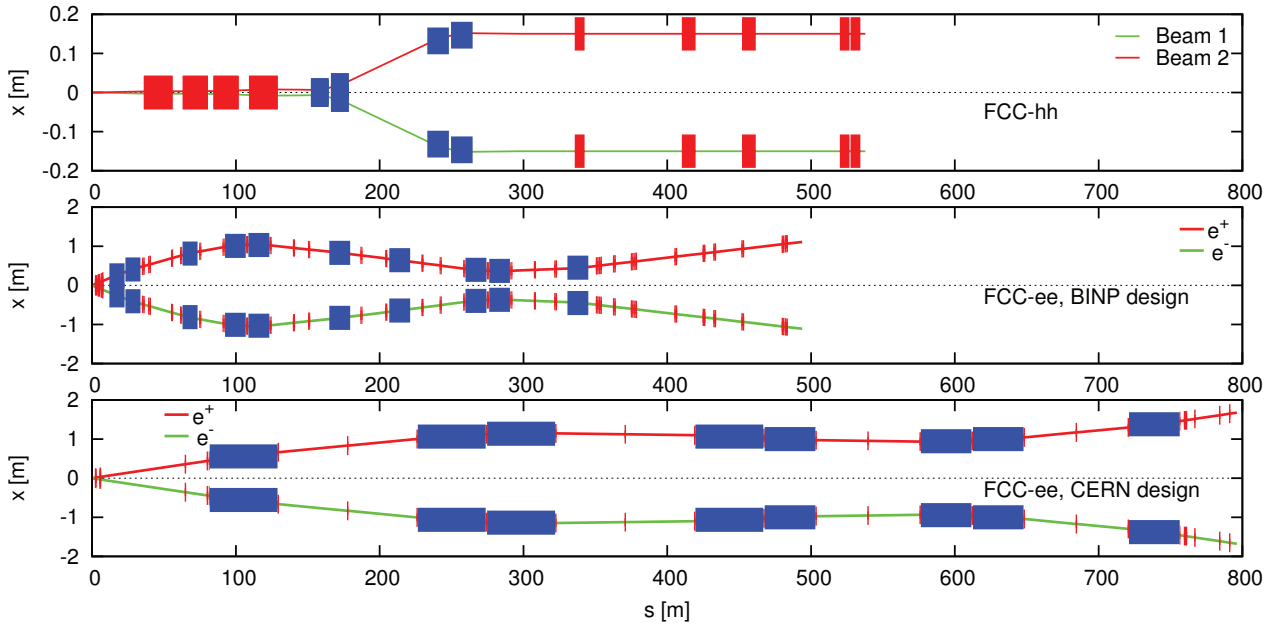


Figure 3: Comparison of the Geometry of the Interaction Region Designs for FCC-hh and FCC-ee [7].

Table 2: List of Baseline Parameters for FCC-hh and the Different Physics Programs of FCC-ee ( [8], [9])

| | FCC-hh | FCC-ee Z | FCC-ee W | FCC-ee H | FCC-ee tt |
|---|---|---|---|---|---|
| Beam energy (GeV) | 50000 | 45.5 | 80 | 120 | 175 |
| Circumference (km) | 100 (80) | 100 | 100 | 100 | 100 |
| Dipole field | 16 (20) | 0.014 | 0.024 | 0.036 | 0.053 |
| Arc filling factor | 0.79 | 0.84 | 0.84 | 0.84 | 0.84 |
| Number of IPs | 2+2 | 4 | 4 | 4 | 4 |
| Peak luminosity ($10^{34}$ cm$^{-2}$s$^{-1}$) | 5 | 28.0 | 12.0 | 5.9 | 1.2 |
| Betatron function at IP $\beta^*$ (m) | | | | | |
| - Horizontal | 1.1 | 0.5 | 0.5 | 0.5 | 1 |
| - Vertical | 1.1 | 0.001 | 0.001 | 0.001 | 0.001 |

quirements for the injection, extraction, collimation regions. While the size of the caverns housing the experiments is defined by the FCC-hh detectors, the straight sections for the final focus system must provide enough space for the geometry of the FCC-ee design. The possible location of a future FCC tunnel depends on geological aspects but also on the already existing infrastructure. The LHC would be a very effective pre-accelerator for FCC-hh, so a possible injection point at FCC-hh should be located close to a LHC straight section but keep a minimum distance to overcome the difference in depth.

Especially in this early stage of the FCC study it is important to consider the compatibility of the sub-studies with each other to ensure a successful development of the project.

## ACKNOWLEDGMENT

This work is supported by the German Bundesministerium für Bildung und Forschung (BMBF).

## REFERENCES

[1] TLEP Design Study group: "Referee report: Answers and actions taken", December, 2013

[2] LBNL Superconducting Magnet Program Newsletter Issue No. 2, "HD-1 Sets New Dipole Field Record", LBNL, Berkeley, CA, USA, October 2003

[3] *LHC Design Report*, (Geneva: CERN, 2004)

[4] M. Sands, *The Physics of Electron Storage Rings. An Introduction*, SLAC-121, 1970

[5] SSCL, "Conceptual Design of the Superconducting Super Collider", SSC-SR-2020, 1986

[6] *LEP Design Report*, (Geneva: CERN, 1984)

[7] R. Martin et al., "Status of the FCC-ee Interaction Region Design", *These Proceedings*, HF2014, Beijing, China (2014)

[8] Future Circular Collider Study, "Hadron Collider Parameters", FCC-1401101315, CERN, 2014

[9] Future Circular Collider Study, "Lepton Collider Paramters", FCC-1401201640, CERN, 2014



ISBN 978-3-95450-172-4

# POLARIZATION ISSUES AND SCHEMES FOR ENERGY CALIBRATION

I.A. Koop, BINP SB RAS, NSU and NSTU, Novosibirsk, Russia

*Abstract*

The paper presents an overview of problems related to production, acceleration and subsequent utilization of the polarized electron and positron beams for the precise energy calibration in the future FCC-ee storage rings. Advantages and disadvantages of the proposed method of free precession spin frequency measurement are discussed.

## INTRODUCTION

As truly stated in [1], the polarized beams can be of interest for two reasons: they allow for an accurate energy calibration using resonant depolarization, which will be a crucial advantage for measurements of $M_Z$, $G_Z$, and $M_W$, with expected precisions of order 0.1 MeV; and they are necessary for physics program with longitudinally polarized beams. Taken seriously into consideration the last request we came to the following polarization scenario:

- No use of self-polarization in a collider - too slow with r=11 km: $\tau$=190 hours at Z-peak.
- Polarized electrons acceleration chain started from a Ga-As photo-gun illuminated by a circularly polarized laser light, followed by acceleration to the energy of an intermediate damping ring (1-2 GeV) and then after cooling by SR again acceleration by a linac up to 20 GeV. After then they will be accelerated by a synchrotron up to the top beam energy of a collider (45 – 175 GeV).
- Positrons produced by the conversion of the accelerated to 5-10 GeV electrons are injected into a damping ring. Main part of the cooled via SR-damping positrons will be utilized for the un-polarized collisions. The remaining fraction of positron bunches will spent much longer time, about few minutes, in a special damping ring equipped by the polarization wigglers. These positrons, after became polarized to 10-40% degree, will be accelerated similarly to electrons via the linac and the synchrotron.
- Preservation of the polarization in the booster synchrotron should be guaranted by the installation there of a number of Siberian Snakes.
- The equilibrium spin direction in both collider rings is vertical. But the spin precession frequency could be determined using two methods: by the resonant depolarization technique, see [2-3], and, alternatively, by measuring a free precession Fourier spectrum.
- In the last approach the injected beam polarization vector is perpendicular to the vertical axis.
- The Compton backscattering longitudinal laser polarimeter we propose to use for detection of a coherent spin precession.
- Our estimations reveal a possibility to measure the average beam energy with the accuracy of the order $10^{-6}$ in single injection shot.

One should keep in mind that resonant depolarization is limited for the use of up to 80-100 GeV per beam. At higher energies the non-polarization methods of the energy monitoring should be considered. Such two possibilities are discussed in [4, 5]. Still calibration by the resonant depolarization shall validate these techniques for the use at higher energies.

## POLARIZED BEAM ACCELERATION WITH SIBERIAN SNAKES

When polarized electron beam is accelerated say from 20 GeV to 80 GeV it crosses more than 130 of integer spin resonances spaced by 440.65 MeV. Due to small field errors it will become fully depolarized even by a single cross of such a resonance.

In 70-th Derbenev and Kondratenko have suggested an idea of the Siberian Snake [6]. This is some kind of a spin rotator which rotates spin by $180^0$ around any axis which is perpendicular to the vertical one. In a ring with equally spaced odd number of snakes the closed spin orbit looks like it is shown in the Fig.1: everywhere in arcs spins are lying in the medium plane of an accelerator.

Another remarkable fact is that with the odd number of snakes the fractional part of the spin tune always equals to $\nu$=0.5, thus all the spin resonances became eliminated! Still strong enough spin perturbation may destroy the regular spin motion making it non-adiabatic. It may happen, if any k-th harmonic amplitude of a perturbation exceeds or approaches to $w_k$~0.5.

Other mechanism, which one should take into account, is the radiative depolarization. More details on that are presented in [7]. Here we want announce only the rough depolarization time estimates, achieved analytically and by running the code ASPIRRIN [8]. With 3 snakes in the isomagnetic ring with the bending radius r=11 km $\tau_p$ =320 s at E=45 GeV and $\tau_p$ =6 s at E=80 GeV.



ISBN 978-3-95450-172-4

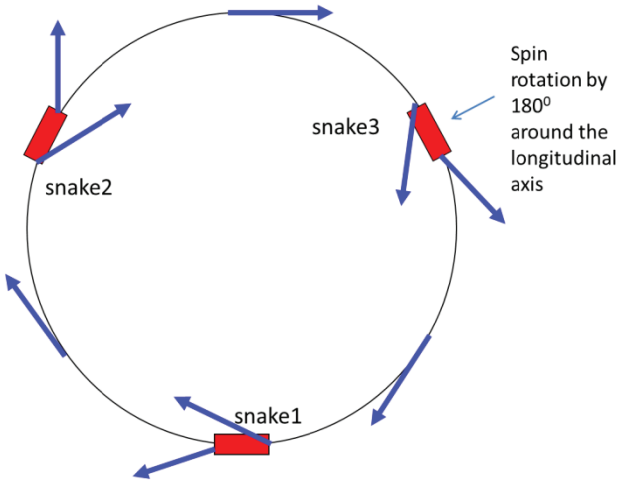


Figure 1: Schematic of spin rotation in a ring by 3 solenoid type snakes.

## LONGITUDINAL COMPTON BACKSCATTERING POLARIMETER

Compton backscattering of the circularly polarized laser light on highly relativistic electron exhibits extremely large analysing power to the longitudinal component of an electron polarization. The unpolarised $\sigma_0(a,x)$ and the polarised fraction $\sigma_1(a,x)$ of differential cross-sections be expressed in units $\pi r_e^2$ are [9]:

$$\sigma_0(a,x) = \frac{1}{1+a(1-x)} + \frac{1}{[1+a(1-x)]^2} - \frac{1-x^2}{[1+a(1-x)]^3}$$

$$\sigma_1(a,x) = -a\left[1+\frac{1}{1+a(1-x)}\right]\frac{x(1-x)}{[1+a(1-x)]^2}$$

Here $a = 2\gamma\omega_0 / m$ is the ratio of the energy of the incident laser photon, taken in the rest system of an electron, to the mass of an electron $m$ and $x = \cos\theta$ is the cosine of the scattering angle in that system.

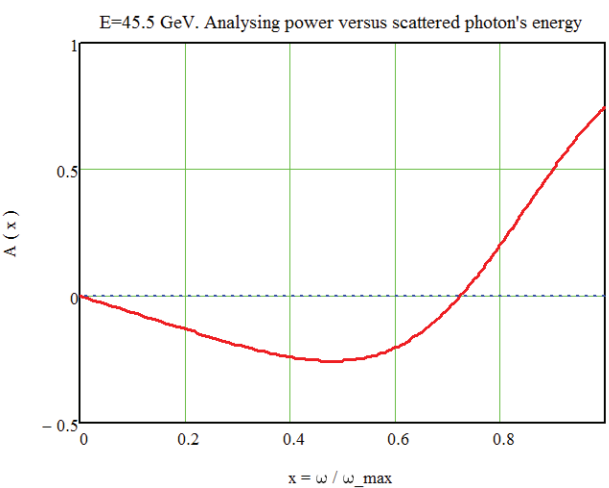


Figure 2: Spectral density of the analysing power of the Compton scattering of the circularly polarized laser light photons with $\omega_0$=2.33 eV on $E$=45.5 GeV electrons.

The analysing power is defined as the ratio of these two cross-sections $\sigma_1(a,x)/\sigma_0(a,x)$. In the Figure 2 is plotted the dependence of the Compton scattering analysing power versus the energy of the scattered photon. At the edge it reaches the huge value of 75%! For polarization measurements we should rely, of course, on detection of such events. But the counting rate of photons might be so high that events overlap in time. Then, one can rely on a measurement of the average over the full spectrum photon energy asymmetry, as it was done by the HERA team [10]. In the lab system the energy of the scattered photon equals to:

$$\omega_{lab} = \gamma m \frac{a(1-x)}{1+a(1-x)}.$$

The edge of the photon spectrum corresponds to the backscattering case: $x = -1$. As example, at $E$=45.5 GeV and with $\omega_0$=2.33 eV one gets $a$=0.812, $\omega_{lab}$=28 GeV. Dramatically large energy loss by the electron, comparable with its initial energy!

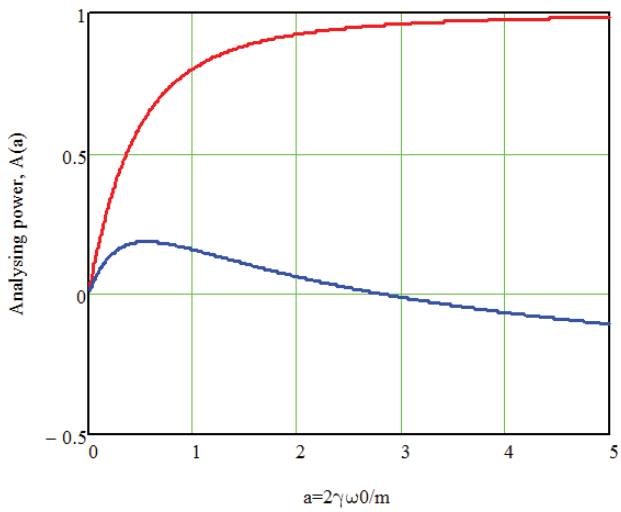


Figure 3: Averaged (blue) and maximal (red) spectral analysing powers of the Compton scattering of the circularly polarized laser light photons with energy $\omega_0$=2.33 eV by 45.5 GeV electrons.

The integrated over $x$ (in other words over a solid angle) total cross-sections are:

$$\sigma_0(a) = \frac{\ln(1+2a)}{a} - \frac{2(1+a)\ln(1+2a)}{a^3} + \frac{4}{a^2} + \frac{2(1+a)}{(1+2a)^2}.$$

$$\sigma_1(a) = \frac{2\left(1+4a+5a^2\right)}{a(1+2a)^2} - \frac{(1+a)\ln(1+2a)}{a^2}$$

Omitting the factor $\gamma m$ from the expression for $\omega_{lab}$ and integrating its product with $\sigma_{0,1}(a,x)$ over $x$ we come to unpolarised and polarized contributions to average over the spectrum photon energy:



ISBN 978-3-95450-172-4

$$E_0(a) = \frac{2(9 + a(51 + a(93 + a(51 - 10a))))}{3a^2(1 + 2a)^3} - \frac{(1 + a)(3 - a)\ln(1 + 2a)}{a^3}$$

$$E_1(a) = \frac{2(6 + a(33 + a(59 + 38a)))}{3a(1 + 2a)^3} - \frac{(2 + a)\ln(1 + 2a)}{a^2}$$

The ratio $E_1(a)/E_0(a)$, shown by blue line in the Figure 3, describes the averaged over the spectrum analysing power dependence on the parameter $a$, while the red curve shows such dependence of the on edge spectral analysing power. Still, average photon energy asymmetry does not exceed 18.5% and even changes a sign for $a$ >2.8.

We suggest detect not photons but lost momentum electrons, which are magnetically well separated according to their energies and do not overlap with softer electrons. Then events, belonging to the spectrum edge of the Compton scattering, could easily be selected.

## FREE SPIN PRECESSION DATA ANALYSIS

Polarization vector of the injected into collider beam could be directed horizontally. This is just the case for the synchrotron with 3 Siberian Snakes: there spins are horizontal everywhere. After injection spin assembly starts free precession around the vertical axis and using the described above a longitudinal laser polarimeter one can measure the fractional part of the spin tune. The first question raised is: how long such free precession may last.

To answer to this question the author has performed a simple the synchrotron and spin motions turn by turn tracking. Parameters of a ring model where taken just that are tabulated to FCC-ee 80 GeV regime. Namely, the synchrotron energy spread $\delta$ was set to $\sigma_\delta$=8·10$^{-4}$ and the damping time was taken $\tau_\delta$=243 turns. Random energy jumps, being normally distributed, and the radiative damping were applied every turn. Linear and the second order spin tune chromaticity also were included into the game. The last one was taken $\Delta\nu=\nu_0\cdot\delta^2$ with $\nu_0$=181.27. Results are presented in the Figures 4-6.

Remark: without the quadratic on energy deviation spin tune dependence the de-phasing of a spin assembly do not develop just after one damping time. The Figure 5 shows how such spread of spin angles develops in time.

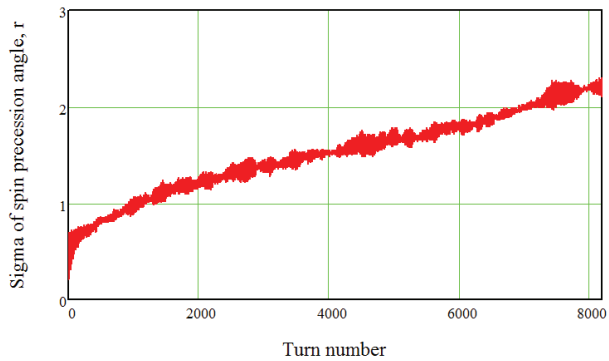


Figure 4: Increase of the spin precession angles spread with the time due to energy spread in a beam in average. The synchrotron amplitudes energy spread is 8·10$^{-4}$ and the energy spread in average is postulated be 6.4·10$^{-7}$.

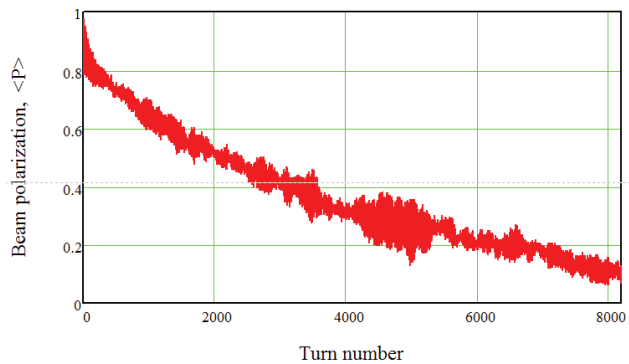


Figure 5: Beam polarization decay due to de-coherence of the spin precession, caused by the dependence of a spin tune on square of the energy deviation, $\Delta\nu=\nu_0\cdot\delta^2$.

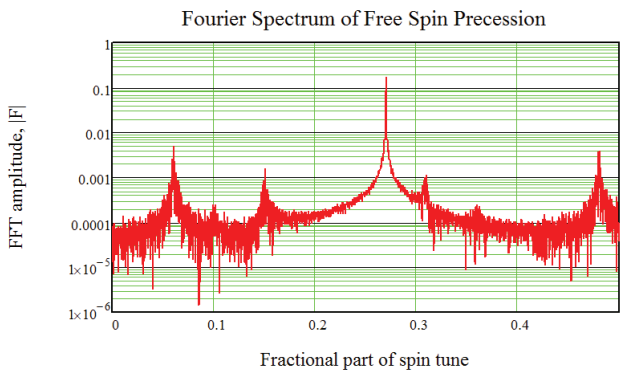


Figure 6: Fourier spectrum of the free spin precession of 250 particles. A spectrum was accumulated in 8192 turns.

Finally a nice Fourier spectrum, accumulated during 8192 turns, is presented in the Figure 6. The first, second and the third order synchrotron side bands are visible ($\nu_s$=0.21) there. The position of the central peak is shifted from a reference particle's value $\Delta\nu_0$=0.27 by the amount $\Delta\nu$=0.00023. This corresponds to about $\Delta E$=100 keV deviation of the energy from the reference value, but the statistical sigma of the energy determination is much smaller.



ISBN 978-3-95450-172-4

## CONCLUSION

The discussed above approach, based on idea to measure the free precession spin frequency looks promising for application at super-high electron-positron storage rings, like FCC-ee. The longitudinal Compton polarimeter can provide very fast and extremely reliable data for the Fourier analysis.

## REFERENCES

[1] F. Zimmermann et al., "FCC-ee Overview", HF2014 Beijing, 9-12 October 2014.
[2] M. Koratzinos et al., "Transverse Polarization and Energy Calibration at Z-peak", HF2014 Beijing, 9-12 October 2014.
[3] E. Gianfelice et al., "Polarization issues in FCC-ee Collider", HF2014 Beijing, 9-12 October 2014.
[4] N. Muchnoi, "FCC-ee Beam Energy Measurement Suggestion", HF2014 Beijing, 9-12 October 2014.
[5] S. Nikitin and E. Levichev, "Possible Applications of Wave-Beam Interaction for Energy Measurement and Obtaining of Polarization at FCC-ee", HF2014 Beijing, 9-12 October 2014.
[6] Ya.S. Derbenev, A.M. Kondratenko , "Acceleration of Polarized Particles", published in Dokl. Akad. Nauk Ser. Fiz. 223 (1975) 830-833 (in Russian), Sov. Phys. Dokl. 20 (1975) 562-564.
[7] I. Koop et al., "Maintaining Polarization in Synchrotrons", HF2014 Beijing, 9-12 October 2014.
[8] V.I. Ptitsyn, Yu.M. Shatunov, S.R. Mane, "Spin response formalism in circular accelerators" Nucl.Instrum.Meth. A608 (2009) 225-233
[9] F.Lipps and H.A.Tolhoek, Physica 20, 85, 395, (1954).
[10] M. Beckmann et al., "The Longitudinal Polarimeter at HERA", Nucl.Instrum.Meth. A479 (2002) 334–348.



ISBN 978-3-95450-172-4

# COST CONSIDERATION AND A POSSIBLE CONSTRUCTION TIMELINE OF THE CEPC-SPPC

W. Chou#, Fermilab, Batavia, IL 60510, USA

*Abstract*

This paper discusses the cost consideration and a possible construction timeline of the CEPC-SPPC study based on a preliminary conceptual design that is being carried out at the Institute of High Energy Physics (IHEP) in China.

## INTRODUCTION

The discovery of the Higgs boson in 2012 at CERN was not only a milestone in particle physics, but also a trigger in the world high-energy physics (HEP) strategic planning for a renewed interest in future circular colliders. Because the Higgs mass is low (125 GeV), a circular *e*+*e*- collider can be built to serve as a Higgs factory. But the ring size must be big in order to combat the synchrotron radiation problem. Such a large size ring would be ideal to house a *pp* collider with an energy much higher than that of the LHC. Based on this consideration, the IHEP proposed to build a 50-100 km ring in China. It would first be used as a Higgs factory with the name Circular Electron-Positron Collider (CEPC), then as a 70-100 TeV Super Proton-Proton Collider (SPPC).

A preliminary conceptual design study of the CEPC-SPPC started in earnest in early 2014. In order to be considered as a line item listed in the Chinese government's next Five-Year Plan (2016-2020), the study was put on a fast track – a preliminary conceptual design report is due the end of 2014.

A general description of the CEPC-SPPC can be found in another presentation at this workshop [1]. This paper will discuss the cost consideration and a possible construction timeline of a 50 km ring.

Table 1 and 2 list the top level parameters of the CEPC and SPPC, respectively. Please note that the luminosity of the SPPC has not yet specified because there is an ongoing debate in the world HEP community about the required luminosity of a future high energy *pp* collider [2].

Table 1: Top Level Parameters for CEPC

| Parameter | Design Goal |
|---|---|
| Particles | *e+, e-* |
| Center of mass energy | 240 GeV |
| Integrated luminosity (per IP per year) | 250 $fb^{-1}$ |
| No. of IPs | 2 |

Table 2: Top Level Parameters for SPPC

| Parameter | Design Goal |
|---|---|
| Particles | *p, p* |
| Center of mass energy | 70 TeV |
| Integrated luminosity (per IP per year) | (TBD) |
| No. of IPs | 2 |

Figure 1 is a layout of the CEPC. The circumference is about 54 km. There are 8 arcs and 8 straight sections. Four straight sections, about 1 km each, are for the interaction regions and RF; another four, about 800 m each, are for the RF, injection, beam dump, etc. The lengths of these straight sections are determined when the future need of large detectors and complex collimation systems of the SPPC are taken into account. The total length of the 8 straight sections is about 14% of the ring circumference, similar to the LHC. Among the four IPs, IP1 and IP2 will be used for *e*+*e*- collision, whereas IP2 and IP4 for *pp* collision.

The tunnel will be underground, about 50-100 m deep. It will accommodate three ring accelerators: the CEPC collider, the SPPC collider, and a full energy booster for the CEPC. Therefore, the tunnel must be big, about 6 m in width as shown in Figure 2. While the two colliders will sit on the floor, the booster will hang on the ceiling, similar to the Recyler in the Main Injector tunnel at Fermilab.

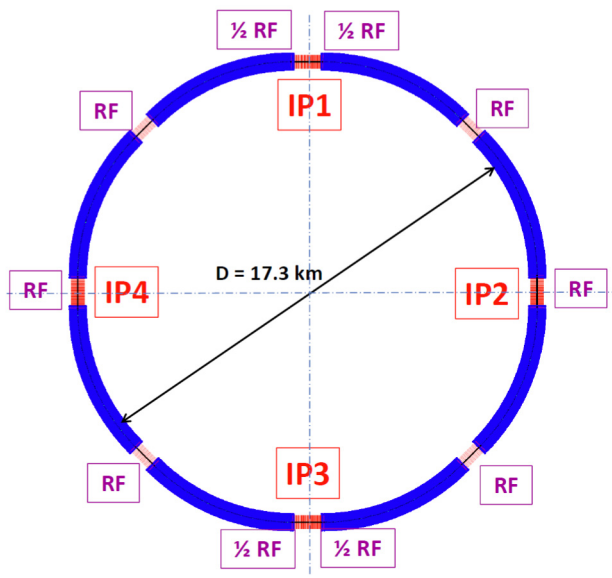


Figure 1: CEPC layout.

ISBN 978-3-95450-172-4

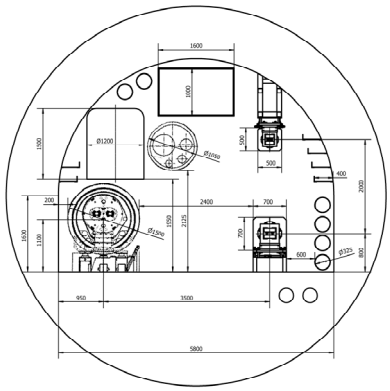

Figure 2: Tunnel cross section. The magnet on the left is the superconducting magnet of the SPPC, the magnets on the right are that for the CEPC collider (bottom) and the Booster (top), respectively. The tunnel width is about 6 m.

## COST CONSIDERATION

The synchrotron radiation power of the *e*+ and *e*- beam is 50 MW each, which must be provided by the RF, Therefore, the most expensive technical systems of the CEPC are: (1) the superconducting RF (SRF) system; (2) the RF power source; and (3) the cryogenic system.

There are two SRF systems:

- 1.3 GHz 9-cell cavities for the booster, similar to the ILC, XFEL and LCLS-II
- 650 MHz 5-cell cavities for the CEPC collider, similar to the ADS and PIP-II

The synergy makes it possible to have a reliable cost estimate based on experiences of the other accelerators,

Two cost references were particularly useful: the actual cost of LEP1 and LEP2, and the cost estimate of the LCLS-II 4 GeV SRF linac.

The LEP1 cost was well documented [3,4]. The total in 1986 prices was 1.3 billion Swiss francs (BCHF). LEP2 added 288 SRF in the 1990s for about 0.5 BCHF [5]. Taking into account the inflation, the construction of LEP1 and LEP2 would cost roughly 2.6 BCHF in today's prices. As the CEPC is twice as large as the LEP, plus a full-energy booster, the cost would be about 7 BCHF if it is built in Switzerland. But the cost in China is lower, especially the civil construction. The goal is to reduce it by half to about 3.5 BCHF, or 20 billion Chinese Yuan.

But, of course, a simple cost scaling will not work. For example, while the civil construction in China can be much cheaper than in Switzerland, the klystron price is the same around the world as only a few vendors can make them.

Two cost estimate exercises were carried out at the IHEP: one by the magnet group, another by the vacuum group. Each group was given the LEP design and was asked to estimate the cost if the identical magnet or vacuum system was built in China. The result showed that the LEP magnet would cost 30% less if fabricated in China. But the saving on the vacuum was smaller because China does not have the advanced aluminium extrusion technology.

The LCLS-II is another useful reference. Its 4 GeV linac uses the 1.3 GHz 9-cell ILC type cavities and cryomodules. The cost is 2.7 million US dollars (USD) per module, or a total of 105M USD for 38 modules. But this cost does not include non-superconducting RF part (klystron, modulator, RF distribution, etc.). The CEPC booster needs 32 cryomodules (1.3 GHz), and the collider 96 cryomodules (650 MHz).

Several measures for cost reduction were taken:

- The guideline is: if there are several options for technology, the cheaper one is chosen for the baseline.
- Two beams (*e*+ and *e*-) will share the same beam pipe as in the LEP and CESR.
- As the CEPC has smaller beam emittance than the LEP, the magnet aperture is reduced by 20%, which saves the construction as well as the operation cost.
- Although solid state is more reliable and easier to maintain than the klystron, the latter is cheaper and has higher efficiency. So klystron is chosen for the baseline.
- For tunnel construction, the tunnel boring machine (TBM) is faster than the explosion method. But the latter can save 20-30% cost and is thus chosen. Moreover, this method can make a city gate-shape tunnel as in Figure 2, which gives more usable space than a circular shape.

A Work Breakdown Structure (WBS) was used for cost estimate. Figure 3 shows the relative cost of each system (excluding the civil, which is under study).

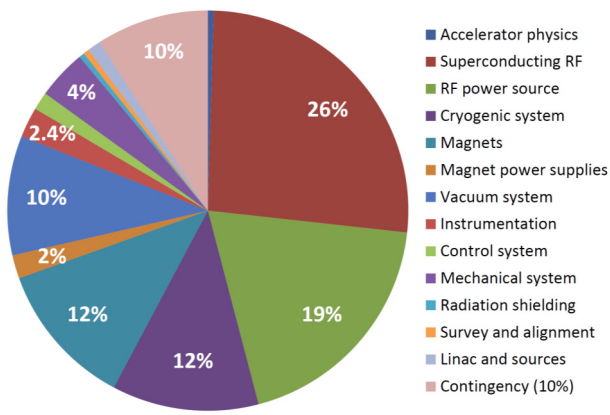


Figure 3: Relative cost of the CEPC technical systems.

It should be pointed out that the cost of the cryogenic system in this plot (12%) is based on a high efficiency HOM damper, which needs to be developed. Both the 1.3 GHz and 650 MHz SRF will operate at 2° K. The Carnot efficiency from the ILS study is listed in Table 2. Because the average beam current in the CEPC is high (16.6 mA for each beam), HOM loss in the cavity is significant (2.3 kW per beam in each cavity). Most of the HOM power



ISBN 978-3-95450-172-4

must be taken out and dissipate at higher temperatures. Table 4 is the required efficiency of the HOM damper, which is very demanding. How to design and implement such a damper is a critical R&D for the CEPC.

Table 3: Carnot Efficiency for CEPC SRF

| | 40 K to 80 K | 5 K to 8 K | 2K |
|---|---|---|---|
| Efficiency in W/W | 16.4 | 197.9 | 703.0 |

Table 4: Required Efficiency of the HOM Damper

| | 40 k to 80 k | 5 k to 8 k | 2k |
|---|---|---|---|
| HOM heat load distribution | 3% | 0.3% | 0.1% |

Power consumption determines the operation cost. When the Tevatron was running, the average total power usage at Fermilab was 58 MW. When the LHC was running, CERN used 183 MW (average over 2012). A consensus for a future circular Higgs factory is that the power should not exceed 300 MW, in which 100 MW is for synchrotron radiation. In other words, the wall plug efficiency (the ratio between the beam power and the wall power) should be 33%. This is a tall order as today's most efficient accelerator, the PSI cyclotron, has only an efficiency of 18%. The design efficiency for the ILC is just 9.6%. In order to have a highly efficient CEPC, one needs a highly efficient SRF system. The recent development of a new type of klystron (Collector Potential Depression, or CPD) is of particular interest as its claimed efficiency can be as high as 80%. Reuse and recycle of waste power from the accelerator is part of a general study nicknamed "green accelerators." Figure 4 shows the relative power consumption of each system in the CEPC.

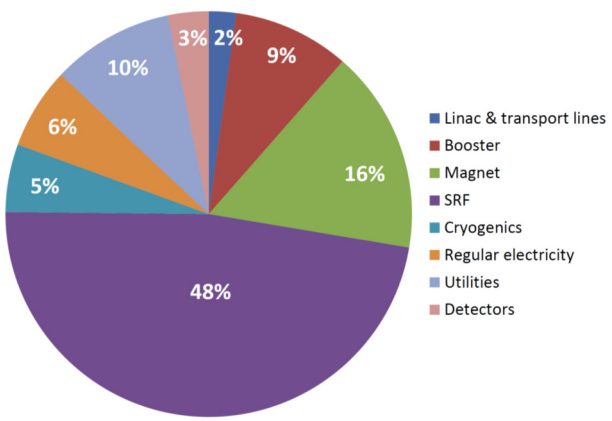


Figure 4: Relative power consumption of each system in the CEPC.

## A POSSIBLE TIMELINE

Figure 5 shows a presently conceived timeline. It consists of following stages:

- The first milestone is to complete a Preliminary Conceptual Design Report (Pre-CDR) by the end of this year. It will be used to apply for R&D fund for the next five years.
- The Chinese government's 13th Five-Year Plan starts in 2016. If the CEPC gets approval, the R&D will take place 2016-2020.
- The construction will (hopefully) start in 2021 in the government's 14th Five-Year Plan and take about 8 years.
- The experiment can start in 2028 during the 15th Five-Year Plan.
- For the SPPC, the focus is to develop cost effective high field superconducting magnet (16-20 Tesla) by means of $Nb_3Sn$ and HTS superconductors. This will take 15 years. The engineering design will start in 2030 and the construction to start around 2035.

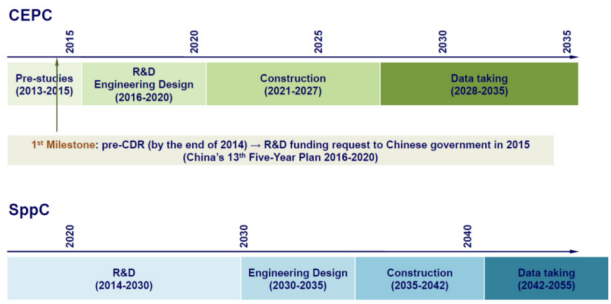


Figure 5: A possible timeline.

Of course the realization of such a fast track timeline depends on many factors. Some are under our control, some are not. At this moment, the effort is focused on meeting the first milestone, namely, to complete the Pre-CDR in the next several months.

A critical path of the CEPC timeline is to have a successful R&D for the two SRF systems:

- Collider: 650 MHz, 384 cavities in 96 cryomodules;
- Booster: 1.3 GHz, 256 cavities in 32 cryomodules.

This would be the largest SRF installation in the world. To succeed with designing, fabricating, commissioning and installation of such a system, a significant investment in R&D, infrastructure and personnel is necessary. The R&D has two parts:

- Prototyping as well as technology development for several critical components, in particular, the power coupler and the HOM damper.
- Pre-series production:
  - 15-20 1.3 GHz cavities and 30-35 650 MHz cavities
  - A large RF facility similar to that at Jlab, Fermilab and DESY for cavity inspection and tuning set ups, RF lab, several vertical test stands, clean rooms, HPR systems, FPC preparation and conditioning facility,



ISBN 978-3-95450-172-4

cryomodule assembly lines, horizontal test stations, high power RF equipment, a cryogenic plant, etc.
- Capable to assemble 1 Booster modules and 2 Collider module each month
- To have at least two vendors for each type of RF
- Personnel development

This R&D plan will absorb enormous resources and take a number of years. If the construction starts in 2021, the tunnel will take 4-5 years to finish. So there should be enough time for the pre-series production to complete before mass production.

## REFERENCES

[1] Q. Qin, "Overview of the CEPC Accelerator", HF2014 Proceedings, THP3H2.
[2] B. Richter, "High Energy Colliding Beams – What is the Future?", to appear in the *Reviews of Accelerator Science and Technology*, Volume 7, World Scientific (2014).
[3] "Financial Position of the LEP Project – Final Report," CERN/FC/3313, May 30, 1990.
[4] H. Schopper, "LEP – The Lord of the Collider Rings at CERN 1980-2000," Springer (2009).
[5] S, Myers, private communication.



ISBN 978-3-95450-172-4

# STATUS OF THE FCC-ee INTERACTION REGION DESIGN

R. Martin*, CERN, Geneva, Switzerland and Humboldt University Berlin, Germany
R. Tomás, CERN, Geneva, Switzerland
L. Medina, Universidad de Guanajuato, Mexico

*Abstract*

The FCC-ee project is a high-luminosity circular electron-positron collider envisioned to operate at center-of-mass energies from 90 to 350 GeV, allowing high-precision measurements of the properties of the Z, W and Higgs boson as well as the top quark. It is considered to be a predecessor of a new 100 TeV proton-proton collider hosted in the same 80 to 100 km tunnel in the Geneva area.

Currently two interaction region designs are being developed by CERN and BINP using different approaches to the definition of baseline parameters. Both preliminary designs are presented with the aim of highlighting the challenges the FCC-ee is facing.

## INTRODUCTION

FCC-ee is foreseen to run at four different center-of-mass energies: the Z-pole at 90 GeV, the W pair production threshold (160 GeV), Higgs resonance (240 GeV) and $t\bar{t}$ threshold (350 GeV). From the accelerator point of view, the Z-pole and $t\bar{t}$ threshold are the most challenging setups due to the high number of bunches per beam and high luminosity target (Z) and beamstrahlung ($t\bar{t}$) so these will be the driving forces of the lattice design. In Table 1 the relevant baseline parameters for the 100 km option of FCC-ee are shown. The parameters are in part determined by the design limit of 50 MW of synchrotron radiation per beam. Another constraint for the design of FCC-ee, in particular of the Interaction Region (IR), is the required compatibility with a possible proton-proton collider (FCC-hh) in order to allow a reuse of the tunnel for both machines. Since not only length, but also diameter of the tunnel are a major cost driver of projects of that kind, the design of both machines has to be closely connected and optimized.

Table 1: FCC-ee Baseline Parameters at Z and $t\bar{t}$ Energy for CERN Design at the 100 km Option [1]

| | Z | $t\bar{t}$ |
|---|---|---|
| Beam energy [GeV] | 45.5 | 175 |
| Crossing angle [mrad] | 11 | |
| Bunches / beam | 16700 | 98 |
| Bunch population [$10^{11}$] | 1.8 | 1.4 |
| Energy loss / turn [GeV] | 0.03 | 7.55 |
| Beta function at IP $\beta^*$ | | |
| - horizontal [m] | 0.5 | 1 |
| - vertical [mm] | 1 | 1 |
| Transverse emittance $\epsilon$ | | |
| - horizontal [nm] | 29.2 | 2 |
| - vertical [pm] | 60 | 2 |
| Beam size at IP $\sigma^*$ | | |
| - horizontal [µm] | 121 | 45 |
| - vertical [µm] | 0.25 | 0.045 |
| Luminosity / IP [$10^{34}$cm$^{-2}$s$^{-1}$] | 28.0 | 1.8 |

## CERN IR DESIGN

The CERN interaction region design is based on a generic lattice originally designed for linear accelerators [2]. This is in part due to the fact that the strong focusing required to reach the high luminosity goals induces high chromaticity that will require a local correction, especially in the vertical plane. The design is shown in Fig. 1 together with the optical functions. It consists of a Final Focus System (FFS), Vertical and Horizontal Chromatic Correction Sections (CCSV, CCSH) and a Matching Section (MS). Each chromatic correction section consists of 4 FODO cells forming two opposed missing dipole dispersion suppressors. All functions are spatially separated which makes the whole lattice very modular. In addition to the sextupoles for chromaticity correction, weaker sextupoles for local correction of nonlinearities were inserted. Currently the CERN design is still in a very early stage of development and only the $t\bar{t}$ settings have been matched.

In the final focus quadrupole, the chromaticity is proportional to $\xi_{x,y} \sim \frac{L^*}{\beta^*_{x,y}}$, thus the length of the last drift $L^*$ should be as small as possible while still leaving enough space to host the detector. At this stage of the design, $L^* = 2$ m is considered reasonable.

From the high number of bunches at lower energies, it is clear that a crossing angle is required to ensure an adequate bunch separation after the IP. While the crossing angle must be large enough to separate the bunches to several $\sigma_x$, a large crossing angle requires either a broad tunnel -a major cost driver- or strong dipole magnets close to the IP bending the beam back. The latter will produce high doses of synchrotron radiation close to the detector, increasing the background noise and potential radiation damage. Thus a compromise has to be found.

A first approach is to choose the crossing angle as small as possible to achieve a certain beam separation and have both beams share the same quadrupoles of the final focus system. In this case, the beams pass the first quadrupole off axis and are deflected due to the magnetic field being non-zero, producing considerable amounts of synchrotron radiation. In

* roman.martin@cern.ch

ISBN 978-3-95450-172-4

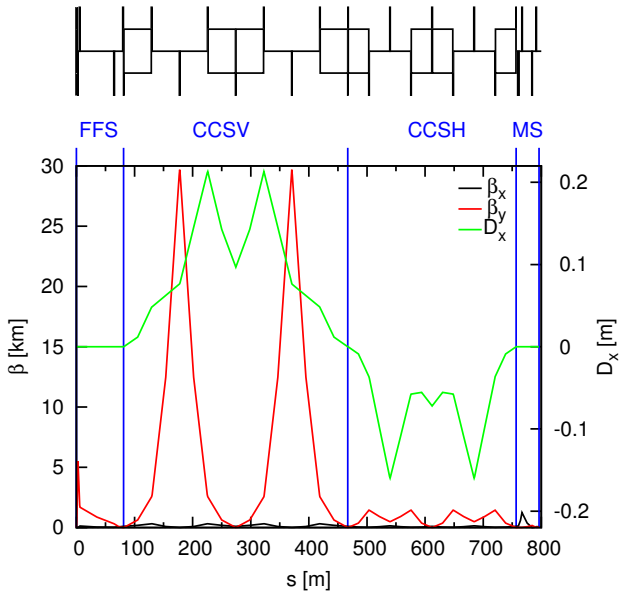


Figure 1: Optical functions of the CERN IR design.

Table 2 the average radiation power is shown, based on calculations with the current CERN IR design and an angular beam separation as small as $6\,\sigma_{P_x}$ . Even for this absolute minimum crossing angle, the radiation power produced in the shared quadrupoles is prohibitively high. Given the fact that there will be little room for absorbers after the last quadrupole, the shared quadrupoles scheme must be considered unfeasible.

Table 2: Average synchrotron power radiated from the shared final focus quadrupoles at an angular beam separation of $6\,\sigma_{P_x}$ . Values are per beam and per quadrupole.

| | Z | $t\bar{t}$ |
|---|---|---|
| average power from Q1 [kW] | 96.8 | 3.5 |
| average power from Q2 [kW] | 423.0 | 15.1 |

For a final focus system with separate apertures for each beam, the crossing angle is determined by $L^*$ and the minimum separation of the magnetic axes of the last quadrupoles that is technically feasible. Design studies of FFS magnets for SuperB [3] and a prototype design by BINP [4] suggest that quadrupole magnets with an axis separation of $\approx$ 22 mm are possible. With an $L^*$ of 2 m this implies a minimum crossing angle of 11 mrad which is used in the current CERN design.

## BINP IR DESIGN

While the CERN design focuses mainly on the feasibility of the high energy option, BINP uses a different approach. The philosophy of the BINP interaction region design is to apply a crab waist collision scheme [5] in order to increase luminosity at low energies (Z,W) by increasing the vertical tune shift. To achieve this the baseline parameters where altered according to Table 3. The parameters where chosen to use the advantages of the crab waist scheme, but at the same time allow running at all energies with the same lattice. At low energies, the crab waist scheme aims at luminosities that are higher by a factor of 8 (Z) and 3 (W) compared to the head-on collision scheme. However, at high energies (H, $t\bar{t}$) the crab waist scheme has no considerable advantages since the beam-beam tune shift, and thereby the luminosity, is limited by beamstrahlung.

Since the BINP design makes use of the crab waist scheme the crossing angle is not chosen as small as possible but to provide an interaction length of the bunches roughly equal to the vertical beta function at the IP for both, Z and W setup. In the case of the BINP design, it is 30 mrad.

The general layout [6] and the optical functions are shown in Fig. 2. Again, a final focus system and vertical and horizontal chromaticity correction sections can be seen as well as a CRAB section providing the necessary phase advance and optical functions for the crab sextupoles. The chromaticity correction sections are much shorter than in the CERN design but this advantage is accomplished at the price of much stronger dipoles. To mitigate the effects of synchrotron radiation at the IP (background in the detector), the first dipole has a rather low magnetic field.

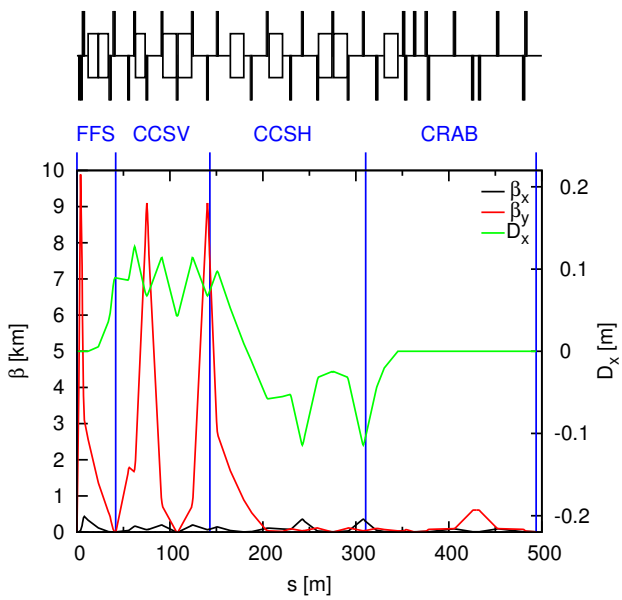


Figure 2: Optical functions of the BINP IR design.

## COMPARISON AND DIFFICULTIES

In Fig. 3 the geometry of both FCC-ee designs are shown, together with the FCC-hh design for $L^* = 36$ m. Both FCC-ee designs require approximately the same tunnel diameter of about 2 m, which is reasonable.

The shown IR for FCC-hh is 540 m long, although this value may increase for a longer $L^*$ (current aim $L^* = 46$ m) and depending on the choice of the dispersion suppressor design. The current design specification for the length is



ISBN 978-3-95450-172-4

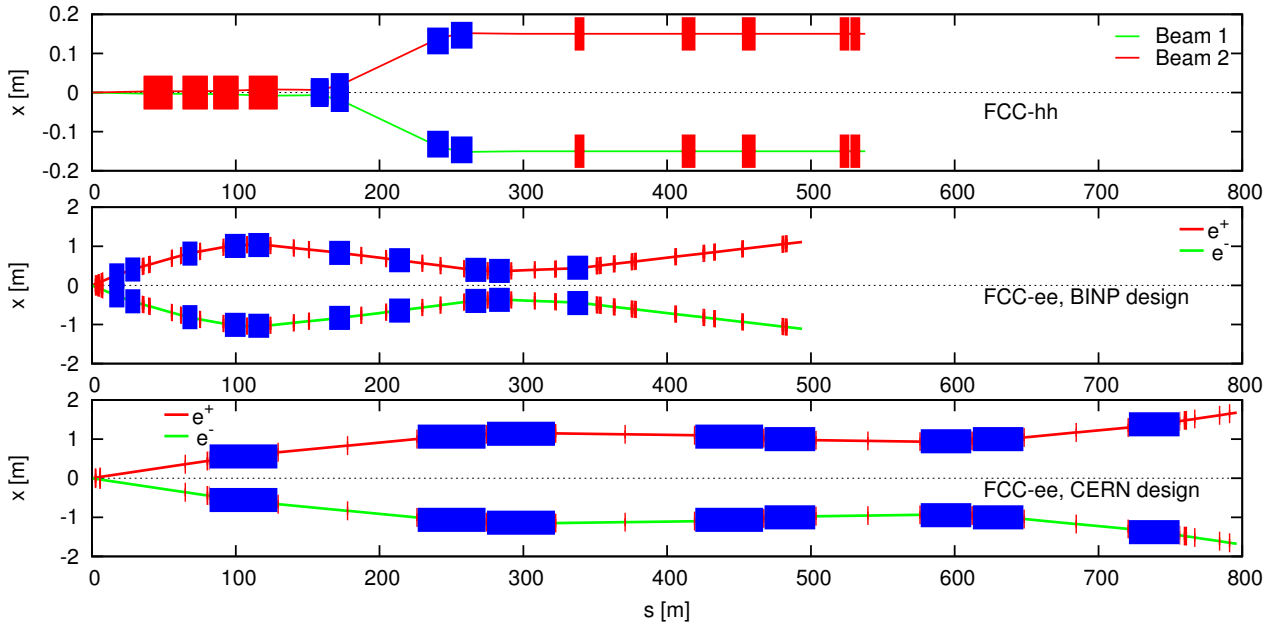


Figure 3: Comparison of the geometry of the current FCC-hh design and both FCC-ee designs. Dispersion suppressors are not included. Red rectangles represent quadrupoles, blue rectangles dipoles. Note the different scales for hadron and electron machines.

Table 3: FCC-ee Baseline Parameters at Z and $\bar{t}t$ Energy for the 100 km Option in the Crab Waist Scheme [7]

| | Z | $t\bar{t}$ |
|---|---|---|
| Beam energy [GeV] | 45.5 | 175 |
| Crossing angle [mrad] | 30 | |
| Bunches / beam | 29791 | 33 |
| Bunch population [$10^{11}$] | 1 | 4 |
| Energy loss / turn [GeV] | 0.03 | 7.7 |
| Beta function at IP $\beta^*$ | | |
| - horizontal [m] | 0.5 | |
| - vertical [mm] | 1 | |
| Transverse emittance $\epsilon$ | | |
| - horizontal [nm] | 0.14 | 2.1 |
| - vertical [pm] | 1 | 4.3 |
| Beam size at IP $\sigma^*$ | | |
| - horizontal [µm] | 8.4 | 0.3 |
| - vertical [µm] | 0.03 | 0.07 |
| Luminosity / IP [$10^{34}$cm$^{-2}$s$^{-1}$] | 212 | 1.3 |

700 m. The designs for FCC-ee have lengths of 500 m (BINP) and 800 m (CERN). Due to the high synchrotron radiation in the arcs, an RF section has to be included in the interaction region, requiring an additional dispersion free straight section somewhere between the dispersion suppressors and the IP. Furthermore, both designs presently end with diverging beams and a beam separation of $\approx 2$ m. It is not yet clear if they can be bent back together in the dispersion suppressors (which means different dispersion suppressors on each side of the IP) or if this recombination requires a dedicated matching section which will add several hundreds of meters to the overall length of the straight sections. If FCC-hh becomes the driving force for building the tunnel, the BINP design might still work out but the CERN design will be too long. Hence, in further steps shortening the IR in order to ensure recombination within a comparable length will be considered. At the Z-pole, the crab waist scheme promises a luminosity almost one order of magnitude higher than the head-on scheme, 3 times higher at the W energy and 1.6 times higher at Higgs energy. On the other hand, the synchrotron radiation produced is also much higher as can be seen in Table 4. The total average power radiated in 4 IRs sums up to 5.6 MW per beam which accounts for more than 10 % of the overall synchrotron radiation budget. The average powers radiated from the dipoles closest to the IP are comparable in both designs, with the crab waist scheme having a higher critical energy. Further studies are needed to determine whether this radiation crosses the detector without hitting the walls of the vacuum chamber or whether it needs to be shielded.

## FIRST TRACKING STUDIES ON THE 100 km RING

First tracking calculations with the full 100 km arc lattice for high energies (Higgs, $\bar{t}t$) [8] were conducted for both designs. All simulations were performed for on-momentum particles, 500 full turns with four IPs and without radiation by MADX and PTC. For these early studies the matching

ISBN 978-3-95450-172-4

Table 4: Characteristics of the Synchrotron Radiation in the Interaction Regions

| | Z | $t\bar{t}$ |
|---|---|---|
| Average total power per IP [kW] | | |
| - CERN | 138 | 138 |
| - BINP | 1460 | 1410 |
| Energy loss per particle per IP [MeV] | | |
| - CERN | 0.8 | 168 |
| - BINP | 2.0 | 440 |
| Average power in last dipole [kW] | | |
| - CERN | 7.3 | 7.3 |
| - BINP | 8.2 | 8.0 |
| Critical Energy in last dipoles $\hbar\omega_c$ [keV] | | |
| - CERN | 8.8 | 503 |
| - BINP | 20 | 1100 |

of arcs and interaction region was rather preliminary. The machines do not yet fully close, no RF section around the IR was included and the Montague W functions have not yet been aligned. The aim of these studies is to provide a first look at the dynamic aperture.

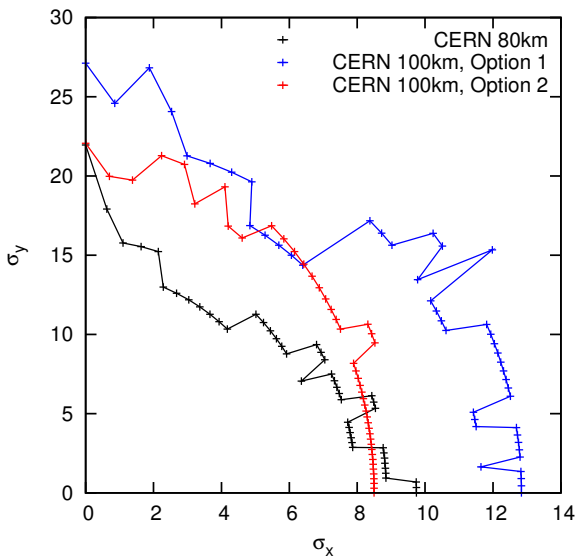


Figure 4: Dynamic apertures of the CERN design for 80 km option and two 100 km options at different working points.

The results for two different working points for the CERN IR are shown in Fig. 4 together with the earlier results with an 80 km arc lattice [9]. The largest dynamic aperture found so far is about 13 $\sigma$ in the horizontal plane and 25 $\sigma$ in the vertical plane. The other two options have dynamic apertures of about 9 $\sigma$ horizontaly and 20 $\sigma$ vertically. For the CERN IR, the aim right now is to find a working lattice with acceptable dynamic aperture and momentum acceptance. Further improvements and refinements are to be considered. For example, the tune will be set to minimise the adverse effects of the beam-beam interaction.

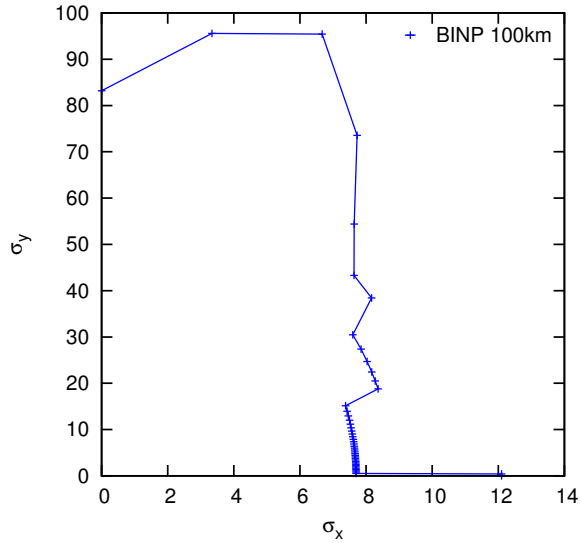


Figure 5: Dynamic aperture of the BINP design for the 100 km option.

Figure 5 shows the tracking results for the BINP design at the 100 km option. It has a dynamic aperture of 8 $\sigma$ horizontaly and almost 100 $\sigma$ vertically. The latter is a very important property because the vertical beam size is rather small so even small errors in the magnetic fields will have a large relative impact.

Table 5: Non-integer Part of the Phase Advance between the IPs for the Tracked Lattices

| | $\psi_x$ | $\psi_y$ |
|---|---|---|
| CERN, 80 km | 0.77 | 0.61 |
| CERN, 100 km, Option 1 | 0.48 | 0.23 |
| CERN, 100 km, Option 2 | 0.77 | 0.11 |
| BINP, 100 km | 0.54 | 0.57 |

Recent beam-beam simulations at $t\bar{t}$ energy suggest beam lifetimes of $\tau_{BS} = 0.39$ min at a momentum acceptance of $\Delta p/p = \pm 1.5\,\%$ or $\tau_{BS} \approx 6$ min for $\Delta p/p = \pm 2.0\,\%$. For lower energies, the requirements are more relaxed [10]. The momentum acceptance of FCC-ee should at least lie between these values, the exact minimum value will depend on the performance of the top-up injection scheme planned for FCC-ee. Although the Montague W functions have not yet been matched to the arcs, preliminary momentum scans were conducted in order to get a first notion of feasibility of these momentum acceptances. The scans (Fig. 6 and Fig. 7) were performed within an intervall of $\Delta p/p = \pm 1.5\,\%$ for the CERN IR lattice at the aforementioned 80 and 100 km options and the BINP lattice at 100 km. The CERN design at 100 km (option 1), which had the largest dynamic aper-



ISBN 978-3-95450-172-4

ture, has a momentum acceptance of only ≈ ±0.1 % with some stable orbits for higher momentum deviation after a resonance crossing. This is mainly due to the fast change of the $\beta$ functions with $\frac{\Delta p}{p}$ and likely to increase, once the Montague W functions are properly matched to the arcs. The scan for the 80 km option showing a momentum acceptance from −0.6 % to 0.9 % before crossing the first integer resonance, as well as the scan for 100 km option 2 (−0.4 % to 0.8 %) reinforce this assumption. The BINP design already offers a considerabe momentum acceptance ranging from −0.6 % to 1.2 %. Considering the preliminary nature of the matching of arcs and IR, the scans give hope that the required momentum acceptance can be achieved by both design principles.

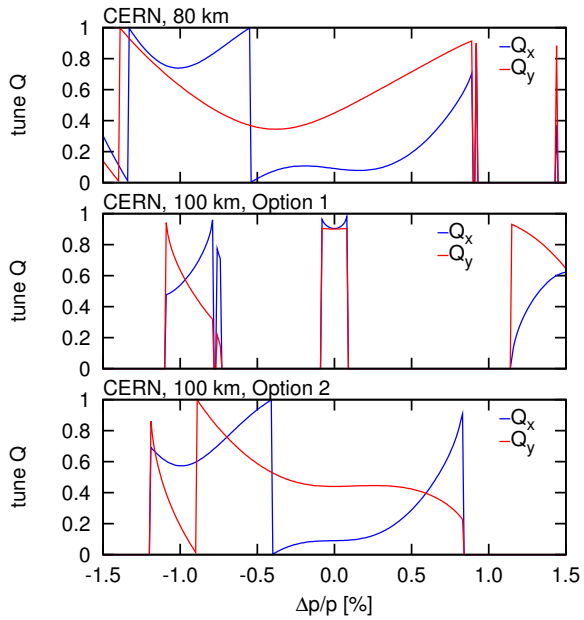


Figure 6: Variation of non-integer part of the horizontal and vertical tunes $Q_x$ and $Q_y$ versus relative momentum deviation $\frac{\Delta p}{p}$ for the CERN designs (80 km and 100 km). For empty sections no stable orbit was found.

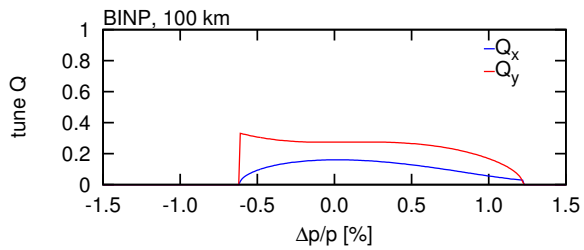


Figure 7: Variation of non-integer part of the horizontal and vertical tunes $Q_x$ and $Q_y$ versus relative momentum deviation $\frac{\Delta p}{p}$ for the BINP design (100 km). For empty sections no stable orbit was found.

## OUTLOOK

The matching sections connecting arcs and interaction region will be refined to properly match the Montague W functions in order to allow optimization of the momentum acceptance. Both designs will be rematched to the arc lattice for lower energies and dynamic aperture and momentum acceptance studies will be performed for these setups. The CERN interaction region is still in a very early stage, currently it still inherits several shortcomings of the generic lattice it is based on. This means there is a lot potential for necessary optimization, especially concerning the dynamic aperture and the momentum acceptance. Different concepts for chromaticity correction will be tested in order to reduce the length of the overall interaction region. The correction of higher order chromaticities will be refined by varying the dipole scheme and adding sextupoles closer to the IP. For both designs, the evolution of the dynamic aperture for changing momentum deviation will be studied, as well as possibilities of shielding the synchrotron radiation from the IP.

## ACKNOWLEDGMENTS

We would like to thank A. Bogomyagkov, B. Holzer, B. Haerer and H. Garcia for fruitful discussions. This work is supported by the Wolfgang-Gentner-Programme of the Federal Ministry of Education and Research, Germany (BMBF).

## REFERENCES

[1] FCC-ee website: `cern.ch/fcc-ee`

[2] O. Napoly, B. Dunham, “FFADA, Computer Design of Final Focus Systems for Linear Colliders”, EPAC’94, London, England, June 1994, p. 698

[3] E. Paoloni et al., “Magnetic Design Studies for the Final Focus Quadrupoles of the SuperB Large Crossing Angle Collision Scheme”, EPAC08, Genoa, Italy, June 2008, WEPD002, p. 2401

[4] A. Bogomyagkov et al., “Draft of the Interaction Region for Crab Waist collision scheme”, FCC Kickoff Meeting, Geneva, February 2014

[5] P. Raimondi, 2nd SuperB Workshop, Frascati, Italy, 2006

[6] A. Bogomyagkov et al., “Interaction Region Lattice for FCC-ee (TLEP)”, THPRI008, IPAC’14, Dresden, Germany (2014).

[7] A. Bogomyagkov et al., “Beam-beam effects investigation and parameters optimization for a circular $e^+e^-$ collider at very high energies”, Phys. Rev. ST Accel. Beams 17, 041004, 2014

[8] B. Haerer, B. Holzer, “Challenges and Status of the FCC-ee Lattice Design”, these proceedings, THT4B3, HF2014, Beijing, China (2014).

[9] H. Garcia et al., “FCC-ee Final Focus with Chromaticity Correction”, THPRI010, IPAC’14, Dresden, Germany (2014).

[10] K. Ohmi, F. Zimmermann, “FCC-ee/CepC Beam-beam Simulations with Beamstrahlung”, THPRI004, IPAC’14, Dresden, Germany (2014).

ISBN 978-3-95450-172-4

# CRAB WAIST INTERACTION REGION FOR FCC-*ee* (TLEP) *

A. Bogomyagkov†, E. Levichev, P. Piminov,
BINP, Novosibirsk 630090, Russia

*Abstract*

Design study of the accelerator that would fit 80-100 km tunnel called Future Circular Colliders (FCC) includes high-luminosity $e^+e^-$ collider (FCC-ee aka (TLEP) ) with center-of-mass energy from 90 to 350 GeV to study Higgs boson properties and perform precise measurements at the electroweak scale [1–3]. Crab waist interaction region provides collisions with luminosity higher than $2 \times 10^{36}\ cm^{-2}sec^{-1}$ at beam energy of 45 GeV. The small values of the beta functions at the interaction point and distant final focus lenses are the reasons for high nonlinear chromaticity limiting energy acceptance of the whole ring. The present paper presents estimations of nonlinear effects and describes practical solutions implemented in the design of the interaction region for correction of linear and nonlinear chromaticity of beta functions, and of betatron tune advances, of second and third order geometrical aberrations from the strong sextupoles pairs. The given design embraces realistic design of final focus quadrupoles, satisfies geometrical constraints of the tunnel layout.

## INTRODUCTION

One of the limiting factors of high energy $e^+e^-$ collider (FCC-ee aka (TLEP) ) is beamstrahlung [4, 5], which limits the beam life time. Consideration of this effect by different authors gave several sets of parameters to achieve high luminosity and feasible beam lifetime. The first one is based on head-on collisions [6], the second is relying on crab waist collision scheme [7, 8] with crossing angle $2\theta = 30$ mrad. Both sets implement the same values of beta functions at the interaction point (IP): $\beta_x^* = 0.5$ m, $\beta_y^* = 0.001$ m and require energy acceptance of the ring more than ±2% to provide feasible beam life time. Advantages of the crab waist set are higher luminosity (7.5 times at 45 GeV) and crossing angle that provides natural separation of the bunches. The list of parameters relevant to present work is given in Table1.

Table 1: Relevant Parameters for Crab Waist IR [7]

| | Z | W | H | tt |
|---|---|---|---|---|
| Energy [GeV] | 45 | 80 | 120 | 175 |
| Perimeter [km] | | 100 | | |
| Crossing angle [mrad] | | 30 | | |
| Particles per bunch [$10^{11}$] | 1 | 4 | 4.7 | 4 |
| Number of bunches | 29791 | 739 | 127 | 33 |
| Energy spread [$10^{-3}$] | 1.1 | 2.1 | 2.4 | 2.6 |
| Emittance hor. [nm] | 0.14 | 0.44 | 1 | 2.1 |
| Emittance ver. [pm] | 1 | 2 | 2 | 4.3 |
| $\beta_x^*/\beta_y^*$ [m] | | 0.5 / 0.001 | | |
| Luminosity / IP [$10^{34}\ cm^{-2}s^{-1}$] | 212 | 36 | 9 | 1.3 |
| Energy loss / turn [GeV] | 0.03 | 0.3 | 1.7 | 7.7 |

Lattice of the interaction region (IR) should satisfy several requirements:

1. Since successor to FCC-ee is proton accelerator, the IR tunnel should be as straight as possible;
2. Small values of IP beta functions produce large chromaticity, which should be compensated as locally as possible in order to minimize excitation of nonlinear chromaticity;
3. Synchrotron radiation power loss should be significantly smaller than in the arcs;
4. Synchrotron radiation at high energy will produce flux of high energy gamma quanta, therefore the lattice should minimize detector background;
5. Small beta functions at IP enhance effects of nonlinear dynamics, decreasing dynamic aperture and energy acceptance of the ring, therefore the lattice should be optimized to provide large dynamic aperture and energy acceptance.

## ESTIMATIONS

The following estimations are performed for vertical plain and marked with subindex $y$. Assuming that action of the first final focus (FF) quadrupole Q0 changes the sign of $\alpha$ function the quadrupole strength could be estimated as $K_1 L = -2/L^*$, where $L^*$ is distance from the interaction point (IP). Chromaticity of beta function is best described by Montague functions [9]

$$b = \frac{1}{\beta}\frac{\partial\beta}{\partial\delta}, \quad (1)$$

$$a = \frac{\partial\alpha}{\partial\delta} - \frac{\alpha}{\beta}\frac{\partial\beta}{\partial\delta}, \quad (2)$$

* Work is supported by the Ministry of Education and Science of the Russian Federation
† A.V.Bogomyagkov@inp.nsk.su



ISBN 978-3-95450-172-4

where $\delta$ is relative energy deviation. Montague functions satisfy evolution equations

$$\frac{\partial b_y}{\partial s} = -\frac{2a_y}{\beta_y}, \quad (3)$$

$$\frac{\partial a_y}{\partial s} = (K_1 - K_2\eta_0)\beta_y + \frac{2b_y}{\beta_y}, \quad (4)$$

where $K_1$ and $K_2$ are quadrupole and sextupole strengths respectively, $\eta_0$ is the first order horizontal dispersion. Assuming that $b = 0$ and $a = 0$ at IP, then after the first quadrupole $Q0$ $a_y$ rises to

$$a_y(Q0) = K_1 L \beta(Q0) \approx -2\frac{L^*}{\beta_y^*}. \quad (5)$$

Influence of the other quadrupoles is significantly smaller, therefore we will neglect it and Montague functions then oscillate at double betatron frequency exchanging values being $\pi/2$ in phase apart

$$b_y(\varphi_y) = -a_y(Q0)\sin\left(2\left(\varphi_y - \varphi_y(Q0)\right)\right), \quad (6)$$

$$a_y(\varphi_y) = a_y(Q0)\cos\left(2\left(\varphi_y - \varphi_y(Q0)\right)\right). \quad (7)$$

The first and second order phase advance $\varphi$ chromaticities are given

$$\frac{\partial \varphi_y}{\partial \delta} = \frac{1}{2}\int_0^{\Pi} \beta_y(K_1 - K_2\eta_0)ds, \quad (8)$$

$$\frac{\partial^2 \varphi_y}{\partial \delta^2} = -2\frac{\partial \varphi_y}{\partial \delta} - \int_0^{\Pi} \beta_y K_2 \eta_1 ds + \frac{1}{2}\int_0^{\Pi} \beta_y b_y (K_1 - K_2\eta_0)ds, \quad (9)$$

where $\eta_1$ is the second order horizontal dispersion. The largest beta function is in the first quadrupole, therefore its contribution in the first order chromaticity is cardinal and gives $\partial\varphi/\partial\delta \approx -L^*/\beta_y^*$. So far the distance from IP to the edge of the first quadrupole Q0 was chosen 2 m, making the distance to the center of Q0 $L^* = 2 + 3.6/2 = 3.8$ m. Substituting numerical values in the formulas above we have

$$\frac{\partial \varphi_y}{\partial \delta}(Q0) = -3.8 \times 10^3, \quad (10)$$

$$a_y(Q0) = -7.6 \times 10^3. \quad (11)$$

using necessary values from the IR lattice we will estimate contributions from the different terms in (9). In the quadrupole at the proper phase ($\pi/4 + n\pi/2$ phase from Q0) $b_y$ reaches maximum of $b_y \approx -7.6 \times 10^3$. If for example such quadrupole has the strength $K_1 L = 0.16 * 2$ m$^{-1}$ and $\beta_y = 100$ m then quadrupole's contribution to second order chromaticity is $\partial^2\varphi/\partial\delta^2 \approx 1.2 \times 10^5$. The strongest sextupoles are exactly $\pi$ in phase away from the FF quadrupoles, thefore the value of $b \approx 0$ making contribution to second order chromaticity rather small, the second order dispersion is $\eta_1 \approx 1$ and $K_2 \times L \approx -9.5 * 0.5$ m$^{-2}$, then contribution to the second order chromaticity is $\partial^2\varphi/\partial\delta^2 \approx 5 \times 10^2$. Hence, the primary source of second order chromaticity is quadrupoles with large beta function chromaticity. Therefore the main sextupoles designed to cancel beta function chromaticity should be as small as possible number of quadrupoles away from the FF quadrupoles, and $L^*$ should be minimized. However minimum distance is limited by detector requirements from one side and by construction design of first quadrupole Q0 from the other.

To finish estimations we will answer the question what values of chromaticity are needed. For that reason we expand tune dependence $Q = \varphi/(2\pi)$ with respect to energy deviation

$$Q(\delta) = Q_0 + Q_0'\delta + Q_0''\frac{\delta^2}{2} + Q_0'''\frac{\delta^3}{6} + \ldots,$$

where "′" denotes $d/d\delta$. Assuming that $Q_0' = 2$ and demanding that $0 \le Q(\delta) - Q_0 \le 0.5$ we can draw an area of possible $Q_0''$ and $Q_0'''$ (Figure 1). Since interaction region will be connected with remaining arcs, which will have their own chromaticities we tried to minimize second order chromaticity in our lattice.

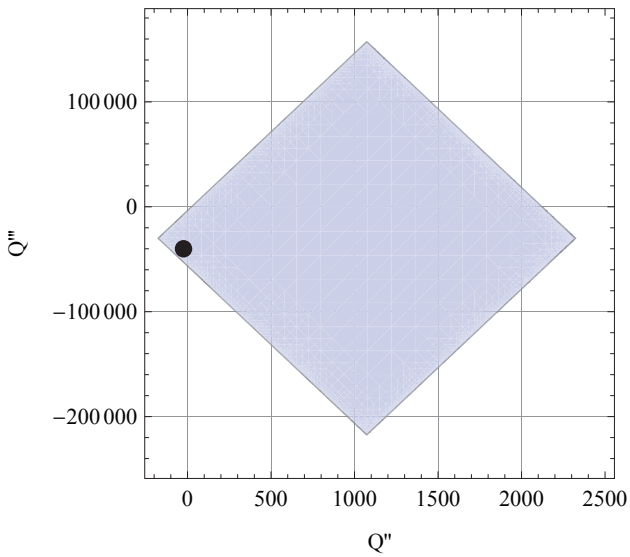


Figure 1: Area of $Q_0''$ and $Q_0'''$ with $Q_0' = 2$ satisfying $0 \le Q(\delta) - Q_0 \le 0.5$ for $\delta \in [-0.02; 0.02]$. A dot represents the present lattice.

## FINAL FOCUS QUADRUPOLES

Having the minimum distance the maximum reliably achievable gradient defines the quadrupole length. In the present study we demanded the quadrupole strength to be lower than 100 T/m, which is a very relaxed condition. We also chose distance from IP to the edge of first quadrupole to be 2 m which at the present moment looks like a good compromise between beam dynamics [10] and detector constraints. Particles trajectories from IP through the FF doublet are shown on Figure 2 together with lines at several angles representing detector blind spot and rectangles for

ISBN 978-3-95450-172-4

bare apertures of the quadrupoles. Quadrupole parameters length, gradient and radius of aperture at $E = 175$ Gev are presented in Table 2. The distance between bare apertures for the first quadrupoles is 3.5 cm, for the second pair the distance is 14.2 cm.

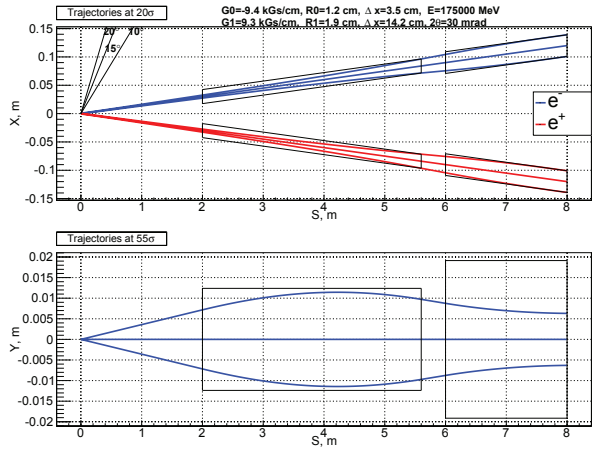


Figure 2: Trajectories of $e^-$ and $e^+$ bunches from IP through FF quadrupoles. Several lines are drown at 10°, 15°, 20° to represent blind solid angle of the detector. Black rectangles over trajectories depict bare quadrupole apertures.

Table 2: Parameters of FF Quadrupoles at 175 GeV

| | L [m] | G [T/m] | R [m] |
|---|---|---|---|
| Q0 | 3.6 | -94.5 | 0.012 |
| Q1 | 2 | 93.3 | 0.019 |

## LATTICE

The IR lattice should provide desired values of optical functions at IP and compensate geometrical and chromatic aberrations which define dynamic aperture (DA) and energy acceptance of the ring. The optics of IR consists of several blocks each having an intrinsic property of telescopic transformation: FFT — final focus telescope, CCSY and CCSX — chromaticity corrections section in horizontal (X) and vertical (Y) planes, CRAB — section that provides necessary phase advances and optical functions for crab waist sextupole [8]. The first dipole from IP is split in two, one closer to IP having a smaller field than the the other. Redistribution of the field between the dipoles gives a useful knob to minimize synchrotron radiation background in the detector. The elements and optical functions are shown on Figure 3, optical blocks are also marked.

The overall geometry of the beam lines is shown on Figure 4. The divergence angle between beam lines is 8.8 mrad and will be intercepted by matching section to bring the beams into the arc.

Synchrotron radiation energy loss for the whole IR from one arc to the other is $2 \cdot 0.11 = 0.22$ GeV at beam energy

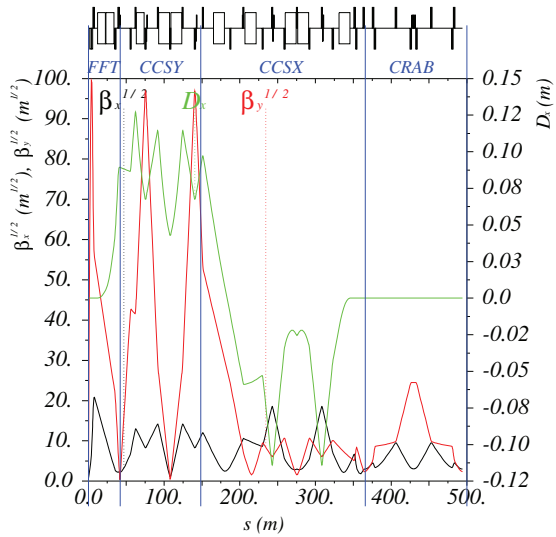


Figure 3: Optical functions of IR (version 6-12).

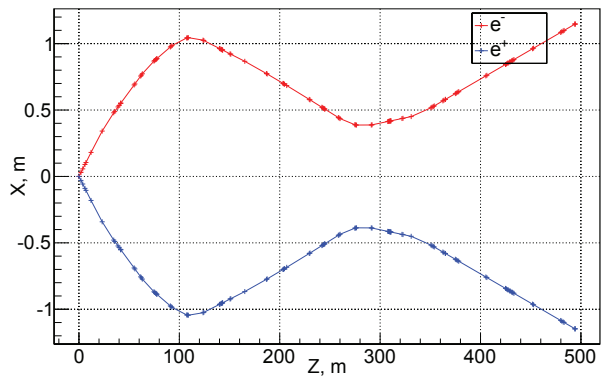


Figure 4: Layout of the electron and positron beam lines. Divergence of the beam lines is 8.8 mrad.

of 175 GeV. The relative power loss of four IPs with respect to the arcs is then $4 \cdot 0.22/7.7 = 0.11$.

## CHROMATICITY

Chromatic functions $W = \sqrt{a^2 + b^2}$ are shown on Figure 5. Obtained phase advance chromaticities are given in Table 3. Shifting the sextupoles pairs in phase relative to corresponding FF quadrupole we minimized the second order chromaticities and satisfied our rough estimations. Introduction of two weak sextupoles in the places with small on-momentum beta function and large second order chromaticity of beta function allows to control third order chromaticity of phase advances and hope for no degradation of dynamic aperture. Results are shown in Table 3 and on Figures 6, 7, 8. Plots of beta function chromaticity at the end of IR are shown on Figures 9, 10, 11 for sextupoles in phase, sextupoles shifted in phase, sextupoles shifted in phase and two additional sextupoles. We need to note that results should be considered as demonstration of efficiency



ISBN 978-3-95450-172-4

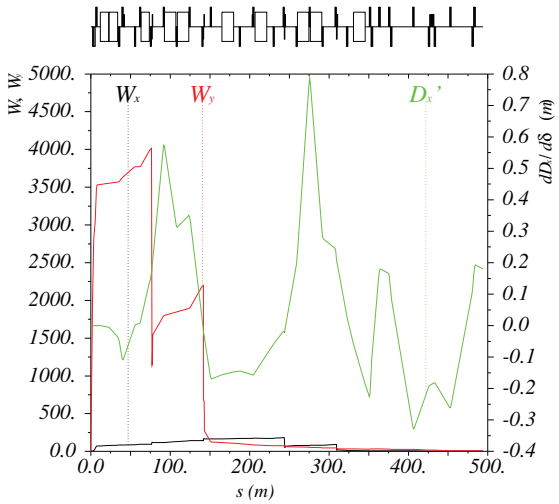


Figure 5: Chromatic (Montague) functions and nonlinear dispersion with sextupoles shifted in phase.

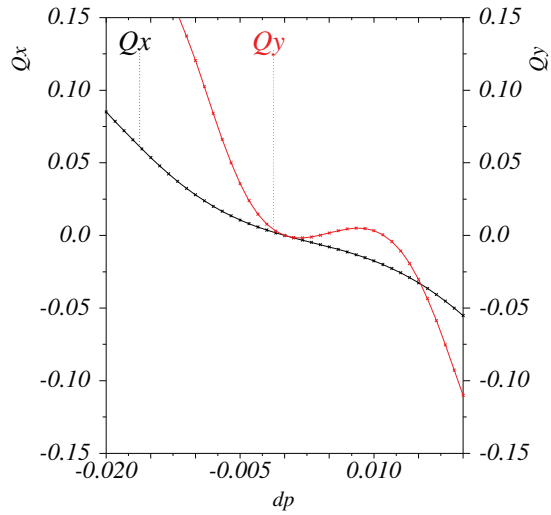


Figure 6: Phase advance variation with sextupoles in phase and no additional sextupoles.

of additional sextupoles, and they will have to be readjusted after the whole ring with realistic arcs is assembled.

Table 3: Chromaticity of Phase Advances from IP to the End of IR

| | Sextupoles in phase | Sextupoles shifted | Sextupoles additional |
|---|---|---|---|
| $Q_x$ | | 4 | |
| $Q'_x$ | −1.71 | −1.62 | −1.27 |
| $Q''_x$ | 110 | −48 | −144 |
| $Q'''_x$ | $-3.6 \cdot 10^4$ | $-3.4 \cdot 10^4$ | $-2.9 \cdot 10^4$ |
| $Q''''_x$ | $-5.3 \cdot 10^5$ | $7.4 \cdot 10^5$ | $8.9 \cdot 10^5$ |
| $Q_y$ | | 3 | |
| $Q'_y$ | −2.15 | −1.22 | −1.51 |
| $Q''_y$ | $1.5 \cdot 10^3$ | −38 | −24 |
| $Q'''_y$ | $-3.1 \cdot 10^5$ | $-3.1 \cdot 10^5$ | $-4 \cdot 10^4$ |
| $Q''''_y$ | $-1 \cdot 10^6$ | $5.8 \cdot 10^6$ | $5.3 \cdot 10^6$ |

## DYNAMIC APERTURE

We closed both shoulders of IR with linear map providing the fractional tunes $\nu_x = 0.54$ $\nu_y = 0.57$ in order to track particles through such a structure and study dynamic aperture. Optimization of sextupole's strengths gave the aperture of $R_x > 100 \cdot \sigma_x$ and $R_y > 200 \cdot \sigma_y$ (Figure 12) with no additional chromatic sextupoles. Each pair of main chromatic sextupoles has a pair of correcting sextupoles, whose strength is numerically adjusted in order to compensate for sextupole length effect [11].

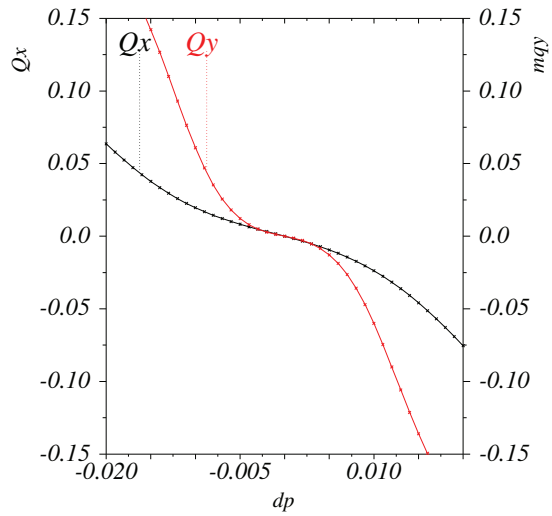


Figure 7: Phase advance variation with sextupoles shifted in phase and no additional sextupoles.

## CONCLUSION

We developed interaction region lattice with crossing angle for crab waist collision scheme. Geometrical layout, synchrotron radiation energy loss requirements are satisfied. Shifting sextupoles in phase with respect to final focus quadrupoles proves to be efficient method to minimize second order chromaticity of phase advances. Introduction of two additional sextupoles in the places with small values of beta functions gives usefull knobs to control third order chromaticity. Chromatic aberrations are compensated and satisfy estimations. Estimation of dynamic aperture is done and found sufficient. Since, IP parameters are the same as in head-on collision scheme the lattice could be used without crab sextupole section in head-on collision scenario. The given lattice of interaction region will be readjusted after the close ring lattice with realistic arcs will be assembled,

ISBN 978-3-95450-172-4

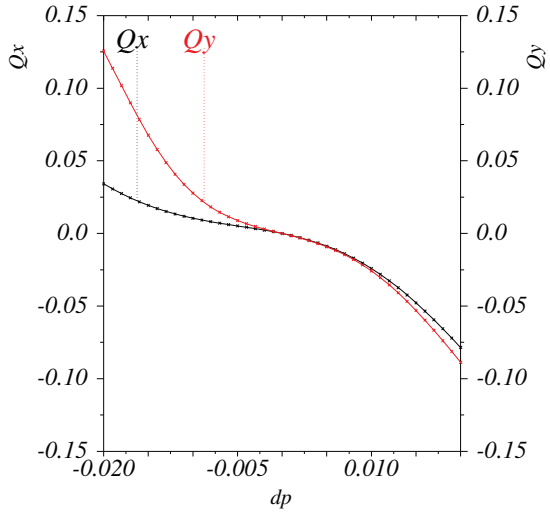


Figure 8: Phase advance variation with sextupoles shifted in phase and two additional sextupoles.

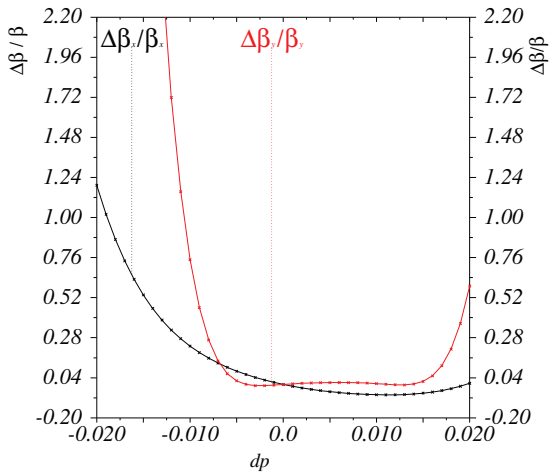


Figure 9: Chromaticity of the beta function at the end of IR with sextupoles in phase and no additional sextupoles.

therefore it needs not be understood as fixed but rather work in progress.

There are several questions which we see important for immediate study.

1. Is it possible to build required final focus quadrupoles?
2. How longitudinal detector field will be compensated?
3. Is there a need to increase $L^*$?
4. Do position and fields of the dipoles allow for synchrotron radiation shielding and detector background minimization?

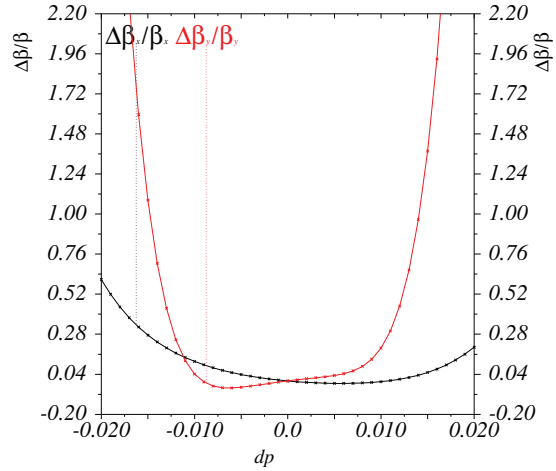


Figure 10: Chromaticity of the beta function at the end of IR with sextupoles shifted in phase and no additional sextupoles.

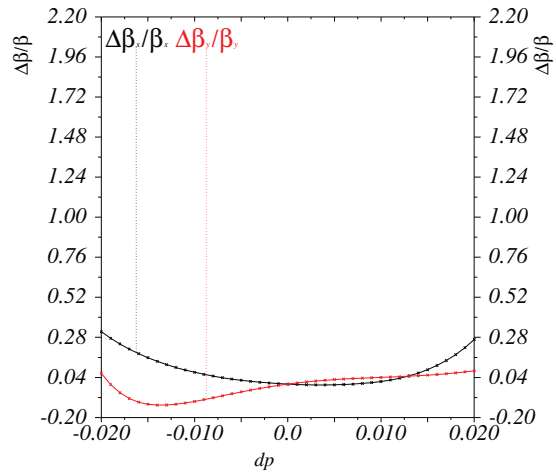


Figure 11: Chromaticity of the beta function at the end of IR with sextupoles shifted in phase and two additional sextupoles.

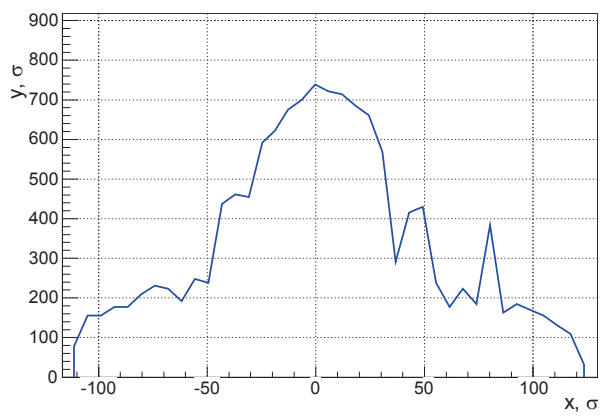


Figure 12: Dynamic aperture of the interaction region closed by the linear map $\sigma_x = 3.26 \cdot 10^{-5}$ m, $\sigma_y = 6.52 \cdot 10^{-8}$ m.



ISBN 978-3-95450-172-4

## REFERENCES


[1] M. Koratzinos et al., "TLEP: A HIGH-PERFORMANCE CIRCULAR e+e- COLLIDER TO STUDY THE HIGGS BOSON", IPAC2013, Shanghai, China, TUPME040 (2013).

[2] A. Blondel et al., "High luminosity e+e- storage ring colliders", submitted to Phys. Rev. Special Topics: Accelerators and Beams; arXiv:1208.0504 [physics.acc-ph], (2012).

[3] "The FCC-ee design study", http://tlep.web.cern.ch/

[4] J.E. Augustin et al., "Limitations on Performance of e+ e- Storage Rings and Linear Colliding Beam Systems at High Energy", ECONF,C781015,009,(1978), http://www.slac.stanford.edu/econf/C781015/pdf/009.pdf

[5] V.I. Telonov, "Restriction on the Energy and Luminosity of $e^+e^-$ Storage Rings due to Beamstrahlung", Phys. Rev. Lett.,110,114801 (2013), http://link.aps.org/doi/10.1103/PhysRevLett.110.114801

[6] Headon parameters (2014), https://tlep.web.cern.ch/sites/tlep.web.cern.ch/files/LeptonColliderParameters_V1.0_0.pdf

[7] A. Bogomyagkov et al., "Beam-beam effects investigation and parameters optimization for a circular e+e- collider at very high energies", Phys. Rev. ST Accel. Beams. 17, 041004 (2014).

[8] P. Raimondi, "Status of the SuperB effort", 2nd Workshop on Super B factory, LNF-INFN, Frascati, March 2006.

[9] B. W. Montague, "Linear Optics For Improved Chromaticity Correction," CERN-LEP-NOTE-165.

[10] A. Bogomyagkov et al., ''Nonlinear properties of the FCC/TLEP final focus with respect to L*", FCC-ee Accelerator VIDYO meeting No. 4 (2014), http://indico.cern.ch/event/286658/

[11] A. Bogomyagkov, S. Glukhov, E. Levichev, P. Piminov, ''Effect of the Sextupole Finite Length on Dynamic Aperture in the Collider Final Focus', http://arxiv.org/abs/0909.4872,2009


ISBN 978-3-95450-172-4

# SUPERKEKB BACKGROUND SIMULATION, INCLUDING ISSUES FOR DETECTOR SHIELDING

H. Nakayama, Y. Funakoshi, Y. Onishi, K. Kanazawa, T. Ishibashi

*Abstract*

The Belle experiment, operated on the KEKB accelerator in KEK, had accumulated a data sample with an integrated luminosity of more than 1 $ab^{-1}$ before the shutdown in 2010. We are preparing upgraded accelerator and detector, called SuperKEKB and Belle-II, to achieve the target luminosity of $8 \times 10^{35} cm^{-1} s^{-1}$. With the increased luminosity, we expect more beam background which might damage our detector components, hide event signals under noise hits, max out readout bandwidth, etc.

Detector shielding is a key to cope with the increased background and protect Belle-II detector. We present how we estimate the impact from each beam background sources at SuperKEKB, such as Touschek-scattering, beam-gas scattering, radiative Bhabha process, etc. We also present our countermeasures to mitigate the beam background, such as tungsten shields installed in the detector to stop shower particles, beam collimators to stop stray beam particles before they reach interaction region, dedicated beam pipe design around interaction point to stop synchrotron radiation, and so on.

## INTRODUCTION

The Belle experiment, operating at an asymmetric electron positron collider KEKB, finished its operation in June 2010. The Belle experiment had accumulated a data sample corresponding to an integrated luminosity of 1 $ab^{-1}$. KEKB recorded the world's highest peak luminosity, $2.1 \times 10^{34} cm^{-2} s^{-1}$. Numerous results of the Belle experiment have confirmed the theoretical predictions of the Standard Model. Especially, measurement of large CP violation in the B meson system has demonstrated that the Kobayashi-Maskawa (KM) mechanism is the dominant source of CP-violation in the standard model,

SuperKEKB, an upgraded of the KEKB collider, will provide a prove to search for new physics beyond the Standard Model, thanks to much larger data sample. The target luminosity of SuperKEKB, $80 \times 10^{34} cm^{-2} s^{-1}$, is 40 times higher than that of KEKB. The upgrade is based on so-called "Nano-beam scheme", which is first proposed by SuperB project planned in Italy [1]. The basic idea of this scheme is to squeeze the vertical beta function at the interaction point (IP). The luminosity of the collider is expressed by the following formula, assuming flat beams and equal horizontal and vertical beam size for two beams at IP:

$$L = \frac{\gamma_{\pm}}{2er_e}\left(\frac{I_{\pm}\xi_{y\pm}}{\beta^*_{y\pm}}\right)\frac{R_L}{R_{\xi_y}}, \qquad (1)$$

where $\gamma, e, and r_e$ are the Lorentz factor, the elementary electric charge and the electron classical radius, respectively. $I, \xi_y, \beta^*_y$ are the beam current, the beam-beam parameter and the vertical beta function at IP. The suffix $\pm$ specifies the positron (+) or the electron (-) beam. The parameters $R_L$ and $R_{\xi_y}$ represent reduction factors for the luminosity and the vertical beam-beam parameter, which arise from the crossing angle and the hourglass effect. At SuperKEKB, the vertical beta function at IP is 20 times smaller than KEKB in the Nano-beam scheme. In addition, the total beam currents will be doubled to achieve 40 times higher luminosity. The basic parameter of SuperKEKB is summarized in Table 1.

Belle II detector, an upgrade of the Belle detector, has better vertex resolution with new pixel detector, better particle identification performance with new type sensors, and better tolerance for the background particles. Details of the Belle II detector are described in [2].

Table 1: Basic parameters of SuperKEKB and KEKB. The former number is for the Low Energy Ring(LER) and the latter for the High Energy Ring(HER).

| | KEKB achieved | SuperKEKB |
|---|---|---|
| Energy [GeV] | 3.5/8.0 | 4.0/7.007 |
| Beam current [A] | 1.637/1.188 | 3.6/2.62 |
| Number of bunch | 1584 | 2503 |
| $\xi_y$ | 0.129/0.090 | 0.0869/0.0807 |
| $\sigma^*_y$ [nm] | 940/940 | 48/63 |
| $\beta^*_y$ [mm] | 5.9/5.9 | 0.27/0.30 |
| $\sigma^*_x$ [$\mu$m] | 147/170 | 10/10 |
| $\beta^*_x$ [mm] | 1200/1200 | 32/25 |
| Luminosity [$cm^{-2} s^{-1}$] | $2.1 \times 10^{34}$ | $80 \times 10^{34}$ |

## BEAM BACKGROUND SOURCES

At SuperKEKB with higher luminosity, the beam-induced background will also increase. Major background sources at SuperKEKB are shown in this section.

### *Touschek Effect*

The first background source is Touschek effect, which is one of dangerous background sources at SuperKEKB with "Nano-beam" scheme. Touschek effect is an intra-bunch scattering. Coulomb scattering between two particles in a same beam bunch changes their energy to deviate from the beam bunch, one with too much and the other with too little energy. The scattering rate of the Touschek effect is proportional to the inverse beam size, third power of the beam energy, the number of bunches and second



ISBN 978-3-95450-172-4

power of the bunch current. Since the beam size of SuperKEKB is much smaller than that of KEKB, background from the Touschek effect will become much higher. At SuperKEKB, simple extrapolation using the machine parameters predicts that Touschek background will increase by factor of ~20 compared to that of KEKB. However, Touschek background is reduced than this prediction because we introduce improved countermeasures to reduce the background. Touschek-scattered particles are lost by hitting the beam pipe inner wall while they propagate around the ring. If their loss position is close to the detector, generated shower might reach the detector. Fake hits generated by the background shower particles deteriorate the detector's physics resolution. Radiation dose by gammas or neutrons in the background shower damage the Silicon devices used in the detector.

To cope with Touschek background, we install horizontal and vertical movable collimators. The movable collimators located along the ring can stop the deviated particles before they reach close to the detector. Touschek background can be reduced effectively by collimating the beam horizontally from both inner and outer sides, since Touschek-scattered particles have more or less energy. At KEKB, we had horizontal collimation only from inner side.

The horizontal collimators are located at the positions where horizontal beta function or the dispersion become local-maximum. The horizontal collimators located just before to the interaction region play important role to minimize the beam loss rate inside the detector. The nearest collimator is only 18 m upstream of IP for LER.

The vertical collimator in LER, which is originally installed to reduce the beam-gas Coulomb background explained in the next subsection, also stops the vertically oscillating Touschek scattered particles. Particles scattered in Fuji-area, which is opposite side of IP in the ring, where LER beam orbit is vertically bending to pass under the HER ring.

The particle loss with various momentum deviations due to the Touschek effect can be evaluated by particle-tracking simulations along each location in the whole ring. The scattering probability is calculated using Bruck's formula, as described in [3].

### *Beam-Gas Scattering*

The second background source is the beam-gas scattering by the residual gas atoms. Coulomb scattering changes the direction of the beam particle, and bremsstrahlung scattering decrease the energy of the beam particles. Scattering rate of the beam-gas scattering is proportional to the vacuum level and the beam current. At SuperKEKB, the beam currents will be ~ 2 times higher than that of KEKB, and the vacuum level except for the interaction region will be the same level as KEKB. Therefore we expected the same order of magnitude (a few times higher) beam-gas background in the past publications [2].

Beam-gas bremsstrahlung loss rate in the detector is well suppressed by horizontal collimators and it is negligible compared to the Touschek loss rate in the detector. However, beam-gas Coulomb scattering rate is found [4] to be higher by factor of ~ 100 than that of KEKB, since Interaction Region (IR) beam pipe aperture is smaller and the maximum vertical beta function is larger. Beam-gas scattered particles are lost by hitting the beam pipe inner wall while they propagate around the ring, just like Touschek-scattered particles. The countermeasures used for Touschek background, movable collimators and the heavy-metal shield, are also effective to reduce beam-gas background. Especially, vertical movable collimator is essential to reduce Coulomb scattering background. However, Transverse Mode Coupling (TMC) instability caused by the vertical collimator should be carefully examined, since vertical beta function is larger than horizontal beta function. Therefore, collimator width should satisfy two conditions at the same time:

- narrow enough to avoid beam loss in the detector
- wide enough to avoid TMC instability

The only way to achieve this is to use the collimator with ~2 mm width. More detailed discussion can be found in [4].

Beam-gas Coulomb scattering probability for given scattering angle is calculated as shown in [3]. The particle loss distribution inside the detector is obtained by particle-tracking simulations along each scattering location in the whole ring, as did in case of Touschek effect.

### *Synchrotron Radiation*

The third background source is synchrotron radiation (SR) emitted from the beam. Since the SR power is proportional to the beam energy squared and magnetic field squared, the HER beam is the main source of this type of background. The energy of SR is few keV to tens of keV. At the first stage of Belle, the inner layer SVD was severely damaged by x-rays with E ~ 2 keV from HER. To absorb the synchrotron radiations before they reach the inner detector (PXD/SVD), the inner surface of the beryllium beam pipe are coated with gold plate. The shape of IR beam pipe is designed to avoid direct SR hits at the detector. Ridge structures on the inner surface of incoming pipes prevent scattered photons to reach interaction point.

Synchrotron radiation is simulated by the physics model implemented in Geant4. We estimate the impact on our inner detectors is tolerable.

### *Radiative Bhabha Process*

The fourth background source is Radiative Bhabha process. Photons from the radiative Bhabha process propagate along the beam axis direction and interact with the iron of the magnets. In these interactions, neutrons are copiously produced via the giant photo-nuclear resonance mechanism. These neutrons are the main background source for the outermost detector, the KL and muon detector (KLM) instrumented in the return yoke of the spectrometer. The rate of neutron production by the radiative Bhabha events is proportional to the luminosity, which is 40 times higher than that of

ISBN 978-3-95450-172-4

KEKB. Additional neutron shield in the tunnel to stop those neutrons is necessary. Both electron and positron energies decrease after radiative Bhabha process. If we employ the shared QCS magnets for incoming and outgoing beams as in KEKB, the scattered particles are over-bent by the QCS magnets. The particles then hit the wall of magnets and electromagnetic showers are generated. In the SuperKEKB case, we use two separate quadrupole magnets and both orbits for incoming and outgoing beams are centered in the Q-magnets. We therefore expect the radiative Bhabha background due to over-bent electrons and positrons will be small and only small fraction of them with very large energy loss($\Delta E$) are lost inside the detector. However, since the luminosity gets 40 times higher, those large $\Delta E$ particles are not negligible and will be comparable to Touschek and Beam-gas background after installation of collimators. Kick from solenoid field due to finite crossing angle is crucial and inevitable cause of those beam loss. Beam intrinsic angular divergence at IP, angular diffusion by radiative Bhabha process, and leak field of the other ring's Q magnets also play a role, but less crucial than solenoid kick.

In addition, radiative Bhabha loss within $|s| < 65$ cm from IP is very dangerous because we cannot put enough shielding in that region. Cryostat is located on $|s| > 65$cm.

Scattering is simulated using the generator called "BBBREM" [5]. The we perform particle-tracking until they hit beam pipes, to obtain loss distribution.

### *Two Photon Process*

The fifth background source is very low momentum electron-positron pair backgrounds produced via the two-photon process: $ee \rightarrow eeee$. Those pairs might reach our inner detectors for vertex measurement.

Scattering is simulated using the generator called "BDK(Diag36)" [6].

## LATEST BACKGROUND SIMULATION RESULTS

Figure 1 shows the latest background picture. Touschek and beam-gas background are rather localized on the position where beam pipe radius changes, while radiative Bhabha background is distributed over wider range in z direction.

Figure 2 shows the loss wattage distribution and Figure 3 summarizes the loss wattage and (effective) loss rate within $|s| < 4$ m. Loss wattage is defined as loss rate multiplied by energy of beam lost particles. One can see now the radiative Bhabha background is the dominant, after the installation of optimized collimators to reduce Touschek and beam-gas background.

## GEANT4 FULL-DETECTOR SIMULATION

Using the estimated loss distribution of each background sources shown in the previous section, we perform the full-detector simulation based on GEANT4. Not only the impact on detector performance but also the radiation/neutron dose on detector components are investigated. Guided by the simulation, we have added tungsten shields inside the cryostat of the final focusing magnets to mitigate the beam background impact on detectors. We also installed several neutron shields to protect Silicon devices.

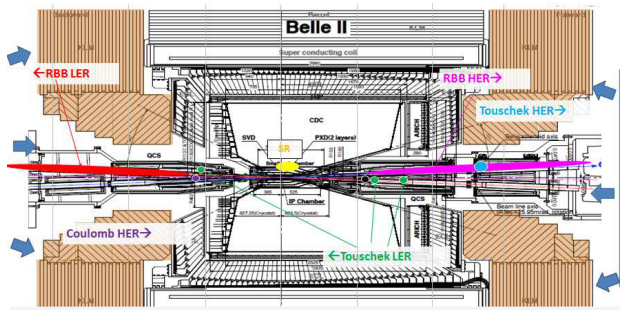


Figure 1: Latest background picture.

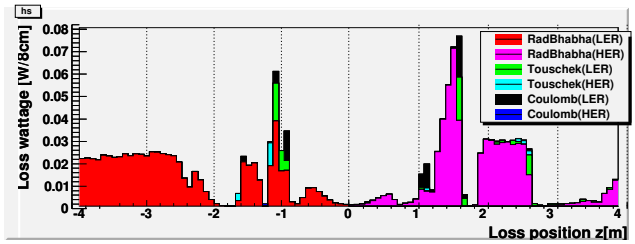


Figure 2: Loss wattage distribution along z position. Loss wattage is defined as loss rate multiplied by energy of lost beam particles.

Assuming the beam background in case of the full design luminosity at SuperKEKB, occupancy on the inner vertex detectors, PXD and SVD, is estimated to be tolerable. Degradation on particle identification (K/$\pi$ separation) performance is also acceptable.

Assuming 10 years of operation at the full luminosity, radiation damage are acceptable for most of detector components. Neutron flux on FPGAs of CDC readout board causes single event upset which needs FPGA reset, but the estimated frequency of the reset is tolerable.

| | LER (4GeV e+) | HER (7GeV e-) |
|---|---|---|
| Rad. Bhabha | 0.74 W (eff. 1.2GHz) | 0.59W (eff. 0.52GHz) |
| Touschek | 0.078W (0.12GHz) | 0.02 W (0.02 GHz) |
| Coulomb | 0.18 W (0.28GHz) | 0.001W (0.001GHz) |

Figure 3: Estimated loss rate and loss wattage within $|s| < 4$ m. Loss wattage is defined as loss rate multiplied by energy of lost beam particles. Effective loss rate is calculated by scaling loss rate by the energy of lost beam particles.



ISBN 978-3-95450-172-4

The only problem we still suffer is TOP PMT photocathode aging issue. We have purchased PMTs with ~1 C/cm$^2$ lifetime, which will be killed in few years of full luminosity operation. The recently developed PMTs has ~7 C/cm$^2$ lifetime, but for now we have budget to buy new PMTs for only half of TOP PMTs. We plan to replace old PMTs after few years of operation.

## REFERENCES

[1] P. Raimondi, talk given at the 2nd SuperB workshop, Frascati, 2006.

[2] Belle II Technical Design Report, `http://xxx.lanl.gov/abs/1011.0352` (not that the beam background section in this TDR is outdated.)

[3] Y. Ohnishi *et al.*, "Accelerator design at SuperKEKB," PTEP **2013**, 03A011 (2013).

[4] H. Nakayama et al, "Small-Beta Collimation at SuperKEKB to Stop Beam-Gas Scattered Particles and to Avoid Transverse Mode Coupling Instability," Conf. Proc. C **1205201**, 1104 (2012)

[5] R. Kleiss and H. Burkhardt, "BBBREM: Monte Carlo simulation of radiative Bhabha scattering in the very forward direction," Comput. Phys. Commun. **81**, 372 (1994) [hep-ph/9401333].

[6] F. A. Berends, P. H. Daverveldt and R. Kleiss, "Monte Carlo Simulation of Two Photon Processes. 3. Complete Lowest Order Calculations for $e^+e^- \to e^+e^-\mu^+\mu^-$ With Large Angle Tagging Conditions," Comput. Phys. Commun. **40**, 309 (1986).

ISBN 978-3-95450-172-4

# ANALYTICAL ESTIMATION OF MAXIMUM BEAM-BEAM TUNE SHIFTS FOR ELECTRON-POSITRON AND HADRON CIRCULAR COLLIDERS*

J. Gao†, M. Xiao, F. Su, S. Jin, D. Wang
Y.W. Wang, S. Bai, T.J. Bian
Institute of High Energy Physics
100049, Beijing, China

*Abstract*

In this paper we will make a brief review of the existing analytical formulae for the beam-beam tune shift limits for electron-positron and hadron circular colliders. The comparison of the estimated beam-beam tune shifts from these formulae with those obtained from existing machines has been made and the validity comparison among these formulae are given as well. Finally, the formulae from J. Gao have been applied in CEPC and SppC parameter optimizations.

## INTRODUCTION

The luminosity of an electron-positron circular collider can be expressed as

$$L = \frac{I_{beam}\gamma\xi_y}{2er_e\beta_y^*}\left(1+\frac{\sigma_y^*}{\sigma_x^*}\right)F_h \quad (1)$$

where $r_e$ is the electron radius ($2.818\times10^{-15}$ m), $\beta_y^*$ is the beta function value at the interaction point, $\gamma$ is the normalized beam energy, $\sigma_x^*$ and $\sigma_y^*$ are the bunch transverse dimensions at the interaction point, respectively, $I_{beam}$ is the circulating current of one beam, $F_h$ is Hourglass reduction factor, and $\xi_y$ is defined as

$$\xi_y = \frac{N_e r_e \beta_y^*}{2\pi\gamma\sigma_y^*(\sigma_x^*+\sigma_y^*)} \quad (2)$$

is the vertical beam-beam tune shift, $N_e$ is the particle population inside a bunch.

$$L = 2.17\times10^{34}(1+r)\xi_y \times \frac{E_0(GeV)N_b I_{bunch}(A)F_h}{\beta_y^*(cm)}[cm^{-2}s^{-1}] \quad (3)$$

where $E_0$ is the beam energy, $r=\sigma_y^*/\sigma_x^*$, $N_b$ is the number of bunches inside a beam, $I_{bunch}$ is the average current of a bunch, and $I_{beam}=N_b I_{bunch}$.

In fact, since ACO [1], it is found that for all circular colliders $\xi_y$ is not a free parameter, and for a given collider, there is a maximum $\xi_y$, or $\xi_{y,max}$, which could not be surpassed no matter how to make working point optimization [2], and beyond $\xi_{y,max}$, the colliding bunch transverse dimensions blow-up and bunch lifetime drops drastically (exponentially in fact). These beam-beam interaction induced phenomena are called beam-beam effects. To understand the beam-beam effects is one of the key subjects for particle accelerator physicists. For a long time, in a collider design, $\xi_{y,max}$ is chosen as a constant value according to some experiences from previous machines independent of specific machine parameters, i.e., regardless whether $\xi_{y,max}$ is a function of the machine energy, damping time, number of interaction points and particle revolution period, etc. In fact, as we know from Ref. [3], for flat colliding electron-positron beams, $\xi_{y,max}$ can be expressed as (without top-up injection)

$$\xi_{y,max} = \frac{H_0}{2\pi}\sqrt{\frac{T_0}{\tau_y\gamma N_{IP}}} \quad (4)$$

where $H_0=2845$, $\tau_y$ is the transverse damping time, $T_0$ is the revolution period, and $N_{IP}$ is the number of interaction points. Or, for isomagnetic case, one has

$$\xi_{y,max,iso} = H_0\gamma\sqrt{\frac{r_e}{6\pi R N_{IP}}} \quad (5)$$

where $R$ is the local dipole bending radius.

Knowing the analytical expression of maximum beam-beam tune shift, $\xi_{y,max}$, one could has luminosity expressed as

$$L_{max}[cm^{-2}s^{-1}] = 2.17\times10^{34}(1+r)\xi_{y,max}\times\frac{E_0[\mathrm{GeV}]N_b I_{bunch}[\mathrm{A}]F_h}{\beta_y^*[\mathrm{mm}]} \quad (6)$$

or

$$L_{max}[cm^{-2}s^{-1}] = \frac{0.158\times10^{34}(1+r)}{\beta_y^*[\mathrm{mm}]}\times I_{beam}[\mathrm{mA}]\sqrt{\frac{U_0[\mathrm{GeV}]}{N_{Ib}}}F_h \quad (7)$$

where $U_0$ is the energy loss due to synchrotron radiation per turn, or

$$L_{max}[cm^{-2}s^{-1}] = \frac{0.158\times10^{34}(1+r)}{\beta_y^*[\mathrm{mm}]}\times\sqrt{\frac{I_{beam}[\mathrm{mA}]P_{sr}[\mathrm{MV}]}{N_{Ib}}}F_h \quad (8)$$

* Work supported by NSFC 11175192
† gaoj@ihep.ac.cn



ISBN 978-3-95450-172-4

where $P_{sr}$ is the synchrotron radiation power of one colliding beam.

If the collider has $N_{IP}$ interaction points, and the total luminosity of the collider is denoted as $L_{total}$, it is clear that $L_{total} = N_{IP}L_{max} \propto \sqrt{N_{IP}}$.

## OTHER TWO MAXIMUM BEAM-BEAM LIMIT SCALING LAWS IN ELECTRON POSITRON STORAGE RING COLLIDERS

Apart from the analytical expression given in eq. 4, which was obtained by improving the corresponding expression in ref. [4], another beam-beam tune limit scaling law was established according to LEP operation experiences at CERN [5]

$$\xi_y = I_{bunch}\sqrt{\frac{1}{A + (I_{bunch}B)^2}} \tag{9}$$

$$A = \left(\frac{2\pi e f_{rev}\gamma}{r_e}\right)^2 \frac{\beta_x^*}{\beta_y^*}\epsilon_x^0\epsilon_y^0 \tag{10}$$

$$B = \frac{1}{\xi_{y,max}} \tag{11}$$

where $e$ is the electron charge, $f_{rev}$ is the revolution frequency, $\epsilon_x^0$ and $\epsilon_y^0$ are zero current emittance, respectively, if $B$ is not zero, means that there exists beam-beam tune limit, $\xi_{y,max}$. It is obvious to see that till now there is no information of how $\xi_{y,max}$ depends on the machine parameters, such as beam energy, revolution frequency, damping time, and number of interaction points. In ref. [5], two papers are cited to indicate that first [6]

$$\xi_{y,max} = f\left(\frac{T_0}{\tau_y N_{IP}}\right) \tag{12}$$

where $f$ denotes a function, and the second [7]

$$\xi_{y,max} \propto \left(\frac{T_0}{\tau_y}\right)^{0.3} \tag{13}$$

Comparing eq. 4 with eq. 12, it is obvious that the $\gamma$ dependance is missing in eq. 12. Comparing eq. 4 with eq. 13, it is obvious that the power dependance on damping decrement, $T_0/\tau_y$, are different, the power dependance on damping decrement in eq. 4 is 0.5 instead of 0.3.

Talman's developed another formulation to estimate analytically the beam-beam tune shift limit [8], which will not be repeated here due to the complication of the formulation.

## COMPARISONS OF THREE ANALYTICAL BEAM-BEAM TUNE LIMIT SCALING LAWS WITH EXPERIMENTS

After reviewing the three analytical formulations to estimate analytically the beam-beam tune limit in the previous two sections, it is high time now to make comparisons between analytical formulae and the experimental results from existing $e^+e^-$ storage ring colliders. As shown in Tabs. 1-3.

From comparison results shown in Tab. 4 and Fig. 1, it is clear to see that Gao's analytical formula expressed in eq. 4 is quite close to the experimental results of machines working on both low and high energy domains, and it is used in CEPC parameter optimizations [10], as shown in Tab. 5.

According to eq. 4 above and eq. 48 in Ref. [9], for CEPC [11],one finds that $\xi_{x,max} = 0.1$ and $\xi_{y,max} = 0.073$ . The $\xi_{y,max} = 0.082$ is chosen little overshot.

## ANALYTICAL BEAM-BEAM TUNE SHIFT LIMIT IN HADRON CIRCULAR COLLIDERS

As for hadron circular colliders, one might want to use eq. 4 by substituting simply $r_e$ in eq. 4 to the radius of the corresponding hadron, for example, proton's classical radius, $r_p$. To many peoples surprise, one can easily find out that it will give ridiculous results! Eq. 4, unfortunately, cannot be applied directly to the hadron particle cases. In the following part of this paper, as one step further, analytical formulae for the beam-beam tune shift limit for hadron circular colliders [12] will be introduced.

In fact, the physical reason for the difference between lepton and hadron circular colliders is very simple. In lepton circular colliders, due to strong strong synchrotron radiation effect, the two colliding buches could be regarded as two bunch of gases, and particles inside are in total mixing. As far as a hadron circular collider is concerned, usually, the stochastic motion will start for some particles only with strong nonlinear beam-beam forces, and the number of these particles moving in a stochastic way is smaller than the particle number in the whole bunch. The question now is to estimate how many particles located in the outer part of the bunch away from the bunche center are moving in a nonlinear beam-beam force driven stochastic motion for a given bunch current. Assuming a round colliding bunch of Gaussian transverse distribution,the number of these "heated" particles, $N_{p,heat}$, can be estimated by $N_{p,heat} = fN_{p,bunch}$, with $N_{p,bunch}$ being the particle number of the bunch. Obviously, for a lepton machine, $f = 1$.

According to ref. [12], one has the general analytical beam-beam tune shift, $\xi_{h,y,max}$ for a hadron circular collider, expressed as follows

$$\xi_{h,y,max} = \frac{H_0\gamma}{f(x_*)}\sqrt{\frac{r_p}{6\pi R N_{IP}}} \tag{14}$$

or

$$\xi_{h,y,max} = \frac{H_0}{2\pi f(x_*)}\sqrt{\frac{T_0}{\tau_y\gamma N_{IP}}} \tag{15}$$

where

$$f(x) = 1 - \frac{2}{\sqrt{2\pi}}\int_0^x \exp\left(-\frac{t^2}{2}\right)dt \tag{16}$$

ISBN 978-3-95450-172-4

Table 1: The Comparison Result of Gao's Formula with Different Machine Experimental Values

| Machine | E（GeV） | R(m) | B(T) | γ | $N_{IP}$ | $\xi_y$ (Gao) | $\xi_y$ (experimental value) | $\xi_y$ (parameter list) |
|---|---|---|---|---|---|---|---|---|
| DAFNE | 0.51 | 1.42 | 1.2 | 998 | 1 | 0.0292 | 0.02 | 0.044 |
| BEPC | 1.89 | 9.23 | 0.903 | 3698 | 1 | 0.0423 | 0.04 | 0.035 |
| BEPCII | 1.89 | 9.31 | 0.677 | 3698 | 1 | 0.0422 | 0.04 | 0.0327 |
| PEP-II(L) | 3.12 | 13.87 | 0.75 | 6106 | 1 | 0.0570 | 0.06 | 0.0510/0.0727 |
| PEP-II(H) | 8.99 | 166.48 | 0.18 | 17593 | 1 | 0.0474 | 0.048 | 0.0703/0.0498 |
| KEKB(L) | 3.5 | 16.20 | 0.72 | 6849 | 1 | 0.0592 | 0.069 | 0.127/0.129 |
| KEKB(H) | 8.0 | 106.667 | 0.25 | 15656 | 1 | 0.0527 | 0.052 | 0.122/0.09 |
| SuperKEKB(L) | 4.0 | 70.18 | 0.19 | 7828 | 1 | 0.0325 | | 0.0028/0.0881 |
| SuperKEKB(H) | 7.0 | 106.06 | 0.22 | 13699 | 1 | 0.0463 | | 0.0012/0.0807 |
| SuperB(L) | 4.2 | 56 | 0.25 | 8219 | 1 | 0.0382 | | 0.002/0.095 |
| SuperB(H) | 6.7 | 42.95 | 0.52 | 13111 | 1 | 0.0696 | | 0.002/0.095 |
| LEP-I | 45.6 | 3096.175 | 0.0491 | 88062 | 4 | 0.0275 | 0.033 | |
| LEP-II | 104.5 | 3096.175 | 0.1112 | 191781 | 4 | 0.0639 | 0.079 | 0.025/0.065 |
| LEP3 | 120 | 2620 | 0.153 | 234834 | 4 | 0.0798 | | 0.09/0.08 |
| CEPC | 120 | 6094 | 0.066 | 234834 | 2 | 0.0739 | | 0.104/0.074 |

Table 2: The Comparison Result of Assmann-Cornelis' Formula with Different Machine Experimental Values

| Machine | E(GeV) | γ | C (km) | $I_b$ (mA) | Bunch number | $f_{rev}$ | $\beta^*_x$ | $\beta^*_y$ | $\varepsilon^0_x$ (10^-9π rad-m) | $\varepsilon^0_y$ (10^-9π rad-m) | $\xi_y$ (calculated value) | $\xi_y$ (experimental value ) | $\xi_y$ (parameter list) |
|---|---|---|---|---|---|---|---|---|---|---|---|---|---|
| DAFNE | 0.510 | 998 | 0.098 | 1000 | 120 | 3.06*10^6 | 0.26 | 0.009 | 260 | 2.6 | 0.0549 | 0.02 | 0.044 |
| BEPC | 1.89 | 3698 | 0.2404 | 40 | 1 | 1.25*10^6 | 1.2 | 0.05 | 660 | 28 | 0.0364 | 0.04 | 0.035 |
| BEPCII | 1.89 | 3698 | 0.2375 | 725 | 88 | 1.26*10^6 | 1.0 | 0.015 | 144 | 2.2 | 0.0341 | 0.04 | 0.0327 |
| PEP-II(L) | 3.12 | 6106 | 2.2 | 3026 | 1732 | 136364 | 0.5 | 0.012 | 24 | 1.8 | 0.1386 | 0.06 | 0.0510/0.0727 |
| PEP-II(H) | 8.99 | 17593 | 2.2 | 1960 | 1732 | 136364 | 0.5 | 0.012 | 48 | 1.8 | 0.02204 | 0.048 | 0.0703/0.0498 |
| KEKB(L) | 3.5 | 6849 | 3.016 | 1637 | 1585 | 99469 | 1.2 | 0.0059 | 18 | 0.56 | 0.09385 | 0.069 | 0.127/0.129 |
| KEKB(H) | 8.0 | 15656 | 3.016 | 1188 | 1585 | 99469 | 1.2 | 0.0059 | 24 | 0.61 | 0.02472 | 0.052 | 0.122/0.09 |
| SuperKEKB(L) | 4.0 | 7828 | 3.016 | 3600 | 2500 | 99469 | 0.032 | 0.00027 | 3.2 | 0.0086 | 2.8704? | | 0.0028/0.0881 |
| SuperKEKB(H) | 7.0 | 13699 | 3.016 | 2600 | 2500 | 99469 | 0.025 | 0.0003 | 4.6 | 0.013 | 0.9584 | | 0.0012/0.0807 |
| SuperB（L） | 4.2 | 8219 | 1.258 | 2400 | 978 | 238474 | 0.026 | 0.00025 | 2.0 | 0.005 | 3.4413? | | 0.002/0.095 |
| SuperB（H） | 6.7 | 13111 | 1.258 | 1900 | 978 | 238474 | 0.032 | 0.00021 | 2.5 | 0.006 | 1.1520 | | 0.002/0.095 |
| LEP-I | 45.6 | 88062 | 26.66 | 1.28 | 4 | 11253 | 2.0 | 0.05 | 55.6 | 0.25 | 0.0383 | 0.033 | |
| LEP-II | 104.5 | 204501 | 26.66 | 4 | 4 | 11253 | 1.5 | 0.05 | 48 | 0.25 | 0.0642 | 0.079 | 0.025/0.065 |
| LEP3 | 120 | 234834 | 26.66 | 7.2 | 4 | 11253 | 0.2 | 0.001 | 25 | 0.10 | 0.0854 | | 0.09/0.08 |
| CEPC | 120 | 234834 | 53.6 | 16.6 | 50 | 5597 | 0.8 | 0.0012 | 6.79 | 0.0204 | 0.07368 | | 0.104/0.074 |



ISBN 978-3-95450-172-4

Table 3: The Comparison Result of Talman's Formula with Different Machine Experimental Values [8]

TABLE III. Parameters of some circular, flat beam, $e^+e^-$ colliding rings, and the saturation tune shift values predicted by Eq. (41). For points not excluded by one of these factors (see table footnotes) the mean and standard deviations of theory/experiment (the last column) are 1.26 ± 0.45.

| Ring | IPs | $Q_x$/IP | $Q_y$/IP | $Q_s$/IP | $\sigma_s$ | $\beta_y^*$ | $10^4\delta_y$ | $\xi_{th}$ | $\Delta Q_{y,exp}$ | $\xi_{th}/\Delta Q_{y,exp}$ |
|---|---|---|---|---|---|---|---|---|---|---|
| VEPP4 | 1 | 8.55 | 9.57 | 0.024 | 0.06 | 0.12 | 1.68 | 0.028 | 0.046 | 0.61 |
| PEP-1IP | 1 | 21.296 | 18.205 | 0.024 | 0.021 | 0.05 | 6.86 | 0.076 | 0.049 | 1.55 |
| PEP-2IP | 2 | 5.303 | 9.1065 | 0.0175 | 0.020 | 0.14 | 4.08 | 0.050 | 0.054 | 0.93 |
| CESR-4.7 | 2 | 4.697 | 4.682 | 0.049 | 0.020 | 0.03 | 0.38 | 0.037 | 0.018 | 2.06 |
| CESR-5.0 | 2 | 4.697 | 4.682 | 0.049 | 0.021 | 0.03 | 0.46 | 0.034 | 0.022 | 1.55 |
| CESR-5.3 | 2 | 4.697 | 4.682 | 0.049 | 0.023 | 0.03 | 0.55 | 0.029 | 0.025 | 1.16 |
| CESR-5.5 | 2 | 4.697 | 4.682 | 0.049 | 0.024 | 0.03 | 0.61 | 0.027 | 0.027 | 1.00 |
| CESR-2000 | 1 | 10.52 | 9.57 | 0.055 | 0.019 | 0.02 | 1.113 | 0.028 | 0.043 | 0.65 |
| KEK-1IP | 1 | 10.13 | 10.27 | 0.037 | 0.014 | 0.03 | 2.84 | 0.046 | 0.047 | 0.98 |
| KEK-2IP | 2 | 4.565 | 4.60 | 0.021 | 0.015 | 0.03 | 1.42 | 0.048 | 0.027 | 1.78 |
| LEP-46 | 4[c] | 22.58 | 19.04 | 0.016 | 0.0076 | 0.05 | 0.958 | 0.128 | 0.034 | |
| LEP-65 | 4[c] | 22.57 | 19.04 | 0.019 | 0.009 | 0.05 | 2.7 | 0.086 | | |
| LEP-98 | 4[c] | 24.59 | 24.05 | 0.029 | 0.0110 | 0.05 | 8.6 | 0.12[b] | 0.052 | |
| PEP-LER | 1 | 38.65 | 36.58 | 0.027 | 0.0123 | 0.0125 | 1.17 | 0.044 | 0.044 | 1.00 |
| PEP-HER | 1 | 24.57 | 23.64 | 0.045 | 0.0115 | 0.0125 | 1.98 | 0.056 | 0.026[a] | |
| KEK-LER | 1 | 45.518 | 44.096 | 0.021 | 0.0057 | 0.007 | 2.34 | 0.042 | 0.032 | 1.31 |
| KEK-HER | 1 | 44.525 | 42.135 | 0.019 | 0.055 | 0.007 | 2.18 | 0.060 | 0.018[a] | |
| BEPC | 1 | 5.80 | 6.70 | 0.020 | 0.05 | 0.05 | 0.16 | 0.068 | 0.039 | 1.74 |

[a]Ion effect blowup of low energy beam may prevent beam-beam saturation.
[b]Theory value is erratic
[c]Unequally spaced IPs.

Table 4: The Comparison Result of The Errors of Three Different Formulae with Different Machine Experimental Values

| Machine | $\xi_y$ Gao's Theory | $\xi_y$ Assmann's theory | $\xi_y$ Talman's theory | $\xi_y$ (experimental value) | $\xi_y$ (parameter list) |
|---|---|---|---|---|---|
| DAFNE | 0.0292 | 0.0549 | | 0.02 | 0.044 |
| BEPC | 0.0423 | 0.0364 | 0.068 | 0.04 | 0.035 |
| BEPCII | 0.0422 | 0.0341 | | 0.04 | 0.0327 |
| PEP-II(L) | 0.0570 | 0.1386 | 0.044 | 0.06 | 0.0510/0.0727 |
| PEP-II(H) | 0.0474 | 0.02204 | 0.056 | 0.048 | 0.0703/0.0498 |
| KEKB(L) | 0.0592 | 0.09385 | 0.042 | 0.069 | 0.127/0.129 |
| KEKB(H) | 0.0527 | 0.02472 | 0.060 | 0.052 | 0.122/0.09 |
| SuperKEKB(L) | 0.0325 | 2.8704? | | | 0.0028/0.0881 |
| SuperKEKB(H) | 0.0463 | 0.9584 | | | 0.0012/0.0807 |
| SuperB（L） | 0.0382 | 3.4413? | | | 0.002/0.095 |
| SuperB（H） | 0.0696 | 1.1520 | | | 0.002/0.095 |
| LEP-I | 0.0275 | 0.0383 | 0.128 | 0.033 | |
| LEP-II | 0.0639 | 0.0642 | 0.12 | 0.079 | 0.025/0.065 |
| LEP3 | 0.0798 | 0.0854 | | | 0.09/0.08 |
| CEPC | 0.0739 | 0.07368 | | | 0.104/0.074 |



ISBN 978-3-95450-172-4

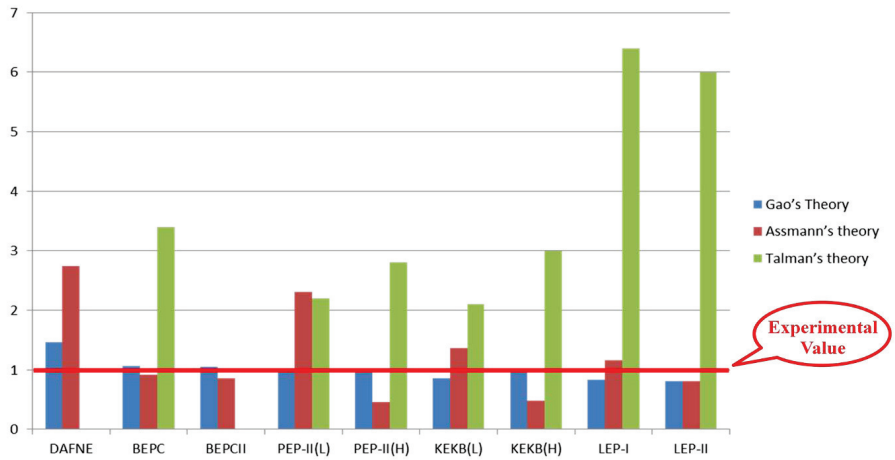


Figure 1: The errors between the analytical estimations and the experimental results vs different machines working on different energys.

Table 5: The CEPC Parameter List

| Parameter | Unit | Value | Parameter | Unit | Value |
|---|---|---|---|---|---|
| Beam energy [E] | GeV | 120 | Circumference [C] | m | 54420 |
| Number of IP[$N_{IP}$] | | 2 | SR loss/turn [$U_0$] | GeV | 3.11 |
| Bunch number/beam[$n_B$] | | 50 | Bunch population [Ne] | | 3.71E+11 |
| SR power/beam [P] | MW | 51.7 | Beam current [I] | mA | 16.6 |
| Bending radius [r] | m | 6094 | momentum compaction factor [$a_p$] | | 3.39E-05 |
| Revolution period [$T_0$] | s | 1.82E-04 | Revolution frequency [$f_0$] | Hz | 5508.87 |
| emittance (x/y) | nm | 6.12/0.018 | $b_{IP}$(x/y) | mm | 800/1.2 |
| Transverse size (x/y) | mm | 69.97/0.15 | $x_{x,y}$/IP | | 0.116/0.082 |
| Beam length SR [$s_{s.SR}$] | mm | 2.17 | Beam length total [$s_{s.tot}$] | mm | 2.53 |
| Lifetime due to Beamstrahlung | min | 80 | lifetime due to radiative Bhabha scattering [$t_L$] | min | 52 |
| RF voltage [$V_{rf}$] | GV | 6.87 | RF frequency [$f_{rf}$] | MHz | 650 |
| Harmonic number [h] | | 117900 | Synchrotron oscillation tune [$n_s$] | | 0.18 |
| Energy acceptance RF [h] | % | 5.98 | Damping partition number [Je] | | 2 |
| Energy spread SR [$s_{d.SR}$] | % | 0.13 | Energy spread BS [$s_{d.BS}$] | % | 0.08 |
| Energy spread total [$s_{d.tot}$] | % | 0.16 | $n_g$ | | 0.23 |
| Transverse damping time [$n_x$] | turns | 78 | Longitudinal damping time [$n_e$] | turns | 39 |
| Hourglass factor | Fh | 0.692 | Luminosity /IP[L] | $cm^{-2}s^{-1}$ | 2.01E+34 |



ISBN 978-3-95450-172-4

Table 6: Comparison of Gao's Formulae to Some Hadron Circular Colliders

| Machine | E(TeV) | R(m) | γ | $N_{IP}$ | f(x) | $\xi_y$(Gao) | $\xi_y$(exp. value) | $\xi_y$(para.list) |
|---|---|---|---|---|---|---|---|---|
| **Tevatron** | 0.98 | 682 | 1048 | 2 | 0.0141217 | 0.00149268 | | 0.012 |
| **HERA(p)** | 0.92 | 588 | 984 | 2 | 0.0140073 | 0.00147705 | | 0.0009 |
| **LHC** | 7 | 2801 | 7458 | 2 | 0.0252262 | 0.00320658 | 0.0034 | 0.005 |
| **SSC** | 22 | 9824 | 23400 | 2 | 0.0313979 | 0.00431618 | | 0.0021 |
| **HL-LHC** | 7 | 2801 | 7458 | 2 | 0.0252262 | 0.00320658 | | 0.0075 |
| **HE-LHC** | 16.5 | 2750 | 17581 | 2 | 0.0363833 | 0.00528936 | | 0.005 |
| **FCC-hh** | 50 | 10416 | 53277 | 2 | 0.0437486 | 0.0068494 | | 0.005 |
| **SppC** | 37.4 | 6236 | 39872 | 2 | 0.0431489 | 0.0067169 | | 0.006 |

Table 7: SppC Parameter (1)

| Parameter | Value | Unit |
|---|---|---|
| **Main parameters** | | |
| **Circumference** | 56 | km |
| **Beam energy** | 37.4 | TeV |
| **Lorentz gamma** | 39891 | |
| **Dipole field** | 20 | T |
| **Dipole curvature radius** | 6236 | m |
| **Arc filling factor** | 0.79 | |
| **Total dipole magnet length** | 39184 | m |
| **Arc length** | 49600 | m |
| **Total straight section length** | 6400 | m |
| **Energy gain factor in collider rings** | 17.8 | |
| **Injection energy** | 2.1 | TeV |
| **Number of IPs** | 2 | |
| **Revolution frequency** | 5.36 | kHz |
| **Physics performance and beam parameters** | | |
| **Peak luminosity per IP** | 1.3E+35 | $cm^{-2}s^{-1}$ |
| **Beta function at collision** | 0.75 | m |
| **Circulating beam current** | 1.0 | A |



ISBN 978-3-95450-172-4

Table 8: SppC Parameter (2)

| | | |
|---|---|---|
| **Max beam-beam tune shift per IP** | **0.006** | |
| **Bunch separation** | 25 | ns |
| **Number of bunches** | 5973 | |
| **Bunch population** | 2.0E+11 | |
| **Accumulated particles per beam** | 1.2E+15 | |
| **Normalized rms transverse emittance** | 4.1 | mm |
| **Beam life time due to burn-off** | 9.3 | hour |
| **Total / inelastic cross section** | 140 | mbarn |
| **Reduction factor in luminosity** | 0.96 | |
| **Full crossing angle** | 71 | mrad |
| **rms bunch length** | 75.5 | mm |
| **rms IP spot size** | 9.0 | mm |
| **Beta at the 1st parasitic encounter** | 19.5 | m |
| **rms spot size at the 1st parasitic encounter** | 46.1 | mm |
| **Stored energy per beam** | 6.3 | GJ |
| **SR power per beam** | 2.1 | MW |
| **SR heat load at arc dipoles** | 63.9 | W/m |
| **Energy loss per turn** | 2.45 | MeV |



ISBN 978-3-95450-172-4

$$x^2 = \frac{4f(x)}{\pi\xi_{y,max}N_{IP}} \quad (17)$$

and $x_*$ in eq. 15 could be solved by the following equation

$$x_*^2 = \frac{4f(x_*)^2}{H_0\pi\gamma}\sqrt{\frac{6\pi R}{r_p N_{IP}}} \quad (18)$$

Before making any application of eqs. 15 and 18 to estimate a hadron circular collider beam-beam tune limit, we made a comparison with the existing machines and some machines under design as shown in Tab. 6 [13]. It is obvious that the analytical estimation gives good prediction.

By using SppC's parameter [11], shown in Tabs. 7 and 8, one gets from eqs. 15 and 18 that $\xi_{SppC,y,max} = 0.06$.

## CONLCUSION

In this paper, we reviewed three analytical formulae of the beam-beam tune limit estimation for $e^+e^-$ circular colliders, and one for hadron colliders. It is shown that Gao's formulae, both for lepton and hadron circular colliders, provide reasonable estimations, and they are used to make CEPC and SppC parameter optimizations.

## REFERENCES


[1] The Orsay Storage Ring Group, Status Report on ACO. http://lss.fnal.gov/conf/C710920/p127.pdf

[2] J. Seeman, in Nonlinear Dynamics Aspects of Particle Accelerators, Lecture Notes in Physics Vol. 247 (Springer-Verlag, New York, 1985), p. 121.

[3] J. Gao, "Emittance growth and beam lifetime limitations due to beamÍCbeam effects in $e^+e-$ storage ring colliders", *Nucl Instr. and Methods*, A533 (2004), p. 270.

[4] J. Gao, "Analytical expression for the maximum beam-beam tune shift in electron storage rings", *Nucl. Instr. and Methods*, A413 (1998), p. 431. (or see Proceedings of PAC97, April 1997, p. 1605)

[5] R. Assmann and K. Cornelis, "The beam-beam interaction with presence of strong radiation damping", EPAC2000, P. 1187.

[6] E. Keil and R. Talman, "Scaling of luminosity data between $e^+e^-$ storage rings", Part. Acc. Vol. 14, 1983, p.109.

[7] S. Peggs, Talk at the Workshop on beam-beam effects (LHC99), CERN, 1999.

[8] R. Talman, "Specific luminosity limit of e+e- colliding rings", PRST-AB, Vol. 5, 081001 (2002).

[9] J. Gao, "Analytical estimation of the beam-beam interaction limited dynamic apertures and lifetimes in $e^+e^-$ circular colliders", it Nucl. Instr. and Methods, A463 (2001), p. 50.

[10] D. Wang, et al., "Optimization parameter design of a circular $e^+e^-$ Higgs factory", Chinese Physics C Vol. 37, No. 9 (2013) 097003.

[11] J. Gao, "Electron Positron Circular Collider, Planning and Progress in China", LCWS2014 Belgrade, Oct. 6-10, 2014.

[12] J. Gao, Private note, 2014, and J. Gao "Analytical formulae for the maximum beam-beam tune shift in circular colliders", LAL-SERA-99-148.

[13] ICFA Mini-Workshop on Beam Beam Effects in Hadron Colliders CERN, Geneva, Switzerland, 18ÍC22 March 2013. CERNÍC2014ÍC004, 17 July 2014.


ISBN 978-3-95450-172-4

# BEAM-BEAM EFFECTS IN CEPC AND TLEP

Kazuhito Ohmi, KEK

*Abstract*

Higgs particles are discovered in LHC at the mass of 126 GeV. The mass is in possible range for circular Higgs factory. Two proposals for high energy electron positron colliders are being submitted from Europe and China. The colliders are called TLEP and CEPC, respectively. It was considered that very high energy lepton colliders are inefficient for two reasons; high beam power loss and strong beamstrahlung in the beam-beam interaction. We discuss the beamstrahlung in two colliders theoretical and simulations.

## INTRODUCTION

Studying the beam-beam effects is essential to determine the beam parameters in colliders. In Higgs factories, beamstrahlung, which is synchrotron radiation emitted by beam-beam collision, seriously affects the bunch length. To get high luminosity $L \sim 10^{34}$ cm$^{-2}$s$^{-1}$, vertical beta function at the interaction point (IP) is squeezed strongly, since the successes and ongoing project of B factories, PEP-II, KEKB and SuperKEKB. The bunch lengthening may break hourglass condition $\beta_y > \sigma_z$. The design parameter should be determined with taking into account the bunch lengthening. The colliders, PEP-II and KEKB, have operated with the condition $\beta_y \leq \sigma_z$. Simulations of beam-beam interaction have worked as powerful tool for optimization of the operating condition. For Higgs factories, highly qualitative design based on the simulations can be made possible. Table 1 shows the parameters of CEPC and TLEP.

Beamstrahlung is inevitable subject in very high energy e+e- circular colliders [1, 3]. Energy of photon emitted by beam-beam force, which is called beamstrahlung, is much harder than that of bending magnet, because of orbit radius is smaller than the bending radius. High relativistic factor $\gamma$ shift photon energy higher. We discuss beam-beam interaction with considering beamstrahlung as a key subject.

## BEAMSTRAHLUNG

Beamstrahlung is synchrotron radiation emitted during the beam-beam interaction. The curvature of beam orbit during the beam-beam interaction is far smaller than that of bending magnets. Energy of emitted photon during the interaction is very high and the number is less than one per collision. Energy spread of the beam is damaged by the emission, which is hard and stochastic.

We first sketch the beamstrahlung using analytic formulae. Linearized Beam-beam force is written as follows,

$$(\Delta p_x, \Delta p_y) = \frac{2N_e r_e}{\gamma} \frac{1}{\sigma_x + \sigma_y} \left( \frac{x}{\sigma_x}, \frac{y}{\sigma_y} \right). \quad (1)$$

where $N_e$ is the bunch population, $r_e$ the classical electron radius, and $\sigma_{x/y}$ is horizontal/vertical beam size at IP. $p_{x,y}$, which is normalized by total momentum $p_0$, is $(1+\delta)dx/ds$, where $\delta = \Delta E/E_0$ is energy deviation for the design beam energy. Substituting $x = \sigma_x$ and $y = \sigma_y$ as typically numbers, the momentum change is expressed by

$$\Delta p_{xy} = \frac{2N_e r_e}{\gamma(\sigma_x + \sigma_y)} \quad (2)$$

The beam-beam force acts during the interaction $\Delta s = \sqrt{\pi/2}\sigma_z$, where it is notified that the colliding beam also moving light speed. The curvature of a beam particle is expressed by

$$\frac{1}{\rho} \approx \frac{\Delta p_{xy}}{\Delta s} = \frac{2Nr_e}{\sqrt{\pi/2}\gamma\sigma_x\sigma_z}. \quad (3)$$

The orbit radii are 23.3 and 38.7 m for CEPC and TLEP-H, respectively. While the radii of bending magnets are 6,094 and 11,000 m, respectively. The radii during the beam-beam interaction are far smaller than those of bending magnets.

The synchrotron radiation is emitted by the beam particles moving with curvature $1/\rho = \sqrt{1/\rho_x^2 + 1/\rho_y^2}$. Characteristic energy of the synchrotron radiation is expressed by

$$u_c = \hbar\omega_c = \frac{3\hbar c\gamma^3}{2\rho}. \quad (4)$$

The energies are 0.16 and 0.099 GeV for CEPC and TLEP-H, respectively. The energies is far less than the beam energy, $E_0 = 120$ GeV.

Spectrum of the synchrotron radiation is expressed using K Bessel function

$$\frac{dn_\gamma(\omega)}{d\omega} = \frac{\sqrt{3}\alpha\gamma\Delta s}{2\pi\rho\omega_c} S(\omega/\omega_c) \quad (5)$$

where

$$S(\xi) = \int_\xi^\infty K_{5/3}(y)dy. \quad (6)$$

$K$ is K-Bessel function and $\alpha = e^2/4\pi\epsilon_0\hbar c \approx 1/137$ is the fine structure constant.



ISBN 978-3-95450-172-4

Table 1: Parameter Table of Higgs Factories

| | CEPC | TLEP-H | TLEP-t | unit |
|---|---|---|---|---|
| circumference | 53.6 | 100 | 100 | km |
| energy | 120 | 120 | 175 | GeV |
| bunch population | 3.71 | 0.46 | 1.4 | $\times 10^{11}$ |
| emittance $\varepsilon_{x/y}$ | 6.8/20 | 0.94/1.9 | 2/2 | nm/pm |
| $\beta^*_{x/y}$ | 800/1.2 | 500/1 | 1000/1 | mm |
| damping time $\tau_{xy/z}/T_0$ | 79.70/39.85 | 144/72 | 46/23 | turns |
| natural bunch length | 2.26 | 0.81 | 1.16 | mm |
| natural energy spread | 0.13 | 0.10 | 0.14 | % |
| synchrotron tune | 0.206 | 0.096 | 0.10 | |
| number of bunches | 50 | 1360 | 98 | |
| number of IP | 2 | 4 | 4 | |
| luminosity | 1.82 | 6.0 | 1.8 | $10^{34}$ cm$^{-2}$s$^{-1}$/IP |
| Beamstrahlung | | | | |
| bunch length | 2.58 | 1.17 | 1.49 | mm |
| energy spread | 0.15 | 0.14 | 0.19 | % |

Number of emitted photon is obtained by integrating over $\omega$.

$$n_\gamma = \int_0^\infty \frac{dn_\gamma(\omega)}{d\omega} d\omega = \frac{5\sqrt{3}\alpha\gamma}{6\rho}\Delta s \tag{7}$$

The number of photon emitted by the radiation is expressed by the beam parameters in Eq.(2)

$$n_\gamma = \frac{5}{\sqrt{3}}\frac{\alpha N_e r_e}{\sigma_x + \sigma_y}. \tag{8}$$

Actually $\rho$ varies along $s$ and depends on $x, y$ due to the nonlinear beam-beam force. Taking into account of the variations, the number of photon is given by [2, 3]

$$n_\gamma = 2.12\frac{\alpha r_e N_e}{\sigma_x + \sigma_y}, \tag{9}$$

Averaged energy of emitted photon is given by integral of the power spectrum as follows,

$$\langle u \rangle = \frac{3}{5\pi}\hbar\omega_c \int_0^\infty \xi S(\xi) d\xi = \frac{8}{15\sqrt{3}}\hbar\omega_c. \tag{10}$$

Multiplying the number of photon, averaged energy loss of a beam particle is obtained as follows,

$$\langle \Delta E \rangle = n_\gamma \langle u \rangle \Delta s = \frac{2\hbar\alpha c\gamma^4}{3\rho^2}. \tag{11}$$

The energy loss is expressed using accelerator parameters as

$$\frac{\langle \Delta E \rangle}{E_0} = \frac{16\sqrt{\pi/2}}{3\pi} r_e^3 \gamma \left(\frac{N_e}{\sigma_z(\sigma_x + \sigma_y)}\right) \sigma_z. \tag{12}$$

Considering trajectory dependence again, the averaged energy loss is given by [2, 3],

$$\langle d\delta_{BS} \rangle = \frac{\langle \Delta E \rangle}{E_0} = 0.864 r_e^3 \gamma \left(\frac{N_e}{\sigma_z(\sigma_x + \sigma_y)}\right)^2 \sigma_z. \tag{13}$$

The square average of photon energy is given by [4]

$$\langle u^2 \rangle = \frac{3}{5\pi}(\hbar\omega_c)^2 \int_0^\infty \xi^2 S(\xi) d\xi = \frac{11}{27}(\hbar\omega_c)^2. \tag{14}$$

The diffusion of beam energy due to the square average is given by

$$n_\gamma \langle u^2 \rangle = \frac{55}{24\sqrt{3}} \frac{r_e \hbar m c^3 \gamma^7}{\rho^3} \Delta s. \tag{15}$$

The contribution to the energy spread is expressed by

$$\frac{\langle \Delta E^2 \rangle}{E_0^2} = \frac{n_\gamma \langle u^2 \rangle}{E_0^2} = n_\gamma \frac{11}{27}(\hbar\omega_c)^2 = \frac{275}{64 n_\gamma}\left(\frac{\langle \Delta E \rangle}{E_0}\right)^2 \tag{16}$$

The other diffusion source is randomness of $n_\gamma$, which is less than 1. The quantum effect had been studied in Ref.[2, 3] The deviation of the energy loss is given for round Gaussian beam as

$$\sqrt{\langle d\delta_{BS}^2 \rangle} = \langle d\delta_{BS} \rangle \sqrt{0.1639 + \frac{5.129}{n_\gamma}}. \tag{17}$$

That for flat Gaussian beam is given by

$$\sqrt{\langle d\delta_{BS}^2 \rangle} = \langle d\delta_{BS} \rangle \sqrt{0.333 + \frac{4.583}{n_\gamma}}. \tag{18}$$

The diffusion is accumulated during the radiation damping time and equilibrium energy spread is realized. Equilibrium energy spread for radiation damping and beamstrahlung is given by

$$\sigma_{\delta,BS} = \frac{1}{2}\sqrt{\tau_z N_{IP}} \sqrt{\langle d\delta_{BS}^2 \rangle}, \tag{19}$$

ISBN 978-3-95450-172-4

Table 2: Parameters Concerning Beamstrahlung

| | CEPC | TLEP-H | TLEP-t | unit |
|---|---|---|---|---|
| $\gamma$ | 2.35 | 2.35 | 3.42 | $10^5$ |
| $\rho$ | 23.3 | 38.7 | 88.6 | m |
| $u_c$ | 0.16 | 0.099 | 0.13 | GeV |
| $n_\gamma$ | 0.21 | 0.092 | 0.13 | |

where $\tau_z$ is the longitudinal radiation damping time in the unit of turn. Taking into account of energy spread due to the synchrotron radiation, total energy spread is given by

$$\sigma_{\delta,tot} = \sqrt{\sigma_{\delta,SR}^2 + \sigma_{\delta,BS}^2}. \quad (20)$$

Enlargement of energy spread induces bunch lengthening, $\sigma_{z,tot} = \sigma_{z,SR}\sigma_{\delta,tot}/\sigma_{\delta,SR}$. The lengthening makes relax the beamstrahlung. Therefore the bunch length and energy spread are solved self-consistently.

Parameters related to beamstrahlung for CEPC and TLEP are summarized in Table 2.

### *Simulation of Beamstrahlung*

Figure 1 sketches the simulation scheme of the beamstrahlung during beam-beam interaction. A beam particle (red line) passes through a bunch (blue ellipse), which is sliced several into pieces. Trajectory of the particle is calculated slice-by-slice by using Bassetti-Erskine formula [5] or Poisson solver based on Particle In Cell method[6]. The bunch is sliced into 20 pieces for the simulations presented in this paper. Synchrotron radiation is emitted by the interaction of slices with the probability of Eq.(7). Both beams move with the light speed. The traveling distance of particles between interactions with i-th and (i+1)-th slices is expressed by

$$ds = \frac{z_i - z_{i+1}}{2}. \quad (21)$$

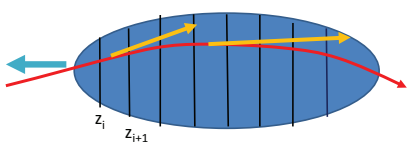


Figure 1: Simulation scheme of the beamstrahlung during beam-beam interaction.

Two types of beam diffusion are examined and compared in this paper.

**Gaussian excitation model** Photon is generated by the probability $n_\gamma$ in Eq.(7). The average energy and square average are given Eqs.(10) and (14). The deviation of the photon energy is expressed by

$$\langle u^2 \rangle - \langle u \rangle^2 = \frac{211}{675}(\hbar\omega_c)^2. \quad (22)$$

Beamstrahlung, energy loss of the beam particle, is evaluated by the photon emission with the energy, which is generated by Gaussian random numbers with the average energy in Eq.(10) and the deviation in Eq.(22).

**Realistic radiation** Photon is generated by the probability $n_\gamma$ in Eq.(7) again. The photon higher than $\hbar\omega$ is generated by the probability as follows,

$$\mathcal{N}_\gamma(\omega) = \frac{3}{5\pi}\int_{\omega/\omega_c}^{\infty} S(\xi)d\xi \quad (23)$$

where $\mathcal{N}_\gamma(0) = 1$ and $\mathcal{N}_\gamma(\infty) = 0$. The energy of emitted photon is determined by the inverse of $\mathcal{N}$,

$$\omega = \mathcal{N}_\gamma^{-1}(\hat{r}) \quad (24)$$

where $\hat{r}$ is uniform random number $0 < \hat{r} < 1$. Figure 2 shows $\mathcal{N}_\gamma(\omega)$.

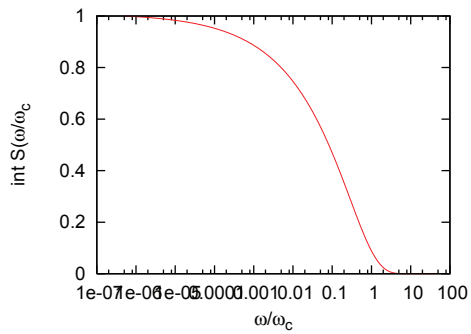


Figure 2: Plot of $\mathcal{N}_\gamma(\xi)$.

## EVOLUTION BEAM ENERGY DISTRIBUTION DUE TO BEAMSTRAHLUNG

Photon energy spectrum is obtained so that macroparticles ($10^7$) collide with Gaussian beam with the design parameters (natural beam sizes determined by synchrotron radiation). Figure 3 shows energy spectrum of the emitted photon. The number of photon emission is 20% of the beam particle ($n_\gamma = 0.2$) for single collision in CEPC (Table 2). The line shown in the figure draw $S(\xi)$, where $u_c = 0.13$ GeV is slightly smaller than the analytical estimate using Eq.(4) and (3), $u_c = 0.16$ GeV. The blue line in the figure is Gaussian distribution using $\langle u^2 \rangle$ in Eq.(10), $0.2N_e(2\pi\langle v^2\rangle)^{-1/2}\exp(-v^2/2\langle v^2\rangle)dv$, where $v \equiv u/E_0$. The tail of energy distribution remarkably spreads higher energy side for K Bessel formula compare than Gaussian. Needless to say, the spectrum of $S(\xi)$ and Gaussian give the same square average $\langle u^2 \rangle$. When $n_\gamma$ is large and characteristic energy ($u_c$) is much smaller than the beam energy like radiation of bending magnet, the tail of energy distribution is not observable in equilibrium distribution. For beamstrahlung in very high energy colliders, $n_\gamma$ is small and $u_c$ is large.



ISBN 978-3-95450-172-4

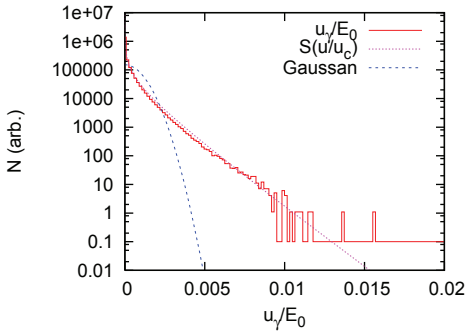


Figure 3: Energy spectrum of emitted photon.

We next focus on evolution of beam energy distribution, in which two beams with the design natural bunch length and energy spread start collision. Figure 4 shows turn-by-turn change of the energy distribution due to the beamstrahlung. Pictures (a) and (b) show evolutions of the energy distribution without and with synchrotron motion, respectively. Each line shows the distribution after beam-beam collisions, whose number is marked in the figure. The macro-particle number is $10^7$. The energy distribution spreads negative direction (loss) for the absence of synchrotron motion. Though the tail is accumulated, the number is not large, several 10 lower then -10$\sigma_\delta$ = 0.13% of the total energy. When synchrotron motion is taken into account, the tail appear in both side, $\sim \pm 10\sigma_\delta$. The number of particles out of $\pm 10\sigma_\delta$ are less. The beam loss just after injection does not seem serious.

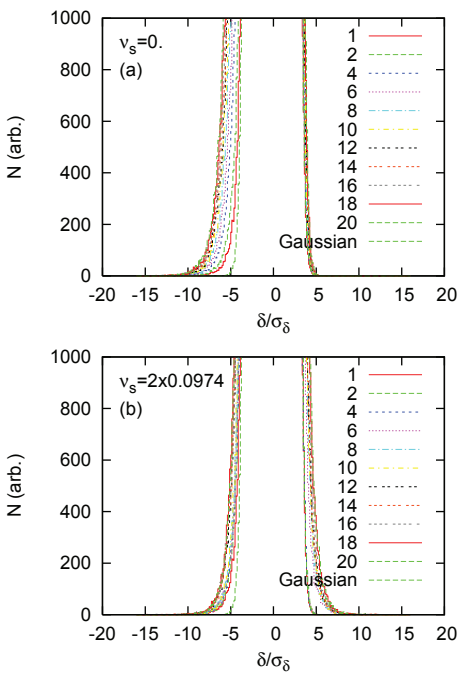


Figure 4: Energy spread change. Pictures (a) and (b) show evolutions of the energy distribution without and with synchrotron motion, respectively.

Figure 5 shows equilibrium distribution of the energy spread. Energy and longitudinal distributions. In the whole distribution of $z$ and $\delta$, those of K Bessel excitations is not distinguished from those with Gaussian. The difference is clear in the tail distribution of the right two pictures.

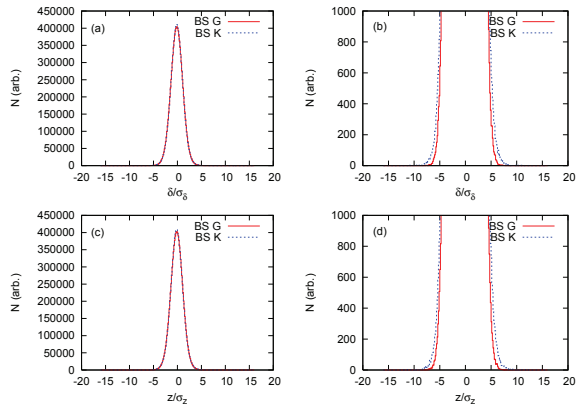


Figure 5: Equilibrium distribution of the energy deviation and z. Pictures (a) and (b) are whole and tail distribution in $z$, respectively. Pictures (c) and (d) are for the energy deviation $\delta$.

## LUMINOSITY EVALUATION USING SIMULATION

Luminosity is evaluated by the weak-strong and strong-strong simulations, which include beamstrahlung treated in previous section.Beamstrahlung causes the energy spreading, which results bunch lengthening. We assume the intensity of both beam is the same, thus bunch length due to beamstrahlung is also the same. The bunch length of the weak beam is calculated turn-by-turn, and is taken average in average 100-1000 turns. The bunch length of the strong beam is revised every 100-1000 turns. The bunch length in the weak-strong simulation is revised self-consistently every 100-1000 turns. The bunch length is calculated turn-by-turn in the strong-strong simulation.

Figure 6 shows evolutions of luminosity and beam sizes $\sigma_x, \sigma_y, \sigma_z$ for CEPC. Three lines are drawn in the figure; red, blue, and green correspond to Gaussian, K Bessel and none for beamstrahlung, respectively. The radiation damping time is 80 turns in transverse, thus the simulation is performed during 12 radiation damping time (1000 turns). Beamstrahlung causes bunch lengthening, which results vertical beam size blowup and luminosity degradation. There is no difference in luminosity and beam sizes between Gaussian and K Bessel for beamstrahlung.

The simulation was done for several bunch populations, 0.6×, 0.8×, 1×,1.2× of the design population, $N_e = 3.71 \times 10^{11}$. Figure 7 shows luminosity and beam sizes as function of bunch population. The horizontal size decreases for increasing bunch population due to dynamic beta $\nu_x/IP = 0.54$. Other parameters, luminosity, $\sigma_y$ and

ISBN 978-3-95450-172-4

$\sigma_z$, increase for higher bunch population. Luminosity does not increase quadratically, since the increases of $\sigma_y$ and $\sigma_z$.

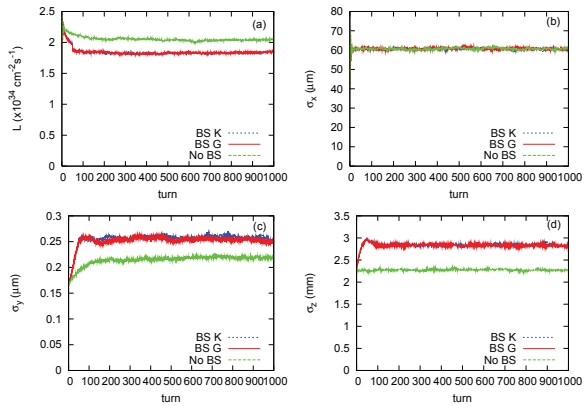


Figure 6: Luminosity and beam sizes for CEPC in a weak-strong simulation (BBWS).

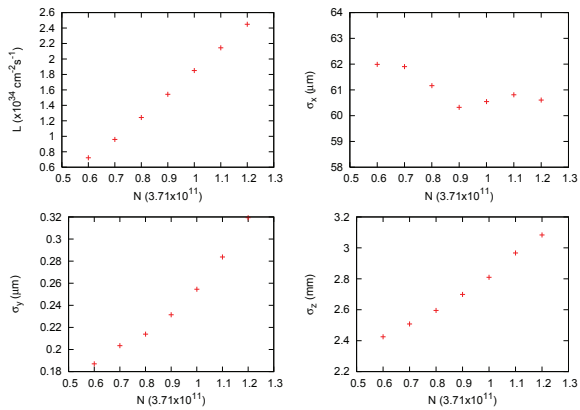


Figure 7: Luminosity and beam sizes depending on the bunch populations for CEPC in a weak-strong simulation using BBWS.

Luminosity and beam sizes are also evaluated by a strong-strong simulation using a code "BBSS"[6]. Figure 8 shows evolution of luminosity and beam sizes, $\sigma_x, \sigma_y, \sigma_z$. Luminosity evolution of three tune operating points are depicted in plot (a). Depending on tune (0.54,0.58), luminosity is unstable. The tune is factional part of IP to IP, the total fractional tune is twice for CEPC. Plots (b)-(d) show evolution of the beam sizes for stable (0.54,0.61) and unstable (0.54,0.58) cases. In unstable case, vertical beam sizes of both beams increase correctively. We use the operating point (0.54,0.61) hereafter [7, 8].

The simulation is performed for several vertical beta function at IP, $\beta_y^* = 1.2$ (design),2,3,4, and 5 mm. Figure 9 shows geometrical beam-beam tune shift and luminosity as function of $\beta_y^*$. Geometrical and simulated luminosities are plotted by blue and red points, respectively, in the plot (b), where "geometrical" means beam-beam parameter and luminosity calculated by design bunch shape. The hourglass effect and bunch lengthening due to beamstrahlung is taken into account in the tune shift. The tune shift is monotonically increases for $\beta_y^*$, but is not linear. Geometrical and simulated luminosity by BBSS are plotted. Geometrical luminosity decreases for higher $\beta_y^*$. The simulation shows mild decrease compare than geometrical one. This behavior is due to dynamic beta and beam-beam limit under hourglass effect.

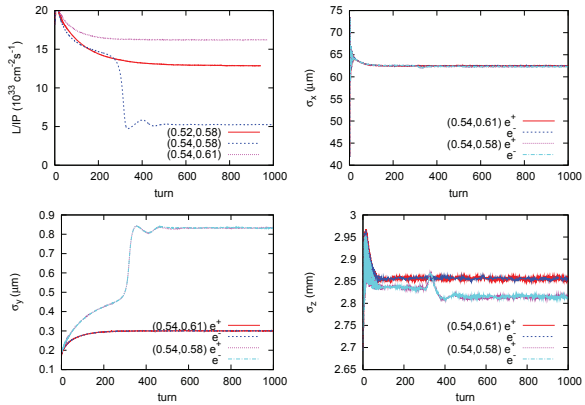


Figure 8: Luminosity and beam sizes in CEPC calculated by a strong-strong simulation (BBSS).

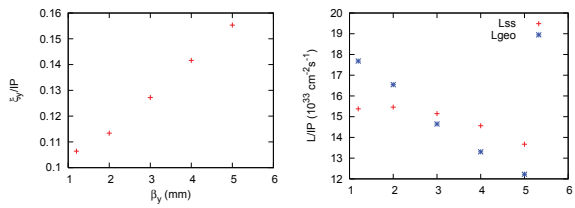


Figure 9: Geometrical beam-beam tune shift and luminosity as function of $\beta_y^*$. Geometrical and simulated luminosities are plotted by blue and red points, respectively, in the plot (b).

In a real operation of an accelerator, beam current of one beam sometimes is lost considerable amount. The accelerator is expected to be operated stably under the occasion. Figure 10 shows evolution of the luminosity and beam sizes for current asymmetry, where one beam (electron beam in this case) has a half intensity of the design. Luminosity degrades one third (not half) and vertical size and bunch length of electron beam increase. The bunch length of positron beam is going toward the design value. The lifetime of the weak($e^-$)-beam is discussed in next section.

Figure 11 shows tolerance of luminosity for vertical dispersion. The luminosity degrades for $\eta_y = 0.02 - 0.05$ mm clearly. This result is requirement for IP optics correction.

Table 3 summarizes luminosity given by the simulations for CEPC and TLEP[9].



ISBN 978-3-95450-172-4

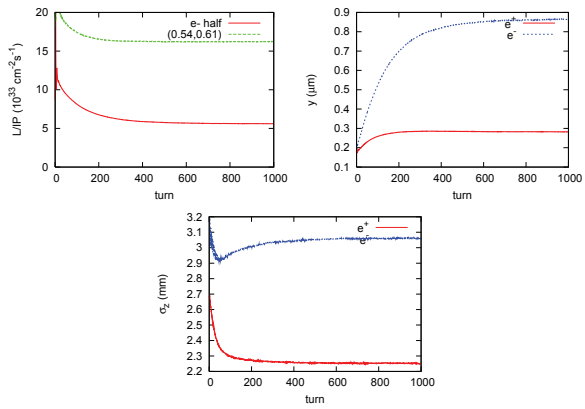


Figure 10: Luminosity and beam sizes for current asymmetry in CEPC calculated by a strong-strong simulation (BBSS).

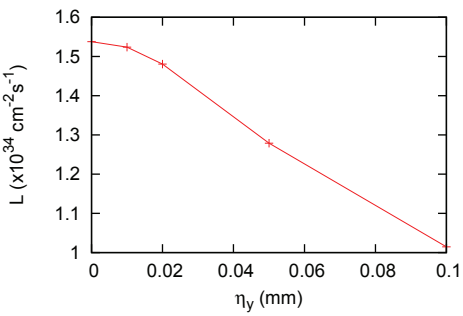


Figure 11: Luminosity as function of vertical dispersion calculated by a strong-strong simulation (BBSS).

Table 3: Calculated Luminosity and Bunch Length[9]

| | TLEP/FCC-ee | | | | | Ce- |
|---|---|---|---|---|---|---|
| | Z | Z (cr. w.) | W | t | H | pC |
| | luminosity [$10^{34}$ cm$^{-2}$s$^{-1}$] | | | | | |
| analyt. | 28 | 219 | 12 | 6.0 | 1.7 | 1.8 |
| w-s. | 21 | 150 | 13 | 6.9 | 2.0 | 1.6 |
| s-strong | — | — | — | 7.5 | 2.2 | 1.6 |
| | $\sigma_z$ [mm] | | | | | |
| w/o BS | 1.64 | 1.9 | 1.01 | 0.81 | 1.16 | 2.3 |
| analyt. | 2.56 | 6.4 | 1.49 | 1.17 | 1.49 | 2.7 |
| w-s. | 2.8 | 7.9 | 1.5 | 1.2 | 1.6 | 2.7 |
| s-strong | — | — | — | 1.3 | 1.72 | 2.9 |

## LIFETIME EVALUATION

Beam lifetime is evaluated by the equilibrium distribution. In the equilibrium, outgoing flow due to diffusion from an aperture is equal to damping flow due to damping[4]. The damping flow is continuously and easily estimated. Another method for the lifetime evaluation is direct simulation, in which number of particle outgoing the aperture is counted.

We consider equilibrium distribution $f(J_i)$ expressed by $J_i$. $J_i$ is constant for betatron/synchrotron oscillation. The incident flow at an aperture $J_{i.max}$ for time step $dt$ is given by multiplication of the density at $J_{i,max}$ and damping of $J_i$ in $dt$,

$$\frac{dN}{dt} = f(J_i)\frac{dJ_i}{dt} \tag{25}$$

The radiation damping time is given by

$$\frac{dJ_i}{dt} = -\frac{2J_i}{\tau_i} \tag{26}$$

The assumption, in which outgoing flow is the same as incident flow, means that the beam lifetime ($\tau_\ell$) is given by

$$\tau_\ell = \frac{N}{\frac{dN}{dt}} = \frac{t_i}{2J_{i,max}f(J_{i,max})} \tag{27}$$

For example of Gaussian distribution, $f(J_i) = \varepsilon_i^{-1}\exp(-J_i/\varepsilon_i)$, the lifetime, which is popular formula, is given by

$$\tau_\ell = \frac{\tau_i}{2}\frac{\varepsilon_i}{J_{i,max}}\exp(J_{i,max}/\varepsilon_i) \tag{28}$$

where $J_{i,max} = \beta_i x_{max}^2$.

Figure 12 shows beam tail distribution $g(r_i)$ in $x, y, z$ directions. The distributions for bunch populations, $(0.6, 0.8, 1.0, 1.2) \times 3.71 \times 10^{11}$ are drawn. The horizontal axes is $r_i = \sqrt{2J_i/\varepsilon_i}$. The lifetime formula is written as

$$\tau_\ell = \frac{\tau_i dr_i}{r_{i,max}g(r_{i,max})dr_i} \tag{29}$$

where $r_{z(y),max} = z(y)_{max}/\sigma_{z(y)}$. Figure 13 shows the lifetime for aperture $r_{i,max}$ in each bunch population. Lifetime limited by horizontal aperture is not plotted, since the horizontal distribution does not have long tail.

We discuss the beam halo and lifetime, when one beam is lost to a half intensity. The beam sizes of the strong beam (without loss) approach to the design values, while those of the weak beam (with loss) blow up. Figure 14 shows the tail distributions of z and y, and related life times. It may be hard to keep the beam, once a loss starts.

Figure 15 shows Luminosity and lifetime dependence on the natural bunch length.

The same simulations are performed for TLEP. Figure 16 and 17 shows tail distributions and lifetime for TLEP. Figure 18 shows results of beam loss simulation with the aperture limit of $\delta_{max} = 1.5\%$. The lifetime is 26 min

ISBN 978-3-95450-172-4

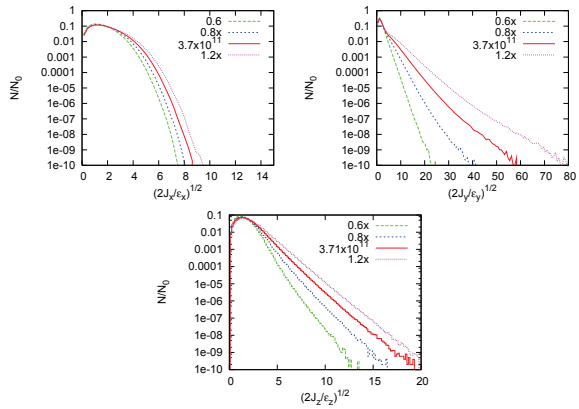


Figure 12: Beam halo distribution in CEPC.

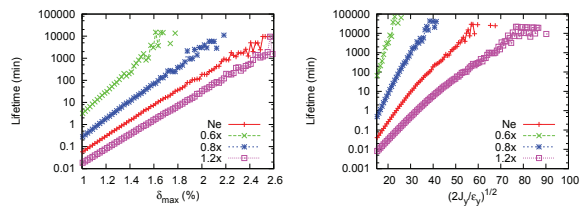


Figure 13: Beam lifetime due to energy and vertical aperture for CEPC.

(H) and 0.31 min (t). The lifetime estimated by the damping flow in Figure 17 agree with that given by the beam loss simulation.

The lifetime is evaluated by analytical formulae [3, 10]. Simulations [10, 11] including results in this paper have shown shorter lifetime than the formulae. Taking into account of the dynamic beta, the formulae gave similar lifetime as these simulations [12].

## CONCLUSIONS

Gaussian and realistic K Bessel beamstrahlung excitation have been examined. Longitudinal beam tail due to beamstrahlung is enhanced. It is essential for lifetime. No difference between Gauss and K Bessel excitations in luminosity and core beam sizes in the both of weak-strong and strong-strong simulations. Strong-strong simulation, (0.54,0.61) is a nice operating point. [7]. Luminosity simulation can be done using effective bunch length and energy spread for beamstrahlung in usual beam-beam codes.

Dependence on luminosity for $\beta_y^* = 1.2-3$ mm is weak. $\beta_y^* = 2$ mm may be a good solution. Tolerance for vertical dispersion, $\eta_y^* < 0.05$ mm. For asymmetric beam, an equilibrium state exists. Lifetime of weak beam should be cared. Long term tracking containing beamstrahlung has been done using weak strong simulation. Beam lifetime was evaluated by the longitudinal and transverse distributions. The lifetime estimated by the damping flow agree with the beam loss simulations. $\delta_{max} > 1.8\%$ (100 min) is required for CEPC. $y_{max}/\sigma_y$¿40 (100 min) is required in transverse.

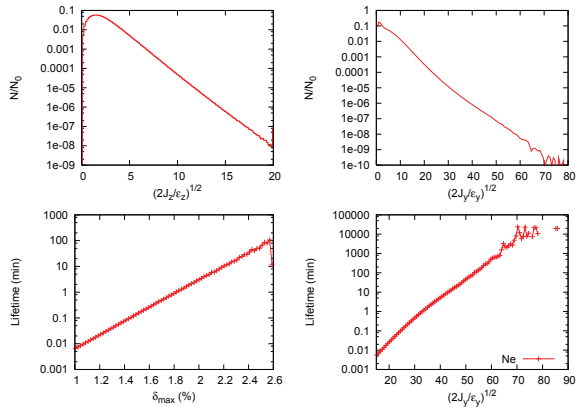


Figure 14: Beam halo distribution and lifetime in CEPC, when one beam is lost to a half intensity.

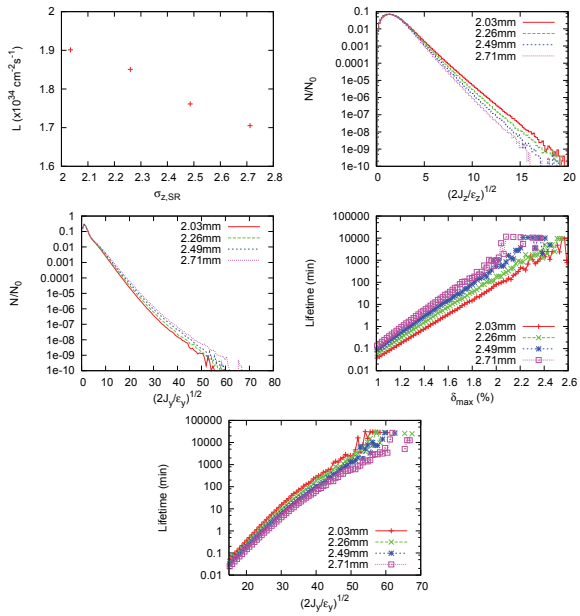


Figure 15: Luminosity and lifetime depending on the natural bunch length.

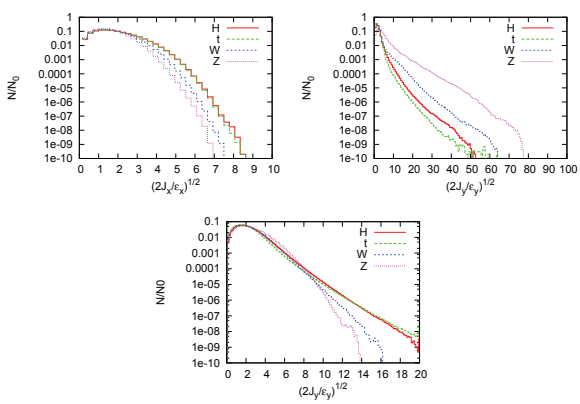


Figure 16: Beam halo distribution in TLEP-H.



ISBN 978-3-95450-172-4

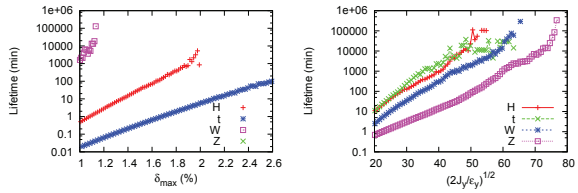


Figure 17: Beam lifetime due to energy and vertical aperture for TLEP.

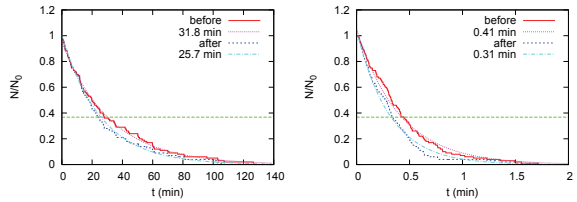


Figure 18: Beam loss in TLEP-H and t.

The author thanks fruitful discussions with W. Chou, M. Koratzinos, D. Shatilov, Y. Zhang, F. Zimmermann.

## REFERENCES

[1] K. Yokoya, "Scaling of High-Energy e+e- Ring Colliders," KEK Accelerator Seminar, 15 March 2012.

[2] K. Yokoya, "Quantum Correction To Beamstrahlung Due To The Finite Number Of Photons," Nucl.Instrum.Meth. A251 (1986) 1.

[3] V. Telnov, "Restriction on the energy and Luminosity of $e^+e^-$ Storage Rings due to Beamstrahlung," Phys. Rev. Lett. 110, 114801 (2013).

[4] M. Sands, "The Physics of Electron Storage Rings," SLAC-R-121 (1970).

[5] M. Bassetti and G. Erskine, CERN-ISR TH/80-06 (1980).

[6] K. Ohmi, Phys. Rev. E62, 7287 (2000). K. Ohmi et. al., Phys. Rev. ST-AB 7, 104401 (2004).

[7] D. Shatilov, Y. Zhang, private communications.

[8] Y. Zhang et al.,IPAC14, THPRI003.

[9] K. Ohmi, F. Zimmermann, IPAC14, THPRI004.

[10]A. Bogomyagkov, et al., "Beam-Beam Effects Investigation and Parameter Optimization for Circular $e^+e^-$ Collider TLEP to study the Higgs Boson," PRST-AB 17, 041004 (2014).

[11]S. White and N. Mounet, "Beam-Beam Studies for TLEP (and Update on TMCI)," 6th TLEP workshop, CERN (2013).

[12]M. Koratzinos, in this proceedings.



ISBN 978-3-95450-172-4

# INTERACTION REGION MAGNETS

E.Paoloni, I.N.F.N. and University of Pisa, Italy

*Abstract*

The magnets of the very final focus are among the most challenging devices of a collider. They must be very compact to leave large acceptance for the surrounding detectors still providing strong focusing power together with excellent field quality not to degrade the collider dynamic aperture. Being all placed very close one respect each other and well inside the detector (which is usually a magnetic spectrometer) several strategies to compensate the cross talk of the leaking field and the coupling introduced by the detector field had been recently proposed and some are now in the construction phase. In this paper I will shortly review these novel compensation techniques, the present status of the interaction region magnets now under construction and the main concepts of their design together with a summary of some of the research and development project in the field.

## MAIN ISSUES OF THE INTERACTION REGION MAGNETS IN $e^+e^-$ HIGH INTENSITY COLLIDERS.

The main strategy followed by the $e^+e^-$ collider community in the last decade to increase the luminosity is to decrease the beam size at the Interaction Point (IP). The recipe seems deceptively simple and straightforward but in reality it implies major advances in almost each aspect of the collider. The prototypical example of the last generation high luminosity $e^+e^-$ colliders based on this approach are SuperKEKB [1] which is now in an advanced construction phase and which is expected to start the first phase of commissioning by 2015, together with its main competitor SuperB [2] whose fate was doomed by the economical crisis in Italy and the shortcoming of the promised funding. Both machines are based on the large Piwinski angle collision scheme [3] in which very low emittance beams are demagnified down to a vertical size of roughly 30 nm and brought in collision with a large crossing angle. The main requirements from the machine designers that are hard to met from the perspective of the magnet builders are the quadrupoles of the final doublet. These magnets must be very short and strong to ease the problem of chromaticity correction, they must provide excellent field quality over a large aperture since the horizontal and vertical beta functions are usually reaching their maxima in the final doublet and any spurious sextupolar component will be detrimental for the dynamic aperture of the ring. Additional complications arise from the requirements of the users (i.e. the detector community). The final doublet must be as compact as possible to leave space for the detector surrounding the IR, moreover the losses near the IP must be kept at a minimum to reduce the detrimental effects of machine backgrounds on the performances and life span of the detector. The most worrisome source of background that must be carefully considered in the design of the magnets of the IR are radiative Bhabha (i.e. beam-strahlung) and Touschek that, at least for SuperKEKB and SuperB, are the driving terms of the loss rate near the IP. It turns out that a conventional design with the two quadrupoles closest to the IP shared among the electron and positron rings in the final doublet is not viable since it is not possible to meet at same time the requirement to have the incoming beam on the magnetic axis to reduce the synchrotron radiation fan impinging on the detector and the requirement to have the outgoing beam on the magnetic axis to reduce the radiative Bhabha losses. In essence each beam line must be equipped with its own set of focusing quadrupoles. The main challenge is the limited amount of space available in between the two beam lines that require a very thin magnet design.

## THE SUPERKEKB IR MAGNETS.

The SuperKEKB collider is a major upgrade of the KEKB Bfactory. It will collide 4 GeV positrons on 7 GeV electrons aiming for a final luminosity of $8 \cdot 10^{35}\,\mathrm{Hz/cm^2}$, that is a 40-fold increase with respect to its ancestor. The final doublet [4] (see Fig. 1) consists of several superconducting magnets: 8 main quadrupoles, 4 compensation solenoids, 35 corrector coils and 8 coils to cancel the leaking field of quadrupoles facing the IP on the Low Energy Ring (LER) that perturbs the High Energy Ring (HER) (see Table 1).

Table 1: SuperKEKB IR magnets name and main parameters. GL is the integrated gradient, Z is the distance of the pole face from the IP, $r_{in}$ is the inner radius of the coil, $r_{out}$ is the outer radius of the collar.

| Magnet | GL, T(T/m × m) | Type | Z, mm | $r_{in}/r_{out}$, mm |
|---|---|---|---|---|
| QC2RE | 13.04 (31.12×0.419) | Yoke | 2925 | 59.3/115 |
| QC2RP | 11.54 (28.15×0.410) | Yoke | 1925 | 53.8/93 |
| QC1RE | 25.39 (68.07×0.373) | Yoke | 1410 | 33.0/70 |
| QC1RP | 22.96 (68.74×0.334) | no Yoke | 935 | 25.0/35.5 |
| QC1LP | 22.96 (68.74×0.334) | no Yoke | -935 | 25.0/35.5 |
| QC1LE | 26.94 (72.23×0.373) | Yoke | -1410 | 33.0/70 |
| QC2LP | 11.48 (28.00×0.410) | Yoke | -1925 | 53.8/93 |
| QC2LE | 15.27 (28.44×0.537) | Yoke | -2700 | 59.3/115 |

The quadrupoles closer to the IP are the QC1RP and QC1LP, two vertical focusing magnets acting on the LER. They are quite strong (68.74 T/m) and very thin (the coil thickness is less than 6 mm). The small crossing angle ( 83 mrad ) together with the small $l^\star$ (935 mm) does not allow to shield the magnet with a return yoke surrounding it



ISBN 978-3-95450-172-4

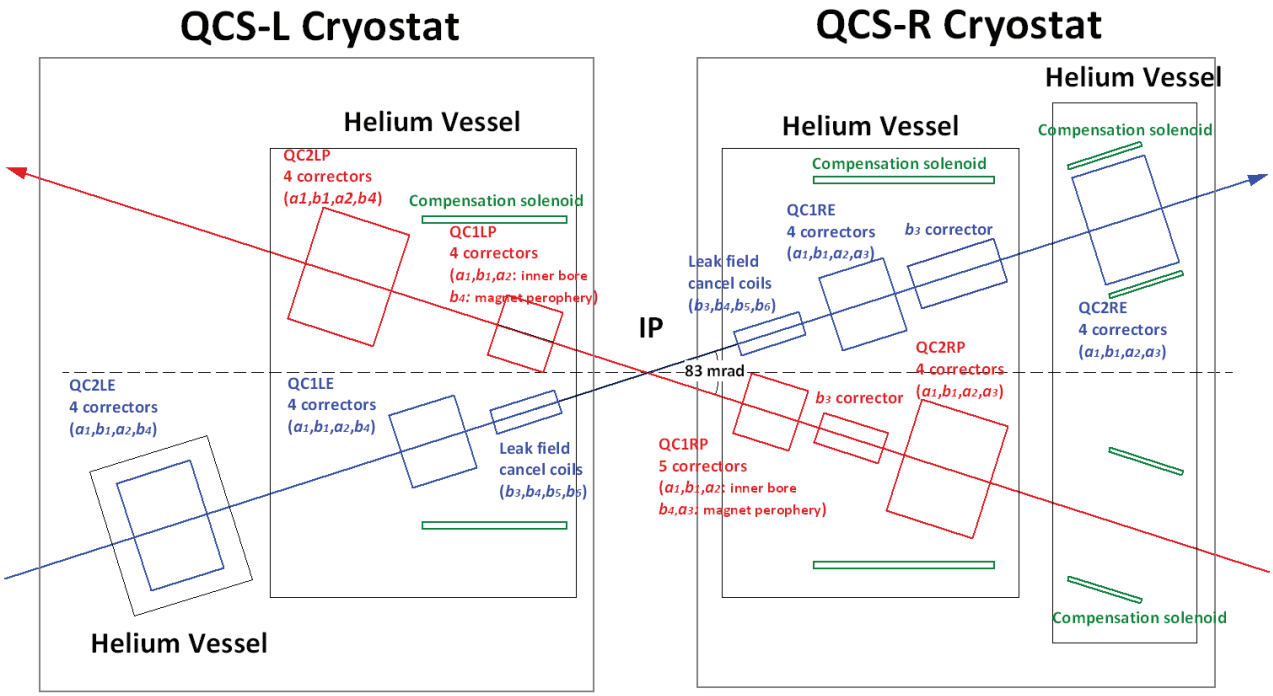


Figure 1: Layout of the Super Conducting magnets of the SuperKEKB IR.

hence a different strategy had been developed to overcome the detrimental effects of the non linear components of the QC1RP and QC1LP on the near running HER.

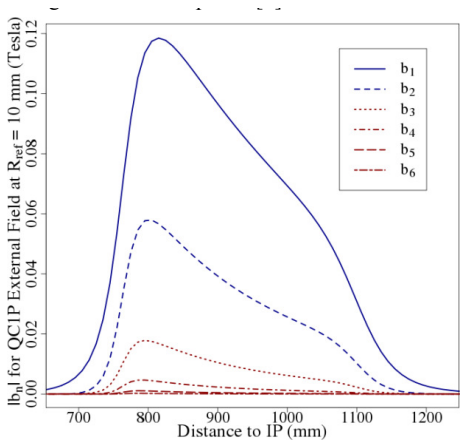


Figure 2: Decomposition into magnetic multipoles for QC1P external field as a function of distance with respect to the IP on the HER beam line. Reference radius 10 mm.

In Fig. 2,from [5], is represented the harmonic decomposition of the external field of the QC1P on a reference radius 10 mm with respect to the HER beam line as a function of distance with respect to the IP. The $b_1$ (dipole) and $b_2$ (quadrupole) components can be accounted for in the model of the HER lattice and can be properly managed. The higher components (see Fig. 3 from [5]) are too large not to impact the HER dynamic aperture hence a set of canceling superconducting coils had been wound around the helium vessel surrounding the HER beam pipe using the serpentine coil design concept [6].

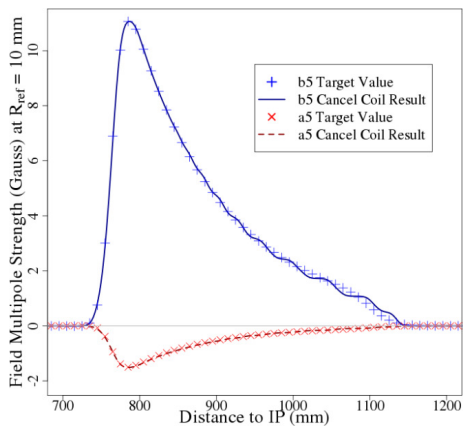


Figure 3: The $b_5$ (decapole) and $a_5$ (skew decapole) field components as a function of distance from the IP. In crosses the target value needed for perfect cancellation of the QC1 leaking field, with continuous and dashed line the field generated by the canceling coils.

## THE SUPERB IR MAGNETS.

The Super*B* collider had been approved by the Italian Research Minister as part of the Italian National Research Plan with a 5 years construction budget and then shut down as a consequence of the economical crisis. It was conceived as an $e^+e^-$ collider composed by an electron LER (4.18 GeV) and a positron HER (6.7 GeV) with a design peak luminosity of $10^{36}$ Hz/ cm$^2$.

ISBN 978-3-95450-172-4

The Super*B* collision scheme required a short focus final doublet to reduce the vertical beta function down to $\beta_y^\star = 0.2$ mm at the IP. The final doublet (see Fig. 4) was designed as a set of permanent samarium cobalt magnets (PM) and superconducting (SC) quadrupoles. The HER (LER in parentheses) PM quadrupoles provided an integrated gradient of 23.1 T (11.2 T) over a magnetic length of 11 cm (7cm). The front pole face had been placed at 38 cm (30 cm) from the IP. The remaining vertical focusing strength would be provided by two (one) SC quadrupoles having an integrated gradient of 39.2 T (28.7 T) over a total magnetic length of 45 cm (30 cm) .

The requested horizontal beam stay clear fixed both the warm bore diameter to 24 mm and the maximum thickness allowed for the cryostat and the SC cold mass to 22 mm. The limited amount of available space together with the requested field purity and gradient strength posed very demanding constraints on the SC magnets design.

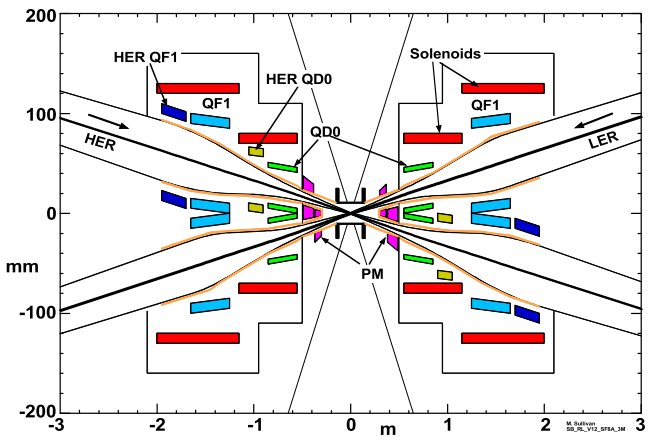


Figure 4: Top view of the IR layout. The PM and the cold masses of the SC magnets are represented together with the horizontal LER and HER beam stay clear.

The main differences with respect to the SuperKEKB layout are the reduced full crossing angle ( 60 mrad vs 83 mrad) and the much shorter $l^\star$, moreover the requirement on the gradient of the QD0 $\sim$ 1 T/ m exceeded by $\sim$ 30% the design gradient of the homologous QC1.

In addition to these, already very demanding, requirements from the beam dynamics team it was also requested to reduce the $l^\star$ of both the HER and the LER to roughly the same value.

It was clear that a solution like the SuperKEKB (i.e. a quadrupole acting on one beam and a set of canceling coils on the other one) was not viable since also the leaking field of the canceling coils would had been a serious problem.

Two solutions were proposed, one was based on double Panofsky quadrupoles and the other exploited the full potential of the double helix [7] concept.

A double helix magnet is composed by an even number of coaxial cylindrical solenoidal coils. The shape of each winding is modulated along the longitudinal direction. The coils are wounded alternating clockwise and counter-clockwise layers so to cancel out the longitudinal solenoidal field. It can be shown using the Biot e Savart law that in the limit of infinitely thin wire the multipolar expansion of the field inside the inner cylinder integrated along the axis of the magnet correspond to the Fourier expansion of the longitudinal displacement of the windings as a function of the azimuthal angle [7].

This idea was used to design a very thin double bore superconducting quadrupole [8] [9] with parallel magnetic axis and a few years later to design a double bore superconducting quadrupole with divergent axis suitable to meet the stringent requirements of the Super*B* IR layout.

The main concept is to parametrize the shape of each spire of the coil by an Hermite polinomial controlled by $2N$ key point. The longitudinal position of these key points can be such that the multipolar expansion of the integrated field is a pure quadrupole.

A prototype of a single core double helix quadrupole magnet had been built by the Super*B* collaboration and it had been tested at 4.2 K [10]. It turned out that the magnet capability to handle the 2650 A nominal current and to survive to quenches exceeded the expectations.



ISBN 978-3-95450-172-4

## REFERENCES


[1] T. Abe *et al.* [Belle-II Collaboration], "Belle II Technical Design Report," arXiv:1011.0352 [physics.ins-det].

[2] M. Bona *et al.*, *Super*B*: A High-Luminosity Asymmetric* $e^+e^-$ *Super Flavor Factory. Conceptual Design Report*, arXiv:0709.0451, 2007.

[3] P. Raimondi, D. N. Shatilov and M. Zobov, "Beam-Beam Issues for Colliding Schemes with Large Piwinski Angle and Crabbed Waist," physics/0702033 [PHYSICS].

[4] N. Higashi, H. Koiso, Y. Ohnishi, N. Ohuchi, T. Oki, M. Tawada, K. Tsuchiya and H. Yamaoka *et al.*, "Design Study of Final Focusing Superconducting Magnets for the SuperKEKB," Conf. Proc. C **110904**, 2457 (2011).

[5] B. Parker, M. Anerella, J. Escallier *et al.* "Superconducting Corrector IR Magnet Production for SUPERKEKB," TH-PBA07, NA-PAC 2013 (Pasadena,CA).

[6] B. Parker, J. Escallier, "Serpentine Coil Topology for BNL Direct Wind Superconducting Magnets," PAC05, Knoxville, TN, May, 2009, pp. 737-739. THPBA07, NA-PAC 2013 (Pasadena,CA).

[7] R.B. Meinke, M.J. Ball,C.L. Goodzeit, Advanced Magnet Laboratory, "Combined Function Magnets Using Double-Helix Coils," In the Proceedings of the 2007 Particle Accelerator Conference, Albuquerque, New Mexico, USA.

[8] E. Paoloni, S. Bettoni, M. E. Biagini and P. Raimondi, "Magnetic design studies for the final focus quadrupoles of the SuperB large crossing angle collision scheme," Conf. Proc. C **0806233** (2008) WEPD002.

[9] E. Paoloni, N. Carmignani, F. Pilo, S. Bettoni, P. Fabbricatore, S. Farinon, R. Musenich and F. Bosi *et al.*, "Advances in the design of the SuperB final doublet," Conf. Proc. C **110904** (2011) 2454.

[10] F. Bosi, P. Fabbricatore, S. Farinon, R. Musenich, U. Gambardella, R. Marabotto and E. Paoloni, "Compact superconducting high gradient quadrupole magnets for the interaction regions of high luminosity colliders," IEEE Trans. Appl. Supercond. **23**, no. 3, 4001004 (2013).




ISBN 978-3-95450-172-4

# BROAD-BAND LONG-FOCUS MIRROR OPTICAL SYSTEM FOR INFRARED DIAGNOSTICS

A. A. Maltsev, K. A. Gusakova, JINR, Dubna, Russia
M. V. Maltseva, V. A. Golubev, JSC "TENZOR", Dubna, Russia
S. A. Kaploukhiy, JSC "Research and Production Enterprise "Integral", Moscow. Russia

*Abstract*

The characteristics of special optics [1] and their use in experiments with IR synchrotron radiation are exemplified by a diagnostics of ring bunches in the compressor at JINR. For the diagnostics of ring bunches of electrons, which use the IR spectrum of synchrotron radiation, the windows to guide radiation out of the accelerator chamber and two variants of long-focus broadband optical channels to focus IR radiation on the sensitive elements of the detector unit were designed and constructed. The difference between the variants is that lenses are used as an objective in one and as spherical mirrors, in the other.

In our article we describe the Mirror Optics.

If a detector should not be exposed to the electromagnetic and radiation fields of an accelerator (this especially relates to high-sensitive detectors with a filled Dewar flask), a special optical channel with the active reflective elements (spherical mirrors) pro-viding the broadband efficiency of the whole channel and allowing for synchrotron radiation to be recorded in a spectral range of $\Delta\lambda \sim 0.3$–$40$ μm was designed and constructed.

One of the chief requirements necessary for multi-cell detectors is that they are screened from pulsed electromagnetic and radiation disturbances of an accelerator. The main source of disturbances is a magnetic field of an accelerator. In order to eliminate the influence of disturbances, a position-sensitive detector where the image of a source is focused at a scale of 1 : 1 should be set no less than two meters from this source. This required an optical channel with long-focus elements to be design.

The spectral broadband efficiency of a tract is implemented by using the reflecting elements (mirrors) only. The reflecting elements were made of the optical glass, had the given curvature, and were coated with a layer of silver evaporated in vacuum. As the temperature and humidity in the laboratory is constant, the evaporated metal was not coated with a protective cover, because it would increase the losses in the optical channel. The short-wave cut-off of a spectral range is determined by the quality of the reflecting surfaces and by a material of coating. The long-wave range is limited by diffraction, and the edge depends on the values of an aperture ratio of a system forming the image. In addition, the long-wave cut-off is connected with the limited number of windows to guide synchrotron radiation out of an accelerator and depends on the sensitivity of detectors.

A principal optical diagram of a mirror channel is shown in Figure 1.

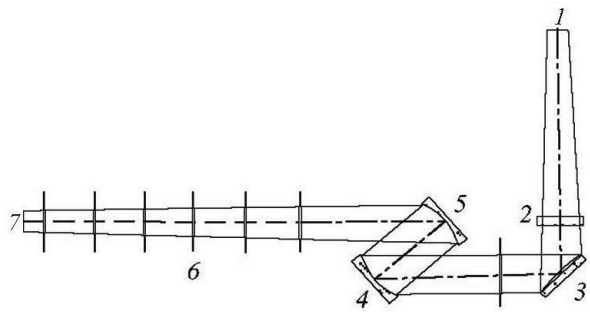


Figure 1: Principal optical diagram of a mirror channel.

As the synchrotron radiation is emit ted into a narrow cone, not all of the electron ring but only its cross section normal to the optical axis of a system is apparent. The synchrotron radiation from the minor cross section (~1/60 part) of an electron ring 1 is extracted from the vacuum chamber of the compressor through IR window 2 in close vicinity to which plane mirror 3 is positioned to deflect the divergent beam of the synchrotron radiation. The first spherical mirror 4 is set so that the object would be in its focus, for the diverging radiation beam would be transformed into the parallel one relative to the optical axis, and thus enabling it to transport it to any distance. The image of an observed object (the cross section of an electron bunch, in our case) is formed in focal plane 7 of second mirror 5 where the sensitive surface of a detector unit is situated. A focal length of both mirrors is the same and equal to 1850 mm. The elements 4 and 5 are concave spherical mirrors, the focal planes of which coincide with the investigated object and its image, which moves along the surface of a position-sensitive multicell photodetector during the compression of an electron ring in an accelerator. Diaphragms 6 limit the influence of glares and stray light.

Deflecting mirror 3 turns the optical axis by 90°. Its surfaces initially had a cylindrical form to correct the spherical mirrors for astigmatism due to oblique beams. Later, in order to obtain optimal image quality, the optical system was analyzed, with the help of computer, frequency-contrast characteristics. It was shown that the best image quality gave plane, not cylindrical, deflecting mirror. The influence of astigmatism seemed to be less



ISBN 978-3-95450-172-4

than that of other aberrations (spherical, coma, etc.) of the optical system. The corresponding frequency-contrast characteristics are shown in Figure 2 and 3.

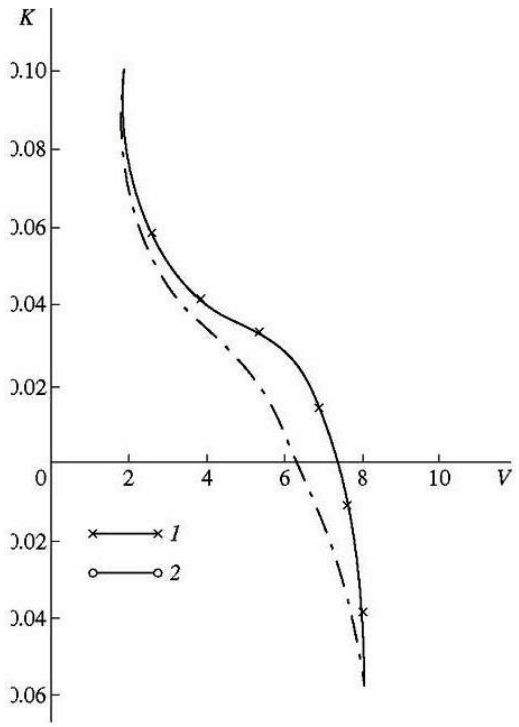


Figure 2: Frequency-contrast characteristic of an optical channel with a deflecting mirror: (1) in the center of the field of view, (2) at the boundary of the view field.

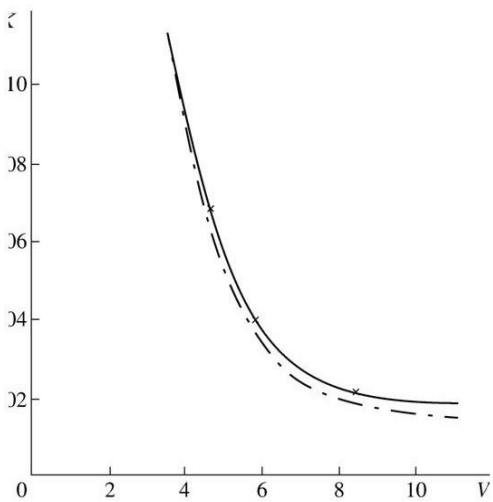


Figure 3: Frequency-contrast characteristic of an optical channel with a deflecting mirror.

Spatial frequency ν, the number of lines per mm in the image, is plotted on the abscissa, and the relative change of image contrast compared with the contrast of object k is laid off as an ordinate. It can be seen from the figures that if a level of 0.02 (the visual resolution) is accepted as the lower limit of the image contrast, the resolution of the optical system in the meridian sys tem plane, the plane of the drawing was 5–6 lines/mm for a cylindrical mirror. The results of computation showed that this is the best resolution of the mirror.

When a plane mirror was used as mirror 3, the resolution was 9–10 lines/mm.

Upper curves (crosses) in Figure 2 and 3 refer to the center of the field of view, the lower ones (dots), to the boundary of the view field.

The photographic resolution of the system is shown in Figure 4.

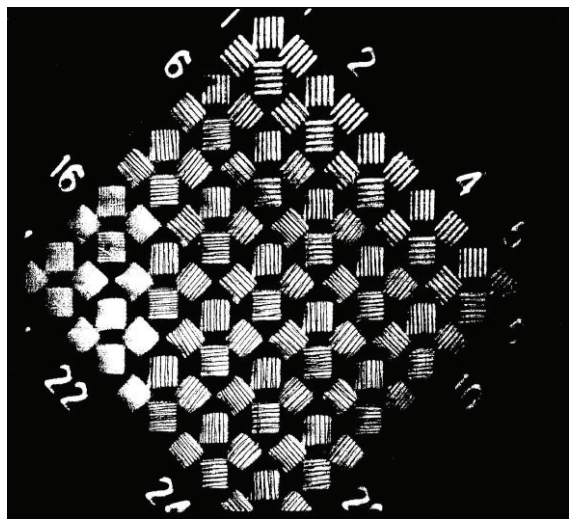

Figure 4: Photographic resolution of the system.

The main technical data and characteristics of the wide-range optical mirror channel are as follows:

The field of application: the system works in the UV and IR ranges of spectrum ($\Delta\lambda \sim 0.3$–$40$ μm), which is limited only by mirror coating and diffraction.

Focal length of the spherical mirrors is $f = 1850$ mm.

Aperture ratio is 1 : 21.

Magnification is 1 : 1.

Photographic resolutions are:

(i) $7^{-1}$ mm in the focal plane of the tract;

(ii) $7^{-1}$ mm in points shifted at ±5 mm; $7^{-1}$ mm, at ±10 mm; $7^{-1}$ mm, at ±15 mm; and $5^{-1}$ mm, at ±20 mm.

The field of view in the plane of an object is ∅34 mm.

The overall dimensions in mm are 2000 × 360 × 370.

The spherical mirrors can be displaced along the optical axis of the optical mirror channel by ±70 mm and rotated ±5° around the intersection point of the mirror surface with the optical axis. The plane mirrors can be rotated ±5°. In order that the focal surface of a detector unit (e.g., photographic camera) perfectly coincided with the focal surface of the second spherical mirror, a ±70 mm aligning interval is provided at the optical axis for the photodetector. The absence of chromatic

ISBN 978-3-95450-172-4

aberration allows the channel to be adjusted with visible light.

One of the advantages of the chosen design is a low radiation loss of the optical channel, which is less than 4% owing to the high reflectance of silver in a spectral range of 0.3–40 μm and the absence of protective coating on the reflecting surfaces. The intensity losses of synchrotron radiation are mainly caused by the materials of an IR window (to 40%) and a detector. All the elements and units of the channel construction are made of nonmetallic, nonconducting, and nonmagnetic materials.

A picture of the mirror system is represented in Figure 5.

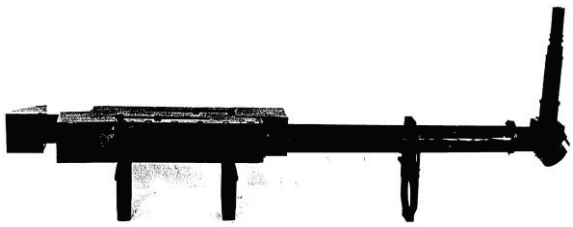

Figure 5: Picture of the mirror system.

The optical tract, in the form of a separate unit, is mounted with tube support to a concrete wall or on a concrete cube, i.e., it is fixed on the rest or base that is free of vibrations.

The channel can be used with various types of IR and non-cooled photodetectors, but mainly with the mosaic photo detectors from silicon, indium antimonide (working temperature of $T_w$ = 77 K), lead selenide ($T_w$ = 250 K), and pyroelectrics. As the mirrors reflect radiation in a wide range of the spectrum, the channel can be also used in the UV and visible ranges of spectrum. The optical channel has the ability to work in the visible and IR ranges of spectrum with a SFR high-speed camera. Photoresistors cooled by liquid nitrogen can be adapted for the channel to record radiation in an IR range. In Figure 5, such a cooled detector is discerned at the exit of an optical tract.

An optical mirror channel was used when synchrotron radiation was first detected and recorded in an accelerator-compressor. The intensity (i.e., the number of electrons) in the first experiments was so low and the spectrum so indefinite that without optical amplification and the ability to record it in a broad range of wave-lengths, the detection of synchrotron radiation would have been impossible.

## REFERENCES

[1] A. A. Mal'tsev and M. A. Mal'tsev, Technical Physics, Vol. 47, No. 6, 777 (2002).



ISBN 978-3-95450-172-4

# BEAM-BEAM LIMIT, NUMBER OF IP'S AND ENERGY

Kazuhito Ohmi, KEK, Tsukuba, Ibaraki, Japan

*Abstract*

FCC-ee has been designed for factories of top (175 GeV), Higgs (120 GeV), W and Z (45 GeV). Number of IP is 4. CEPC has been designed for H with two IP. Limit of the beam-beam tune shift depends on the damping time. Number of IP affects the beam-beam performance, because the superperiodicity between is broken in real accelerators. We discuss beam-beam limit based on LEP experiences.

## INTRODUCTION

Systematic study for energy/damping time and number of IP's are performed for LEP. LEP had been operated in several energy. The beam-beam tune shift limit is measured in each energy. The experiences should be helpful for FCC-ee design.

We study the beam-beam limit of LEP using simulations and compare the results with experimental results. LEP had operated with several energies. The number of IP is 4. Difference between LEP and FCC-ee is the fact that the bunch length ($\sigma_z$) is longer than vertical beta at IP ($\beta_y^*$). The effects of the difference will be discussed elsewhere.

Table 1 summarizes parameters of LEP. LEP had been operated at three stages with energy of 45.6, 60 and 100 GeV which are called LEP1, LEP1.5 and LEP2, respectively. The radiation damping time is faster for increasing the beam energy with cubic dependence. Luminosity and beam-beam tune shift limit increase for the energy increase.

## SIMULATION RESULTS

We executed beam-beam simulation for LEP. Both of strong-strong and weak-strong simulations was performed using the code named BBSS [2, 3] and BBWS [3, 4]. Beam particles are tracked during 10 damping time under the beam-beam interaction. The number of macro-particles are 1,000,000 for the strong-strong and 65,536 for the weak-strong simulation. Though the bunch length is shorter than $\beta_y$, the bunch is sliced into 7 pieces. Because beam-beam induced head-tail instability is sometimes seen in the simulations.

Figure 1 shows the evolution of the luminosity for LEP2. The radiation damping time is 300 turns/IP. Equilibrium value is realized around 1-2 damping time Luminosity for several cases of bunch populations is plotted in the figure.

The beam-beam tune shift per IP is evaluated by the equilibrium luminosity per IP,

$$\xi_y = \frac{2r_e\beta_y L}{\gamma N_e f_0}. \quad (1)$$

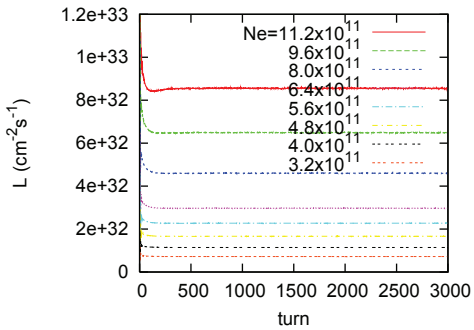


Figure 1: Evolution of luminosity for LEP2. The turn number is 4 times of actual turn number.

Figure 2 shows $\xi_y$ per IP and vertical beam size evolution as function of the equilibrium bunch population. The vertical beam size evolutions are for $(\nu_x, \nu_y)$=(0.5775,0.0425)/IP. There are no remarkable signal related to luminosity degradation in $x, \sigma_x$. The beam-beam tune shift per IP is saturated at 0.12 for $(\nu_x, \nu_y)$=(0.5775,0.0425)/IP, while is not saturated over 0.18 at (0.51,0.57). The fractional tune operating point (0.5775,0.0425) is given by the tune in Table 1 divided by 4. LEP had been operated at the tune area (0.57,0.04) in every energy. CESR, KEKB, PEPII, BEPC-II had operated at the tune area $(\nu_x, \nu_y)$=(0.51,0.58). The electron positron colliders were successful by adopting the tune operating point.

At $(\nu_x, \nu_y)$=(0.5775,0.0425)/IP, beam-beam limit is seen $\sim 0.12$ at $N_e = 3 \times 10^{11}$. This value is very higher than experimental value 0.044 at $N_e = 1.2 \times 10^{11}$ in Table 1.

Figure 3 shows evolutions of $\langle y \rangle$ and $\langle yz \rangle$ at $N_e = 3 \times 10^{11}$. Coherent oscillation of $\pi$ mode is seen in $\langle y \rangle$ motion (1st and 2nd pictures). $\langle yz \rangle$ (3rd) of two beams, which is related to head-tail motion, oscillate with an opposite phase.

Figure 4 shows the results for LEP15; beam-beam parameter (1st) as function of the bunch population and coherent motion in $\langle y \rangle$ (2nd) and $\langle yz \rangle$ (3rd).

Figure 5 show $\xi_y$ as function of bunch population for LEP2 and LEP2.1. The tune shift is saturated at 0.3 for both cases. Coherent motion was not seen in LEP2 and 2.1. Fast radiation damping may suppress the coherent motion. Figure 6 shows evolution of the vertical beam sizes. Flip-flop of two beam sizes are reason of the beam-beam limit.

Weak-strong simulation is performed using LEP pa-

ISBN 978-3-95450-172-4

Table 1: Parameter Table of LEP [1]

| | LEP1 | LEP15 | LEP2 | LEP2.1 | unit |
|---|---|---|---|---|---|
| circumference | 26658 | | | | m |
| number of IP | 4 | | | | |
| energy | 45.6 | 65 | 94.3 | 97.8 | |
| bunch population | 1.2 | 2 | 4 | 4 | $\times 10^{11}$ |
| emittance $\varepsilon_{x/y}$ | 19.3/0.23 | 24.3/0.16 | 21.5/0.31 | 21.1/0.215 | nm |
| $\beta^*_{x/y}$ | 200/5 | 250/5 | 125/5 | 150/5 | cm |
| damping time $\tau_y/IP$ | 2888 | 1000 | 326 | 293 | turns |
| natural bunch length | 0.86 | 1.05 | 1.2 | 1.17 | cm |
| natural energy spread | 0.71 | 1.02 | 1.84 | 2.04 | $10^{-3}$ |
| horizontal tune | 90.31 | 90.258 | 98.285 | 98.34 | |
| vertical tune | 76.17 | 76.166 | 96.155 | 96.18 | |
| synchrotron tune | 0.065 | 0.076 | 0.101 | 0.116 | |
| luminosity | 1.51 | 2.11 | 8.84 | 9.73 | $10^{31}$ cm$^{-2}$s$^{-1}$/IP |
| $\xi_y$ per IP | 0.044 | 0.051 | 0.073 | 0.0785 | |

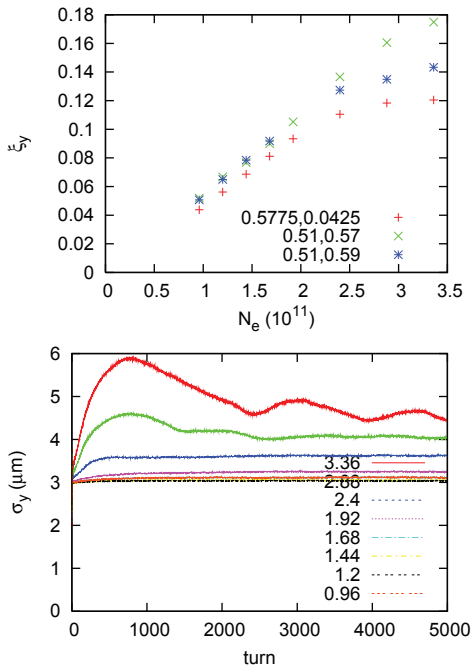


Figure 2: Beam-beam limit for LEP1. $\xi$ in left picture is tune shift per IP. The vertical beam size for bunch populations for (0.5775,0.0425) are plotted in 2-nd picture.

rameters. Coherent phenomena like coherent motion or flip/flop seen in the strong-strong simulation are basically suppressed in the weak-strong. Purely incoherent emittance growth due to nonlinear beam-beam resonances is seen. Figure 7 shows $\xi_y$ and $\sigma_y$ as function of bunch population. The tune shift limit per IP is 0.2, 0.3, 0.3 and 0.35 for LEP1-LEP2.1, respectively at tune (0.57,0.04)/IP area. There is no limit in this tune shift level for (0.51,0.57)/IP. The tune shift limit per IP exceed 0.5 for LEP2 and 2.1.

The tune shift limit is summarized in Figure 8 for the

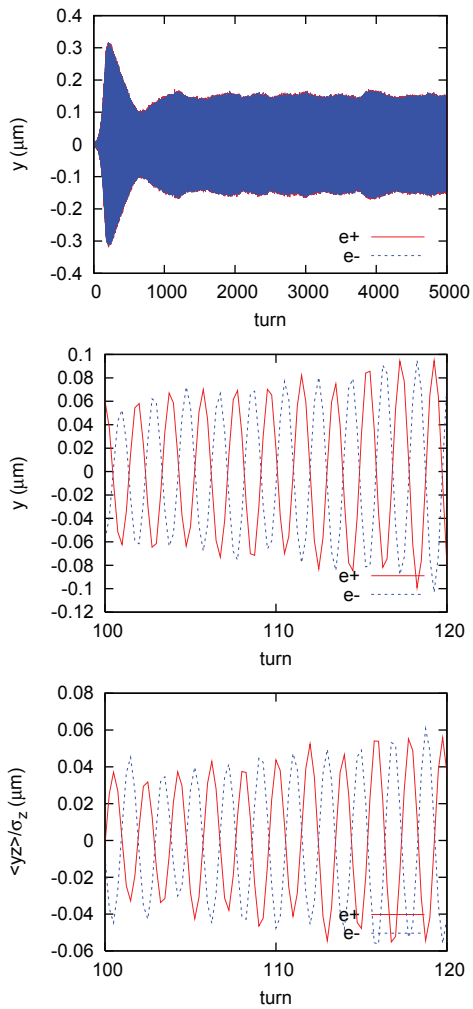


Figure 3: Coherent motion seen in LEP1 simulation at $N_e = 3 \times 10^{11}$. 1st and 2nd pictures show $\langle y \rangle$ motion. 3rd picture shows $\langle yz \rangle$ motion.



ISBN 978-3-95450-172-4

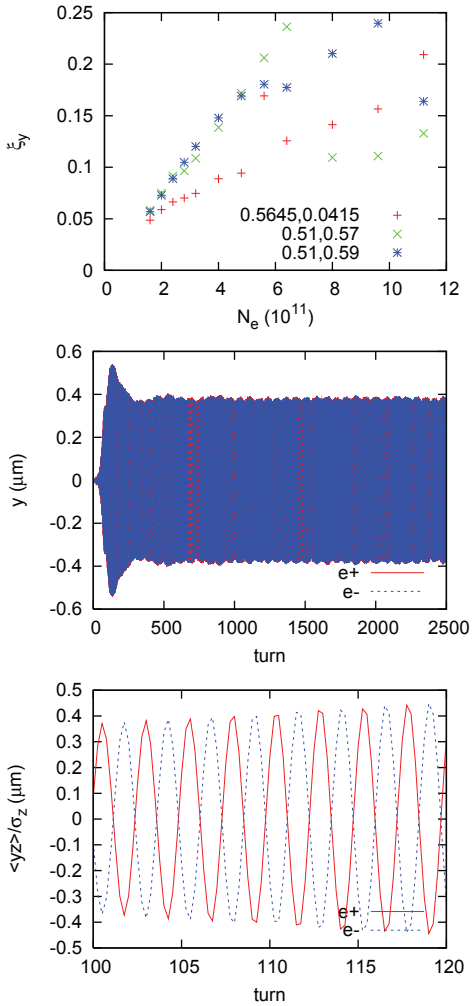


Figure 4: Beam-beam limit for LEP1.5.

damping time. $\xi_y$ in experiments are plotted in 1st picture. The line is a scaling formula $0.5\tau^{-0.4}$ [5]. The formula agrees with $\xi_y$ of LEP, but deviates for those in other machines with lower energy. Simulation and experimental results are plotted in right picture. Simulations especially weak-strong give much higher $\xi_y$ than experiments. Strong-strong simulations at $(\nu_x, \nu_y) = (0.57, 0.04)$/IP and experimental data for low energy colliders scales $1.6\tau^{-0.4}$.

## NUMBER OF IP'S

When superperiodicity between IP's is perfect, the beam-beam system is equivalent to a single IP collider with circumference divided by the number of IP's.

When betatron phase advances between IP's are different, or $\beta^*$, x-y coupling and dispersion at IP are different IP by IP, the superperiodicity is broken. Such errors degrade luminosity performance.

We now assume the phase variation of IP-by-IP (1) $\Delta(\phi_{y,12}, \phi_{y,23}, \phi_{y,34})/2\pi = (0.01, 0.02, 0.01)$, where $\Delta\phi_{y,41} = -\sum_{i=1}^{3} \phi_{y,i,i+1}$. We also tried

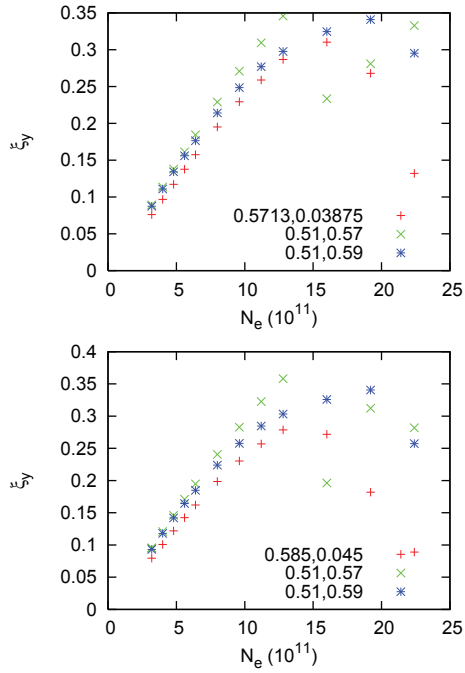


Figure 5: Beam-beam limit for LEP2 (1st) and LEP2.1 (2nd).

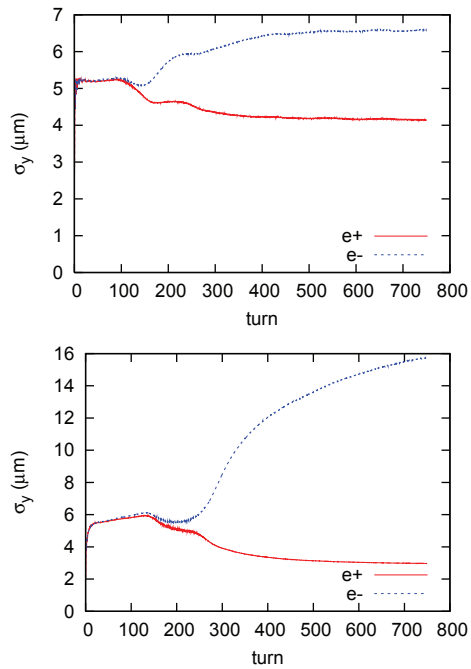


Figure 6: Beam size evolution at $N_e = 20 \times 10^{11}$ for LEP2(1st) and LEP2.1(2nd).

ISBN 978-3-95450-172-4

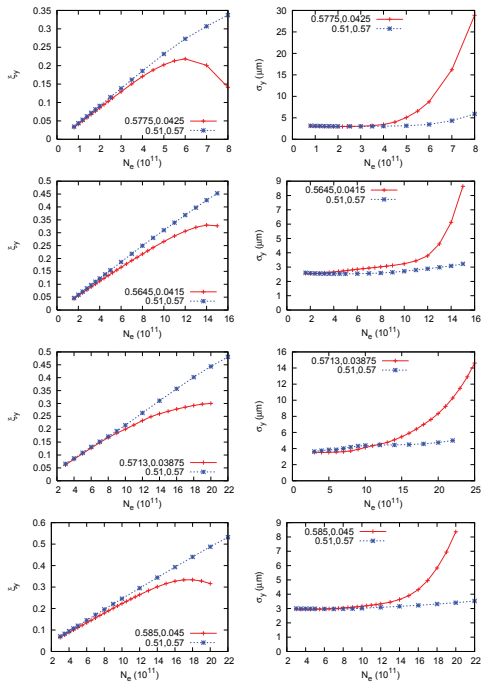


Figure 7: Beam-beam limit for LEP in weak-strong simulations. Tune shift per IP $\xi_y$ is plotted in odd pictures and vertical beam size is ploeed even pictures. LEP1 1st-2nd, LEP1.5 3rd-4-th, LEP2 5-6-th, LEP2.5 7-8-th.

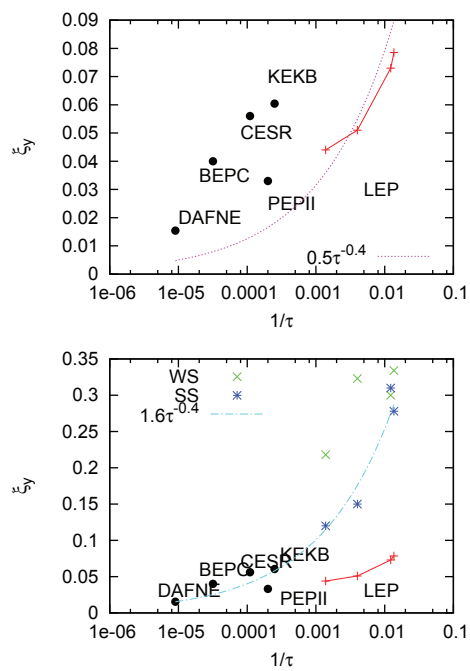


Figure 8: Beam-beam limit as function of vertical damping time. 1st picture depict tune shift in experiments. Simulation results are added in 2nd picture.

(2) (0.02,0.04,0.01)
(3) 0.04,-0.02,-0.01.

The third parameter is given by a measurement in LEP.

Strong-strong simulations are performed with taking into account the phase errors. Figure 9 shows beam-beam tune shift/IP as function of the bunch population for LEP2 containing the phase errors. Red line is no error as reference. Green and magenta lines are given for the phase errors for the cases (1) and (3), respectively. The limit values are 0.2 and 0.15 for the errors, respectively. Vertical beam size are plotted in 2nd picture as function of $N_e$. Coherent quadrupole motion is seen at the stage of the beam-beam limit. 3rd picture depicts evolution of $\sigma_y$ of two beams at $N_e = 8 \times 10^{11}$.

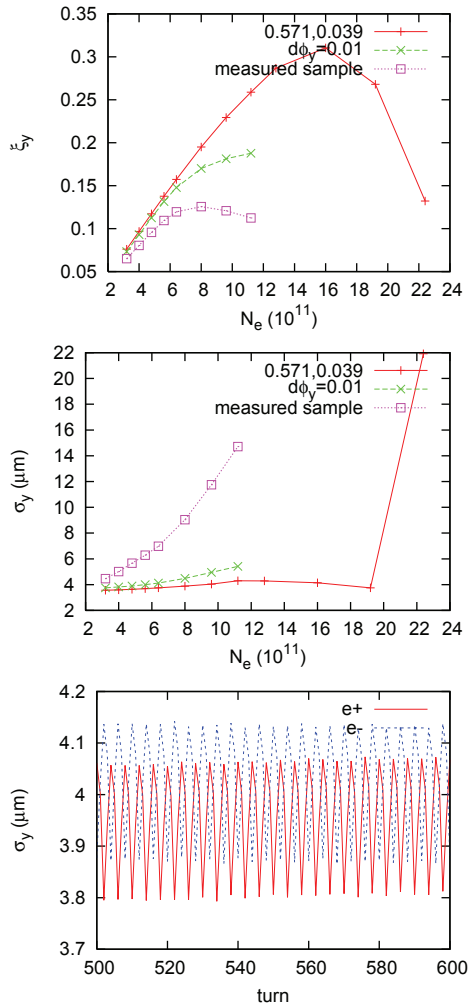


Figure 9: Beam-beam limit for LEP2 with vertical betatron phase errors. Tune shift beam size as function of the bunch population are seen in 1st and 2nd pictures, respectively. 3rd picture depicts coherent quadrupole motion onset of beam-beam instability.

The same simulations are performed using weak-strong simulation. Figure 10 shows $\xi_y$ as function of the bunch population with phase error between IP's.



ISBN 978-3-95450-172-4

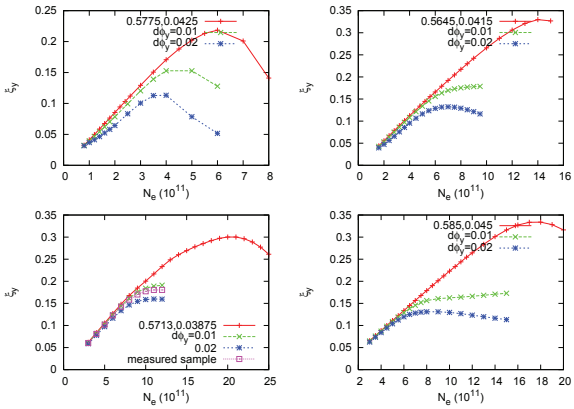


Figure 10: Beam-beam limit for LEP in weak-strong simulations. Tune shift of LEP1, LEP15, LEP2 and LEP2.1 are plotted in 1st, 2nd, 3rd and 4-th pictures.

x-y coupling and collision offset are different in IP-by-IP. We studied cases $r_2 = 0.0024, -0.0024, 0.0048, -0.0024$ and offset $\Delta y/\sigma_y = (0, 0.25, 0.5, -0.25)$ for each IP. Strong-strong simulation was performed with the errors in x-y coupling and collision offset for LEP2. Figure 11 shows $\xi_y$ with x-y coupling and offset at IP's. Red is without error as reference. Green and blue lines are given for the errors of $r_2$ and $\Delta y$, respectively. No clear degradation for the reference is seen.

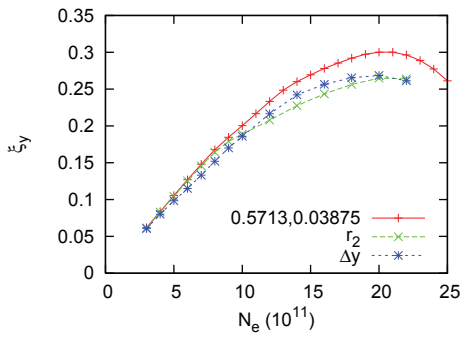


Figure 11: Beam-beam tune shift per IP as function of bunch population with errors in x-y coupling and offset.

## SUMMARY

Beam-beam limit in LEP is studied using strong-strong and weak-strong simulations. Equilibrium luminosity is calculated for various currents and energies. Tune shift is calculated by equilibrium luminosity for each current and energy in simulations. Tune shift limits in strong-strong simulations are smaller than those of weak-strong simulations. Coherent instability appears in LEP operating point (0.57,0.04)/IP for LEP1 and 1.5 in the strong-strong simulations. Flip-flop of the beam sizes appears in LEP2 and 2.1.

The tune shift limit is compared with experimental results. Maximum tune shift is much higher than measured ones. The tune shift per IP measured in LEP is satisfied a scaling for the damping time per IP in unit of turn $0.5\tau^{-0.4}$. The tune shift of KEKB, CESR, BEPC is higher than the scaling. Tune shifts of the strong-strong simulation and the three colliders scale as $1.6\tau^{-0.4}$.

Superperiodicity is broken when betatron phase, IP optics parameters and collision offset are different in IP-by-IP. Luminosity degradation due to the errors. The betatron phase errors $\sim 0.02 \times 2\pi$ affect luminosity performance. x-y coupling ($r_2 \sim 0.0024$) and collision offset $(0.25 - 0.5\sigma_y)$ IP-by-IP do not affect clearly.

Difference between LEP and FCC-ee is the fact that the bunch length ($\sigma_z$) is longer than vertical beta at IP ($\beta_y^*$). The same study should be performed using FCC parameter.

The author thanks fruitful discussions with Y. Funakoshi.

## REFERENCES

[1] H. Burkhardt, private communications.

[2] K. Ohmi, Phys. Rev. E62, 7287 (2000).

[3] K. Ohmi, M. Tawada, Y. Cai, S. Kamada, K.Oide, J.Qiang, Phys. Rev. ST-AB 7, 104401 (2004).

[4] K. Hirata et al., Partcle Accelerators 40,205 (1993).

[5] R. Assmann and K. Cornelis, proceedings of EPAC2000, Vienna.



ISBN 978-3-95450-172-4

# LONG-RANGE BEAM-BEAM INTERACTION WITH THE BUNCH TRAIN OPERATION*

David Rice, CLASSE, Cornell University, Ithaca,NY 14853, USA
David Rubin, CLASSE, Cornell University, Ithaca,NY 14853, USA

Abstract

For the past three decades, colliders have realized increased luminosity by adding beam bunches beyond the traditional $N_{interaction\ points}$ / 2. CESR has operated since 1983 with pretzel orbits to realize substantial improvements in luminosity. In 1994 bunch trains with horizontal crossing angle were introduced. We review some of the fundamentals of the long-range beam-beam effects, including bunch trains, and suggest some guidelines in the design of a circular e+e- Higgs Factory.

## MULTI-BUNCH OPERATION IN E+E- CIRCULAR COLLIDERS

Ideally a circular colliding beam facility should have full flexibility in number of bunches to maximize performance with attention to bunch charge limits (head-on beam-beam effects, TMCI and other single bunch effects), total current limitations (RF, instabilities), and beam-beam tune shift limits. There are, unfortunately, also effects on performance resulting from the choice of adding bunches.

Where separate rings are not practical, the counter-rotating beams share a common vacuum chamber and guide fields with separation at crossing points provided by electrostatic or RF separators. The resulting closed orbits are generally referred to as pretzel orbits (Fig. 1).

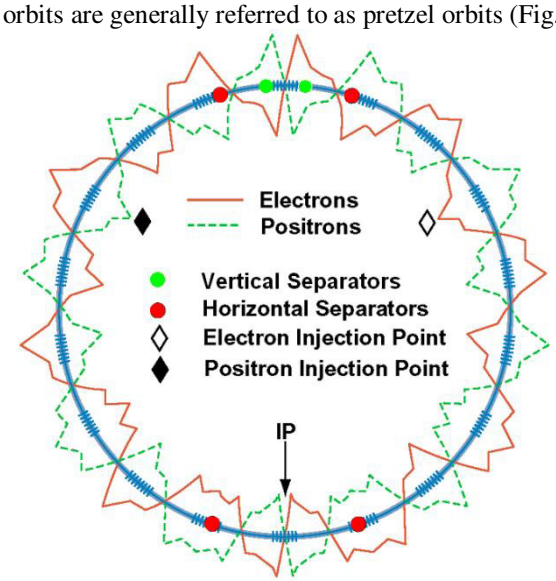


Figure 1: Pretzel orbits in CESR. Blue tic marks show crossing points for 9 trains of 5 bunches each.

Both the pretzel orbit and the multiple crossings where bunches experience the electromagnetic fields from the opposing beam impact the beam dynamics.

* Work supported by multiple grants from the U.S.National Science Foundation

## PRETZEL AND PARASITIC CROSSING EFFECTS

### *Overview*

We start with a brief outline of potential pretzel optics and parasitic crossing effects outlined in Table 1. The pretzel orbits themselves bring about multiple changes in optics. These are inherently different for electrons and positrons, but some effects are mitigated by choosing the appropriate symmetry in the ring.

The electromagnetic fields from the opposing beam cause multiple beam-beam effects (long range beam-beam interaction, or LRBBI) at each parasitic crossing. The effects of the LRBBI include kicks, tune and chromaticity shifts, and nonlinear coupling. The magnitude of the effects of these parasitic crossings depends on local pretzel amplitudes, twiss parameters and dispersion, as well as the charge in the opposing bunch and therefore do not affect all bunches uniformly.,. The variation of the lattice parameters at the parasitic crossing as well as the non-uniformity in the intensities of the opposing bunches makes mitigation difficult as compared with the usual head-on beam-beam effects, or impossible in many cases.

The distortion of the closed orbit distorts the optics of a single beam. If the separation scheme has the appropriate symmetry, the change in global parameters like tune and chromaticity is common to both beams. But local distortions are generally different for electrons and positrons. There is therefore a tension between minimizing pretzel effects (smaller pretzel amplitude) and minimizing LRBBI effects (larger pretzel amplitude).

Table 1: Pretzel and Long Range BBI Effects

| Type | Source |
|---|---|
| Pretzel Optics | |
| Betatron phase errors | Sextupoles |
| Dispersion errors | Sextupoles |
| Damping partition #'s | Quadrupoles |
| Enhanced Synch. Rad. | Quadrupoles |
| H_V coupling | Sextupoles, etc. |
| Instr. Nonlinearities | BPMs |
| | |
| Parasitic Crossings | (Opposing beam - ) |
| Orbit distortion | Far E&M fields |
| Coherent tune split | Far E&M fields |
| Nonlinearity | Core E&M fields |
| Chromatic Effects | Far E&M + Dispersion |



ISBN 978-3-95450-172-4

### *Pretzel Optics*

Dispersion errors will be introduced at each quadrupole where the pretzel orbit is non-zero. Betatron phase, coupling, and dispersion errors are generated at each sextupole.. When separation is in the horizontal plane, the phase advance and horizontal dispersion will be affected. For vertical separation, coupling terms will be introduced along with vertical dispersion. Skew quadrupole components will in general generate out of plane dispersion. These effects are calculable and can be assessed early in the design stage. These effects are more easily addressed if they are the same for both beams, i.e. common changes in tune, chromaticity etc. Differential global effects can be reduced significantly by maintaining anti-symmetric pretzels as much as possible. Further correction may require introduction of additional quadrupole and sextupole and skew sextupole controls.

As the closed orbit passes through quadrupoles off center, in addition to enhanced radiation losses, the radiation damping is modified. The damping parameter D is modified approximately as [1]:

$$J_x \cong 1 - \frac{2\int K_1^2(s)(D_x - D_{x0})x_p(s)ds}{\int G^2(s)ds} \qquad (1)$$

resulting in changes in the horizontal emittance, $\varepsilon_x$ that can be difficult to correct.

Synchrotron radiation losses will be enhanced as:

$$\Delta P_\gamma \propto \int K_1^2(s)\, x_p^2(s)\, ds \qquad (2)$$

Since the losses scale overall as $E^4$, the enhanced synchrotron radiation must be considered in the design of a Higgs factory.

In the following $d_{x,y}$ is design pretzel separation between beams at parasitic crossings and $x_{1,2}$ or $y_{1,2}$ is the displacement of a particle in beam 1 or 2 from the equilibrium orbit.

Horizontal to vertical as well as dispersion coupling is introduced by vertical displacements in sextupoles. The magnitude of this coupling depends on the separation scheme and alignment and field errors. Additionally the betatron phase errors previously described may compromise pre-existing coupling corrections.

The effects of large closed orbit displacements on instrumentation may be significant. Beam position detectors may exhibit significant nonlinear behaviour when the pickup electrodes have a spacing comparable to the peak-to-peak pretzel amplitude. In this case compensation must be made before using the data for correction or analysis. A map of measured positions against a background of actual beam (wire) positions is shown in Fig. 2.

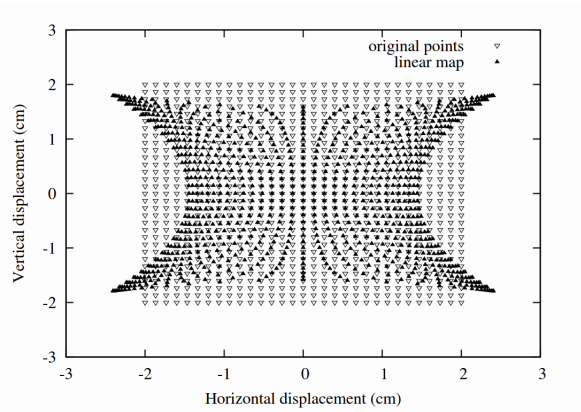


Figure 2: Nonlinear response of a CESR BPM against a background of actual positions.

### *Parasitic Crossings Beam-beam Effects*

For reasonably large separation (>5σ) between opposing beams the angle imparted to a bunch during a horizontally separated passage is [2]:

$$\Delta x_1' = -\frac{2N_2 r_0}{\gamma_1 d_x} - \frac{2N_2 r_0}{\gamma_1 d_x^2}(x_1 - x_2) \qquad (3)$$

with a similar result in the vertical plane. The subscripts refer to the two beams, $d_x$ is the nominal pretzel separation between closed orbits and x is the displacement from the closed orbit for each bunch.

The closed orbit distortion is the vector sum of the kicks from the first term on the RHS. This can give rise to position or angle errors at the primary interaction points.

The second term represents a variable deflection turn-by-turn depending on the bunches' oscillations about their equilibrium (pretzel) orbits, producing a coherent focussing force and coupling between the two beams. The tune shift parameter is then:

$$\Delta\nu_x^{(bb)} = -\frac{r_0 N \beta_x}{4\pi\gamma d_x^2} \qquad (4)$$

The coherent beam-beam modes resulting from these tune shifts are given by the eigenvalues and vectors of the single-turn matrix resulting from inclusion of all the parasitic crossings.

While the orbit distortions and coherent modes may produce operational problems, they generally will not result in excessive particle loss, particularly with a good bunch-by-bunch feedback system

If individual particles approach within 2 or 3 sigma of the opposing beam core the beam-beam kick will become very large since the beta functions at most parasitic crossing points are huge compared to a low-beta IR insert. Analysis and tracking studies have shown that, with horizontal separation, the vertical motion is most strongly affected, and particle loss is generally in the vertical beam motion. [3] Fig. 3 below shows tracking results for a separation of 6.5 $\sigma_x$ between beams (bunch profile shown on RHS.).



ISBN 978-3-95450-172-4

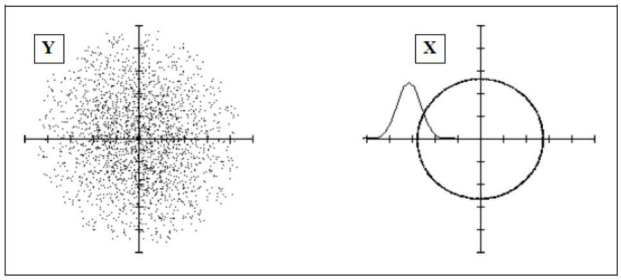


Figure 3: Phase space of particles tracked with 6.5 $\sigma_x$ between beams. From reference [3]

The beam-beam tune shift will be modulated by the energy oscillations and local dispersion at the parasitic crossing points. Considering the horizontal plane only, adding the dispersion causes a modulation of the chromaticity as [4]:

$$\Delta\nu_x'^{(bb)} = -\frac{2D_x}{d_x}\Delta\nu_x^{(bb)} \quad (5)$$

The factor $D_x/d_x$ can be quite large, leading to significant shifts in chromaticity depending on crossing point parameters and bunch intensities.

### *Minimum Separation Requirements*

As a general rule, all of the following separation requirements should be met [5]:

1. $d_i > n\sigma_i$ where $n \approx 5.5\text{-}7$
2. $\Delta\nu_x^{(bb)} < \Delta\nu_{max}^{(bb)}$ where $10^{-4} < \Delta\nu_{max}^{(bb)} < 10^{-3}$
3. $\sum_i \Delta\nu_x^{(bb)} < \sim 10^{-3}$

(Horizontal parameters are shown, the same applies to vertical where relevant.)

Several plausible phenomenological models for minimum required separation were tested at CESR [6] with several optics configurations. Of note, the 4 (out of 11) best models all had a $\beta_y$ dependence (with horizontally separated beams). CESR optics were designed to minimize both horizontal and vertical tune shifts at each of the parasitic crossings as well as to maximize separation. For operation with symmetric pretzels, differential path length, tunes, and partition numbers were constrained. Maximum tolerable individual and accumulated tune shifts were determined experimentally. Beam energy dependence emerged through the constraints on parasitic tune shifts.

## BUNCH TRAINS

Once the bunch charge has reached the (head-on) beam-beam limit, beyond which luminosity increases only linearly with current, adding more bunches is desirable. If available anti-nodes of the pretzel are filled with bunch crossings (i.e., one bunch per beam per integer tune), increasing bunch numbers requires using closely spaced groups, or trains, of bunches. The trains must be short enough so the crossing points are all encompassed, with sufficient separation, between pretzel nodes.

Since we are trying to pack as many bunches as possible into each train, the parasitic collision points will be spread across each pretzel anti-node, generally resulting in a wider variation in beam-beam related parameters. Fig. 4 below shows the horizontal separation in units of $\sigma_x$ in CESR during the 1990's. [7] Fig. 5 shows the vertical difference at the interaction point (coupling by experiment solenoid), and the tune shifts for the configuration in Fig. 4. Obviously compensating these effects bunch-by-bunch would be challenging. With the total flexibility in quadrupole/sextupole distributions in CESR it is possible to optimize these parameters. [8]

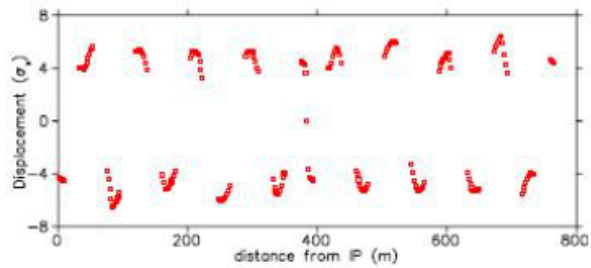


Figure 4: Horizontal separation at each parasitic crossing point with 9 trains of 5 bunches each in CESR. Beams are separated vertically at the point in the center.

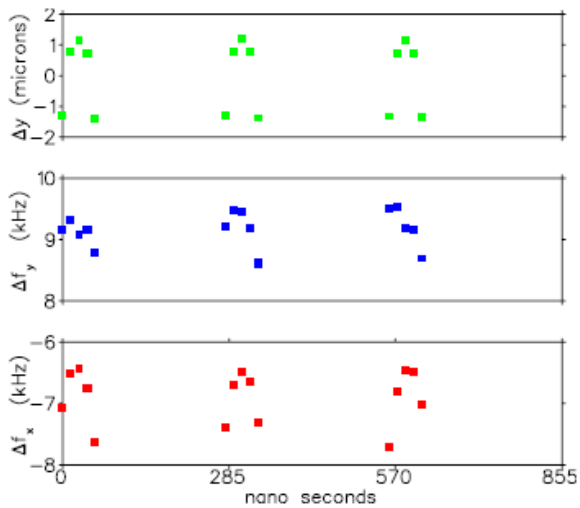


Figure 5: Vertical displacement at the interaction point and parasitic crossing induced tune shifts ($\Delta Q \times 390$ kHz) for a strong beam 9 trains of 5 bunches, each with 1.2 x $10^{11}$ e-. Only 3 trains are shown since there is a 3 train periodicity in the 9 trains. From reference [7]

There is also the issue of separation around the interaction point of a collider – common to both single and two-ring colliders. Several options have been used at various colliders, including crossing angle (CESR, DAΦNE, LHC), electrostatic separators (LEP, Tevatron), and for asymmetric energies, magnetic separation (KEK-B, PEP-II). The parasitic crossings around each interaction point introduce the same beam-beam phenomena as crossings in the arc. A crossing angle also introduces potential vertical errors at the interaction point if the detector has a strong solenoid field.



ISBN 978-3-95450-172-4

If the single bunch current is limited by LRBBI, then adding more bunches may be helpful. One may ask, however, if the effects of closely-spaced parasitic crossings add coherently, nullifying the advantage for LRBBI.

If the parasitic crossings in a train have a coherent LRBBI then current limits will scale only as the total train current, $I_t$. If they are incoherent, then the scaling would be as $I_t/\sqrt{N_{bt}}$. ($N_{bt}$ is the number of bunches in the train.) Measurements were made at CESR [9] to give guidance for limits to bunch train spacing from effects of coherency between bunches. A weak probe bunch experienced multiple parasitic crossings (but no head-on collision) from a drive beam consisting of one of three configurations: 1) a single bunch; 2) two bunches with separation 14 ns; 3) two bunches with separation 28 ns. The minimum pretzel amplitude for ~50 minute lifetime vs. total drive train current was recorded. Results are shown in Fig. 6 below.

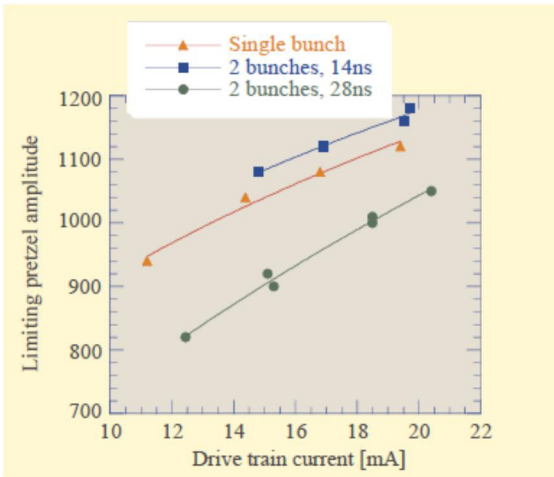


Figure 6: Pretzel amplitude for 50 minute lifetime of a test bunch interacting with opposing drive beam. Coherency between interactions becomes significant between 28 and 14 ns separation. From reference [9].

## MITIGATION OF PRETZEL AND LRBBI EFFECTS

### *Mitigation of Pretzel Effects*

Mitigation of pretzel effects begins with designing anti-symmetric pretzels, or as nearly so as possible with respect to the interaction points. This will reduce the differential effects of pretzels such as orbit kicks, but leaving a possible crossing angle.

Strategically placed sextupoles can control the tune splitting of the two beams as well as dispersion errors. CESR conveniently has independent control of all sextupoles and quadrupoles, permitting substantial compensation of $\Delta\nu_x^{(bb)}$, variation of $J_x$, crossing point angle, "pretzel efficiency" (separation at parasitic crossings relative to peak pretzel closed orbit), and an empirical figure of merit $\sum_i \epsilon_x \beta_{xi} \beta_{yi} / x_i^2$ [8]. Sextupoles are optimized to minimize local chromaticity, optics variation with closed orbit (pretzel), and amplitude dependence of optics, including coupling.

However, CESR is the only ring with pretzels that has the luxury of independently controlled quadrupoles and sextupoles. Selected sets of quadrupoles and achromatic sextupoles were used to compensate pretzel effects in LEP. [10,11] In addition, vertical trim separators and separator scans minimized orbit differences at interaction points. As with most colliders, fine tuning to achieve "golden orbits" is necessary to realize peak luminosity.

### *Mitigation of LRBBI Effects*

Given sufficient flexibility in sextupole configuration, the coherent LRBBI effects may be effectively reduced by splitting the betatron tunes for the two beams beyond any coherent tune shift from parasitic crossings. This is routinely employed at CESR. [12] The perturbation to vertical motion by LRBBI may be reduced by increasing the vertical emittance of the "strong" beam. While this may help during injection, it is not necessarily productive for maximum luminosity. Effective bunch-by-bunch feedback can help damp residual coherent motion.

Observing that the magnetic field from a wire next to the beam mimics the LRBBI field, use of such a wire to compensate the parasitic crossings was suggested for hadron colliders [13] and has been extensively modelled. Some experimental investigation has been carried out with inconclusive results [14]. Fields from wires have also been used to simulate parasitic crossings effects. [15] We mention in passing that electron beam lenses for hadron colliders have been investigated at the Tevatron with some success. [16,17]

Wire compensation for lepton colliders has been studied and tested at DAΦNE [18]. While some improvement in lifetime of the traditionally weak beam was obtained in one configuration, no benefit was found in a second configuration of the interaction region.

With individual control of quadruples, it may be possible to mitigate parasitic crossing effects by changing focussing local to each parasitic crossing as a function of bunch currents. This was modelled and tested at CESR [19] with some success, using the calculated focussing at the core of the "weak" bunch. Models showed some increase in dynamic aperture, and a 20% increase in beam current was obtained in a test configuration emphasizing the parasitic crossing limitations compared to the head-on BBI. This configuration was not optimum for luminosity however.

## LRBBI IN CIRCULAR HIGGS FACTORIES

The choices for mitigation of parasitic crossing effects in large circular colliders are limited, or at least more difficult, compared to the lepton machines discussed above.

Since extensive installation of trim or compensating elements will be costly, a solid program for modelling the

ISBN 978-3-95450-172-4

optics and beam dynamics is essential, and a sizable part of the R&D effort should be budgeted for modelling and simulations.

The LEP experience is most relevant for the size (energy) of the ring. The beam lifetime in a Higgs Factory precludes low energy injection so this is one LEP effect that will not have to be managed.

Compensating quadrupole families and achromatic sextupole groups will likely be essential, as will trim of differential beam positions.

## REFERENCES

(Note: Papers cited from accelerator conferences (EPAC, IPAC, PAC) may be found at http://jacow.org)

[1] J.M. Jowett, "Beam Dynamics at LEP," CERN SL/98-029 (AP)

[2] A.B. Temnykh, J.J. Welch, "Some Aspects of the Long Range Beam-Beam Interaction in Storage Rings," PAC May,1993, Washington D.C., p. 3476

[3] A.B. Temnykh, D. Sagan, "The Incoherent Long Range Beam-Beam Interaction in CESR," PAC May, 1997, Vancouver, p. 1768

[4] Y. Alexahin, T. Sen, M. Xiao, "Beam-Beam Excited Synchro-Betatron Resonances in the Tevatron Run II Lattice," Proc. Of Workshop on Beam-beam Effects in Circular Colliders, Batavia 2001, http://www.slac.stanford.edu/econf/C0106258/

[5] J.M. Jowett in Handbook of Accelerator Physics and Engineering, World Scientific,1999

[6] A.B. Temnykh, J.J. Welch, D.H. Rice, "The Long Range Beam-Beam Interaction at CESR – Experiments, Simulation and Phenomenology," PAC May, 1993, Washington D.C., p. 2007

[7] D.L. Rubin, "CESR Status and Performance," PAC June, 2001, Chicago, p. 3520

[8] D. Sagan, D. Rubin, "CESR Lattice Design," PAC June, 2001, Chicago, p. 3517

[9] A.B. Temnykh, J.J. Welch, "Coherency of the Long Range Beam-Beam Interaction at CESR," PAC May, 1995, Dallas, p. 2771

[10] R. Bailey, et al., "Commissioning and Operation of the LEP Pretzel Scheme," PAC May, 1993, Washington D.C., p. 2013

[11] R. Bailey, et al., "Operational Procedures to Obtain High Beam-Beam Tune Shifts in LEP Pretzel Operation," PAC May, 1995, Dallas, p. 548.

[12] M.G. Billing, J.A. Crittenden, M.A. Palmer, "Investigations of Injection Orbits at CESR based on Turn-by-Turn BPM Measurements," PAC May, 2005, Knoxville, p. 1228

[13] J.P. Koutchouk, "Correction of the Long-Range Beam-Beam Effect in LHC using Electromagnetic Lenses," Batavia 2001, Op.cit.

[14] H.J. Kim, T. Sen, "Long-Range Beam-Beam Compensation in RHIC," IPAC May, 2010, Kyoto, p. 2072

[15] V. Shiltsev, "Tevatron Electron Lens for Beam-Beam Compensation: First Experimental Results," Batavia 2001, Op.cit.

[16] U. Dorda et al., "Wire Excitation Experiments in the CERN SPS," EPAC'08, May, 2008, Genoa, p. 3176

[17] V. Shitsev, et al., New Jour,Phys., **10** (2008) 043042

[18] C. Milardi et al., "DAΦNE Lifetime Optimization with Compensating Wires and Octupoles," CARE-HHH-APD IR'07 Workshop, Frascati, Nov. 2007, arxiv-web3.library.cornell.edu /pdf/0803.1544v1

[19] M.G. Billing, J.A. Crittenden, "Beam-Beam Interaction Studies at the Cornell Electron Storage Ring," Phys. Rev. ST Accel. Beams **9**, 121001 (2006)



ISBN 978-3-95450-172-4

# MONTE-CARLO SIMULATION OF SYNCHROTRON RADIATION IN THE DESIGN OF CEPC VACUUM CHAMBER

DING Ya-dong, MA Zhong-jian, WANG Qing-bin, WANG Pan-feng
Institute of High Energy Physics, Chinese Academy of Sciences, Beijing 100049 China

*Abstract*

The circular electron positron collider (CEPC) has been proposed by IHEP. Two 120GeV beams circulate around the 54km accelerator rings, which produce intense synchrotron radiation with photon energies up to a few of mega-electron volts. It is very important to analysis the source of synchrotron radiation. Two techniques of designing vacuum chamber which are contained Al covered by Pb and totally by Cu are put forward to protect sensitive machine components. A Monte-Carlo program called MCNP has been used to calculate dose rate, heat and energy spectrum of synchrotron radiation in the tunnel in former two designing cases. The results including dose rate, heat and energy spectrum which performed in various components of the CEPC are shown in this article.

## INTRODUCTION

Synchrotron radiation (SR) is a kind of electromagnetic radiation which is released by charged particles, when the speed of particles is close to the speed of light ($v \approx c$), while particles are moving in the magnetic field along the arc track. In CEPC, 120GeV electrons and positrons pass through the dipole magnets and focusing (quadrupole) magnets, which are always accompanied by the emission of SR. The spectrum of SR extends from the region of visible light through the energy range of ordinary diagnostic X-rays (hundreds of kilo-electron volts) up to ten mega-electron volts in the vacuum chamber. By calculation, the power of SR emitted per unit length is huge, which is up to 1KW/m. Hence, SR can bring about very high radiation dose rates in many components of accelerator and Air of the tunnel, which will induce the problems of heating of the vacuum chamber, radiation damage to machine elements, formation of ozone and nitrogen oxides in the air, further lead to corrosion of machine components and act [1],[2]. At present, two methods of designing vacuum chamber are proposed, there are including manufactured by Aluminum material [3],[4] and covered by lead shield, or fabricated totally by copper. Therefore, it is essential to confirm relevant parameters of these two choices, such as energy deposition, energy spectrum in every part of the tunnel, which could be used to calculate heat quantity, dose rate, the amount of harmful gases.

## ANALYSIS OF SYNCHROTRON RADIATION SOURCE

In the accelerator, the spectrum of SR depends on the charge, the mass and energy of the particle and the bending radius. When determining the effects of SR, there are two important parameters including: the radiated power per unit beam path and the critical energy. The power of the synchrotron radiation emitted by the electrons and positrons per unit length is given by the simple expression:

$$P(W/m) = 14.08\frac{E(GeV)^4 I(mA)}{\rho(m)^2} \quad (1)$$

With $P$, the synchrotron power loss is in W/m;
$E$, the energy of electrons and positrons is in GeV;
$I$, the current of the circulating particles is in mA;
$\rho$, is the bending radius in meter.

The critical energy of synchrotron spectrum divides the emitting radiation power in two halves, which is defined by the following expression:

$$E_c(keV) = 2.218\frac{E(GeV)^3}{\rho(m)} \quad (2)$$

With $E_C$, the critical energy is in keV.

The energy spectrum of synchrotron radiation can be calculated by the following formula:

$$S\left(\frac{\omega}{\omega_c}\right) = \frac{9\sqrt{3}}{8\pi}\frac{\omega}{\omega_c}\int_{\omega/\omega_c}^{\infty} K_{5/3}(\eta) \quad (3)$$

With $\omega$, the angular frequency of the synchrotron radiation photon in rad/s;
$\omega_c$, the angular frequency of the critical energy photon in rad/s;
$S$, the relative share of spectrum in different frequency separation;
$K$, Bessel function.

992 blocks of magnets will be equipped in the main ring of CEPC, the bending angle would be given in this condition. Meanwhile, synchrotron radiation itself distributes as a solid degree, and the half angle of light cone is $1/\gamma$, which is focused by 85% power of synchrotron radiation, $\gamma$ can be expressed as:

$$\gamma = \frac{E_e}{mc^2} = 1957E_e(GeV) \quad (4)$$

ISBN 978-3-95450-172-4

Table 1: Designing and Calculating Parameters of Synchrotron Radiation

| Parameters of synchrotron radiation | | | values |
|---|---|---|---|
| Beam energy | $E$ | GeV | 120 |
| Beam current | $I$ | mA | 16.60 |
| Bending radius | $\rho$ | m | 6094 |
| Power per unit length | $P$ | W/m | 1305.06 |
| Critical energy | $E_c$ | keV | 628.93 |
| Bending angle | $\theta$ | mrad | 3.1669 |
| Solid degree | $\varphi$ | μrad | 4.2582 |

According to formula 3, if photon energy is lower than 200keV, the following expression could be satisfied the energy spectrum.

$$S\left(\frac{\omega}{\omega_c}\right) = 1.333\left(\frac{\omega}{\omega_c}\right)^{1/3} \quad (5)$$

Though integration of the above formula and calculation of formula 3, it is only a small share of photons number in low energy area to compare with the total number of photons. And, these photons contribute a little of total heat and dose due to their energy. Although, the number of photons decreases with energy reduction when photon energy is lower than 200keV, we do a hypothesis that the number of these photons only contributes to heat in the vacuum chamber, the 1305.06M/m power of synchrotron radiation is totally contributed by the energy higher than 200keV for heat and dose in the air as shown in Figure 1. In this situation, calculation of heat and dose which are harmful to equipment would be conservative.

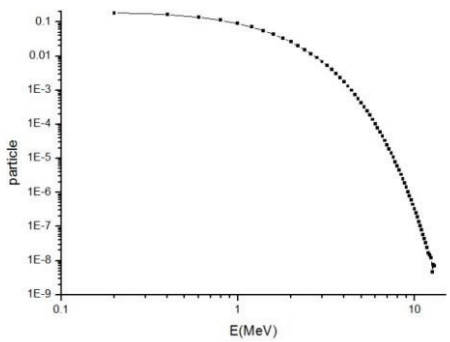


Figure 1: The photon spectrum of synchrotron radiation.

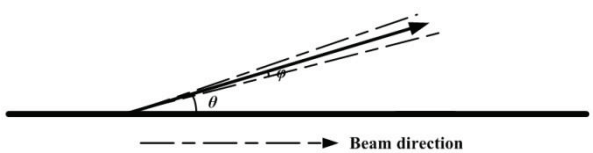


Figure 2: The direction of synchrotron radiation.

The photon spectrum of synchrotron radiation is calculated by formula 3. From energy spectrum and power, we could obtain the total number of photons in different energies. The average energy of photons is 0.9466MeV from the photon spectrum, and total number of photons is $8.62\times1015S^{-1}m^{-1}$. Due to previous hypothesis, power of the photons energy lower than 200keV is less than 40W/m which could be calculated by integration of average energy and total photon counting.In every point of beam direction, conical light of synchrotron radiation emits along a certain angle as shown in Figure 2.

## MONTE-CARLO SIMULATION

In Monte-Carlo simulation, the tunnel and vacuum chamber of CEPC are regarded as straight sections, because the bending radius is larger than the distance which photons pass though vacuum chamber. As we know, the vacuum chamber may be manufactured by aluminum (Al), lead (Pb) or copper (Cu), it is necessary to acquaint shielding effective of these three kinds of materials. In Figure 3, the mass attenuation coefficients of Cu are between Al's and Pb's, so the vacuum chamber fabricated by Cu could instead of Al and Pb. In the real situation, the expression of $e^{-\mu x}$ is not suitable to calculate flux, spectrum or even dose.

Therefore, A Monte-Carlo program called MCNP is used to study the influence of synchrotron radiation for CEPC main ring, which could be directly used to calculate the energy deposition in the various regions, and use to determine the photon spectrum streaming out from vacuum chamber. The vacuum chamber is composed by a few millimeters of Al covered by 3 or 8mm of Pb or totally by a few millimeters of Cu, while the photons of synchrotron radiation hits the vacuum chamber at a grazing angle of 3.1669mrad, the photon energy streaming into tunnel is rather small, concentrating on hardening of the spectrum.

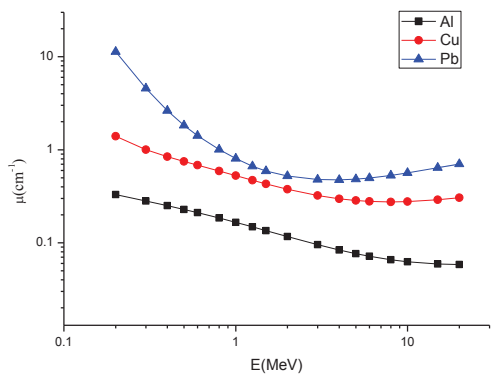


Figure 3: Mass attenuation coefficients of Al, Pb and Cu.

The geometric model is established by MCNP program. The cross section of vacuum chamber is shown in Figure 4, the picture "a" shows chamber is made of Al and Pb, the left and the right ends of the chamber is covered by 8mm Pb, the picture "b" shows chamber is totally manufactured by Cu, the size is as same as the left one. It



ISBN 978-3-95450-172-4

is hard to describe the whole chamber as the arc structure, fortunately the radius of curvature of main ring is up to 6000m, the chamber seems as a straight line in tens of meters distance. Hence, the vacuum chamber is designed as 80 meters long as long as the photon source. If the cross section is regarded as XY plane consistent with the Descartes coordinate system, Z axis is along our sight direction perpendicular to the XY plane, the origin is in the center of the ellipse. Then, the direction of photon could be considered in the XZ plane, with the Z axis direction of 3.1669mrad.

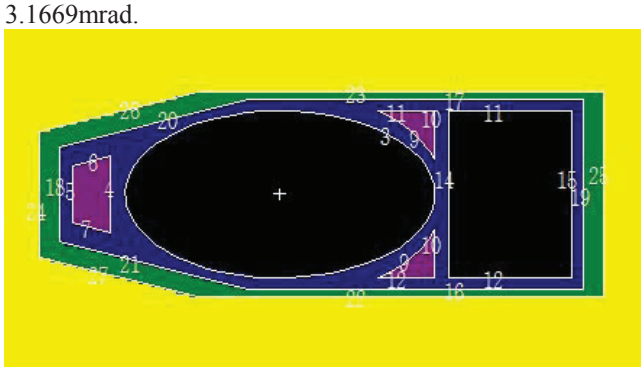

(a)

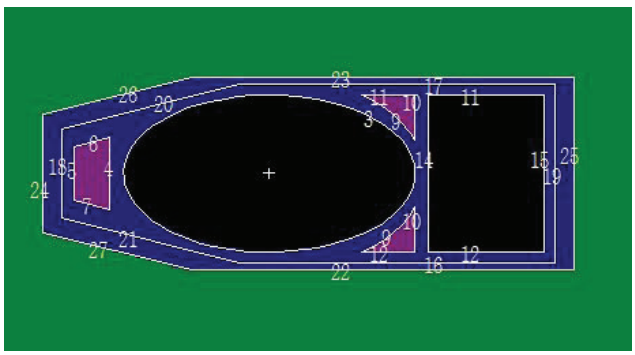

(b)

Figure 4: The cross section of vacuum chamber (a: Al&Pb, b: Cu).

In the input file of MCNP, the 80 meters long tunnel is divided into eight sections, any section is 10 meters long, what is aimed to record energy deposition and spectrum accurately. In the source description, it is a linear source of 80 meters long, and every point on the linear source emits cone light at a certain angle with the linear source. Spectrum is given by discrete points as shown in Figure 1. F6 card is used to record energy deposition of an equivalent photon. F4 card is used to record energy spectrum of photons. The energy deposition of air is in a radius of 2.25m of the tunnel center.

Table 2: Energy Deposition of an Equivalent Photon (in MeV/g), Dose Rate (Gy/h) and Heat (W/m) in Different Areas

| Al&Pb | | | |
|---|---|---|---|
| Materials | Energy Deposition (MeV/g) | Dose rate (Gy/h) | Heat (W/m) |
| Left $H_2O$ | $4.0\times10^{-8}$ | $1.5888\times10^{4}$ | ------ |
| Right$H_2O$ | $1.2\times10^{-7}$ | $4.7664\times10^{4}$ | ------ |
| Al | $5.3\times10^{-7}$ | $2.1052\times10^{5}$ | $7.092\times10^{2}$ |
| Pb | $7.5\times10^{-8}$ | $2.9790\times10^{4}$ | $2.990\times10^{2}$ |
| Air | $3.5\times10^{-10}$ | $1.3902\times10^{2}$ | ------ |

| Cu | | | |
|---|---|---|---|
| Materials | Energy deposition (MeV/g) | Dose rate (Gy/h) | Heat (W/m) |
| Left $H_2O$ | $2.4\times10^{-8}$ | $9.5328\times10^{3}$ | ------ |
| Right$H_2O$ | $5.0\times10^{-8}$ | $1.986\times10^{4}$ | ------ |
| Inner Cu | $2.18\times10^{-7}$ | $8.6594\times10^{4}$ | $9.673\times10^{2}$ |
| Outer Cu | $1.9\times10^{-8}$ | $7.5468\times10^{3}$ | $8.43\times10^{1}$ |
| Air | $2.9\times10^{-10}$ | $1.1519\times10^{2}$ | ------ |

Energy deposition of an equivalent photon, dose rate and power in different areas are given in Table 2. In this model, there is only a vacuum chamber in the tunnel without magnets and other components, so the dose rate in the air is large. Most of the power is converted into heat deposited in the metal.

The spectrum of photons in the air (Al&Pb, Cu) is shown in Figure 5, which is recorded by F4 card. Energy of most of photons is between 100keV and 300keV, the vertical axis represents the flux of photons produced by an equivalent photon. The flux out of Cu is obviously lower than Al&Pb's.

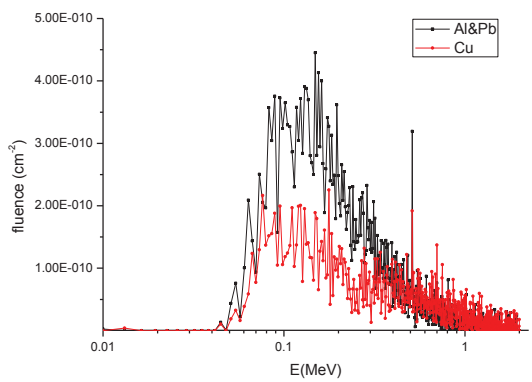


Figure 5: The spectrum of photons in the air (Al&Pb, Cu).

ISBN 978-3-95450-172-4

## CONCLUSIONS

In this study, we use MCNP program to simulate synchrotron radiation problems of vacuum chamber in the accelerator tunnel. MCNP is a useful tool to solve the problems of synchrotron radiation. Though the calculation, it is obviously to obtain the energy deposition of an equivalent photon, which could be used to calculate deposition of heat in the vacuum chamber. Meanwhile, the spectrum of photons in each component could get from simulation. In order to obtain a more adequate result, the physics model which is including a lot of physical entities should be more realistic.

## REFERENCES

[1] A.Fasso, G.R.Stevenson and R.Tartaglia. Monte-Carlo simulation of synchrotron radiation transport and dose calculation to the components of a high-energy accelerator, CERN/TIS-RP/90-11/CF (1990).

[2] K.Burn, A.Fasso, K.Goebel and etal. Dose estimations for the LEP main ring, HS divisional report and LEP note 348 (1981).

[3] A.Fasso, K.Goebel and M.Hoefert. Lead shielding around the LEP vacuum chamber, HS divisional report and LEP note 421 (1982).

[4] A.Fasso, K.Goebel and M.Hoefert. Radiation problems in the design of the large electron- positron collider (LEP), CERN 84-02 Technical Inspection and Safety Commission (1984).



ISBN 978-3-95450-172-4

# VACUUM SYSTEM REQUIREMENTS FOR A HIGGS FACTORY e+e- COLLIDER

R. Kersevan#, CERN, Geneva, Switzerland

*Abstract*

Several proposals for a new class of accelerators called Higgs Factories (HF) have been made in the recent years. The LEP machine, formerly installed in what is today the 26.7 km LHC tunnel, had already given a glimpse of the issues which such machines would have to face. Since the stop and dismantling of LEP, big advancements have been made by the accelerator physics community to develop smart ways of increasing the luminosity. At the same time, the synchrotron radiation (SR) community has worked towards the development of so called "ultimate light sources", which have lately been grouped under the name of "ultra-low emittance" light sources. The merging of the two fields has allowed the development of new magnetic lattices which would allow a HF machine to obtain a very low beam emittance, which in turn would generate, with proper design of the interaction regions (IRs) unprecedented values of the luminosity at center of mass energies in excess of several hundred GeVs. These state-of-the-art accelerators necessarily need state-of-the-art implementation of technologies for their sub-systems, such as radio-frequency (RF), vacuum, feedback and control, etc…

The paper looks into the specific vacuum system requirements stemming from the large size of any HF, its high beam energy, its rather large beam currents and attendant synchrotron radiation losses and loads, just to name a few. It is shown that an optimization of the vacuum system based on discrete, localized absorbers would allow a minimization of the number and size of the pumps, especially if implemented in conjunction with distributed pumping along most of the machine, like was done in LEP. Localized absorbers would also allow concentrating the radiation background generated by the MeV-range critical energy of the SR, and minimizing the radiation damage and material activation in the tunnel.

Delving into the details, and taking into account what has been done for the Long Straight Sections (LSS) of the LHC, it becomes clear that a cost-optimization of the vacuum system is possible under the assumption that an industrial-scale development of the vacuum chamber fabrication and preparation could be carried out.

In principle, there seems to be no major technological show-stopper, since modern B-factories and light sources have already found solutions for dealing with extremely high linear photon flux and power densities.

Based on LEP experience, particular care must be taken in case damping- and beam-polarization- wigglers are installed on the rings.

#e-mail: roberto.kersevan@cern.ch

This paper does not address any specific vacuum issues relevant to the IR regions or to the injectors, which are treated in separate talks.

## BACKGROUND

A wealth of information on the vacuum issues relevant to very high energy e- e+ accelerators has been accumulated during the 12 years of operation of LEP, under its various forms ([1-10], and references therein). In addition to those seen on LEP, a new class of vacuum issues can be expected in HFs due to the extremely low emittance specifications for these machines, which call for narrower gaps in the magnets and stronger focusing gradients. These effects have already appeared in all their magnitude in B-factories, in particular the electron-cloud generated in the $e^+$ ring, an effect which had not affected LEP since it hosted both $e^-$ and $e^+$ beam in the same vacuum chamber.

For the sake of clarity, the well documented case of LEP is taken as a guideline for the discussion, and extrapolations to the design and performance of future HFs are made.

## SYNCHROTRON RADIATION AND GAS LOADS

### *Synchrotron Radiation*

Any multi-GeV $e^+$ and/or $e^-$ accelerator is bound to generate a huge amount of synchrotron radiation (SR). Standard formulae [11] show that the total flux varies linearly with the beam energy, while the total power varies with the $4^{th}$ power of the energy and is inversely proportional to the radius of curvature. For reasons related to obtaining a very low emittance, the radius of curvature of the dipoles for the proposed HFs is always very large, as is the number of dipoles. In the case of the FCC-ee versions proposed by CERN (FCC-ee Z, W, H, tt), the radius of curvature is presently ~ 11 km, i.e. ~3.5x that of LEP (3096 m) [12]. This helps with keeping down the linear flux and power densities, in ph/s/m and W/m respectively, which dictate the local vacuum conditions along the ring. As explained in the nice retrospective review paper [4], SR-induced desorption is the main source of residual gas in the vacuum chamber of a LEP-like accelerator, and is also the source of other different problems. All photons with energies above 4 eV are considered capable of inducing the emission of molecules from the surface of the vacuum chamber, and migration/diffusion from the bulk of it. These molecules in turn move randomly around the chamber until either they reach a pump and are removed or are hit by one of the circulating $e^-/e^+$. In that case the collision can lead to beam losses following different well known mechanisms, and energy deposition, both locally and away from the

ISBN 978-3-95450-172-4

point of collision, as explained in [13]. HFs, in comparison with the higher linear power density of the B-factories, are characterized by the extremely high critical energy of their SR spectra. The critical energy varies with the third power of the beam energy, and is inversely proportional to the bending radius. LEP2 had reached, at 104 GeV, critical energies in excess of 800 keV, and had shown clear signs of additional heating and outgassing loads due to Compton scattered radiation, which becomes a major source as soon as the photon energy reaches few hundreds keV [3]. It becomes therefore mandatory to design the vacuum system in concert with the people dealing with radiation deposition, like has been done in [14].

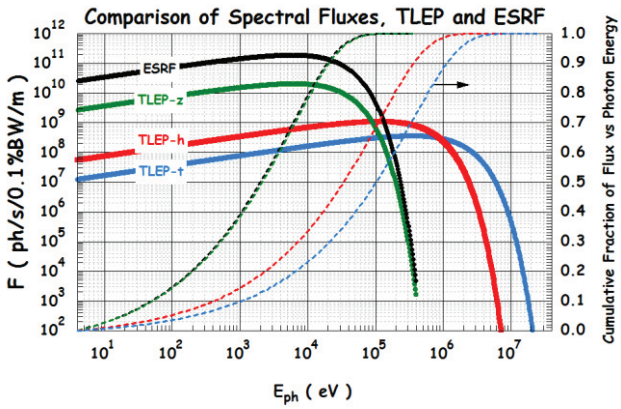


Figure 1: Comparison of the SR spectral fluxes, per meter of dipole length, for various "TLEP" flavours (now called FCC-ee), compared to that of a well-known SR light source, the ESRF. Dotted lines: scale on the right.

## *Gas Loads*

Depending on the solution chosen for the SR absorbers, distributed vs discrete, the gas load of a HF will change a lot. It will also depend on the pumping choice made, since if the NEG-coating solution is employed, the SR-induced desorption yield will be substantially lower as compared to a non-coated solution [15], as indicated in figure 2:

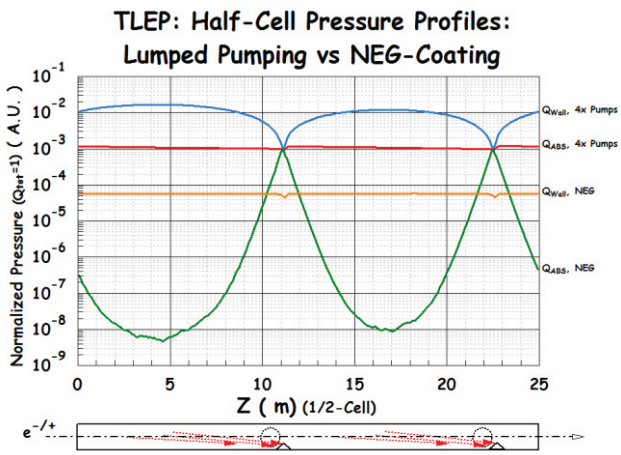


Figure 2: Comparison of calculated normalized pressure profiles for a lumped pumping with distributed SR absorption vs distributed NEG-coating with discrete absorbers. Same total flux [16]. The lower SR-induced desorption yield of NEG-coating has not been taken into account [14].

For some of the HFs under study at this time [12], gas loads of relevant magnitude should only be expected for the high-current, 45.5 GeV Z-pole version, with its 1450 mA beam. Looking at figure 1, it can be seen that the spectrum of such a HF is almost identical to the one generated by the SR light source ESRF, in Grenoble. With a critical energy of about 20 keV, practically all of its photon flux would be capable of desorbing molecules (limited amount of photons escaping the vacuum chamber via Compton scattering, see [2], Sec.5). The linear photon flux, in ph/s/m, at nominal current I and energy E is given by the formula

$$F' = 8.08E + 17 \cdot E(GeV) \cdot I(mA) / (2\pi\rho(m)) \qquad (1)$$

where ρ(m) is the bending radius of curvature.

Inserting the appropriate values in (1) yields the value of F'=8E+17 ph/s/m. This can be converted into practical vacuum outgassing units, for instance mbar·liter/s, via the conversion unit k, 1 mbar·liter = 2.47E+19 molecules (at 20 ºC temperature).

Dividing F'(ph/s/m) by k and multiplying by the photo-desorption yield (PDY) η(molecules/ph) we can obtain a reasonable estimate of the specific gas load Q', in mbar·liter/s/m: Q'=3.24E-2·η.

## *Commissioning Scenarios*

For a non vacuum-conditioned accelerator, η can initially be as high as 0.01 mol/ph. Experimentally it conditions with a slope proportional to $D^{-\alpha}$, with D being the integrated beam dose in mA·hour, and α a coefficient typically ranging between -1 and -0.5 [17]. What is important to notice here, is that the initial η, at machine start-up, can vary by more than 2 orders of magnitude, depending on: 1) the choice of the material of the vacuum chambers; 2) their cleaning procedure; 3) bake-out cycle (or lack of it); 4) eventual presence of low-PDY coatings [15]. These parameters could, in principle, be combined in many different ways, and each combination would yield a different conditioning curve. The time to condition the vacuum system, which in literature is typically obtained when η decreases to 1.0E-6 mol/ph, also has a strong dependence on the combination chosen.

It is of course the responsibility of the vacuum scientists and engineers, to implement the best combination, in agreement with the project team, plan, budget and schedule.

It is important here to notice that there are clear implications of the chosen combination also on the operational constraints in case of vacuum failure, such as the time to recover the conditions prior to the failure, costs associated with the recovery, etc.



ISBN 978-3-95450-172-4

### *Examples*

*Example 1*: Just to clarify this last point, recovering a large vacuum leak in a NEG-coated section would need bake-out and activation of the full sector. Therefore, it would be important to have vacuum sector which are not too long (LEP had ~ 500 m long sectors), but the additional capital and operational cost of a large number of all-metal gate valves (GVs) with RF-contacts has to be weighted in. An 11 km bending radius HF with 200 m vacuum sectors would need of the order of 350 GVs per ring, excluding those installed in the LSS, and those around special non-vacuum equipment (SRF cavities, pulsed magnets, diagnostics, etc...).

*Example 2*: The equations above give a worst case initial value of the specific gas load Q' of ~3.0E-4 mbar·l/s/m and a best case, "fully conditioned" value of ~3.0E-8 mbar·l/s/m. Setting a target average pressure of ~1.0E-9 mbar for being able to run the HF with reasonably low beam-gas scattering levels (~100 hours beam-gas scattering lifetime, [13]), the former value of Q' would need the implementation of an effective specific pumping speed S' of 300,000 l/s/m, which is physically impossible to obtain, while the latter value would imply S'=30 l/s/m, which can certainly be obtained even taking into account the conductance limitations of the chambers, as can be seen in figure 3. In particular, it has been shown that NEG-coating, once activated, can provide an initial η of the order of 1.0E-5 mol/ph [15], meaning that initially a HF like FCC-ee-Z could store beams of the order of ½ its nominal current in a very short time. This simplified numerical estimate does not take into account the additional, and possibly large, gas load generated by any non NEG-coated components facing vacuum which would be hit by stray, scattered photons. This is clearly the case for present day design of sliding contact fingers inside the bellows, an item which has been under close scrutiny by the vacuum community since several decades.

## VACUUM HARDWARE

### *Vacuum Chamber Materials*

LEP had been built using aluminium alloy, mainly for ease of fabrication (good extrusion and machining) and cost, but this choice had a strong impact on its vacuum performance .

First of all, SR-induced desorption from aluminium is well known to be higher compared to that of austenitic steels or copper alloys [3], and therefore needed a more efficient pumping mechanism. Aluminum is also more transparent to high-energy photons, and therefore lets a larger fraction of the SR spectrum escape the vacuum chamber, deposit energy, and create radiation damage and activation on components outside of the vacuum chamber [1-4]. This in turn may generate a higher concentration of ozone in the tunnel, which may provoke corrosion. In order to reduce these effects, a lead cladding had to be installed all around the vacuum chamber [7], and this in turn created other unexpected problems (de-polarization of the beams due to nickel in the Al-to-Pb bonding layer, and localized heating of the chamber). Aluminium chambers also dictated, in LEP, a low bake-out temperature and the need to develop custom sealing flanges based on soft, pure aluminium, with diamond-shaped rings, which could only be baked at low temperatures. This low temperature bake-out, maximum 150 ºC via super-heated water, reduced the effectiveness of the bake-out procedure.

On the other hand, modern B-factories have accumulated experience with copper for the fabrication of their vacuum chambers (typically for the high-energy ring), and therefore a natural choice would be to employ Cu, due to its superior mechanical strength, better electrical conductivity and thermal dissipation higher density and attenuation factor. On the other hand, copper alloys cannot be extruded as easily as aluminium ones, and are more expensive. They can be baked to higher temperatures as compared to aluminium ones, and this may help for the passive activation of NEG-coatings during bake-out (see sections below).

Austenitic stainless steel is the best known material and the one most used for the fabrication of vacuum components. It has strengths and weaknesses as compared to aluminium and copper, though. In particular it has a very low electrical conductivity, and has a low thermal conductivity as well. On the other hand, it is easily weldable and via the ConFlat design of the flanges, can be baked at high temperatures, therefore assuring water vapour-free residual gas composition, and passive activation of NEG-coatings (see sections below).

### *Vacuum Hardware*

Contrary to LEP, the proposed HFs have all in common a very low emittance target, which demands a very careful design of all components such as bellows, flanges, tapered transitions, beam-position monitors (BPMs), feed-back and control instrumentation (horizontal or vertical electrostatic separators, stripline monitors, injection and ejection kickers and septa, beam scrapers, SR-light monitors, low-gap wigglers or undulators, etc…). The analysis and design of such components must be carried out in close collaboration with people doing impedance studies, as there is ample evidence that adverse effects take place in low-emittance machines whenever there is a change of cross-section of the vacuum chamber, or material properties change (e.g. with regards to coatings of surfaces). Also, the bake-out cycle demands a careful placement of a sufficient number of low-impedance bellows, in order to take care of the elongation of the chamber, and possible misalignment, during bake-out. In particular, LEP suffered a number of failures at bellows, especially when affected by high-order mode (HOM) radiation leaking from RF cavities or other components capable of trapping HOMs, and stray SR from strong quadrupoles in the LSS [4]. Clearly, all vacuum hardware components must be carefully integrated into the CAD model and a series of ray-tracing runs, taking into account any possible positioning tolerances for the beam orbits and

ISBN 978-3-95450-172-4

vacuum chambers, must be carried out. Modern computing tools allow to do this, either open-domain software [18, 19], or commercial ones.

Another accelerator hardware category to mention is the RF cavities. For reasons of energy conservation and needed acceleration gradients, superconducting RF technology (SRF) is mandatory whenever high beam energies are to be reached. This was the case for the LEP-2 upgrade, which more than doubled the initial energy of 45 GeV. SRF cavities need a very good vacuum in the sections between different cryomodules, and those preceding and following them, in order to minimize the possibility of polluting the surface of the cavities, which is kept at liquid He temperatures. For the HFs under study now, the LSS seem to be sufficiently long so as to guarantee the possibility of placing the SRF cavities sufficiently far from the nearest dipoles and their powerful SR fans. Alternatively, the SRF cavities must be protected by carefully designed SR absorbers with large-conductance pumping systems. This kind of analysis and technology has already been developed for high-current B-factories and SR light sources, and therefore it should not constitute a major hurdle towards the design and construction of a HF.

### *Pumping System*

Contrary to the custom of the times, which employed either lumped pumps or distributed ion-pumps inside the dipoles, a novel pumping solution was proposed and finally adopted for LEP [20]. The NEG strip, combined with the possibility to extrude complicated shapes out of aluminium, allowed the implementation of distributed pumping along the arcs of LEP. Distributed pumping is much more effective than lumped pumping in conductance-limited vacuum systems [21]. The St101 NEG strip of LEP installed in the ante-chamber generated about 260 l/s/m of average pumping speed along the dipole chambers: in order to obtain the same average pumping speed using lumped pumps of 500 l/s, they should be installed at ~2 m spacing from each other, which would be impractical and extremely expensive. For LEP, with its ~ 3 km radius of curvature, it would have meant of the order of 8,800x 500 l/s pumps (as a best case, without considering further restrictions coming from the conductance limitation at the pumps' throats, e.g. RF-shielding grids).

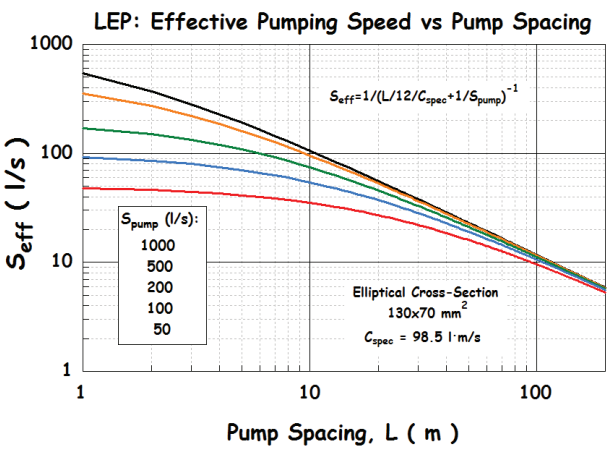


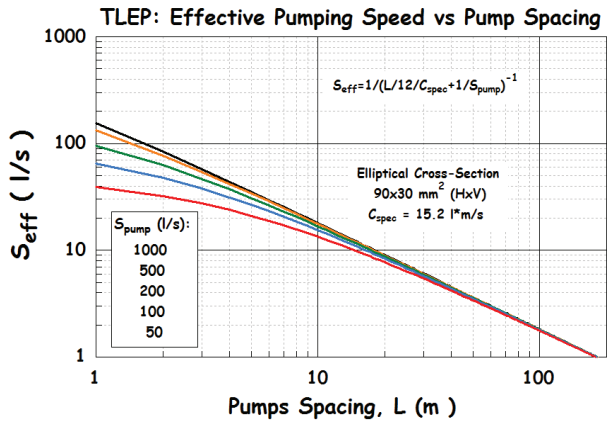


Figure 3: (top) LEP elliptical chamber: effective pumping speed vs pump spacing for different pump sizes; (bottom) same for the proposed FCC-ee chamber [10, 14].

Trying to obtain the same pressure inside of a FCC-ee-like machine would be physically impossible even using 1000 l/s pumps installed at 1 m spacing, as figure 3 (bottom) shows: an effective pumping speed slightly above 150 l/s/m would be obtained. This is the consequence of the fact that the specific conductance of the proposed FCC-ee chamber is ~ 6.5 times smaller than that of the elliptical LEP chamber. This demonstrates once more the effectiveness of distributed pumping vs discrete pumping in conductance-limited vacuum systems.

The importance of the specific conductance is evident when comparing the value for different cross-sections. In figure 4 the parabolic pressure profiles obtained along 5 different 5 m-long chambers is shown. We have chosen the two cross-sections of the KEK-B machine [22], the 130x70mm$^2$ elliptical chamber of LEP (without antechamber), and the proposed FCC-ee elliptical 90x30mm$^2$. The KEK B chambers are round 94 mm ID,and racetrack 150x94 (HxV) mm$^2$.

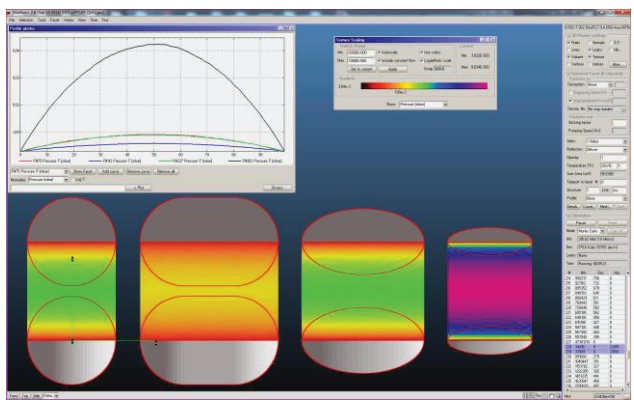

Figure 4: Parabolic pressure profiles along the 5m-long chambers. From left to right: KEK B round and racetrack, LEP, FCC-ee. 160 l/s pumps are assumed at each extremity of the chambers. A unitary outgassing rate is also assumed. The colour-coded pressure along the rectangular transparent facet on the plane of the orbit is in logarithmic scale.



ISBN 978-3-95450-172-4

It has already been shown [16] that for an effective reduction of the outgassing rate and effective pumping to take place, a discrete absorber design of the vacuum system should be preferred as compared to a distributed absorption of SR along all chambers (as had been the case for LEP). It is interesting to note that the LEP design team had, in effect, considered the possibility of implementing such a discrete absorber design (page 30 of [9], and [10]), but their estimation of needing a ~1.5 m spacing between adjacent absorbers led them to the conclusion that it was not practical to do it. Although not clearly stated in their report, it is our impression that the 1.5 m spacing was dictated by the fact that LEP was a two-beams-in-one-chamber accelerator, with need to accommodate future changes in the pretzeled orbits. Clearly, a separated-ring design, where the $e^-$ and $e^+$ have each dedicated arc chambers, with a larger bending radius would help in this direction, as is the case for the FCC-ee study machine. As shown in [14,16], a single-beam HF with ~ 9 km bending radius of curvature would need a spacing of about 12 m, in order to absorb all primary photons [16] (i.e. except those scattered on discrete absorbers), see figure 5, and ~6 m for minimizing the amount of radiation scattered on the magnet coils and in the tunnel (creation of ozone) [14], see figure 6. On the other hand, the $e^+$ beam would suffer from the e-cloud effect, as seen in all machines dedicated to $e^+$, and appropriate mitigation mechanisms should be envisioned in that case (low secondary electron yield – SEY– coatings or solenoids).

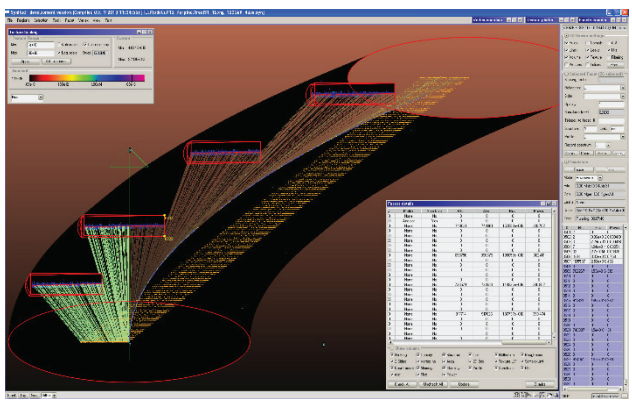

Figure 5: Ray-tracing (SYNRAD+ code [18]), of a half-cell FCC-ee arc chambers, with 4 discrete absorbers [16]. 100 percent of the primary SR fan is intercepted by the Cu absorbers. Elliptical chamber, 90x30 mm$^2$ (HxV).

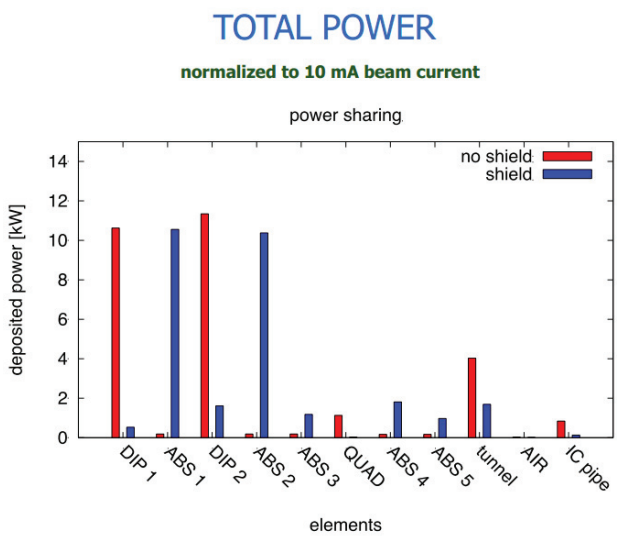


Figure 6: Four absorbers per 25 m section of the FCC-ee FODO arc elements. Copied from [10]. In addition to covering 100% of the primary photon hits, the additional 4 absorbers/half-cell minimize also the Compton-scattered radiation to the coils of the magnets and to the tunnel.

## CONCLUSIONS

### *General Remarks*

This paper has used a retrospective view and analysis of data of the operation of the vacuum system of LEP, as the natural ancestor of today's high-energy Higgs Factories. It has been shown that the vacuum technology available today is adequate to deal with the demands of such machines. This good news does not, in any way, eliminate or alleviate the need for a careful analysis, based on all available software tools and literature bibliography, of the design of the vacuum system of a HF. In particular, careful 3D ray-tracing, i.e. employing real CAD models of the vacuum chambers, is mandatory, in order to avoid the appearance of hot-spots during the operation of the machine.

Also, the paper has given indication of possible choices which could be made in terms of vacuum equipment (materials, treatments, sectorization, bake-out cycle, NEG-coatings, etc…) which would lead to different commissioning scenarios, or scenarios to recover from vacuum leaks/problems, and including rather wide budget envelopes for the total cost of the vacuum system.

Just to stress this important point once more, a ~66.5 km arc section (FCC-ee, [8]) pumped by lumped pumps installed every 12 meters would mean the need for 5500 pumps per ring, with most of the pumps needing a cable (like in the case of ion-pumps) subject to radiation damage by the high-critical energy SR beams, and an additional couple of flanges plus a spool piece to connect each pump to the beam chamber, in contrast to a NEG-coating solution which has an initial non-negligible capital cost for the coating plant or contract to industry, but then does not need more than one "holding" ion-pump per 50~100 m (depending on the conductance of the chamber).

ISBN 978-3-95450-172-4

*Requirements*

- Cross-section of the vacuum chamber as big as possible (to maximize the specific conductance)
- Implementation of distributed pumping scheme
- Choice of a combination of vacuum chamber material and treatments which assure the lowest possible photon-induced desorption
- Careful analysis and design based on 3D ray-tracing
- Optimization of the vacuum sector length
- Capability to bake-out the vacuum chamber to, at least, 200 ºC
- Implementation of e-cloud suppression measures in case of separated-rings option

## ACKNOWLEDGEMENTS

Many thanks to F. Cerruti, L. Esposito of the CERN FLUKA Team for providing several figures and data, and to P. Chiggiato and P. Cruikshank for reading the manuscript.

## REFERENCES

[1] P.M. Strubin et al., "Reliability of the LEP vacuum system", PAC-95, http://www.JACoW.org
[2] M. Jimenez et al., "Experience with the LEP vacuum system at energies above 90 GeV and future expectations", EPAC-98, Stockholm, http://www.JACoW.org
[3] O. Groebner, "Experience with the LEP vacuum system", Workshop on an e+e-ring at VLHC, Illinois Institute of Technology, March 2001, http://www.capp.iit.edu/workshops/epem/Transparencies/Grobner.pdf
[4] M. Jimenez, "LEP2 synchrotron-radiation issues", LEP3 Meeting, Jine 2012
[5] P. Lepeule R. Veness, C.Menot, "Design and Implementation of Synchrotron Radiation Masks for LEP2", LHC/96-08 (VAC) Note, https://cds.cern.ch/record/307861/files/lhc-96-008.pdf
[6] R. Bailey et al., "Synchrotron radiation effects at LEP", EPAC-98, http://www.JACoW.org
[7] O. Groebner et al., "SR lead shielding of the vacuum chambers for LEP", PAC 1983 p2340, http://accelconf.web.cern.ch/AccelConf/p83/PDF/PAC1983_2340.pdf
[8] M. Jimenez et al., "Synchrotron Radiation Power from Insertion Quadrupoles onto LEP Equipment", CERN-SL-98-058 (EA)
[9] A.Zichichi ed., "ECFA-LEP Working Group, 1979 Progress Report", https://cds.cern.ch/record/124218/files/CM-P00100391-e[1].pdf
[10] J.S. Kouptsidis, "Vacuum system design considerations for electron storage rings above PETRA energies", DESY Note M-79/26, June 1979
[11] A. Hofmann, "Characteristics of synchrotron radiation", https://cds.cern.ch/record/375972/files/p1.pdf
[12] J. Wenninger et al., "Future Circular Collider Study – Lepton Collider Parameters", FCC-ACC-SPC-0003, 2014-09-05.
[13] M. Boscolo, "Beam lifetime in low emittance rings", IPAC-13, Shanghai, http://www.jacow.org
[14] F. Cerutti, "Impact of synchrotron radiation in arcs", FCC Study Kick-off Meeting, Univ. of Geneva, February 2014, https://indico.cern.ch/event/282344/contributions
[15] P. Chiggiato, R. Kersevan, "Synchrotron radiation-induced desorption from a NEG-coated vacuum chamber", Vacuum 60 (2001) 67-72
[16] R. Kersevan, " Synchrotron radiation & vacuum concepts", FCC Study Kick-off Meeting, Univ. of Geneva, February 2014, https://indico.cern.ch/event/282344/session/2/contribution/25
[17] A. G. Mathewson et al., "Vacuum design of synchrotron light sources", Proceedings, 2nd Topical Conference, Argonne, USA, November 13-15, 1990 - Amer, Y.G. et al. editors, New York, USA: AIP (1991) 428 p. ; AIP conference proceedings, 236). (American Vacuum Society series, 12
[18] R. Kersevan, M. Ady, SYNRAD+ code, http://test-molflow.web.cern.ch/content/synrad-downloads
[19] FLUKA Team, "FLUKA code", http://www.fluka.org/fluka.php
[20] C. Benvenuti, "A new pumping approach for the Large Electron Positron Collider (LEP)", NIM 205 (1983) 391-401
[21] T. Xu et al., "Monte Carlo simulation of the pressure and f the effective pumping speed in the LEP collider", CERN-LEP-VA/86-02
[22] K.Kanazawa et al., "The vacuum system of KEK B", NIM A 499 (2003) 66-74



ISBN 978-3-95450-172-4

# SHIELDING OF ELECTRONICS IN THE TUNNEL

L.S. Esposito#, M. Brugger, F. Cerutti, A. Ferrari, R. Losito, CERN, Geneva, Switzerland

*Abstract*

Radiation to Electronics (R2E) represents a crucial issue to be taken into account as design criterion of any high energy and intensity machine. The different effects on the concerned equipment and the microscopic mechanisms underneath are reviewed. Evaluation and mitigation strategies are presented, based on the support of dedicated Monte Carlo calculations. In the specific context of a future e+e- HF, the relevant radiation sources and their possible impact are discussed.

## INTRODUCTION TO R2E

The study of the electronics sensitivity to radiation requires a multi-disciplinary approach, spanning from the knowledge of the electronic components, to the radiation environment, and to the physics models that describe the interaction of the radiation with the matter. The goals are: (1) to define and quantify the effects of the radiation on the electronics; (2) to monitor and/or estimate the radiation levels in the concerned area; (3) to test and develop radiation-hard or sufficiently tolerant electronics; (4) to implement mitigation options.

R2E is often considered for space applications, where application design, test and monitoring standards are already well defined. However, it is important to note that the radiation environment encountered in a high energy and intensity accelerator, the high number of electronic systems and components exposed to radiation, as well as the actual impact of radiation-induced failures on the machine operation, pose challenges that might strongly differ from the context of space applications.

For a high intensity and energy machine, typical sources of radiation are luminosity debris, direct losses on collimators and dumps, and beam interactions with the residual gas inside the vacuum chamber all along the accelerator, as well as with dust fragments falling into the beam path. But, for the specific case of a lepton machine, an additional main source of radiation in the tunnel is represented by the synchrotron radiation.

In order to evaluate the impact of the radiation on the machine equipment, Monte Carlo simulations represent an indispensable tool. They need to rely both on a refined implementation of physics models of the particle interaction with matter and an accurate 3D-description of the region of interest.

Typically the mixed particle type and energy field of interest in a high-energy environment is composed of charged and neutral hadrons (protons, pions, kaons and neutrons), photons, electrons and muons ranging from thermal energies up to the GeV range. This complex field has been extensively simulated by the FLUKA Monte Carlo code [1,2] and benchmarked in detail for radiation damage issues at the LHC [3,4].

The proportion of the different particle species in the field depends on the distance and on the angle with respect to the original loss point, as well as on the amount (if any) of installed shielding material. In this environment, electronic components and systems exposed to a mixed radiation field will experience three different types of radiation damages:

- damage from the Total Ionizing Dose (TID).
- displacement damage (DD) or non-ionizing dose.
- so-called Single-Event-Effects (SEEs).

The latter ones range from single or multiple bit upsets (SEUs or MBUs), transients (SETs) up to possible destructive latch-ups (SELs), destructive gate ruptures or burn-outs (SEGRs and SEBs).

The first two groups are of cumulative nature and are measured through TID and non-ionizing energy deposition (NIEL [1], generally quantified through accumulated 1-MeV neutron equivalent fluence), where the steady accumulation of defects cause measurable effects which can ultimately lead to device failure.

Being of stochastic nature, SEE failures form an entirely different group. They are due to the direct ionization by a single particle, able to deposit sufficient energy through ionization processes in order to perturb the operation of the device. They can only be characterized in terms of their probability of occurring as a function of accumulated High Energy (> 5 ÷ 20 MeV) Hadron (HEH) fluence. The probability of failure will strongly depend on the device as well as on the flux and nature of the particles.

For accelerator applications, the installed control systems are either fully commercial or often based on so-called COTS (Commercial-Off-The-Shelf) components, both possibly affected by radiation. This includes the immediate risk of SEE with a possible direct impact on beam operation, as well as in the long-term, cumulative dose effects (impacting the component/system lifetime) which additionally have to be considered.

As example, for the tunnel equipment in the existing LHC, radiation was only partially taken into account as design criteria prior to construction, and most of the equipment placed in adjacent and partly shielded areas was not conceived nor tested for their actual radiation environment. Therefore, given the large amount of electronics being installed in these areas, during the past years a CERN wide project called R2E (Radiation To Electronics) [5] was then initiated to quantify the risk of radiation-induced failures and to mitigate the risk for nominal beams and beyond to below one failure a week for all exposed electronic systems together. The respective

#Luigi.Salvatore.Esposito@cern.ch

[1] Non-Ionizing Energy Losses.

ISBN 978-3-95450-172-4

mitigation process included a detailed analysis of involved radiation fields, intensities and related Monte Carlo calculations; radiation monitoring [6] and benchmarking; the behavior of commercial equipment/systems and their use in the LHC radiation fields; as well as radiation tests with dedicated test areas and facilities [7]. In parallel, radiation induced failures were analyzed in detail in order to confirm early predictions of failure rates, as well as to study the effectiveness of implemented mitigation measures.

For the design of a new machine, it is therefore essential to take into account already at an early stage the impact of the radiation on the equipment in order to adopt all the necessary measures to mitigate its effect and develop radiation tolerant electronics.

In the next Section, a case study for a possible FCC-ee tunnel is presented in order to estimate the radiation levels induced by synchrotron light and evaluate its impact on the electronic equipment.

## CASE STUDY

For this study, the FCC arc cell model described in [8] has been used. Table 1 summarizes the main parameters of the 80 km option considered. The geometry consists of a 25 m long half FODO cell, with five 24 cm long absorbers. The latters are shaped with an inner 25 mm copper wing (see Fig. 1). The internal dimension of the elliptical beam pipe considered is 90×30 mm (H×V).

Table 1: Key Parameters of A Possible 80 Km Long E+E-Collider

| Main parameters | 80 km |
|---|---|
| Beam Energy [GeV] | 175 |
| Dipole Bending Radius [km] | 9.8 |
| Critical Energy [MeV] | 1.21 |
| Energy lost per turn [GeV/turn] | 8.5 |
| Energy lost in the dipole [keV/cm] | 1.375 |
| Beam current [mA] | 10 |
| Power lost in the whole accelerator [MW] | 85 |
| Power lost in the dipole [W/cm] | 13.75 |
| Operation time per year [s] | $10^7$ |

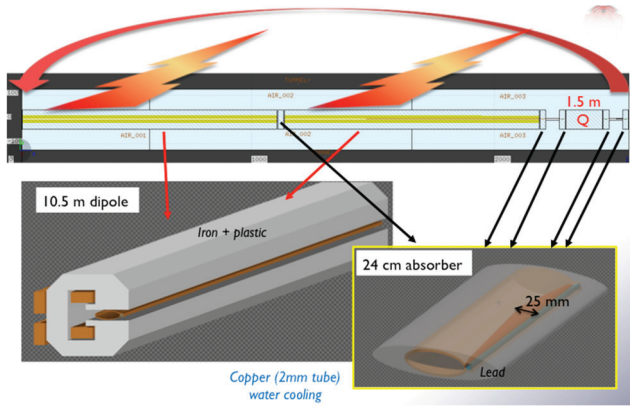


Figure 1: FLUKA geometry layout of the half FODO cell on top, details of the geometry implementation on the bottom: the 10.5 m dipole is shown on the left, while the preliminary design of a possible absorber is on the right, including an external lead shielding of 5 cm.

The synchrotron radiation as implemented in the FLUKA allows to sample from any synchrotron radiation spectrum and accounts for the photon angular distribution and polarization. A proper change of coordinates is applied to particles exiting from the end of the half FODO cell, re-injecting them back at its beginning, in order to account for the contribution of all relevant upstream cells.

The particle spectra at the height of 1 meter from the beam line in correspondence of the interconnect between the second dipole and the arc quadrupole are shown in Fig. 2. The particle fluence is dominated by the photons peaked at about few hundred keV. The spectrum of neutrons produced in photonuclear interaction ranges from about MeV down to thermal energies.

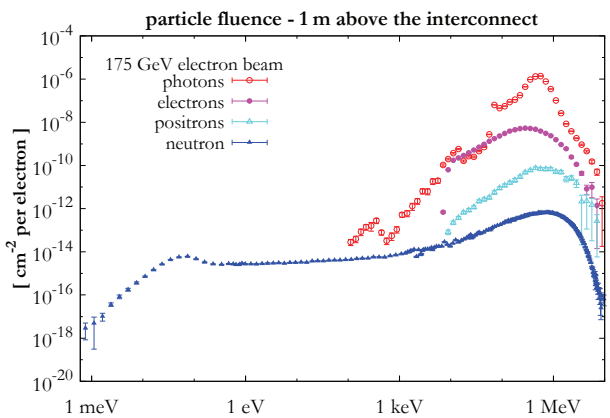


Figure 2: Energy spectra of different particle species in air at the height of 1 meter from the beam line, in correspondence of the interconnect between the dipole and the arc quadrouple.

Figure 3 shows HEH fluence, Silicon 1 MeV-neutron equivalent fluence and dose in the tunnel of a FCC-ee for an accumulated charge equal to 10 mA × $10^7$ s. The values are azimuthally averaged.



ISBN 978-3-95450-172-4

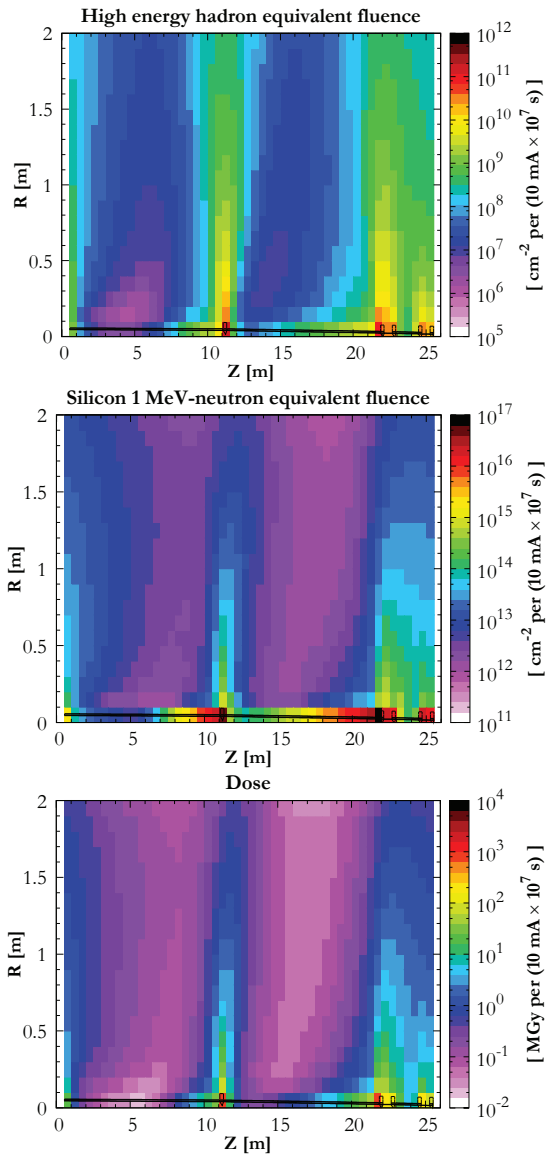


Figure 3: HEH fluence (top), Silicon 1-MeV neutron equivalent fluence (middle), dose (bottom) expected in the tunnel of a FCC-ee arc half FODO cell for an accumulated charge equal to 10 mA × $10^7$ s.

The patterns present hot spots along the beam pipe in correspondence of the interconnects where the synchrotron radiation absorbers are placed.

The resulting values indicate that, depending on the location, any equipment installed in the tunnel might not only suffer SEE failures, but will mainly be heavily impacted by the TID effects thus limiting the equipment lifetime.

In particular, TID values of the order of 100 kGy ÷ 1 MGy represents a problem for the use of any active electronics. Fully commercial systems (COTS based) are to be avoided, because only after careful selection and qualification they can rarely stand more than a kGy level, while special radiation hard component might stand up to a few 10 kGy. In case they are required, their failure impact and mitigation measures have to be studied in the context of accelerator operation. Therefore, a detailed study is needed in order to coherently design the areas housing the required control electronics that can sustain significant radiation levels and mitigation measures must be addressed during the early design phase (shielding measures, minimal requirement of control electronics, maximum cable lengths, etc.).

In parallel, also with respect to material damage, a careful choice is necessary because some material, especially organic, can withstand radiation levels only in the order of ten kGy and start deteriorating afterwards.

## CONCLUSION

The design of a FCC-ee machine should carefully address R2E and general radiation damage issues. The main concern is represented by the damage from TID that can eventually lead to device destruction. For the tunnel equipment (and in adjacent and partly shielded areas), a full understanding of the radiation levels is necessary. The efficient use of benchmarked Monte Carlo codes such as FLUKA is an indispensable tool to anticipate radiation issues and to implement a correct protection strategy, by means of dedicated shielding and/or electronics hardening.

## REFERENCES

[1] G. Battistoni et al., “The FLUKA code: Description and benchmarking”, AIP Conf.Proc. 896 (2007) 31-49.

[2] A. Ferrari et al., “FLUKA: A multi-particle transport code (Program version 2005)”, CERN-2005-010; http://www.fluka.org

[3] M. Brugger et al., “FLUKA capabilities and CERN applications for the study of radiation damage to electronics at high-energy hadron accelerators”, Progress in Nuclear Science and Technology, PNST10184-R1 (2010).

[4] K. Roed et al., “FLUKA simulations for SEE studies of critical LHC underground areas”, Nuclear Science, IEEE Transactions on, vol. 58, no. 3, p. 932, (2011).

[5] R2E website, www.cern.ch/r2e

[6] G. Spiezia et al., “The LHC accelerator Radiation Monitoring System – RadMON”, in Proceedings of Science, 2011.

[7] M. Brugger et al., “R2E Experience and Outlook for 2012”, Proceedings of LHC Performance workshop, Chamonix 2012.

L. Lari et al. “Beam-machine Interaction at TLEP: First Evaluation and Mitigation of the Synchrotron Radiation Impact”, IPAC2014, THPRI011.



ISBN 978-3-95450-172-4

# CHOICE OF L*: IR OPTICS AND DYNAMIC APERTURE(*)

A. Bogomyagkov, E. Levichev#, P.Piminov, BINP, Novosibirsk 630090, Russia

*Abstract*

A design of interaction region (IR) optics from the viewpoint of nonlinear motion and dynamic aperture limitation is discussed for the FCCee Crab Waist collision scheme. We use the first order tune-amplitude shift as a figure of merit to characterize the strength of nonlinear perturbation caused by different sources including the final focus kinematic terms, quadrupole fringe field, octupole field error in QD0 and chromatic sextupoles. Theoretical prediction is compared with the tracking results. Dynamic aperture limited by different nonlinearities in the IR is presented and analyzed.

## INTRODUCTION

A drift L* from the interaction point (IP) to the first quadrupole (QD0) in the collider final focus (FF) is an important parameter not only from the viewpoint of a machine detector interface or detector background condition. This drift length also influences the beam optics and dynamics and hence determines the design of the whole IR and beyond. It is essential especially for the Crab Waist (CW) beam-beam collision [1] because this approach assumes that the bulk of luminosity increase comes from an extremely low vertical beta at the IP ($\beta_y^* \le 1$mm), resulting in large chromaticity (for both vertical betatron tune and function) and ~1÷10-km beta in the FF quadrupoles.

Large chromaticity must be corrected by strong sextupole magnets which usually are arranged in pairs and separated by the –I optical transformation [2]. For the ideal kick-like sextupoles such a scheme cancels all geometrical aberrations. For the realistic length sextupoles, the second order aberrations are cancelled exactly while the higher order terms remain and spoil the DA [3].

Very large beta in QD0 amplifies influence of nonlinear imperfections in quadrupole fields (including the fringe fields and the field errors inside) on nonlinear beam dynamics. These effects can also provide the DA reduction.

One more source of the DA shrink is kinematic terms which originated from the fact that due to a large transverse momentum in the first drift, usual paraxial approximation is not still valid and the next momentum terms should be taken into account.

All the above-mentioned effects are discussed and estimated below. The problem is that there is no general criterion to evaluate relative contribution of a particular nonlinear perturbation to the DA size. Fortunately all important effects are of the forth power (octupole-like) in Hamiltonian canonical variables. Basing on this fact we suggest using vertical nonlinear detuning coefficient as a figure of merit to compare different effects depending on L*. Numerical simulation of the DA shows strong and weak points of such approach.

(*) Work supported by the Ministry of Education and Science of the Russian Federation

#E.B.Levichev@inp.nsk.su

## IR ARRANGEMENT

Typical CW IR consists of several optical modules as it is shown in Figure 1. Strong FF quadrupole doublet squeezes the beam at the IP. The final focus telescope (FFT) matches the IP lattice functions to the rest of the IR. The chromaticity correction section YXCCS consists of the sextupoles Y1-Y2 and X1-X2 combined in two pairs with –I transformation inside of each pair.

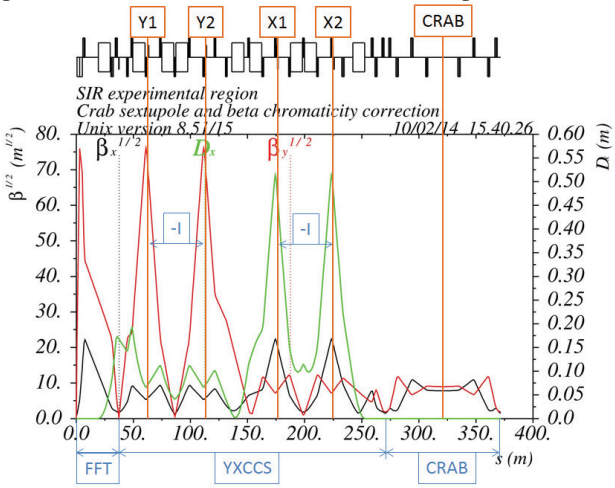


Figure 1: Optical arrangement of the FCCee IR (one half) in the CW mode for L* = 0.7 m.

Dispersion function in the chromaticity correction section is excited by a dipole magnet (BM in Figure 2) and the vertical beta in the Y sextupole pair is as large as in the QD0. Finally the crab sextupole is placed at the end of IR at the proper phase advance with respect to the IP.

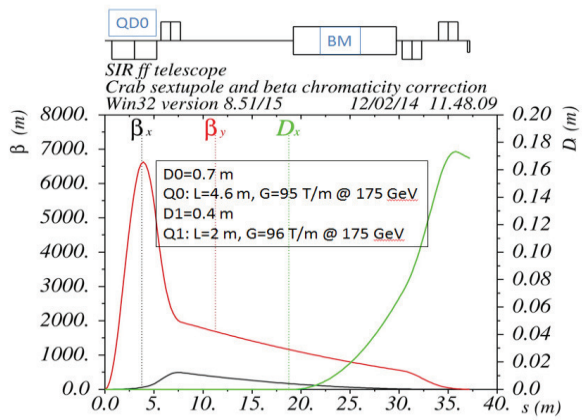


Figure 2: Final focus arrangement.

For the FF parameters shown in Figure 2, $\beta_y^* = 1$ mm yields almost 7 km beta in the middle of QD0.



ISBN 978-3-95450-172-4

## QD0 CHROMATICITY

Assuming the vertical beta derivative changes its sign in the middle of QD0 $\alpha_{yOUT} = -\alpha_{yIN}$, one can find the relevant integrated quadrupole strength as

$$(-k_1 L)_{QD0} = 2 / L^* . \quad (1)$$

Then, taking into account the beta behaviour over the quadrupole length, the chromaticity produced by QD0 is expressed as (one arm of the IR)

$$\mu'_y \approx -L^* / \beta^*_y . \quad (2)$$

The tune chromaticity associates with the Montague chromatic function $a_y$ [4] excited by QD0 and determining the optical functions behaviour with non-zero $\delta = \Delta p / p_0$ as

$$2\mu'_y = a_y = \frac{d\alpha_y}{d\delta} - \frac{\alpha_y}{\beta_y}\frac{d\beta_y}{d\delta} .$$

To compensate tune and beta chromaticities, we place a pair of vertical sextupoles with $\Delta\mu_y = n\pi$ from QD0 and determine the integrated sextupole strength from the following equation (sextupole pair)

$$\mu'_y + \frac{1}{2}(k_2 2L_s)\beta_{ys}\eta_s = 0 . \quad (3)$$

More details on the FCC-ee IR chromatic functions calculation and control can be found in [5].

## NONLINEAR TUNE SHIFT

Due to the extremely low vertical beta at the IP and, consequently, extremely large vertical beta in QD0 and chromatic sextupoles, nonlinear motion in the vertical plane determines the IR DA in both directions (in the horizontal one through the coupling terms). To compare relative "power" of different nonlinearities in the IR as a function of $L^*$, we suggest to use a nonlinear detuning coefficient $\alpha_{yy}$ providing the tune shift according to

$$\Delta\nu_y = \alpha_{yy} J_y, \; J_y = A_y^2 / 2\beta_y .$$

where $J_y$ is the vertical action. Fortunately all the nonlinearities we consider here are of the 4th power in canonical variables

$$\Delta H_2 \sim y^n p_y^m, \qquad n+m=4 .$$

and for such (octupole-like) perturbation $\alpha^{yy}$ can be found easily in the first order of perturbative calculation. Moreover, $\alpha_{yy}$ is additive for different sources over the lattice section

$$\alpha_{yy} = \alpha_{yy1} + \alpha_{yy2} + ... = \int_{s_1}^{s_2} (F_1 + F_2 + ...) ds .$$

so one can estimate a combined contribution of several nonlinearities or find a way how to compensate them by introducing nonlinear correctors.

### *Kinematics Nonlinearity*

For large transverse momentum the first order correction of non-paraxiality is given by

$$\Delta H_2 = \frac{1}{8}\left(p_x^2 + p_y^2\right)^2, \alpha^k_{xx} = \frac{3}{16\pi}\int \gamma_x^2(s) ds .$$

$$\alpha^k_{xy} = \frac{1}{8\pi}\int \gamma_x(s)\gamma_y(s) ds, \; \alpha^k_{yy} = \frac{3}{16\pi}\int \gamma_y^2(s) ds .$$

where $\gamma_{x,y}(s)$ is the Twiss parameter. The main contribution comes from the first drift [6]

$$\alpha^k_{yy} = \frac{3}{16\pi}\frac{2L^*}{\beta^{*2}_y} \approx -\frac{3}{16\pi}\frac{2\mu'_y}{\beta^*_y} . \quad (4)$$

where $2L^*$ is the distance between two 2QD0s, hence this expression includes both arms of the IR.

### *QD0 Fringe Fields*

Quadrupole fringe field nonlinearity in the hard-edge approximation is described by the following Hamiltonian

$$\Delta H_2 = -k'_1(s) x^2 y p_y / 2 + k''_1(s)\left(y^4 - 6x^2 y^2\right)/24 .$$

and the vertical detuning coefficient is given by [6]

$$\alpha^f_{yy} = \frac{1}{16\pi} k_{10}\left(\beta_{y1}\beta'_{y1} - \beta_{y2}\beta'_{y2}\right) .$$

where $k_{10}$ is the central gradient of QD0 and lower digital indices correspond to the entrance and the exit of the quadrupole. Calculating the betas and their derivatives at the QD0 edges

$$\beta_{yeQD0} \approx \frac{L^{*2}}{\beta^*_y}, \qquad \beta'_{yeQD0} \approx \pm\frac{2L^*}{\beta^*_y} .$$

one can obtain the following simple estimation (2×QD0)

$$\alpha^f_{yy} \approx -\frac{1}{2\pi} k_{10}\frac{L^{*3}}{\beta^{*2}_y} \approx -\frac{1}{2\pi} k_{10} L^* \mu'^2_y . \quad (5)$$

ISBN 978-3-95450-172-4

### *Octupole Error in QD0*

An octupole field error (or corrector) in QD0 is described by

$$\Delta H_2 = k_3(s)\left(x^4 - 6x^2y^2 + y^4\right)/24.$$

$$\alpha^o_{yy} = \frac{1}{16\pi}\int k_3(s)\beta_y^2(s)ds = \frac{1}{16\pi}k_3\bar{\beta}_y^2 L_{QD0}. \quad (6)$$

Introducing the relative octupole field error at the aperture radius $r_a$

$$q = \frac{\Delta B_o(r_a)}{B_Q(r_a)} = \frac{k_3}{6k_1}r_a^2.$$

we can rewrite (2×QD0)

$$\alpha^o_{yy} = \frac{3}{4\pi}\frac{q}{r_a^2}k_{10}L_{QD0}\bar{\beta}_y^2 \approx \frac{3}{2\pi}\frac{q}{r_a^2}\frac{L^{*3}}{\beta_y^{*2}} \approx \frac{3}{2\pi}\frac{q}{r_a^2}L^*\mu_y'^2.$$

### *Chromatic Vertical Sextupoles*

Two defocusing sextupoles (Y1-Y2 in Figure 1) located at $\Delta\mu_y = n\pi$ with respect to QD0 correct locally the tune $\mu_y'$ and the beta $a_y$ chromaticity. Their strength can be found from (3). To find the vertical detuning coefficient we can use the first order map through the sextupoles separated by –I transform [3]

*Sextupole pair* $$p_y = -p_{y0} - \frac{(k_2L_s)^2L_s}{6}\left(y_0^3 + x_0^2y_0\right).$$

*Octupole* $$p_y = p_{y0} - \frac{k_3L_o}{6}\left(y_0^3 - 3x_0^2y_0\right).$$

By analogy of the sextupole pair map with the octupole one, we can directly use (6) with replacing of $(k_2L_s)^2 \to k_3$:

$$\alpha^{sp}_{yy} = \frac{1}{16\pi}(k_2L_s)^2\bar{\beta}_y^2L_s \quad .$$

for one IR arm. Substituting $\mu_y'$ from (3) and taking into account two vertical chromatic sections, one can find

$$\alpha^{sp}_{yy} = \frac{1}{8\pi}L_s\cdot\mu_y'^2/\eta_s^2. \quad (7)$$

### *Discussion*

Kinematics nonlinearity scales as $\alpha^k_{yy} \sim L^*/\beta_y^{*2} \sim \mu_y'/\beta_y^*$. QD0 fringe field effect grows fast with $L^*$ increase and vertical beta decrease as $\alpha^f_{yy} \sim L^{*3}/\beta_y^{*2} \sim \mu_y'^2L^*$. Octupole error field inside the QD0 demonstrates the same dependence as the fringe field $\alpha^o_{yy} \sim L^{*3}/\beta_y^{*2} \sim \mu_y'^2L^*$ and with the $L^*$ increase, tolerance for QD0 field quality becomes tougher. The vertical sextupoles for local chromaticity correction introduce the amplitude dependent tune shift which scales with the first drift length as $\alpha^{sp}_{yy} \sim \mu_y'^2/\eta_s^2$, and there is a possibility to mitigate effectively this effect by increase of the dispersion function in the sextupoles.

## ESTIMATION VS SIMULATION

The given above expressions were applied to the Crab Waist FCCee IR lattice provided by A.Bogomyagkov [7]. For a range of $L^*$ from 0.7 m to 3 m an appropriate optical solution was found, the chromaticity was corrected and the vertical detuning coefficient was calculated for various perturbation sources. The vertical beta at the IP is $\beta_y^* = 1$ mm. The QD0 strength $k_1 = -0.16\,\mathrm{m}^{-2}$ is the constant for different $L^*$ but its length changes to fit (1). The estimation results are listed in Table 1.

Table 1: $\alpha_{yy}$ for the CW FCCee IR Lattice

| $L^*$(m) | 0.7 | 1 | 2 | 3 |
|---|---|---|---|---|
| $-2\mu'_y$ | 1400 | 2000 | 4000 | 6000 |
| $10^{-6}\alpha^k(\mathrm{m}^{-1})$ | 0.08 | 0.11 | 0.24 | 0.34 |
| $10^{-6}\alpha^f(\mathrm{m}^{-1})$ | 0.009 | 0.025 | 0.21 | 0.71 |
| $10^{-6}\alpha^{sp}(\mathrm{m}^{-1})$ | -8 | -16 | -64 | -144 |

One can see that the sextupole nonlinearity due to the finite length effect dominates in Table 1. The reason is a rather low dispersion $\bar{\eta}_s \approx 0.05$ m in the Y chromatic section because of the strong requirement to match IR in the tunnel as straight as possible (see details in [5]). A larger dispersion could significantly suppress the Y-sextupoles influence (see comments later to SuperKEKB case).

We checked the estimation by particle tracking with the help of MAD8 and the BINP home-made accelerator design code Acceleraticum [8] for $L^*$ = 0.7 m. The IR optics was closed artificially by the linear matrix with the resulting fractional tunes (0.53, 0.57) providing optimum luminosity. The comparison results are given in Table 2.

Table 2: Nonlinear Detuning: Estimation vs Simulation

| | Kin | Fringe | Sext.pair |
|---|---|---|---|
| Simulation | | | |
| $\alpha_{xx}$ ($\mathrm{m}^{-1}$) | 60 | 1100 | -2300 |
| $\alpha_{xy} = \alpha_{yx}$($\mathrm{m}^{-1}$) | 380 | 15300 | $-0.07\times10^6$ |
| $\alpha_{yy}$ ($\mathrm{m}^{-1}$) | $0.075\times10^6$ | $0.1\times10^6$ | $-14\times10^6$ |
| Estimation | | | |
| $\alpha_{yy}$ ($\mathrm{m}^{-1}$) | $0.084\times10^6$ | 8700 | $-8\times10^6$ |



ISBN 978-3-95450-172-4

Table 2 clearly indicates prevailing of the vertical non-linearity over the horizontal one. The most critical contribution comes from the Y chromatic correction section as it was predicted by the simple estimation.

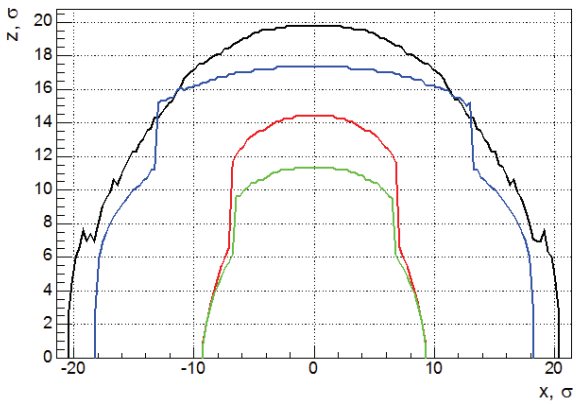


Figure 3: FCCee IR DA for $L^* = 0.7$ m (black), $L^* = 1$ m (red), $L^* = 1.5$ m (green) and $L^* = 2$ m (blue).

A discrepancy in results is explained by the fact that the tracking takes into consideration other sources (like X chromatic section or quadrupole fringes in the Y chromatic module, etc.). Closed ring solution allowed us to find the transverse dynamic aperture for a set of $L^*$. The relevant plot (in the rms beam sizes) is shown in Figure 3 at the IP azimuth with $\sigma_x = 3.24\times10^{-5}$m, $\sigma_y = 6.52\times10^{-8}$m, $\beta_x^* = 0.5$m, $\beta_y^* = 0.001$m.

With $L^*$ increase the DA in Figure 3 predictably shrinks, but for $L^* = 2$ m it surprisingly grows up. The explanation is a more fortunate design of the optics for the Y chromaticity correction section as it is shown in Figure 4. For $L^* = 2$ m the dispersion function inside the Y sextupoles is slightly larger than that for $L^* = 0.7$ m (≈ 10 cm against ≈ 5 cm) while the vertical beta is almost the same so according to (7) the dispersion function increase compensates enlargement of the first drift length in such a way that the DA is almost equal for both cases.

Anyway, even the largest DA in Figure 3 is not so large, only $\approx 20\sigma_x \times 20\sigma_y$, and the question is if it is possible to open it additionally?

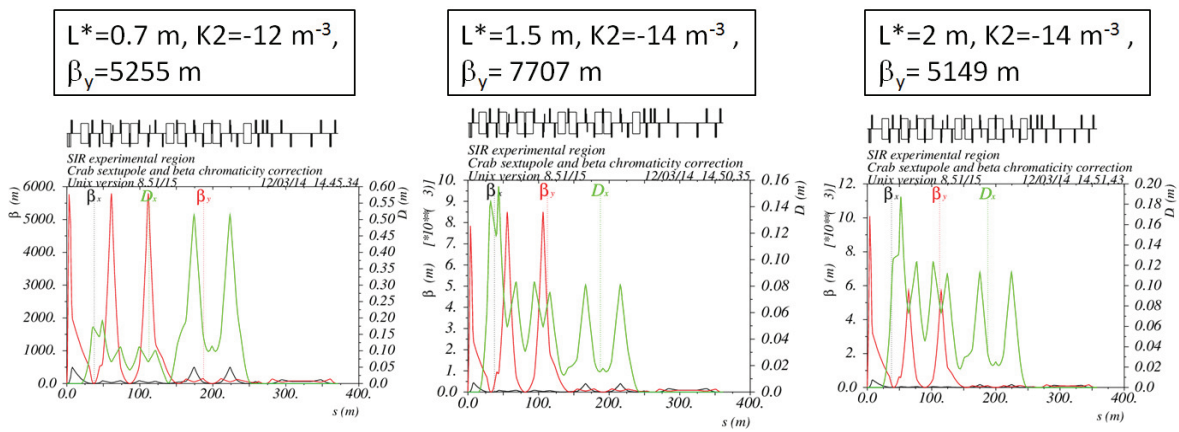


Figure 4: IR optics for three $L^*$ lengths. Vertical betas are indicated in the vertical sextupoles.

The third order aberrations in the sextupole pair with –I transform coming from the finite magnet length can be mitigated by inserting of additional sextupole correctors as it was proposed in [3]. Two low strength (~10% of the main ones) sextupoles also separated by the –I transformation are placed near the main chromatic sextupoles and (if the DA is limited by the sextupoles) can significantly enlarge the DA.

We applied this technique to the FCCee IR with different length of the first drift and indeed obtained sizable improvement of the DA as it is demonstrated in Figure 5. With the sextupole correctors the DA increased up to ~70÷100 sigma in horizontal direction and ~700-800 sigma in vertical direction. This fact confirms that the chromatic sextupoles provide major contribution to the nonlinear beam motion as it was predicted by the α-test.

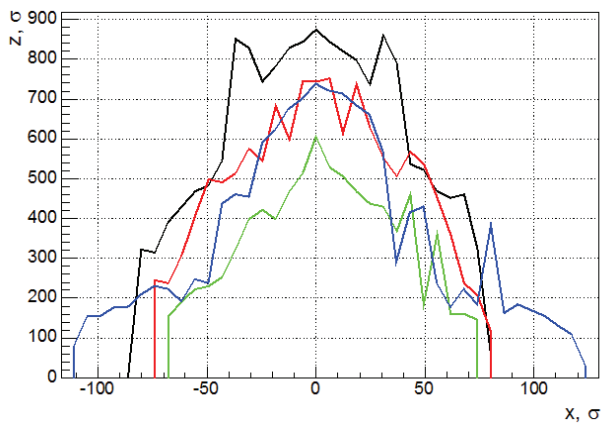


Figure 5: IR DA improved by the sextupole correctors. Colours are the same as in Figure 3.

ISBN 978-3-95450-172-4

The question is which values of $\alpha_{yy}$ correspond to the enlarged DA? The answer is given in Table 3 which compares the vertical nonlinear detuning before and after the sextupole correction for $L^*$= 0.7 m (uncorrected values are taken from Table 2).

Table 3: $\alpha$ Before and After Correction

| | Before | After |
|---|---|---|
| $\alpha_{xx}$ ($m^{-1}$) | -2300 | 51200 |
| $\alpha_{xy}=\alpha_{yx}$($m^{-1}$) | -72000 | 14000 |
| $\alpha_{yy}$ ($m^{-1}$) | $-14\times10^6$ | $0.4\times10^6$ |

It is clearly seen that the vertical and the coupling alphas are reduced substantially providing the DA enlargement shown in Figure 5. The horizontal alpha has increased but it is still less than the vertical one.

## CONCLUSION

To explore nonlinear features of the FCCee collider IR section without knowing in detail the remained lattice we suggested using the vertical amplitude dependent tune shift. One can easily calculate the relevant coefficient by the first order perturbation theory and compare relative contribution of different sources of nonlinear force. We have considered analytically the following nonlinearities: kinematics due to a large transverse momentum at the IP, first quadrupole QD0 fringe field and possible octupole field imperfection, and the sextupoles correcting the vertical FF chromaticity.

It was found that for all considered sources of nonlinearity the vertical detuning is inversely proportional to the IP beta in square $\alpha_{yy} \sim 1/\beta_y^{*2}$, but dependence on $L^*$ differs for them: for kinematic term it is $\alpha_{yy}^{*} \sim L^{*}$ while for sextupole pair and for fringe field it is $\alpha_{yy}^{sp} \sim L^{*2}$ and $\alpha_{yy}^{f} \sim L^{*3}$, respectively.

Due to the moderate dispersion function in the sextupole location $\overline{\eta}_s \approx 0.05\,\mathrm{m}$, the sextupole strength is large and this effect determines the size of the IR dynamic aperture. Low strength sextupole correctors can significantly supress the effect of the chromatic sextupoles and open the DA.

## REFERENCES

[1] P. Raimondi, 2nd SuperB Workshop, LNF, Frascati, March 2006, P. Raimondi, M. Zobov, DAΦNE Techn. Note G-58, April 2003; D. Shatilov, M. Zobov, ICFA BDN37:99-109, 2005.
[2] K.L.Brown, IEEE Trans. Nucl. Sci. NS-26, 3490 (1979).
[3] A. Bogomyagkov, S. Glukhov, E. Levichev, P.Piminov, Effect of the Sextupole Finite Length on Dynamic Aperture in the Collider Final Focus, 4872 (2009). http://arxiv.org/abs/0909
[4] B Montague , LEPNotel65 (1979).
[5] A.Bogomyagkov et al. Crab waist interaction region for FCCee (TLEP), Proc. of ICFA HF2014.
[6] E.Levichev, P.Piminov, arXiv: 0903.3028. A.V.Bogomyagkov et al. IPAC13, WEREA049, 2615.
[7] A.Bogomyagkov, FCCee IR lattice v.11, 2014 (private communication).
[8] P.Piminov, PhD Thesis, BINP, Novosibirsk, (1979).



ISBN 978-3-95450-172-4

# SYNCHROTRON RADIATION ISSUES FOR THE CEPC IR*

M. Sullivan#, SLAC National Accelerator Laboratory, Menlo Park, CA 94025, USA

*Abstract*

This is a preliminary investigation of some of the issues concerning Synchrotron Radiation (SR) generated in and nearby the Interaction Region (IR) of the CEPC e+e- Higgs Factory design. Background issues are discussed as well as power levels and power absorption of the SR in this region. Implications as to final focus magnet parameters, including L*, and nearby bending magnet strengths and positions are explored.

## INTRODUCTION

The IR of any collider is one of the more difficult sections of the accelerator. There are several conflicting requirements related to this area that need to be satisfied. The ultimate performance of the accelerator (the luminosity) is manifest here by the event rate of the physics coming out of the collision between the beams. Low β* values are needed which in turn requires large beta functions in the final focus magnets (usually a doublet). The distance from the final focus magnets and the Interaction Point (IP) called L* plays an important role. The physics detector prefers as much space as possible around the collision point in order to collect as much physics as it can. However, areas close to the beams and to the vacuum beam pipes are populated with backgrounds from the beam particles directly (lost beam particles through various mechanisms: Beam-Gas scattering (BGB), Coulomb scattering, Touschek scattering, Inter-bunch scattering (IBS), beamstrahlung, to name a few. In this paper, I will concentrate on the backgrounds and implications of the large amount of SR generated in this area.

## CEPC INTERACTION REGION

The high energy of the colliding beams (120 GeV) makes high power fans and beams of SR. This radiation must be controlled and designed to either be absorbed in local masks and shields or to pass harmlessly through the IR to be absorbed at some location away from the IP. The intensity of the SR generated in this area is high enough to instantly (seconds to minutes) destroy unprotected detectors if it is not properly controlled. Usually at least 4 orders of magnitude (and in some cases much more) suppression is needed in order to create an environment suitable for detectors to collect the physics from the collision point.

Table 1 lists some of the accelerator parameters important for the study of SR backgrounds in the IR. This is not a complete parameter list but emphasizes features important to IR designs.

*Work supported by Dept. of Energy number DC-AC02-76SF00515
#sullivan@slac.stanford.edu

Table 1: Some accelerator parameters important for SR background studies in the interaction region.

| Accelerator Parameters related to IR designs | |
|---|---|
| Beam energy (GeV) | 120 |
| Current (mA) | 16.6 |
| Number of bunches | 50 |
| Particles/bunch | $3.79\times10^{11}$ |
| L* (m) | 1.5 |
| Emittance x/y (nm-rad) | 6.12/0.018 |
| β* x/y (mm) | 800/1.2 |
| QD0 L(m) and G(T/m) | 1.25/300 |
| QF1 L(m) and G(T/m) | 0.72/300 |

## SYNCHROTRON RADIATION SOURCES

The sources of SR come from nearby magnets. The important magnets are the final focus magnets and the last bend magnet before the collision point. We will first take a look at the last bend magnet in the design.

### *Last Bend Magnet before the IP*

In an earlier design, the last bend magnet from the local chromaticity correction block had the following parameters: length 3.375 m and a bend angle of 4.416 mrad. These values gave a field strength of 5.275 kG for this bend magnet. This is a very intense magnetic field for this beam energy (the arc bend magnets have a field strength of about 600 G). This bend magnet would have generated 8965 kW of SR power. This was quickly recognized as too much local power and a new design has emerged in which the bend magnet has been lengthened to 15.5 m and the strength has been reduced to 1 kG. This reduces the SR fan power from this magnet to 47 kW, still a significant amount of power, but greatly reduced from the initial design. The new bend magnet also starts 30 m from the IP which is about 15 m farther away from the IP.

Figure 1 shows a drawing of a possible beam pipe with a 2 cm radius for the pipe outboard of the final focus (FF) quads. There is a 1.5 cm radius cryogenic pipe under the final focus quads and the collision point beam pipe has a 1.5 cm radius and is ±0.1 m long. As one can see, the SR fan from the last bend magnet passes entirely through the region and the detector beam pipe and the cryogenic beam pipes under the FF quads must be shielded from this fan. The power incident on the beam pipe from the SR fan is shown. The power density for each section of the fan and for various surfaces of the beam pipe is listed in Table 2. For reference, an acceptable beam pipe surface power is usually about 10 W/mm. The highest beam pipe wall power that can be absorbed is about 20 W/mm and a material called GlipCop™ which is dispersion strengthened copper is one of the few materials that can stand up under this power density.

ISBN 978-3-95450-172-4

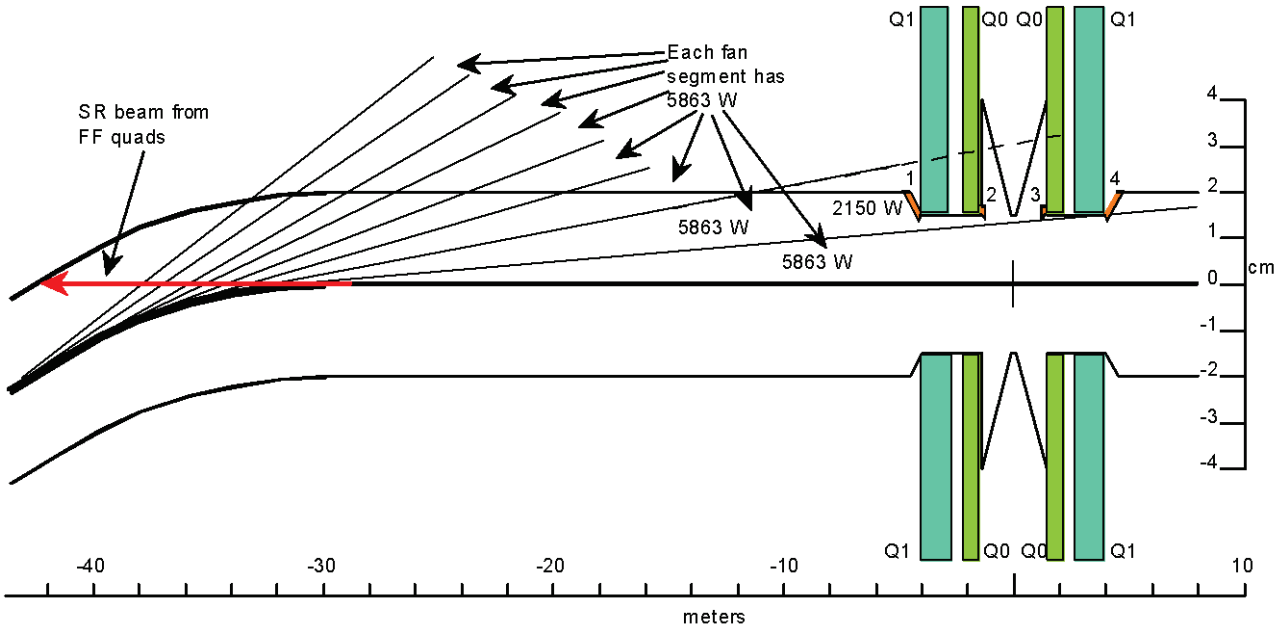


Figure 1: Drawing of the synchrotron radiation fan from the last bend magnet coming from the beam that enters from the left side of the picture. This layout reflects the latest IR design. The SR fan from this magnet is shown in 8 sections. Each section generates 5.863 kW of power. The critical energy of these fans is 958 keV. The amount of SR power to strike mask #1 is estimated to be 1250 W. Assuming the shield is stretched out over 0.5 m (as drawn) then the power density on this surface is 2.5 W/mm which is an acceptable number. This surface as well as all of the upstream beam chamber surfaces (from both sides) will have to be water cooled. The large red arrow to the left indicates where the intense SR beam generated by the FF quads will hit the beam pipe. In this picture, the SR power in the red arrow comes from the other beam.

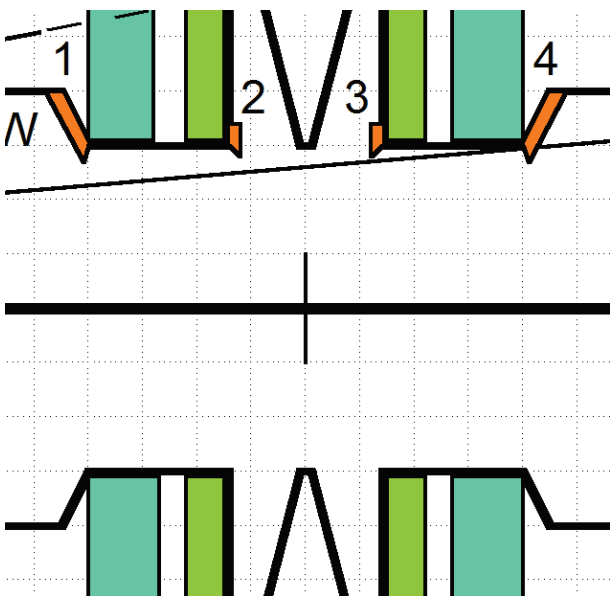


Figure 2: Close up of the IR region. This shows more clearly the suggested masking needed to shield the cryogenic beam pipes inside the final focus magnets from the bend radiation of the last horizontal dipole magnet. The masking is necessarily right/left symmetric in order to shield the cryogenic beam pipes from the bend radiation coming from the other beam (not shown in this picture). So, masks 1 and 3 are used to protect the beam pipes from the left beam fan and masks 2 and 4 are needed to shield the beam pipes from the right beam fan.

The depicted masking scheme in Figs 1 and 2 is only a suggested solution. A detailed simulation of the photons coming from this bend magnet needs to be done to insure that the shielding is adequate. As we see from the example here, there will be forward and backscattering from these masks and that will also have to be carefully modeled. In addition, because the energy spectrum is high, many photons will penetrate most masking schemes and a tally of these photons will also be needed in order to correctly estimate the background rate in the detector and onto the cryogenic beam pipes.

Table 2: Power levels on the beam pipe from the last bend magnet SR fan. The fan is broken into 8 separate fans of equal SR power (5683 W) in order to more correctly estimate the surface power on the beam pipe.

| Fan number | Est. beam pipe length (m) | Power density (W/mm) |
|---|---|---|
| 1 | 2.0 | 2.93 |
| 2 | 2.2 | 2.67 |
| 3 | 2.2 | 2.67 |
| 4 | 3.1 | 1.89 |
| 5 | 4.4 | 1.33 |
| 6 | 8.6 | 0.68 |
| 7 | 5.9 | 0.38* |
| 8 | >20 | 0.29# |

*This is only part of a fan section. See Fig 1.
#This fan segment travels completely through the IP and strikes downstream surfaces.



ISBN 978-3-95450-172-4

### *Final Focus Quadrupoles*

The final focus quadrupoles are the last magnets before the collision point. They generally have fairly high magnetic field strengths and perform the final focus of the beam to the small β values at the IP. Table 3 lists the parameters of the final focus quads for the CEPC design.

Table 3: Parameters for the Final Focus Doublet

| Magnet | QD0 | QF1 |
|---|---|---|
| Length (m) | 1.25 | 0.72 |
| Z of Face (m) | 1.5 | 3.25 |
| Gradient (T/m) | 300 | 300 |
| Beam pipe radius (mm) | 16 | 16 |
| Coil radius (mm) | 20 | 20 |

As we can see from the table the magnet strengths are quite high. Since the beam energy is also very high, these magnets will generate significant SR.

### *Beam-stay-clear and Beam Tails*

A crucial aspect of finding out whether or not the beam produces background SR from these magnets is the definition of the Beam-Stay-Clear (BSC) and the beam particle population in the high beam sigma region. The BSC is defined as the transverse region around the beam where no physical object can intrude. This means all beam pipes and other physical objects must be outside of this boundary. Most storage ring beams require a minimum of 10 $\sigma_x$ and 10 $\sigma_y$. A storage ring collider needs more vertical space because high luminosity means a high vertical tune shift. This means that more beam particles are pushed vertically out away from the beam core, hence the necessity of more vertical aperture. The vertical BSC is usually described as between 35 and 60 $\sigma_y$ depending on the accelerator emittance ratio. In addition, the BSC definition has a dispersion term to account for regions of high dispersion. The equations describing the BSC are:

$$BSC_x = n\,\sigma_x + COD_x \;\; and \;\; BSC_y = m\,\sigma_y + COD_y$$

$$where \;\; \sigma_x = \sqrt{\varepsilon_x \beta_x + \left(D_x(\delta p/p)\right)^2}$$

$$and \quad \sigma_y = \sqrt{\varepsilon_y \beta_y + \left(D_y(\delta p/p)\right)^2}$$

$COD_x$ and $COD_y$ are the allowed orbit differences from ideal (typically between 0.5 and 1 mm) and n and m are the number of agreed upon beam sigmas. The distribution of beam particles in the high sigma region is the next important piece of information. Figure 3 shows the assumed transverse beam distribution that was used to simulate the beam profile for the PEP-II B-Factory.

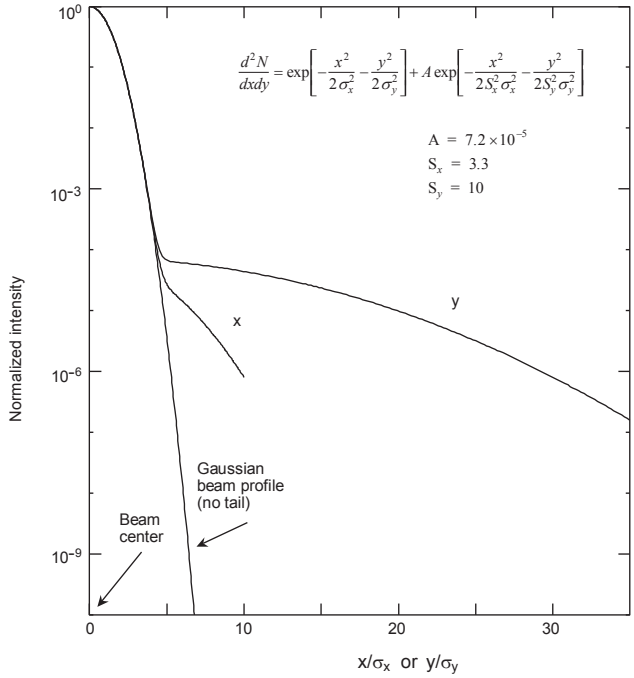


Figure 3: Transverse beam profile plot that was used in the PEP-II B-Factory background simulations for SR. The particle density at the ends of the tail distributions reflect an approximate beam lifetime of 1 hour assuming the beam particles at a distance greater than 10 $\sigma_x$ and 35 $\sigma_y$ are lost either through collimation or through dynamic aperture limits. The emittance ratio for the PEP-II B-factory was about 0.05. This was significantly larger than the proposed emittance ratio of the CEPC design which is 0.003.

### *Final Focus Synchrotron Radiation*

In the CEPC design, the final focus quadrupoles produce a synchrotron radiation beam of gamma rays (here we define a gamma ray as a photon that is > 1 MeV) along the colliding beam axis. The intensity of this beam grows rapidly as the distance to the beam axis decreases. Table 4 shows the photon rate per bunch crossing as a function of radius at the IP (Z=0.0). The photon values in the larger radii data points are dominated by the choice of beam tail parameters. One can see from the table that the photon rate and the power density climb rapidly as the radius gets smaller. Near the beam axis nearly all of the particles in the beam are contributing to the generation of SR.

Table 4: Photon rates and power densities of the synchrotron radiation photons from the FF quads. The photon numbers are for each bunch crossing. Each row of numbers in the table are for an annulus with an inner radius given by R1 and an outer radius given by R2. This table shows the numbers for one beam. These numbers double for both beams. The values in this table come from a beam profile distribution shown in Figure 3. The beam profile is traced out to 12 $\sigma_x$ and 65 $\sigma_y$ for the CEPC FF design. There were no photon hits above 23 mm radius at the IP for this particular scenario.

ISBN 978-3-95450-172-4

| R1 mm | R2 mm | Total γ/bun xing | Watts | γ/bun xing > 10 MeV | Each ring W/mm² |
|---|---|---|---|---|---|
| 22 | 23 | 6.22E+02 | 2.45E-04 | 1.55E+02 | 0.0000 |
| 21 | 22 | 6.86E+03 | 2.72E-03 | 1.71E+03 | 0.0000 |
| 20 | 21 | 2.01E+04 | 7.71E-03 | 4.91E+03 | 0.0001 |
| 19 | 20 | 5.26E+04 | 1.94E-02 | 1.24E+04 | 0.0002 |
| 18 | 19 | 1.31E+05 | 4.61E-02 | 3.00E+04 | 0.0004 |
| 17 | 18 | 3.14E+05 | 0.105 | 6.94E+04 | 0.0010 |
| 16 | 17 | 7.18E+05 | 0.228 | 1.52E+05 | 0.0022 |
| 15 | 16 | 1.57E+06 | 0.474 | 3.19E+05 | 0.0049 |
| 14 | 15 | 3.30E+06 | 0.941 | 6.38E+05 | 0.0103 |
| 13 | 14 | 6.64E+06 | 1.79 | 1.22E+06 | 0.0211 |
| 12 | 13 | 1.28E+07 | 3.25 | 2.23E+06 | 0.0414 |
| 11 | 12 | 2.38E+07 | 5.64 | 3.88E+06 | 0.0781 |
| 10 | 11 | 4.23E+07 | 9.4 | 6.46E+06 | 0.142 |
| 9 | 10 | 7.26E+07 | 15 | 1.03E+07 | 0.251 |
| 8 | 9 | 1.20E+08 | 23.1 | 1.57E+07 | 0.432 |
| 7 | 8 | 1.93E+08 | 34.6 | 2.32E+07 | 0.734 |
| 6 | 7 | 3.02E+08 | 50.5 | 3.32E+07 | 1.23 |
| 5 | 6 | 4.66E+08 | 72.4 | 4.66E+07 | 2.09 |
| 4 | 5 | 7.01E+08 | 99.9 | 6.25E+07 | 3.53 |
| 3 | 4 | 9.99E+08 | 128 | 7.61E+07 | 5.82 |
| 2 | 3 | 1.56E+09 | 1667 | 8.98E+07 | 106.1 |
| 1 | 2 | 3.03E+10 | 1487 | 3.47E+08 | 157.7 |
| 0 | 1 | 4.87E+11 | 10803 | 7.72E+08 | 3438.7 |

It is possible that some rate of SR photons incident on the central detector beam pipe is acceptable. A simulation of the detector beam pipe and of the first layers of the silicon tracker is necessary to see what level of hit rate is acceptable. It is also possible that some shielding may be installed that can absorb some of the incident photons. Again, this needs to be simulated in detail to see if shielding can help.

Almost all of this radiation will travel through the nearby IP area and strike the beam pipe where the first bend magnet occurs for the outgoing beam. This is shown in Fig 1 by the large red arrow. The red arrow depicts the SR beam that comes from the opposite beam as it travels through both sets of final focus magnets. In this drawing, the beam pipe surface is sloped by about 3.4 mrad with respect to the collision axis and this means the power from this SR beam is spread out over as much as 0.3-1 m. Since both sets of FF quads contribute to the SR beam the total power striking the beam pipe surface is about 30 kW. The power density on the beam surface is then about 90-30 kW/m which is too high for any material to withstand. A careful beam pipe design will be needed in this area in order to properly control and absorb this radiation. Either a thin beam pipe that absorbs only part of the power and/or a more sloped surface are possible solutions but a detailed simulation will again be needed in order to properly design this beam pipe.

## CHECKLIST FOR SR STUDIES

Below I have an incomplete list of items to investigate or check for any general SR design. There are bound to be topics missed in this list so the best a designer can do is to try to imagine where the photons might go after they strike a surface and to keep in mind that the answer is essentially all directions.

- The very first concern is the number of SR photons that directly strike the detector beam pipe and the cryogenic beam pipes under the FF quads. Ideally this number is zero after introducing appropriate shielding but some small number of hits per bunch crossing might be acceptable.
- The shielding used to protect these chambers from direct hits will now be a new source of SR photons through forward and back scattering photons from these shield surfaces.
- These now become significant new sources because they are relatively close to the chambers that need to be protected and these chambers hence have a fairly large solid angle acceptance for the scattered photons. These new source rates may force moving the shields farther upstream in order to decrease the solid angle acceptance. This may not always be possible and a careful choice of shielding materials may help.
- One may ultimately be forced to increase the radius of the chambers that must be protected from SR.
- The radiation from the last bend magnet is always an issue and introducing a very low field final section to this bend magnet can sometimes help.
- Allowances must be made for non-ideal beam orbits since this will most likely increase photon hits on sensitive beam pipe chambers.
- In addition, one must check for forward scattering photons from upstream beam pipes as far away as the last bend magnet before the IP.
- One must also check for backscattered photons coming from beam pipe surfaces as much as tens of meters downstream of the IP.

## CONCLUSION

I have taken a very preliminary look at SR issues in the IR area of the CEPC accelerator design. There are several things to be aware of and many of the desires for both the detector and for the accelerator must be carefully checked to make sure these requests can survive the intense SR fans and beams in this area.

## ACKNOWLEDGMENT

I would like to acknowledge the organizers of the workshop for setting up the program and presenting this very interesting accelerator design for a Higgs Factory. The IR has several very interesting design issues especially with respect to synchrotron radiation that must be addressed. The issues are challenging and this makes them all the more intriguing. I also want to thank the local CEPC design team for their help in giving me the details of the latest design. This has made this paper much more accurate and (I hope) helpful.



ISBN 978-3-95450-172-4

# LOST PARTICLES IN THE IR AND ISSUES FOR BEAM INDUCED BACKGROUNDS IN HIGGS FACTORIES

M. Boscolo, INFN Frascati, Italy; H. Burkhardt, CERN, Geneva, Switzerland

*Abstract*

The loss of beam particles has to be well under control in high energy and high luminosity e+e- colliders -namely Higgs Factories- especially at the interaction regions. In the design stage the main beam related effects causing particle losses need to be studied in details by means of full simulation to check that machine induced background rates are tolerable for the experiments and, if not, conceive an efficient collimation system to intercept particles that would eventually be lost in the Interaction region (IR). These studies can also give a realistic evaluation of beam lifetime.

We will review how main beam backgrounds have been handled at SuperB and DAΦNE and we will mention the LEP experience. A first tracking simulation of the Touschek and radiative Bhabha particles for the CEPC IR case are presented as a starting point for losses evaluation.

Synchrotron Radiation, essentially determined by the beam energy, is a key issue for the IR design of Higgs Factories. A first description of the tools under development for the SR evaluation in view of the FCC-ee design study is given.

## INTRODUCTION

We can distinguish backgrounds from two main sources: losses of beam particles and synchrotron radiation (SR). Particle effects that cause beam losses can be generated by single beam effects -mainly Touschek and beam-gas scattering- or they can be generated at the IP -mainly beamstrahlung, radiative Bhabha, $e^+e^-$ pairs production- usually referred to as *IP backgrounds*.

Both sources have been deeply studied for past and present machines; beam particles effects have been studied extensively for upgrades of B factories; on the other hand LEP has been the highest energy lepton collider, experience on this machine can be very helpful.

Unlike linear colliders, circular machines have to cope also with beam halo. For lepton high-energy colliders this issue has to be considered particularly for the vertical plane, where the emittance is low. An off-momentum halo at the IR may be generated by beam-beam effects and by beamstrahlung, which gets stronger as the beam energy increases.

The first concern for particle losses is the implication of beam degradation itself, with a consequent loss of luminosity, lifetime reduction and need of increase the frequency injection. The second concern is the background that beam losses can generate at the IR: particle losses may shower into detectors causing damages and they may fake triggers.

## BEAM PARTICLE LOSSES

In this section a short description of the main effects for beam losses is presented, with a summary of the approach used for SuperB factories and LEP. First considerations for future high energy colliders, such as the Chinese HF CEPC [1] and FCC [2] are also presented.

Depending on machine's parameters such as energy, beam density and energy spread, the beam particle losses will be driven by one of the processes mentioned in the introduction. We can say that for rings with beam energies of $E_{beam}$=120 GeV such as CEPC and even higher (maximum energy foreseen for FCC-ee is 175 GeV), beamstrahlung will typically be the dominant effect, followed by radiative Bhabha, e+e- pairs production, beam-gas and Touschek.

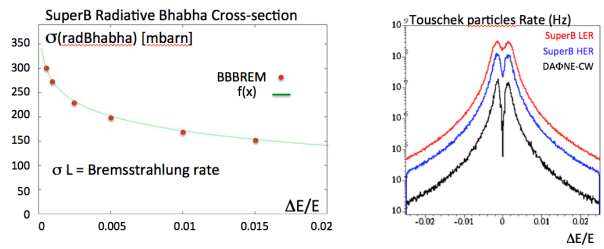


Figure 1: Left: SuperB radiative Bhabha cross-section vs ΔE/E; right: rate of Touschek particles in SuperB LER (red), HER (blue) and DAFNE Crab-waist (black) for 1 single bunch nominal current (1.49 and 10 mA, respectively).

For CEPC and FCC which are in the design phase, dedicated calculations for backgrounds are planned. As an example in Table 1, we report the lifetime evaluation performed for the SuperB factory with a Monte Carlo numerical tracking code developed for this purpose. SuperKEKB used an analogous approach [3].

Table 1: Lifetime Contributions at SuperB Calculated with the Code, Beam Parameters in [4] and Collimators at Set.

| Loss effect | HER Lifetime (s) | LER Lifetime (s) |
|---|---|---|
| Radiative Bhabha | 290*/280+ | 380*/420+ |
| Touschek | 1320 | 420 |
| Elastic beam-gas | 3040 | 1420 |
| Inelastic beam-gas | 72 hrs | 77 hrs |
| Total Lifetime | 220 | 180 |

* 1% momentum acceptance assumed in integrated formula;
+ momentum acceptance calculated with tracking MonteCarlo

ISBN 978-3-95450-172-4

Some of these processes are very non-linearly dependent on energy acceptance (see two examples in Fig. 1). Numerical tracking gives accurate particle losses and lifetime estimation, more realistic than the one obtained by assuming the ring's energy acceptance. Fig. 2 gives an example of the Touschek Monte Carlo tracking, where for each longitudinal position *s* it is not simply calculated the momentum aperture, but also its corresponding loss probability.

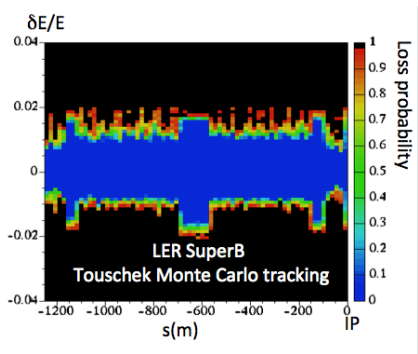


Figure 2: Energy acceptance (left axis) with loss probability of Touschek particles (right axis) through the LER SuperB.

## *Beamstrahlung*

Beamstrahlung is synchrotron radiation in the field of the opposing beam [5]. When two charged bunches collide, the electro-magnetic field of each bunch bends the trajectories of the opposite bunch particles and energetic photons are emitted, and the off-energy bunch particles can get lost in the IR producing backgrounds from debris, luminosity drop and enlargement of the beam energy spread. It is very strongly dependent on the ring's energy acceptance [6], so, for a given machine parameter's set, the remedy is to increase the energy acceptance as high as possible at the IP.

This effect is the dominant one at the high energies of the HF. Full simulation is needed for tracking of the lost IR particles into the detector; multi-turn tracking are also envisaged.

## *Radiative Bhabha*

Radiative Bhabha scattering is enhanced by the expected luminosity increase with the crab-waist collision scheme, being proportional to luminosity. And, in fact, being the dominant effect for Super-B factories it has been studied in great details. The particle losses due to this effect are essentially determined by the energy acceptance at the IP, that needs to be larger than 1% to get acceptable lifetimes. This condition is challenging due to the strong squeezing of the beams in the IR obtained with the crab-waist scheme [7].

In order to estimate this effect as a background source, the off-energy e+/e- need to be tracked after the IP, as well as the emitted photons, which may produce neutrons in secondary interactions. Radiative Bhabha scattering occurs only at the IP. We distinguish two cases:

- Bhabha final states particles have large energy deviation;
- Bhabha final states particles have small energy deviation, so that they can be lost after few machine turns.

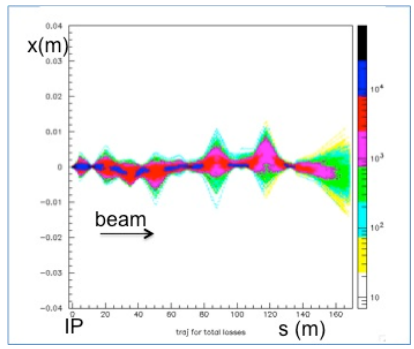


Figure 3: CEPC radiative Bhabha trajectories upstream the IP, in the FFS (April 2014 lattice).

In the first case spent particles get lost immediately, close to detectors. These particles are well simulated with the BBBREM [8] generator and then tracked into detectors with GEANT4. There is little dependence on the machine lattice, only the Final Focus design really matters. In the second case a multi-turn tracking code is needed to simulate spent particles from the IP through the ring. At SuperB, as well as SuperKEKB it has been found that most of these particles get lost in the first, or, in a small percentage, in the second turn.

Figure 3 shows first tracking simulations for radiative Bhabha trajectories, assuming a constant physical aperture of 3 cm through the CEPC IR using the same Monte Carlo tracking code as used for SuperB studies. The April 2014 CEPC lattice [9] has been used.

The CEPC IR beam sigmas calculated from the lattice are shown in Fig. 4.

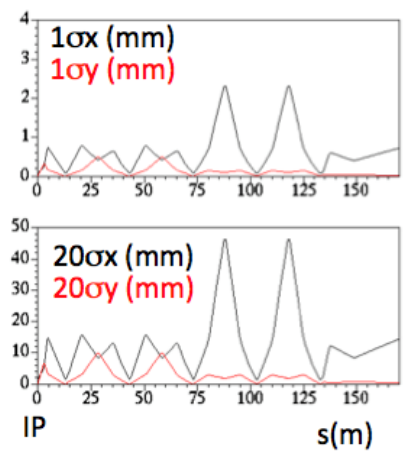


Figure 4: CEPC IR: $\sigma_x$ and $\sigma_y$ (0 is at IP).

## *Beam-gas Scattering*

The beam-gas scattering is a single beam effect in which beam particles can get lost by an elastic or inelastic



ISBN 978-3-95450-172-4

scattering with the residual gas molecules, either with nuclei or electrons, in the vacuum chamber, affecting beam lifetime. The circulating particle gets scattered to high amplitude or it loses energy and it can get lost either for physical/dynamic aperture or for exceeding the RF acceptance.

Coulomb beam-gas scattering is proportional to the gas pressure in the beam pipe, to the beam current and to the average and peak β-functions [10]. The rate follows longitudinally the pressure maps. It is not energy dependent at the first order but if there is high gas pressure due to SR outgassing (dynamic pressure), then the scattering rate is proportional to $I^2$. This effect is increased in the factories with the CW scheme, due to the high β-functions in the IR doublet. For HF this effect could be important as well, given the squeezing of the beams at IP, so we think dedicated studies with particle tracking are recommended, similarly to SuperB and SuperKEKB approach. In fact, most losses are located in the vertical plane at the defocusing low-β quadrupoles, which are much larger than at B factories (see the numbers in second row of Table 2 which should be compared to about 12 km for CEPC).

Table 2: Coulomb Beam-gas Main Parameters for Three LER *B*-Factories.

| | unit | KEK LER | SuperKEKB LER | SuperB LER |
|---|---|---|---|---|
| Vert. apert. at QD0 | mm | 35 | 13.5 | 6 |
| $\beta_y$ (max) at QD0 | m | 600 | 2900 | 1497 |
| $<\beta_y>$ | m | 23 | 48 | 47 |
| Coulomb Lifetime | hrs/min | >10 | 35 min | 24 min |

At LEP off-energy particle background was generated by both beam-gas bremsstrahlung and thermal photon scattering [11] : $\tau_B$=430 hours with P = $10^{-10}$ Torr; from 45 GeV to 65 GeV the dynamic pressure increased by a factor 5. An example of beam-gas bremsstrahlung simulation for the LER SuperB is shown in Fig. 5; left plot indicates that it is mainly a first and second turn effect, right plot is useful for finding good locations for horizontal collimators. Similar approach is proposed for Higgs factories.

A general requirement for elastic and inelastic beam-gas scattering is a pression below $10^{-9}$ Torr, but this has to be checked with the lattice and physical apertures.

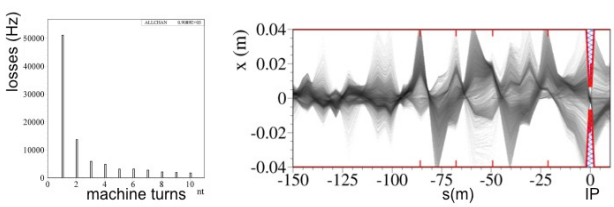


Figure 5: LER SuperB beam-gas bremsstrahlung Monte Carlo simulations.

### *Touschek Losses*

Touschek effect [12] is a Coulomb scattering between particles in a stored bunch that induces an energy exchange between transverse and longitudinal motions; in this process small transverse momentum fluctuations are transformed into magnified longitudinal fluctuations due to the relativistic Lorentz factor in the transformation. Off-momentum particles can exceed the RF momentum acceptance, or they may hit the aperture when displaced by dispersion. The Touschek effect is determined by many parameters, like the beam energy, the bunch density, the H-invariant, dispersion and phase advance; of course also the physical aperture through the ring plays a role. The scattering rate is proportional to beam density $1/\gamma^3$, so it stronger the lower the beam energy.

For a low-energy collider as DAΦNE the Touschek effect determines lifetime and induced backgrounds. For this machine great effort has been spent during the years of runs to control this effect. However, this effect is important for all the upgrades of the flavour factories, even at energies higher than the Φ–factory not only because of their relatively low energy, but also because they have dense colliding beams, and the super-squeezed beams are obtained with large low-β quads at the IR that give a reduced momentum acceptance. So, if we consider that the data taking can be fruitful only if the luminosity to backgrounds ratio is acceptable -and not only by increasing the luminosity- in this sense the real limit of these storage rings performance comes from the non-linear dynamics and the momentum aperture.

There are different possibilities to calculate the Touschek lifetime:

- Assume as input the machine momentum acceptance and perform the calculation averaging on the whole lattice;
- Calculate the momentum acceptance and the formula locally for each small section of the lattice and sum up;
- Perform the tracking of the macro-particles with the Monte Carlo technique with non-linear kicks included; in this case the momentum acceptance is calculated for each macro-particle (see Fig. 2).

This last approach, the most accurate one, has been used for the DAΦNE, Superb and τ/charm studies [13].

Generally, from the scaling law Touschek rate is inversely proportional to $\gamma^3(\sigma_x\,\sigma_y\,\sigma_z)$, so that we can argue that for low emittance synchrotron light sources, which have no IP and relatively low energy, Touschek effect is a major issue impacting lifetime: the cure is continuous injection by topping-up. In low-ε colliders and relatively low energy Touschek effect is a major issue as well, but now both for lifetime and IR losses: the cure is top-up injection and collimation, together with a good design of the IR physical aperture. In low-ε colliders and very high energies (Higgs Factories) Touschek effect is not the dominant effect. However, tracking simulation is useful to check that Touschek losses are not dangerous. First



ISBN 978-3-95450-172-4

tracking of Touschek particles has been done for CEPC IR [9] assuming a constant physical aperture of 3 cm. Touschek trajectories generated upstream the final focus, starting from -150 m from IP are tracked and shown in Fig. 6. The blue lines indicate possible attempt for horizontal collimators, to be checked with simulations.

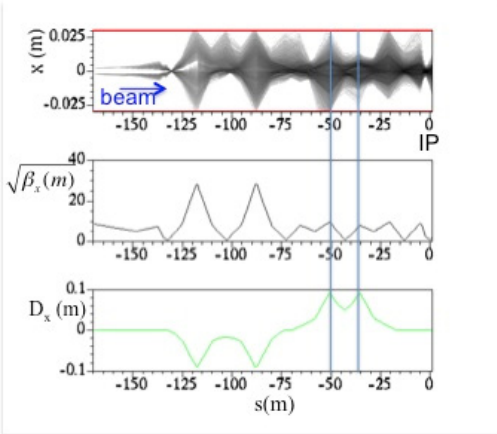


Figure 6: Touschek trajectories through CEPC Final Focus upstream the IP (upper) showing larger amplitude in correspondence of high $\beta_x$ (middle) and $D_x$ (lower plot).

## IR SYNCHROTRON RADIATION

There are many issues to be addressed regarding SR in the IR in a new design of HF, some are:

- SR power from IR dipoles and quadrupoles;
- Calculation of the rate of photons through the detector beam pipe;
- Scattering rate and incidence on detector beam pipe;
- Add in the calculation the compensating solenoids and the detector field;
- Calculation of the backscattered photons;
- Forward scattered photon rate from upstream bend magnets.

Table 3: Typical Fields for FCC-ee with LEP Ones

| | unit | LEP | FCC-ee |
|---|---|---|---|
| Energy | GeV | 100 | 175 |
| Bending fields | Tesla | 0.1 | 0.06 |
| Mean γ energy | MeV | 0.2 | 0.4 |

Some of the concerns regard the compatibility of the stay-clear apertures with effective masking of incoming SR; the edge scattering from upstream the SR masks; the backscattering from downstream aperture limitations.

The LEP physics beam energy was between 45 GeV and 104.5 GeV with a bending radius of 3026 m. LEP had a circumference of 26658.9 m, 8 straight sections with +/- 284 m around IPs and 4 IRs. The distance of the first superconducting quadrupole L* was 3.7 m. The tunnel construction started in September 1983, and LEP operated from 1989 to 2000. It was a flat and symmetric machine with no crossing angle and few (4-12) bunches. The maximum power in synchrotron radiation was 18 MW, with a maximum energy loss per turn in synchrotron radiation 3.5 GeV. There were about 100 collimators to reduce the machine-induced backgrounds and to eliminate any direct or single reflected radiation to experiments in the IP region [11]. Still the dominant backgrounds were synchrotron radiation followed by backgrounds from off-momentum particles generated in beam-gas or thermal photon scattering.

At LEP systematic measurements of beam halo were performed using scrapers and loss monitors [14, 15]. Significant non-Gaussian tails were observed, in particular in the vertical plane. They were generated by beam-beam effects and particle scattering and enhanced by high chromaticity. Typical fields are shown in Table 3. Fig. 7 shows the layout of one LEP IR with horizontal and vertical collimators.

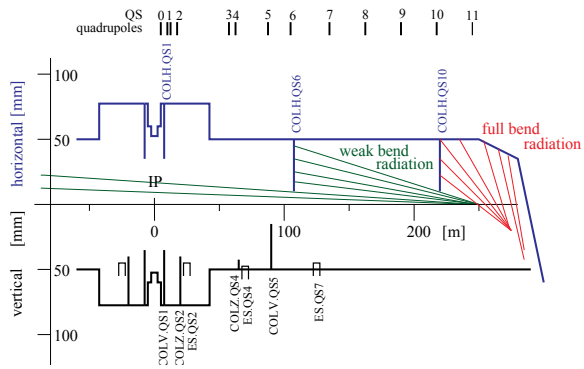


Figure 7: LEP: Straight section at a LEP IP in the horizontal (top) and vertical (bottom) planes.

## CONCLUSIONS

The design of the IR is critical for the success of a collider. A careful trade-off between the constraints of machine and detector has to be found. In this frame the simulations of all the effects that induce machine backgrounds are essential, and they should be as realistic as possible.

We are approaching the FCC-ee IR challenges starting to develop the software tools for these dedicated studies: a SR Monte Carlo integrated in Geant4 is under development. The basis is MAD-X lattice using ROOT as main geometry and interface tool. SR fans and estimate of energy flows are evaluated for the desired IR, combining machine tracking and detector model.

Provided the estimates of beam losses at IR, the Machine Detector Interface issues such as shielding, masking, collimation system, will follow, as well as estimates on the radiation limits: peak residual dose rate in the tunnel in non-controlled areas, ground water activation, peak energy deposition and absorbed dose, air activation. The general approach for background handling is quite straightforward: collection of background generators for generating primaries, transport of primaries with



ISBN 978-3-95450-172-4

GEANT4 into sub-detectors, shieldings design to intercept showers, background impact determination in the subsystems with the implemented shieldings.

## ACKNOWLEDGEMENTS

This work was partly funded by the European Commission under the FP7 Research Infrastructures project EuCARD-2, grant agreement no.312453.

## REFERENCES

[1] Q. Qin *et al.* "Overview: CEPC", presented at the 55th ICFA ABDW Workshop on High Luminosity Circular $e^+e^-$ Colliders – Higgs Factory (HF2014), Beijing, China, paper THP3H2, these proceedings.

[2] F. Zimmermann *et al.*, "FCC-ee Overview", presented at the 55th ICFA ABDW Workshop on High Luminosity Circular $e^+e^-$ Colliders – Higgs Factory (HF2014), Beijing, China, paper FRT3A1, these proceedings.

[3] H. Nakayama *et al.,* "SuperKEKB Background Simulations, Including Issues for Detector Shielding", presented at the 55th ICFA ABDW Workshop on High Luminosity Circular $e^+e^-$ Colliders – Higgs Factory (HF2014), Beijing, China, paper FRT3A1, these proceedings.

[4] M.E. Biagini *et al.*, "SuperB CDR2", arXiv: 1009.6178v3, (2010).

[5] V.I. Telnov, PRL 110 (2013) 114801.

[6] K. Ohmi, "Beam-beam Effects in CEPC and TLEP", presented at the 55th ICFA ABDW Workshop on High Luminosity Circular $e^+e^-$ Colliders – Higgs Factory (HF2014), Beijing, China, paper FRT3B1, these proceedings.

[7] M. Zobov *et al.*, Phys. Rev. Lett. **104** 174801 (2010).

[8] R. Kleiss, H. Burkhardt, Comp.Phys.Comm.81 372 (1994).

[9] CEPC April 2014 lattice, Q. Qin private communication.

[10] J. Le Duff, NIM A239 (1985) 83.

[11] NIM A 403 (1998) 205-246.

[12] C. Bernardini *et al.*, Phys. Rev. Lett., **10** 407 (1963).

[13] M. Boscolo, P. Raimondi, PRST-AB 15 104201 (2012) and ref. therein.

[14] H. Burkhardt, "BEAM LIFETIME AND BEAM TAILS IN LEP." CERN-SL-99-061-AP and Proc. e+ e+ Factories 1999, KEK, Tsukuba 1999.

[15] Transverse beam tails due to inelastic scattering, Phys. Rev. ST Accel. Beams 3, 091001 (2000).



ISBN 978-3-95450-172-4

# SYNCHROTRON RADIATION ABSORPTION AND VACUUM ISSUES IN THE IR*

J. T. Seeman†, SLAC, Menlo Park, CA 94025 USA

*Abstract*

The PEP-II B-Factory (3.1 GeV e+ x 9.0 GeV e-) at SLAC operated from 1999 to 2008, delivering luminosity to the BaBar experiment. PEP-II surpassed by four times its design luminosity reaching $1.21 \times 10^{36}$ cm$^{-2}$ s$^{-1}$. It also set stored beam current records of 2.1 A e- and 3.2 A e+ in 1732 bunches. Continuous injection was implemented with BaBar taking data. PEP-II was constructed by SLAC, LBNL, and LLNL with help from BINP, IHEP, the BaBar collaboration, and the US DOE OHEP [1, 2].

The interaction region at PEP-II had to bring the multi-ampere beams into collisions at one point, produce small vertical beta functions (~1 cm), provide beam separation for parasitic beam crossings, provide low backgrounds to the detector, and remove heat generated by synchrotron radiation and higher order modes. All of these constraints made the IR design very complicated. The synchrotron radiation generated by the many dipole and quadrupole magnets had to be absorbed without generating a lot of emitted gas which would cause beam-gas interaction, lost particles, and detector backgrounds. A complication was the permanent magnet dipoles and quadrupoles near the collision point inside the Babar detector used to focus the beam and to provide the beam separation [3, 4]. The IR region extended away from the collision point by about 65 m on each side to accomplish all the needed requirements.

Table 1: PEP-II Collision Parameters

| Parameter | Units | Design | April 2008 Best | Gain Factor over Design |
|---|---|---|---|---|
| I+ | mA | 2140 | 3210 | x 1.50 |
| I- | mA | 750 | 2070 | x 2.76 |
| Number bunches | | 1658 | 1732 | x 1.04 |
| $\beta_y$* | mm | 15-25 | 9-10 | x 2.0 |
| Bunch length | mm | 15 | 11-12 | x 1.4 |
| $\xi_y$ | | 0.03 | 0.05 to 0.06 | x 2.0 |
| Luminosity | $10^{34}$ /cm$^2$/s | 0.3 | 1.2 | x 4.0 |
| Int lumin per day | pb$^{-1}$ | 130 | 911 | x 7.0 |

*Supported by US DOE contract DE-AC02-76SF00515.

†seeman@slac.stanford.edu

## PEP-II PARAMETERS

In PEP-II the Low Energy Ring (LER) was mounted 0.89 m above the High Energy Ring (HER) in the 2.2 km tunnel as shown in Figure 1. The interaction region is shown in Figure 2 where the beams were collided head on. Figure 3 shows the Be vacuum chamber inside the detector with the permanent magnet dipoles on either side. The interface cone angle at the IR between BaBar and PEP-II was at 300 mrad. To bring the beams into collision, LER was brought down 0.89 m to the HER level and then with a horizontal deviation for both rings were made to collide. Since both rings have the same circumference, each bunch in one ring only collides with one bunch in the other ring making the beam-beam interaction much easier. Parameters are shown in Table 1.

Figure 1:PEP-II tunnel with LER above the HER.

The high beam currents were supported large RF systems consisting of 1.2 MW klystrons at 476 MHz and high power copper cavities with HOM absorbing loads. An RF cavity had three HOM loads with the capability of 10 kW each. At the peak currents the HER cavities each received 285 kW and the LER cavities 372 kW. The average klystron power was 1.01 MW. An overhead of about 20% in power was needed to allow the RF feedback systems to be stable. The power from synchrotron radiation was ultimately deposited in the walls of the vacuum system and had to be removed by water cooling.

The vacuum systems were extruded copper in the HER arcs and extruded aluminium with antechambers and photon-stops in the LER arcs. Both rings had stainless steel double walled chambers in the non-IR straight



ISBN 978-3-95450-172-4

sections. The chambers were water cooled continuously over their 2.2 km lengths due to beam heating from synchrotron radiation, HOM heating, and resistive wall heating. From beam-off to beam-on the vacuum chambers expanded and high power expansion bellows were needed (Figure 4).

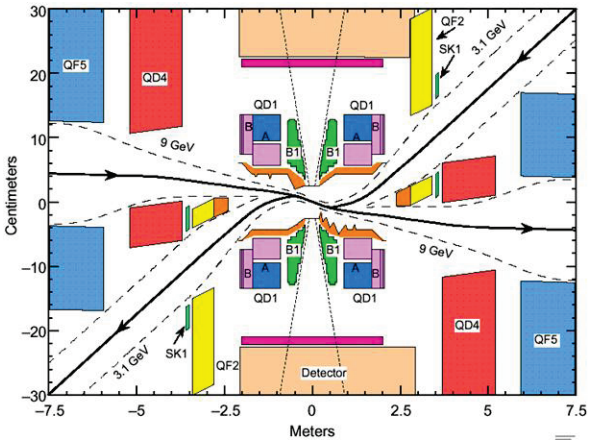


Figure 2:PEP-II Interaction Region (IR) with head-on collisions. There are four permanent magnets within the BaBar 1.5 T solenoidal field covering +/- 2.5 m. B1 is a dipole. A is a fixed quadrupole. The two magnets "B" were rotatable quadrupoles with two longitudinal slices each so that a skew quadrupole term could be introduced or an adjustable quadrupole (S. Ecklund, M. Sullivan).


Figure 3:IR double-walled Be collision chamber with nearby water cooling and permanent magnet dipoles.

The vacuum chambers were cooled with water using various techniques. The first was double walled chambers with several mm layer of water between the walls which was used in the straight sections and some in the IR region. The second was cooling channels extruded into the vacuum chamber seen mostly in the LER arcs and some of the IR chambers (Q4 and Q5). The third was copper cooling lines e-beam welded or brazed onto the outside of the copper chambers. The fourth was stainless tubing welded or brazed on the outside of smaller odd shaped components such as stainless steel flanges, discrete masks, and collimator jaws.

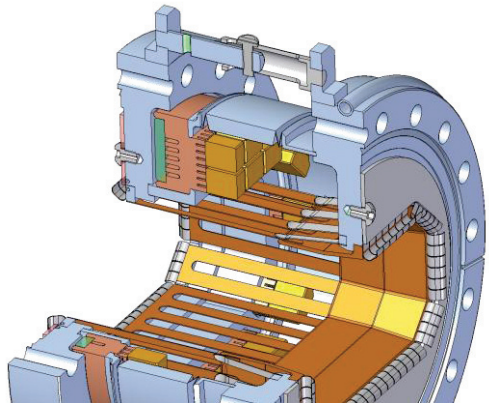

Figure 4:Ultimate design of the PEP-II high power expansion bellows module with sliding fingers, compression (hold down) fingers, beam RF seals at the ends, and water cooled HOM absorbers tiles. This bellow could handle over 3 amperes with 1700 bunches with a bunch length (sigma) of 1 cm (N. Kurita).

## IR VACUUM SYSTEM

The beams in a circular e+e- collider emit synchrotron radiation photons in the dipoles and quadrupoles in the interaction region and deposit them in the nearby vacuum chambers [5]. These photons must be absorbed in the vacuum chambers with the deposited power taken away and the emitted gasses pumped away not to cause beam-gas backgrounds. A discussion of how this was done in the PEP-II IR will be presented and implications for a Higgs Factory will be shown. The beam-stay-clears in the two rings as a function of distance from the IP are shown in Figures 5 and 6.

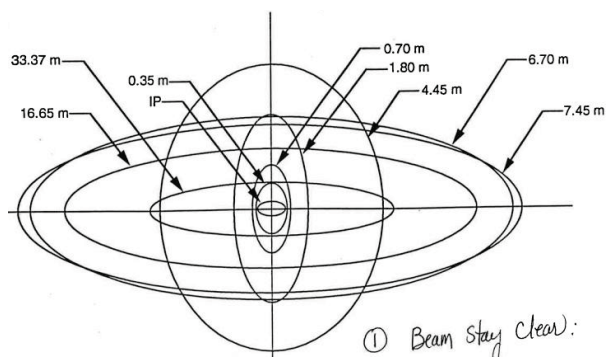


Figure 5:HER horizontal and vertical beam stay clears as a function of distance from the interaction point. This information is used to design the vacuum chamber dimensions (M. Sullivan).

ISBN 978-3-95450-172-4

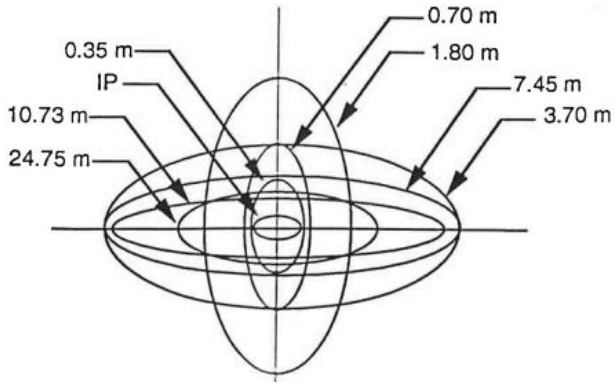


Figure 6:LER horizontal and vertical beam stay clears as a function of distance from the interaction point. This information is used to design the vacuum chamber dimensions (M. Sullivan).

The two energy beams produced x-ray fans inside the detector depending on the location and strength of the quadrupole and dipole magnets. The radiation fans for the incoming HER beam is shown in Figure 7 and for the incoming LER in Figure 8. The masking was designed so that no single scattered x-ray off a mask tip could hit the Be chamber at the IP in the detector.

The Be chamber was a double walled chamber with about 1 mm of water in radius that flowed along its length. The cooling could remove about 1 kW of power safely. The cooling lines were arranged so that the water flowed in one side, travelled down the length and then return back on the other side. The cooling water system had a sub-atmospheric pressure so that if a leak developed, no water would enter the BaBar detector. The Be chamber and the permanent magnets were support in a "support tube" that was stainless steel on both ends and a Be cylinder on the center. The diameter was about 60 cm.

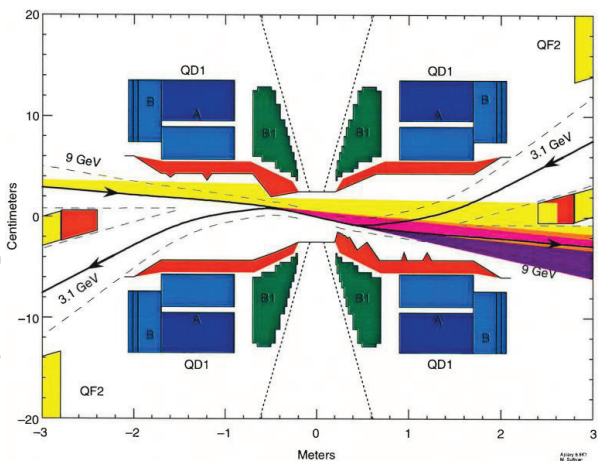


Figure 7:Radiation fans on the incoming HER beam showing the masking for backgrounds and the exiting high power photon beam (M. Sullivan).

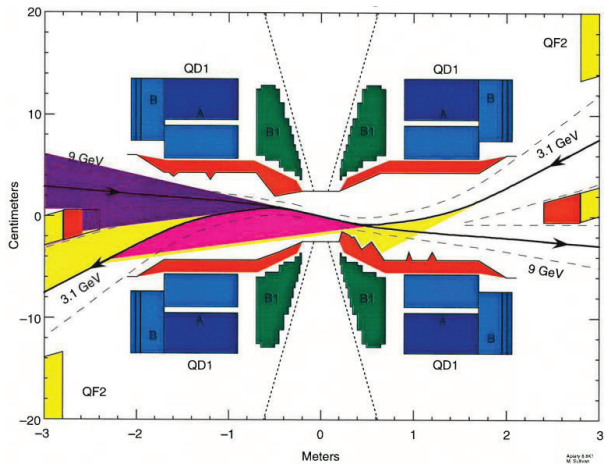


Figure 8:Radiation fans on the incoming LER beam showing the masking for backgrounds and the exiting high power photon beam (M. Sullivan).

A vacuum chamber schematic near the entrance and exit of BaBar is shown in Figure 9. Here, the chamber divides from one to two for the two accelerators as the beam separate. The various styles of vacuum pumps can be seen in the drawing using any space available. An enlargement of the vacuum chambers in the B1 dipole and the Q2 quadrupole are shown in Figures 10 and 11 showing their three dimensional shapes.

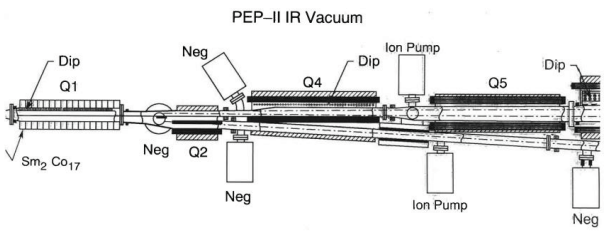


Figure 9:Schematic layout of the vacuum chambers just outside of BaBar showing the pumping arrangement.

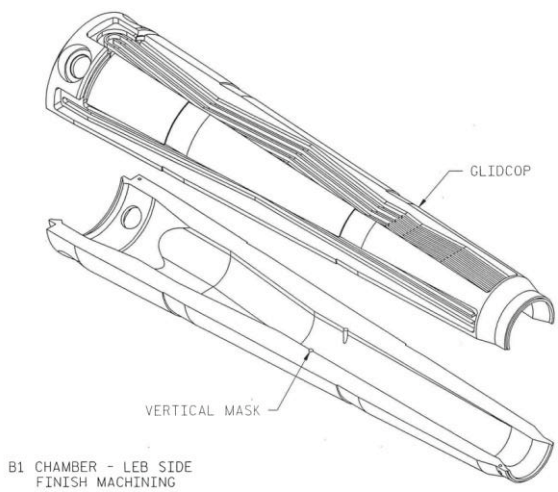


Figure 10:B1 chamber showing taper and masking.



ISBN 978-3-95450-172-4


Figure 11:Q2 chamber showing taper, masking and heavy duty water cooling with tapered sided to reduce local synchrotron radiation heat loading and stresses (S. Ecklund, N. Kurita).

The vacuum pressure in a heavily heating chamber from synchrotron radiation will outgas. But with time as a function of dose the outgassing rate will reduce. In Figure 12 is shown the reduced outgassing rate with an integrated dose of over $10^{25}$ photons/m. The reduction with dose does not saturate but keeps reducing.

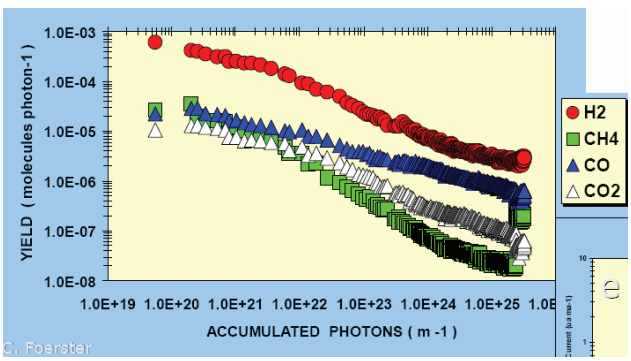


Figure 12:Outgassing rates as a function of synchrotron radiation dose (N. Kurita).

The reduced transverse dimensions of the vacuum chambers in the IR plus the addition of x-ray masks allow for the capture of HOM fields and associated power deposition from a high power beam. A calculation of HOM fields and frequencies for the PEP-II IR geometry is shown in Figure 13 and the associated modes are shown in Figure 14. The HOM modes added several kilowatts of integrated local power that had to be cooled. The fields were excited by both beams. Because of geometry with two oppositely traveling beams, the two sets of fields could either coherently add or subtract. PEP-II had some modes that added and some that subtracted fields with two beams. A lot of the generated fields were not trapped in the IR chamber but flowed out along the beam line and were dissipated in the vacuum chambers away from the IR, sometime many 10s of meters away.

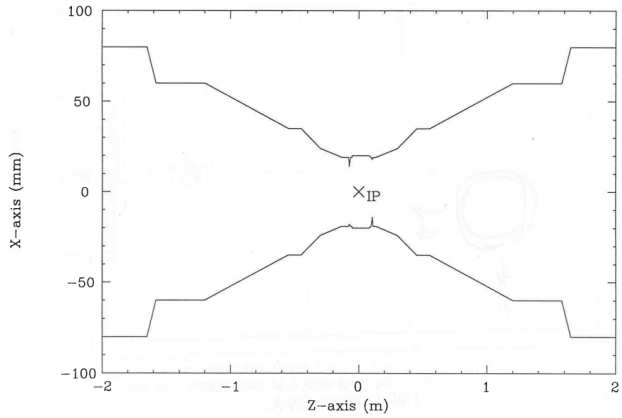


Figure 13:Schematic of the IP showing where higher order modes could be trapped between x-ray masks.

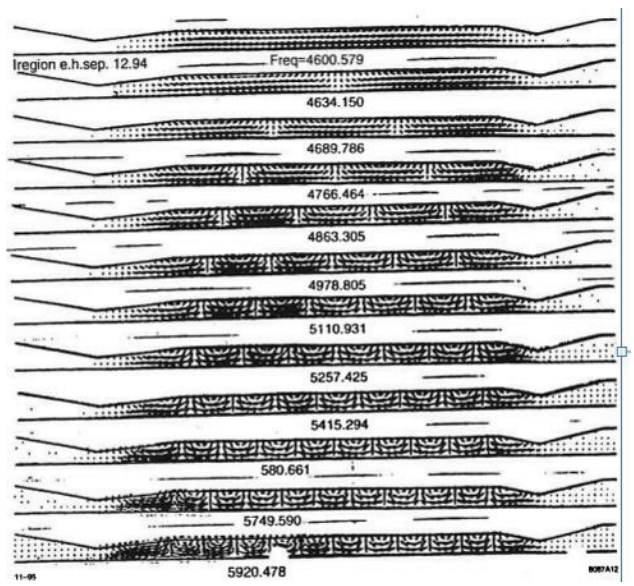


Figure 14:Various frequency HOM modes from the bunched beam as displayed in the IR vacuum chamber.

## IR PERFORMANCE IMPROVEMENTS

Over the years several improvements to the vacuum system in the IR were done.

A) The small (10 cm diameter) expansion bellows on each end of the IP Be chambers had to have extra air and water cooling installed to survive the higher combined beam currents.

B) The synchrotron and lost particle masking near detector was improved as the currents were raised.

C) The high power vacuum expansion bellows went through several designs being able to handle ever increasing HOM powers. See Figure 6 for the best design.

D) The HOM screens for the NEG pumps in the IR had to be replaced as some beam HOM power was leaking through the screens and heating the NEG strips to several hundred degrees causing vacuum issues.



ISBN 978-3-95450-172-4

## CONCLUSIONS

In the design of an interaction region for an e+e- Higgs factory the designer must minimize the SR power lost in various components and their vacuum chambers. It is important to find creative possibilities to provide vacuum pumping near the IR. Pumping inside of the detector is important if possible. Finally, it is important to shield carefully the detector from x-rays and lost particles for detector data integrity.

## ACKNOWLEDGMENTS

The author and the PEP-II team wish to thank the operations staff, the maintenance crews, the safety teams, and all other supporting staff at SLAC for their hard work and support. The author thanks N. Kurita, S. Ecklund and M. Sullivan for discussions about IR vacuum systems.

## REFERENCES

[1] "PEP-II an Asymmetric B Factory", Conceptual Design Report, CALT-68-1869, LBL-PUB-5379, SLAC-418, UCRL-ID-114055, UC-IIRPA-93-01, June 1993.

[2] J. Seeman, et. al., "PEP-II at $1.2 \times 10^{34}/cm^2/s$ Luminosity", PAC 2007, pg. 37.

[3] M. Sullivan, et. al., "Results from a Prototype Permanent Magnet Dipole-Quadrupole Hybrid for the PEP-II B-Factory", PAC 1997, pg. 3330.

[4] M. Sullivan, et. al., "Further Progress on a Design for a Super-B Interaction Region," PAC 2009, pg. 51.

[5] U. Wienands, "Vacuum Performance and Beam Lifetime in the PEP-II Storage Rings", PAC 2001, pg. 597.



ISBN 978-3-95450-172-4

# INFRARED SYNCHROTRON METHODS AND SYSTEMS FOR MONITORING AND CONTROLLING PARTICLE BEAMS IN REAL TIME

M. V. Maltseva, JSC "TENZOR", Dubna, Russia

A. A. Maltsev, L. A. Gusakova, JINR, Dubna, Russia

*Abstract*

We present the methods and infrared position-sensitive detection systems for nondestructive diagnostics and study of charged-particle beams or bunches based on the use of their synchrotron radiation in a wide spectral range. The detection systems contains of the optoelectronic and spectral detectors working in real time with the computer system.

The synchrotron radiation spectrum that is used mainly in the infrared region (wavelength range > 1 μm). The radiation is detected in the spectral region 0.3-45 μm by infrared detectors operating at low temperature or room temperature. Results are presented on the measurement of the number of electrons in the ring bunch, the equilibrium radius and dimensions of the small cross section of bunch, and the angular divergence of the synchrotron radiation relative to the median plane of the ring bunch.

The extension of the spectral range of positively diagnosed synchrotron radiation opens up new possibilities and prospects for solving scientific and applied problems.

## INTRODUCTION

Synchrotron radiation of relativistic charge-particles is a well-known effect observed in electron-ring accelerators and storage systems and is widely used in various experiments and investigations, in particular, for passive, nondestructive diagnostics of electron bunches during formation and acceleration of the bunches [1,2]. Synchrotron radiation can be used to measure the current, energy, and geometrical dimensions of electron and proton beams and bunches without affecting the accelerated particles, as well as for nondestructive studies of fast processes. The objectives of this work are as follows – we present the methods and systems of nondestructive diagnostics and study of charged-particle (electron, electron-ion, and proton) bunches (beams) based on the use of their magnetic-bremsstrahlung (synchrotron) radiation in a wide spectral range, from the ultraviolet to the far long-wave infrared region. In this paper, we describe the infrared one-element integration detectors and position sensitive one-coordinate detectors (the sensitive elements are arranged in line) and present the results of measurements with these detectors.

The extension of the spectral range of positively diagnosed synchrotron radiation opens up new possibilities and prospects for solving scientific and applied problems.

## INFRARED SOURCES

Synchrotron radiation is a well understood effect which is widely used at electron ring accelerators and storage rings. All charged particles, including protons, emit synchrotron radiation as they move along a curved trajectory in a magnetic field. However, since the proton rest energy E0p (938 MeV) is larger than the electron rest energy E0e (0.511 MeV) by a factor of 1835.6, the intensity of the synchrotron radiation for protons is lower by the same factor for a given particle energy and curvature of the trajectory. Therefore, for the energies available until recently at proton accelerators, synchrotron radiation has hardly been used at all. This explains the limited number of publications on this topic. Such publications have begun appearing only since the late 1970s and deal with the production of synchrotron radiation by the 400 GeV SPS proton synchrotron at CERN (synchrotron radiation at the edges of the displacement magnets at wave-lengths 0.6 μm). The construction of accelerator-storage-ring complexes like SSC or LHC for protons of energy 3-20 TeV may significantly effect the monopoly of electron ring accelerators as the main producers of synchrotron radiation. Analysis of the synchrotron radiation spectra of proton ring accelerators at the leading accelerator laboratories around the world shows that the bulk of the spectral distribution of the radiation for protons of energy up to 1 TeV lies in the infrared region. Estimating the intensity of the proton radiation and comparing it with that of the synchrotron radiation of low-energy electrons at, for example, the JINR accelerator – compressor electron-ring bunch (see we find that the techniques and systems of infrared synchrotron diagnostics developed for the JINR accelerator and later used in accelerator experiments may also be useful for the diagnostics of proton beams with energies above 100 GeV. So far we know of no cases of diagnostics of proton beams with proton energy above 400 GeV. The calculation of the characteristics of synchrotron radiation and the choice of techniques and diagnostics systems have been made and demonstrated for the example of the ring-shaped bunches during bunch compression in the high-current low-energy accelerator – compressor of ring-shaped electron (electron-ion) bunches are based on the measurements of synchrotron radiation [1]. The spectrum of synchrotron radiation from the compressor (electron energy $\Delta E \approx$

ISBN 978-3-95450-172-4

2.5-20 MeV, electron orbit ΔR ≈ 40-4 cm) corresponds largely to the far-infrared range. An important feature of synchrotron radiation is the fact that its characteristics can be predicted theoretically and an exact quantitative description of it can be obtained. The spectral distribution of the instantaneous power of synchrotron radiation emitted by an ultrarelativistic particle of energy E moving along a circular orbit of radius R in the wavelength λ per unit wavelength interval is given by the expression.

## METHODS

Basing on these methods there were elaborated measurement systems for the diagnostics of current and geometrical ring parameters [1,2].

Generally number electrons Ne of proportionally complete the synchrotron-radiation intensity of a ring:

$$N_e = \frac{U_{sr} G_{sr}}{S} \left( \int_0^\infty w(\lambda)\varepsilon(\lambda)\tau(\lambda)d\lambda \right)^{-1}$$

where:

Usr – electrical signal on the detector synchrotron radiation proportional to radiation intensity, got on the detector and registered by it, V;

S – calibration constant of the detector, its integrated sensitivity expressed in volts on unit of falling intensity and measured in calibration experiments;

Gsr – geometrical factor determined by geometry of experiments and angular distribution of synchrotron radiation intensity;

$w(\lambda)$ – radiation intensity of one electron;

$\varepsilon(\lambda)$ – relative spectral sensitivity of the detector;

$\tau(\lambda)$ – spectral transmission of intermediate optical environments.

The constant S is defined on a thermal source, at which, as is known, spectral distribution of radiation intensity is close to distribution of synchrotron-radiation intensity. As a reference source tungsten tape lamp calibrated on an absolutely black body was used.

The geometrical factor is defined on measured angular divergence of flow synchrotron radiation rather median plane of the ring-shaped bunch:

$$G_{sr}(\theta) = \frac{1}{w(0)} \int w(\theta) d\theta$$

where

w(0) – intensity of synchrotron radiation in a median plane of a bunch;

w(θ) – measured experimentally distribution of a flow of radiation in function of a corner θ between a direction of radiation and median plane of the ring-shaped bunch.

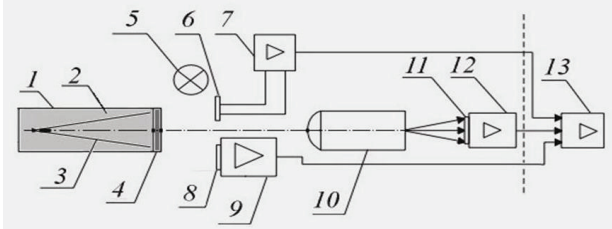


Figure 1: Typical diagram of the SR-diagnostics.

1 – channel of SR;
2 – vacuum;
3 – SR-beam;
4 – window for extracting SR;
5 – reference source;
6 – precision integral detector;
7, 9, 12 – amplifier;
8 – one-coordinate detector of SR-beam;
10 – long-focal-length optical channel;
11 – one-coordinate detector of the profile of the proton-beam;
13 – electronic equipment for accumulating and processing information using a computer.

The measurement suite is formed from a series of computerized optoelectronic and spectrometric detecting systems working in real time on-line to a computer. Those systems contain current-induction sensors and radiation detectors: for gamma rays, characteristic x-rays, and synchrotron infrared radiation. The suite measures several parameters simultaneously: current, energy, geometry, and so on, which characterize the formation and compression of a ring bunch of relativistic electrons and involves the interaction of the charged particles (electrons and heavy ions) in the compressor.

The diagnosis of the charged-particle bunches is analogous to that for the electronuclear plant and involves the following operations.

The infrared radiation beam 3 is extracted through a special heated high-vacuum window 4 [3], which passes infrared radiation over a wide wavelength range, from the planar-cylindrical chamber 1 in the compressor (Fig. 1), which is generated by the bunch 2 of relativistic electrons (the object). The infrared radiation at the output from the compressor is recorded by the noise-immune precision detectors 6 and 7 [4], which are located close to the window 4 and can measure the discrete or integral infrared intensities in various parts of the spectrum. Part of the flux passes to the input pupil of the long-focus wide-band mirror-lens optical channel 9 [5], which transports the radiation with minimal loss to a set distance (over 2.5 m) and transfers it to the detector. The radiation is focused either as an image of the small cross section of the bunch on the sensitive surface of the coordinate detector 10 [6], which measures the geometrical parameters of the ring and the electron distribution over the cross section, or else as an image of the input pupil of the optical channel on the sensitive surface of the one-element precision electron number detector (one of the detectors 6 and 7).



ISBN 978-3-95450-172-4

The infrared radiation is recorded by the detector units 6, 7, and 10, which convert the intensity to a signal that is isolated from the background of the pulsed electromagnetic and radiation interference from the accelerator and is amplified in units 8, 11, and 12. The amplified analog signal passes along the cable highway to the control panel, where there are electronic units for recording, processing, and storing the information 13. The processed results are output in the required form and are stored in the computer.

The controlled source 5 is used to check and calibrate the detectors.

### *Number of Charge-particles*

The electron number measurement method is based on the direct dependence of the synchrotron radiation intensity on the electrons number and the synchrotron radiation registration is made in the spectral region $\lambda >> \lambda c$, when the radiation intensity is independent of the energy of electrons. If the total power W of the radiation of the e-bunch is proportional to the number Ne of electrons in the ring bunch, for a given number of electrons the total power of the radiation is $W = Ne \times w$. The electrons number Ne in the ring bunch can be calculated if one-electron synchrotron radiation power w is known and synchrotron radiation total power W is measured:

$Ne = W / w = [USR / S] \times f(E, R, G, \lambda)$.

The power of the radiation of a single electron for $\gamma >> 1$ is given by

$w = \int \lambda d\lambda = 4.6 \times 10\text{-}16\ \gamma 4\ R\text{-}2[cm]$.

The total synchrotron radiation power can be determined if we know: the signal on the radiation detector – USR; the calibration constant of the detector – S; the energy electrons – E; the orbit radius – R; the coefficient of synchrotron radiation flow using, from G – geometrical factor determined by solid angle of the synchrotron radiation detector; relative spectral characteristic $\varepsilon(\lambda)$ of the detector; the coefficient of spectral passing $\tau(\lambda)$ of interval pass limits environment (window, filters, optics) and the synchrotron radiation polarization properties. In general case the signal on the radiation detector-receiver can be the following:

$USR = Ne\ S\ G \int w(\lambda)\ \varepsilon(\lambda)\ \tau(\lambda)\ d\lambda$.

where: S is the calibration constant of the detector (V/W), measured with the help of the known methods at the thermal source – tungsten filament lamp. There are two variants of synchrotron radiation intensity measurement: the approximate one when the radiation is measured only in the median plane of the electron ring with the detector and the more precise one when the detectors system involves the greater part of the solid angle, where the most part of the synchrotron radiation is concentrated. The first method is good by simplicity of the apparatus and bad by the absence of operative, for every accelerator pulse, information about the angular distribution of the synchrotron radiation.

### *Geometrical Parameters*

Since a bunch of the charged particles in an accelerator can be considered as an ensemble of oscillators with three degrees of freedom (longitudinal (synchrotron) and two transverse (betatron) – radial and axial ones), the diagnostic set must provide the measurements of the corresponding geometrical parameters of the bunch and possibility of observing the bunch dynamics. The method of measuring the sizes of the bunch and its location inside the accelerator, as well as studies of the bunch dynamics during the compression involves the facilities for extraction of synchrotron radiation from the accelerator chamber, its transportation, and detection. The appropriately reduced image of the bunch cross section is focused on and recorded by a detector unit with sensitive elements arranged in line.

### *Angular Divergence*

An important parameter for the diagnostics of a ring bunch is the angular divergence of the synchrotron radiation in the direction perpendicular to the median plane of the ring bunch. Measurement of this quantity gives information about the electron energy and angular distribution (axial betatron oscillations). A method has been developed to measure the divergence of the radiation beam and the characteristics related to this divergence. This method is based on repeated (throughout the acceleration cycle) measurement of the intensity of the synchrotron radiation as it exits the accelerator chamber by means of an infrared detector whose length covers most of the synchrotron radiation flux in the direction perpendicular to the plane of rotation of the charged particles.

This technique makes it possible to:

1. Estimate the electron energy in the bunch.
2. Measure the power of the synchrotron radiation, taking into account its actual angular distribution, thereby raising the accuracy of absolute measurements of the number of electrons in the bunch.
3. Use the nature of the broadening of the angular distribution of synchrotron radiation to estimate the frequency of betatron oscillations of electrons in the bunch and the intensity of the ion component of the bunch loaded with ions.

## EXPERIMENTAL APPARATUS

The diagnostics of the parameters of the ring bunch are performed simultaneously by several information-measuring systems which realize the various methods listed in the preceding section. Synchrotron radiation from the electron ring is extracted through an infrared window of the vacuum chamber of the accelerator, then it is transported along the optical channel over the given

ISBN 978-3-95450-172-4

distance and is received by a detectors unit with a power sources. The detector signals are registered and processed by an electronic facility, and then transferred to a computer for the real-time processing. In the immediate vicinity of the accelerator, there is only the detector units, which includes a single-element and multielement coordinate infrared detectors with a preamplifier in each of the recording channels, a cryogenic system (in the case when the detector is cooled to the temperature of the liquid nitrogen), and a power sources. The detectors unit can be moved in the image plane by electric motors, which is remotely controlled by a unit. The processing facilities are outside the region of the radiation damage. The synchrotron light is extracted from the accelerator through windows made of various optical materials. The optical channel designed for the extraction and transportation of synchrotron radiation includes an output window and a long-focus wide-band optical mirror channel; at the output of the channel, radiation is focused on the sensitive surface of the coordinate detector. The synchrotron radiation extracted from the accelerator is recorded by three independent infrared detection systems forming a single information-measuring complex. Each system performs a specific task, operating synchronously on a common time scale. The device with a single-element detector is designed for measuring the absolute number of electrons. The geometrical parameters of the bunch are measured using a system containing a multi-element coordinate detector system located at the focus of the optical channel. The angular divergence of the synchrotron radiation and its intensity are measured by an infrared coordinate detector with linear arrangement of the elements. The information obtained from the measuring systems is collected and processed in the units, which incorporate a computer. This information significantly raises the overall accuracy and information content of the measurements. The choice of detectors for the diagnostics systems is determined by the intensity and spectral characteristics of the recorded synchrotron radiation, and also by the conditions of operation of the accelerator. The main requirements in choosing the detectors were the following:

- High spectral sensitivity in the wavelength range $\lambda \approx$ 0.4-40 μm.
- Time resolution (speed of response) $t = 0.1\text{-}5 \cdot 10^6$ s.
- Simplicity of operation (absence of complicated cryogenic systems).

Various types of infrared collector were considered. Five types of photocollector sensitive to the given region of the infrared spectrum were proposed to conform with the above requirements. The synchrotron radiation of the electrons can be recorded either by all the measuring systems simultaneously or by each separately. The radiation intensity is recorded by detectors and output as an analog signal, which is preamplifier to the required amplitude and fed via a cable to the control panel of the accelerator, where it is transformed into digital from and processed by computer. The measurement channels allow repeated (up to 10 times) recording of a ring compression cycle in the compressor of the accelerator. The duration of the measurement date is 0.1 μs. The time interval between successive measurements can be varied from 100 μs and more for a total duration of the synchrotron radiation pulse of about one millisecond.

## CONCLUSION

Methods for measuring the current and geometrical parameters and estimating the energy parameters of bunch in ring accelerators using synchrotron radiation in the infrared region are reviewed, together with the information-measuring systems designed to detect synchrotron radiation and realize these methods. The synchrotron radiation spectrum that is used lies mainly in the infrared region. The detection systems incorporate specially designed infrared-optical elements (a high-vacuum window of optical ceramics and broad-band, long-focus optical channels). The radiation is detected in the spectral region $\Delta\lambda$ = 0.3-45 μm by infrared detectors operating at low temperature or room temperature. It should be noted that the range of applicability of these results is fairly broad. Most of the techniques and information-measuring systems described here can be used in the same or slightly altered form at other electron and proton ring accelerators which generate synchrotron radiation, for example, LHC, SPS the synchrotron radiation spectrum at which lies mainly in the infrared region. They are useful both for the diagnostics of bunches and beams during their dynamical development, and for carrying out various types of scientific research and solving applied problems based on the use of infrared synchrotron radiation, including beam diagnostics and research at electron-positron storage rings The objectives of this work are as follows:

- We present the methods and systems of nondestructive diagnostics and study of charged-particle (electron, electron-ion, and proton) bunches and beams based on the use of their magnetic-bremsstrahlung (synchrotron) radiation in a wide spectral range, from the ultraviolet to the far long-wave infrared region.
- We draw attention to the great diversity of problems, both in accelerator experiments (for example, the study of the coherence of synchrotron radiation or of the coherent processes at colliders) and in other, sometimes quite unrelated fields, such as metrology, high-temperature superconductivity, biology, etc., which might be solved by means of infrared synchrotron diagnostics, covering the interval of wavelengths $\Delta\lambda$ = 0.3-45 μm, which is much larger than the spectral range that is widely used at present (basically, the range $\Delta\lambda$ = 0.3-1.1 μm) in various experiments and investigations.
- The extension of the spectral range of positively diagnosed synchrotron radiation opens up new possibilities and prospects for solving scientific and applied problems.



ISBN 978-3-95450-172-4

## REFERENCES

[1] A.A. Maltsev, Phys. Part. Nucl., Vol. 27, №3, 330 (1996)
[2] M.V. Maslova, A.A. Mal'tsev, M.A. Mal'tsev, Measurement Techniques, Volume 45, №7, 773 (2005
[3] A. A. Mal'tsev, Prib. Tekh. Eksper., №3, 177 (1994).
[4] A. A. Mal'tsev and M. A. Mal'tsev, At. Énerg., 79 Issue 2, 121 (1995).
[5] A. A. Mal'tsev and M. A. Mal'tsev, Prib. Tekh Eksper. № 4, 210 (1995).
[6] A. A. Mal'tsev, Phys. Plazm., 23, № 5, 419 (1997).

ISBN 978-3-95450-172-4

# DETECTOR BEAM BACKGROUND SIMULATIONS FOR CEPC

H. Zhu*, X. Lou, Q. Xiu
Institute of High Energy Physics, CAS, Beijing, China

*Abstract*

Detector backgrounds of different sources expected at the Circular Electron Positron Collider are reviewed. Their potential impacts on the interaction region design and detector performance are discussed. The backgrounds originating from beam-beam interactions are evaluated with Monte Carlo simulation and preliminary results are presented.

## INTRODUCTION

The Circular Electron Positron Collider (CEPC), proposed by the Chinese High Energy Physics community, is designed to operate at the center-of-mass energy of $\sqrt{s}$ = 240 GeV, with an instantaneous luminosity of $2 \times 10^{34}$ cm$^{-2}$s$^{-1}$. The CEPC $e^+e^-$ collider will produce millions of clean Higgs events over a period of 10 years, allowing for detailed studies of the properties of the Higgs boson discovered at the LHC experiments [1,2].

To fully exploit the physics potential of machine and to optimise the detector performance, it is important to understand the detector backgrounds at the CEPC, which is among the most critical issues for the project. Different sources of backgrounds can give rise to either primary particles that enter the detector directly or generate secondary debris that ultimately hit the detector. It is mandatory to study thoroughly those backgrounds and their impacts on detector performance with Monte Carlo simulation. In this report, results of the main backgrounds from the beam-beam interactions, including beamstrahlung, electron positron pair production, hadronic backgrounds and radiative Bhabha events, are presented and their impacts on the CEPC detector are discussed. Other critical backgrounds, in particular synchrotron radiation, beam-gas interactions and beam loss, are important topics for future studies.

## THE INTERACTION REGION LAYOUT

The interaction region (IR) of the CEPC consists of the beampipe, the surrounding silicon detectors, the luminosity calorimeter and the interface to the last final focus quadrupoles, namely QD0 and QD1. Its preliminary IR layout is depicted in Figure 1. The current design features a rather short focal length of $L^*$ = 1.5 m, *i.e.* the distance between QD0 and the interaction point (IP). Such short $L^*$ allows for the realisation of high luminosity without large chromaticity corrections, but at the same time it imposes certain constraints on the CEPC detector layout and can have significant impact on the choice of detector technologies. Therefore thorough understandings of the effects of the short $L^*$ on both detector and machine performance will be a critical topic for future studies.

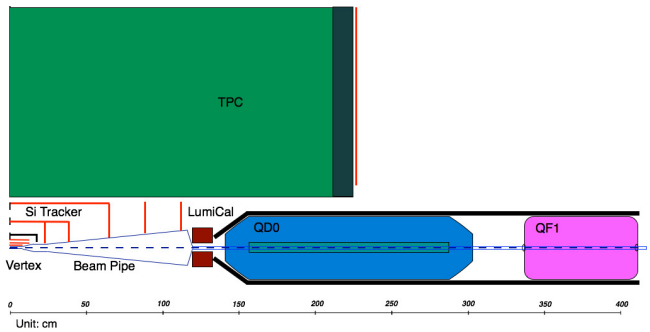


Figure 1: Preliminary layout of the interaction region for the CEPC.

## BACKGROUNDS FROM THE BEAM-BEAM INTERACTIONS

At the IP of the $e^+e^-$ collider, the two crossing bunches of opposite-charge attract each other, called "Pinch Effect", which is illustrated in Figure 2. The self-focusing effect during this process leads to higher luminosity for head-on collisions. However, the charged particles deflected by the strong forces will emit radiation called "beamstrahlung". The actual beam-beam effects can be estimated with Monte Carlo simulation, which shall take into account the dynamically changing bunch effects, reduced particle energies and their impacts on the fields. The GUINEA-PIG [3] program has been adopted to simulate the beam-beam interactions for the CEPC. The machine and beam parameters used as the input into the program are listed in Table 1.

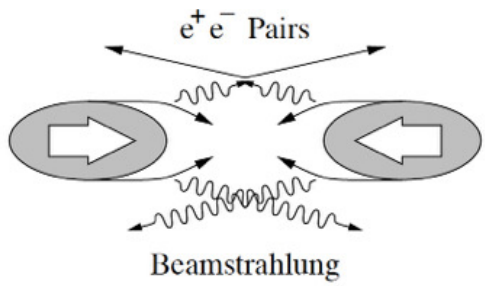


Figure 2: Illustration of the Pinch Effect between two crossing bunches of opposite-charge.

The main backgrounds from the beam-beam interactions are beamstrahlung, electron positron pair production,

* email: zhuhb@ihep.ac.cn

ISBN 978-3-95450-172-4

Table 1: Input CEPC Beam and Machine Parameters to the GUINEA-PIG Simulation Program

| Machine Parameters | Unit | Value |
|---|---|---|
| $E_{cm}$ | GeV | 240 |
| Particles per bunch | | $3.7 \times 10^{11}$ |
| Beam size $\sigma_x/\sigma_y$ | $\mu$m | 73.7/0.16 |
| Beam size $\sigma_z$ | $\mu$m | 2260 |
| Emittance $\varepsilon_x/\varepsilon_y$ | mm·mrad | 1595/4.8 |

hadronic background and radiative Bhabha events. Preliminary results from each of the sources are presented in the following.

### *Beamstrahlung*

Due to the Pinch Effect, the trajectories of the particles in the bunches are bent and they emit beamstrahlung photons. The beamstrahlung photons can have potentially large impacts on the beam energy spread and the luminosity spectrum of the CEPC machine. However, as illustrated in Figure 3, the beamstrahlung photons are dominantly produced with very low transverse momentum and small polar angle along the beam axis. They are negligible background for the CEPC detector.

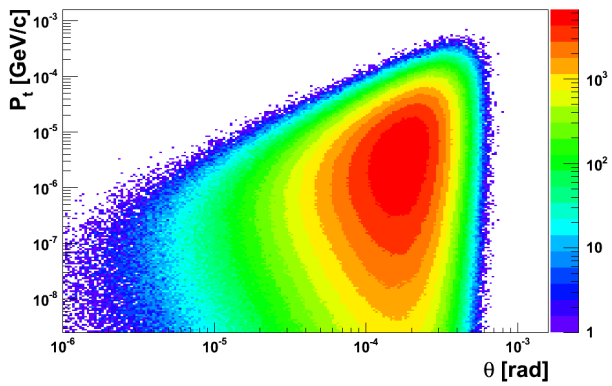


Figure 3: Transverse momentum distribution vs polar angle of the beamstrahlung photons for the CEPC.

### *Pair Production*

The electron-positron pairs can be produced with either coherent or incoherent processes:

- **Coherent Production**: $e^+e^-$ pairs produced via the interaction of virtual or real photons (e.g. beamstrahlung photons) with the coherent field of the oncoming bunch. The particles can be highly energetic but dominantly produced with small angle and confined in the beampipe.
- **Incoherent Production**: $e^+e^-$ pairs produced via the interactions involving two real and/or virtual photons. Most of the particles are confined in the beampipe with the strong detector solenoid field. But a small fraction of the particles are with high transverse momenta and large polar angles and can enter the detector. Incoherent pair production is considered as one of the most important background sources for the CEPC detector.

Figure 4 shows the transverse momentum distribution vs. the polar angle of the incoherent $e^+e^-$ pairs, after deflection through beam-beam interaction. It also shows the sharp kinematic edge (green band in the figure) developed by the pairs. Any detector component, including the detector beampipe, must be placed away from the particles in that region to avoid introducing particle shower. In addition, it is necessary to introduce mask to protect the CEPC detector from secondaries created by the pair-produced particles interaction with the quadrupole.

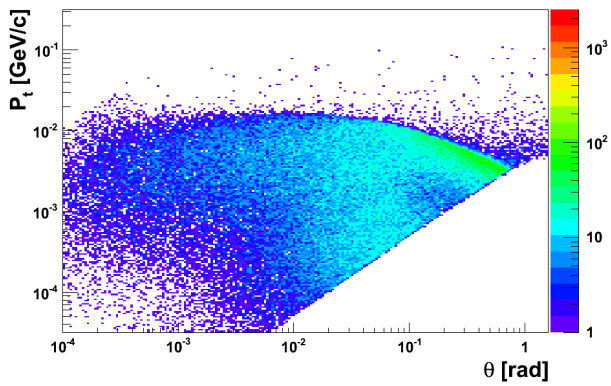


Figure 4: Transverse momentum distribution vs the polar angle for the particles from the incoherent $e^+e^-$ pair production. Events are integrated over 50 bunch crossings.

### *Hadronic Background*

The interaction of photons can also produces quark pairs (e.g. the $\gamma\gamma \to q\bar{q}$ process), forming hadronic background events. But fortunately the production rate of this type of events is orders of magnitude smaller than the dominant $e^+e^-$ pair production. To evaluate the effects, the energetic photons produced from the beam-beam interactions using GUINEA-PIG are passed to PYTHIA [4] for generation of the hard interaction, followed by hadronisation. Preliminary results confirm that most of the hadronic background events are of low energy and small polar angle, which make them negligible for the CEPC detector. However, there is a very small fraction of events, in which jets can be produced with sufficiently large transverse momenta (called "mini-jets"). Their exact impacts on the CEPC detector, in particular the calorimeter, needs to be studied with detailed detector simulation.

### *Radiative Bhabha Events*

Radiative Bhabha scattering ($e^+e^- \to e^+e^-\gamma$) events can be dominant background for $B-$factories (see the

ISBN 978-3-95450-172-4

SuperKEKB report in the same proceeding), but become less important for high energy electron positron colliders. Their effects have been studied with GUINEA-PIG, and cross-checked with BBBREM [5]. The preliminary result demonstrates that they are negligible background for the CEPC detector. Nevertheless radiative Bhabha scattering provides an important handle to determine precisely the machine luminosity. It has been planed to perform more detailed studies with the BHWIDE [6] program dedicated for large angle scattering, and the general-purpose generator WHIZARD [7].

## RADIATION LEVELS

The radiation backgrounds can degrade the performance of the CEPC detector. Among the sub-detectors, the vertex detector that will be constructed with silicon pixel sensors and placed closest to the IP, will be most vulnerable to the radiation backgrounds. The radiation damage, characterised as Total Ionisation Dose (TID) and Non-Ionising Energy Loss (NIEL), has to be estimated reliably to guide the design of the silicon pixel sensors. The NIEL contribution from the particles originating from the beam-beam interactions is presented in 1MeV equivalent neutron fluence and shown in Figure 5.

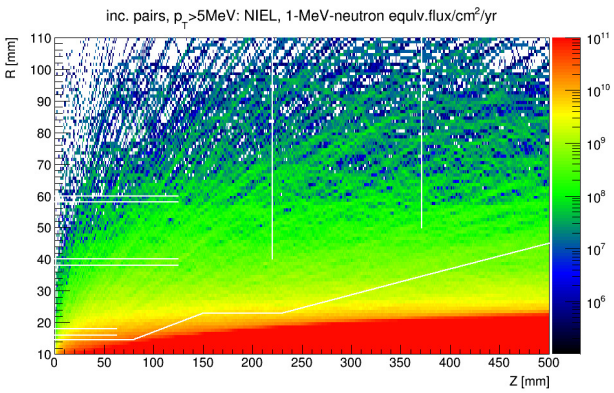


Figure 5: The NIEL distribution introduced by the particles originating from the beam-beam interactions. The white lines indicate the positions of the barrel layers of the vertex detector, the first two forward disks of the silicon tracker and the beampipe for the CEPC.

The first layer of the vertex detector of the CEPC detector will be positioned at $r = 1.6$ cm from the IP. The averaged hit density at this distance is estimated to be $0.2/\mathrm{cm}^2/\mathrm{BX}$. The corresponding annual values for NIEL and TID are estimated to be $10^{11}$ $\mathrm{n}_{eq}/\mathrm{cm}^2$ and 100 kRad, respectively. In both NIEL and TID calculations, a safety factor of 5 has been taken into account.

## OPTIMISATION OF THE VERTEX DETECTOR LAYOUT

The low hit density presented in the first layer and benign radiation levels may make it possible to place the vertex detector layer closer to the IP. Shortening the distance from the first measurement to the IP can reduce the extrapolation uncertainty, hence enhance the performance of heavy-flavour tagging, which can improve precision measurement of the Higgs branching fractions. Therefore it becomes important to find out other limiting factors and make sure such improvements could be realised. From the detector background point of view, it must avoid direct hitting of the synchrotron radiation photons on any detector component. In addition, as it has been already pointed out, the beampipe must be places sufficiently far away from the kinematic edge ("Pair Edge") developed by the $e^+e^-$ pair production. The current beampipe position and the "Pair-Edge" are shown in Figure 6, assuming a solenoid magnetic field of 3.5 Tesla for the CEPC detector. It shall be feasible to place the beampipe closer by ~1 mm, and the first vertex detector layer accordingly. This change needs to be validated and justified with further studies and the impacts on final physics results need to evaluated with full detector simulation in future studies.

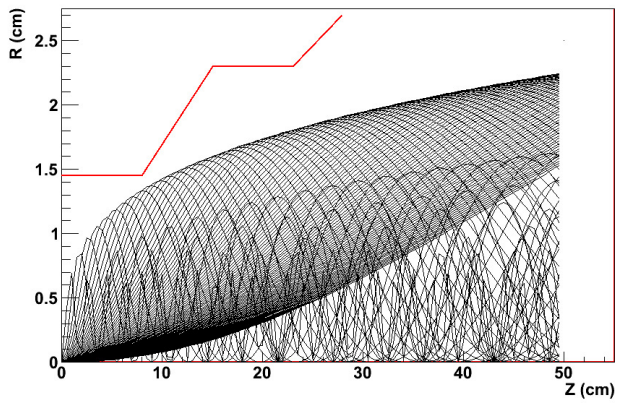


Figure 6: "Pair Edge" developed by the $e^+e^-$ pair production within a solenoid magnetic field of 3.5 Tesla and projected to the R-Z plane. The read line indicates the current beampipe position.

## SUMMARY

The proposed Circular Electron Positron Collider (CEPC) will offer great opportunities to perform precision measurement of the recently discovered Higgs boson. To fully exploit the physics potential and to optimise the detector performance, it is critical to understand thoroughly the detector backgrounds from different sources. Preliminary results on the detector backgrounds from the beam-beam interactions are obtained and their potential impacts on detector performance have been briefly discussed. It is important to refine those estimations and include more background sources in future studies.



ISBN 978-3-95450-172-4

## REFERENCES

[1] ATLAS Collaboration, "Observation of a new particle in the search for the Standard Model Higgs boson with the ATLAS detector at the LHC", Phys. Lett. B 716 (2012) 1-29.

[2] CMS Collaboration, "Observation of a new boson at a mass of 125 GeV with the CMS experiment at the LHC", Phys. Lett. B 716 (2012) 30-61.

[3] D. Schulte, "Beam-beam simulation with GUINEA-PIG", In 5th International Computational Accelerator Physics Conference, September 1998, CLIC-NOTE 387.

[4] T. Sjostrand, S. Mrenna, and P. Z. Skands, "PYTHIA 6.4 Physics and Manual", JHEP 0605 (2006) 026.

[5] R. Kleiss and H. Burkhardt, "BBBREM – Monte Carlo simulation of radiative Bhabha scattering in the very forward direction", Computer Physics Communications 81 (1994), no. 3 372 – 380.

[6] S. Jadach, W. Placzek, and B. Ward, "BHWIDE 1.00: O(alpha) YFS exponentiated Monte Carlo for Bhabha scattering at wide angles for LEP-1 / SLC and LEP-2", Phys.Lett. B390 (1997) 298–308.

[7] W. Kilian, T. Ohl, and J. Reuter, "WHIZARD: Simulating Multi-Particle Processes at LHC and ILC", Eur. Phys. J. C71 (2011) 1742.



ISBN 978-3-95450-172-4

# DESIGN STUDY OF THE CEPC BOOSTER

C. Zhang, IHEP, CAS, P.O.Box 918, Beijing 100049, China

*Abstract*

Design study of the CEPC booster is reported. The booster provides 120 GeV beams for the collider with top-up injection frequency of 0.1 Hz. To save cost, energy of the linac injector for the booster is chosen as 6GeV, corresponding to the magnetic field of 30 Gs. In this paper, lattice of the booster is described; the low injection energy issues are studied; beam transfer from linac to booster and from booster to collider are discussed.

## GENERAL DESCRIPTION

Soon after discovery of the Higgs boson, the Circular Electron-Positron Collider (CEPC) was proposed. The Super Proton-Proton Collider (SPPC) could be installed later in the same tunnel of CEPC for $e^+e^-$, pp, ep and ion collisions [1].

The booster is in the same tunnel of the collider with about same circumference, while bypasses are arranged to keep away from detectors in IP1 and IP3. Electron and positron beams are injected from the linac to the booster through the transfer line LTB (Linac To Booster) in one of the 850 m long straight sections. The beam extraction at top energy takes place in other two straight sections. Electron and positron beams are injected to the collider through $BTCe^+$ and $BTCe^-$ (Booster To Collider) transfer lines. Figure 1 illustrates the layout of the booster on the upside of the CEPC collider.

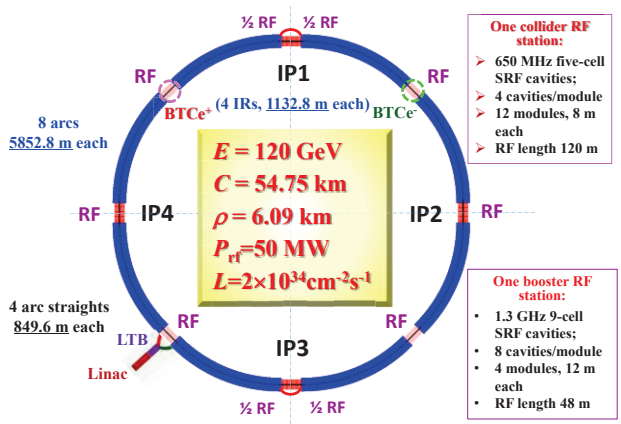


Figure 1: Layout of CEPC and its booster.

As shown in Fig.1, the collider is designed with four interaction points, where IP1 and IP2 are for $e^+e^-$ collisions of luminosity $2\times10^{34}cm^{-2}s^{-1}$ each, while other two IP's are reserved for future pp collider SPPC. The circumference of CEPC collider is 54.75 km, including 8 arcs of 5852.8m, 4 arc straights of 849.6 m each and 4 interaction region straights of 1132.8 m each. The RF frequency of the booster is chosen as 1.3 GHz, factor of two higher than that in the collider. There are eight RF stations in the booster, providing total RF voltage of 5.12 GV. One RF station consists of 4 cry-modules of 12 m long each, each of them contains eight 9-cell super-conducting cavities. Table 1 lists the main parameters of the CEPC booster.

Table 1: Main Parameters of the CEPC Booster

| Parameter | | Unit | Value |
|---|---|---|---|
| Injection energy | | GeV | 6 |
| Ejection energy | | GeV | 120 |
| Circumference | | km | 52.75 |
| Bending radius | | km | 6.519 |
| Bending field | @ 6 GeV | T | 0.0614 |
| | @ 120 GeV | | 0.00307 |
| SR loss/turn | | GeV | 2.814 |
| Bunch number | | | 50 |
| Bunch population | | $10^{10}$ | 2.0 |
| Beam current | | mA | 0.87 |
| RF frequency | | GHz | 1.3 |
| Total RF voltage | | GV | 5.12 |
| SR power @ 120GeV | | MW | 2.46 |
| SR power density @120GeV | | W/m | 45 |

The bunch number in the booster is chosen the same as in the collider. The bunch population is based on the assumption of 5% current decay in the collider between two top-ups. Synchrotron radiation power density of 45W/m at 120 GeV in CEPC booster is much lower than in BEPCII of 415W/m [2].

For the very low synchrotron radiation damping rate, a scheme of single bunch injection from linac to booster is adopted. The electron and positron beams with bunch population of $2\times10^{10}$ and emittance of 0.3 mm·mrad are injected into central orbit of the booster. Overall transfer efficiency from linac to the collider is assumed to be 90 %.

The booster operates with a repetition frequency of 0.1 Hz, the typical magnetic cycle is given in Fig. 2. Shown in Fig.2, the beam injection from the linac to the booster takes 1 second, the energy ramp takes 4 seconds, 1 second flat top is for beam extraction to the collider, and 4 seconds for magnets ramping down.

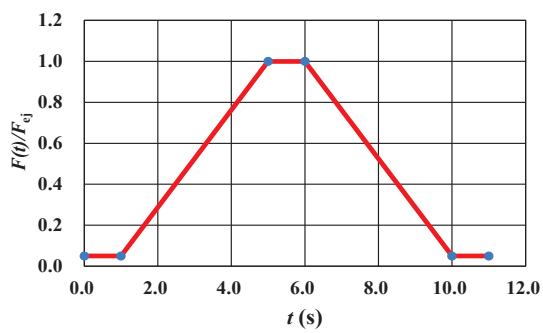


Figure 2: Typical magnetic cycle in the booster.



ISBN 978-3-95450-172-4

## LATTICE

### *Choice of Cell Length*

For the booster is installed in the CEPC tunnel, its arc arrangement should be similar to the collider. However, the length of the cells can be optimized with required beam property and other parameters in order to improve cost performance. Lattice parameters scaling to the cell length are presented in Table 2.

Table 2: Lattice Parameters Scaling to the Cell Length

| Parameter | Value | | | Unit |
|---|---|---|---|---|
| $L_{cell}$ | 47.2 | 71.7 | 94.4 | m |
| $\|k_Q l_Q\| \propto L^{-1}$ | 0.044 | 0.029 | 0.022 | $m^{-1}$ |
| $\beta_{max} \propto L$ | 81.2 | 123.3 | 162.3 | m |
| $D_x \propto L^2$ | 0.38 | 0.87 | 1.52 | m |
| $\nu_{x,y} \propto L^{-1}$ | 189.2 | 124.6 | 94.6 | |
| $\alpha_p \propto L^2$ | 3.43 | 7.91 | 13.72 | $10^{-5}$ |
| $\xi \propto L^{-1}$ | 86.4 | 56.9 | 43.2 | |
| $\|k_{SF} l\| \propto L^{-3}$ | 0.15 | 0.043 | 0.019 | $m^{-2}$ |
| $\|k_{SD} l\| \propto L^{-3}$ | 0.24 | 0.070 | 0.030 | $m^{-2}$ |
| $\varepsilon_{x0} \propto L^3$ | 6.8 | 23.8 | 54.40 | nm |
| $\nu_s \propto L$ | 0.204 | 0.31 | 0.41 | |
| $\sigma_{x\beta} \propto L^2$ | 0.74 | 1.71 | 2.97 | mm |
| $\sigma_{y\beta} \propto L^2$ | 0.53 | 1.21 | 2.10 | mm |
| $\sigma_{xE} \propto L^2$ | 0.49 | 1.14 | 1.97 | mm |
| $\sigma_x \propto L^2$ | 0.89 | 2.06 | 3.57 | mm |
| $\sigma_z \propto L$ | 1.84 | 2.76 | 3.68 | mm |

It is indicated in Table 2 that longer the cell, the larger the beta functions, dispersion, emittence and beam size, and also smaller the chromaticity, weaker the sextuples, and, more importantly, the less cell number and machine components. The cell length of the booster is then chosen as 71.7m, about 1.5 times of the collider of 47.2 m, as the baseline design. The total FODO cells in the booster is 764.

### *Lattice Functions*

The lattice of the booster is based on 60° FODO cells. The structure of two types of super-periods in the booster is indicated in Fig.3.

| | | | | |
|---|---|---|---|---|
| Arc straight | -DIS | 18 FODO cells | DIS | IR straight |
| Arc straight | -DIS | 18 FODO cells | DIS | Bypass |

Figure 3: Layout of CEPC and its booster.

There are 8 arcs in the booster, each of them consists of 78 FODO cells and two dispersion suppressors (each contains one regular FODO cell and one straight FODO cell). There are two quadrupoles of 1 m each, 8 dipoles of 8 m each, two sixtupoles of 0.2 m each in a regular FODO cell of 71.7 m. Total length of an arc is 5846.6 m. There are 12 straight FODO cells in the arc straight and 15 straight FODO cells in the IR straight (for IR2 and IR4). In IR1 and IR3, two bypasses are designed to keep away from the detectors. The computer code MAD [3] is applied for the optics design. The lattice functions in the booster are shown in Fig. 4.

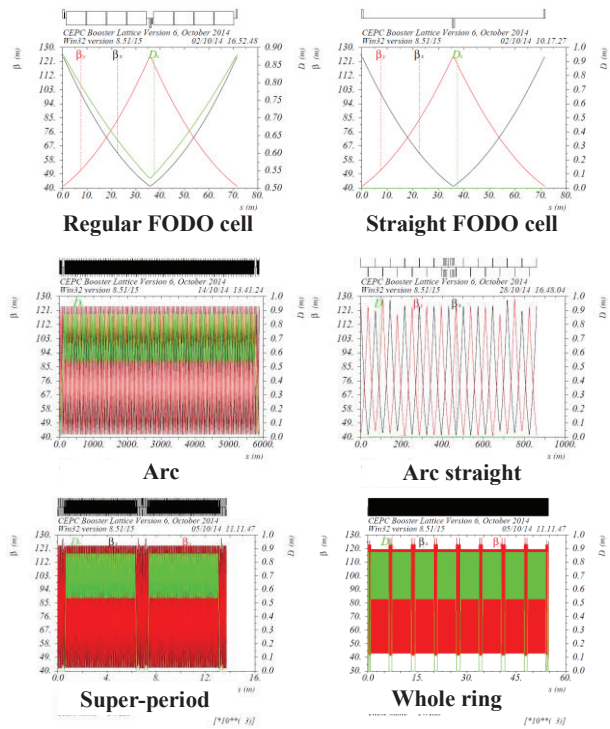


Figure 4: Lattice functions in the booster.

### *Bypasses*

Two bypasses are arranged in the booster to make the beamline skirting the detectors at IP1 and IP3 of the collider. The structure of a half bypass is shown in Fig. 5.

| | | | | | | |
|---|---|---|---|---|---|---|
| -3*FODO<br>$-3L_c$ | -DIS<br>$2L_c$ | BPI1<br>$4f_1 \cdot L_c$ | -DIS<br>$2L_c$ | FODO<br>$2L_c$ | DIS<br>$2L_c$ | BPI2<br>$1.5f_2 \cdot L_c$ |

Figure 5: Structure of half bypass.

Seen in Fig.5 the bypasses are also based on FODO cells. The idea of the booster bypass design is to move out 3 regular FODO cells in arcs to the bypasses and keep the straight sections BPI1 and BPI2 dispersion free. The advantage of this design is that no additional bending magnet is required. The length of a bypass is $L_{bp}=2\times(6+4f_1+1.5f2)\cdot L_c$ and the width of the bypass is $W_{bp}=(9.5+9f_1)\cdot\theta_c L_c$. By properly choosing the factors $f_1$ and $f_2$, both length and width of bypasses can be adjusted to meet the length of interaction region and detector width. In present design, we take $f_1=1.0$ and $f_2=1.0$ making bypass width of 13.0m and total length of 2×820 m, and the circumference about the same as the collider.

ISBN 978-3-95450-172-4

Lattice functions in long straights in IP2 & IP4 and half bypass in IP1 & IP3 are shown in Fig. 6.

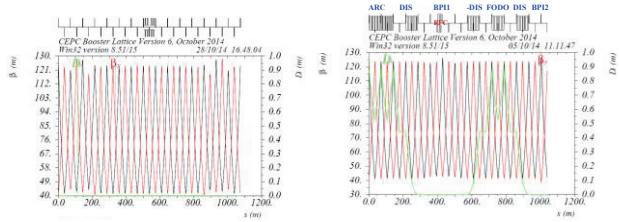

Figure 6: Lattice functions in long straights in IP2 & IP4 and half bypass in IP1 & IP3.

### *Dynamic Aperture*

Dynamic aperture of the booster is studied with optics computing code SAD [4]. Two family of sixtupoles SF and SD near quadrupoles QF and QD in FODO cells are used for chromaticity correction with corrected $\xi_x = \xi_y = 0.5$. Figure 7 plots the dynamic aperture for particles of $\Delta p/p = 0$, ±1%, ±2% by tracking of 3 damping times assuming the transverse coupling $r = \varepsilon_y/\varepsilon_x = 0.01$.

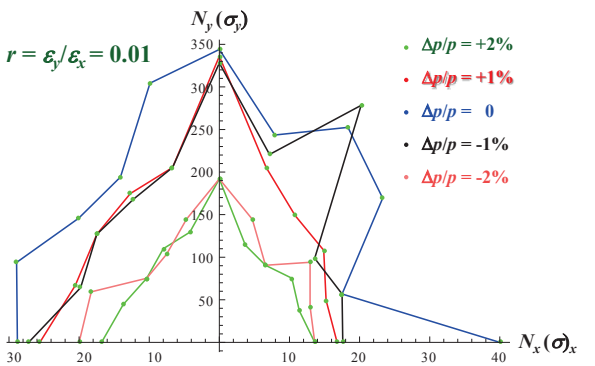


Figure 7: Dynamic aperture plot.

As a summary of this section, the lattice related parameters of the booster are given in Table 3.

Table 3: Lattice Parameters of the Booster

| Parameter | Unit | Value |
|---|---|---|
| FODO cell length | m | 71.665 |
| Total number of FODO cells | | 764 |
| Phase advance in a cell (H/V) | | 60°/60° |
| Length of D/Q/S magnets | m | 8.0/1.0/0.2 |
| Maximum β function (H/V) | m | 123.8/123.0 |
| Transverse betatron tune (H/V) | | 127.2/127.3 |
| Maximum dispersion function | m | 0.879 |
| Length of bypass | m | 1640 |
| Width of bypass | m | 13.0 |
| Emittance (H/V) | nm·rad | 20.5/0.205 |
| Damping time (Trans./Long.) | ms | 15.6/7.8 |
| Momentum compaction factor | $10^{-5}$ | 7.69 |
| Beam energy spread | % | 0.127 |
| Synchrotron oscillation tune | | 0.32076 |
| Bunch length ($V_{rf}$=5.12 GV) | mm | 2.66 |
| Maximum beam size (H/V) | mm | 1.948/0.159 |

## LOW INJECTION ENERGY ISSUES

It is seen in Table 1, the bending field of CEPC booster is 614Gs at 120 GeV. To reduce the cost of linac injector, the injection beam energy for booster is chosen as low as 6 GeV with the magnetic field as low as 30.7 Gs, about 1/7 of the injection field of LEP [5]. The question is if the magnetic field is stable enough at such a low field against the earth field of 0.5-0.6 Gs and its variation. To mitigate the low field problem, effort is also made to increase the bending field at injection with the proposed wiggling band scheme. Moreover, the beam instability at 6 GeV is discussed.

### *Low Field Stability Test*

Taking advantage of the existing BEPC bending magnet and power supply, low magnetic field stability was tested. The stability of the power supply is better than $1\times10^{-4}$. A Hall probe system is used for field measurement with accuracy of 0.1Gs or $\Delta B/B$ of $3\times10^{-3}$. The setup for the test is shown in Figure 8.

Figure 8: The magnetic field test setup.

The test was performed by IHEP magnet group [6]. The magnetic field outside and inside of the magnet with zero excitation current was measured first. As shown in Figure 9, the earth field (outside the magnet) is about 0.8 Gs, with $B_x$=0.55 Gs (south-to-north), $B_y$=0.45 Gs (vertical) and $B_z$=0.25Gs (east-west); while the field inside the magnet is dominated by its residual field.

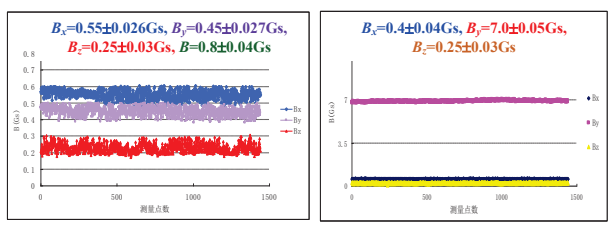


Figure 9: Measured field outside & inside of the magnet.

The 24-hour magnetic field stability was measured for different excitation currents, given in Figure 10.

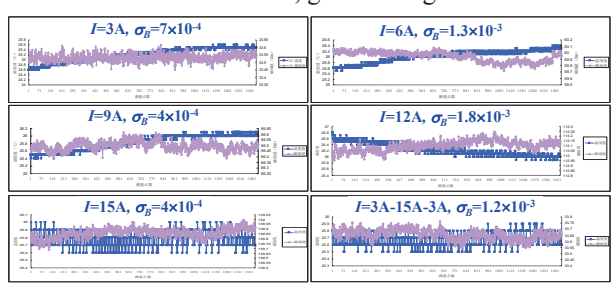


Figure 10: 24-hour magnetic field stability test for different excitation currents.



ISBN 978-3-95450-172-4

The test shows that the magnetic field stability around 30 Gs is about $1\times10^{-3}$, which indicates the injected beam energy for booster of 6 GeV could be feasible in view of field stability.

### *Low Field Stability Test*

The idea of wiggling bend scheme comes from wiggler magnets applied in synchrotron radiation facilities that higher field cancelation makes zero or lower integrated field. The proposed scheme is shown in Figure 11. There are four bending magnets in half cell of the booster, two outside bends are excited by a bipolar power supply making the wiggling bands so that the operating magnetic field gets higher.

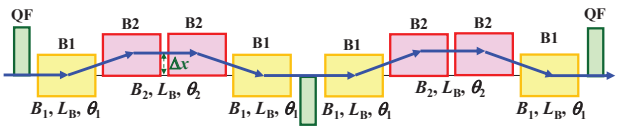


Figure 11: The magnetic field test setup.

The magnetic field of the bending magnets is properly set during energy ramp to keep total bending angle constant, i.e. $\theta_{B2}+\theta_{B1}=2\theta_B$. In principle, the oppositely excited bends $B_1$ can be as low as $-0.9B_{ej}$ at injection for $B_2=B_{ej}$. However, the orbit offset $\Delta x=\theta_1\times(L_B+L_D)$ may get too large, where $L_B$ and $L_D$ are length of bending magnets and the drift space between the magnets. Here we take $B_1=-0.1B_{ej}=60$Gs, and $B_2=0.2B_{ej}$, i.e. double the magnetic field of the baseline design with $\Delta x$ =20 mm. Magnetic field and energy ramping curves are given in Fig.12.

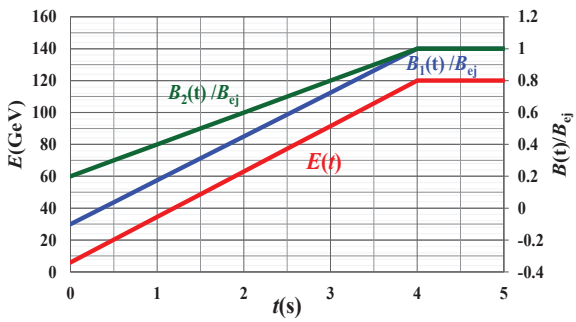


Figure 12: Magnetic field and energy ramping curves in wiggling bend scheme.

### *Instability Issue*

The low injection energy not only results in the low magnetic field, but also beam instability. The beam energy in the booster at injection is 1/20 of that in the collider, while the beam intensity in the booster is also 1/20 of the collider. However, beams may get unstable for almost no synchrotron radiation damping in the booster. The special concern is on transverse mode coupling instability, coupled bunch instability excited by high order modes in 1.3 GHz superconducting cavities and resistive wall effect. Study on beam instability in the booster is in progress. In any case, bunch-by-bunch feedback system should be equipped in the booster to provide damping mechanism in order to stabilize beams.

## BEAM TRANSFER

6 GeV electron and positron beams from the linac are injected into the booster ring through the transfer line LTB, accelerated to the top energy of 120 GeV and then extracted to the collider through the transfer line BTC.

### *Beam Transfer from Linac to Booster*

The function of the transfer line LTB is to bring electron and positron beams from the linac to booster and to match to its phase space functions. The layout of LTB is illustrated in Fig. 13.

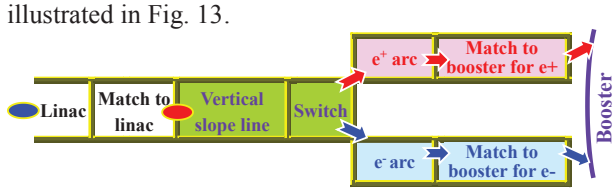


Figure 13: Layout of beam transfer line LTB.

As shown in Fig. 13, the transfer line LTB is comprised of a vertical slope line (VSL), a switch yard and $e^+e^-$ branch lines. The vertical slope line connects the linac of ground level to the booster of 50 m deep. It consists of a bend down section making a 1:10 slope, successive 15 straight 90° FODO cells and a bend down section making dispersion free at the end of VSL. The switch yard matches the Twiss parameters with VSL and delivers electron and positron beams to their individual branch lines. In the $e^+$ and $e^-$ branch lines, beams are transferred in two arcs and then matched to the booster through the final matching sections. Each arc contains 2 dispersion suppressors and 6 regular 90° FODO cells. The dispersion suppressors are carefully arranged to avoid conflict of the magnets in two branches. The lattice functions in the transfer line LTB are shown in Fig. 14.

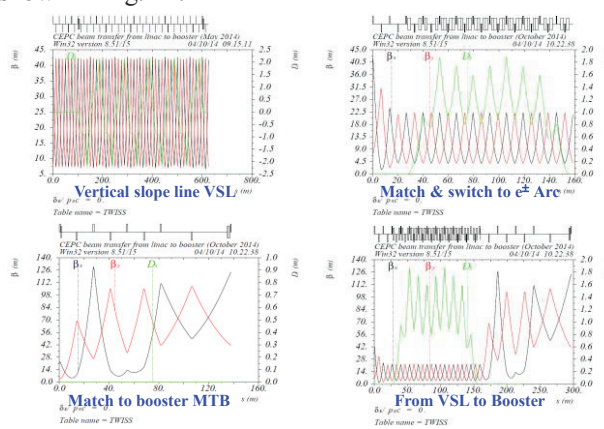


Figure 14: The lattice functions in the transfer line LTB.

### *Beam Injection to Booster*

Through the transfer line LTB, electron and positron beams are injected into the booster from outside of the ring. Horizontal septum is used to bend beams into the booster, and a single kicker downstream of injected beams kicks the beams to the booster orbit with maximum injection rate of 100 Hz. Figure 15 pictures the injecting bunch in the septum and the injected bunch in the booster. The kicker

ISBN 978-3-95450-172-4

needs to deflect the beam with displacement of $x_k=12\sigma_{x,ej}+3\sigma_{x,inj}+d$ at the entrance of the septum in order to avoid particle loss of both injecting and injected bunches.

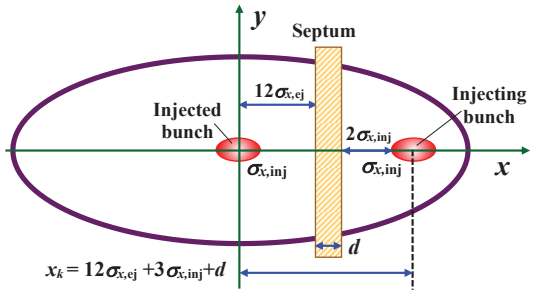


Figure 15: Injecting and injected bunches at entrance of septum.

Main parameters of the injection septum and kicker are listed in Table 4. The strength of the septum and the kicker corresponds to the energy of 12 GeV for future upgrade.

Table 4: Main Parameters of the Injection Septum and Kickers

| Magnet type | Length (m) | $\theta$ (mrad) | Field (T) | Aperture | |
|---|---|---|---|---|---|
| | | | | H (mm) | V (mm) |
| Septum | 2.0 | 9.1 | 0.18 | 41.4 | 13.4 |
| Kicker | 0.5 | 0.40 | 0.032 | 41.4 | 13.4 |

### *Beam Extraction From Booster*

Single kicker and 4 orbit bumps are used for beam extraction horizontally from the booster with maximum extraction rate of 100 Hz. A Lamberstson magnet is applied to bend beams vertically into the transfer line BTC. Main parameters of the extraction septum and kicker are listed in Table 5.

Table 5: Main Parameters of the Injection Septum and Kickers

| Magnet type | Length (m) | $\theta$ (mrad) | Field (T) | Aperture | |
|---|---|---|---|---|---|
| | | | | H (mm) | V (mm) |
| Septum | 10.0 | 9.1 | 0.41 | 41.4 | 18.6 |
| Kicker | 2.0 | 0.33 | 0.046 | 41.4 | 13.6 |

### *Beam Extraction from Booster*

The booster is mounted in the CEPC tunnel 2m above the collider. The Lamberstson septum bends beams down to the transfer line BTC. Beams are transferred and matches their Twiss parameters to the collider in BTC. Detail BTC design needs to be carried out together with collider injection. The lattice functions in BTC are shown in Fig. 16.

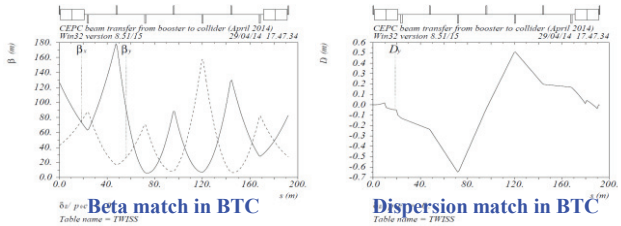


Figure 16: Lattice functions in the transfer line BTC.

## SUMMARY

The pre-conception design study on CEPC booster described in above sections finds no showstopper in view point of lattice, bypasses, dynamic aperture, beam transfer and requirement to technical systems. The issues related to the low energy injection, including the low magnetic field performance and beam instabilities, remain a central concern in the design. The wiggling bend scheme is proposed to mitigate this problem, while schemes of extending the linac injector with damping rings and adding a pre-booster are being considered. There are some technical challenges, such as the low HOM 1.3 GHz SC cavities, supports & alignment, as well as low cost components. The design study needs to be detailed and deepened.

## ACKNOWLEDGMENT

The author would like to thank all members of the CEPC design team for their perfect collaboration.

## REFERENCES

[1] Q.Qin, Overview of the CEPC Accelerators, HF2014 proceedings, THP3H2.
[2] BEPCII Team, Performance and Prospects of BEPCII, Proc. IPAC2012, 1030-1034, May 2012.
[3] H. Grote, C. Iselin, The MAD Program User's Reference Manual, CERN/SL/90-13(AP).
[4] SAD Home Page, Strategic Accelerator Design, http://acc-physics.kek.jp/SAD/.
[5] LEP Design Report, CERN-LEP/TH/83-29, June 1983.
[6] Z. Zhang, Low field stability test of the BEPC dipole, IHEP Internal Report, June, 2014.



ISBN 978-3-95450-172-4

# MAINTAINING POLARIZATION IN SYNCHROTRONS

I.A. Koop, BINP SB RAS, NSU and NSTU, Novosibirsk, Russia

*Abstract*

The paper describes a method of the preservation of the polarization of the electron beam during the acceleration in a synchrotron. It is proposed to install in the ring equally spaced Siberian Snakes. Advantages to use the odd number of snakes are discussed. Preliminary results of the analytical estimations and of numerical spin tracking simulation are shown.

## INTRODUCTION

The polarized beams are needed, first of all, for precise energy calibration using either resonant depolarization or free precession frequency measurement technique; and they are necessary for physics program with longitudinally polarized beams. Acceleration of polarized beams in a synchrotron has many advantages in comparison with the use of self-polarization directly in the collider: 1) full intensity polarized of up to 80%-90% electron beam could be accelerated and used for the experiments; 2) a polarized up to 50%-70% positron beam with only about 10 times lower intensity also should be available – it will become polarized in about 5 min in a 1-1.5 GeV wiggler damping ring; 3) free spin precession frequency measurement technique [1] is much faster and robust method of the energy determination – it measures every injection shot not only the average beam energy with the accuracy in the order of $10^{-6}$ , but also many other parameters, such as spin de-coherence rate, strength of first and high order synchrotron spin resonances etc.

A method of Siberian Snakes for preservation of the polarization during acceleration in a synchrotron was proposed by Derbenev and Kondratenko in 70-th [2]. They suggested install along a circumference the odd number of $180^0$ spin rotators. We will briefly discuss the applicability of that approach for acceleration of the polarized electron and positron beams in a booster synchrotron of FCC-ee collider.

## POLARIZED BEAM ACCELERATION WITH SIBERIAN SNAKES

When polarized electron beam is accelerated say from 20 GeV to 80 GeV it crosses more than 130 of integer spin resonances spaced by 440.65 MeV. Due to small field errors it will become fully depolarized even by a single cross of such a resonance. A Siberian Snake may help to solve this problem quite radically.

It is some kind of a spin rotator which rotates spin by $180^0$ around any axis which is perpendicular to the vertical one. In a ring with equally spaced odd number of snakes the closed spin orbit looks like it is shown in the Fig. 1 - everywhere in arcs spins are lying in the medium plane of an accelerator.

Another remarkable fact is that with the odd number of snakes the fractional part of the spin tune always equals to $\nu$=0.5, thus all the spin resonances became eliminated! Still strong enough spin perturbation may destroy the regular spin motion making it non-adiabatic. It may happen, if any k-th harmonic amplitude of a perturbation exceeds or approaches to $w_k$~0.5.

Other mechanism, which one should take into account, is the radiative depolarization. The spin relaxation rate is described by the famous DK formula [3]:

$$\tau_p^{-1} = \frac{5\sqrt{3}}{8}\lambda_e r_e c\gamma^5 \left\langle \frac{1-\frac{2}{9}\left(\vec{n}\vec{\beta}\right)^2+\frac{11}{18}\vec{d}^2}{|r^3|} \right\rangle$$

Here $\vec{n}(\theta)$ is a unity vector aligned along the equilibrium spin direction of a reference particle, $\vec{d}(\theta) \equiv \gamma \frac{\partial \vec{n}}{\partial \gamma}$ is the so-called a spin-orbit coupling vector, which describes the dependence of $\vec{n}$ from the energy, r is the bending radius and other symbols have the obvious meaning.

In a flat normal ring without snakes $\vec{n}(\theta)$ is vertical and $\vec{d}(\theta) = 0$. In the ring with the odd number of snakes $\vec{n}(\theta)$ is horizontal in arcs, as shown in the Figure 1, $|\vec{d}|$ scales $\sim \gamma$ and $\tau_p^{-1} \sim \gamma^7$.

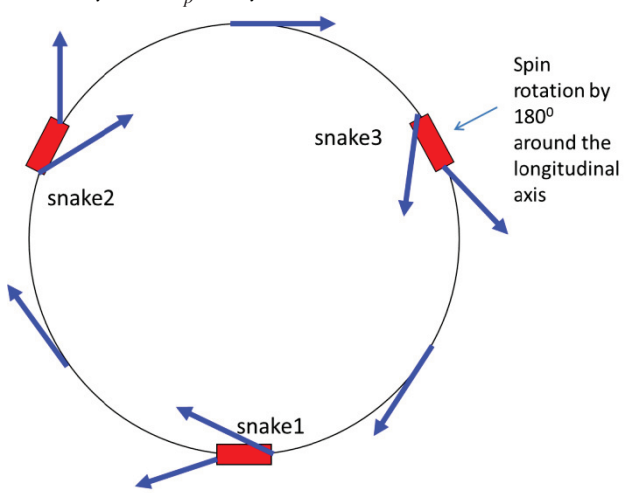


Figure 1: Schematic of spin rotation in a ring by 3 solenoid type snakes.

The averaged over the azimuth $\theta$ value of the spin-orbit coupling vector depends on the number of snakes N as follows:

ISBN 978-3-95450-172-4

$$\left\langle \vec{d}^{\,2} \right\rangle \simeq \frac{\pi^2}{3}\frac{\nu_0^{\,2}}{N^2}\,.$$

Here $\nu_0 = \gamma a$ is a spin tune, $a$ is the anomalous magnetic moment.

So, increasing the number of snakes one will reduce the depolarization rate $\tau_p^{-1} \sim N^{-2}$. With 3 snakes in the isomagnetic ring with the bending radius $r$=11 km $\tau_p$ =320 s at $E$=45 GeV and $\tau_p$ =6 s at $E$=80 GeV – very strong energy dependence! In the Figure 2 it is shown calculated by the code ASPIRRIN [4] dependence of the factor $|d(s)|$ (or equivalently |F5|) along the azimuth $s$, counted there in meters.

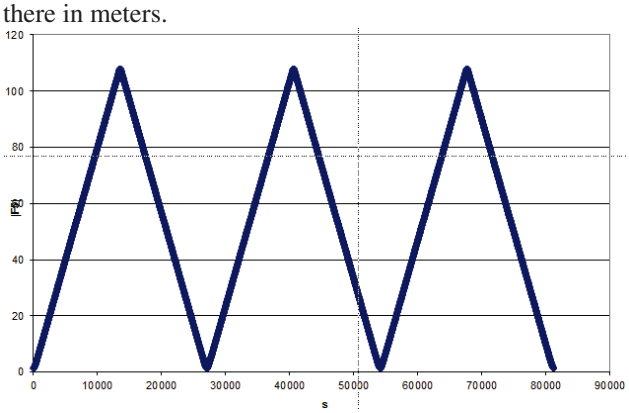


Figure 2: Azimuth dependence of the modulus of the spin-orbit coupling vector |$d(s)$|.

Its linear behaviour is dictated by the chromaticity of the $\vec{n}$ direction in arcs, which is proportional to the factor $\nu_0 / N$, we discussed above.

Let's estimate the polarization loss during acceleration in a synchrotron. Assuming that energy ramp proceeds linearly during a time $T$ one can calculate:

$$\tau_p^{-7} \sim E^7$$

$$P_{rad}(T) = \exp\left(-\int_0^T \frac{dt}{\tau(t)}\right) = \exp\left(-\frac{T}{8\tau_T}\,\frac{1-\left(\frac{E_0}{E_T}\right)^8}{1-\frac{E_0}{E_T}}\right).$$

For $E_0$=20 GeV, ET=80 GeV and taken $\tau_T = 6$ s, T=10 s, one gets Prad(T)=0.79 – not too small! With T=20 s the result is also not very bad: Prad(T)=0.79. And even with T=30 s the loss of the polarization during acceleration is only 50%, which may be considered as acceptable.

## SOLENOID TYPE SPIN ROTATORS

Different optics schemes for compensation of by the solenoid induced coupling were suggested in 80-th by Litvinenko and Zholentz [5]. Most simple for realization is a scheme shown in the Figure 3. The total solenoid is divided in two halfs. Each half rotates spin around the longitudinal axis by the angle

$$\frac{\varphi}{2} = (1+a)\frac{\int Bdl}{Br}$$

The coupling is compensated by the normal quadrupole lenses inserted between the solenoids providing that the 2x2 transportation matrices satisfy to the condition $T_x = -T_y$.

Main advantage of such a scheme is a flexibility in tuning the optics of a spin rotator. One can switch off the solenoids completely and retune the quads to provide the same beam transport as it was before.

The other requirement comes from the spin transparency condition. To cancel the contribution of the horizontal betatron oscillations to beam depolarization the transport matrix of such a partial spin rotator should be of the type [6] shown in the Figure 3. In case of a full Snake the total spin rotation angle φ=π and $T_x$–matrix becomes the unity matrix, while $T_y$ becomes minus unity matrix.

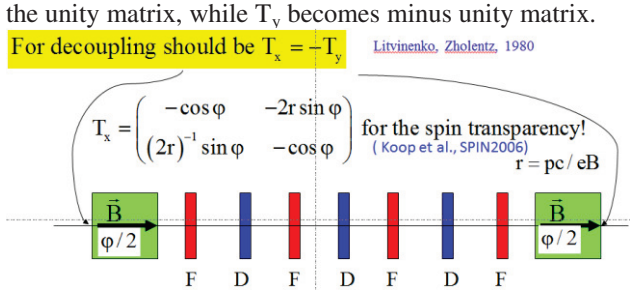


Figure 3: Spin transparent rotator optics scheme for the solenoid partial Snake.

## MINIMIZATION OF SPIN TUNE CHROMATICITY

In a flat ring without snakes the spin tune chromaticity equals just to the tune $\nu_0$:

$$\gamma\frac{\partial\nu}{\partial\gamma} = \nu_0 = 180 \qquad \text{for} \quad E=80 \ \text{GeV}$$

With a single snake it becomes very small:

$$\left|\gamma\frac{\partial\nu}{\partial\gamma}\right| \le \frac{1}{2}\,.$$

With N-odd equally spaced snakes it may become N times larger. Alternation of a sign of the longitudinal field will make spin tune chromaticity again less than ½.

With such a small spin tune chromaticity the synchrotron satellites of intrinsic and integer spin resonances will disappear. This is very profitable for the



ISBN 978-3-95450-172-4

acceleration of polarized beams to super-high energies [7, 8].

## CONCLUSION

Use of Siberian Snakes for the acceleration of a polarized beam in a synchrotron is an obvious tool to solve such a difficult task. Three snakes (odd number) will ensure preservation of the polarization in a booster synchrotron of FCC-ee complex up to 80 GeV.

Spin tracking simulations should validate this statement and provide the solid basis for the choice of the number of snakes needed to solve a task.

Remark: the radiative diffusion effects need to be incorporated into the tracking code!

## ACKNOWLEDGEMENTS

The author expresses his gratitude to Yu. Shatunov, S.R. Mane and A. Otboev for stimulating discussions and interest to this work.

## REFERENCES

[1] I. Koop, “Polarization issues and schemes for energy calibration”, HF2014 Beijing, 9-12 October 2014.

[2] Ya.S. Derbenev, A.M. Kondratenko , “Acceleration of Polarized Particles”, published in Dokl. Akad. Nauk Ser. Fiz. 223 (1975) 830-833 (in Russian), Sov. Phys. Dokl. 20 (1975) 562-564.

[3] Ya.S. Derbenev, A.M. Kondratenko , “Polarization kinetics of particles in storage rings”, Zh. Eksp. Teor. Fiz. 64 (June 1973) 1918-1929 (in Russian); Sov. Phys. JETP, vol.37, No.6 (Dec. 1973), pp. 968-973.

[4] V.I. Ptitsyn, Yu.M. Shatunov, S.R. Mane, “Spin response formalism in circular accelerators” Nucl.Instrum.Meth. A608 (2009) 225-233

[5] A.A. Zholents, V.N. Litvinenko, “On the compensation of solenoid field effects by quadrupole lenses”, Preprint IYF 1981-080, Novosibirsk; see also DESY-L-TRANS-289

[6] I.A. Koop et al., “Spin transparent Siberian Snake and spin rotator with solenoids”, 17th International Spin Physics Symposium, Kyoto, Japan, 2-7 October, 2006; AIP Conference Proceedings Volume 915, American Institute of Physics, 2006, p.948-954.

[7] S.R. Mane, “Polarization at TLEP/FCC-ee: ideas and estimates”, preprint arXiv: 1406.0561v1 [physics.acc-ph] 3 June 2014.

[8] Yu. Shatunov, a talk at SPIN14 conference, October 2014, Beijing, China.



ISBN 978-3-95450-172-4

# HOM DAMPER HARDWARE CONSIDERATIONS FOR FUTURE ENERGY FRONTIER CIRCULAR COLLIDERS*

Sergey Belomestnykh#
Brookhaven National Laboratory, Upton, NY 11973-5000, U.S.A.
and
Stony Brook University, Stony Brook, NY 11794, U.S.A.

*Abstract*

Future high luminosity energy frontier $e^+e^-$ circular colliders CEPC and FCC-ee will operate with high average beam currents. Radio-frequency systems in these machines utilize superconducting RF (SRF) structures with strong damping of higher order modes (HOMs). In this paper I will consider HOM damping options for the colliders under consideration, review HOM damper hardware, both existing and under development, and outline R&D necessary to develop efficient HOM damping in the future circular colliders.

## INTRODUCTION

Superconducting RF systems of the future energy frontier $e^+e^-$ circular collider CEPC and FCC-ee will have to deal with high average current particle beams consisting of a large number of short bunches [1]. The machines will be very big with a circumference between 50 and 100 km. As a result, the beams will have very wideband spectra with densely spaced frequency lines. Therefore HOM damping schemes for future colliders are quite challenging. Any selected scheme will have to be capable of handling kilowatts of HOM power via a combination of HOM couplers and beam pipe absorbers, see [2], for example. The latter are required to intersect the high-frequency part of HOM power, which propagate through the beam pipes. Typically required loaded quality factors of HOMs are in the $10^2$ to $10^4$ range. In this paper I review HOM dampers, existing and under development, with an emphasis on their applicability to the future energy frontier circular colliders.

## COUPLER TYPES

There are a large variety of HOM damper designs for SRF cavities, many of them reviewed in references [3]-[4]. However, very few of those dampers are designed to handle high average HOM power and even fewer demonstrated this in operation. The three main HOM damper configurations are based on different transmission lines and coupling circuits. These are: beam pipe absorbers, rectangular waveguide HOM couplers and loop/antenna HOM couplers to a coaxial line [4]. In this section we discuss pros and cons of different HOM damper types and consider existing designs.

*Work is supported by Brookhaven Science Associates, LLC under contract No. DE-AC02-98CH10886 with the US DOE.
#sbelomestnykh@bnl.gov

### *Beam Pipe Absorbers*

The beam pipe absorbers (HOM loads) are arguably the most efficient in HOM damping and will be required to absorb the high frequency part of HOM power, which propagates along the beam pipe. The absorber is a section of beam pipe with its inner surface covered by a layer of microwave-absorbing material, e.g. lossy ferrite or ceramics. Drawbacks of the beam pipe absorbers are: i) most absorber materials are brittle, can create particulates that contaminate SRF cavities; ii) parasitic beam-absorber interaction is significant and contributes to the overall HOM power; iii) the main disadvantage for large SRF systems is that the HOM loads occupy real estate along the beam axis and thus reduce the SRF system fill factor.

Room temperature HOM loads were originally developed at Cornell University and KEK for very high average power HOM absorption in the high-current $e^+e^-$ colliders CESR and KEKB [5]-[6]. These HOM loads utilize lossy ferrite materials and demonstrated capacity to absorb several kilowatts of HOM power in operation: 2.9 kW per load at CESR and 8 kW per load at KEKB. In both cases the loads were used in conjunction with single cell SRF cavities as illustrated in Figure 1.

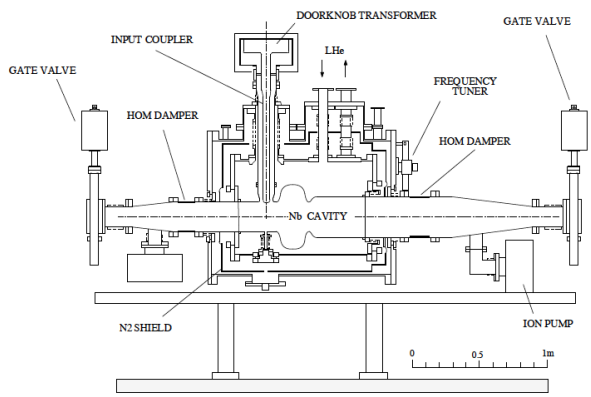


Figure 1: Single cell KEKB SRF cavity with beam pipe HOM dampers [7].

The CESR HOM loads, as the one shown in Figure 2, are used in many high-current storage rings around the world as well as in the R&D ERL at BNL [8]. The KEKB loads are installed in BEPC-II and are planned to be used at SuperKEKB, where the HOM power is expected to reach 15 kW per absorber.

The beam pipe absorbers operating at cryogenic temperatures have dissipation capacity of ~100 W [4] and are not suitable for the future circular colliders.



ISBN 978-3-95450-172-4

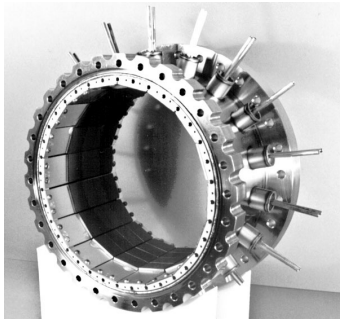

Figure 2: CESR-type HOM load [5].

### *Rectangular Waveguide Couplers*

The waveguide couplers can provide very efficient damping in a broad frequency range and don't compromise the fill factor. In theory, these couplers should be able to handle high HOM power, but it has not been demonstrated in operation yet. The main disadvantage of using waveguides is that their large size complicates the cavity and cryomodule designs.

This damping scheme is worked on at Jefferson Lab primarily in the context of developing SRF structures for high-current ERLs and for the electron-ion collider MEIC. For multi-cell cavities, the waveguides are configured in a Y-shape on each of the cavity's beam pipes as shown in Figure 3. The waveguides are then routed through the cryomodule and terminated with water-cooled loads at room temperature either outside or inside the vacuum vessel as illustrated in Figure 4.

Figure 3: 750 MHz ERL cavity (courtesy of JLab).

### *Coaxial Antenna/Loop Couplers*

The coaxial loop/antenna HOM couplers can provide strong HOM damping, but they require means of rejecting the fundamental mode. Rejection filters are typically very narrowband and must be carefully tuned. Also, these couplers are more difficult to cool than two other types.

First couplers of this type were developed for HERA and LEP. Later on, experience with LEP couplers was used to design couplers for SOLEIL, LHC, and Super-3HC cryomodules at SLS and ELETTRA. In addition to the LEP2 dipole mode coupler, the LHC SRF cavities have broadband couplers. The LHC couplers, depicted in Figure 5, were designed for ~1 kW HOM power level, but operate at lower HOM power levels so far.

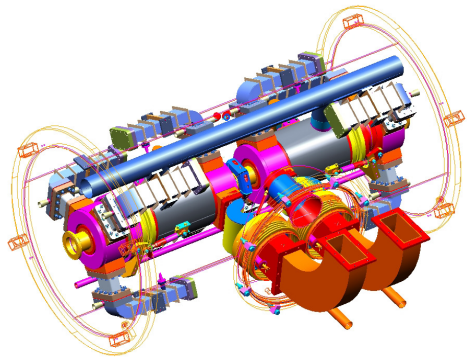

Figure 4: The cryomodule concept with rectangular waveguide HOM couplers (courtesy of JLab).

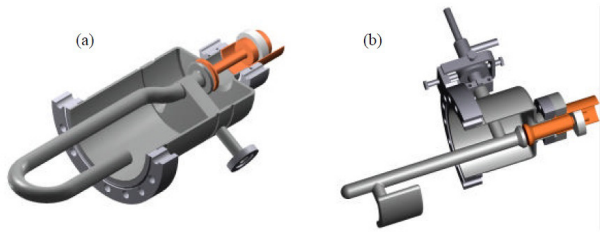


Figure 5: LHC HOM couplers: (a) narrow band dipole; (b) broadband [9].

## HOM COUPLERS UNDER DEVELOPMENT

Several new designs, that might be suitable for the future circular colliders, are under development. Here we consider design efforts at JLab and BNL.

For single cell cavities, JLab is developing an "on-cell" waveguide damper scheme, which allows satisfying very stringent HOM damping requirements of MEIC. A concept of such cavity is shown in Figure 6.

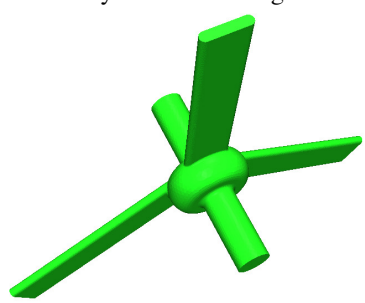

Figure 6: A concept MEIC cavity with an "on-cell" waveguide HOM damping (courtesy of JLab).

To avoid difficulties associated with the narrowband rejection filters in coaxial couplers, one can use high-pass filters. The high-pass filters, if properly designed, should be easy to tune and should have relaxed fabrication tolerances. BNL is developing several new designs capable of transmitting ~1 kW of HOM power.

ISBN 978-3-95450-172-4

A couple of designs are under development for the 704 MHz five-cell BNL3 cavity [10, 11]. One of the designs utilizes a two-stage Nb band-stop filter [12], shown in Figure 7. Three such couplers will be connected to the BNL3 cavity at each beam pipe for an efficient HOM damping.

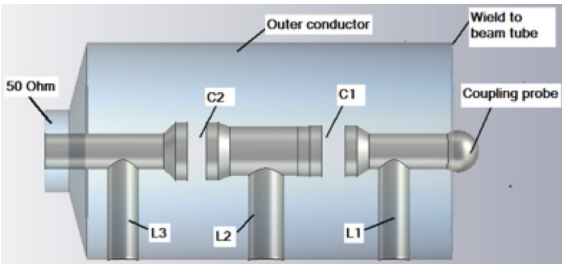


Figure 7: Two-stage band-stop filter [12].

The second design uses a dual ridge waveguide as a natural high-pass filter. A dual ridge waveguide provides a compact cross-section as compared to a rectangular waveguide. The most critical component in this layout is an antenna-to-waveguide transition. A broadband transition, shown in Figure 8, was designed and modeled. It has RF performance better than that of the two-stage coupler design, as illustrated by Figure 9 [13]. However, at this moment it is not clear, which design would be i) easier to fabricate and ii) less prone to multipacting.

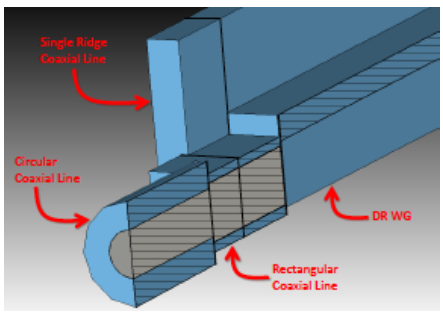


Figure 8: Layout of the broadband coaxial line to dual ridge waveguide transition [13].

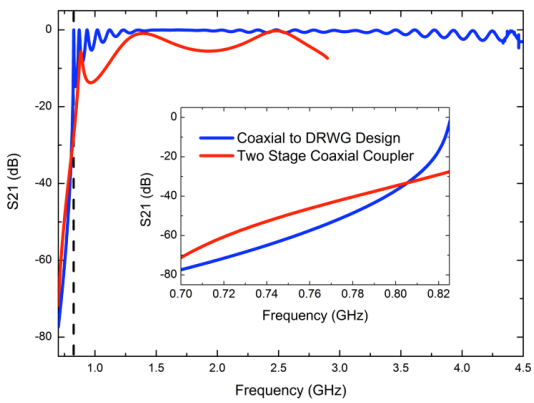


Figure 9: Comparison of the dual ridge waveguide and two-stage filters. The inset shows data from the fundamental mode to the first HOM [13].

Yet another high power HOM filter design, which might be suitable for the future colliders, is being worked on for the HL-LHC compact double quarter wave crab cavity [14]. The filter layout [15] is shown in Figure 10.

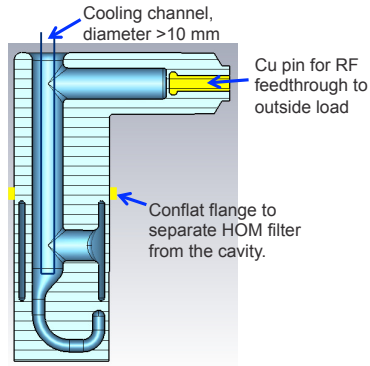


Figure 10: HOM coupler of the double quarter wave crab cavity for HL-LHC.

## SUMMARY

There are many proven designs of HOM dampers. However, only beam pipe absorbers demonstrated so far performance level of interest for CEPC and FCC-ee. The LHC HOM couplers were designed for ~1 kW HOM power levels, but operate at lower HOM power levels thus far. There are several promising new designs under development, which might be suitable for future circular colliders.

## ACKNOWLEDGMENT

The author would like to thank Robert Rimmer and Haipeng Wang for providing materials about development of HOM damped cavities at Jefferson Lab.

## REFERENCES

[1] F. Zimmermann et al., "Challenges for highest energy circular colliders," IPAC'14, Dresden, Germany (2014) pp. 1-6.

[2] J. Zhai, "CEPC SRF system," these proceedings, HF2014, Beijing, China, (2014).

[3] J. Sekutowicz, "HOM damping and power extraction from superconducting cavities," LINAC'06, Knoxville, TN, USA (2006) pp. 506-510.

[4] S. Belomestnykh, "Superconducting radio-frequency systems for high-$\beta$ particle accelerators," *Reviews of Accelerator Science and Technology* **5** (21012) 147-184.

[5] E. Chojnacki et al., "Beam line RF load development at Cornell," PAC'99, New York, NY, USA (1999) pp. 845-847.

[6] T. Tajima et al., "Development of HOM damper for B-factory (KEKB) superconducting cavities," PAC'95, Dallas, TX, USA (1995) pp. 1620-1622.

[7] K. Akai et al., "RF system for the KEK B-Factory," *Nucl. Instr. Meth. Phys. Res. A* **499** (2003) 45-65.



ISBN 978-3-95450-172-4

[8] H. Hahn et al., "Higher-order-mode absorbers for energy recovery linac cryomodules at Brookhaven National Laboratory," *Phys. Rev. ST Accel. Beams* **12** (2010) 121002.
[9] D. Boussard and T. Linnecar, "The LHC superconducting RF system," *Adv. Cryogen. Eng. A* **45** (2000) 835.
[10] Wencan Xu et al., "High current cavity design at BNL," *Nucl. Instr. Meth. Phys. Res. A* **622** (2010) 17.
[11] Wencan Xu, "704 MHz BNL3 cavity as an option for CEPC/FCC," these proceedings, HF2014, Beijing, China, (2014).
[12] Wencan Xu et al., "New HOM coupler design for high current SRF cavity," in PAC'11, New York, NY, USA (2011) pp. 925–927.
[13] C. Marques, "A Comprehensive Investigation and Coupler Design for Higher-Order Modes in the BNL Energy Recovery Linear Accelerator," M.S. Thesis, Stony Brook University, 2014.
[14] B. Xiao et al., "Design, prototyping and testing of a compact superconducting double quarter wave crab cavity," to be submitted to *Phys. Rev. ST Accel. Beams*.
[15] B. Xiao, "Overview of the HOM damping in deflecting cavity," HOMSC'14, Batavia, IL, USA (2014).



ISBN 978-3-95450-172-4

# FREQUENCY TUNERS, OPERATING EXPERIENCE AND PERFORMANCE RECOVERY

Yoshiyuki Morita#, KEK, Oho 1-1, Tsukuba, Ibaraki, Japan

*Abstract*

Several important issues for the SRF cavity system will be discussed. One issue is a tuner system. Recent tuner systems have significantly advanced at many laboratories and a number of tuner technologies now exist for a variety of requirements. We will review those tuner systems and discuss applicability.

The second issue is stability of cavity operation. The SRF systems for the Higgs factory must have as low trip rate as possible. Maintenance work is necessary to keep the trip rate at low level. The SRF cavity design that takes into account the ease of maintenance is required. Operational experience of KEKB is an useful example for practical considerations.

The third issue is performance degradation and its recovery method. In a long-term operation, cavity performance gradually degrades. A recovery method with a low risk, low cost and in a short period of time is desirable. We have developed a horizontal high pressure rinsing that can be applied directly to the cavity in a cryomodule. Our degraded cavities successfully recovered using this method.

In this paper, we will report the tuner systems for SRF cavities for appropriate design choice, the operating experience and cavity performance recovery.

## INTRODUCTION

There are several important issues for designing SRF cavities and cryomodules. In this report three main issues will be discussed. Those are frequency tuners, operating experience and performance recovery.

Frequency tuner is an important system for the cavity. Its functions are to tune the cavity to its resonant frequency, detune to compensate the beam loading, and help to stabilize its RF amplitude and phase. At an early stage of the SRF cavity development, many types of tuners were tried and applied. Now frequency tuners have advanced for a variety of requirements. One can select an appropriate tuner design for one's cavity. It is useful to review tuner designs developed at many laboratories.

Operating experience gained elsewhere provides very useful information for designing suitable system for the machine operation. Since the Higgs factory requires high integrated luminosity, RF trip rates and down time of the SRF cavities should be as low as possible. In order to keep the low trip rate, maintenance works are essential. Cavity performance degradation in a long term operation also gives a useful information. As an example, cavity RF trip rates, maintenance work, troubles of the cavity operation and performance degradation of the SRF cavities at KEKB are presented.

Performance recovery is needed or desired for a long-term operation. A recovery method should be low risk, low cost and in short period of time. KEK recently developed a horizontal high pressure rinsing method that can be directly applied to a cavity in a cryomodule. Two degraded KEKB cavity modules successfully recovered after the horizontal high pressure rinsing. The R&D effort, details of horizontal high pressure rinsing and application to cryomodules are presented.

## FREQUENCY TUNERS

### *Tuners at An Early Stage*

Four frequency tuner systems at an early stage of development are reviewed [1]. The TRISTAN tuner at KEK had a lever system. The lever was driven by a screw jack with a stepping motor. The jack has a piezoactuator for fine tuning. The CESRIII tuner at Cornell University had a flex hinge system with no backlash driven by a stepping motor. The CEBAF tuner system at JLab had a gear shaft system driven by a stepping motor and harmonic gear combination exterior to the cryomodule. The LEPII tuner system at CERN utilized thermal expansion and contraction of three Ni bars. He gas cools the bars for contraction while coil heater warm up the bars for expansion. Exciting coils surrounded those bars to produce magnetostrictive effect for fine tuning. There were a variety of mechanism of the main tuners. The fine sub-tuner was a piezoactuator or a magneto-strictive tuner. Table 1 summarises tuner parameters.

Table 1: Tuner Parameters

| | CEBAF | TRISTAN | CESR III | LEP II |
|---|---|---|---|---|
| Frequency (MHz) | 1500 | 508 | 500 | 325 |
| Mechanism | Drive shaft | Lever arm | Flex hinge | Ni bars |
| Driver | Stepping motor | Stepping motor | Stepping motor | He cooling and coil heating |
| Sub-tuner | | Piezo 4kHz | | Magneto-strictive ±1kHz |
| Sensitivity (kHz/mm) | 500 | 80 | 320 | 40 |
| Frequency range (kHz) | 400 | 800 (10 mm) | 600 | 50 (10Hz/s) |
| Precision (Hz) | 2 | 20 | 10 | - |

#yoshiyuki.morita@kek.jp



ISBN 978-3-95450-172-4

### *TRISTAN Tuner Development*

We present development of tuner systems for the TRISTAN cavity [2]. A 508 MHz, 3-cell test cavity had a scissor jack mechanism in a helium vessel. The cavity had a piezoactuator for fine tuning at the beam pipe exterior to a cryostat. This scissor jack was soon replaced with a screw jack tuner system with a piezoactuator at the beam pipe for a 5-cell test cavity. Finally a lever system was applied for the TRISTAN 5-cell cavities as shown in Figure 1. The lever expand the cavity at the beam pipe by a screw jack driven by a stepping motor and a piezoactuator.

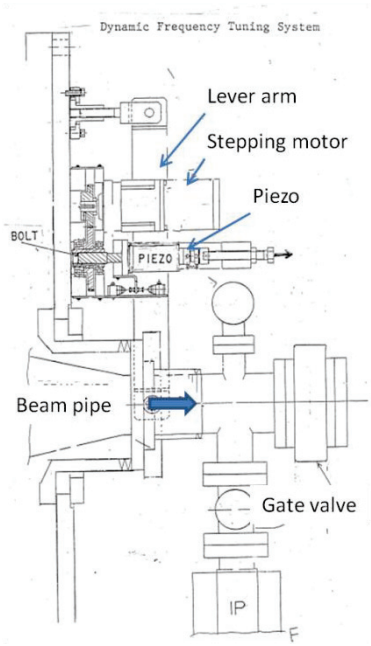


Figure 1: TRISTAN tuner system.

Several piezoactuators broke at the first stage of the operation. However, no piezoactuator broke after improvements of the sintering conditions of piezoelectric elements and reinforcement of the radiation shield. The same screw jack systems were used for lever arm tuners of the KEKB 509 MHz single cell cavity. The tuners will be used for the SuperKEKB operation without major change. However, stepping motors, harmonic gears, piezoactuators, etc. were renewed for the purpose of easy maintenance. The renewed tuner parameters are listed in Table 2.

Table 2: Tuner Parameters of SuperKEKB

| Parameter | SuperKEKB |
|---|---|
| Frequency (MHz) | 509 MHz |
| Bandwidth (Hz) | 10 kHz |
| Lever ratio | 0.5 |
| Piezo stroke | 64μm/800V |
| Sensitivity | 400 kHz/mm |
| Frequency range | 400 KHz |
| Stiffness | 400 kg/mm |

### *S1 Global Cavity Tuners*

Three frequency tuners of S1 global string test cavities at KEK are reviewed [3]. Those cavities are TESLA type or TESLA-like cavities produced by FNAL, DESY and KEK as shown in Figure 2. Two TESLA cavities of FNAL have coaxial blade tuners developed by INFN, Milan. Tow TESLA cavities of DESY have double lever tuner systems developed by DESY based on the Saclay design. Other four TESLA-like cavities of KEK have slide jack tuner systems developed by KEK.

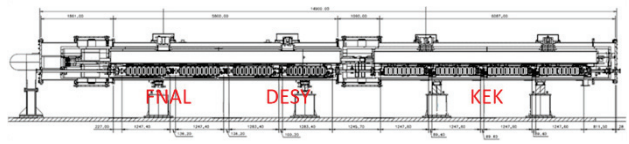


Figure 2: S1 global cavities.

The blade tuner transfers an azimuth motion to longitudinal strain with zero backlash. A CuBe threaded shaft was used for a screw nut system. A stepping motor and harmonic gear combination drives the screw nut. Two piezoactuators are set for fine tuning. All components are located in a cold section in vacuum. Figure 3 shows the blade tuner.

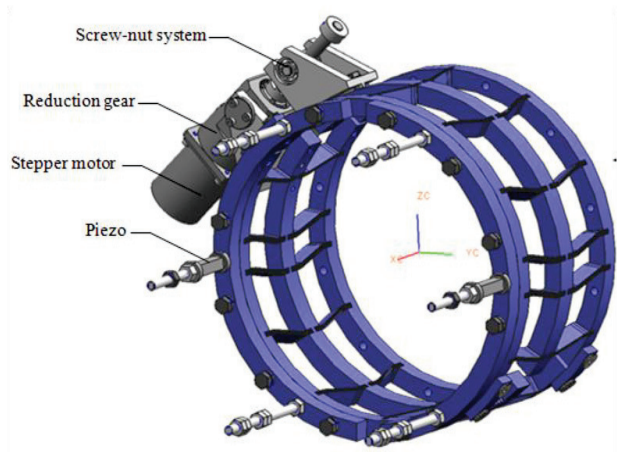


Figure 3: Blade tuner.

The DESY/Saclay tuner has a unique double lever system, whose lever ratio is 1:25. A stepping motor and harmonic gear combination drives a screw nut system. Two piezoactuators are set in a preloaded frame for a fast action. All components are located at a cold section in vacuum. Figure 4 shows the DESY/Saclay tuner.

The KEK slide jack tuner has two sliding rollers that push a tapered section. A single high voltage piezoactuator is set for a fast action. Two rollers are driven by a stepping motor located at a warm section via driving shaft. Figure 5 shows the slide jack tuner. Table 3 summarizes those three advanced tuner parameters.



ISBN 978-3-95450-172-4

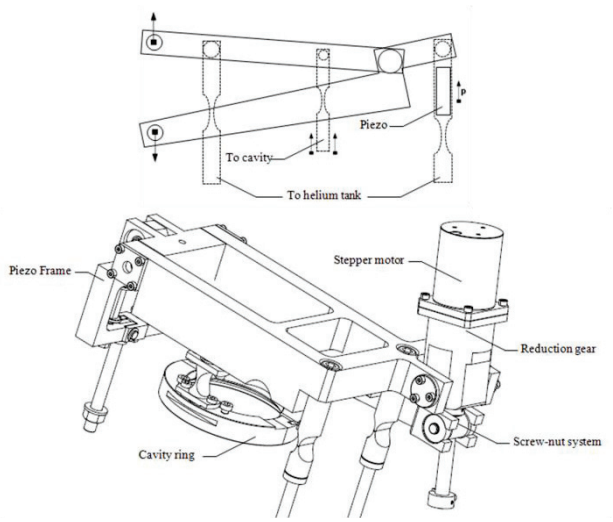


Figure 4: DESY/Saclay tuner.

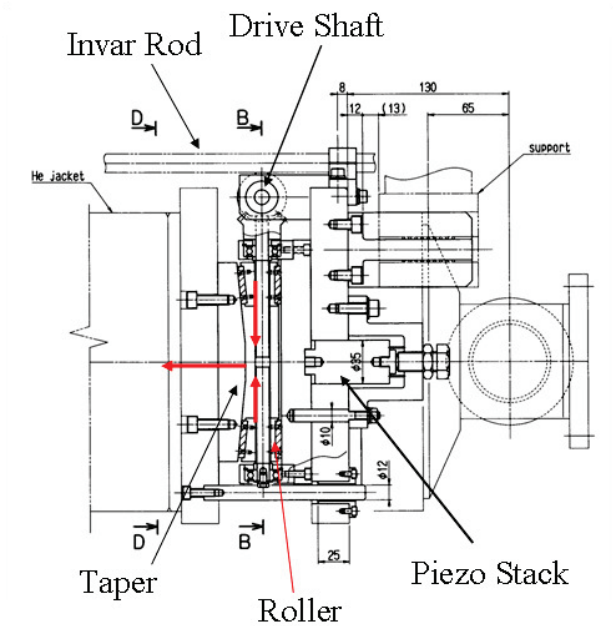


Figure 5: KEK tuner.

Table 3: Tuner Parameters of S1 Global Cavity

| | Blade | DESY/Sacray | KEK |
|---|---|---|---|
| Main tuner | Coaxial blade | Double lever | Slide jack |
| Driver location | Cold, vacuum | Cold, vacuum | Warm, air |
| Piezoactuator | Double | Double | Single |
| Sensitivity | 1.5Hz/step | 1 HZ/step | 3 Hz/step |
| Frequency range (kHz) | 600 | 500 | 900 |
| Stiffness (kN/mm) | 30 | 40 | 290 |

### *Other Excellent Tuners*

Saclay's two levers and eccentric shafts system has a tuning range of +/- 460 kHz with a resolution of 1.2 HZ (4nm) [4]. Two piezoactuators are set with a tuning range of 1.4 kHz. All components are located at a cold section. This tuner is compact compared to other tuning systems.

CEBAF upgrade cavity has a scissor jack system with a warm driver exterior to cryomodule [5]. The driver has three low voltage , 50mm stroke piesoactuators.

### *Summary*

As we have reviewed many tuner designs, resent tuners have advanced. One is able to select the design for one's cavity. On consideration to be taken into account is a location of a tuner driver. A cold location makes a tuner system compact and efficient, while it makes the maintenance difficult and time consuming. On the other hand, a warm location of a tuner driver exterior to its cryomodule makes the maintenance easy. Another consideration of selection is a long life and reliability. The lever system with a piezoactuator is used for long time and reliable system. The TRISTAN/KEKB tuner system has really long life (~30 years old) and will be used for the SuperKEKB operation.

## OPERATING EXPERIENCE

### *Overview of KEKB and SRF Cavities*

KEKB is an electron positron double ring collider accelerator for B meson physics at KEK [6]. Its circumference is 3 km. A 3.5GeV low energy ring stored positron beams of 1.7 A and 8GeV high energy ring stored electron beams of 1.4A. Both rings were filled with the top-up injections with no ramp-up. The achieved peak luminosity is 2.1x1034/cm2/s and total integrated luminosity from 1999 to 2010 was 1040/fb.

The RF system of the HER was a hybrid of eight SRF cavities and twelve normal conducting cavities [7]. The SRF cavity was a 509MHz, single cell, heavily damped cavity. Figure 6 shows the KEKB SRF cavity. Its operating voltage was 1.2-1.5 MV depending on the KEKB machine operation. Delivered beam powers per cavity were 350-400 kW and total absorbed HOM powers were 14-16 kW. Designed and achieved parameters of SRF cavity is listed in Table 4. The external Q factor of the input coupler was first set at $7x10^4$. It was then replaced to $5x10^4$ for the increase of beam currents.

Table 4: Designed and Achieved RF Parameters

| Parameter | Designed | Achieved |
|---|---|---|
| No. of cavities | 8 | 8 |
| RF voltage (MV) | 1.5 | 1.2-2 |
| Beam current (A) | 1.1 | 1.4 |
| RF power (kW/cav) | 250 | 350-400 |
| HOM power (kW/cav) | 5 | 14-16 |



ISBN 978-3-95450-172-4

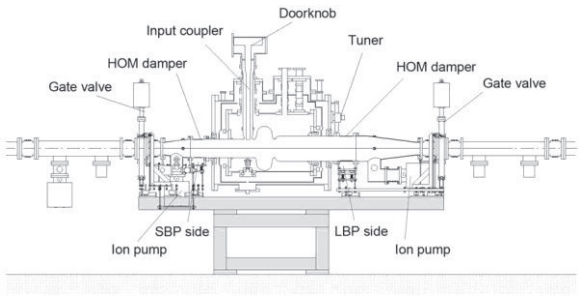


Figure 6: KEKB SRF cavity.

### *RF Trip Rate*

Figure 7 shows trip statistics of SRF, normal conducting and crab cavities from 2002 to 2010. RF trips of the SRF cavities were mainly due to discharging in the cavity or input coupler. The trip rate was 0.5 times per day for eight SRF cavities at the 1.4 A operation. The trip rate decreased to 0.1 times per day at the 1 A HER operation.

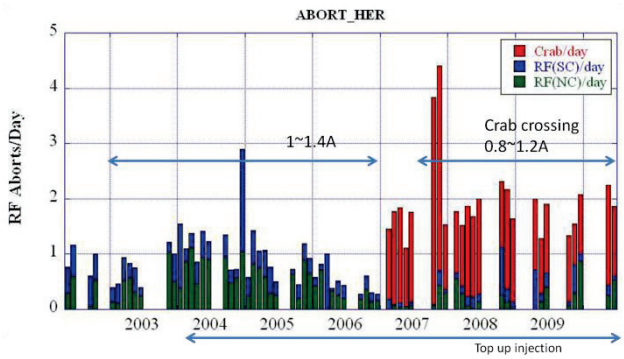


Figure 7: RF trip statistics.

### *Maintenance Work*

In order to keep low trip rates, maintenance works are essential. SRF cavities were warmed up twice a year in summer and winter shutdowns. During the shutdown, several maintenance works were done;

- Safety inspection of safety valves and pressure gauges once a year
- Greasing of the screw jack of the frequency tuners once a year
- Coupler RF conditioning with voltage biasing every before cool-down.
- Cavity RF conditioning up to 2-2.3 MV after cool-down.

Furthermore cavities were RF conditioned during the regular maintenance stop every two or three weeks. It is emphasized that the RF conditioning of the input coupler with voltage biasing up to +/- 2000 V with a full reflected RF power up to 300 kW was effective to reduce trip rates in the coupler.

### *SRF Cavity Troubles*

More than 20 heat cycles were experienced during the KEKB operation. The cool-down rate was 3 K/h. Two vacuum leakages of helium vessels, five leakages of SRF cavities at the indium seal, one leakage at the HOM damper flange and one leakage at the high voltage connector of an ion pump were occurred. Three cavities were re-assembled to repair the leakage of the indium seal with no additional surface treatments and other two cavities were repaired by re-tightening the indium flange bolts. All leakages at the indium seal occurred during the cool-down or warm-up. One piezoactuator broke during the KEKB operation

### *Performance Degradation*

All SRF cavities can provide 2 MV after 10 years of operation. However unloaded Q factors at 2 MV (Eacc=8MV/m) significantly degraded from $2x10^9$ to several $10^8$ with strong field emission. One apparent cause of degradation is a vacuum trouble during repair of leakage. Some amount of air dusts contaminated the cavity. Other causes are particle contamination at the air exposure of the cavity during the gasket exchange of the input coupler or during the repair of the indium seal.

## PERFORMANCE RECOVERY

Cavity performance degraded after 10 years of KEKB operation. Those cavity performances are still acceptable for the SuperKEKB operation. However further degradation will make the operation difficult. Performance recovery is desirable. The recovery method should be low risk, low cost and in short period of time. High pressure rinsing is suitable for this purpose. Therefore we developed a horizontal high pressure rinsing (HHPR) directly applied to a cavity in a cryomodule [8]. This method uses a horizontal insertion of high pressure water nozzle and aspirator pump for wasted water extraction. We started R&D using a test cavity.

After the application of HHPR to the test cavity in a clean room, we developed an automatic nozzle driving system. A schematic diagram of the HHPR system is shown in Figure 8. This system was applied to the test cavity in a clean booth at the cryomodule assembly area to simulate the application to SRF module. Parameters of the HHPR are listed in Table 5. The rinsing was applied in the cell and iris area only.

Table 5: Parameters of HHPR

| **Parameters** | |
|---|---|
| Water pressure | 7 MPa |
| Nozzle | ϕ0.54mm x 6 |
| Driving speed | 1 mm/sec |
| Rotational speed | $6^0$/sec |
| Rinsing time | 15 min |

ISBN 978-3-95450-172-4

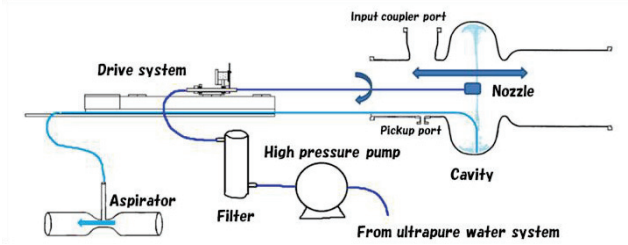


Figure 8: HHPR system.

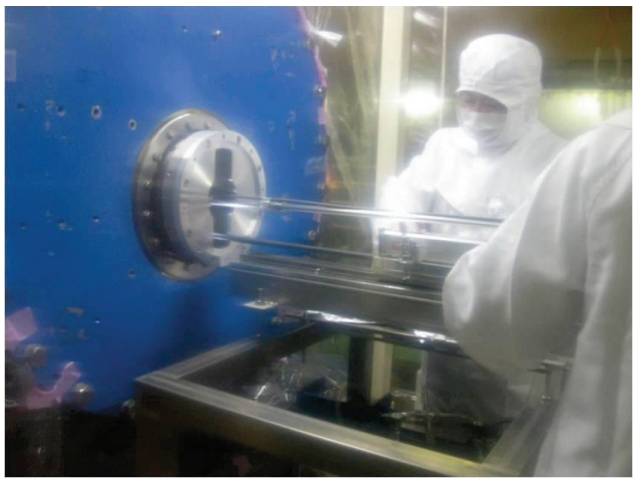

Figure 9: HHPR applied to the degraded cavity module.

We applied the HHPR to our degraded cavity module. The cavity (D11B) was degraded after the repair of vacuum leakage at the indium seal. Before the HHPR the inner conductor of the input power coupler and beam pipes on both sides including HOM dampers were dismounted from the cavity module. The cell and iris areas of the degraded cavity was rinsed with HHPR for only 15 minutes with the same conditions listed in Table 5. A picture at the HHPR in the clean booth is shown in Figure 9. The degraded Q factors sufficiently recovered after the HHPR. Figure 10a shows unloaded Q factors before the vacuum leakage, after the degradation at the repair of indium joint and after the HHPR. The recovered cavity was installed in the KEKB tunnel and replaced with another degraded cavity module by the vacuum trouble. We applied HHPR to this cavity and drastically recovered its Q factors as shown in Figure 10b.

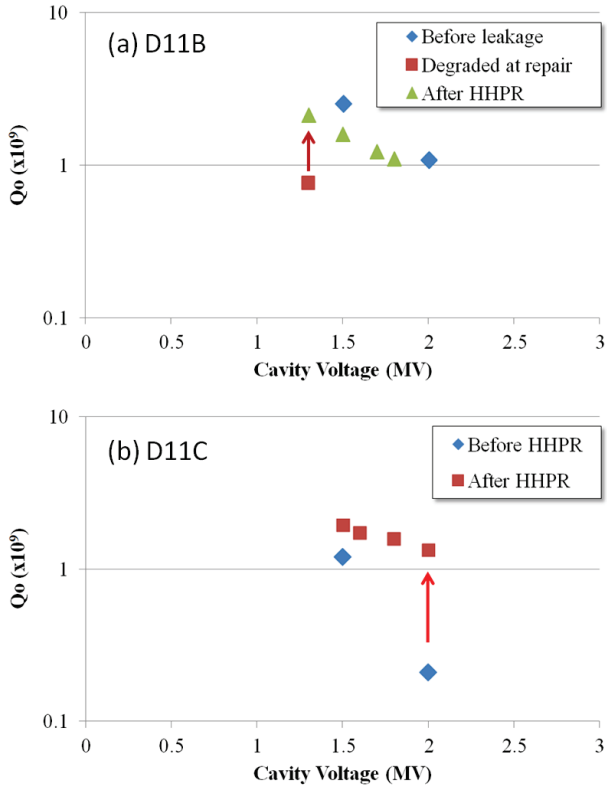


Figure 10: Recovery of unloaded Q factors . a) Unloaded Q factors of D11B cavity, b) Unloaded Q factors of D11C cavity.

## REFERENCES

[1] H. Padamsee, Jens Knobloch and Tomas Hays, RF Superconductivity for Accelerators, 2nd Edition, John Wiley & Sons, Inc., 2008.
[2] S. Mitsunobu, private communications.
[3] Kako et al.,"S1-Global Report", KEK Report 2013-3, May (2013).
[4] Pierre Bosland, "Tuning systems for superconducting cavities at Saclay", (2007); https://www.cells.es/old/ESLS-RF/ESLS-RF/2007/07-ESLS07-PBosland.pdf
[5] Jean Delayen, "Tuning Systens", (2008); http://uspas.fnal.gov/materials/08UMD/Tuning_Systems.pdf
[6] T. Abe et al., Prog. Theor. Exp. Phys. (2013) 03A001.
[7] T. Abe et al., Prog. Theor. Exp. Phys. (2013) 03A006.
[8] Y. Morita et al., “Horizontal High Pressure Water Rinsing for Performance Recovery”, SRF2013, Paris, Sept. 2013, TUP051, p. 521 (2013); http://ipnweb.in2p3.fr/srf2013/



ISBN 978-3-95450-172-4

# TOP UP INJECTION AT PEP-II AND APPLICATIONS TO A CIRCULAR e+e- HIGGS FACTORY*

J. T. Seeman†, SLAC, Menlo Park, CA 94025 USA

*Abstract*

The PEP-II B-Factory at SLAC (3.1 GeV e+ x 9.0 GeV e-) operated from 1999 to 2008, delivering luminosity to the BaBar experiment. The design luminosity was reached after one and a half years of operation. PEP-II surpassed by four times its design luminosity reaching 1.21 x $10^{36}$ $cm^{-2}$ $s^{-1}$. It also set stored beam current records of 2.1 A e- and 3.2 A e+ in about 1732 bunches.

Top-off injection, or continuous injection, was developed in PEP-II using the linac injector to allow constant luminosity with the BaBar detector being fully operational during injection. The electron beam top-off was developed initially as its lifetime was the shortest and thus made the luminosity nearly constant. Second, the positron beam top-off was developed making the luminosity fully constant. Either electrons or positron could be injection up to 30 Hz if needed, deciding pulse-by-pulse which beam (bunch) was needed. Technical details of PEP-II top-off will be discussed. The implications for top-off into a circular Higgs factory are also presented. For this article top-up injection, top-off injection, trickle injection, and continuous injection mean the same thing [1-9].

The SLAC linac as built for the SLC was used for the injector of PEP-II with up to 30 Hz of either positrons or electron injected into the two rings. The injections for top-up typically were about 3 to 10 Hz for HER and 5 to 15 Hz for LER in steady state operations.

Table 1: PEP-II Collision Parameters

| Parameter | Units | Design | April 2008 Best | Gain Factor over Design |
|---|---|---|---|---|
| I+ | mA | 2140 | 3210 | x 1.50 |
| I- | mA | 750 | 2070 | x 2.76 |
| Number bunches | | 1658 | 1732 | x 1.04 |
| $\beta_y$* | mm | 15-25 | 9-10 | x 2.0 |
| Bunch length | mm | 15 | 11-12 | x 1.4 |
| $\xi_y$ | | 0.03 | 0.05 to 0.06 | x 2.0 |
| Luminosity | $10^{34}$ /$cm^2$/s | 0.3 | 1.2 | x 4.0 |
| Int lumin per day | $pb^{-1}$ | 130 | 911 | x 7.0 |

*Supported by US DOE contract DE-AC02-76SF00515.
†seeman@slac.stanford.edu

## PEP-II PARAMETERS

In PEP-II the Low Energy Ring (LER) was mounted 0.89 m above the High Energy Ring (HER) in the 2.2 km tunnel as shown in Figure 1. To bring the beams into collision at the single IP, LER was bent down 0.89 m to the HER level and then with horizontal deviations for both rings are made to collide. Since both rings had the same circumference, each bunch in one ring only collides with one bunch in the other ring.

The high beam currents were supported large RF systems consisting of 1.2 MW klystrons at 476 MHz and high power cavities with HOM absorbing loads. Each cavity had three HOM loads each with the capability of 10 kW. At the peak currents the HER cavities received 285 kW and the LER cavities 372 kW. The average klystron power was 1.01 MW. An overhead of about 20% in power was needed to allow the longitudinal bunch-by-bunch RF feedback systems to be stable.

Figure 1: PEP-II tunnel with LER above the HER.

## TECHNICAL ITEMS FOR TOP-UP

There are seven technical items that need to be accomplished to achieve successful top-up injection. 1) Each bunch charge in real time must be measured and determined when it needs to be refilled. 2) In the ring and injector, a timing signal is produced to generate a bunch so to deliver it after all the transport gymnastics (gun, linac, damping rings, transport lines) to the needed particular bunch (bucket) in the ring. 3) The linac bunch or bunches need to be injected into the collider with very low losses. 4) The injected beam backgrounds in the

ISBN 978-3-95450-172-4

particle physics detector need to be measured. 5) Cures for the injection backgrounds need to be found using gating and collimation. 6) Methods to monitor relevant backgrounds need to be developed for the accelerator operators to tune on in real time to keep top-up operating efficiently. 7) Trigger masking for the detector physics need to be developed by taking accelerator turns and azimuthal variations into account.

## PEP-II TOP-UP INJECTION

The parameters for PEP-II top-up injection are listed here.

Energy = 3.5 x 9 GeV.
Ring circumference = 2200 m.
One collision point (IR) at luminosity = 1.2 x $10^{34}$.
Full energy injection from the linac and damping rings.
Number of bunches = 1732 per ring.
Beam currents = 2.1 A x 3.2 A.
Particles = 1.0/1.5 x $10^{14}$ / beam (HER/LER).
Lifetimes:
Vacuum = ~10 hours
Touschek = ~3 hours (LER)
Luminosity = ~1 hour
Lost particles per second = 4.2 x $10^{10}$ / second.
Top-up injection = one bunch per linac pulse.
Injection rate: ~3-15 Hz (30 Hz max).
Particles per injection: 3 to 9 x $10^{9}$ per pulse.
There are several discrete injection quanta.
Bunch injection controller: picked the lowest bunch.
Injection efficiency = ~ 80%, but can be as high as 95%.
Injection kicker pulse length = 0.4 microsecond.
Ring path length = 7.3 microsecond.

The resulting luminosity 24 hour plots of top-up injection before and after are shown in Figure 2 and 3.

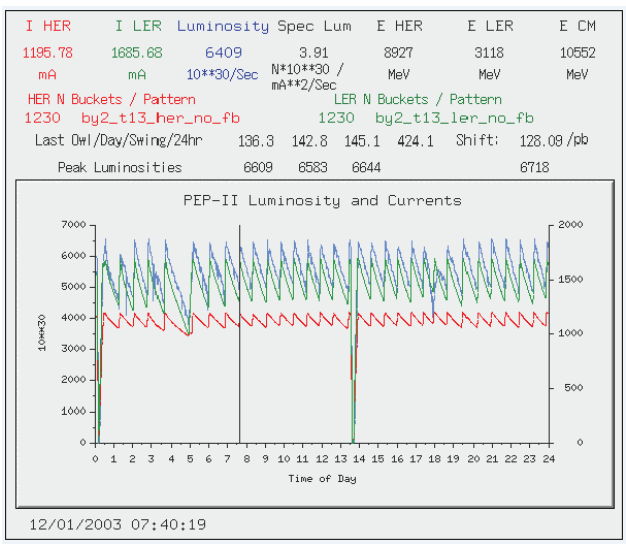


Figure 2: PEP-II collisions for 24 hours before top-up injection with HER beam current (red), LER beam current (green), and luminosity (blue). Fills every 45 minutes.

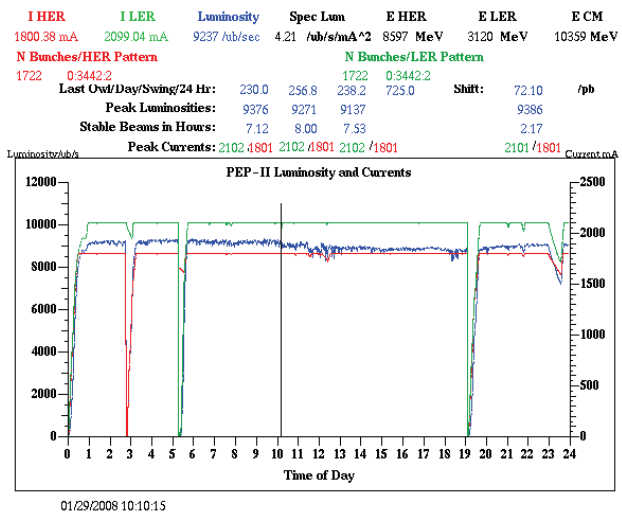


Figure 3: PEP-II collisions for 24 hours after top-up injection with HER beam current (red), LER beam current (green), and luminosity (blue). The luminosity varied somewhat with time due to changing orbits day to night which resulted in changing lattice functions at the IR and around the rings.

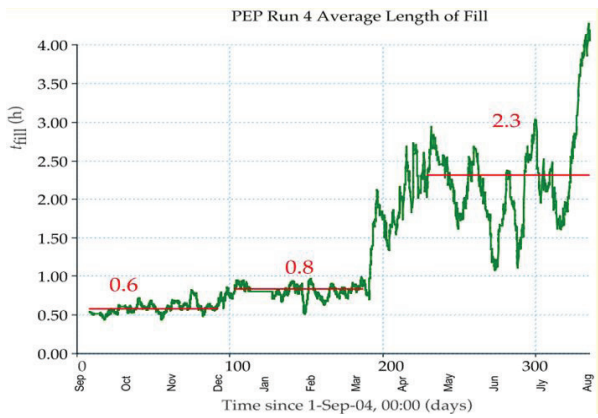


Figure 4: Increase in fill duration for PEP-II collisions after one ring trickle (HER only, center) and two ring trickle (adding LER, right).

After, PEP-II had 35% increased integrated luminosity achieved and the run length was greatly increased as shown in Figure 4. In Figure 5 are shown the time allocations during operating PEP-II of different activities corresponding to BaBar data taking, PEP-II machine development, tuning and filling, unscheduled off and scheduled off averaged over a long time period. The time for integrating luminosity increased by 35% and the time for filling and tuning reduced by 50% after trickle injection.

The injected beam particles were collimated carefully before injection to reduce the particles that would be lost later after injecting into the ring. Also, internal to the rings the injected beam transverse and energy tails were



ISBN 978-3-95450-172-4

carefully controlled and collimated as best possible but without reducing the stored beam lifetimes.

## BABAR MASKING AND VETO

BaBar trigger masking included masking all of ring for a few tens of turns, followed by a small part of the ring turn for a longer time of about 0.9-1.3 msec. The plots of BaBar backgrounds and masking are shown in detail

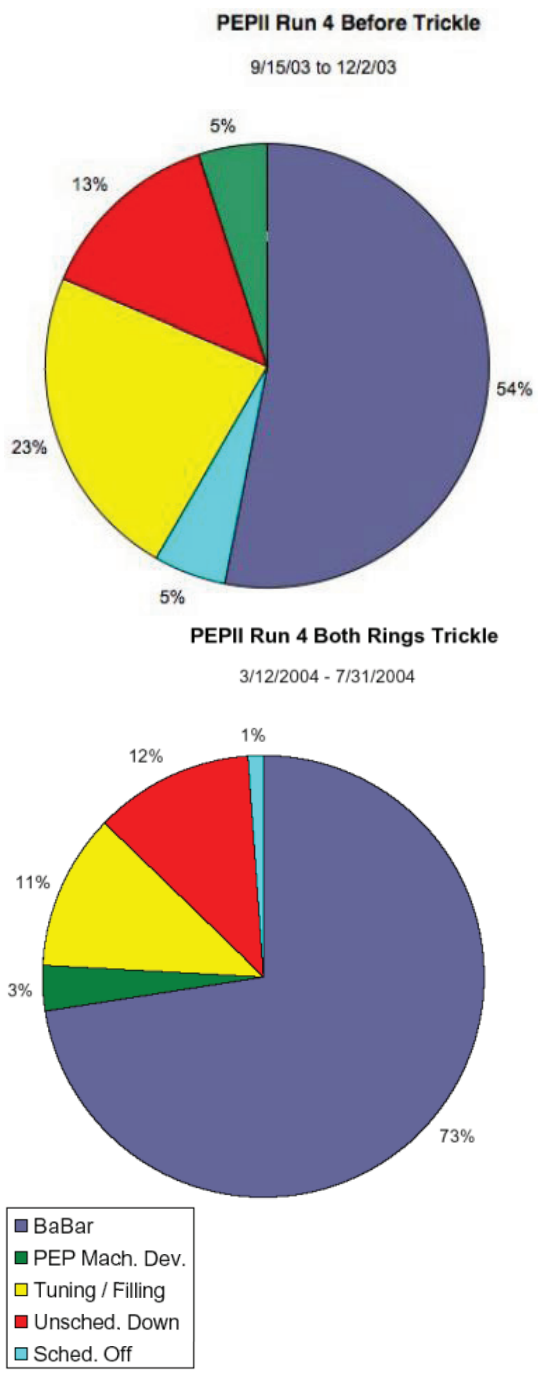


Figure 5: Time accounting in PEP-II operation before (upper) and after trickle (top-up) injection (lower) was implimented. The improvement was 35% in BaBar physics data taking and reduded by 2 in filling time.

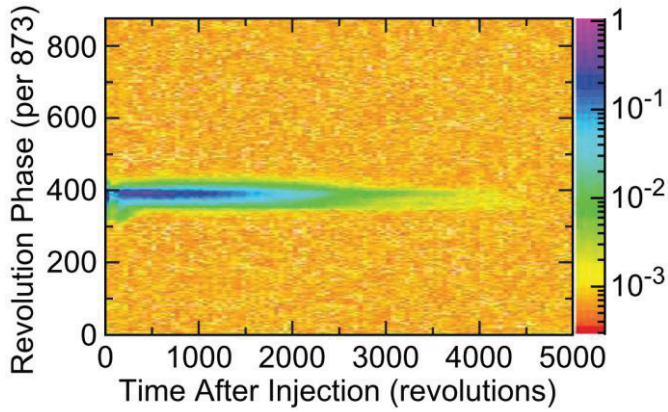


Figure 6: The injection background signal in BaBar as a function of time (left to right) and the azimuthal position around the ring (i.e. bunch number) (vertical). Only the time near the injected bunch makes long term backgrounds.

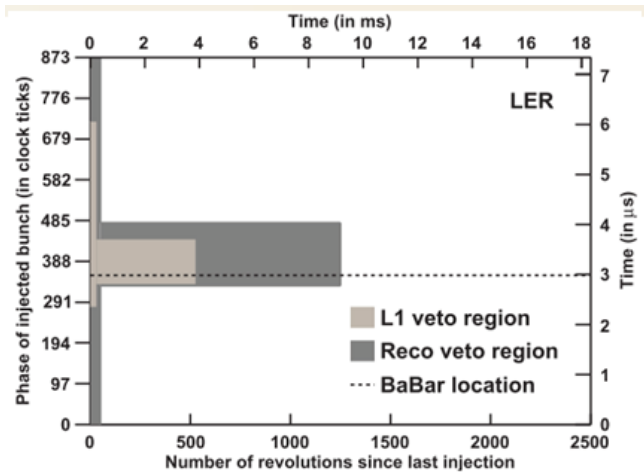


Figure 7: The BaBar trigger vetoes associated with the background signals in Figure 6.

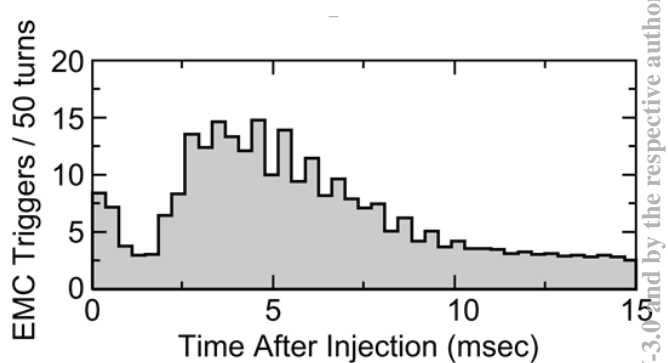


Figure 8: The total injection background signal as a function of time after injection.

in Figures 6,7,8,and 9. Note the long term backgrounds are only in time with the injected bunch and not all around the ring. The needed trigger vetoes only mask the

ISBN 978-3-95450-172-4

event triggers near the injected bunch. The vetoes for HER injection are different than LER injection as the backgrounds have slightly different time structures. The vetoes only last for up to about 2000 turns and were shorter for LER injection.

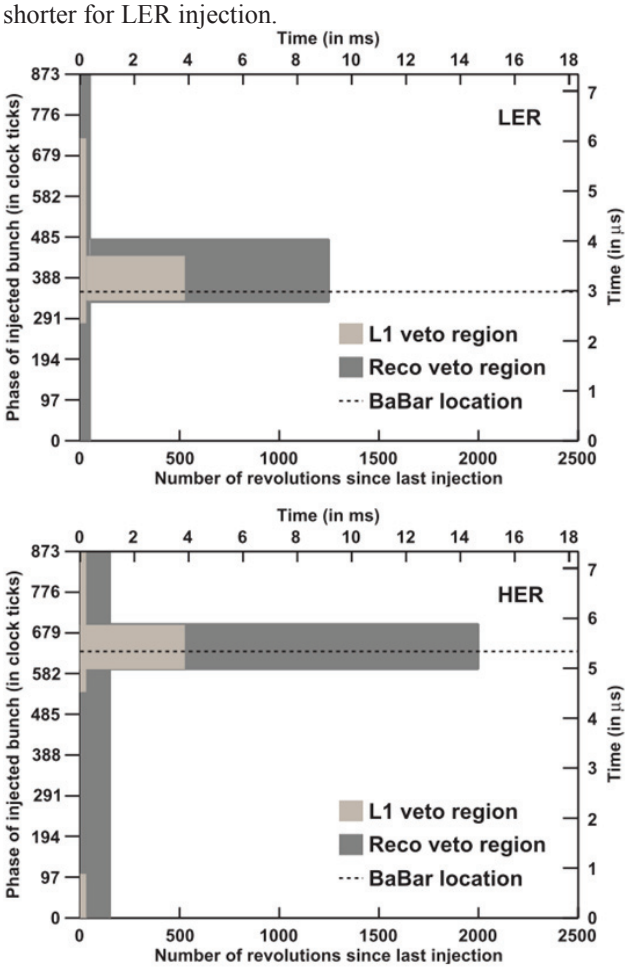


Figure 9: Veto masks in BaBar for LER injection (above) and HER injection (below).

## HIGG FACTORY TOP-UP INJECTION

The parameters assumed for e+e- Higgs factory at the injection septum are listed here.

$\beta_x$ at injection septum (stored) = ~200m
$\beta_x$ at injection septum (injection) = ~30m
$\varepsilon_{xstored}$ (stored) =6 nm
$\varepsilon_{xinj}$ (injected) =40 nm
$\sigma_{xstored}$ at septum (stored) = 1.1 mm
$\sigma_{xinj}$ at septum (injected) = 1.1 mm
$X_s$ = Septum blade thickness =~ 5 mm
$X_c$ = septum clearance distance = ~$6\sigma_x$
Xinj < $A_x$
Xinj = $4\sigma$inj+$X_s$+Xc = ~16 mm
$A_x$ = machine aperture > ~20 mm

The stored beam is bumped to near the septum with pulsed dipoles in the ring as shown in Figure 10. The duration of the pulse can be much less than a ring turn. The injected bunch enters via the septum and is captured in the main ring after the pulse bump is removed. The injected bunch then damps to the enter the stored bunch after several damping times.

The requirements for a Higgs Factory injector are similar to what has been done before in terms of particle numbers. The CEPC stores about 2 x$10^{13}$ e+ per ring. The CEPC with 1 hour lifetime needs 1.25 x$10^{13}$ e-/e+ per hour or ~3.5 x$10^9$ e+ and e- per second at full energy. As examples, the CERN LEP injection complex delivered ~$10^{11}$ e+ per second. Alternatively, the SLAC SLC injection complex delivered ~6 x $10^{12}$ e+ per second.

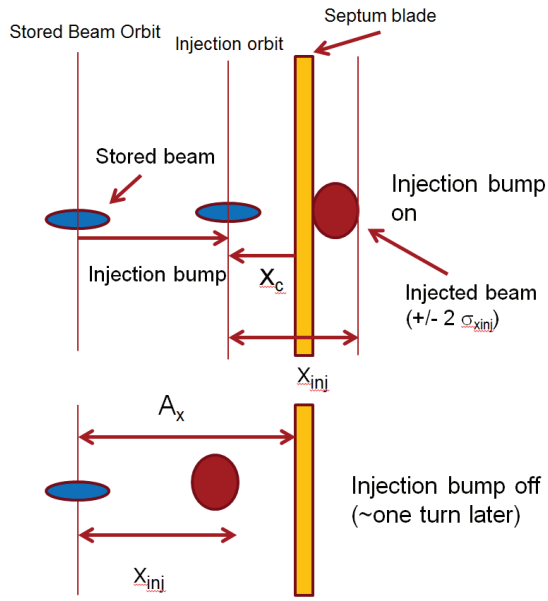


Figure 10: Schematic injection spacings at the injection septum showing the bumped stored bunch and the injected beam bunch. Horizontal injection is shown here, although vertical injection can be done as in PEP-II. Note the injected bunch can have different beta functions than the stored bunch to allow it to be closer to the septum.

## SLOW RAMP INJECTOR

The slow injector (Figure 11) can be a ramped storage ring. The ramping rate can be small going from low to high energy in a few minutes. The field quality in the ring have to be good to allow the stored and ramped beam to have good lifetimes. The CERN LEP ring is a good example. Parameters of a ramped storage ring for a Higgs Factory:

Top-up injection = 50 bunches / pulse / beam.
Slow ramp due to magnet laminations.
Injection rate: Once every 4 minutes.
Particles per ring injection: 8.4 x $10^{11}$ / pulse.
Particles per injected bunch: 1.7 x $10^{10}$ / pulse.
Bunch injection controller: Fill all bunches at once.
Need to tailor (charge) each bunch separately.



ISBN 978-3-95450-172-4

Ring path length = 182 microsecond.
Injection kicker pulse length = 182 microsecond.
Kickers = 13 stronger than PEP-II but long flat top.
Luminosity varies from 100% to 74% over 8 minutes with 4 minutes injection cycles per ring.
As an example: CERN LEP: 26.7 km with a ramping speed of 0.5 GeV/sec. Thus, 120 GeV needs 4 minutes.


Figure 11: Slow ramped injector for a Higgs Factory.

## FAST RAMP INJECTOR

The injector (Figure 12) can be a rapidly cycling synchrotron similar to the 60 Hz cycling Cornell synchrotron (12 GeV) except 10 times longer but with the same magnets. Some parameters for a rapid cycling Higgs Factory injection are:

Fast Cycling Synchrotron with laminated dipoles and quadrupoles
Top-up injection = 50 bunch / pulse.
Cycle rate = 3 Hz.
Injection rate: 1 Hz e+, 1 Hz e-, 1 Hz e- to make e+.
Particles per injection: 4 x $10^9$ / pulse over 50 bunches with 90% injection efficiency.
Produces 8 x $10^7$ /bunch which means low instability effects and RF feedback.
Easy positron source at 120 GeV e-.
Bunch injection controller: Tailor the charge of each bunch as needed
Magnet laminations same as AC transformers.
Injection kicker pulse length = 183 microseconds (= 53 km)
Kickers = 13 stronger than PEP-II but 7 times slower.
Ring path length = 183 microseconds (53 km).
The luminosity stays within 0.12% of the peak.

An example is the Cornell synchrotron of 768 m with a biased sine wave-magnet excitation. It ramps from 0.2 GeV to 12 GeV in 8.3 msec at 60 Hz. The ramping cycle does not affect the CESR storage ring operation just 1.5 m away.

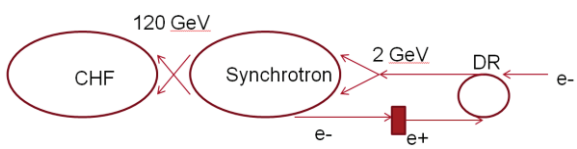


Figure 12: Fast cycling synchrotron injector for a Higgs Factory.

## DETECTOR MASKING FOR HIGGS

The physics detectors for CEPC need to the mask the injection bunches. The masking will depend on the type of injector.

For the slow ramped storage ring injector the detector must mask all of ring for about 10 microseconds every 4 minutes but the luminosity is only constant to ~16%.

For the synchrotron injector the detector must mask only part of the ring for about 10 microsecond at 1 Hz but the injected bunches and injection charge are 200 times smaller and luminosity is constant to 0.1%. Thus, the fast cycling synchrotron is far superior.

There is a pressing need to make an initial complete scale design of a full energy 1 Hz synchrotron injector.

## CONCLUSIONS

There is no doubt that top-up injection will work for a Circular Higgs Factory as done at PEP-II and KEKB. A full energy injector is needed because of beam lifetimes which are on the order of 10 minutes. A synchrotron injector will work the best if it is fast cycling and will have enough capacity to be more than is needed (60 Hz). A ramped storage ring is barely adequate (4 min) but will likely be marginally satisfactory. Also, a slowly ramped storage ring injector doesn't make the luminosity constant enough. The detectors will need to mask out the buckets with damping injected bunches during data taking. Both the accelerator and detector designs must work together to make this top-up injection successful.

## ACKNOWLEDGMENTS

The author and the PEP-II team wish to thank the operations staff, the maintenance crews, and all other supporting staff at SLAC for their hard work and support. The author thanks U. Wienands, James Turner, and M. Sullivan for trickle injection discussions. Many thanks go to the DOE Office of High Energy Physics for support.

## REFERENCES

[1] "PEP-II an Asymmetric B Factory", Conceptual Design Report, CALT-68-1869, LBL-PUB-5379, SLAC-418, UCRL-ID-114055, UC-IIRPA-93-01, June 1993.
[2] J. Seeman, et. al., "PEP-II at 1.2x$10^{34}$/$cm^2$/s Luminosity", PAC 2007, pg. 37.
[3] J. Seeman, "Last Year Of PEP-II B-Factory Operation," EPAC 2008, Geneva, pg. 946.
[4] J. L. Turner, et. al., "Trickle-charge: a New Operational Mode for PEP-II", EPAC 2004, pg. 881.
[5] U. Wienands, et. al., "High-temperature Kicker Electrodes for High-beam-current Operation of PEP-II", EPAC 2004, pg. 2843.
[6] P. A. McIntosh, et. al., "PEP-II RF System Operation and Performance", EPAC 2004, pg. 1087.
[7] U. Wienands, et. al., "Tracking Down a Fast Instability in the PEP-II LER", EPAC 2006, pg. 658.
[8] M. Sullivan, et. al., "Anomalous High Radiation Beam Aborts in the PEP-II B-factory", EPAC 2006, pg. 652.
[9] BaBar "BaBar and PEP-II Operations", NIM-U 2014.

ISBN 978-3-95450-172-4

# INJECTION WITH PRETZELS AT CESR*

David Rice, CLASSE, Cornell University, Ithaca,NY 14853, USA
David Rubin, CLASSE, Cornell University, Ithaca,NY 14853, USA

*Abstract*

CESR has operated with pretzel orbits since 1983. With separation in the horizontal plane, the parasitic crossings reduce the acceptance for horizontal betatron stacking of injected particles. Furthermore, both coherent and incoherent long range beam-beam effects reduce tune plane working space. Each bunch will have a particular coherent tune shift depending on parasitic crossing points and bunch currents in the opposing beam. We present the experience at CESR and discuss applicability to the circular Higgs factories.

## CESR RING AND INJECTOR

CESR operated as an electron-positron collider from 1979 to early 2008. Ring and injector parameters are listed in Table 1. The synchrotron ring circumference is precisely 60/61 times the CESR circumference, permitting filling of many CESR bunches each injector cycle.

Table 1: CESR Ring and Injector Parameters

| Parameter & Units | Value |
|---|---|
| CESR Ring | |
| Circumference [m] | 768.44 |
| Operating beam energy [GeV] | 1.8-6 |
| Transverse damping time [ms] | 24 |
| Current per beam (mA) | 400 |
| Number of bunches | 40 |
| RF Frequency [MHz] | 499.7594 |
| | |
| CESR Injector | |
| Injector repetition rate [/s] | 60 |
| Linac Energy (e+/e-) [MeV] | 160/300 |
| Linac max bunch number | 24 |
| Linac charge/bunch (e+/e-) [nc] | |
| Linac RF frequency [MHz] | 2855.77 |
| Synchrotron Circumference [m] | 755.84 |
| Synchrotron RF frequency [MHz] | 713.943 |
| Highest common frequency [MHz] | 71.394 |
| Smallest common bunch spacing [ns] | 14.007 |

The numerology of the various RF systems in the injector chain enables acceleration and injection of bunches spaced at 14 ns intervals (7 CESR RF buckets) in a single injection cycle. The maximum number of bunches is limited to about 24 by loading of the linac RF accelerating cavities. Intercalary buckets may be filled by shifting the injector RF phases between injection cycles. Bunch currents in CESR are monitored and the linac bunch pattern adjusted to equalize the bunch currents.

* Work supported by multiple grants from the U.S. National Science Foundation

Figure 1 below shows a layout of the CESR accelerator complex. Two important features of CESR are critical to optimization of injection with pretzeled orbits:

1. All quadrupoles and sextupoles are independently powered, enabling total flexibility in designing optics and creating group knobs for orthogonal adjustment of specific accelerator physics parameters.
2. The linac/synchrotron provide trains of bunches each (60 Hz) cycle for rapid filling in multi-bunch mode.

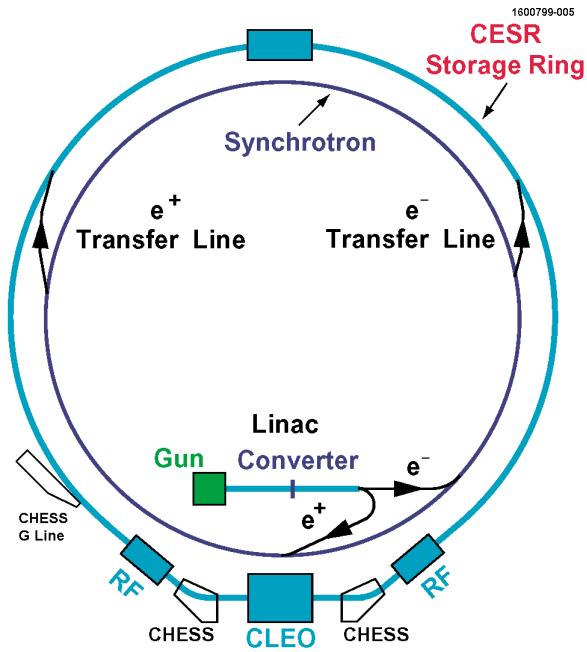


Figure 1: CESR accelerators layout.

Injection into CESR takes place, nominally at least, in the horizontal plane. The beam is extracted from the synchrotron in a single turn by a fast (2.5 μsec) kicker and a pair of septum magnets to bring the beam through the synchrotron fringe field into transfer lines shown above. The transfer lines (Figure 2) have five quadrupoles each (two of them off-center), three horizontal bending magnets and two or three steering trim magnets in each plane. A pulsed septum magnet provides a final bend to bring the injected bunches roughly parallel to the stored beam that has been brought next to the septum magnet by three pulsed kicker ("bumper") magnets forming a closed orbit bump. Injection efficiency can be as high as 90% for a single beam, but is reduced significantly in the presence of a counter-rotating beam as described below.

When all of the beam sizes and hardware parameters are accounted for, the center of the injected bunch has an



ISBN 978-3-95450-172-4

oscillation amplitude about the closed orbit of about 2.2 mm/√β or about +/- 12 mm for a typical focussing quadrupole.

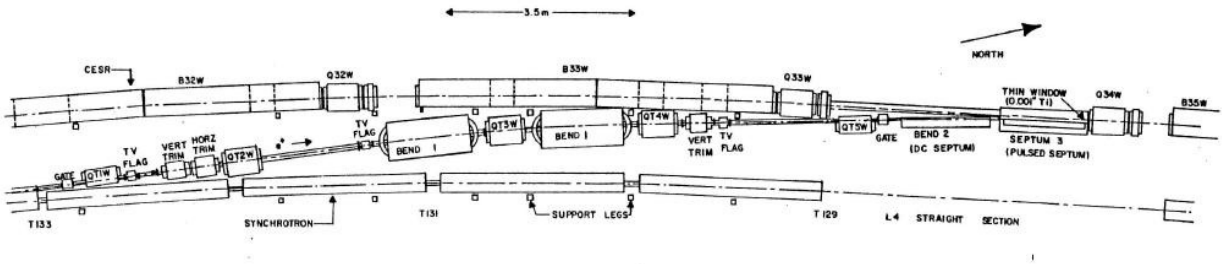


Figure 2: CESR west (positron) transfer line layout.

## PRETZEL ORBITS

Pretzel orbits are established by four horizontal electrostatic deflectors placed roughly as shown in Figure 3. The peaks of the pretzel are roughly ±20 mm in the 90 mm full horizontal aperture vacuum chamber. This geometry is illustrated in Figure 4.

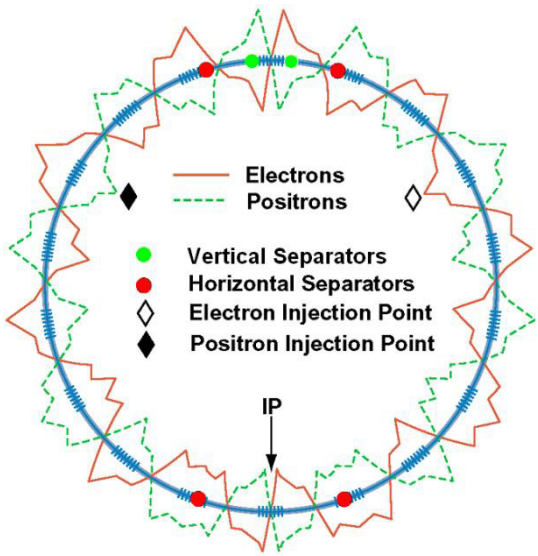


Figure 3: Pretzel layout of CESR with ±3.5 mr crossing angle in the IP and vertical separation in the opposite IP.

Storage ring optics are optimized to maximize the "pretzel efficiency" or minimum separation at the crossing points divided by the peak pretzel amplitude, both normalized to $\sqrt{\beta_x}$. Using bunch trains, up to 9 trains of 5 bunches each, necessarily reduces the pretzel efficiency since the crossings cover an appreciable part of each pretzel anti-node, pushing toward the nodes. Figure 5 below shows the separation at parasitic crossings in units of horizontal beam size for the 9 train x 5 bunch configuration.

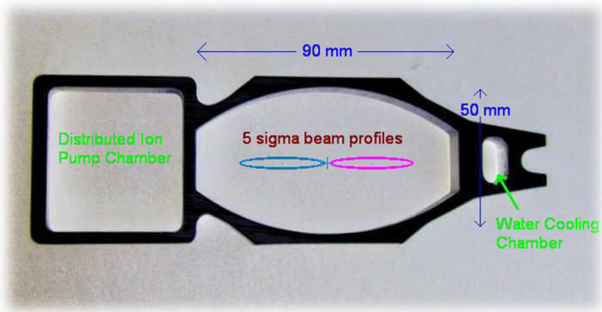


Figure 4: CESR's vacuum chamber showing relative position and size of beams at a crossing point.

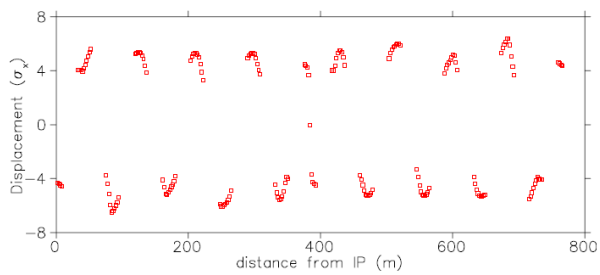


Figure 5: Separation at parasitic crossing points in units of $\sigma_x$. [1]

When the injection oscillations are included, it is clear that some of the electrons occasionally pass close to the core of the opposite beam until they damp. In fact the injection efficiency drops significantly. The clearances between injected bunches and the counter-rotating bunches at each parasitic crossing were calculated for CESR 1.9 GeV conditions and are shown in Figure 6. Clearly the bunches that have crossings at 380, 590, and 630 m azimuth will likely be difficult to fill.

## INJECTION WITH PRETZELS

With a single beam in CESR the injection efficiency was typically 50% to 80%, occasionally approaching 100%. With a full counter-rotating beam present, the efficiency dropped to 20%-30% in the best of conditions, and below 10% in bad. Generally certain bunches,



ISBN 978-3-95450-172-4

usually at the end of trains, dominated the injection losses.

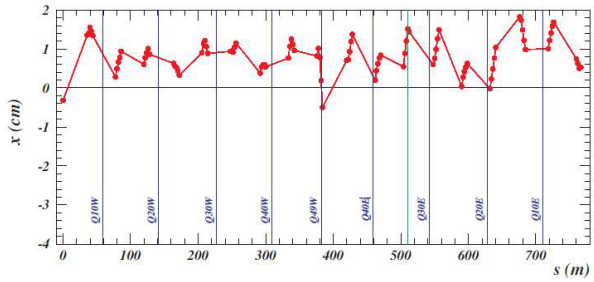


Figure 6: Clearance of injected electrons from stored positron beam (CESR 1.9 GeV, 9 trains x 5 bunches each). [2]

Several steps [2] to mitigate the LRBBI effects were taken, beginning with separation of electron and positron betatron tunes to avoid variable bunch-to-bunch coherent effects. This was easily achieved at CESR by creating a group knob control of sextupoles to change the two beams' tunes differentially while maintaining chromaticity and minimizing large local optics perturbations. Tune differences of 0.025 are generally used.

Beam losses from the LRBBI are primarily in the vertical dimension. [3] The vertical size of the "strong" beam plays a fundamental role in driving resonances. By placing the horizontal and vertical tunes near a coupling resonance, the vertical emittance is increased and horizontal decreased, both desirable in reducing the parasitic crossing effects. The application of this technique may have to be limited to avoid compromising luminosity.

A one-turn kicker, or "pinger" is frequently used to decrease the amplitude of oscillation of the injected beam within a few turns after transfer to the storage ring. The small increase in stored beam motion is generally inconsequential.

We have used mismatch of energy between the injector and storage ring to share horizontal and longitudinal phase space during injection. Empirical exploration has generally been more successful than detailed modelling.

Bunch-by-bunch beam stabilizing feedback decreases the damping time of coherent motion resulting from errors in pulsed element amplitudes and timing as well as the pinger mentioned above.

Allowing vertical ripple from the interaction region separators to propagate around the arcs was used when effective to vertically separate beams at particularly bad crossing points.

When initially injecting, it is sometimes helpful to fill one beam evenly to half current then the other, finally returning to the first.

We have only rough experimental information regarding energy dependence of LRBBI effects. When operations transitioned from B to Charm physics (beam energy 5.3 GeV to 1.9 GeV) the LRBBI effects were proportionately greater, lowering maximum sustainable current per beam from 375 to 75 mA during colliding beam operation. 1.8 T wigglers controlled horizontal emittance and kept damping times within a factor of 2 compared to 5.3 GeV operation.

While acceptable conditions usually persisted with minor adjustments once achieved, equipment failure or extended shutdown periods would sometimes require extended tuning to recover performance. Good injection was dependent on filling profiles of bunches in each beam. Some irregular profiles would exacerbate losses or decrease the injection rate of the opposing beam. This is not unexpected given the bunch-by-bunch dependence on individual parasitic crossing parameters and opposing beam bunch currents.

## HIGGS FACTORY INJECTION

Of the mitigation measures used at CESR, several may be applicable to a Higgs Factory circular collider.

1) Splitting tunes of the two beams is feasible if appropriate sextuple control is available.
2) Control of vertical emittance may be possible depending on beam-beam parameters, but separate conditions for injection would require fast pulsed elements.
3) A pinger to share oscillation amplitudes between stored and injected beams may be useful.
4) Energy mismatch should be considered.
5) Bunch currents should usually be kept as even as possible.

A two-ring machine will still have parasitic crossings near the interaction points, especially at lower energies where more (~10,000) bunches are optimum. Here other options such as vertical separation might be considered.

## REFERENCES

Note: References from conference proceedings (PAC, EPAC) may be found at http://jacow.org

[1] D.L. Rubin et al., "CESR Status and Performance," PAC 2001, Chicago, p, 3520

[2] M.G. Billing, J.A. Crittenden, M.A. Palmer, "Investigations of Injection Orbits at CESR Based on Turn-by Turn BPM Measurements," PAC 2005, Knoxville, p. 1228

[3] A.B. Temnykh, D. Sagan, "The Incoherent Long Range Beam-Beam Interaction in CESR," PAC 1997, Vancouver, p. 1768



ISBN 978-3-95450-172-4

# LATTICE OPTIMIZATION FOR TOP-OFF INJECTION

Richard Talman
Laboratory of Elementary-Particle Physics,
Cornell University

*Abstract*

This paper discusses Higgs factory injection. Full energy, top-off injection is assumed. Vertical injection seems preferable to horizontal and kicker-free, bunch-by-bunch injection concurrent with physics running may be feasible. Achieving high efficiency injection justifies optimizing injector and/or collider lattices for maximum injection efficiency. Stronger focusing in the injector and weaker focusing in the collider improves the injection efficiency. Scaling formulas (for the dependence on ring radius $R$) show injection efficiency increasing with increasing ring circumference. Scaling up from LEP, more nearly optimal parameters for both injector and collider are obtained. Maximum luminosity favors adjusting the collider cell length $L_c$ for maximum luminosity and choosing a shorter injector cell length, $L_i < L_c$, for maximizing injection efficiency.

## INJECTION STRATEGY: STRONG FOCUSING INJECTOR, WEAK FOCUSING COLLIDER

### *Introduction*

I take it as given that full energy top-off injection will be required for the FCC electron-positron Higgs factory. Without reviewing the advantages of top-off injection, one has to be aware of one disadvantage. The cost in energy of losing a full energy particle due to injection inefficiency is the same as the cost of losing a circulating particle to Bhabha scattering or to beamstrahlung or to any other loss mechanism. Injection efficiency of 50% is equivalent to doubling the irreducible circulating beam loss rate. To make this degradation unimportant one should therefore try to achieve 90% injection efficiency.

Achieving high efficiency injection is therefore sufficiently important to justify optimizing one or both of injector and collider lattices to improve injection. The aspect of this optimization to be emphasized here is shrinking the injector beam emittances and expanding the collider beam acceptances by using stronger focusing in the injector than in the collider. What are the dynamic aperture implications? They will be shown to be progressively more favorable as the ring radius $R$ is increased relative to the LEP value. The dynamic-aperture/beam-width ratio increases as $R^{1/2}$ and is the same for injector and collider. Before addressing this optimization other injection issues will be surveyed.

Handling the synchrotron radiation at a Higgs Factory is difficult and replenishing the power loss is expensive. Otherwise the RF power loss is purely beneficial, especially for injection. Betatron damping decrements $\delta$ (fractional amplitude loss per turn) are approximately half the energy loss per turn divided by the beam energy, (e.g. $\delta \approx 0.5{\times}2.96/120 = 1.25$ %.) Also the energy dependence is large enough for injection efficiency to improve significantly with increasing energy.

According to Liouville's theorem, increasing the beam particle density by injection is impossible for a Hamiltonian system. The damping decrement $\delta$ measures the degree to which the system is *not* Hamiltonian. Usually bumpers and kickers are needed to keep the already stored beam captured while the injected beam has time to damp. If $\delta$ is large enough one can, at least in principle, inject with no bumpers or kickers.

### *Advantages of Vertical Injection and Bumper-Free, Kicker-Free, Top-Off Injection*

The most fundamental parameter limiting injection efficiency is the emittance of the injected beam. The vertical emittance in the booster accelerator can be very small, perhaps $\epsilon_y < 10^{-10}$ m. This may require a brief flat top at full energy in the booster. For injection purposes the beam height can then be taken to be effectively zero. The next most important injector parameter is the septum thickness. For horizontal injection this septum also has to carry the current to produce a horizontal deflection. Typically this requires the septum thickness to be at least 1 mm. For vertical injection, with angular deflection not necessarily required, the septum can be very thin, even zero. The remaining (and most important) injection uncertainty is whether the ring dynamic aperture extends out to the septum. If not, it may be possible to improve the situation by moving the closed orbit closer to the wall using DC bumpers. (However this may be disadvantageous for vertical injection as vertical bends contribute unwanted vertical emittance to the stored beams.)

A virtue of top-off injection is that, with beam currents always essentially constant, the linear part of the beam-beam tune shift can be designed into the linear lattice optics. One beam "looks", to a particle in the other beam, like a lens (focusing in both planes). Large octupole moments makes this lens far from ideal. Nevertheless, if the beam currents are constant the pure linear part can be subsumed into the linear lattice model. And the octupole component, though nonlinear, does not necessarily limit the achievable luminosity very severely.

With injection continuing during data collection there would be no need for cycling between injection mode and data collection mode. This could avoid the need for the always difficult "beta squeeze" in transitioning from injection mode to collision mode. Runs could then last for days, always at maximum luminosity. This would improve both average luminosity and data quality.

ISBN 978-3-95450-172-4

Kicker-free vertical injection is indicated schematically in Figure 1. Let $n_{\text{inj.}}$ be a small integer indicating the number of turns following injection before the injected beam threatens to wipe out on the injection septum. The fractional shrinkage of the Courant-Snyder invariant after $n_{\text{inj.}}$ turns is $n_{\text{inj.}}\delta$. By judicious choice of vertical, horizontal, and synchrotron tunes this shrinkage may be great enough that less than, say, 10 % of the beam is lost on the septum.

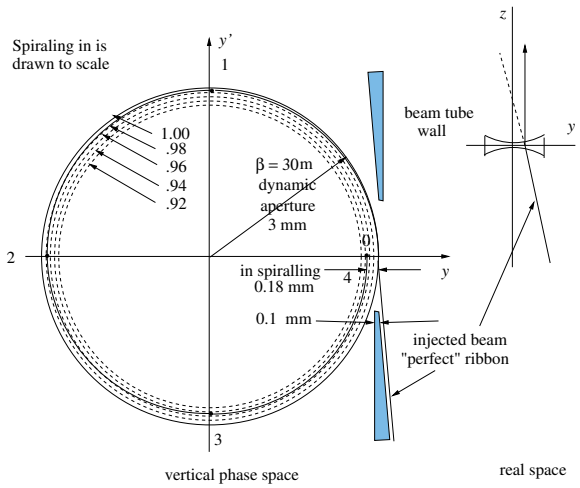


Figure 1: A cartoon of kicker-free, vertical injection. The dashed line shows the Courant-Snyder amplitude of the injected particle with the fractional shrinking per turn drawn more or less to scale.

## CONSTANT DISPERSION SCALING WITH BEND RADIUS *R*

### *Linear Lattice Optics*

Most of the following scaling formulas come from Jowett [1] or Keil [2] or from reference [3]. For simplicity, even if it is not necessarily optimal, assume the Higgs factory arc optics can be scaled directly from LEP values, which are: phase advance per cell $\mu_x = \pi/2$, full cell length $L_c = 79\,\text{m}$. (The subscript "c" distinguishes the collider lattice cell length from the injector lattice cell length $L_i$.) At constant phase advance, the beta function $\beta_x$ scales as $L_c$ and dispersion $D$ scales as bend angle per cell $\phi = L_c/R$ multiplied by cell length $L_c$;

$$D \propto \frac{L_c^2}{R}. \tag{1}$$

Holding $L_c$ constant as $R$ is increased would decrease the dispersion, impairing our ability to control chromaticity. Let us therefore *tentatively adopt the scaling*

$$L_c \propto R^{1/2}, \quad \text{corresponding to} \quad \phi \propto R^{-1/2}. \tag{2}$$

This can be seen to be tantamount to holding dispersion $D$ constant, and is consistent with electron storage ring design trends over the decades.

These quantities and "Sands curly H" $\mathcal{H}$ then scale as

$$\beta_x \propto R^{1/2}, \quad D \propto 1, \quad \mathcal{H} \propto \frac{D^2}{\beta_x} \propto \frac{1}{R^{1/2}}. \tag{3}$$

Copied from Jowett [1], the fractional energy spread is given by

$$\sigma_\epsilon^2 = \frac{55}{32\sqrt{3}}\frac{\hbar}{m_e c}\gamma_e, \quad \text{where}$$
$$F_\epsilon = \frac{<1/R^3>}{J_x <1/R^2>} \propto \frac{1}{R}, \tag{4}$$

and the horizontal emittance is given by

$$\epsilon_x = \frac{55}{32\sqrt{3}}\frac{\hbar}{m_e c}\gamma_e F_x, \quad \text{where}$$
$$F_x = \frac{<\mathcal{H}/R^3>}{J_x <1/R^2>} \propto \frac{1}{R^{3/2}}. \tag{5}$$

The betatron contribution to beam width scales as

$$\sigma_{x,\text{betatron}} \propto \sqrt{\beta_x \epsilon_x} \propto 1/R^{1/2}. \tag{6}$$

Similarly, at fixed beam energy, the fractional beam energy (or momentum) spread $\sigma_\delta$ scales as

$$\sigma_\delta \propto \sqrt{B} \propto 1/R^{1/2}. \tag{7}$$

### *Scaling with R of Arc Sextupole Strengths and Dynamic Aperture*

At this stage in the Higgs Factory design, it remains uncertain whether the IP-induced chromaticity can be cancelled locally, which would promise well over than a factor of two increase in luminosity, but would require strong bends close to the IP. For the time being I assume the IP chromaticity is cancelled in the arcs. Individual sextupole strengths can be apportioned as

$$S = S^{\text{arc chr.}} + S^{\text{IP chr.}} \tag{8}$$

The IP-compensating sextupole portion $S^{\text{IP chr.}}$ depends on the IP-induced chromaticity. A convenient rule of thumb has the IP chromaticity equal to the arc chromaticity. By this rule doubling the arc-compensating sextupole strengths cancels both the arc and the IP chromaticity.

With dispersion $D \propto 1$, quad strength $q \propto 1/R^{1/2}$, and $S^{\text{arc chr.}} \propto q/D$, one obtains the scaling of sextupole strengths and dynamic aperture scaling;

$$S \propto \frac{1}{R^{1/2}}, \quad \text{and} \quad x^{\text{dyn. ap.}} \propto \frac{q}{S^{\text{arc chr.}}} \propto 1. \tag{9}$$

The most appropriate measure of dynamic aperture is

$$\frac{x^{\text{dyn. ap.}}}{\sigma_x} \propto \frac{1}{1/R^{1/2}} \propto R^{1/2}. \tag{10}$$

The increase of dynamic aperture divided by beam size with increasing $R$ would allow the IP optics to be more aggressive for the Higgs factory than for LEP. Unfortunately it is



ISBN 978-3-95450-172-4

the chromatic mismatch between IP and arc that is thought to be more important in limiting the dynamic aperture than is the simple compensation of total chromaticity. The constant dispersion scaling formulas derived so far are given in Table 1.

## INJECTION-OPTIMIZED SCALING FOR INJECTOR AND COLLIDER

### *Revised Injector and Collider Parameters*

What has been discussed so far has been "constant dispersion scalling". But, as already stated, we wish to differentiate the injector and collider optics such that the injector emittances are smaller and the collider acceptances are larger. This can be accomplished by shortening injector length $L_i$ and lengthening collider cell length $L_c$. The resulting $R$-dependencies and scaling formulas are shown in Table 2. They yield the lattice parameters in Table 3 for both the 50 km and 100 km circumference options.

### *Implications of Changing Lattices for Improved Injection*

According to these calculations there is substantial advantage and no disadvantage to strengthening the injector focusing and weakening the collider focusing. This is achieved by shortening the injector cell length $L_i$ and increasing the collider cell length $L_c$. Weakening the collider focusing has the effect of increasing the transverse beam sizes

As indicated in the caption to Table 3, the improvement in the injector emittance/collider acceptance ratio is probably unnecessaily large, at least for a 100 km ring, where the improvement is seven-fold.

Furthermore there is at least one more constraint that needs to be met. Maximum luminosity results only when the beam aspect ratio at the crossing point is optimal. Among other things this imposes a condition of the horizontal emittance $\epsilon_x$. At the moment the preferred method for controlling $\epsilon_x$ is by the appropriate choice of cell length $L_c$. With lattice manipulations other than changing the cell length it may be possible to increase, but probably not decrease $\epsilon_x$.

According to Table 3 of my WG 2 paper, "Ring Circumference and Two Rings vs One Ring", with $\beta_y^* = 5$ mm the optimal choice of $\epsilon_x$ is 3.98 nm. According to Table 3 of the present report the actual value will be $\epsilon_x = 7.82$ nm. These values can be considered "close enough for now", or they can be considered different enough to argue that further design refinement is required (which is obvious in any case). But the suggestion is that the $L_c = 213$ m collider cell length choice in this paper may be somewhat too long.

Unfortunately the optimal value of $\epsilon_x$ depends strongly on the optimal value of $\beta_y^*$, which is presently unkown. These considerations show that the arc and intersection region designs cannot be separately optimized. Rather a full ring optimization is required.

## REFERENCES

[1] J. Jowett, *Beam Dynamics at LEP,* CERN SL/98-029 (AP), 1998

[2] E. Keil, *Lattices for Collider Storage Rings,* Section in Accelerator Handbook, edited by A. Chao and M. Tigner.

[3] R. Talman, *Accelerator X-Ray Sources,* Wiley-VCH Verlag, 2006



ISBN 978-3-95450-172-4

Table 1: *Constant dispersion* scaling is the result of choosing cell length $L \propto R^{1/2}$. This is empasized by the shaded row, where the 1 in the final column indicates constancy as the ring radius is changed. The table gives the scaling with $R$ of other lattice and beam parameters.

| Parameter | Symbol | Proportionality | Scaling |
|---|---|---|---|
| phase advance per cell | $\mu$ | | 1 |
| cell length | $L$ | | $R^{1/2}$ |
| bend angle per cell | $\phi$ | $= L/R$ | $R^{-1/2}$ |
| quad strength $(1/f)$ | $q$ | $1/L$ | $R^{-1/2}$ |
| dispersion | $D$ | $\phi L$ | 1 |
| beta | $\beta$ | $L$ | $R^{1/2}$ |
| tunes | $Q_x, Q_y$ | $R/\beta$ | $R^{1/2}$ |
| Sands's "curly H" | $\mathcal{H}$ | $= D^2/\beta$ | $R^{-1/2}$ |
| partition numbers | $J_x/J_y/J_\epsilon$ | = 1/1/2 | 1 |
| horizontal emittance | $\epsilon_x$ | $\mathcal{H}/(J_x R)$ | $R^{-3/2}$ |
| fract. momentum spread | $\sigma_\delta$ | $\sqrt{B}$ | $R^{-1/2}$ |
| arc beam width-betatron | $\sigma_{x,\beta}$ | $\sqrt{\beta\epsilon_x}$ | $R^{-1/2}$ |
| -synchrotron | $\sigma_{x,synch.}$ | $D\sigma_\delta$ | $R^{-1/2}$ |
| sextupole strength | $S$ | $q/D$ | $R^{-1/2}$ |
| dynamic aperture | $x^{\max}$ | $q/S$ | 1 |
| relative dyn. aperture | $x^{\max}/\sigma_x$ | | $R^{1/2}$ |
| pretzel amplitude | $x_p$ | $\sigma_x$ | $R^{-1/2}$ |

Table 2: To improve injection efficiency (compared to constant dispersion scaling) the injector cell length can increase more weakly, for example $L_i \propto R^{1/4}$, and the collider cell length can increase more strongly, for example $L_i \propto R^{3/4}$. The shaded entries assume circumference $C$=100 km, $R/R_{\rm LEP}$=3.75.

| Parameter | Symbol | Proportionality | $L \propto R^{1/4}$ injector | $L \propto R^{1/2}$ | $L \propto R^{3/4}$ collider |
|---|---|---|---|---|---|
| phase advance per cell | $\mu_x$ | | 90° | 90° | 90° |
| cell length | $L$ | | $R^{1/4}$ | $R^{1/2}$ | $R^{3/4}$ |
| | | | 110 m | 153 m | 213 m |
| bend angle per cell | $\phi$ | $= L/R$ | $R^{-3/4}$ | $R^{-1/2}$ | $R^{-1/4}$ |
| momentum compaction | | $\phi^2$ | $R^{-3/2}$ | $R^{-1}$ | $R^{-1/2}$ |
| quad strength $(1/f)$ | $q$ | $1/L$ | $R^{-1/4}$ | $R^{-1/2}$ | $R^{-3/4}$ |
| dispersion | $D$ | $\phi L$ | $R^{-1/2}$ | 1 | $R^{1/2}$ |
| beta | $\beta$ | $L$ | $R^{1/4}$ | $R^{1/2}$ | $R^{3/4}$ |
| tune | $Q_x$ | $R/\beta$ | $R^{3/4}$ | $R^{1/2}$ | $R^{1/4}$ |
| | | | 243.26 | 174.26 | 125.26 |
| tune | $Q_y$ | $R/\beta$ | $R^{3/4}$ | $R^{1/2}$ | $R^{1/4}$ |
| | | | 205.19 | 147.19 | 106.19 |
| Sands's "curly H" | $\mathcal{H}$ | $= D^2/\beta$ | $R^{-5/4}$ | $R^{-1/2}$ | $R^{1/4}$ |
| partition numbers | $J_x/J_y/J_\epsilon$ | 1/1/2 | 1/1/2 | 1/1/2 | 1/1/2 |
| horizontal emittance | $\epsilon_x$ | $\mathcal{H}/(J_x R)$ | $R^{-9/4}$ | $R^{-3/2}$ | $R^{-3/4}$ |
| fract. momentum spread | $\sigma_\delta$ | $\sqrt{B}$ | $R^{-1/2}$ | $R^{-1/2}$ | $R^{-1/2}$ |
| arc beam width-betatron | $\sigma_{x,\beta}$ | $= \sqrt{\beta\epsilon_x}$ | $R^{-1}$ | $R^{-1/2}$ | 1 |
| -synchrotron | $\sigma_{x,synch.}$ | $= D\sigma_\delta$ | $R^{-1}$ | $R^{-1/2}$ | 1 |
| sextupole strength | $S$ | $q/D$ | $R^{1/4}$ | $R^{-1/2}$ | $R^{-5/4}$ |
| dynamic aperture | $x^{\rm da}$ | $q/S$ | $R^{-1/2}$ | 1 | $R^{1/2}$ |
| relative dyn. aperture | $x^{\rm da}/\sigma_x$ | | $R^{1/2}$ | $R^{1/2}$ | $R^{1/2}$ |
| separation amplitude | $x_p$ | $\sigma_x$ | N/A | $R^{-1/2}$ | 1 |



ISBN 978-3-95450-172-4

Table 3: Lattice parameters for improved injection efficiency. The shaded row indicates how successfully the injector emittance has been reduced relative to the collider emittance. The factor of seven improvement, 7.82/1.08, in this ratio for a 100 km ring, seems unnecessarily large, indicating that less radical scaling should be satisfactory.

| Parameter | Symbol | LEP(sc) | Unit | Injector | | Collider | |
|---|---|---|---|---|---|---|---|
| mean bend radius | $R$ | **3026** | m | **5675** | **11350** | **5675** | **11350** |
| beam Energy | | 120 | GeV | 120 | 120 | 120 | 120 |
| circumference | $C$ | 26.7 | km | 50 | 100 | 50 | 100 |
| cell length | $L$ | 79 | m | 92.4 | 110 | 127 | 213 |
| momentum compaction | $\alpha_c$ | 1.85e-4 | m | 0.72e-4 | 0.25e-4 | 1.35e-4 | 0.96e-4 |
| tunes | $Q_x$ | 90.26 | | 144.26 | 243.26 | 105.26 | 125.26 |
| | $Q_y$ | 76.19 | | 122.19 | 205.19 | 89.19 | 106.19 |
| partition numbers | $J_x/J_y/J_\epsilon$ | 1/1.6/1.4 | | 1/1/2 | 1/1/2 | 1/1/2 | 1/1/2 |
| main bend field | $B_0$ | 0.1316 | T | 0.0702 | 0.0351 | 0.0702 | 0.0351 |
| energy loss per turn | $U_0$ | 6.49 | GeV | 3.46 | 1.73 | 3.46 | 1.73 |
| radial damping time | $\tau_x$ | 0.0033 | s | 0.0061 | 0.0124 | 0.0061 | 0.0124 |
| | $\tau_x/T_0$ | 37 | turns | 69 | 139 | 69 | 139 |
| fractional energy spread | $\sigma_\delta$ | 0.0025 | | 0.0018 | 0.0013 | 0.0018 | 0.0013 |
| emittances (no BB), $x$ | $\epsilon_x$ | **21.1** | nm | **5.13** | **1.08** | **13.2** | **7.82** |
| $y$ | $\epsilon_y$ | 1.0 | nm | 0.25 | 0.05 | 0.66 | 0.39 |
| max. arc beta functs | $\beta_x^{\max}$ | 125 | m | 146 | 174 | 200 | 337 |
| max. arc dispersion | $D^{\max}$ | 0.5 | m | 0.37 | 0.26 | 0.68 | 0.97 |
| quadrupole strength | $q \approx \pm 2.5/L_p$ | 0.0316 | 1/m | 0.027 | 0.0227 | 0.0197 | 0.0117 |
| max. beam width (arc) | $\sigma_x = \sqrt{2\beta_x^{\max}\epsilon_x}$ | $1.6\sqrt{2}$ | mm | $0.865\sqrt{2}$ | $0.433\sqrt{2}$ | $1.62\sqrt{2}$ | $1.62\sqrt{2}$ |
| (ref) sextupole strength | $S = q/D$ | 0.0632 | $1/m^2$ | 0.0732 | 0.0873 | 0.0290 | 0.0121 |
| (ref) dynamic aperture | $x^{\mathrm{da}} \sim q/S$ | ~0.5 | m | ~0.370 | ~0.260 | ~0.679 | ~0.967 |
| (rel-ref) dyn.ap. | $x^{\mathrm{da}}/\sigma_x$ | ~0.313 | | ~0.428 | ~0.600 | ~0.417 | ~0.621 |
| separation amplitude | $\pm 5\sigma_x$ | $\pm 8.0\sqrt{2}$ | mm | | | $\pm 8.1\sqrt{2}$ | $\pm 7.8\sqrt{2}$ |

ISBN 978-3-95450-172-4

# IMPEDANCE AND COLLECTIVE EFFECTS STUDIES IN CEPC*

N. Wang#, H. J. Zheng, D. Wang, Y.W. Wang, Q. Qin, IHEP, Beijing, China
W. Chou, Fermilab, Batavia, USA
D. Zhou, K. Ohmi, KEK, Ibaraki, Japan

*Abstract*

Circular electron-positron collider (CEPC) is a 120GeV storage ring-based collider. Due to the small beam size and high single bunch population, the collective effects may bring new challenges to the physical design of the machine. A thorough evaluation of the coupling impedance is necessary in controlling the total impedance of the ring, which can accordingly prevent the occurrence of the beam instability. The primary studies on the impedance and collective effects in CEPC are presented.

## INTRODUCTION

Interaction of an intense charged particle beam with the vacuum chamber surroundings may lead to collective instabilities. These instabilities can induce beam quality degradation or beam loss, and finally restrict the luminosity of the machine. Therefore, beam instability study is essential for designing a new machine. In this paper, the primary calculations of the impedances are first given. Based on the impedance studies, beam instabilities due to single bunch and multi bunch effects are estimated. Instabilities due to interaction of electron beam with the residual ions and positron beam with the electron cloud are also investigated. The main parameters used in the calculation are listed in Table 1.

Table 1: Main Parameters of CEPC

| Parameter | Symbol, unit | Value |
|---|---|---|
| Beam energy | $E$, GeV | 120 |
| Circumference | $C$, m | 54752 |
| Beam current | $I_0$, mA | 16.6 |
| Bunch number | $n_b$ | 50 |
| Bunch length | $\sigma_z$, mm | 2.65 |
| RF frequency | $f_{rf}$, GHz | 0.65 |
| Energy spread | $\sigma_e$ | $1.63\times10^{-3}$ |
| Slipping factor | $\alpha_p$ | $3.36\times10^{-5}$ |
| Betatron tune | $\nu_x/\nu_y$ | 179.08/179.22 |
| Synchrotron tune | $\nu_s$ | 0.18 |
| Damping time | $\tau_x/\tau_y/\tau_z$, ms | 14/14/7 |

*Work supported by NSFC (Project No. 11205171)
#wangn@ihep.ac.cn

## IMPEDANCE

Since most of the engineering designs of the vacuum objects are not done yet, only the RF cavities and the resistive wall impedance are considered here. A more complete impedance budget will be obtained as more vacuum components are designed.

### *RF Cavities*

A five cell superconducting RF cavity structure with RF frequency of 650 MHz will be used in CEPC. Given an accelerating gradient of 15.5 MV/m, 384 cavities will be needed. Since the RF cavities are axisymmetric, the impedance and wake are calculated with the code ABCI [1]. The short range wake at nominal bunch length is shown in Fig. 1. We fit the bunch wake with the analytical model [2]

$$W(s) = -Rc\lambda(s) - Lc^2\lambda'(s), \qquad (1)$$

where $L$ and $R$ are effective inductance and resistance, respectively. The calculated loss factor for one RF cavity is $k_l$=2.332 V/pC.

### *Resistive Wall*

The resistive wall wake for a Gaussian bunch in a cylindrical beam pipe is calculated analytically [3]

$$W(s) = \frac{cl}{8\sqrt{2}\pi a}\frac{1}{\sigma_z^{3/2}}\sqrt{\frac{Z_0}{\sigma_c}}f(s/c), \qquad (2)$$

where

$$f(x) = \sqrt{|x|^3}e^{-x^2/4}\left(I_{1/4} - I_{-3/4} \pm I_{-1/4} \mp I_{3/4}\right)\Big|_{x^2/4}, \qquad (3)$$

and $I_n(x)$ is the modified Bessel function of the first kind.

Aluminium beam pipes will be used in CEPC. The beam pipe has an elliptical cross section with half height of dimension of $a_x$=52 mm and $a_y$=28 mm. We use the vertical aperture in the calculation and obtain the longitudinal wake as shown in Fig. 1.

Impedance budget of the objects considered is given in Table 2.

Table 2: Summary of the Impedance Budget

| Objects | $R$, kΩ | $L$, nH | $k_{loss}$, V/pC |
|---|---|---|---|
| RF cavities | 28.1 | -- | 895.5 |
| Resistive wall | 9.7 | 126.8 | 309.6 |
| Total | 37.8 | 126.8 | 1205.1 |



ISBN 978-3-95450-172-4

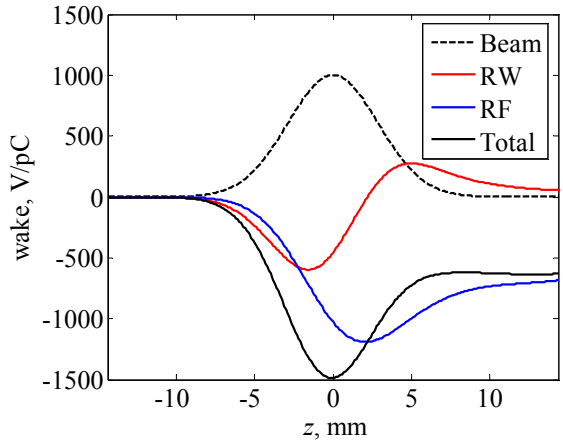


Figure 1: Longitudinal short range wake of different vacuum components at nominal bunch length.

## SINGLE BUNCH EFFECTS

### *Bunch Lengthening*

Interaction of the beam with broadband impedance can change the bunch length and longitudinal distribution due to potential well distortion. The longitudinal bunch density distribution is obtained by numerically solving the Haissinski equation [4, 5]

$$\rho(z)=\rho(0)\exp\left[-\frac{1}{2}\left(\frac{\omega_s z}{\eta c\sigma_\delta}\right)^2+\frac{r_0}{\eta\sigma_\delta^2\gamma C}\int_0^z dz''\int_{z''}^{\infty}dz'\rho(z')W_0'(z''-z')\right]. \quad (4)$$

The Pseudo-Green function wake with bunch length of 0.5mm as shown in Fig. 2 is used in the instability calculation. The longitudinal bunch density with the influence of the wake is shown in Fig. 3. We can see that the bunch is shortened due to the capacitive property of the RF cavity.

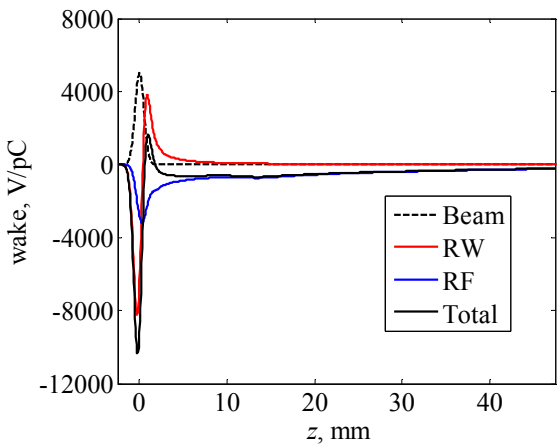


Figure 2: Pseudo-Green function wake with $\sigma_z$=0.5mm.

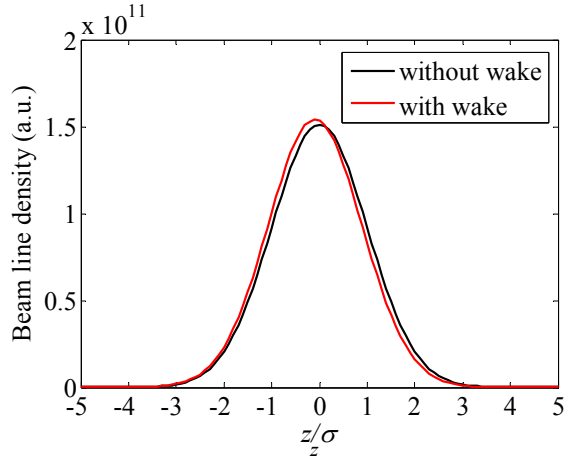


Figure 3: Steady-state longitudinal bunch distribution.

Here, only the impedances of resistive wall and RF cavity are considered in the calculation. Since it is impossible to get a complete impedance model at the present stage, we used SuperKEKB's wake model to do the estimation. The total wake is the SuperKEKB HER or LER's wake scaled by the ratio of the circumference of CEPC to SuperKEKB. The bunch lengthening with different bunch population is simulated. The result is shown in Fig. 4. The red and green curves are the cases with simple scaling by the ratio of the circumference, while the blue and pink ones with a more careful scaling, in which the total wake includes the wake of

- CEPC RF+RW
- bellows, flanges, pumping ports, SR masks, BPMs scaled by the ratio of the circumferences
- feedback kicker and longitudinal kicker without scaling
- collimators, IR duct scaled by the number of IP

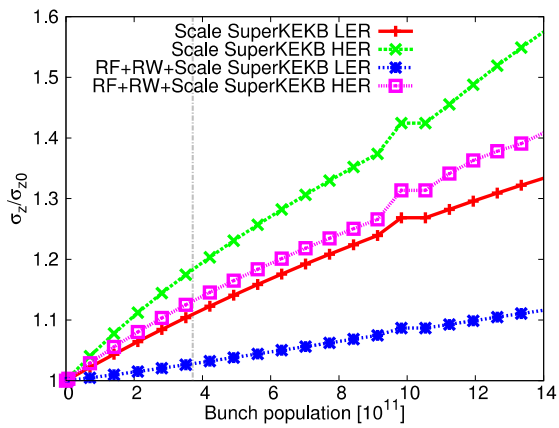


Figure 4: Bunch lengthening vs. bunch population. The grey dashed line indicates the design bunch population.

### *Microwave Instability*

The average threshold current for the longitudinal microwave instability is estimated according to the Boussard or Keil-Schnell criterion [6, 7]

ISBN 978-3-95450-172-4

$$I_{th} = \frac{\sqrt{2\pi}\alpha_p \frac{E}{e}\sigma_e^{\,2}\sigma_z}{R\left|\frac{Z}{n}\right|_{eff}}. \quad (5)$$

For nominal design current, the threshold impedance is 0.025Ω. The microwave instability is also simulated with the scaled SuperKEKB's wake. The result is shown in Fig. 5. The red and green curves correspond to rough scaling, while the blue and pink ones correspond to careful scaling. We can see that, with LER wake, the threshold bunch population is higher than $10^{12}$, while with the HER wake, the threshold bunch population is about $9\times10^{11}$.

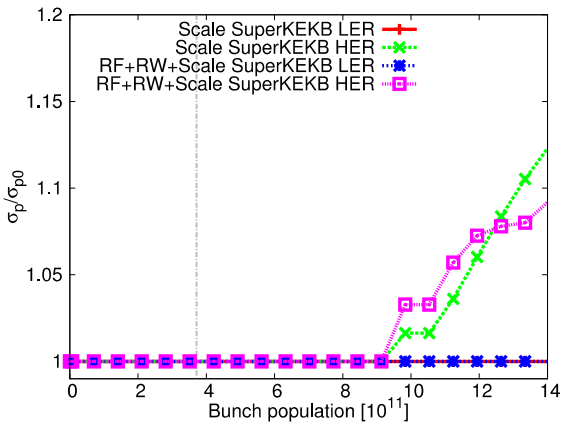


Figure 5: Energy spread vs. bunch population. The grey dashed line indicates the design bunch population.

### *Transverse Mode Coupling Instability*

The threshold bunch current for the transverse mode coupling instability is estimated using eigen mode analysis. Figure 6 shows the dependence of the frequency shift of the head-tail modes with the bunch current. As a primary study, only the resistive wall impedance is considered. The threshold bunch current is 3.4 mA.

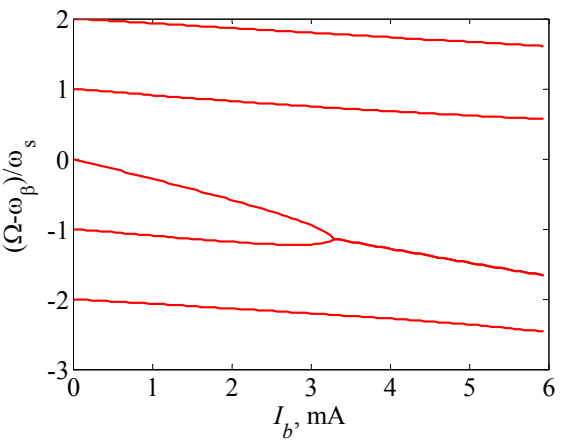


Figure 6: Dependences of the head-tail mode frequencies on the bunch current.

### *Beam Tilt Due to Transverse Wake Fields*

When a beam passes through an impedance with a transverse offset, the tail particles will receive transverse kicks and induce bunch shape distortion. The transverse kick experienced by a particle located at longitudinal position $z$ is given by [4]

$$\Delta y'(z) = \frac{Ne^2}{E}\int_0^\infty dz'\rho(z'+z)W_\perp(y_b, z'). \quad (6)$$

This will lead to a transverse displacement of the bunch tail at IP [8, 9]

$$\Delta y = \sqrt{0.5\beta_y^*\beta_y}\,\Delta y', \quad (7)$$

where $\beta_y^*$ and $\beta_y$ are the vertical beta function at the IP and at the location of the impedance, respectively.

Considering a pretzel orbit of 5 mm in the horizontal plane and closed orbit of 1mm in the vertical plane, the transverse kicks along the bunch excited by the impedance of one RF cavity in both planes are shown in Fig. 7 and Fig. 8.

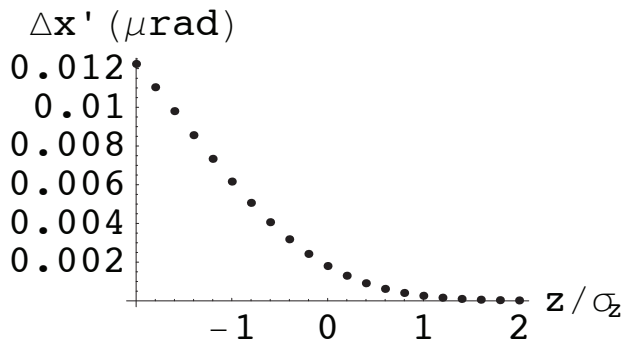


Figure 7: Transverse kick along the bunch in horizontal.

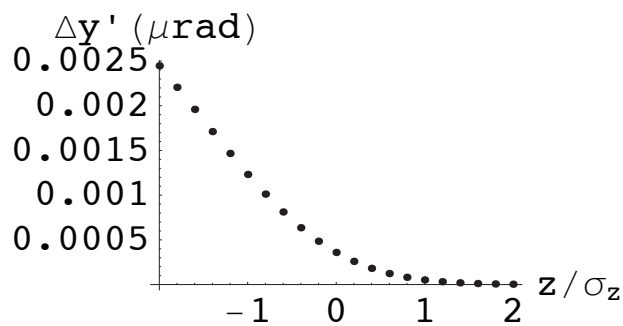


Figure 8: Transverse kick along the bunch in vertical.

The maximum kick angle excited by the transverse impedance of one RF cavity is 12nrad in horizontal and 2nrad in vertical. The corresponding displacements at IP are 54.0nm (horizontal) and 0.42nm (vertical). Since there are 384 cavities located in 8 positions in the ring, the



ISBN 978-3-95450-172-4

displacement at IP is $48\sqrt{8}\times54.0$nm=7.3μm in horizontal and $48\sqrt{8}\times0.42$nm=57nm in vertical.

### *Coherent Synchrotron Radiation*

In evaluating the coherent synchrotron radiation (CSR) effect, the beam is assumed to be moving in a circle of radius $\rho$ between two parallel plates at locations $y = \pm h$. From the linear theory, the condition for the onset of coherent synchrotron radiation is given by the threshold current $S_{th}$, which is given as a function of shielding parameter Π [10]

$$S_{th} = 0.50 + 0.12\Pi, \tag{8}$$

where

$$S = \frac{r_e N_b \rho^{1/3}}{2\pi\nu_s\gamma\sigma_\delta\sigma_z^{4/3}}, \quad \Pi = \frac{\sigma_z\rho^{1/2}}{h^{3/2}}. \tag{9}$$

The CEPC design parameters give Π=16, which means CSR is well shielded. The threshold bunch population is about $7.3\times10^{12}$, which is much higher than the designed value of $3.79\times10^{11}$.

## MULTI-BUNCH EFFECTS

### *Transverse Resistive Wall Instability*

One of the main origins for exciting the transverse multi-bunch instability is due to the interaction of the beam with the resistive wall impedance. Considering $n_b$ uniformly distributed bunches, the rise time of the transverse multi-hunch instability can be estimated by [4]

$$\frac{1}{\tau_\perp} = \frac{n_b I_b c}{4\pi(E/e)\nu_{x,y}} \sum_{p=-\infty}^{\infty} e^{-(\omega_p-\xi\omega_0/\alpha_p)^2\sigma_\tau^2} \mathrm{Re}Z_\perp(\omega_p). \tag{10}$$

where $\omega_p = (pn_b+\mu+\nu_\beta)\omega_0$.

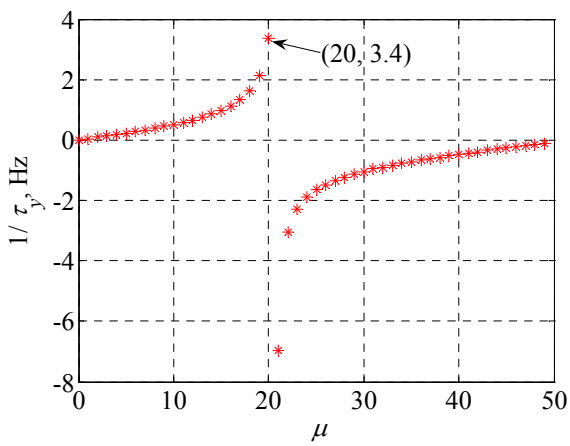


Figure 9: Resistive wall instability growth rate versus oscillation mode number.

Figure 9 shows the growth rate of the transverse resistive wall instability with different mode numbers. We can see that the rise time for the most dangerous mode is about 0.3s. The rise time is much higher than the transverse radiation damping rate.

### *Coupled Bunch Instability Induced by the RF HOM's*

Another dominant contribution to the coupled bunch instability is the higher order modes (HOM) of the accelerating cavities. In the resonant condition, i.e. when the resonant frequency is coincident with the beam spectrum, the growth time can be given by [4]

$$\frac{1}{\tau_\parallel} = \frac{\alpha_p I_0 \omega_R R_\parallel}{4\pi\nu_s(E/e)}, \tag{11}$$

and

$$\frac{1}{\tau_\perp} = \frac{\beta_{x,y} I_0 \omega_0 R_\perp}{4\pi(E/e)}, \tag{12}$$

To keep the beam stable, the radiation damping time should be less than the rise time of any of the oscillation modes. Then we obtain the threshold for the longitudinal impedance is shown in Fig. 10. The threshold for the transverse impedance is 3.9MΩ/m.

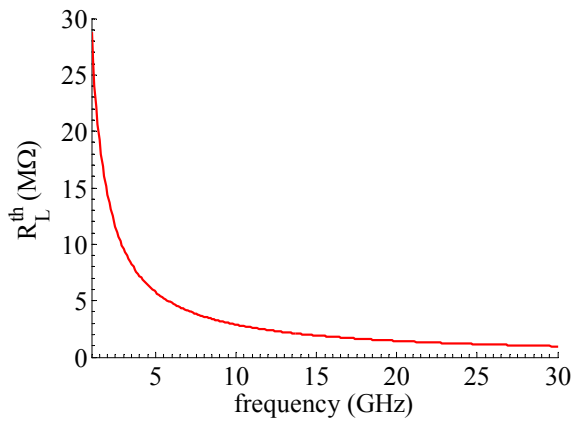


Figure 10: Longitudinal impedance threshold of the RF HOM's.

## ELECTRON CLOUD INSTABILITY

The threshold volume density of the electron cloud for the head-tail instability is given by [11, 12]

$$\rho_{e,th} = \frac{2\gamma\nu_s\omega_e\sigma_z/c}{\sqrt{3}KQr_0\beta L}, \tag{13}$$

where $K=\omega_e\sigma_z/c$, $Q$=min $(Q_{nl}, \omega_e\sigma_z/c)$, $Q_{nl}$ depends on the nonlinear interaction, and $\omega_e$ the electron oscillation frequency. Here, we take $Q_{nl}$ = 7 for analytical estimation, and get the threshold density for the single bunch instability is $9.3\times10^{11}$m$^{-3}$.

ISBN 978-3-95450-172-4

For the multi-bunch instability, the electron cloud is considered as a rigid Gaussian beam with the chamber size. The characteristic frequency is

$$\omega_{G,y}^2 = \frac{2\lambda_b r_e c^2}{(\Sigma_x + \Sigma_y)\Sigma_y}, \quad (14)$$

where $\Sigma_x$ and $\Sigma_y$ are horizontal and vertical electron cloud sizes, and $\Sigma_{x(y)} >> \sigma_{x(y)}$. The phase angle between adjacent bunches is $\omega_G L_{sp}/c$=32.3. So the electrons are not supposed to accumulate and the multipacting effect is low.

## BEAM ION INSTABILITY

In an electron ring, instabilities can be excited by the ions of the residual gas accumulated in the potential well of the electron beam. With uniform filling, the ions with relative molecular mass greater than $A_{x,y}$ will be trapped

$$A_{x,y} = \frac{N_b r_p S_b}{2(\sigma_x + \sigma_y)\sigma_{x,y}}. \quad (15)$$

Figure 11 shows the critical mass number $A_{x,y}$ along the ring. As the threshold is quite high, the ions will not be trapped by the beam.

Fast beam ion instability is a transient beam instability excited by the beam generated ions accumulated in a single passage of the bunch train. The phase angle between adjacent bunches is $\omega_i L_{sep}/c$=42. So the ions will not accumulate due to the over-focus inside the bunch train.

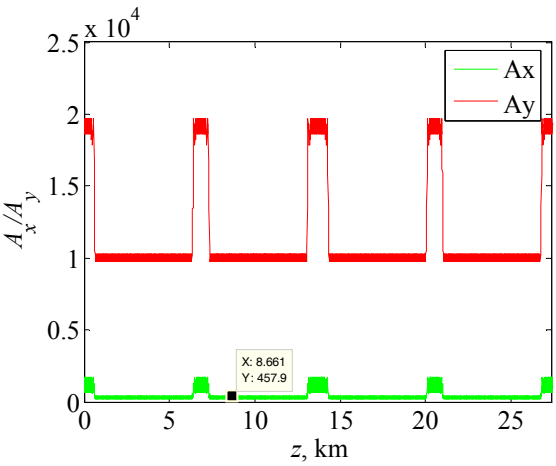


Figure 11: Critical mass number along half of the ring.

## SUMMARY

According to the primary analysis, CEPC should be safe from the microwave instability and transverse mode coupling instability. With only the impedance of resistive wall and RF cavities, the bunch length is reduced due to the capacitive property of the RF cavity. Analysis based on SuperKEKB's geometry impedance shows bunch lengthening of about 10%.

Bunch shape distortion due to the transverse wake is another potential restriction to the high luminosity. More detail analysis take into account impedance localization are needed.

Coupled bunch instabilities are less serious compare to the single bunch effects since the bunch spacing is large. Electron cloud and ion instability should not be a problem due to the overfocus inside the bunch train.

The above analyses are based on a very rough impedance model. A complete impedance model is needed to get more accurate instability estimations. On the other hand, the impedance should be carefully studied and well controlled to suppress the single bunch effects.

## ACKNOWLEDGMENT

Many thanks to Alexander Wu Chao, Gang Xu, Yuan Zhang, YuHong Zhang, Gennady Stupakov, Jiyuan Zhai, Jie Gao and Huiping Geng for their useful discussions and suggestions.

## REFERENCES

[1] abci.kek.jp/abci.htm.
[2] K. Bane et al., SLAC-PUB-14151, 2010.
[3] A.W. Chao, M. Tigner, "Handbook of Accelerator Physics and Engineering", Word Scientific, 1999.
[4] A.W. Chao, "Physics of Collective Beam Instabilities in High Energy Accelerators", JOHN WILEY & SONS, INC., 1993.
[5] J. Haissinski, Nuovo Cimento 18B, 72, 1973.
[6] D. Boussard, CERN II/RF/Int. 75-2, 1975.
[7] E. Keil and W. Schnell, CERN ISR-TH-RF 69/48, 1969.
[8] A.W. Chao and S. Kheifets, SLAC-PUB-3052, 1983.
[9] D. Zhou, K. Ohmi, A. W. Chao, IPAC2011, p.601~603, 2001.
[10] K. Bane, Y. Cai and G. Stupakov, PRST-AB 13, 104402 ,2010.
[11] K. Ohmi and F. Zimmermann, PRL, 85, 3821, 2000.
[12] H. Fukuma, ECLOUD'12, pp.27-30, 2012.



ISBN 978-3-95450-172-4

# TRANSVERSE POLARIZATION FOR ENERGY CALIBRATION AT THE Z PEAK

M. Koratzinos, University of Geneva and CERN, Geneva, Switzerland

*Abstract*

In this paper we deal with aspects of transverse polarization for the purpose of energy calibration of proposed circular colliders like the FCC-ee and the CEPC. The main issues of such a measurement will be discussed. The possibility of using this method to accurately determine the energy at the WW threshold as well as the Z peak will be addressed. The use of wigglers for reducing long polarization times will be discussed and a possible strategy will be presented for minimising the energy uncertainty error in these large machines.

## INTRODUCTION

Accurate energy determination is a fundamental ingredient of precise electroweak measurements. In the case of LEP1 the centre of mass energy at and around the Z peak was known with an accuracy of around $2\times10^{-5}$. The exact contribution of the energy error to the mass and the width of the Z are presented in [1].

The proposed circular colliders FCC-ee [2] and CEPC [3] are capable of delivering statistics a factor ~$10^5$ larger than LEP at the Z and WW energies, therefore there is a need not only to achieve similar performance as far as energy determination is concerned, but to do significantly better.

The only method that can provide the accuracy needed is the so-called resonant depolarization technique, each measurement of which has an instantaneous accuracy of $O(10^{-6})$.

The resonant depolarization technique [4] is based on the fact that the spin precession frequency of an electron in a storage ring is proportional to its energy, $E$. More precisely the spin tune $\nu$ will precess $a\gamma$ times for one revolution in the storage ring, where $a$ is the anomalous magnetic moment and $\gamma$ the Lorenz factor of the electron

$$\nu = a\gamma = \frac{aE}{mc^2} = \frac{E[MeV]}{440.6486(1)[MeV]} \quad (1)$$

The average of all spin vectors in a bunch is defined as the polarization vector $\vec{P}$.Therefore the average energy of a bunch can be computed by selectively depolarizing a bunch of electrons or positrons which have been polarized to an adequate level and measuring the frequency at which this depolarization occurs. A polarimeter measures the change of polarization level. The accuracy with which the instantaneous average energy of the bunch is computed using this method is O(100KeV) – a value much smaller than the beam energy spread of the storage rings considered here.

## TRANSVERSE POLARIZATION

Electron and positron beams in a storage ring naturally polarize due to the Sokolov-Ternov effect [5]. For the purposes of energy calibration important figures of merit are the asymptotic value of polarization that can be reached and the time constant of polarization build-up.

### *Asymptotic Polarization Value*

The maximum achievable polarization value is given by the theory as

$$P_{max} = \frac{8}{5\sqrt{3}} \cong 0.924 \quad (1)$$

however machine imperfections usually limit this number to lower levels. There can be numerous depolarizing effects in a storage ring.

### *Polarization Time Constant*

For a beam with zero polarization the time dependence for build up to equilibrium is

$$P(t) = P_{max}\left[1 - \exp(-t/\tau_{pol})\right] \quad (2)$$

Where the built up rate is (in natural units)

$$\tau_{pol}{}^{-1}[s^{-1}] \approx \frac{2\pi}{99}\frac{E[GeV]^5}{C[m]\rho[m]^2} \quad (3)$$

Where C is the circumference of the storage ring and $\rho$ its bending radius. Therefore polarization times increase dramatically with the machine circumference and decrease with energy. The use of wigglers [6] can decrease this time if needed, at the expense of increasing the energy spread and the synchrotron radiation (SR) budget of the machine.

Polarization times for relevant machines and energies can be seen in Table 1.

**Table 1:** Polarization Times without the Help of Wigglers

| Storage ring | Circumference (kms) | E (GeV) | $\tau_{pol}$ (hours) |
|---|---|---|---|
| LEP | 27 | 45 | 5.8 |
| FCC-ee | 100 | 45 | 290 |
| FCC-ee | 100 | 80 | 16 |
| CEPC | 55 | 45 | 48 |



ISBN 978-3-95450-172-4

## POLARIZATION AND ENERGY SPREAD

One important limitation on achievable polarization levels comes from the energy spread of the beam: Off momentum particles reaching an integer spin resonance depolarize quickly. As seen from eqn. (1), these spin resonances sit 440MeV apart. Energy spread scales approximately like

$$\sigma_E \propto \frac{E^2}{\sqrt{\rho}} \tag{4}$$

The maximum energy at which useful levels of polarization can be measured cannot easily be calculated. However, we can extrapolate from the measurements done at LEP [7] where the maximum energy where polarization was observed was 60.6GeV (at a level of around 8%). Using eqn. (4) this extrapolation to storage rings with different diameters can be seen in Table 2.

**Table 2:** Extrapolation of LEP data to other machines regarding the maximum energy below which polarization levels will be adequate for resonant depolarization measurements.

| Storage ring | C(kms) | Maximum energy with polarization (GeV) |
|---|---|---|
| LEP | 27 | 61 |
| CEPC | 55 | 72 |
| FCC-ee | 100 | 84 |

As can be seen from the above table, polarization at the W pair threshold (80GeV) at FCC-ee seems possible. This is in contrast of what was achieved at LEP and another input to the physics case of this unique machine.

There are also LEP measurements (figure 8 in [7]) where the maximum energy spread compatible with reasonable polarization levels has been measured - wigglers were used to change the energy spread. An energy spread larger than about 52MeV leads to a significant drop of polarization levels. In the absence of detailed simulation work we shall use the above figure as the maximum permissible energy spread compatible with polarization.

## RESONANT DEPOLARIZATION

The way the resonant depolarization measurement is performed is the following: Only one bunch is targeted at a time. Since the colliding rate is much larger than the polarization rate, for polarization to build up this bunch needs to be a non-colliding bunch. It should be stated here that operation with colliding and non-colliding bunches might be a challenge due to the different tune shifts of the two species of bunches involved. The measurement proper consists of measuring the spin precession frequency by introducing a resonance in a 'trial and error' fashion. If no depolarization is observed (failure) the frequency used is not the correct depolarizing frequency. The bunch remains polarized. If the bunch depolarises (success) the frequency corresponds to the exact mean energy of the bunch at that moment. To observe the polarization change, polarization levels of 5-10% are needed – the better the polarimeter, the lower the values of polarization necessary for a successful measurement.

## THE ENERGY MODEL

The beam energy of large storage rings continuously changes due to internal and extraneous causes. This evolution can be modelled but energy changes are many orders of magnitude larger than the instantaneous accuracy of a depolarization measurement. For example, small changes in the diameter of the ring due to elastic deformations of the earth's crust (due to, for instance, tidal forces) can have a big effect on the energy of the electrons and positrons. This is due to the small momentum compaction factor $\alpha_c$ which relates changes in energy to changes in the orbit length of a storage ring:

$$\frac{\Delta E}{E} = -\frac{1}{\alpha_c}\frac{\Delta L}{L} \tag{5}$$

Where $L$ is the orbit length. Momentum compaction factors vary from $2 \cdot 10^{-4}$ for LEP to $5 \cdot 10^{-6}$ at FCC-ee. So a 1mm orbit length change at FCC-ee (a change of $10^{-8}$) leads to a large 90MeV change in energy, to be contrasted with the O(100keV) accuracy of the depolarization method. Table 3 shows changes in energy for a 1mm circumference change (typical for tide-induced changes at LEP) for the three storage rings discussed here.

**Table 3:** Change in energy of a 45GeV beam for a circumference change of 1 mm in the three storage rings discussed here.

| Storage ring | Circumference (kms) | $\alpha_c$ | $\Delta E$ (MeV) |
|---|---|---|---|
| LEP | 27 | $2 \cdot 10^{-4}$ | 8 |
| CEPC | 55 | $4 \cdot 10^{-5}$ | 20 |
| FCC-ee | 100 | $5 \cdot 10^{-6}$ | 90 |

The time constant for elastic deformation changes varies between hours (for tides) to months (for rainfall variations). Other effects that contribute to change of the energy include temperature changes (time constant of a few hours), parasitic currents (time constant of some minutes) and many other effects discussed in some detail in [4].

Moreover, the RF configuration can give rise to different energies for electrons and positrons, therefore both species should be measured with the resonant depolarization technique, something that was not done at LEP. This necessitates the use of two polarimeters for both species.

There are also corrections to be applied in deriving the centre of mass energy per experiment from the mean energy of the electrons and positrons measured with the resonant depolarization method.

Therefore for ultimate precision we need to



ISBN 978-3-95450-172-4

- Measure the energy using the resonant depolarization every few minutes
- Measure independently electrons and positrons
- Measure continuously from the beginning of physics to the end of physics

## WIGGLERS

The natural polarization time for large rings is very long as seen from Table 1. As we only need polarization levels of 5-10% to perform a polarization measurement, we can divide the numbers in the table by 10 to 20. But this is still too long compared to the mean time between failures which cannot be assumed to be more than a few hours or a day at most. A way to reduce polarization time is the use of wigglers [6]. Wigglers are dipole magnets with two parts: a low field region and a high field region so that the integral field seen by the electrons is zero. However they help polarization as polarization time scales with the square of the field and polarization levels are not affected provided that the wiggler asymmetry (the ratio of lengths of the positive and negative field magnets) is larger than ~5.

Wigglers have, however, two undesired effects: They increase the energy spread and they contribute to the SR power budget of the machine. Therefore a possible strategy would be to use them is such a way that the energy spread is less than some pre-determined maximum and to switch them on only where necessary.

The maximum energy spread that can be tolerated as discussed earlier is around 52MeV. In the absence of a new design, we consider the wigglers suggested for LEP [6] that have an asymmetry of 6.15 and pole lengths of 0.65m and 4m for the strong and the weak field respectively.

The polarization time and wiggler SR power dissipated for various configurations can be seen in Table 4. In each case we have pushed the wiggler field until the maximum allowed energy spread of 52MeV is reached. B+ is the field of the strong pole. As can be seen, polarization times are reduced by a large factor - to 21 hours (TLEP) and 7 hours (CEPC) when using wigglers. Interestingly, polarization times depend only weakly on the number of wigglers installed (but a higher field per wiggler is needed)

Therefore useful polarization levels (5-10%) are reached after 60-130 minutes (TLEP) and 21-42 minutes (CEPC). These times are not too different from the fill up times of the machines.

The SR power dissipated by the wigglers (last column of Table 4, for both beams) is rather large, although it is reduced if one operates one wiggler at a high field rather than many at a reduced field.

**Table 4:** The effect of the use of wigglers on polarization times, energy spread and wiggler power dissipation using the analytic approach in **[6]** and for the wiggler design described therein. B+ is the magnetic field of the short (strong) dipole of the wiggler.

| Machine | Energy (GeV) | No. of wigglers | B+ (T) | Polarization time (hours) | Energy spread (MeV) | Wiggler SR power (MW) |
|---|---|---|---|---|---|---|
| TLEP | 45 | 0 | 0 | 253 | 17 | 0 |
| TLEP | 45 | 12 | 0.62 | 21 | 52 | 20 |
| TLEP | 45 | 1 | 1.35 | 24 | 52 | 9 |
| CEPC | 45 | 0 | 0 | 41 | 23 | 0 |
| CEPC | 45 | 12 | 0.72 | 7 | 52 | 17 |
| CEPC | 45 | 1 | 1.58 | 7 | 52 | 7 |

### *Wiggler Operation*

A possible strategy therefore emerges to solve the problem of very long polarization times at large storage rings while wasting as little of the power budget of the machine (which costs in terms of luminosity) as possible: Wigglers need to be used, but they need to be on just enough time to polarise enough non-colliding bunches. For the case of FCC-ee, 250 non-colliding bunches are sufficient and for the case of the CEPC 40 non-colliding bunches. The wigglers can be switched on as soon as the machine starts filling up and they can be switched off when 5% polarization is achieved. Machine fill-up times are expected to be around 30 minutes, therefore in the case of the FCC-ee an extra ~40 minute dead time is introduced while polarization builds up and during which period no meaningful energy measurement can be performed. Also, due to the power taken up by the wigglers, the luminosity of the machine will be lower than during normal operation. Physics studies which do not need the precise energy determination can take place, though.

When the required level of polarization for the non-colliding bunches has been achieved, the wigglers can be turned off and the depolarization measurements can start. Measuring and replacing 5 bunches for 5 depolarization measurements per hour, the FCC-ee will exhaust all 250 non-colliding bunches in 50 hours, during which time new non-colliding bunches will have been polarized to more than 5%.

ISBN 978-3-95450-172-4

We here assume that the number of electrons in a non-colliding bunch would be similar to the number of electrons of a normal (colliding) bunch. For the FCC-ee this number is $\sim 1.8 \cdot 10^{11}$ (similar to the LEP1 value). Having 250 out of 16700 bunches not colliding leads to an inefficiency of 1.5%.

The SR budget for the wigglers is reasonable, especially considering that they can be switched off after a short period of time. A single wiggler with a high field, if it can be constructed at a reasonable cost, is better than many wigglers with a smaller field in this respect. It should be noted here that wigglers introduce more damping and might help to achieve higher beam-beam parameters, partly compensating the luminosity loss due to wiggler SR power – this is a topic that needs to be investigated.

## CONCLUSIONS

The resonant depolarization method seems accessible at the Z (45GeV) and W (80GeV) energies of the FCC-ee and at the Z energy of the CEPC. Both lepton species should be measured. Long polarization times necessitate the use of wigglers, which however are needed only during a short period at the beginning of a fill. Resonant depolarization measurements should be performed routinely at a rate of a few her hour to profit from their instantaneous accuracy and help reduce the energy uncertainty to the unprecedented levels needed by the high statistics of the proposed large circular colliders.

## REFERENCES

[1] R. Assmann et al., "Calibration of centre-of-mass energies at LEP1," *Eur. Phys. J. C 6, 187-223 (1999).*

[2] Wenninger, J. et al., "Future Circular Collider Study Lepton Collider Parameters," *CERN EDMS no. 1346082,* 2014.

[3] Q. Qin, "Overview of the CEPC Accelerator," in *55th ICFA Advanced Beam Dynamics Workshop on High Luminosity Circular e+e- Colliders – Higgs Factory (HF2014)*, Beijing, 2014.

[4] L. Arnaudon et al., "Accurate Determination of the LEP Beam Energy by resonant depolarization," *Z. Phys. C 66, 45-62 (1995).*

[5] A.A. Sokolov, I.M.Ternov, "On Polarization and spin effects in the theory of synchrotron radiation," *Sov. Phys. Dokl. 8, 1203 (1964).*

[6] A. Blondel and J.M. Jowett, "Dedicated Wiglers for Polarization," LEP note 606, CERN, 1988.

[7] R. Assmann et al., "Spin dynamics in LEP with 40–100 GeV beams," in *AIP Conf. Proc. 570 , 169* , 2001.



ISBN 978-3-95450-172-4

# LONGITUDINAL POLARIZATION AND ACCELERATION OF POLARIZED BEAMS

I.A. Koop, BINP SB RAS, NSU and NSTU, Novosibirsk, Russia

*Abstract*

The paper describes a scheme of creation of the longitudinally polarized electron beam at the collision point of the future FCC-ee collider. A scheme is based on use of two 90-degrees spin rotators placed in appropriate points of the interaction region. The solenoid type spin rotators are proposed to use for that purpose. Advantages and disadvantages of the proposed approach are discussed.

## INTRODUCTION

There is a clear request for the longitudinal polarization at Z-peak [1]. Even collisions of un-polarized positrons with polarized electrons are of interest for the Weinberg angle measurement experiment, as it was done at SLC.

Still, a positron beam polarization would help very much in study and minimization of different systematics. In principle, a polarized of up to 50%-70% positron beam with only about 10 times lower intensity should be available – it can become polarized in about 5 min in 1-1.5 GeV wiggler damping ring and then be pre-accelerated in a linac to 20 GeV and finally ramped to a full energy by the booster synchrotron.

The full intensity polarized of up to 80%-90% electron beam will be produced like at SLC by a photoemission gun. After acceleration in a linac to 20 GeV it similarly to positrons will be accelerated in a booster synchrotron. Maintaining of the polarization in a synchrotron is discussed briefly in [2].

The effective control of the polarization in the collider and in a synchrotron will be provided by the longitudinal Compton backscattering polarimeter [3, 4]. In contrast to the transverse case the longitudinal one has an extremely large analyzing power, approaching to 75% at Z-peak and almost to 100% at W-threshold.

Below we will discuss two possibilities of organizing of the longitudinal orientation of the stable spin direction at the IP. In both cases the solenoid type spin rotators are proposed to be used.

## LONGITUDINAL POLARIZATION AT Z-PEAK

A combination of two $\pm 90^0$ spin rotators and an anti-symmetric horizontal chicane in between with 15 mr deflection angle at IP (relative to the solenoid axis) provides the needed longitudinal spin direction in the collision point, see the Figure 1. Such setup does not disturb the global spin motion due to mirror symmetry of all spin rotations. Therefore the stable spin axis remains a vertical all around a ring, as also the spin tune remains be as same $\nu=\nu_0=\gamma a$, as without any spin rotators. So, a spin precession frequency measurement can be used further for monitoring of the energy stability and for the energy calibration.

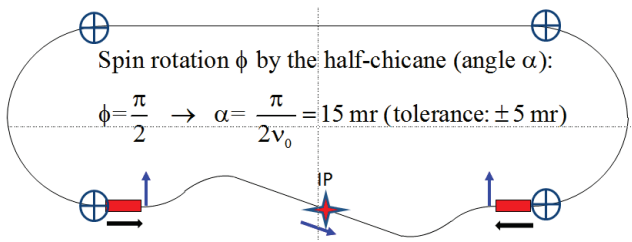


Figure 1: Top view on anti-symmetric layout of a set of $90^0$ spin rotations produced by solenoids and by bends in horizontal plane. The orbit deflection angle 15 mr provides $90^0$ spin rotation exactly at E=45.5 GeV.

The radiative depolarization rate is expected to be very small because of zero value of the spin-orbit coupling vector $\vec{d}$ everywhere in arcs, except the chicane bends. The spin relaxation rate is described by the famous DK formula [5]:

$$\tau_p^{-1} = \frac{5\sqrt{3}}{8}\lambda_e r_e c \gamma^5 \left\langle \frac{1 - \frac{2}{9}\left(\vec{n}\vec{\beta}\right)^2 + \frac{11}{18}\vec{d}^2}{|r^3|} \right\rangle$$

Here $\vec{n}(\theta)$ is a unity vector aligned along the equilibrium spin direction of a reference particle, $\vec{d}(\theta) \equiv \gamma \frac{\partial \vec{n}}{\partial \gamma}$ is the so-called a spin-orbit coupling vector, which describes the dependence of $\vec{n}$ from the energy, $r$ is the bending radius and other symbols have the obvious meaning.

In a flat normal ring $\vec{n}(\theta)$ is vertical independently of energy, hence $\vec{d}(\theta) = 0$. Some small contribution to $\vec{d}$ from dipoles of the chicane will decrease depolarization time from 190 hours to about 24 hours, if the field strength in these bends is same as in arcs.

ISBN 978-3-95450-172-4

## SOLENOID TYPE SPIN ROTATORS

Different optics schemes for compensation of by the solenoid induced coupling were suggested in 80-th by Litvinenko and Zholentz [5]. Most simple for realization is a scheme shown in the Figure 2. The total solenoid is divided in two halfs. Each half rotates spin around the longitudinal axis by the angle

$$\frac{\varphi}{2} = (1 + a)\frac{\int B\,dl}{Br}$$

The coupling is compensated by the normal quadrupole lenses inserted between the solenoids providing that the 2x2 transportation matrices satisfy to the condition [6]:

$$T_x = -T_y .$$

Main advantage of such a scheme is a flexibility in tuning the optics of a spin rotator. One can switch off the solenoids completely and retune the quads to provide the same beam transport as it was before.

The other requirement comes from the spin transparency condition. To cancel the contribution of the horizontal betatron oscillations to beam depolarization the transport matrix of such a partial spin rotator should be of the type shown in the Figure 2 [7]. In case of the $90^0$ total spin rotation angle both matrices $T_{x,y}$ became anti-diagonal.

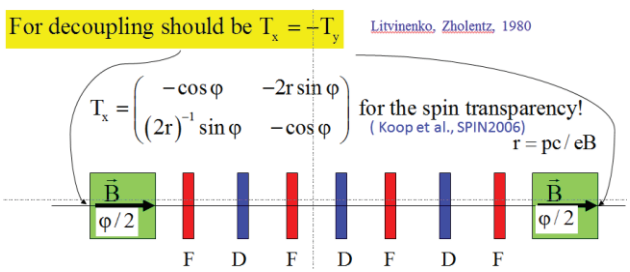


Figure 2: Spin transparent rotator optics scheme for the solenoid type partial Snake.

## LONGITUDINAL POLARIZATION AT HIGHER ENERGIES

At higher than 60 GeV beam energies the synchrotron satellites of integer and intrinsic resonances may overlap and make polarization life time very short. That is one of the plausible explanations of the LEP's observations [8].

The strength of the synchrotron satellites is proportional to a spin tune chromaticity. In a flat ring without snakes the spin tune chromaticity equals just to the tune $\nu_0$:

$$\gamma\frac{\partial\nu}{\partial\gamma} = \nu_0 = 180 \qquad \text{for} \quad E=80 \ \text{GeV}$$

We see that at 80 GeV the tune chromaticity becomes extremely large. But there is a trick which can help to solve a problem.

We can make same polarity of the longitudinal field in two $90^0$ spin rotators - one on the left and another on the right side from the IP. Then the whole device became a Siberian Snake. Now, let do the longitudinal polarization not in one but in 2 or 4 detectors, placed as shown in the Figure 3. In this example four interaction points divide $360^0$ ring azimuth on unequal segments and spin changes the direction from a vertical to anti-vertical after passing of each snake. Let $f < 0.5$ is a fraction of the total circumference occupied by two short arcs, interleaved by two long arcs. Then the spin tune is equal to:

$$\nu = (1 - 2f)\nu_0$$

With $f$ chosen close to 0.5 it becomes arbitrarily small, but still not zero! Accordingly, the spin tune chromaticity becomes also much smaller than $\nu_0$, and this could make the polarization life time much longer.

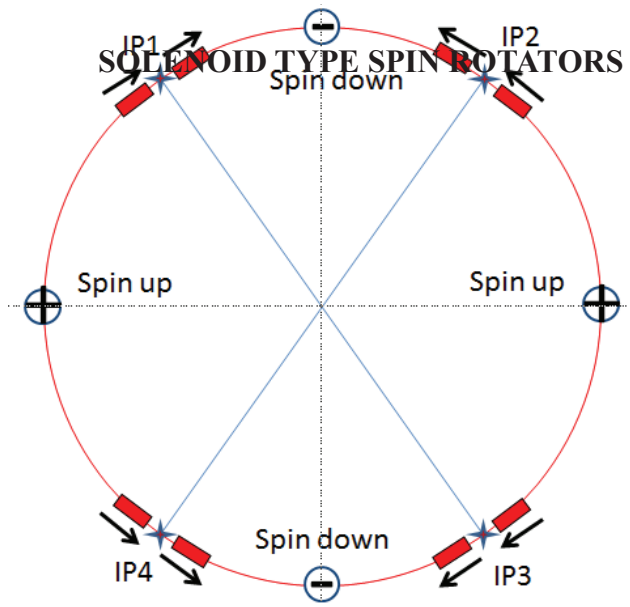


Figure 3: The longitudinal polarization scheme with 4 Siberian Snakes which divide a ring into 4 unequal sectors. The equilibrium spin direction is vertical in long sectors and is rotated by $180^0$ by each snake, which consists in turn of two $90^0$ spin rotators of solenoid type. Chicane magnets, which rotate spin in the horizontal plane and create the longitudinal spin component at IP (not perfectly in general), are not shown.

Such asymmetric division of the circumference on 2 or 4 sectors by the even number of snakes (in general) looks very profitable also for the acceleration of polarized beams to super-high energies [8, 9]. The only drawback is that spin tune is not constant during the energy ramp and may cover a wide dynamic range, say: $0.1 < \nu < 0.9$.

## CONCLUSION

Using $90^0$ spin rotators and ±15 mr magnet chicanes it is possible to organize a perfect longitudinal polarization



ISBN 978-3-95450-172-4

at IP of each interaction region at Z-peak. At higher energies one should care on minimization of the spin tune chromaticity. Siberian Snake approach provides a solution based on a choice of unequal arc angles between 4 interaction points. Still, the polarization vector becomes perfectly longitudinal only at a set of discrete energies: say at 45 and 135 GeV, depending on the chicane deflection angle.

Future spin tracking simulations should prove validity of the discussed above ideas.

## ACKNOWLEDGEMENTS

The author expresses his gratitude to Yu. Shatunov, S.R. Mane and A. Otboev for stimulating discussions and interest to this work.

## REFERENCES

[1] A. Blondel, “Physics motivation and requirements”, HF2014 Beijing, 9-12 October 2014.
[2] I. Koop, “Maintaining polarization in synchrotrons”, HF2014 Beijing, 9-12 October 2014.
[3] I. Koop, “Polarization issues and schemes for energy calibration”, HF2014 Beijing, 9-12 October 2014.
[4] M. Beckmann et al., “The Longitudinal Polarimeter at HERA”, Nucl.Instrum.Meth. A479 (2002) 334–348.
[5] Ya.S. Derbenev, A.M. Kondratenko , “Polarization kinetics of particles in storage rings”, Zh. Eksp. Teor. Fiz. 64 (June 1973) 1918-1929 (in Russian); Sov. Phys. JETP, vol.37, No.6 (Dec. 1973), pp. 968-973.
[6] A.A. Zholents, V.N. Litvinenko, “On the compensation of solenoid field effects by quadrupole lenses”, Preprint IYF 1981-080, Novosibirsk; see also DESY-L-TRANS-289
[7] I.A. Koop et al., “Spin transparent Siberian Snake and spin rotator with solenoids”, 17th International Spin Physics Symposium, Kyoto, Japan, 2-7 October, 2006; AIP Conference Proceedings Volume 915, American Institute of Physics, 2006, p.948-954.
[8] S.R. Mane, “Polarization at TLEP/FCC-ee: ideas and estimates”, preprint arXiv: 1406.0561v1 [physics.acc-ph] 3 June 2014.
[9] Yu. Shatunov, a talk at SPIN14 conference, October 2014, Beijing, China.



ISBN 978-3-95450-172-4

# FCC-ee BEAM ENERGY MEASUREMENT SUGGESTION*

N.Yu. Muchnoi†, Budker INP & Novosibirsk State University, Russia

*Abstract*

An approach for beam energy calibration at future circular electron-positron collider (FCC-ee) is suggested. The method is based on a magnetic spectrometer, but does not require absolute knowledge of its bending field. Inverse Compton scattering of laser radiation on the electron beam provides accurate calibration of the bending force. Due to scattering kinematics, the beam energy determination is based on the laser wavelength together with accurate measurement of the ratio of deflection angles. The approach has no serious limitations in the electron beam energy range. The same apparatus allows to measure the electron beam polarization.

## INTRODUCTION

Accurate knowledge of the beam energy in experiments on lepton colliders provides direct access to collision energy. This knowledge has always been a tremendous advantage for performing precise measurements of particle masses, shapes of the resonance structures, etc.

The present accuracy of the mass scale in high-energy physics is established mostly due to the resonant depolarization technique, which had been used at various $e^+e^-$ colliders like VEPP-2M, SPEAR, DORIS, CESR, VEPP-4(M), LEP. The resonant depolarization approach provides ultimate precision ($\Delta E_0/E_0 \simeq 10^{-6}$) for instant beam energy determination through measurement of the spin precession frequency. However, preparation of and control over polarized beams is not always possible and usually consumes significant amount of time and decreases the overall luminosity integral. At high beam energies the beam polarimetry is usually based on laser backscattering, a process which is sensitive to both transverse and longitudinal polarization of electrons [1, 2].

In case when an experiment requires precise measurement of the beam energy, it is very important to have several complementary approaches possessing high sensitivity at least to relative beam energy changes. This helps to determine the beam energy behaviour during data acquisition time as well as to perform various cross-checks and eliminate possible errors. In storage rings the beam energy is usually derived from continuous measurements of the bending fields in a number of dipoles. The relationship between the measured fields and the beam energy is defined via magnetic model of the storage ring, which is calibrated against precise measurements of the beam energy, e. g. by resonant depolarisation [3, 4].

At LEP 2 the beam energy "was verified by three independent methods: the flux-loop, which is sensitive to the bending field of all the dipoles of LEP; the spectrometer, which determines the energy through measurements of the deflection of the beam in a magnet of known integrated field; and an analysis of the variation of the synchrotron tune with the total RF voltage".

### *Compton Backscattering of Laser Radiation*

Here let us make a brief introduction to another approach for the absolute beam energy determination. It was implemented for the last ten years at $e^+e^-$ colliders VEPP-4M [3], BEPC-II [5] and VEPP-2000 [6, 7].

When the photon with energy $\omega_0$ is scattered towards the relativistic electron with energy $E_0$, this electron gives significant part of its energy to the scattered photon, even in case when $\omega_0 \ll E_0$. Maximum energy loss of the electron occurs when the scattered photon propagates exactly along the electron momentum, carrying out $\omega_{max}$ energy:

$$\omega_{max} = E_0 \frac{\kappa}{1+\kappa}\,, \qquad (1)$$

where $\kappa = 4\omega_0 E_0/m^2$. Electron mass $m$ is a well established parameter, $\Delta m/m \simeq 2 \cdot 10^{-8}$. If one uses a laser as a source of photons for scattering, the order of about 1 ppm relative accuracy for the $\omega_0$ value is practically not a problem. Thus, if one can measure $\omega_{max}$ in absolute units, electron energy $E_0$ could be easily obtained from Eq. 1 with roughly twice better relative precision than $\omega_{max}$ measurement.

The particular case when this approach is good enough is when $\omega_{max}$ belongs to the energy range between 100 keV and 10 MeV. Here the HPGe[1] detectors possess *high energy resolution* and *sufficient efficiency*. What is also very important is that in this energy range the *absolute scale calibration is possible* due to well-known energies of nuclear $\gamma$-sources. By now the backscattering of laser radiation is a well established approach for beam energy measurement with an accuracy $\Delta E_0/E_0 \lesssim 5 \cdot 10^{-5}$, but its application is limited for the beam energies $E_0 \lesssim 2$ GeV.

For further consideration we note that for a relativistic electron one can neglect $\omega_0$ in the energy balance of scattering, i. e. the minimal electron energy after scattering $E_{min} = E_0 - \omega_{max}$, and from Eq. 1 one has:

$$E_{min} = E_0 \frac{1}{1+\kappa}\,. \qquad (2)$$

## THE SUGGESTION

One of the beam energy measurement approaches at LEP (1997-2000) was the LEP spectrometer [4]. The similar concept was proposed for the ILC upstream beam energy spectrometer [2]. When the electron beam passes through

* Work supported by the Ministry of Education and Science of the Russian Federation, NSh-4860.2014.2

† muchnoi@inp.nsk.su

[1] HPGe – High Purity Germanium detector



ISBN 978-3-95450-172-4

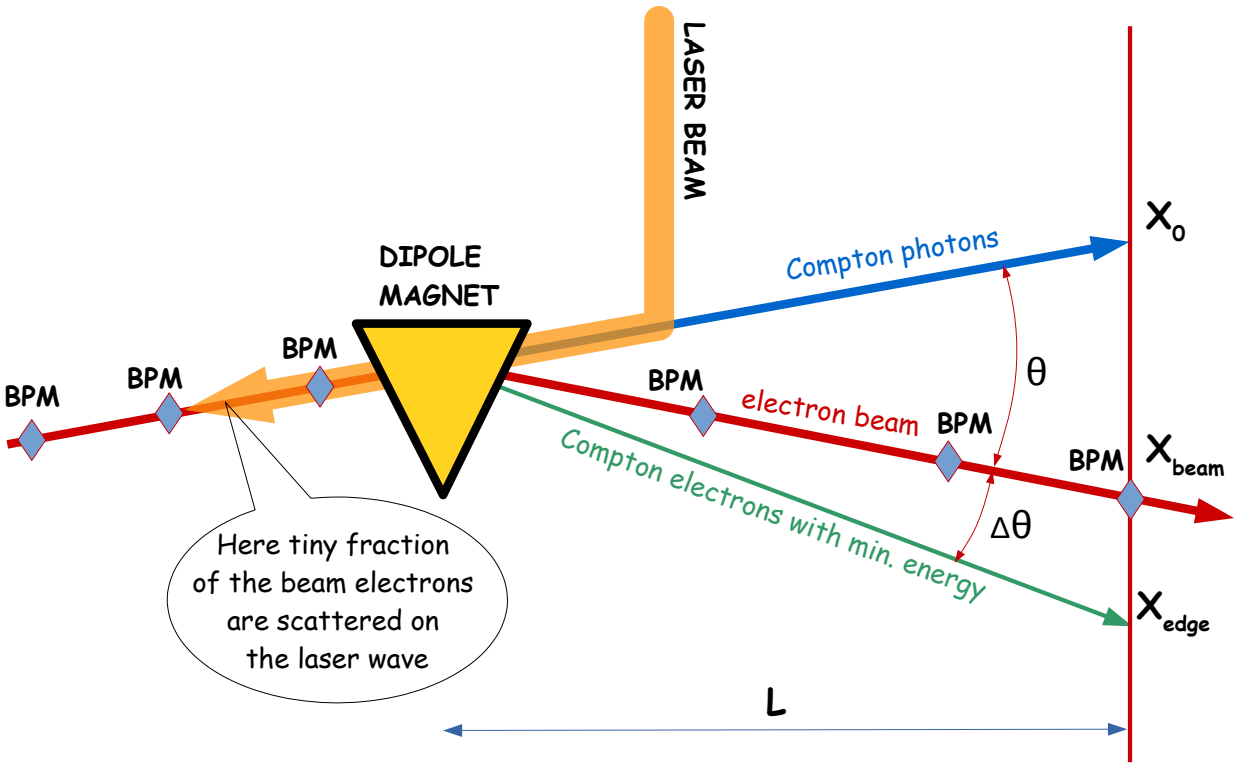


Figure 1: Apparatus layout. If one measures $\theta$ and $\Delta\theta$, the beam energy $E_0$ is determined by equation (5).

the bending magnet, mean electron energy $E_0$ is derived from the bending field integral and deflection angle $\theta$:

$$\theta = \frac{c\int Bds}{E_0} \,. \tag{3}$$

Layout of the apparatus for FCC-ee beam energy calibration is shown in Fig. 1. Beam position monitors (BPM) are installed along the beam orbit before and after the bending magnet, allowing to measure the beam deflection angle and thus completely reproduce the conventional spectrometer approach.

In addition (see Fig. 1), laser radiation propagates towards the electron beam, and the electron-photon interaction occurs before electrons enter the dipole magnet. This interaction produces scattered photons and electrons. The number of scattered particles is only a few pieces per bunch, so the affordable low-power laser system may be used, satisfying the requirements of non-destructive instrument.

The electron beam bending angle, $\theta$ in Fig. 1, is inverse proportional to the mean beam energy $E_0$ (see Eq. 3). A deflection angle for the electrons with the energy $E_{min}$ could be obtained by substitution of $E_{min}$ from Eq. 2 instead of $E_0$ to Eq. 3. Finally, we find that:

$$\frac{\Delta\theta}{\theta} = \kappa = \frac{4\omega_0 E_0}{m^2} \,. \tag{4}$$

Of course, this simple equality is exact only in the case when the integrals of the magnetic field $\int Bds$ are equal for electrons with either $E_0$ or $E_{min}$ energies. However, Eq. 4 is not obvious, it was first mentioned as a tool for the beam energy spectrometer calibration in [8].

$\Delta\theta/\theta$ is proportional to $\omega_0$ and $E_0$, in case when $E_0$ = 100 GeV and $\omega_0$ = 1 eV one has $\Delta\theta/\theta \simeq 1.53$. With a green laser ($\omega_0$ = 2 eV) this ratio may be doubled, while with IR laser ($\omega_0$ = 0.1 eV) it will be ten times lower.

We suggest to obtain the mean energy of beam electrons from the measurements of deflection angles $\theta$ and $\Delta\theta$:

$$E_0 = \frac{\Delta\theta}{\theta} \times \frac{m^2}{4\omega_0} \,. \tag{5}$$

Vertical line on the right of Fig. 1 is the "detection line", located at the distance $L$ from the dipole, where one of downstream BPMs is installed: this BPM will measure $X_{beam}$.

The photon detector measures the space distribution of backscattering photons and determine its mean value $X_0$. The up-down asymmetry appears in this distribution when the circular polarized laser light is scattered on the electron beam with transverse polarization [1].

The scattered electrons detector provides their distribution along the detection line. This distribution has a sharp edge at $X_{edge}$, corresponding to the electrons with $E_{min}$ energy. The width (spread) of the edge will be equal to the unscattered beam transverse size at the detection line due to Eq. 4. $X_{edge}$ is going to be obtained from fitting the edge with erfc-like function. The height of the edge depends on lon-

ISBN 978-3-95450-172-4

gitudinal electrons polarization when the circular polarized laser light is scattered on the electron beam [2].

The data of both detectors is collected for many laser shots during some time by the order of several minutes. If $\theta, \Delta\theta \ll 1$ one has

$$\frac{\Delta\theta}{\theta} \simeq \frac{X_{edge} - X_{beam}}{X_{beam} - X_0}\ , \qquad (6)$$

which allows to use these measurements for beam energy determination by Eq. 5.

Alternatively, the value of $\theta$ may be taken from the BPMs data only.

### *A Rough Accuracy Estimation*

Suppose that we can measure both $[X_{beam} - X_0]$ and $[X_{edge} - X_{beam}]$ with 10 $\mu$m accuracy, which seems to be technically possible. In order to achieve the precision of beam energy measurement at the level of $\Delta E/E \simeq 10^{-5}$, one needs to have both $[X_{beam} - X_0]$ and $[X_{edge} - X_{beam}]$ to be about 1 m. This is the case, for example, if the beam bending angle $\theta \simeq 10$ mrad and a free space between the magnet and the "detection line" $L \simeq 100$ m (see Fig. 1). The only way to reduce the bending angle and overall size of the system is to improve the accuracy of coordinate measuremets, it is a challenge that requires more studies.

## CONCLUSION

The problem of the beam energy calibration for high energy colliders still does not have a perfect solution. Extensive way of solving the problem is to increase the accuracy of existing methods. In the opinion of the author, no less important is to search for innovative approaches. Let's list the strengths of the present suggestion:

- it aims to measure the absolute energy of the electron beam and does not require precise measurements of magnetic fields in absolute scale;
- backscattering of laser radiation is a proven tool for beam energy calibration at low energy machines;
- conventional spectrometer remains in service and provides *independent information* about the beam energy;
- the calibration procedure for coordinate-sensitive detectors does not directly depend on particles energies;
- looks tempting the possibility to measure both energy and polarization of the beam by the same apparatus;
- use of different laser wavelengths will definitely help to control some of possible systematic uncertainties.

The weaknesses are:

- it is necessary to ensure equality of integrals of magnetic field for electrons with very different energies;
- the installation dimensions seems to be larger than one would like to have;
- three different types of coordinate detectors must work together to measure distances with high precision in absolute units.

## ACKNOWLEDGMENT

The author wants to express his gratitude to M. N. Achasov, I. A. Koop, E. B. Levichev and V. N. Zhilich for useful discussions.

## REFERENCES

[1] M.Placidi, R.Rossmanith, "$e^+e^-$ Polarimetry at LEP", Nucl. Instrum. Meth. A274 (1989) 79-94.

[2] S.Boogert et al., "Polarimeters and energy spectrometers for the ILC Beam Delivery System", JINST 4 P10015 (2009), http://iopscience.iop.org/1748-0221/4/10/P10015

[3] V.E.Blinov et al., "Review of beam energy measurements at VEPP-4M collider", Nucl. Instrum. Meth. A598 (2009) 23-30.

[4] R.Assmann et al., "Calibration of centre-of-mass energies at LEP 2 for a precise measurement of the W boson mass", Eur. Phys. J. C39 (2005) 253-292. SLD

[5] E.V.Abakumova et al., "The beam energy measurement system for the Beijing electron-positron collider", Nucl. Instrum. Meth. A659 (2011) 21-29.

[6] E.V.Abakumova et al., "Backscattering of laser radiation on ultra-relativistic electrons in transverse magnetic field: evidence of MeV-scale photon interference", Phys. Rev. Lett. 110 (2013) 140402.

[7] E.V.Abakumova et al., "A system of beam energy measurement based on the Compton backscattered laser photons for the VEPP-2000 electron-positron collider ", Nucl. Instrum. Meth. A744 (2014) 35-40.

[8] N.Muchnoi, H.J.Schreiber, M.Viti., "ILC beam energy measurement by means of laser Compton backscattering", Nucl. Instrum. Meth. A607 (2009) 340-366.



ISBN 978-3-95450-172-4

# POSSIBLE APPLICATIONS OF WAVE-BEAM INTERACTION FOR ENERGY MEASUREMENT AND OBTAINING OF POLARIZATION AT FCCee

E. Levichev, S. Nikitin*, BINP, Novosibirsk, Russia

*Abstract*

Possibility to monitor beam energy in FCCee with an accuracy of $10^{-4}$ using Compton scattering on a waveguide wave is under consideration. Methods based on interaction of a beam with circularly polarized photons for obtaining beam polarization, proposed and theoretically substantiated in the past but not yet approved anywhere, are briefly discussed in regard to parameters of FCCee.

## INTRODUCTION

The aim of the work is an attempt to imagine some new possibilities which a beam-wave interaction can impart to the FCCee project development in regard to beam energy monitoring and obtaining of spin polarization.

One of them is an application of waveguide wave for a beam energy determination by the Compton scattering.

The precision beam energy calibration with an accuracy of $10^{-6}$ using the resonant depolarization technique will be applied at FCCee in the experiment of the Z mass measurement [1]. Such calibration procedures will be conducted periodically depending on the timing cycles of obtaining and utilization of beam polarization. The gained experience of the similar experiments (see, for example, [2]) shows an acute need to continuously monitor a beam energy in the intervals between these procedures with an accuracy of at least the order of a beam energy spread. The reason for this is a long-term instability of guide field and violations of a storage ring geometry due to temperature changes and tidal effects.

Compton Back Scattering (CBS) on a relativistic electron beam in a storage ring is applied now to monitor the beam energy with an accuracy of up to a fraction of the beam energy spread which makes diffuseness of the Compton spectrum edge. In the top quark experiments the Compton scattering may be considered as a main method for beam energy determination because of growing problems [1] with obtaining spin polarization at energies >100 GeV.

Accuracy of the VEPP-4M CBS monitor of beam energy with the working laser wavelength of 10 $\mu$m amounts $2.5 \times 10^{-5}$ at the beam energy spread of $3 \times 10^{-4}$ [2]. Question of possibility to apply a similar CBS monitor at 45-175 GeV FCCee turns on the issue of the use of significantly longer wavelengths of incident waves providing a limit of scattered photon energy of the order of 5 MeV which is feasible for detecting [3]. Taking into account such limitation we should take the wavelength $\lambda > 8$ mm. Such a problem definition looks like obvious but the corresponding possibility still has not been studied.

In the past the original proposals to obtain spin polarization in storage rings of the LEP energy range using laser waves were developed at Budker Institute [4, 5]. But no experiments have been performed to approve these proposals anywhere till now. We briefly discuss them in regard to the FCC project general parameters.

## WAVEGUIDE COMPTON MONITOR OF BEAM ENERGY

### *Compton Scattering Kinematics in Waveguide Mode*

According to the Compton kinematic scheme in Figure1 a momentum $k_2$ of a scattered photon is related to an analogous parameter before scattering ($k_1$) by the equation (the useful formulae on the Compton effect are presented in [6])

$$k_2 = \frac{k_1(1 - \beta\cos\theta_1)}{1 + \frac{k_1}{E}[1 - \cos(\theta_2 - \theta_1)] - \beta\cos\theta_2}, \qquad (1)$$

where $E = m\gamma$ and $\beta$ are the initial energy and velocity of an electron. When a microwave radiation with a frequency

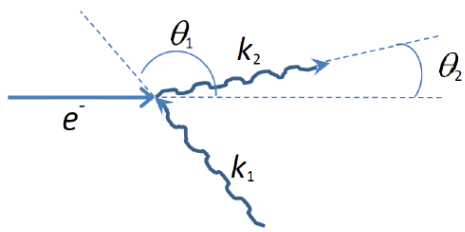


Figure 1: Kinematic scheme of Compton scattering.

$\omega = 2\pi c/\lambda$ induced in the FCC vacuum chamber propagates towards the beam one can observe the Compton Back Scattering of the corresponding photons. In the limit of very small wavelengths $\lambda << \lambda_c$ ($\lambda_c$ is a critical wavelength) the incident photons fly practically along an axis of the chamber-waveguide ($\theta_1 = \pi$) and energy of scattered photons equals to

$$\omega' \approx \frac{4\gamma^2\omega}{1 + \gamma^2/\theta_2^2}, \qquad (2)$$

or $\omega' = 4\gamma^2\omega$ at $\theta_2 = 0$. This is valid for laser beam because of its high directedness. In the general case a geometric description of Compton scattering of waveguide waves undergoes change. The easiest way to consider this change is to use the Brillouin approach based on partial plane waves (see Figure 2). Direction of the partial waves are given by the angle

* nikitins@inp.nsk.su

ISBN 978-3-95450-172-4

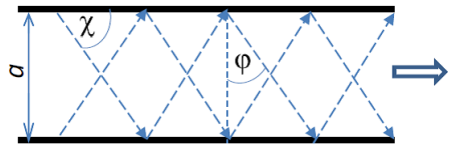


Figure 2: Geometry of partial waves in a plane waveguide.

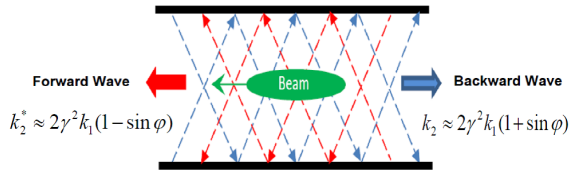


Figure 3: Scheme with the backward and forward waveguide waves.

$\chi = \chi_n$ (relative to the axis) or $\varphi = \varphi_n$ (relative to a normal to the axis) which take strictly determined values related to the type ($H_{m,q}$ or $E_{m,q}$) and the order ($n = \{m, q\}$) of the waveguide wave and corresponding critical wavelength ($\lambda_c = \lambda_c^{(n)}$):

$$\cos\chi = \sin\varphi = \frac{\lambda}{\Lambda} = \sqrt{1 - \frac{\lambda^2}{\lambda_c^2}} = \frac{c}{v_{ph}}, \qquad (3)$$

$\Lambda = \lambda v_{ph}/c$ is a waveguide mode period; $v_{ph}$ , a phase velocity in a smooth waveguide, is larger than the light speed ($v_{ph} > c$). Scattering of backward partial waveguide waves at the incident angle $\varphi$ (see Figure 2.) yields the CBS Compton spectrum edge which is shifted down according to (1) ($k_1/E << 1$) as

$$k_2 \approx 2\gamma^2 k_1(1 + \sin\varphi). \qquad (4)$$

Next, we use as a base example the wave in a round waveguide with the following parameters and features:

- $a = 4$, cm, the waveguide diameter;
- $\lambda = 5.5$ cm, the wavelength parameter of the plane waves with the frequency of 5.45 GHz;
- $\lambda_c = 3.41a/2 = 6.82$ cm, the critical wavelength for the lowest round waveguide mode - $H_{11}$;
- 5.24 cm is the critical wavelength of the next nearest mode - $E_{01}$ and, thus, the "mono-wave" condition $2.6a < 2\lambda < 3.41a$, meaning that only the lowest mode $H_{11}$ survives, is fulfilled - this is important for one-valuedness of the CBS spectrum edge determination;
- $\varphi = 36°$ so the collision angle $\theta_1 \neq 180°$ but 127°;
- CBS spectrum edge goes down regarding that in the "head on" case resulting in their ratio $k_2(\varphi)/k_2(\pi/2) = (1 + \sin\varphi)/2 = 0.795$.

Since the critical wavelength depends on the waveguide transverse size, the CBS spectrum edge also depends on it. From here one can conclude that the use of the Waveguide Compton CBS for monitoring of a beam energy with a reasonable accuracy of $10^{-4}$ is not possible without knowing the waveguide sizes of the same accuracy along the wave-beam interaction region.

## *Two Wave Scheme*

In this work we suggest to avoid the obstacle mentioned above using two waves instead of one - the backward ($\theta_1 = \pi/2 + \varphi$) and forward ($\theta_1 = \pi/2 - \varphi$) waves of the same frequency (Figure 3). The latter is excited at the opposite end of the waveguide section with respect to the backward wave (BW). The spectrum edge for the forward wave (FW) is given by a formula:

$$k_2^* \approx 2\gamma^2 k_1(1 - \sin\varphi). \qquad (5)$$

Let us introduce the ratio $R = k_2/k_2^*$. Then combining (4) and (5) we find

$$\sin\varphi = \frac{R-1}{R+1}. \qquad (6)$$

That disposes of difficulty to know exactly the waveguide sizes as the beam energy can be determined from

$$\gamma = \sqrt{\frac{k_2}{2k_1} \cdot \frac{(R+1)}{R}} = \sqrt{\frac{k_2 + k_2^*}{2k_1}}, \qquad (7)$$

where $k_1$ is known with a good accuracy by the frequency of the GHz signal source; $k_2$ and $k_2^*$ are determined owing to measurement of the gamma quanta spectrum edges in the BW and FW cases using the same detector. For the base example with the $H_{11}$ wave parameters described above the ratio $R$ amounts

$$R = \frac{1 + \sin\varphi}{1 - \sin\varphi} = 2.69, \qquad (8)$$

Sketch in Figure 4 shows a variant of the two wave scheme at FCCee basing on the straight sections where an interaction of FW and BW with the electron and positron beams occurs. The length of interaction can be limited with ceramic insertions in the vacuum chamber at the ends of sections.

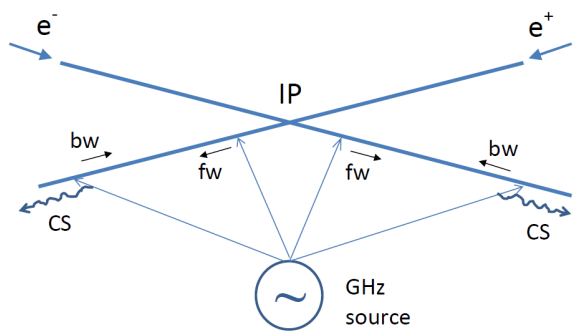


Figure 4: Scheme of organization of waveguide sections at FCCee with the Compton monitor on the backward and forward waveguide waves.



ISBN 978-3-95450-172-4

### *Monochromaticity and Effective Length of Interaction*

Beam-wave interaction region scale is determined by the requirement on the extent of inmonochromaticity. This extent can be found from the uncertainty relation for a moving sinusoid bit which characterizes a monochromaticity of the wave train at the effective interaction length $L_i$:

$$\frac{\delta\lambda}{\lambda} = \frac{\lambda}{L_i} \tag{9}$$

The effective length $L_i$ depends on a number of the wave crests intersecting a particle during its motion in the wave. Hence we obtain for the backward wave

$$L_i = 2v_{ph}\frac{L}{\beta c}. \tag{10}$$

taking into account that the partial plane waves make a longer path in the waveguide of the length $L$ as compared with the light signal directed along the waveguide axis but in a free space. Factor "2" arises due to the fact that in a time of passage of the beam in the waveguide $T$ the counter wave train forms in a length corresponding to the time $2T$. As consequence the inmonochromaticity extent in the BW case equals to

$$\frac{\delta\lambda}{\lambda} = \frac{\lambda}{2L}\sin\varphi = \frac{\lambda}{2L}\sqrt{1-\frac{\lambda^2}{\lambda_c^2}}. \tag{11}$$

At the base example parameters and the length $L = 100$ m of a straight section occupied by the waveguide the inmonochromaticity of interaction is $\delta\lambda/\lambda = 1.6\times10^{-4}$.

At the same time the analogous quantity in the FW case is expressed through the effective length

$$L_i = \left(\frac{v_{ph}}{\beta c} - 1\right)\cdot L, \tag{12}$$

and then

$$\frac{\delta\lambda}{\lambda} = \frac{\lambda}{L}\frac{\sin\varphi}{(1-\sin\varphi)}. \tag{13}$$

This gives the FW inmonochromaticity $\delta\lambda/\lambda = 7.9\times10^{-4}$ at $L = 100$ m. Assuming that $\delta\lambda/\lambda = \delta k_2/k_2$ we find the error of the energy determination from (7)

$$\frac{\delta\gamma}{\gamma} = \frac{1}{2}\frac{(\delta\lambda/\lambda)_{FW} + (\delta\lambda/\lambda)_{BW}(1+\sin\varphi)(1-\sin\varphi)^{-1}}{[1+(1+\sin\varphi)(1-\sin\varphi)^{-1}]}$$

$$+\frac{1}{2}\frac{\delta k_1}{k_1} = 1.4\times10^{-4}$$

(we suppose $\delta k_1/k_1 << \delta k_2/k_2$).

### *Relation of Scattering Angle and Monochromaticity Bandwidth*

Let us define a monochromaticity bandwidth in the spectrum of scattered photons as a quantity equal to the inmonochromaticity extent determined above in the BW case:

$$\frac{\delta\omega_s}{\omega_s} = \frac{\delta\lambda}{\lambda} \sim 10^{-4}. \tag{14}$$

Scattered photons fly in a cone at small angles $\theta \sim 1/\gamma << 1$ in accordance with the differential cross section

$$\frac{d\sigma}{d\Omega} \approx \frac{r_e^2\gamma^2}{1+\gamma^2\theta^2}. \tag{15}$$

In the interval $0 < \theta < \theta_c$ a corresponding portion of the cross section amounts

$$d\sigma_c \approx 2\pi r_e^2\gamma^2\theta_c^2.$$

The relation between the scattering angle and the photon energy is found from (1):

$$\omega_s \approx \frac{2\gamma^2\omega(1+\sin\varphi)}{1+\theta^2\gamma^2}. \tag{16}$$

Combining (14) and (16) we obtain the characteristic angle of scattering in the interval of monochromaticity $\delta\omega_s/\omega_s \sim 10^{-4}$ ($\lambda_s = 2\pi c/\omega_s$):

$$\theta_c = \sqrt{\frac{\lambda_s}{L_i}} \sim 10^{-7}. \tag{17}$$

Corresponding portion of total cross section $d\sigma_c \approx 10^{-4}2\pi r_e^2 \sim 10^{-4}\sigma_T$ where $\sigma_T = (8/3)\pi r_e^2 = 6.6\cdot10^{-25}\text{cm}^2$ is the Thomson cross section.

In the presence of quads at the waveguide section a particle trajectory is variable in direction with characteristic angular spread $\sqrt{\mathcal{E}_x/\beta_x} \sim 10^{-5}$ (in the FCCee project $\mathcal{E}_x \sim 10$ nm, the horizontal beam emittance; $\beta_x \sim 100$ m), that is much larger than the characteristic scattering angle $\theta_c \sim 10^{-7}$. Therefore, a real interaction length is determined by a mean distance between the quads $L_q < L$ where the particles move straight [7]. Waveguide section should not contain quads. The section length $L = 100$ m can be acceptable since the beta function in FCCee may be of the same scale. Also one needs to provide a magnetic shield decreasing the Earth magnetic field inside a waveguide chamber down to level of $\sim 10^{-3}$ Gs with the aim to limit a rotation angle of the beam axis to $\theta_c$ .

### *Estimate of CBS Photon Statistics*

Number of photons scattered on a moving electron at an interaction length $l$ is given as

$$dN_s = \sigma_T\cdot n_i\cdot l\cdot(1+\cos\chi). \tag{18}$$

where $\chi$ is an angle of incidence of photons to a beam; $n_i \approx W/(Sc\hbar\omega)$ is a photon density expressed through a wave power $W$, a waveguide cross section $S$ and the photon energy $\hbar\omega$ ($\approx 2\cdot10^{-5}$ eV at $\lambda = 5.5$ cm). The resulting statistics of scattered photons will be as $\delta N_s \approx 5\times10^{-7}$ photons from a single electron and $dN_s = 5\times10^4$ photons from a single bunch per a single passage in the waveguide section for the base example parameters, $L = 100$m, a bunch population $N_e = 10^{11}$, the waveguide power $W = 100$ Watt.

To measure Compton spectrum one needs to shift down the number $dN_s$ to $dN_s \le 1$ photon:

ISBN 978-3-95450-172-4

- $W < 1$ Watt;
- $N_e \leq 10^9$ a bunch population;
- $dN_s = 1$ scattered photons/bunch/passage;
- $N_b = 10^3$ a number of bunches;
- $f_0 = 3$ kHz, a revolution frequency;
- $1 \times N_b \times f_0 = 3$ MHz, a total rate of the CBS photons;
- 300 Hz is a $10^{-4}$ portion of scattered photons in the interval $d\omega_s/\omega_s \sim 10^{-4}$ at the spectrum edge.

An injection can be organized to maintain, for instance, every tenth bunch with a $10^9$ population. It allows monitoring the particle energy during an acquisition of statistics in the experiments on colliding beams In this case the useful counting rate of the CBS photons will be 300 kHz.

### *Background Conditions*

Compton scattering on thermal radiation photons ($trp$) [8] can be a source of background for the Waveguide Compton beam energy monitor at FCCee. Let us base on the estimates made for LEP and experimentally approved. At $E = 50$ GeV and 300 K, the room temperature, the main parameters of the thermal radiation photons are as following: $n_{trp} = 5.45 \times 10^8$ cm$^{-3}$, the trp density; $\bar{\omega}_{trp} = 0.07$ eV, the characteristic $trp$ energy; $x = 4E\bar{\omega}_{trp}/m^2 = 0.055$, the interaction parameter; $xE = 2.75$ GeV, the scattered photon energy. The large energy loss $\Delta E/E = x = 5.5\%$ means that a knockout of electron from a beam is unavoidable. The corresponding beam lifetime makes up $\tau_{trp} = 92000$ s $\sim 10^5$ s. Applying these characteristics for the case of Waveguide Compton monitor at the 50 GeV FCCee ($N_e = 10^9$, $f_0 = 3$ kHz, $L = 100$ m) we obtain :

- $\delta N_{trp} = \frac{N_e}{\tau_{trp}} \frac{L}{c} = 0.003$ photons from a single bunch with $N_e = 10^9$ per a single passage;
- $\frac{\delta N_{trp}}{dt} = \delta N_{trp} \frac{N_b f_0}{10} \approx 1$ kHz a background counting rate due to trp when using an every tenth bunch for CBS monitoring.

The $trp$ background for the proposed conditions (1kHz) is much less than the rate of useful events (300 kHz). For comparison: the VEPP-4M CBS monitor yields 10 kHz taking $5 \times 10^6$ events in 10 min providing an accuracy $5 \times 10^{-5}$. According to the Telnov's calculation for LEP at energies $E \geq 50$ GeV the beam lifetime due to $trp$ and that due to Bremsstrahlung are of the same order at the typical average residual gas pressure $\sim 10^{-9}$ Torr. All this suggests that the eficiency of the Waveguide Compton monitor of beam energy at FCCee can be fairly high.

## LASER METHODS FOR OBTAINING BEAM POLARIZATION

In the framework of the FCCee project the polarized beams are needed, in particular, for precise measurement of the beam energy using the resonant depolrization technique in the experiment on Z- mass measurement. Sokolov-Ternov polarization time in the 80 km FCCee ring is very large: $\tau_0 \approx 150$ h at 45.6 GeV. It makes the task of obtaining polarization directly in Main Ring or in Injector Ring rather difficult. In [4, 5] two methods using interaction of beam with circularly polarized photons were proposed and theoretically substantiated to obtain polarization in e+e- storage rings in the cases when other methods are ineffective :

- "Soft Photons" ($\chi = 2\gamma\hbar\omega/m << 1$, $c = 1$) is based on multiple scattering of electrons in the wave field. There is no output of scattering particles from a beam. Principle role belongs to a special spin-orbital coupling created in the region if beam-wave interaction (IR), for instance, with a solenoid of a fixed field integral (11 kGs·m regardless the beam energy);
- "Hard Photons" ($\chi = 2\gamma\hbar\omega/m >> 1$) consists in dominating knock-out of electrons of one of helicity signs from a beam. It requires an organization of equilibrium longitudinal direction of polarization in the wave-beam interaction region.

The authors of [4, 5] noted that the usual quantum lasers can be applied in certain cases. In the long term wider possibilities would be realized using Free Electron Lasers.

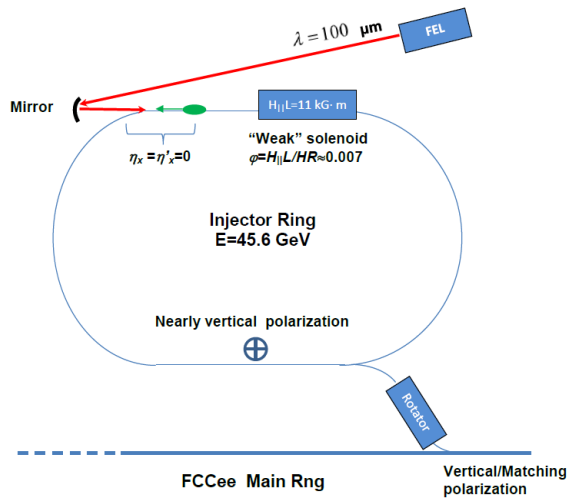


Figure 5: The possible variant of Soft Photon scheme for FCCee. At the interacion region the condition of zero dispersion ($\eta_x = \eta'_x = 0$) should be fulfilled to minimize an increase of transverse beam sizes.

The Soft Photon polarizing mechanism is based on indirect action of a field of radiation on a spin - through a perturbation of particle trajectory due to a change in energy. This is called the "spin-orbit coupling" and takes into account the effect of variation in a particle momentum on a precession axis $\vec{n}$. The variant of the Soft Photon scheme is shown in Figure 5. According to [4, 5] the scheme provides in IR the optimal spin-orbit coupling $\gamma\partial\vec{n}/\partial\gamma = \sqrt{10/7}\vec{\beta}$ and the direction of polarization axis transverse in regard to a particle velocity (the unit vector $\vec{\beta}$): $\vec{n} \cdot \vec{\beta} \approx 0$. It is assumed that polarization occurs at the spin precession frequency paramerer close to half integer values ($\nu = \gamma a \approx 103.5$ at $E = 45.6$ GeV). We have made the preliminary estimates for FCCee which show that Soft Photons using a 100 $\mu$m FEL with reasonable parameters can speed up notably the polarization process at 50 GeV. For instance, the polarization



ISBN 978-3-95450-172-4

time can be made as $A = 26$ times lower than that due to synchrotron radiation in bending magnets. At the same time such a method fundamentally results in significant increase of the beam energy spread: by a factor of $\sqrt{1 + (63/110) \cdot A}$ times (= 4 at $A = 26$). In this relation the Soft Photons competes poorly with the usual method using a set of strong wigglers with a non-zero average cube of field which can provide a tenfold speed up of polarization doubling the energy spread [9]. Nevertheless, in contrast to the wiggler method, the Soft Photons allows polarization of a beam without noticeable energy consumption in the RF cavities. This follows from the fact that an increase of particle energy diffusion rate in the wave field leading to speeding up of the polarization process is owing not to an increase of field intensity but rather to an increase of radiation hardness.

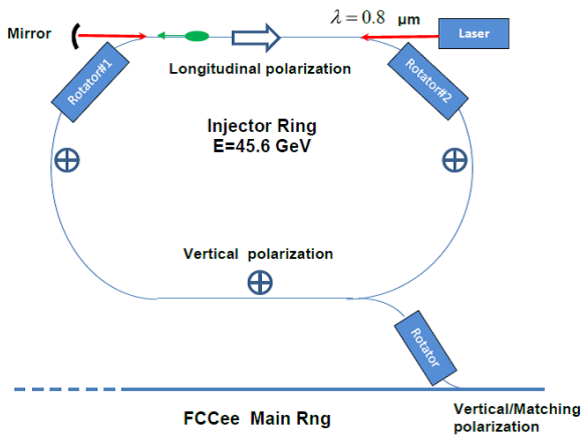


Figure 6: The variant of Hard Photon scheme for FCCee.

Another method, Hard Photons, does not increase a beam energy spread. The possible variant of Hard Photon scheme is presented in Figure 6. In the region of interaction of a cirularly polarized laser beam with electrons the precession axis must lie along the particle velocity. It should be organized in the scheme with localization of longitudinal polarization using the spin rotators. The polarization anywhere outside IR remains vertical. It allows to minimize depolarization effects due to SR in the bending magnets.

Time to reach an extent of beam polarization $\eta$ is given by an equation [4, 5]

$$\tau_w = |\dot{N}_w \zeta (\sigma_\uparrow - \sigma_\downarrow)|^{-1} \ln \frac{1+\eta}{1-\eta}, \qquad (19)$$

with $\dot{N}_w$ , an average photon fluence density ($\mathrm{cm}^{-2}\cdot\mathrm{s}^{-1}$);

$$|\sigma_\uparrow - \sigma_\downarrow| = 4\pi r_e^2 \left[ \frac{1+\chi}{2\chi^2} \ln(1+2\chi) - \frac{1+4\chi+5\chi^2}{\chi(1+2\chi)} \right], \qquad (20)$$

a difference of the cross sections for electrons with opposite signs of helicity; $\zeta$, a circular polarization extent of photons. The quantity $|\sigma_\uparrow - \sigma_\downarrow|$ characterizes a dependence of the method efficiency in regard to polarization rate on the laser wavelength chosen. In the limit of large photon energies ($\chi \to \infty$) one can obtain a full polarization ($\eta \to 1$) at the cost of losing half of the particles : $N/N_0 \to 1/2$. At that the time of polarization in the wave grows as $\tau_w \propto \chi \ln \chi$ [4, 5]. Thereby, a wish to obtain the polarization close to unity and to keep more of the beam population contradicts a wish to make the polarization process shorter in time.

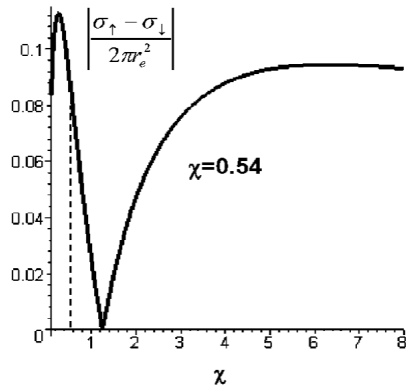


Figure 7: Hard Photon efficiency vs the interaction parameter. The specified value of this parameter is given for $\lambda = 0.8$ $\mu$m at $E = 45.6$ GeV.

Practically, the extent of polarization $\eta \approx 10\%$ is still enough for the precise beam energy calibration by the resonant depolarization technique because of a high efficiency of the laser polarimeter in the FCCee energy range [9]. By this reason one would choose the working wavelength corresponding to not very high values of the $\chi$ parameter. For instance, the wavelength $\lambda = 0.8$ $\mu$m, typical for the Ti:Al203 lasers, corresponds to $\chi = 0.54$ at $E = 45.6$ GeV. Thus the Hard Photon efficiency is close to an optimal one (see Figure7).

An optimal focusing of the laser beams with the help of mirrors and a proper choice of the laser pulse duration in both methods imply that the laser and electron beams are similar in sizes. Examples of the required power and timing performances of the free electron lasers are given in the original papers [4, 5] as applied to the LEP project. The FCCee project is different in regard to its size and the number of bunches. To be competitive the methods basing on the beam-wave interactions should provide the polarization time of about ten minutes or less.

## SUMMARY

- Possibility to apply the Compton scattering of a waveguide wave to measure a beam energy in the FCCee has been considered for the first time. The two wave concept of the Waveguide Compton beam energy monitor has been proposed allowing to diminish uncertainties related to variation of the waveguide transverse sizes. Preliminarily, the method looks promising because provides a reasonable accuracy with high registration efficiency at low wave power.
- One needs to search and consider the competitive schemes to realize the known ideas on application of

ISBN 978-3-95450-172-4

the incident circularly polarized waves for obtaining beam polarization at FCCee.

## ACKNOWLEDGMENT

The authors are grateful to N.Vinokurov, I.Koop, G.Kurkin, N.Muchnoi, V.Telnov and G.Tumaikin for discussions.

## REFERENCES

[1] I. Koop, Talk at this ICFA Workshop.

[2] V.E. Blinov et al., NIM(A) 598 (2009) 23.

[3] N. Muchnoi, private communication.

[4] Ya.S. Derbenev, A.M. Kondratenko, E.L. Saldin, NIM(A) 165 (1979) 15.

[5] Ya.S. Derbenev, A.M. Kondratenko, E.L. Saldin, NIM(A) 165 (1979) 201.

[6] I.F. Ginzburg et al., NIM 205 (1983) 47, 219 (1984) 5.

[7] N. Vinokurov. private communication.

[8] V.I. Telnov, NIM(A) 260 (1987) 304.

[9] A.Blondel, Presentation at TLEP-6 Polarization 2013-10-17.



ISBN 978-3-95450-172-4

# LESSONS LEARNED FROM THE B-FACTORIES AND IMPLICATIONS FOR A HIGH-LUMINOSITY CIRCULAR e+e- HIGGS FACTORY

Y. Funakoshi
KEK, High Energy Accelerator Organization, Oho 1-1, Tsukuba, Ibaraki 305-0801, Japan

*Abstract*

Experiences on the electron clouds, optics corrections, an orbit feedback at IP and luminosity tuning at KEKB are described. An emphasis is placed on the beam instrumentations and the beam control.

## INTRODUCTION

KEKB [1] is an energy-asymmetric double-ring collider for B meson physics. KEKB consists of an 8-GeV electron ring (the high energy ring: HER), a 3.5-GeV positron ring (the low energy ring: LER) and their injector, which is a linac-complex providing the rings with both of the electron and positron beams. The construction of KEKB started in 1994, utilizing the existing tunnel of TRISTAN, a 30 GeV $\times$ 30 GeV electron-positron collider. The machine commissioning of KEKB started in December 1998. The physics experiment with the physics detector named Belle was started in June 1999. The peak luminosity surpassed the design value of $1.0 \times 10^{34}\mathrm{cm}^{-2}\mathrm{s}^{-1}$ in May 2003. The maximum peak luminosity of KEKB is $2.11 \times 10^{34}\mathrm{cm}^{-2}\mathrm{s}^{-1}$, which was recorded in June 2009. This value has been the world-record since then. The KEKB operation was terminated at the end of June 2010 for the works to upgrade KEKB to SuperKEKB. The commissioning of SuperKEKB is expected to start in autumn in 2015. The total integrated luminosity collected by the Belle detector was 1041 $\mathrm{fb}^{-1}$. The history of KEKB is shown in Figure 1. In this report, some experiences at KEKB are described. An emphasis is places on the beam instrumentation and the beam control. Some of them may be useful in future colliders such as a high-luminosity circular e+e- Higgs factory. Achievements of KEKB and details of commissioning are described elsewhere [2] [3].

## ELECTRON CLOUDS

A beam size enlargement depending on the beam current in the LER has given one of the most serious luminosity restrictions to KEKB. This type of beam-blowup was not considered in the design phase of KEKB. It turned out that the cause of the blowup is the electron clouds. Although the electron clouds are formed by the bunch train, the blowup is induced by a single bunch instability. The mechanism of this blowup has been studied theoretically by F. Zimmermann and K. Ohmi. They showed by simulations that the blowup can be explained by a fast head-tail instability caused by wake fields by the passage of the bunch particles though the electron clouds [4]. This explanation has been experimentally confirmed by observing vertical betatron sideband due to the electron clouds at KEKB LER [5]. Figure 2 shows a typical results of the sideband measurements. More detailed explanations and an experimental setup for this measurement are described in [5].

To suppress this instability, solenoid coils have been wound around approximately 95% of the drift space in the LER ring with a maximum field at the center of the beam pipe of ~60 Gauss [6]. Although the solenoids drastically improved the luminosity, performance of KEKB was still affected by the effects of electron clouds with a higher beam current of the LER than about 1.6 A. The luminosity of KEKB did not increase with a higher LER beam current than about 1.6 A. It is believed that this is due to the effects of electron clouds. For this reason, the operation beam current in LER of 1.6 A is much lower than the design beam current, 2.6 A. Another impact of the electron clouds to the beam operation at KEKB is the choice of bunch spacing. In the design, the bunch spacing is one RF bucket, which means that every RF bucket is filled with beam particles. However, in the actual operation, the bunch spacing is approximately 3 RF buckets. With shorter bunch spacing, the specific luminosity lowered. This restriction to bunch spacing is also believed to come from the effects of the electron clouds. Figure 3 shows a result of an experiment on bunch spacing carried out on March 21st 2008. For the experiment, a special filling pattern was used. In the beam filling pattern of KEKB, the same pattern should be repeated every 49 RF-buckets to be compatible with the two bunch injection. Due to the synchronization problem between the injector linac and the KEKB rings, only the two bunches in 49 RF-buckets in the rings can be injected from linac to the rings. In the filling pattern used in the experiment, 17 RF-buckets out of 49 RF-buckets were filled with the beam and the same patterns repeated 99 times. Most of bunch spacing between adjacent bunches was 3 RF-buckets but only 2 bunches out of 17 bunches in a unit of 49 RF-buckets followed the preceding bunches at a distance of 2 RF-buckets. In Fig. 3, the specific luminosity per bunch is plotted as function of bunch ID in a unit of 49 RF-buckets. Note that the specific luminosity of each bunch ID in the figure is the average of 99 bunches in the equivalent position in the units of 49 RF-buckets. The error bars in the graph show the standard deviations of the 99 bunches. As is seen in the figure, the specific luminosity after 2 RF-buckets is ~15 % lower than that of the other bunches. It is believed that this degradation in the specific luminosity comes from the effects of the electron clouds. In the case of short bunch trains, this degradation was not observed and then we can deny the possibility that the degradation in the specific luminosity after short bunch spacing is caused by the effects of the parasitic collisions.

Another instrument for the electron clouds measurement used at KEKB is an retarding field analyzer (RFA) [7]. A

ISBN 978-3-95450-172-4

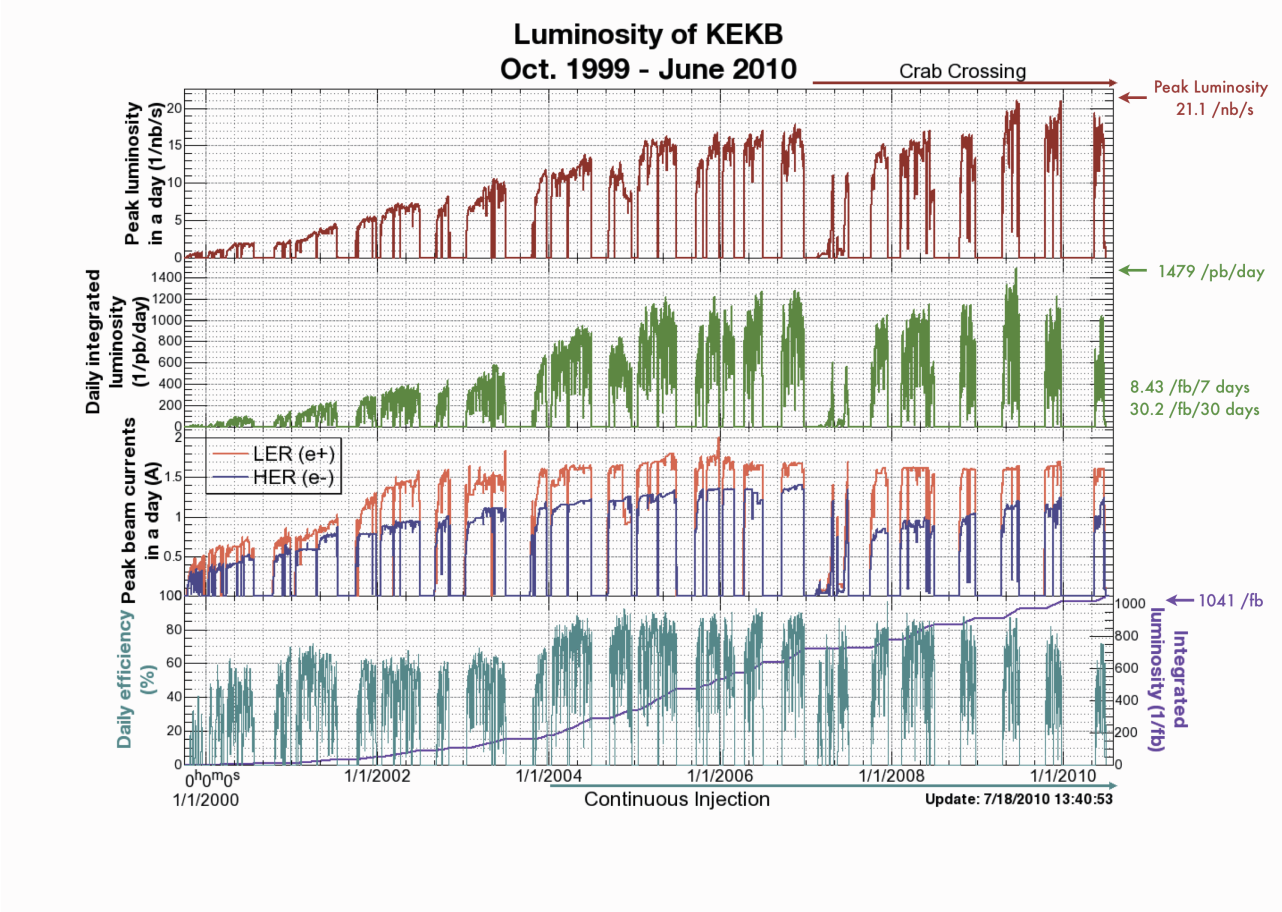


Figure 1: History of the performance of KEKB from October 1999 until June 2010. The rows represent (top to bottom) the peak luminosity in a day, the daily integrated luminosity, the peak stored currents in the LER and HER in a day, the daily efficiency, and the total integrated luminosity at Belle, respectively. The integrated luminosities are the numbers recorded by Belle. The daily efficiency is defined as (Daily integrated luminosity)/(Peak luminosity times 1 day), and was boosted in January 2004 by the Continuous Injection Mode. The crab crossing scheme has been in use since February 2007.

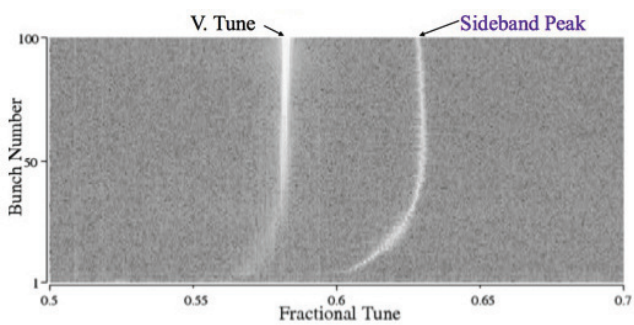


Figure 2: The horizontal axis is the fractional tune, from 0.5 on the left edge to 0.7 on the right edge. The vertical axis is the bunch number in the train, from 1 on the bottom edge to 100 on the top edge. The bunches in the train are spaced 4-rf buckets (about 8 ns) apart. There are two peaks corresponding to the vertical tune and the sideband beak.

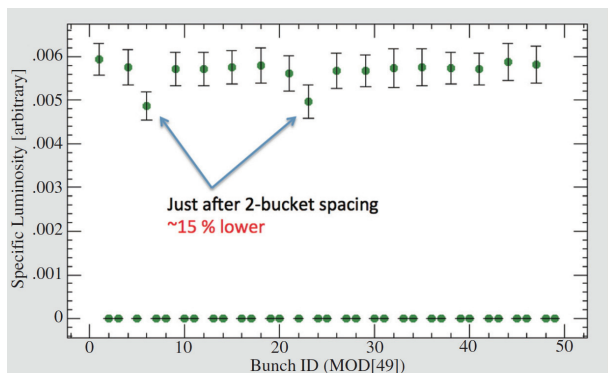


Figure 3: Specific luminosity per bunch depending on the bunch position in the unit 49 RF-buckets. Each datum is the average of 99 bunches in the equivalent position in the unit 49 RF-buckets and the error bars are the standard deviations of the 99 bunches.



ISBN 978-3-95450-172-4

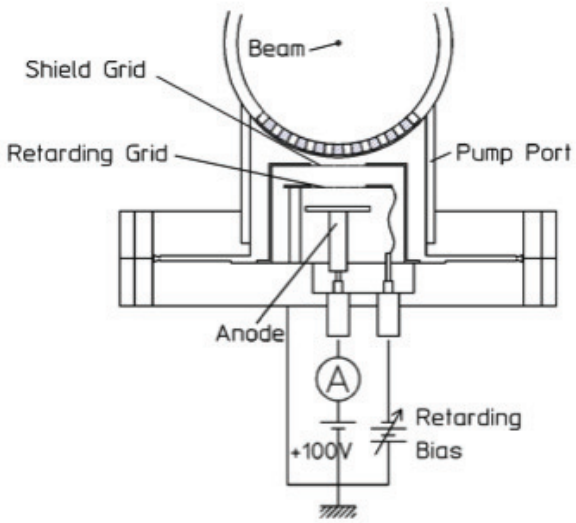


Figure 4: Conceptual drawing of the RFA monitor.

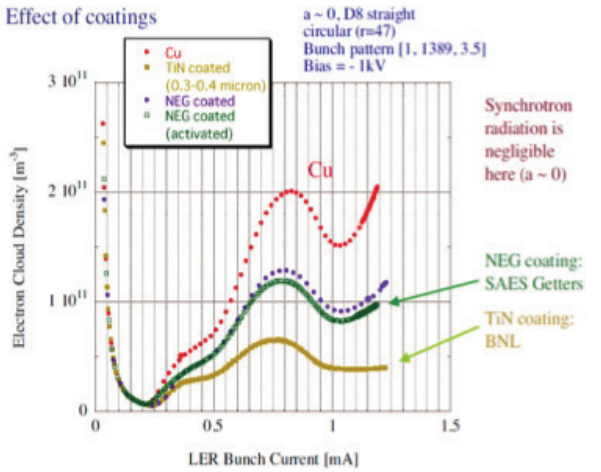


Figure 5: Typical result of the electron clouds density measurement using the RFA monitor.

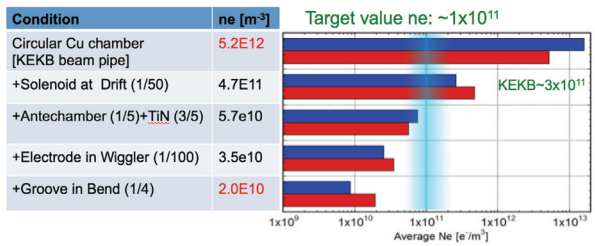


Figure 6: Effectiveness of countermeasures for suppressing the effects of the electron clouds at SuperKEKB. The data in blue and red are those from simulations and the measurements using the RFA monitor, respectively.

conceptual drawing of the monitor is shown in Fig. 4. This monitor has been used for measuring electron cloud density in KEKB LER using various materials for R&D's. A typical result of the measurements is shown in Fig. 5. In this experiment, the electron cloud density was measured in three conditions, *i.e.* a bare circular Cu chamber, the chamber with a NEG coating and with a TiN coating. The beam fill pattern was a single train, 1389 bunches and 3.5 RF-bucket spacing. The bias (retarding) voltage of RFA was set to -1 kV. As is seen in the figure, the electron clouds density is reduced by a factor 3 ~ 5 by TiN coating. In SuperKEKB we will adopt ante-chambers with the TiN coating. The chambers with other countermeasures for SuperKEKB such as electron cloud clearing electrodes for the wiggler sections and grooved chambers in bending sections are tested with the RFA monitor. Figure 6 summarizes effectiveness of countermeasures for the electron clouds [8]. The data bars in blue and red are those from simulations and the measurements using the RFA monitor, respectively. The consistency between the measurements and the simulations is not so bad. With bare circular Cu beam pipes, an expected average density of the electron clouds is $\sim 3 \times 10^{11}$electrons $m^{-3}$. With all of countermeasures in Fig. 6, the expected electron cloud density will be reduced down to $\sim 2 \times 10^{10}$electrons $m^{-3}$. This value is about 1/5 of the target density of $\sim 1 \times 10^{11}$electrons $m^{-3}$ and seems to be well below the threshold of the instabilities due to the electron clouds.

### *Summary of Experiences with Electron Clouds at KEKB*

The electron clouds at LER of KEKB gave serious effects on the KEKB performance. Winding solenoid coils in the drift space in the ring was effective to suppress the effects, although there remained some effects even after almost all drift spaces were covered with the solenoid fields. To analyze phenomena, bunch-by-bunch measurement systems such as the bunch-by-bunch BPM and the bunch-by-bunch luminosity monitor have been important. A RFA monitor has been used to measure electron cloud density and the data was very helpful to design the vacuum system for SuperKEKB.

## BPMS AND OPTICS CORRECTIONS

### *BPMs*

At KEKB, every quadrupole magnet is equipped with a BPM and the number of BPMs is about 450 for each ring for measuring the closed-orbit distortion (COD) [9]. In order to avoid picking up the RF leakage from the highpower RF system, the 1 GHz (twice the RF frequency) component of the beam-induced button signal is detected by a spectrum analysis method using a digital signal processor (DSP). The effective bandwidth of the signal detection is widely programmable, and it is easy to optimize the measuring time and the accuracy for the various operation modes of the accelerator. The CODs of both rings are continuously measured every 2~3 s and corrected every 20~30 s based on the BPM data to suppress any orbit drift appearing in both rings.

ISBN 978-3-95450-172-4

A typical resolution of the COD measurement at 30 mA is a few $\mu$m.

To ensure the reliability of an orbit measurement, the center offset of each BPM relative to the quadrupole nearby was corrected by a beam-based alignment. In addition, BPMs near sextuploles have capacitive sensors to measure relative transverse position of BPMs to the sextupoles and the measured values were automatically applied as offsets to the BPM readings. Another important beam based diagnostics for BPMs is gain mapping of BPM electrodes [10]. By using beams, calibration was done to find the relative gains of all KEKB BPM heads. With this BPM gain mapping, the consistency of BPM measurement was drastically improved. Each BPM has four electrodes and the BPM consistency is defined as an rms value of four beam position data using four different sets of combinations of three electrodes. We needed to do this gain mapping for all BPMs typically every month.

At KEKB, 38 turn-by-turn BPMs were used. The monitor heads are common to the BPMs for COD measurement and the electronics were switched for turn-by-turn measurements. The turn-by-turn BPMs were not used for routine operation but for the orbit measurement before beam storage after a long shutdown and for the beam studies such as a x-y coupling measurements.

### *Optics Correction*

The optics correction is the basis of the machine operation [12]. Typically every two weeks after a regular maintenance time, we did the optics corrections. At KEKB, the optics corrections of the x-y coupling, the dispersion and beta-beating around the each ring were done. Since there are not many turn-by-turn BPMS at KEKB, the corrections were done by measuring COD using the BPMS. A loop of corrections for the x-y coupling, the dispersion and the beat-beating took 30~60 minutes per ring to converge. Each correction took 3.5 to 7 minutes. With this method, we do not have to solve the entire problem at once by a single big matrix. Although these corrections are not independent, their cross-talks are smaller than the diagonal parts, so the iteration converged quickly. The optics corrections gave a basis of the luminosity tuning shown below.

As for the slow ground deformation, a relatively large subsidence has been observed at KEKB as shown in Fig. 7. A cumulative amount of the tunnel deformation of the South arc section amounted to 25mm. Although there are a couple of speculations as to why the South arc section continues to sink, there has not been any clear explanation determined yet. In the construction period of KEKB (1998), all magnets were aligned on a horizontal plane. The vertical positions of the magnets have been changing according to the tunnel deformation. However, almost no degradation of performance has been observed with the position shifts of the magnets owing to the optics corrections developed at KEKB and the best luminosity of KEKB was achieved with the deformed ground. A simulation confirmed that the effects of the alignment errors which are slower than the betatron wave length are small.

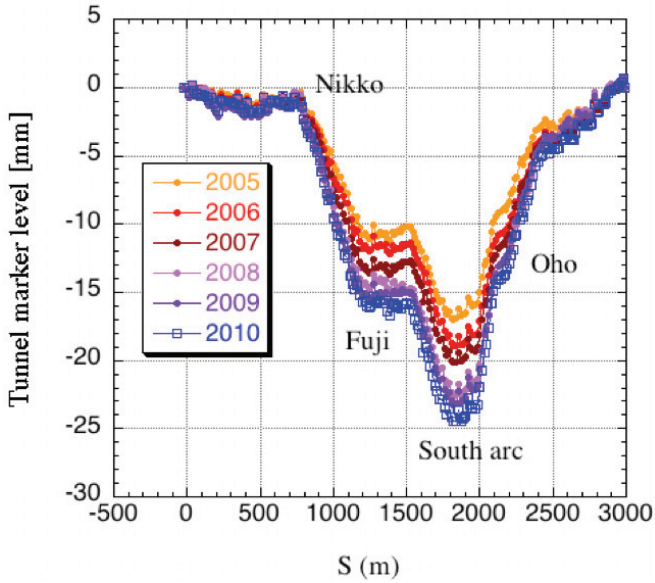


Figure 7: Tunnel level marker height with respect to that at the interaction point over years.

### *Day Night Difference of Luminosity*

In the process of increasing the luminosity, we encountered a peculiar problem. This problem became first conspicuous in March 2003. The problem has the following features. 1) The luminosity degrades in the daytime. The difference in the luminosity between day and night is about 20 % at the worst. 2) The difference seems to depend on the temperature difference between day and night. The difference is not remarkable in winter or on a rainy day. 3) When the luminosity drops in the daytime, the HER beam blowup *is observed. Tuning on the x-y coupling parameters at IP is* somewhat effective to mitigate the luminosity drop, although its effectiveness is insufficient. A lot of efforts have been devoted in vain to solve the problem. Eventually, we found that the BPM consistency also shows the day-night difference. The consistency is defined as the standard deviation of four BPM readings by using four different combinations of BPM electrodes (choice of three electrodes out of four). Orbit corrections based on changing BPM offsets bring optics deformation and may result in the luminosity degradation. The mechanism that we found is that a part of BPM cables goes through the outside of buildings and is affected by the day-night temperature change. To solve the problem, we installed thermal insulator sheets to the BPM cables in the outside. An example of the thermal insulator sheets is shown in Fig. 8. After the installation, the day-night change of the BPM consistency error decreased by 30 or 50 % and the day-night difference in the luminosity became almost invisible.



ISBN 978-3-95450-172-4

Figure 8: A thermal insulator sheet for BPM cables installed near the local control building (LC4).

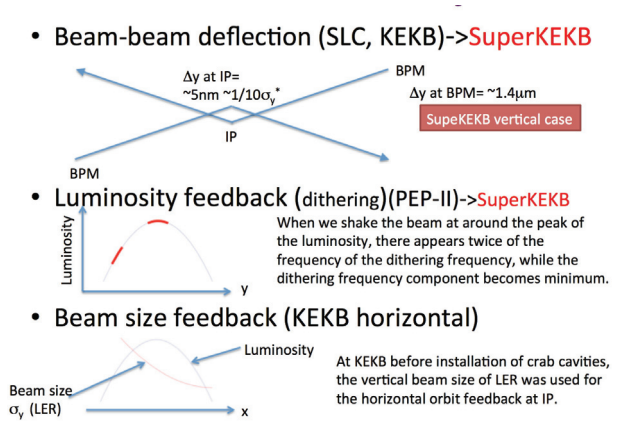


Figure 9: Three algorisms for orbit feedback at IP.

### *Summary of Experiences on Optics Corrections Based on COD Measurement.*

At KEKB, the optics corrections were done based on the COD measurement, since KEKB did not have many turn-by-turn BPMs. In the following, some experiences on the optics corrections are summarized.

- Global COD correction was done continuously every 20 seconds.
- Optics corrections were done every 2 weeks.
- Method of iteration of x-y coupling, dispersions and $\beta$-beating was used.
- The methods worked very well even with the large tunnel deformation based on BPM measurements.
- However, when the BPMs give the incorrect values, the luminosity tuning has a trouble such as the day-night problem which KEKB encountered.
- It seems that the BPM gain mapping and Quad-BPM tuning are very important at high luminosity machines.

## COLLISION FEEDBACK

In double ring colliders such as KEKB, we have to solve some special problems which we never encountered in conventional single ring colliders. One such critical problem is how to maintain optimum beam collision conditions. For this purpose, we have developed a special system which manipulates beam orbits around the IP [13]. As is schematically shown in Fig.9, there are three possible ways to maintain optimum beam collision condition, *i.e.* a beam-beam deflection method, the luminosity dithering method and the method relying on the beam size measurement [13]. Of these algorisms, KEKB mainly used the beam-beam deflection method. As is shown in Fig.10, a set of 4 QCS BPMs (A,B,C and D) or another set of 2 OctoPos BPMs (E and F) gives sufficient information to the feedback system. In

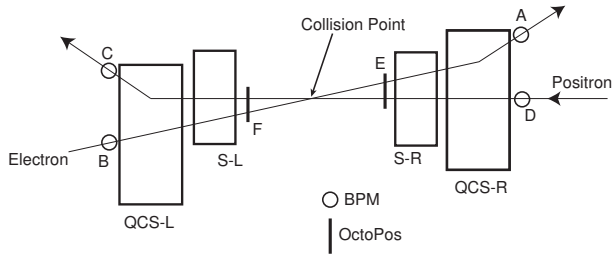


Figure 10: Schematic view of BPM configuration. Tow of six BPMs (E and F) are special BPMs called “OctoPos". The OctoPos BPMs are located closer to the IP than the other usual BPMs. They have 8 electrodes and can measure orbits of the two beams simultaneously.

actual beam operation, we usually use the set of 4 regular BPMs, since the beam current dependence in the orbit measurements is larger with the set of OctoPos BPMs than with the regular BPMs. The orbit feedback system around IP at KEKB worked by making orbit bumps so as to reduce orbit offsets at IP which are measured using the BPMs. The speed of the feedback is ~ 1/4Hz. The resolution of the BPMs is ~ 2$\mu$m.

Figure 11 shows a typical behavior of the orbit feedback system. In the figure, plotted is the history of the vertical bump amplitude at the IP created by the orbit feedback system for two hours. During this period, the machine condition was very stable and the luminosity was kept almost constant owing to the orbit feedback system. The beam currents were also kept almost constant thanks to the continuous beam injection mode. The period was not special one but was chosen rather randomly on the condition that the machine status is stable. The change of the vertical offset during this period is much larger than the vertical beam size. This means that the vertical offset at the IP would largely change in a short time without the feedback. The amount of the offset change is unexpectedly large. Some part of the offset change may be created by the CCC (Continuous Closed orbit Correction) system. Therefore, the orbit feedback system is vital for KEKB.



ISBN 978-3-95450-172-4

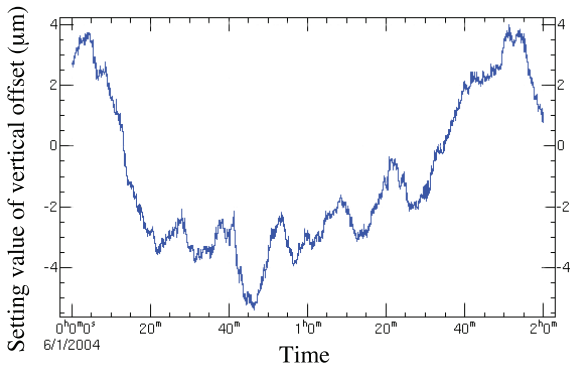


Figure 11: History of the vertical bump amplitude at the IP.

### *Some Experiences of IP Orbit Feedback at KEKB*

In the following, some experiences with the IP orbit feedback system at KEKB are summarized.

- In double ring colliders such as KEKB, an orbit feedback system for maintaining the beam orbits around IP is vital. Without such a system, we cannot maintain the luminosity even for a short period.
- With the system based on BPM measurement, we could prevent luminosity loss due to orbit change almost completely.
- One of the problems with the system was the stability of the target values (feedback points) of the feedback.
  - To trace their changes, we frequently (typically once an 8-hour shift) had to do the target scan for optimum values.
  - The origin of the target change was thought to be mechanical movement of the BPMs or the QCS magnets.
  - We experienced that the target changes greatly after beam aborts.
  - Our observations have shown that heating of vacuum chambers brings sizable mechanical movement of the vacuum chamber and BPMs (and even of the quadrupole magnets).
  - Countermeasures for this problem was reinforcement of the cooling power of the IR vacuum chambers, displacement sensors for BPMs, introduction of continuous beam injection scheme.

## LUMINOSITY TUNING

There are a number of knobs to tune up the luminosity. Only a few of them can be tuned up with independent observables besides the luminosity. Table 1 lists the tuning parameters and its observables. Tuning parameters related to the crab cavities are not listed in the table. We found that the liner optics correction is important for suppressing the beam-beam blowup. In usual beam operation, we frequently (typically every 2 weeks) made optics corrections where we corrected global beta functions, x-y coupling parameters and dispersions [6]. Sometimes, the optics corrections were done with a different set of strength of the sextupole magnets to narrow the stop-band of the resonance ($2\nu_x + \nu_s$ = integer) or ($2\nu_x + 2\nu_s$ = integer). The optics correction is the basis of the luminosity tuning. On this basis, we carry out tuning on the other parameters in Table 1. At KEKB, we found that the local x-y coupling and the vertical dispersion at IP are very important for increasing the luminosity. We have developed tuning knobs to adjust those parameters. In the conventional method of tuning at KEKB, most of these parameters (except for the parameters optimized by observing their own observables) were scanned one by one just observing the luminosity and the beam sizes. As a more efficient method of the parameter search, we introduced in autumn 2007 the downhill simplex method for twelve parameters of the x-y coupling parameters at IP and the vertical dispersions at IP and their slopes, which are very important for the luminosity tuning from the experience of the KEKB operation. These twelve parameters can be searched at the same time in this method. We have been using this method since then. However, even with this method an achievable specific luminosity has not been improved, although the speed of the parameter search seems to be rather improved.

For the luminosity tuning, only the luminosity monitor [14] and the beam size monitor based on the SR interferometer [11] are used and so these monitors are particularly important at KEKB. Also, the continuous injection scheme (top-up injection) made the luminosity tuning easier through more stable beam conditions [3]. With the scheme, the beam currents were almost constant and heating effects by the beams were saturated at some points. Generally speaking, a machine has a tendency that its operation becomes more stable with operation conditions unchanged. As an example in the KEKB operation, in the conventional injection scheme we used different working points during the injection and the physics run and the beam abort sometimes occurred in changing the tunes due to wrong setting of the tunes. We can avoid this problem with the continuous injection. Of course, the direct motivation of the continuous injection was to increase the integrated luminosity. Roughly speaking, the gain of the continuous injection in the integrated luminosity was about 30%. One third of it came from elimination of the loss time, while two third from keeping the maximum beam currents. We started the beam operation with the continuous injection scheme in the middle of January 2004. Since then, this scheme has been very successfully applied to the KEKB operation and has brought an enormous gain in the integrated luminosity to Belle. In Table 2, we show a comparison of luminosity performance before and after the continuous injection. For comparison, we took two shifts that were stable and gave record integrated luminosities. The beam operations of the two shifts are shown in Fig. 12 and Fig.13.



ISBN 978-3-95450-172-4

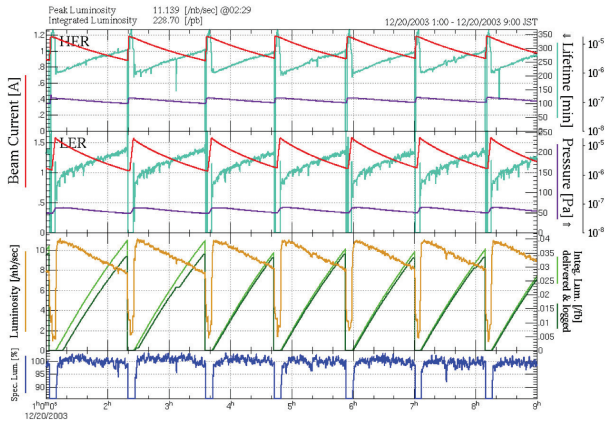


Figure 12: Beam currents and luminosity trend before continuous injection.

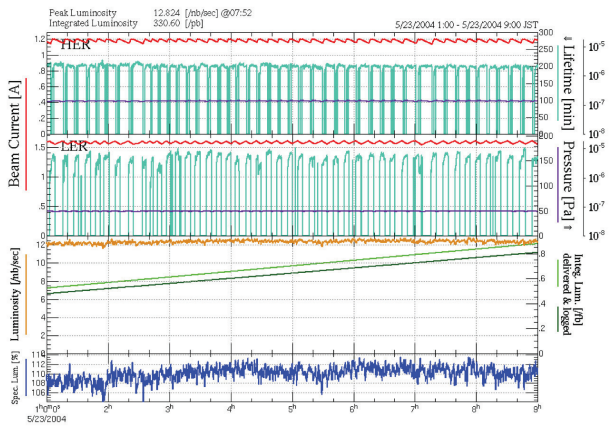


Figure 13: Beam currents and luminosity trend after continuous injection.

### *Some Experiences of Luminosity Tuning at KEKB*

In the following, some experiences of luminosity tuning at KEKB are summarized.

- The KEKB luminosity has been increased by many and continuous parameter scans.
  - The machine operators did almost always (even in physics run) parameter scans. (scan, scan, scan...)
  - An introduction of downhill simplex method for the parameter search speeded up the parameter search. However, the achievable luminosity was not increased with this method.
- Most of the luminosity tuning used the luminosity monitors and the beam size monitor (SR interferometer) as observables. Reliability of those monitors were important.
- The continuous injection scheme (top-up injection) made the luminosity tuning easier through more stable beam conditions.

## REFERENCES

[1] KEKB B-Factory Design Report, KEK-Report 95-7, 1995.

[2] T. Abe et al., Prog. Theor. Exp. Phys. (2013) 2013 (3), 03A001.

[3] T. Abe et al., Prog. Theor. Exp. Phys. (2013) 2013 (3), 03A010.

[4] K. Ohmi and F. Zimmermann, Phys. Rev. Lett. 85, 3821 (2000).

[5] J W. Flanagan et al., Phys. Rev. Lett. 94, 054801 (2005).

[6] K. Akai et al., Nucl. Instrum. Methods A 499, 191 (2003).

[7] K. Kanazawa et al., Prog. Theor. Exp. Phys. (2013) 2013 (3), 03A005.

[8] T. Abe et al., SuperKEKB design report to be published in KEK report.

[9] M. Arinaga et al., Prog. Theor. Exp. Phys. (2013) 2013 (3), 03A007.

[10] K. Satoh and M. Tejima, Proc.PAC 97, Vancouver, B.C., Canada, pp. 2087 (1997).

[11] M. Arinaga et al., Nucl. Instrum. Methods Phys. Res., Sect. A 499, 100 (2003).

[12] H. Koiso et al., Prog. Theor. Exp. Phys. (2013) 2013 (3), 03A0019.

[13] Y. Funakoshi et al., Phys. Rev. ST AB, 10, 101001 (2007).

[14] V. Zhilich, Nucl. Instrum. Methods Phys. Res., Sect. A 494, 63 (2002).



ISBN 978-3-95450-172-4

Table 1: Tuning knobs for the luminosity and their observables. Many depend only on the beam size at the synchrotron radiation monitor (SRM), besides the luminosity.

| Knob | Observalbe | frequency |
|---|---|---|
| Beam offset at IP (orbit feedback) | Beam-beam kick (BPMs) | ~1 s |
| Crossing angle at IP (orbit feedback) | BPMs | ~1 s |
| Target of orbit feedback at IP (offset) | vertical size at SRM, luminosity | ~1/2 day |
| Target of orbit feedback at IP (angle) | vertical size at SRM, luminosity | ~1/2 day |
| Global closed orbit | BPMs | ~ 20 s |
| Betatron tunes | tunes of non-colliding bunches | ~ 20 s |
| Relative RF phase | center of gravity of the vertex | ~ 10 min |
| Global coupling, dispersion, beta-beat | orbit response to kicks, RF freq. | ~ 14 days |
| Vertical waist position | vertical size at SRM, luminosity | ~ 1/2 day |
| x-y coupling and dispersion at IP | vertical size at SRM, luminosity | ~ 1/2 day |
| Chromaticity of x-y coupling at IP | vertical size at SRM, luminosity | ~ 1/2 day |

Table 2: Comparison of the continuous injection with the conventional injection scheme. *: due to injection and HV up/down.

| Injection mode | Continuous | Conventional | |
|---|---|---|---|
| Reference shift | Dec. 20 2003 owl | May 23 2004 owl | |
| Integrated luminosity per shift | 330.6 | 228.7 | $pb^{-1}$ |
| Peak luminosity | 12.824 | 11.139 | $nb^{-1}s^{-1}$ |
| Loss time* | 0 | ~13.4 | % |
| Veto time during injection | 3.5 | 0 | ms |
| Increase of dead time due to Veto | ~2.3 | 0 | % |
| Linac repetition rate | 10 | 50 | Hz |
| Injection rate (e+) | ~0.39 | ~3.1 | $mAs^{-1}$ |
| Injection rate (e-) | ~0.71 | ~4.5 | $mAs^{-1}$ |
| Peak beam current (e+) | 1600 | 1570 | mA |
| Peak beam current( e-) | 1200 | 1175 | mA |



ISBN 978-3-95450-172-4

# CHALLENGES IN BEAM INSTRUMENTATION AND DIAGNOSTICS FOR LARGE RING COLLIDERS – BASED ON THE LHC EXPERIENCE

R. Jones, M. Wendt#, J. Wenninger, CERN, Geneva, Switzerland

*Abstract*

An overview on some of the major challenges for beam instrumentation and diagnostics for large ring colliders is given. In the Introduction the general challenges are listed, independent of particle type and accelerator specifics. After a short LHC introduction, examples from the LHC experience are presented, related to observed issues, and to the present upgrade and improvement efforts, made during the long shutdown 1. A list, however not comprehensive, of relevant beam instrumentation R&D activities closes this summary.

## INTRODUCTION

The next generation of a ring collider for high energy physics (HEP) will have >50 km circumference, and collide leptons, as a Higgs factory, or hadrons, for beyond standard model physics exploration, at highest energies (up to 100 TeV center-of-mass) and luminosities. At the time of this article we operate the Large Hadron Collider (LHC) at CERN (Geneva, Switzerland) for the HEP community at the energy frontier, colliding proton beams with up to 7+7 TeV [1].

Table 1: Large Ring Colliders for HEP

| Collider | Years of operation | Circum ference *[km]* | Beam type | Beam Energy *[GeV]* | Luminosity *[$cm^{-2}s^{-1}$]* |
|---|---|---|---|---|---|
| Tevatron | 1983-2011 | 6.3 | p-$\bar{p}$ | 980-980 | 4e32 |
| LEP | 1989-2000 | 27 | $e^+$-$e^-$ | 104.5-104.5 | 2.1e31 |
| HERA* | 1992-2007 | 6.3 | p-e | 920-27.5 | 5.1e31 |
| **LHC** | **2008-…** | **27** | **p-p/$Pb^{82+}$** | **4000-4000**** | **7.7e33**** |

* achieved >50 % longitudinal polarization of the e-beam
** achieved performance in 2012

Table 1 summarizes recent large ring colliders, which all have common goals, i.e. highest center-of-mass (CoM) energy, high integrated luminosity (reliable operation), reasonable low investment and operation costs, and in case of leptons high spin polarization. All these ring accelerators made heavy use of superconductive technologies for magnets, RF or both. For any future large ring accelerator project the time span from the initial concept to the first stored beam will be large, 20 years, or more. With the LHC now in operation, the case for a future HEP machine has to be made, this also includes first thoughts on the challenges for the beam instrumentation.

The beam instrumentation and diagnostics systems have to characterize mission critical beam parameters, e.g.:

#manfred.wendt@cern.ch

**Intensity** Beam and bunch intensities, beam life time, abort gap, etc.

**Orbit and Position** Beam position monitors (BPM) with bunch-by-bunch, turn-by-turn and high resolution beam orbit measurement capabilities. All BPMs integrated into the orbit feedback system, some BPMs integrated into technical interlock systems. Special BPMs for specific tasks, e.g. BPMs integrated into collimator jaws.

**Beam Losses** The beam loss monitors (BLM) are the central element of the machine protection system (MPS).

**Tunes and Instabilities** Monitoring and feedback of the betatron tunes should be accomplished with no or minimum beam excitation. The measurement on the tunes of individual bunches (single bunch tunes) is desirable. A system for the early detection of instabilities, e.g. head-tail motion is of great benefit.

**Beam Profile (Emittance) and Halo** A non- or minimum invasive measurement of the transverse beam profile, with single bunch capability is essential to monitor the beam emittance. Techniques with high dynamic range have to be developed to monitor the transverse beam halo, which need to be eliminated.

**Chromaticity** measurement based on a direct, non-invasive measurement technique, e.g. monitoring of the *Schottky* bands.

### *Challenges*

Regardless of beam type and exact machine layout, all future large ring accelerators will have some major challenges for the beam instrumentation in common:

- The large physical size requires a large number of components and subsystems, thus a tight control on costs and reliability. E.g. the use of copper cables over long distances is not adequate, optical fibers have to replace copper wherever possible.
- Low temperatures for superconductive operation of magnets and/or RF give additional challenges for nearby beam monitors, e.g. cryogenic RF vacuum feedthroughs, RF cables, beam monitors (BPMs, BLMs) inside the cryostat.
- High order mode (HOM) and wakefield effects of beam detectors have to be well understood to minimize their impact on the accelerator's impedance budget, and to prevent damages e.g. due to RF heating.
- Basically all beam detection methods have to be non-invasive as of the damage and residual loss potential of high intensity, high brilliance beams.
- An early observation and damping of beam instabilities, e.g. head-tail, e-cloud, etc. will be crucial.

ISBN 978-3-95450-172-4

- As with all past HEP machines, the beam instrumentation systems for a future ring accelerator have to be prepared for small and major changes in the lifespan, e.g. different beam formatting and timing, changes in beam / bunch intensities, different particle species, changes in the machine optics and lattice, etc.
- The high stored energy of the high brightness beam goes along with a severe damage potential. This results in a substantial challenge for the MPS and all the related components and subsystems, particular the BLM system.

## THE LARGE HADRON COLLIDER

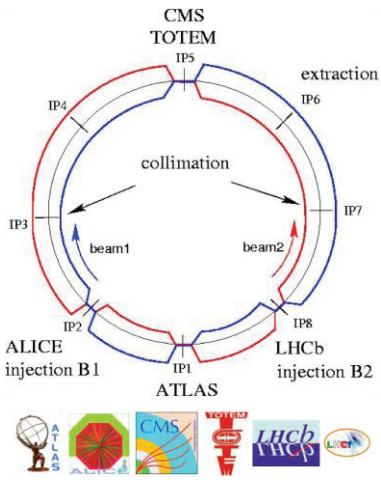


Figure 1: LHC layout.

Figure 1 shows the layout of the LHC, with two separate rings, each 26.7 km circumference, which provide proton and lead ion collisions at 4 interaction points (IP). The machine is divided symmetrically in eight arc sectors, each ~3 km long, and eight long straight sections, each ~700 m long. The guide fields for the beams are provided by ~8000 superconducting magnets, fed by 1600 power supply circuits. The 2-in-1 design dipole magnets are ramped to a field of 8.3 T.

Also for some of the beam diagnostics the quantities are impressive, about 1000 BPM systems to monitor and correct the beam orbit, and 4000 BLM systems based on ionization chambers for beam loss detection and machine protection.

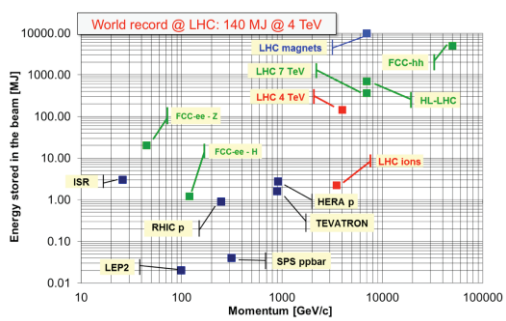


Figure 2: Stored energy in ring accelerators.

At nominal operation, i.e. 7 TeV beam energy and 0.58 A beam current, the stored energy of each proton beam is 360 MJ, equivalent to a 200 m long train travelling at 155 km/h, or 90 kg of TNT. The related high damage potential requires particular attention on the BLMs, some of the BPMs, and all other systems that are in direct contact to the MPS [2]. Figure 2 compares beam energy and the stored energy of different ring accelerators, showing some relaxation for colliding leptons in future rings (FCC).

A severe power incident at the LHC, in September 2008 during no beam operation, required a safety limit to 4 TeV beam energy. Starting 2015, after 1-1/2 years of consolidation the full beam energy operation will be restored.

## EXAMPLES OF LHC BEAM INSTRUMENTATION CHALLENGES

Regardless if the next large ring accelerator is a "*Higgs* factory" lepton collider or an energy frontier proton machine, the lessons learned and challenges from the present LHC will be of great benefit, of course not only for the subject of beam instrumentation [3,4]. The following list of examples is neither complete nor comprehensive.

### *Minimizing Radiation to Electronics*

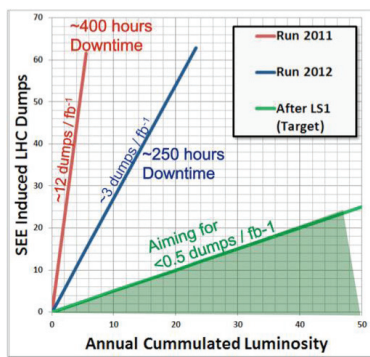


Figure 3: Beam dumps and downtime due to single event effects in LHC front-end electronics.

To cope with reasonable cable installation lengths and signal levels, most of the front-end electronics is installed in the LHC tunnel, or in the alcoves running parallel to the straight sections. Therefore the electronics hardware is exposed to residual radiation from the accelerator, namely highly energetic ionized particles (>20 MeV) causing single event effects (SEE) in the active silicon areas of the electronics chips. SEEs are further divided into categories, i.e. single event upset (SEU), single event latchup (SEL), single event burnout (SEU), all have a malfunction of the transistor in common. Figure 3 shows the number of LHC beam aborts, along with the caused downtime per fb integrated luminosity for the years 2011 and 2012 due to electronics SEEs (not only those of beam diagnostics electronics). Major shielding and electronics relocation efforts in the long shutdown 1 (LS1) aiming for a



ISBN 978-3-95450-172-4

substantial reduction of these SEEs, the goal is <0.5 dumps/fb$^{-1}$.

### *Beam Loss Monitors (BLM)*

The BLM system is the "primary line of defence", feeding the machine protection system (MPS), and has to cope with several substantial challenges [5].

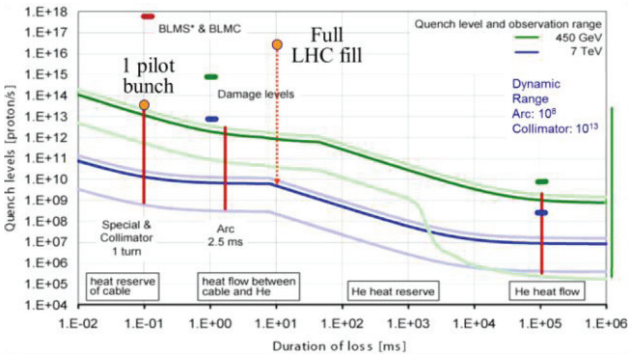


Figure 4: LHC quench and damage thresholds.

As Figure 4 indicates, with beam energies of >6.5 TeV at Run II, the quench and damage thresholds are significantly reduced. A single 5e9 protons pilot bunch is at 7 TeV already close to the damage level, and losses of >3e-7 of the nominal beam current over a time period of 10 ms will cause a quench at this energy.

The BLMs have to cover a large, ~8 orders of magnitude dynamic range to detect small losses at the quench level, as well as scraping losses at the collimators. The LHC collimation system [6] consists out of 100 movable devices, arranged in a multi-stage layout with a cleaning efficiency of 99.98 %. The gap of the primary collimators is set to 2.2 mm.

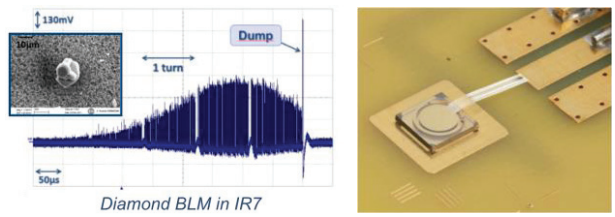


Figure 5: Beam loss induced dump due to UFOs (left), Diamond-BLM detector (right, courtesy E. Griesmayer).

During LHC Run I a series of beam aborts, e.g. 14 dumps at 4 GeV under stable luminosity run conditions have been triggered by the BLM system. Figure 5 shows in post-mortem the beam loss just before abort (last turn) of a prototype diamond-based BLM [7]. The fast response time of the BLM, typically ~1 ns, shows the loss pattern of the individual batches and bunches, the reason for the sudden beam loss is not yet fully understood [8]. The best explanation so far: "unknown flying objects" (UFO), i.e. small dust particles, perhaps from the injection elements. Even though only 21 events caused a BLM triggered beam abort, ~17000 below dump threshold UFO candidates have been found when analysing the BLM data for the same loss pattern. To increase the system sensitivity (up to a factor 30) BLM detectors have been redistributed more uniformly, they are not anymore located only at high beta areas, i.e. quadrupole magnets.

Other efforts are made on BLM detector R&D, e.g. to locate the BLM inside the cryostat, keeping the distance to the beam pipe short. Diamond, silicon and liquid-He ionization chambers are candidates for cryogenic BLMs.

### *Beam Position Monitors (BPM)*

The LHC BPM read-out electronics design goes back to the time of analog signal processing, and is based on the wideband amplitude-to-phase normalizer, capable to acquire the beam position of each passing bunch – at 25 ns bunch spacing – at each of the ~1000 BPM pickups [9]. The single bunch-processing schema minimizes the requirements for the dynamic range, and as of the fast, low latency electronics also allows BPMs at critical locations to be included into the MPS.

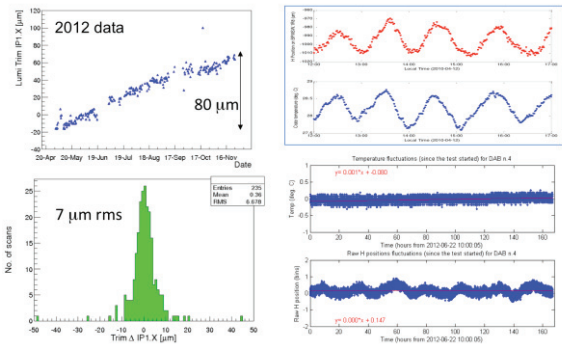


Figure 6: LHC orbit stability at the IP (left), correlation of BPM data and ambient temperature before and after BPM rack modifications (right).

While the LHC BPM system operates flawless and in general very reliable, the orbit stability was not completely satisfactory. Figure 6 (left) shows, the orbit at the IP varies over the course of year 2012 by ~80 µm, however stays within 7 µm from run to run, which is smaller than the beam size at the IP. The main reason is found to be the temperature dependence of the BPM analog electronics [3], which now is improved by the implementation of temperature controlled racks (<0.1 degree), see Figure 6 (right).

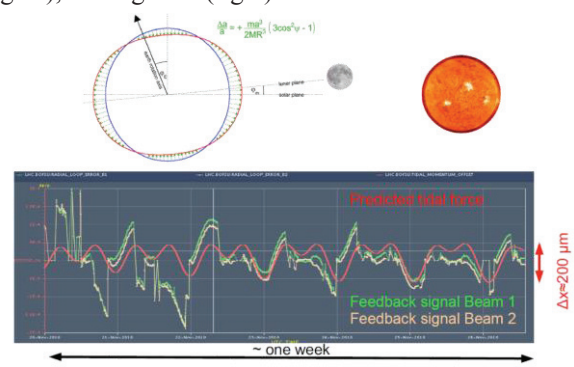


Figure 7: Correlation between tidal forces (red) and the orbit feedback signals (green – beam 1, yellow – beam 2).

ISBN 978-3-95450-172-4

The beam orbit of the LHC, as of any future large ring accelerator, relies heavily on a seamless operating orbit feedback system. Figure 7 illustrates the correlation between the tidal forces and the orbit feedback error signals, which accounts for ~200 µm orbit deviation.

To speed up the setting of ~100 collimators at the beginning of a physics run, button BPMs are now embedded in the 18 tertiary LHC collimators [10], see Figure 8. Instead of operating one-by-one on the rather slow BLM response, the local beam position is used for positioning of the collimator jaws, measured with a resolution of ~100 nm, based on the direct diode detection principle [11]. This system will speed up the setting procedure by two orders of magnitude, all collimator jaws can be aligned simultaneously within 20 s [12].

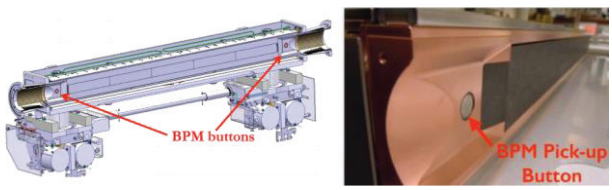


Figure 8: Button BPM electrodes embedded inside a collimator jaw.

Another upcoming BPM challenge is related to the position monitoring of both beams near the IP in the shared vacuum chamber, foreseen for the high luminosity upgrade HL-LHC. Stripline BPMs have directivity properties, but there is some remaining cross-coupling between upstream and downstream signals. A different arrival time of the bunches of each beam can be used in the signal processing to further entangle the individual position signals. For the BPM system of a future ring collider the decision one vs. two rings is of great relevance, as two beams in a single chamber with many bunches will give this additional challenge to the BPM system.

### *Wakepotential, HOM Effects and RF Heating*

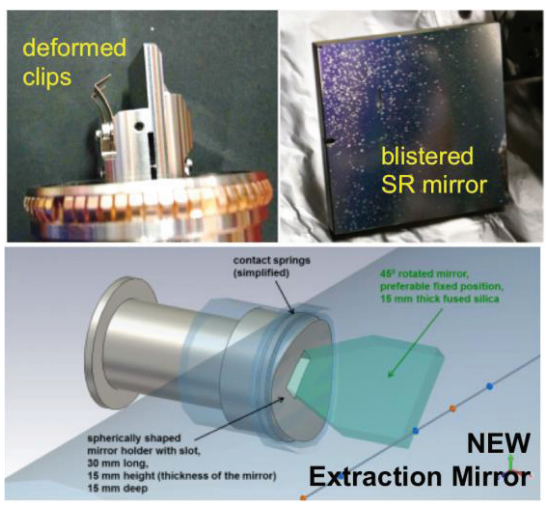


Figure 9: RF heating issues on the LHC BSRT synchrotron light extraction mirror.

A bad surprise during LHC run I was related to beam excited RF resonance effects of various components, including beam pickups [13]. Particular the light extraction mirror of the beam synchrotron radiation telescope (BSRT) suffered from RF heating [14], which damaged the mirror and its holder substantially, see Figure 9. Modifications and redesign, including extensive studies on wakepotential and RF impedances had to be undertaken, still the operation with 25 ns bunch spacing could give further surprises.

### *Early Detection of Beam Instabilities*

A broadband stripline monitor connector to a wideband oscilloscope is currently used to detect transverse beam instabilities. These head-tail motions are also observed by the fast beam current monitor, as single bunch intensity modulation, and by the BSRT synchrotron light monitor, as emittance blow-up of individual bunches. The limited dynamic range of the oscilloscope however limits the resolution to ~100 µm. At those oscillation amplitudes the instability has already grown significantly, too late to generate an early trigger for other beam monitors.

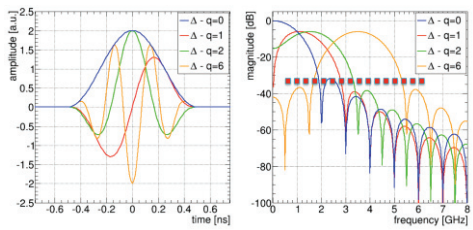


Figure 10:Transverse head-tail modes in time and frequency domain.

A new multiband instability monitor is under development [15], dividing the observed frequency range 0.4-6.4 GHz in 16 individually monitored bands, spaced by 400 MHz. Figure 10 illustrates how head-tail modes map in the frequency domain, indicating the foreseen observation bands. A measurement of magnitude and phase of each band may also allow reproducing the time domain signal. The present stripline pickup and Δ-hybrid installation could be replaced by an electro-optical front-end system, which could cover the entire frequency range.

The early detection of beam instabilities will receive more attention with the 25 ns bunch spacing in the upcoming run II, which has the potential to generate higher electron-cloud densities, and therefore will lower the head-tail instability threshold [16].

### *Non-invasive Beam Profile Monitors*

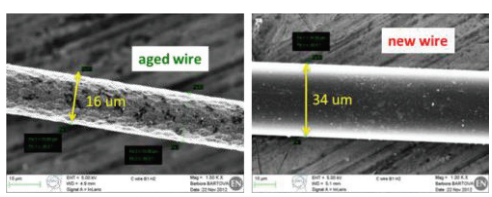


Figure 11: Aging effect of the LHC carbon wire.



ISBN 978-3-95450-172-4

The monitoring of the beam profile of the LHC is one of the biggest challenges, as it is for any high intensity, high brightness accelerator. Physical wires producing secondary emission for monitoring the beam profile during the wire-scan have several drawbacks, e.g. wire heating and sublimation, residual losses, and at higher beam intensities, wire destruction. Figure 11 shows the aging effect of the LHC carbon wire [17]. This limits the use of the LHC wire-scanner to low beam intensities, a total of 2.7e13 protons at 450 GeV injection energy, and only 2.7e12 protons at 7 TeV (equivalent ~20 bunches). However, the wire scanner remains relevant for calibration and beam commissioning purposes.

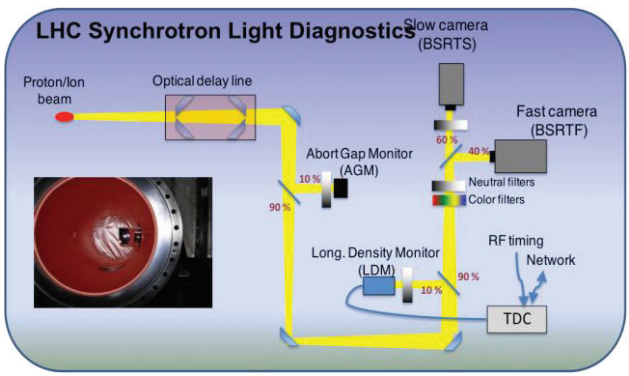


Figure 12: The LHC beam synchrotron radiation telescope (BSRT).

The BSRT synchrotron light monitor [18] is the primary non-invasive beam profile monitor (Figure 12). With its gated camera it allows to display the transverse beam profile at injection energy, utilizing the synchrotron light generated by a superconducting undulator, and at higher beam energies (>1 TeV) using the light from a SC dipole. Beside single bunch beam profile measurements, it also monitors the longitudinal beam profile and unwanted residual particles in the beam abort gap. However, at the nominal 7 TeV beam energy the system operates at the diffraction limit, therefore an interferometer setup is under investigation [19].

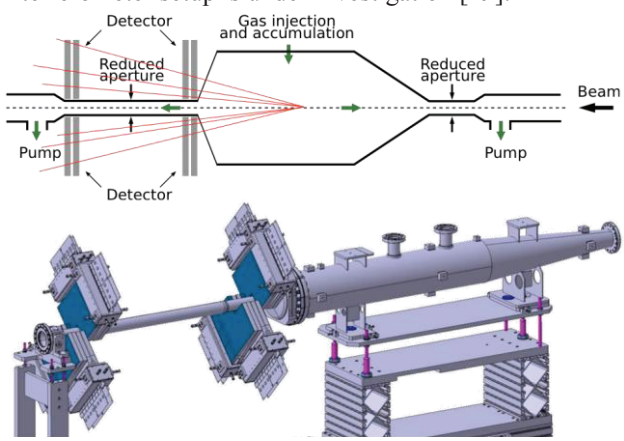


Figure 13: The LHC beam gas vertex detector (BGV).

A variety of other non-invasive beam profile monitors are studied, e.g. the ionization profile monitor (IPM) [20,21], and the beam gas vertex detector (BGV) [22]. The BGV system is based on the LHCb vertex detector principle [23,24], see Figure 13. It requires some statistics, i.e. integration time to reproduce the transverse beam profile from the particle tracks after their collision with residual gas molecules, detected by the two multichannel detector planes.

### *Beam Halo Mitigation*

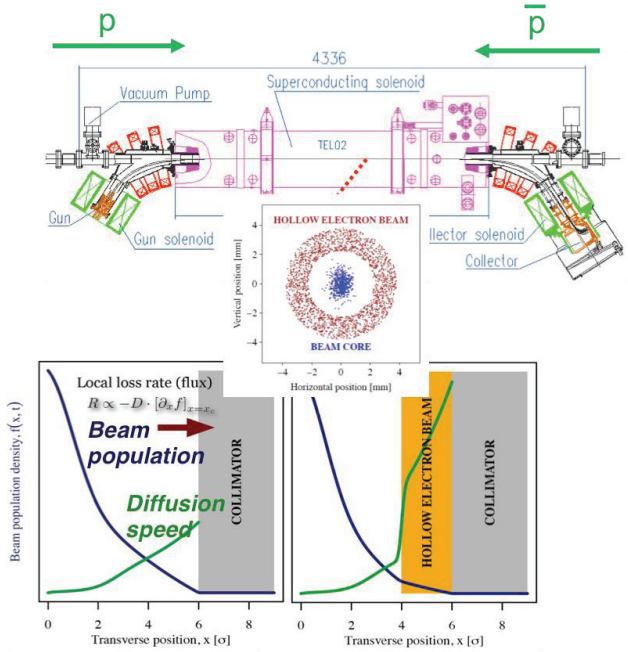


Figure 14: Hollow electron lens.

The unwanted transverse beam halo can be mitigated, e.g. by a hollow electron lens [25] (see Figure 14). Particles experience a non-linear field, which increase the diffusion speed towards the collimator jaws, and results in a clean up of the beam tails.

## BEAM INSTRUMENTATION R&D

There is much more R&D on beam instrumentation, as well as trends in electronics, digital signal processing and electro-optical systems. Some of these developments are very valuable for future large ring accelerators, e.g.:

- R&D on radiation tolerant chips, including FPGAs
- Radiation tolerant optical fibers and related transceivers for the transmission of high volume digital data and broadband analog signals.
- Laser-based wire scanners and emittance monitors are further developed towards a turnkey operational system.
- In-depth studies, analyses and minimization of impedance effects of BPM button electrodes.
- Development of a high resolution gas-jet beam profile monitor.



ISBN 978-3-95450-172-4

- Non-invasive hadron beam profile monitor R&D based on coulomb interaction with a perpendicular electron beam (e-beam scanner).
- Schottky monitor R&D for bunched hadron and ion beams.
- R&D on beam halo detectors.
- Broadband, bunch-by-bunch and intra bunch feedback systems.

State-of-the art developments and technologies on beam instrumentation are presented at the yearly IBIC and IPAC conferences, past events of interest are also the BIW and DIPAC workshops.

## REFERENCES


[1] S. Myers, "The First Two Years of LHC Operation", Proc. of IPAC 2012, New Orleans, LA, USA, May 20-25, 2012, pp.1-5; http://www.JACoW.org

[2] J. Wenninger, "State-of-the-Art and Future Challenges for Machine Protection Systems", Proc. of IPAC 2014, Dresden, Germany, June 15-20, 2014, pp.4060-4064; http://www.JACoW.org

[3] R. Jones, "The Beam Instrumentation and Diagnostics Challenges for LHC Operation at High Energy", Proc. of IBIC 2014, Monterey, CA, USA, September 14-18, 2014.

[4] R. Jones, "First Years Experience of LHC Beam Instrumentation", Proc. of IPAC 2011, San Sebastian, Spain, September 4-9, 2011, pp.3779-3783; http://www.JACoW.org

[5] B. Dehning, et.al., "The LHC Beam Loss Measurement System", Proc. of PAC 2007, Albuquerque, NM, USA, June 25-29, 2007, pp.4192-4194; http://www.JACoW.org

[6] D. Wollmann, et.al., "First Cleaning with LHC Collimators", Proc. of IPAC 2010, Kyoto, Japan, May 23-28, 2010, pp.1237-1239; http://www.JACoW.org

[7] E. Griesmayer, "A Fast CVD Diamond Beam Loss Detector for LHC", Proc. of DIPAC 2011, Hamburg, Germany, May16-18, 2011, pp.143-145; http://www.JACoW.org

[8] T. Baer, et.al., "UFOs in the LHC", Proc. of IPAC 2011, San Sebastian, Spain, September 4-9, 2011, pp.1247-1249; http://www.JACoW.org

[9] E. Calvo Giraldo, et.al, "The LHC Beam Position System: Performance during 2010 and Outlook for 2011", Proc. of DIPAC 2011, Hamburg, Germany, 2011, pp.323-325; http://www.JACoW.org

[10] C. Boccard, et.al., "Embedded Collimator Beam Position Monitors", Proc. of DIPAC 2011, Hamburg, Germany, May 16-18, 2011, pp.80-82; http://www.JACoW.org

[11] M. Gasior, et.al., "BPM Electronics based on Compensated Diode Detectors – Results from Recent Development Systems", Proc. of BIW 2012, Newport News, VA, USA, 2012, pp.44-46; http://www.JACoW.org

[12] G. Valentino, et.al., "Development and Beam Tests of an Automatic Algorithm of LHC Collimators with Embedded BPMs", Proc. of IPAC 2013, Shanghai, China, May 12-13, 2013, pp.3439-3441; http://www.JACoW.org

[13] B. Salvant, et.al., "Update on Beam Induced RF Heating in the LHC", Proc. of IPAC 2013, Shanghai, China, May 12-13, 2013, pp.1646-1648; http://www.JACoW.org

[14] R. Roncarolo, et.al., "Electromagnetic Coupling between High Intensity LHC Beams and the Synchrotron Radiation Light Extraction System", Proc. of IPAC 2013, Shanghai, China, May 12-13, 2013, pp.1493-1495; http://www.JACoW.org

[15] R. Steinhagen, "A Multiband-Instability-Monitor for High-Frequency Intra-Bunch Beam Diagnostics", Proc. of IBIC 2013, Oxford, UK, September 16-19, 2013, pp.327-330; http://www.JACoW.org

[16] G. Iadarola and G. Rumolo, "Electron Cloud in the CERN Accelerators (PS, SPS, LHC)", arXiv: 1309.6795v1, September 26, 2013.

[17] M. Sapinski, et.al., "Carbon Fiber Damage in Particle Beam", Proc. of HB 2010, Morschach, Switzerland, September 27 - October 1, 2010, pp.231-234; http://www.JACoW.org

[18] R. Roncarolo, et.al., "Design and Performance of the Upgraded LHC Synchrotron Light Monitor", Proc. of IBIC 2013, Oxford, UK, September 220-223, 2013, pp.327-330; http://www.JACoW.org

[19] G. Trad, et.al., "A Novel Approach to Synchrotron Radiation Simulation ", Proc. of IPAC 2014, Dresden, Germany, June 15-20, 2014, pp.3687-3689; http://www.JACoW.org

[20] M. Sapinski, et.al., "The First Experience with the Beam Gas Ionization Profile Monitor", Proc. of IBIC 2012, Tsukuba, Japan, October 1-4, 2012, pp.489-491; http://www.JACoW.org

[21] M. Patecki, et.al., "Electron Tracking Simulations in the Presence of the Beams External Fields", Proc. of IPAC 2013, Shanghai, China, May 12-13, 2013, pp.741-743; http://www.JACoW.org

[22] P. Hopchev, et.al., "A Beam Gas Vertex Detector for Beam Size Measurements at the LHC", Proc. of IPAC 2014, Dresden, Germany, June 15-20, 2014, pp.3680-3683; http://www.JACoW.org

[23] M. Ferro-Luzzi, Nucl. Instrum. Methods Phys. Res., Sect. A 553, 3 (2005), pp.388-399.

[24] LHCb Collaboration, J. Instrum. 7 P01010 (2012).

[25] G. Stancari, et.al.,"Collimation with Hollow Electron Beams", Phys. Rev. Lett. 107, 084802, August 17, 2011.




ISBN 978-3-95450-172-4

# SUMMARY OF HF2014 WORKING GROUP 1 – "PARAMETERS"

E.B. Levichev, BINP Novosibirsk, Russia; F. Zimmermann, CERN, Geneva, Switzerland

*Abstract*

The ICFA Higgs Factory workshop ("HF2014") was held in Beijing from 9 to 12 October 2014. Here we summarize the presentations and discussions from the three sessions of Working Group no. 1, which looked after the "Parameters."

## INTRODUCTION

The HF2014 WG1 sessions featured the following nine presentations:

1) Physics motivation and requirements, Alain Blondel (U. Geneva)
2) Choice of circumference, minimum & maxim energy, number of collision points, and target luminosity, Michael Koratzinos (U. Geneva)
3) Ring circumference and two rings vs. one ring, Richard Talman (Cornell U.)
4) Beam-beam effects in high-energy colliders: crab waist vs. head-on, Dmitry Shatilov (BINP)
5) Optimizing beam intensity, number of bunches, bunch charge, and emittance, Chuang Zhang (IHEP)
6) Polarization issues in *FCC-ee* collider, Eliana Gianfelice (FNAL)
7) Constraints on the *FCC-ee* lattice from the compatibility with the *FCC* hadron collider, Bastian Haerer (CERN)
8) Polarization issues and schemes for energy calibration, Ivan Koop,
9) Optimizing costs of construction and operation, possible construction time line, Weiren Chou (FNAL)

## PHYSICS REQUIREMENTS

Alain Blondel reviewed the physics requirements for the next generation of high-energy $e^+e^-$ colliders [1].

Table 1 presents a sample of essential physics studies.

For FCC-ee and CepC the precision of the luminosity measurement will be improved compared with LEP-2. As systematic errors are likely to dominate the need for small-angle measurement should be revisited.

The duration of the desired $e^+e^-$ runs is of order ~20 years, including staging. A possible *FCC-ee* physics programme conceived in 2013 (for the then *TLEP*) would be as follows:

1. ***ZH* threshold scan and 240 GeV running** (covering energies from 200 GeV to 250 GeV): more than 5 years at 2 x $10^{35}$ $cm^{-2}s^{-1}$ would produce 2x$10^6$ *ZH* events. Later one will need to return to the *Z* peak with the *FCC-ee-H* configuration for the detector and beam energy calibration. The physics programme includes Higgs boson *HZ* studies, while running at the *ZH* measuring of cross sections and decay rates of the copiously produced *WW* and *ZZ* pairs, etc.
2. **Top threshold scan and 350 GeV running:** more than 5 years at 2x$10^{34}$ $cm^{-2}s^{-1}$ would produce $10^6$ $\bar{t}t$ events. Also this configuration should be operated at the *Z* peak for calibration purposes. The physics covered would include top quark mass, *WW* fusion (with *H* and two neutrinos in the final state), etc.
3. ***Z* peak scan and peak running in the *FCC-ee-Z* configuration** delivering more than $10^{12}$ (possibly $10^{13}$) *Z* decays. This running mode includes transverse polarization of 'single' bunches for precise $E_{beam}$ calibration. At least 2 and preferably 4 years of running in this configuration are required to accomplish the physics goals related to $M_z$, $\Gamma_Z$, $R_b$ etc, with emphasis on precision tests and searches for rare decays.
4. ***WW* threshold scan for precision *W* mass measurement and *W* pair studies** during another 1-2 years would yield some $10^8$ *W* pairs. Again energy and beam energy calibration would be accomplished by operating with the same configuration at the Z peak.
5. **Operation with polarized beams** (requiring spin rotators) at the *Z* peak during 1 year at a beam-beam tune shift of 0.01 per IP would yield $10^{11}$ *Z* decays, enabling precision measurements of $A_{LR}$, $A_{FB}^{pol}$ etc.

Achieving polarization will be more difficult for *CepC* than for *FCC-ee,* due to the intrinsically larger energy spread of a smaller machine.

For precision studies of the *Z* pole and of various thresholds mono-chromatization schemes (see e.g. [2]) could be of interest. Such schemes could provide a 10 times smaller collision energy spread, probably at the expense of lower luminosity.

Table 1: Sample of *FCC-ee* Physics Studies [1]

| X | physics | present precision | | FCC-ee stat//syst. precision | FCC-ee key | challenge |
|---|---|---|---|---|---|---|
| $M_Z$ MeV/$c^2$ | Input | 91187.5 ±2.1 | Z line shape scan | 0.005 MeV/ <±0.1 MeV | $E_{cal}$ | QED corrections |
| $\Gamma_Z$ MeV/$c^2$ | Δρ (T) (no Δα!) | 2495.2 ±2.3 | Z line shape scan | 0.008 MeV/ <±0.1 MeV | $E_{cal}$ | QED corrections |
| $R_l$ | $\alpha_s$, $\delta_b$ | 20.767 ± 0.025 | Z peak | 0.0001/ ± 0.002 - 0.0002 | statistics | QED corrections |
| $N_\nu$ | unitarity of PMNS, sterile ν's | 2.984 ±0.008 | Z peak<br>Z+γ (161 GeV) | 0.00008/ ±0.004<br>0.001/- | lumi meas.<br>statistics | QED corrections to Bhabha scattering |
| $R_b$ | $\delta_b$ | 0.21629 ±0.00066 | Z Peak | 0.000003/ ±0.000020 – 60 | statistics, small IP | hemisphere correlations |
| $A_{LR}$ | Δρ, ε3 Δα (T, S ) | 0.1514 ±0.0022 | Z peak, polarized | -/±0.000015 | 4 bunch scheme | design experiment |
| $M_W$ MeV/$c^2$ | Δρ, ε1, ε2, Δα (T, S, U) | 80385 ± 15 | tThreshold (161 GeV) | 0.3 MeV/ <1 MeV | $E_{cal}$ & statistics | QED corections |
| $m_{top}$ MeV/$c^2$ | Input | 173200 ± 900 | threshold scan | 10 MeV/- | $E_{cal}$ & statistics | theory limit at 100 MeV? |

ISBN 978-3-95450-172-4

## OPTIMIZED PARAMETERS: SIZE, IPS, BEAM-BEAM, LUMINOSITY

Mike Koratzinos discussed the optimization of key parameters such as circumference, minimum & maximum energy, number of collision points, and target luminosity [3].

In particular, he presented optimized parameters for *CepC*. With these 80% higher luminosity in *ZH* running appears possible.

Other conclusions from his presentation are: A ring of 70 km circumference would produce 20% more luminosity than a 53 km ring. With 4 IPs there is 53% more luminosity than with 2 IPs. At 45 GeV, *CepC* could reach a luminosity of $4\text{x}10^{34}$ $\text{cm}^{-2}\text{s}^{-1}$ with 10 MW of SR power (160 bunches). At 175 GeV the luminosity of the 53 km *CepC* would be a factor 5 lower than for the 100 km long *FCC-ee*.

A key limitation at high energy is beamstrahlung. Two analytical formulae exist, one by V. Telnov [4] and the other by A. Bogomyagkov [5], as well as - at least - one thorough simulation, by K. Ohmi [6]. Figure 1 compares the two analytical predictions with the simulated beamstrahlung lifetime, for the *H* and *t* running modes. The agreement between the three predictions for a realistic momentum acceptance of 1.5%-2% is within a factor of 5. At 350 GeV there is a nearly perfect consistency between the simulation and Bogomyakgkov's formula, while for 240 GeV the simulation results are closer to Telnov's prediction.

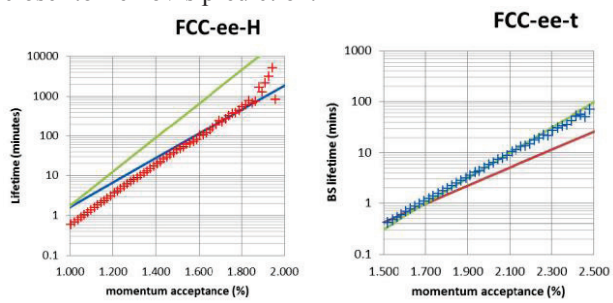


Figure 1: Comparison of beamstrahlung lifetime according to analytical formulae from V. Telnov (blue on the left, red on the right) and A. Bogomyagkov (green) with simulation by K. Ohmi (red on the left, blue on the right) for *FCC-ee* at 240 GeV (left) 350 GeV c.m. (right), from M. Koratzinos [3].

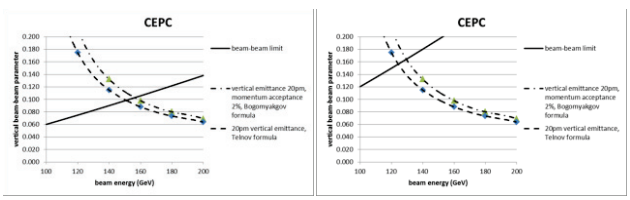


Figure 2: $\xi_y$ vs beam energy for the current *CepC* design (left) and extrapolation from *FCC-ee* (right), from M. Koratzinos [3].

M. Koratzinos pointed out that the current *CepC* design may be conservative, as it assumes a vertical emittance 10 times larger than for *FCC-ee*. Figure 2 illustrates the two limiting regimes and how the *CepC* design might be further improved. In both cases, the 120 GeV running is limited by the beam-beam effect.

In addition, the present *CepC* design features different beam-beam parameters for the horizontal and vertical plane, while these values might conceivably be equal for an optimized parameter set.

## 1 VS 2 RINGS & CIRCUMFERENCE

Richard Talman addressed the (controversial) question whether to choose one or two rings [4]. He argued that an optimized design should reach all limits – e.g. on power, beam-beam tune shift, and beamstrahlung lifetime – at the same time. Maximizing the ring circumference will be of paramount importance and should always been chosen if money were available rather than converting a single ring to a double-ring machine.

R. Talman modelled the total cost as the sum of two terms, one proportional to the size and one proportional to the RF power, the latter scaling as luminosity divided by the radius. The optimum size is obtained by minimizing the sum. He concluded that with the (assumed) lower civil engineering costs in China the Chinese ring should have a larger radius than rings in Europe or the US – exactly opposite to the relative sizes of the machine designs presently proposed in the various regions.

R. Talman's beam-beam simulation "dead-reckons" the saturated beam-beam tune shift. The result is shown in Fig. 3.

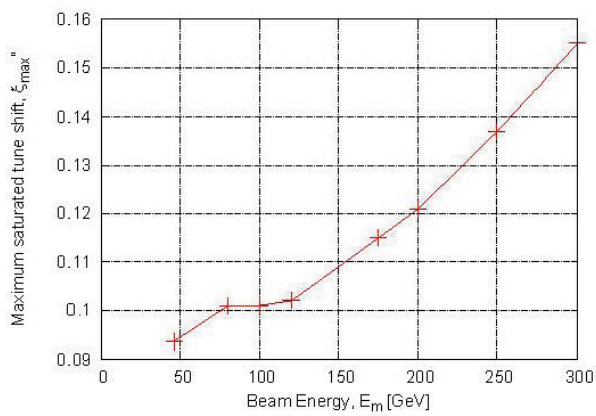


Figure 3: Simulated maximum tune shift $\xi_{max}$ vs. beam energy for rings such that $E \propto R^{5/4}$, assuming that $\sigma_z = \beta_y^*$, from R. Talman [4].

## BEAM-BEAM EFFECTS: CRAB WAIST VERSUS HEAD-ON

Dmitry Shatilov discussed the parameter optimization vis-à-vis the beam-beam effects [5]. The operation of *FCC-ee-Z* with head-on collisions is characterized by



ISBN 978-3-95450-172-4

strong bunch lengthening, transverse blow-up and long tails, all of which are related to the weak damping. Figure 4 illustrates the harmful impact of the bunch lengthening on the transverse dynamics. For longer bunches with noticeable hourglass effect both the transverse tails grow and resonances are enhanced.

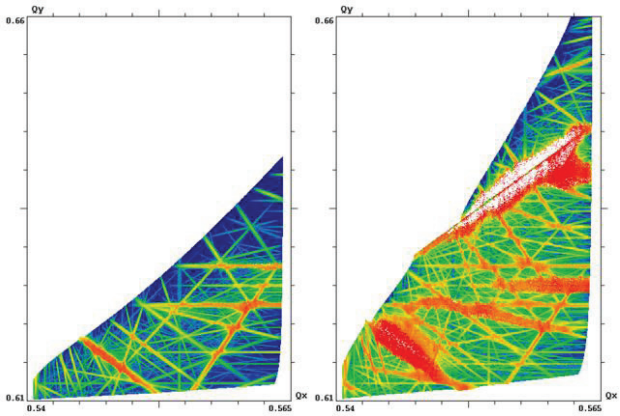


Figure 4: Footprints in the plane of betatron tunes, obtained by a frequency map analysis, for fixed synchrotron amplitude of $A_s = 1\ \sigma_z$, considering $\sigma_z = \beta_y$ (left) and $\sigma_z = 3\ \beta_y$ (right). Other parameters are those for *FCC-ee-Z* in Ref. [6] with $\xi_x \approx \xi_y \approx 0.03$ (nominal values), from D. Shatilov.

Table 2: Luminosity at Low Energies (*Z* and *W*) with Head-on and Crab-waist Schemes, from D. Shatilov

| energy | *FCC-ee-Z* | | *FCC-ee-W* | |
|---|---|---|---|---|
| collision scheme | head-on | crab waist | head-on | crab waist |
| $N_p$ [$10^{11}$] | 1.8 | 1.0 | 0.7 | 4.0 |
| $\theta$ [mrad] | 0? | 30 | 0 ? | 30 |
| $\sigma_z$ (SR / total) [mm] | 1.64 / **3.0** | 2.77 / **7.63** | 1.01 / **1.76** | 4.13 / **11.6** |
| $\varepsilon_x$ [nm] | 29.2 | 0.14 | 3.3 | 0.44 |
| $\varepsilon_y$ [pm] | 60.0 | 1.0 | 7.0 | 1.0 |
| $\xi_x$ / $\xi_y$ [nominal] | 0.03 / 0.03 | 0.02 / 0.14 | 0.06 / 0.06 | 0.02 / 0.20 |
| $L$[$10^{34}$ cm$^{-2}$s$^{-1}$] | **17** | **180** | **13** | **45** |

Table 3: Luminosity at High Energies (*H* and *tt*) with Head-on and Crab-waist Schemes, from D. Shatilov

| energy | *FCC-ee-H* | | *FCC-ee-t* | |
|---|---|---|---|---|
| collision scheme | head-on | crab waist | head-on | crab waist |
| $N_p$ [$10^{11}$] | 0.46 | 4.7 | 1.4 | 4.0 |
| $\theta$ [mrad] | 0 ? | 30 | 0? | 30 |
| $\sigma_z$ (SR / total) [mm] | 0.81 / **1.29** | 4.82 / **9.33** | 1.16 / **1.60** | 5.25 / **6.78** |
| $\varepsilon_x$ [nm] | 0.94 | 1.0 | 2.0 | 2.13 |
| $\varepsilon_y$ [pm] | 1.9 | 2.0 | 2.0 | 4.25 |
| $\xi_x$ / $\xi_y$ [nominal] | 0.093 / 0.093 | 0.02 / 0.13 | 0.092 / 0.092 | 0.03 / 0.07 |
| $\tau_{bs}$ [min] | **> 500** | **70** | **2** | **20** |
| L [$10^{34}$ cm$^{-2}$s$^{-1}$] | **7.4** | **8.4** | **2.1 ?** | **1.3** |

Introducing a crab waist solves all these problems. Specifically, it is proposed to change the effective crossing angle from ~0 to 30 mrad. The gain from the crab waist schemes is illustrated in Table 2. Numbers obtained in simulations (by the Lifetrac code) are shown in bold.

The luminosity for *FCC-ee-Z* can be further increased if the vertical emittance can be reduced to values below 1 pm. Another important result is that for operation at the *Z* and *W* the energy acceptance can be reduced, namely from 2% to 1% (for *Z*) or 1.7% (for *W*).

In general, at high energies head-on and crab-waist collisions provide similar luminosities as is shown in Table 3. Again a small vertical emittance is of crucial importance. Indeed, $\xi_y$ can be raised further by decreasing $\varepsilon_y$, but this requires an emittance ratio of, or below, ~0.1%, which would still need to be demonstrated. When running for *H* or *t* production, the $\beta_y^*$ can be increased (which will improve the energy acceptance) with an associated luminosity drop which is weaker than $1/\sqrt{\beta_y^*}$. For example, increasing $\beta_y^*$ from to 1.5 (2) mm lowers the luminosity only by 2.5% (7.5%) for *FCC-ee-H*, and by 1.5% (5%) for *FCC-ee-t*.

## OPTIMIZING BEAM INTENSITY, NO. OF BUNCHES, CHARGE, AND EMITTANCE

Chuang Zhang reviewed the design optimization of Higgs factories [7]. The complex interplay of the key design parameters is sketched in Fig. 5.

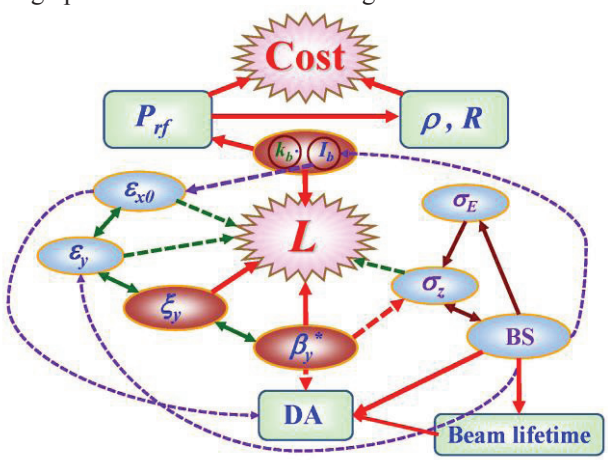


Figure 5: Schematic illustrating the parameter optimization of circular Higgs factories, from C. Zhang [7].

Table 4 and Fig. 6 compare (damping-time dependent) maximum beam-beam parameters extrapolated from LEP with the design values for *CepC* and *FCC-ee*. For *CepC* the design is a factor two more conservative than the extrapolation. It was argued that for *CepC* there might not be much margin in $\xi_y$ and luminosity, since the large hourglass (Fig. 7) implies a large actual beam-beam tune



ISBN 978-3-95450-172-4

shift even if the nominal beam-beam parameter is low. The situation for *FCC-ee-Z* appears even less favourable, however, which may require further studies.

Table 4: Comparison of Damping Times and Beam-Beam Parameters for *CepC* and Four Running Modes of *FCC-ee*, from C. Zhang

| parameter | | *CepC* | *FCC-ee* | | | |
|---|---|---|---|---|---|---|
| $E$ (GeV) | | 120 | 45.5 | 80 | 120 | 175 |
| $\tau_E$ (turns) | | 39 | 1320 | 243 | 72 | 23 |
| $\xi_y^{max}$ | calcul. | 0.15 | 0.028 | 0.056 | 0.090 | 0.143 |
| | design | 0.083 | 0.03 | 0.059 | 0.093 | 0.092 |

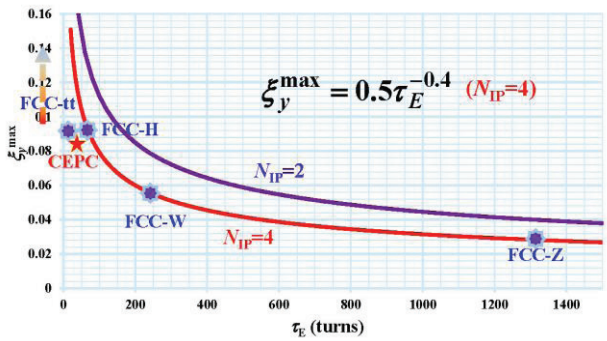


Figure 6: Maximum beam-beam parameter versus damping time extrapolated from LEP for two and four IPs, together with the actual design parameters, from C. Zhang [7].

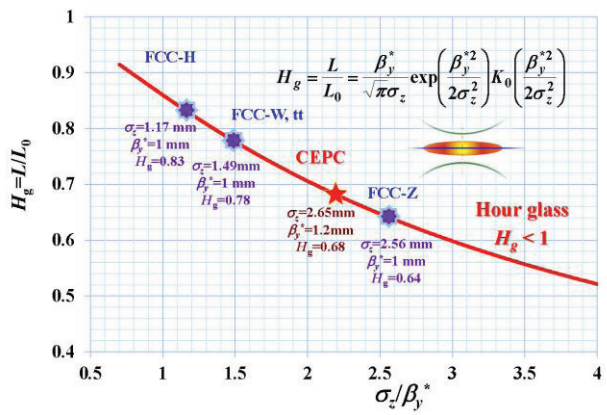


Figure 7: Hourglass factor versus ratio of rms bunch length, $\sigma_z$, and vertical IP beta function $\beta_y^*$ together with the working points of the proposed machines, from C. Zhang [7]

## POLARIZATION ISSUES

Eliana Gianfelice discussed polarization issues for the *FCC-ee* [8], considering a toy model of the ring. To reduce the polarization time at the *Z* pole one could add polarization wigglers (such as the LEP wigglers of Blondel and Jowett [9]) installed in dispersion-free sections. The beam energy spread including the effect of the wigglers would need to remain below the critical value where polarization is lost; in this regard a field of 0.6 T field could be about optimum, as was pointed out by A. Blondel.

First SITROS spin-tracking simulations were executed for the toy model, including quadrupole misalignments, but without any corrections, and also without any wigglers. Figure 8 displays the results, which illustrate that rather high levels of polarization may be attained. A vertical "kink" of the machine would lead to spin diffusion, as sketched in Fig. 9, which can lower the achievable polarization level or may even eliminate the possibility of polarization altogether. The concrete effect of a non-planar layout and the maximum acceptable deviation from planarity could be explored through similar SITROS simulations.

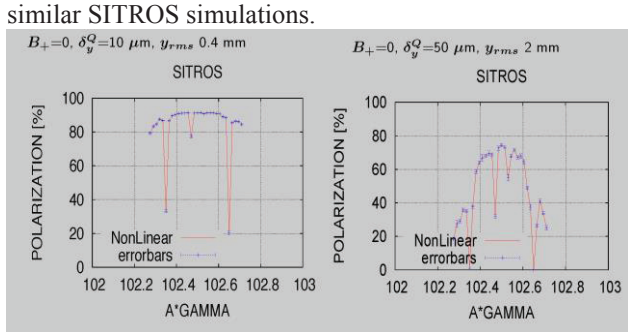


Figure 8: SITROS spin tracking results for an *FCC-ee* toy model at 45.5 GeV, considering smaller (left, 10 μm rms) and larger random quadrupole displacements (right, 50 μm rms), from E. Gianfelice [8].

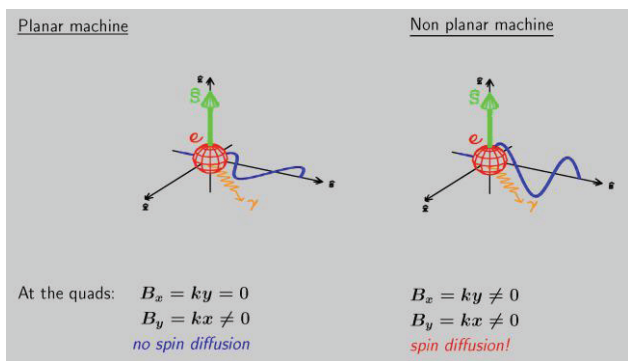


Figure 9: Schematic showing how a non-planar machine leads to spin diffusion, from E. Gianfelice [8].

In any case, for energies far above the *WW* threshold the polarization is expected to be lost due to too large an energy spread from arc synchrotron radiation. However, a classical paper [10] predicts a resurrection of polarization at high energy if the synchrotron tune, $Q_s$, is large.

## CONSTRAINTS FROM PP COLLIDER

Bastian Haerer reviewed the constraints imposed by the required compatibility with a hadron collider sharing the same tunnel infrastructure [11]. For the *FCC-hh*, the



ISBN 978-3-95450-172-4

functional requirements of injection, beam dump, collimation and experiments define the lengths of the various straight sections. In addition, the geology, together with the *FCC-hh* transfer lines, determines the optimum location of the *FCC*. This relation is illustrated in Fig. 10. Namely, the *FCC* and LHC should "overlap," if LHC is used as the injector. The minimum distance $L$ for transfer lines depends on the difference in depth $d$, the magnet technology used for the transfer line, the beam energy, and the maximum slope of the tunnel (<5%).

In particular, the layout of the FCC interaction region IR should be compatible between the two colliders. Figure 11 compares the layout of the hadron IR with two different IR versions for the leptons, one shorter, the other much longer (with rather different values for the synchrotron-radiation power emitted in the IR, as well as with different collision schemes). Both lepton collider IR versions consider $\beta_y^* = 1$ mm, and $l^* = 2$ m (both much shorter/smaller than for the hadron collider). They also feature a large crossing angle of 30 mrad or 11 mrad, respectively. The bottom picture of Fig. 11 suggests that the IR for the leptons might become longer than for the hadrons, which would be opposite to the LEP/LHC experience, and might be attributed to the additional space required for a (semi)-local chromatic correction. The latter is necessary to achieve the small $\beta_y^*$ with adequate momentum acceptance.

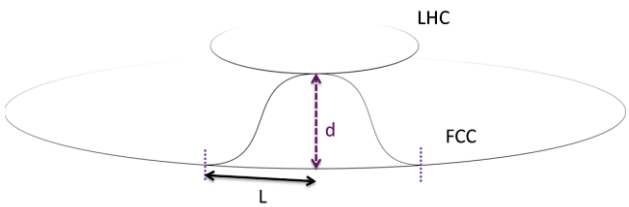


Figure 10: Sketch of the optimum FCC location with respect to the LHC, highlighting the injection transfer lines, from W. Bartmann and B. Haerer [11].

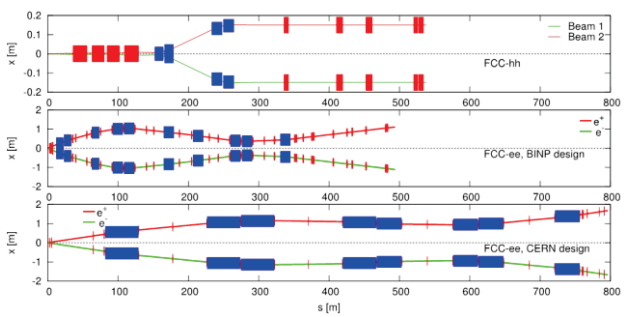


Figure 11: Preliminary FCC interaction region designs for *FCC-hh* (top) and *FCC-ee* – version 1 (center) and version 2 (bottom) –, from B. Haerer [11].

## POLARIZATION & ENERGY CALIBRATION

Ivan Koop proposed a scheme based on a polarized $e^-$ source, in which one would accelerate a polarized beam, and measure the energy in the collider at every injection shot [12]. For $e^+$ beams one could exploit the self-polarization in a 1-2 GeV intermediate ring. The beam polarization could be preserved during acceleration thanks to several snakes in the booster ring. A spin transparent rotator for the solenoid type snake which would suit this purpose is shown in Fig. 12. Here two solenoids, each 40 m in length and with a field of 5 T would provide a spin rotation by 180° at a beam energy of 45.5 GeV. An extension up to 120 GeV with $B$=10 T looks feasible. This rotator system contains no skew quadrupoles. For a full snake, the optics should be set to $\cos\phi$=-1, and $\sin\phi$=0.

In I. Koop's scheme there would be no rotators and one would inject into the collider with the polarization vector oriented in the horizontal plane. Directly after injection the modulation of the Compton back scattering due to the spin precession could be measured, e.g. over the first 10,000 turns, by means of Compton polarimetry. The subsequent analysis of the free spin precession data will be based on the Fourier spectrum as sketched in Fig. 13. This method should provide a beam-energy measurement accuracy of $10^{-6}$. However, in order to obtain so good an accuracy, the nearby resonance strength must be known or cancelled (e.g. through harmonic spin matching; or by measuring several points). For beam energies above about 100 GeV, other purely Compton based energy measurements could be employed. In these cases, without polarization, the energy precision will be of order $10^{-4}$.

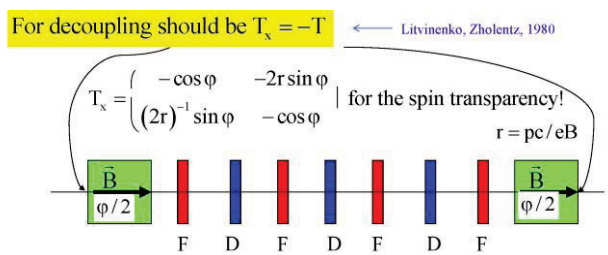


Figure 12: Spin transparent rotator for the solenoid based snake [13], from I. Koop [12].

ISBN 978-3-95450-172-4

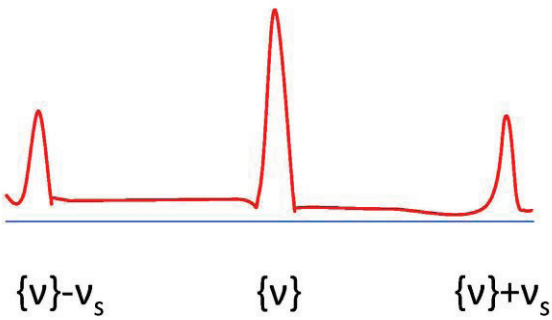


Figure 13: Schematic of free spin precession data analysis using the Fourier spectrum of the modulated turn-by-turn Compton-scattering signal, from I. Koop [12]. Weaker synchrotron sidebands appear around the primary signal. Coherent betatron oscillations may give rise to additional peaks.

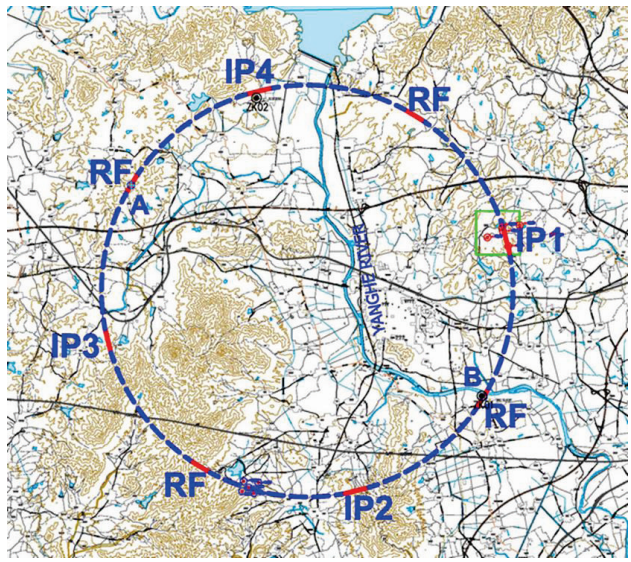


Figure 14: Proposed *CepC/SppC* construction site with indication of *CepC* RF locations, from W. Chou [14].

## COST & PLANNING

Weiren Chou discussed the cost and schedule for *CepC/SppC* [14]. His presentation covered the cost optimization and the construction time line. For *CepC/SppC* a tunnel diameter of 6.5 m has been chosen, almost twice the size of the LEP tunnel. The SRF frequency is 1.3 GHz for the booster and 650 MHz for the collider. IHEP already has the required SRF expertise to construct these systems, as it is presently building 58 cryomodules for the XFEL in Hamburg.

For the construction site considered (Fig. 14), the classical dig & blast technique for the tunnel is estimated to be 20-40% cheaper than the use of a tunnel boring machines (TBMs). For the beam pipe the baseline is copper, which is expected to be cheaper than using *Al* with a *Pb* cladding.

The relative cost estimate of the *CepC* accelerator components is displayed in Fig. 15, and the relative power consumption in Fig. 16. Figure 17 presents the "dream" project time lines of *CepC* and *SppC*.

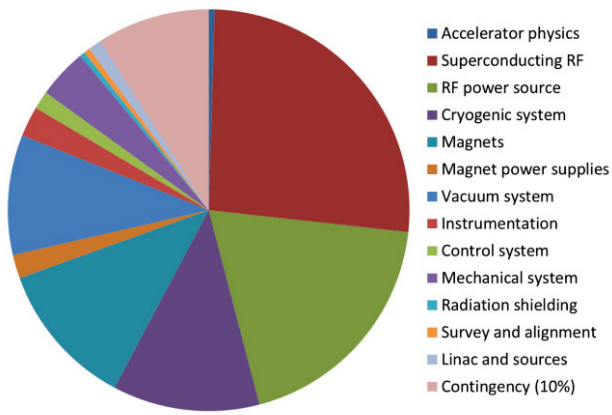


Figure 15: Relative cost estimate of *CepC* accelerator components, from W. Chou [14].

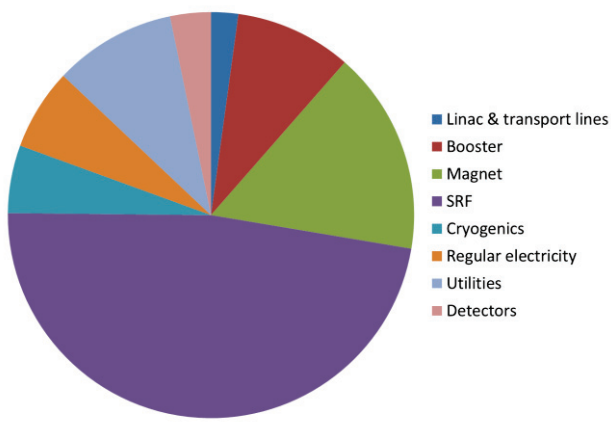


Figure 16: Relative *CepC* power consumption, from W. Chou [14].



ISBN 978-3-95450-172-4

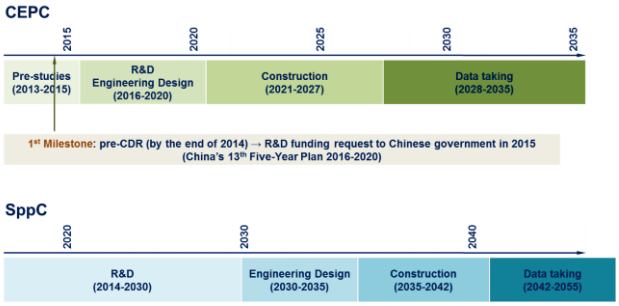


Figure 17: Optimistic project time line of CepC/SppC, from W. Chou [14].

## DISCUSSION TOPICS

Questions and topics raised during the WG1 discussion included the following:

- length of hadron-collider interaction region;
- choice of the free length from the IP, $l^*$ , for the hadron collider;
- effect of beamstrahlung on polarization;
- beam-beam limit for *FCC-ee-Z*;
- novel CPD klystron from Toshiba, which has demonstrated an efficiency of 70-80;
- how cost estimates are taking into account the evolution of currency differences, e.g. CHF/$;
- installation of electronics in the tunnel;
- HOM losses with many short bunches;
- multi-cell SRF cavities at high beam current;
- detuning and feedback required to combat the second Robinson instability;
- relative cost of the RF system for a single or double ring.

Concerning the latter point, the *FCC-ee* consists of a double ring using separate RF systems when running at the *Z*, *W* and *H* energies with many bunches, and a combined single RF system providing maximum voltage for operation above the $t\bar{t}$ threshold, where the number of bunches is small. Figure 18 illustrates these two configurations.

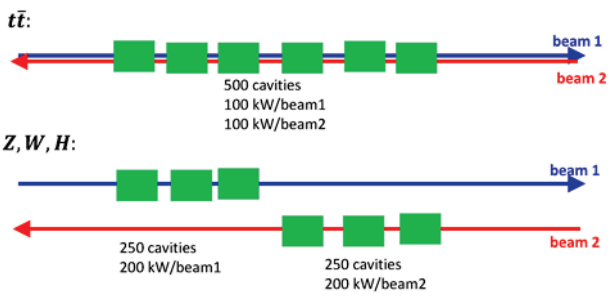


Figure 18: Proposed RF system configurations for different running modes of *FCC-ee*: (1) with many bunches at low total voltage for *Z*, *W*, and *H* physics [top] and for operation with few bunches and largest total voltage at highest energy near the $t\bar{t}$ threshold [bottom].

There are at least two ways to accomplish the transition: (1) physical motion of cavities by some tens of cm in a winter shutdown, or (2) using a switching scheme as proposed by Alain Blondel [15]. The latter is sketched in Fig. 19. It requires bunch trains of an appropriate length (in the example of Fig. 19 two bunch trains of length $2A+L$ in a machine that has a total circumference of $8A+8L$ where $A$ denotes the length of the arcs and $L$ the one of the straight section). If the RF is located at different points than the IPs, one can arrange for the trains to collide in the interaction points, but to avoid each other in the common RF sections by way of timing. At the IP crossing at an angle will avoid the harmful effect of parasitic collisions. The switch over from the *FCC-ee-H* to *FCC-ee-Z* can then be achieved by a magnetic separation such that one beam (e.g. $e^+$) sees the RF in points 1 and 5, and the other (e.g. $e^-$) at points 3 and 7 (assuming the IPs to be at the event points 2, 4, 6, and 8), while the combination at high energy can be achieved using electrostatic separators.

For the lower-energy operation modes based on high beam current and many bunches, the double ring with separate RF system reduces both the cavity-related impedance and the HOM losses by a factor of two, which could be a decisive advantage and translate into considerable cost saving. The HOM losses in the RF cavities can be lowered further by colliding longer bunches, which is an additional argument in favor of the crab-waist scheme [5]. Figure 20, taken from [16], illustrates how the longitudinal loss factor for typical SRF cavities steeply increases as bunches get shorter.

## ACKNOWLEDGEMENTS

Our warm thanks go to Weiren Chou for organizing the HF2014 workshop, for inviting a summary presentation, and for diligently making sure, together with Ning Zhao, that this paper was written and submitted.

This work was partly funded by the European Commission under the FP7 Research Infrastructures project EuCARD-2, grant agreement no.312453.



ISBN 978-3-95450-172-4

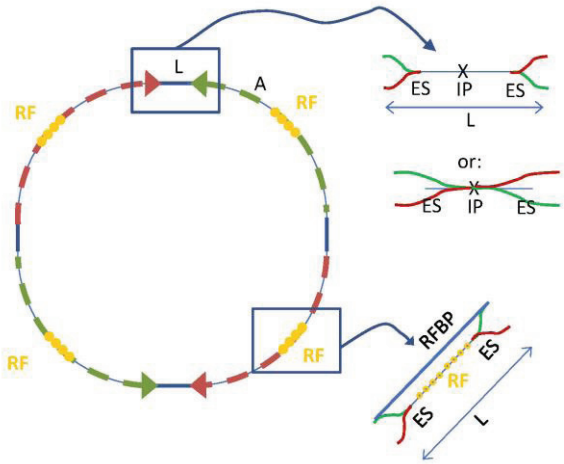


Figure 19: Example of Bunch Train scheme for RF management at *FCC-ee* [15]. Total length of ring: 8*L* + 8*A*; total length of each of two bunch trains: 2*A*+*L*; IP: Interaction Point; ES: Electrostatic Separator followed by quadrupole or split-field dipole; RFBP: possible RF bypass for one or the other beam activated by dipoles, from A. Blondel.

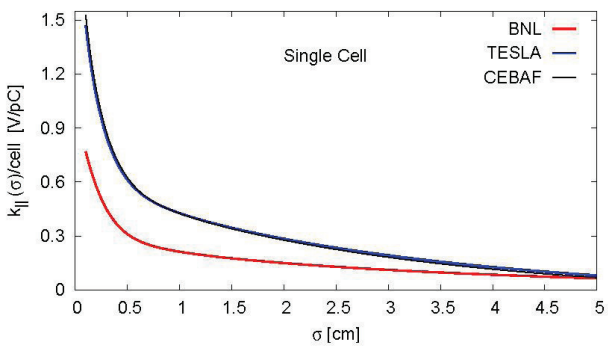


Figure 20: Longitudinal loss factor as a function of bunch length [16].

## REFERENCES

[1] A. Blondel, "Physics motivation and requirements, Alain Blondel," HF2014 Beijing, 9-12 October 2014.

[2] J.M. Jowett, "Feasibility of a Monochromator Scheme in LEP," LEP Note 544 (1985).

[3] M. Koratzinos, "Choice of circumference, minimum & maxim energy, number of collision points, and target luminosity," HF2014 Beijing, 9-12 October 2014.

[4] R. Talman, "Ring circumference and two rings vs one ring," HF2014 Beijing, 9-12 October 2014.

[5] D. Shatilov, "Beam-beam effects in high-energy colliders: crab waist vs. head-on," HF2014 Beijing, 9-12 October 2014 .

[6] J. Wenninger et al., "Lepton Collider Parameters," CCC-ACC-SPC-0003, v1.0 (2014).

[7] C. Zhang, "Optimizing beam intensity, number of bunches, bunch charge, and emittance," HF2014 Beijing, 9-12 October 2014.

[8] E. Gianfelice, "Polarization issues in FCC-ee collider," HF2014 Beijing, 9-12 October 2014.

[9] A. Blondel, J.M. Jowett, "Dedicated Wigglers for Polarization," CERN-LEP-NOTE-606 (1988).

[10] Ya.S. Derbenev, A.M. Kondratenko and A.N. Skrinsky, "Radiative Polarization at Ultrahigh-Energies," Part. Acc., v. 9, 247-266 (1979).

[11] B. Haerer, "Constraints on the FCC-ee lattice from the compatibility with the FCC hadron collider," HF2014 Beijing, 9-12 October 2014.

[12] I. Koop, "Polarization issues and schemes for energy calibration," HF2014 Beijing, 9-12 October 2014.

[13] A.A. Zholents and V.N. Litvinenko, "On the Compensation of Solenoid Field Effects by Quadrupole Lenses," Novosibirsk preprint IYF-81-80 (1981).

[14] W. Chou, "Optimizing costs of construction and operation, possible construction time line," HF2014 Beijing, 9-12 October 2014.

[15] A. Blondel, private communication, 22 November 2013.

[16] R. Calaga, "Linear Beam Dynamics and Ampere Class Superconducting RF Cavities at RHIC," PhD thesis, U. Stony Brook, UMI-32-38968 (2006).



ISBN 978-3-95450-172-4

# SUMMARY OF WORKING GROUP 2: OPTICS*

Kazuhito Ohmi, KEK, National Laboratory for High Energy Physics, Oho, Tsukuba, Ibaraki 305, Japan
Yunhai Cai, SLAC National Accelerator Laboratory, Menlo Park, CA 74024, USA

## INTRODUCTION

We had four sessions of optics in the Higgs Workshop 2014, Beijing. The first section was dedicated to the overall consideration of optics in circular Higgs factory (CHF), and the existing designs from IHEP and CERN. The second one focused on single-particle beam dynamics, in particular dynamic aperture in SuperKEKB and CHF. The third session was a joined one together the working group 3: interaction region (IR) and machine detector interface. The topic was final focus system (FFS) and local chromatic compensation. Three approaches by IHEP, CERN, and BINP were presented. In the final session we had a discussion of beamstralung, beam-beam interaction, and IR magnets.

## TALKS

There were 15 talks in the optics sessions:

1. “Overall consideration, main challenges and goals", Yunhai Cai (SLAC)
2. “Single ring multi-bunch operation and beam separation", Richard Talman (Cornell)
3. “Challenges and status of the FCC-ee lattice design", Bastian Harer (CERN)
4. “Status of the CEPC lattice design", Huiping Geng (IHEP)
5. “Analysis of nonlinear dynamics", Yunhai Cai (SLAC)
6. “Dynamic aperture optimization in SuperKEKB", Yukiyoshi Ohnishi (KEK)
7. “The effect of IR imperfection on dynamic aperture in SuperKEKB / dynamic aperture study of CEPC", Hiroshi Sugimoto (KEK)
8. “Beam lifetime and Injection consideration", Cui Xiaohao (IHEP)
9. “CEPC IR optics", Yiwei Wang (IHEP)
10. “Status of the FCC-ee interaction region design", Roman Martin (CERN)
11. “Crab waist interaction region", Anton Bogomyagkov (BINP)
12. “Beamstrahlung and energy acceptance", Kazuhito Ohmi (KEK)
13. “Interaction region magnets", Eugenio Paoloni (INF)
14. “Beam-beam effects in the CEPC", Yuan Zhang (IHEP)
15. “Wide-band long-focus optics for detection systems infrared synchrotron accelerator diagnostics", Marina Maltseva (TENZOR)

Here are our conclusive remarks on the optics in CHF.

## MAIN CHALLENGES

Compared with LEP2, we need a factor of 100 increase of luminosity at beam energy of 120 Gev with an affordable cost. Without any major technology advances, we have put all burdens squarely on the optics:

- Low emittance lattice at high energy,
- High packing factor of magnets,
- Strong final focusing,
- Large momentum acceptance,
- Short bunches.

Any one of the listed item represents a significant challenge. With all of them combined, we have not yet found any solution since the last workshop two years ago. Most likely, something has to give or new concept has to be discovered.

## ARC LATTICE

To reduce synchrotron radiation of the bending magnets, we all use FODO cell in CHF because of its large packing factor. It lacks of flexibility in optics. Specifically, the interlaced sextupoles generated huge tune shifts at high betatron amplitudes. As a result, any perturbation will degrade the dynamic aperture, mostly noticeable with a pretzel orbit or insertion of the IR. A way to mitigate this effect is to consider increase circumference to accommodate other type of cells with non-interlace sextupoles in arcs.

## FINAL FOCUS SYSTEM

Many progresses have been made since the last meeting (Feb, 2014), but the momentum aperture of the collider with realistic arcs remains too small. Possible solutions:

- Add octupoles near the final doublet,
- Consider asymmetric dispersion at the paired sextupole in FFS,
- Simplify the transition between CCY and CCX to reduce the phase advance from $3\pi$ to $2\pi$

* Work supported by the Department of Energy under Contract Number: DE-AC02-76SF00515.

ISBN 978-3-95450-172-4

## PARAMETER

The bunch length is lengthened to 2.8 mm after adding the contribution from the beamstrahlung. It is too long compared to the 1.2 mm beta function at the interaction point (IP) in the vertical plane due to the hour-glass effects. The simulation shows a further degradation of luminosity in the beam-beam interaction. In fact, there is not much gain from the 1.2 mm beta compared to the 2 mm one. Therefore, we strongly recommend increasing the vertical beta function at the IP to 2 or 3 mm. This change will greatly help to develop a lattice with a large dynamic aperture.

## TECHNICAL ISSUES

There are many technical issues in the design of CHF. Some R&D may be necessary. Among them, most important ones are:

- 300 T/m gradient of quadupole near the IP
- a thin septum (2 mm) or alternative injection scheme
- Dipole in the interaction region may be still too strong
- Injected beam may be too large, especially with a pretzel scheme

## GOALS

Here are a set of goals for our working group:

- Clarify where we are and identify main design issues,
- Compare different designs and identify their trade-offs,
- Collect ideas to resolve the technical blocks such as off-momentum aperture,
- Obtain a set of requirements that consistent with other systems,
- Define or have a baseline design?

We believe that they can be useful to the near-term development of the lattice in CHF. A definable baseline not only adds credibility to the project but also lays a foundation for further improvement. Technically, it simplifies any comparisons among different designs.

## ACKNOWLEDGMENT

We would like to thank all speakers in our working group for their contributions and many stimulating discussions.



ISBN 978-3-95450-172-4

# SUMMARY OF WORKING GROUP 3*

M. Sullivan#, SLAC National Accelerator Laboratory, Menlo Park, CA 94025, USA
Y. Funakoshi, KEK, 1-1 Oho, Tsukuba, Ibaraki 305-0801 Japan

*Abstract*

This is a brief summary of the talks and issues that came up in Working Group 3 (IR and MDI). There were many excellent presentations and several issues were raised regarding the CEPC design and the FCC-ee design.

## INTRODUCTION

The working group looked at issues for backgrounds in the detector from synchrotron radiation and from beam particles. In addition, the needs of the detector were also addressed and several discussions were entertained that revolved around these various issues. The CEPC interaction region design is quite challenging and there were many points of interest raised that will require further study. The interaction region of the FCC-ee design is equally challenging and has its own set of unique issues.

## PRESENTATIONS

There were a total of 6 sessions and 14 presentations. We also had 3 joint sessions with working groups 2 and 4. We list the presentations here.

1. CEPC IR Optics, Y. Wang (IHEP)
2. Status of FCC-ee Interaction Region Design, R. Martin (CERN) **FRT2B2**
3. Crab Waist Interaction Region, A. Bogomyagkov (BINP) **FRT2B3**
4. SuperKEKB Background Simulations, H. Nakayama (KEK) **FRT3A1**
5. Beam-beam limit vs. number of IPs and Energy II: scaling law, M. Xiao (IHEP) **FRT3A2**
6. Beam-beam limit vs. number of IPs and Energy I: beam-beam simulation, K. Ohmi (KEK) **FRT4A1**
7. Long-Range beam-beam interaction with the CESR bunch train operation, D. Rice (Cornell U.) **FRT4A2**
8. Choice of L* I and SR in the HF IR, M. Sullivan (SLAC) **SAT1B1**
9. Choice of L* II: IR optics and dynamic aperture, E. Levichev (BINP) **SAT1A2**
10. Choice of L* III: requirement from the detector, G. Li
11. Lost particles in the IR and Touschek effects, M. Boscolo (INFN-LNF) **SAT1B2**
12. Infrared synchrotron methods and systems for monitoring and controlling particle beams in real time, M. Maltseva (TENZOR) **SAT1B4**
13. Detector beam background simulations for CEPC, H. Zhu (IHEP) **SAT2A2**
14. Synchrotron radiation absorption and vacuum issues in the IR, J. Seeman (SLAC) **SAT1B3**

*Work supported by Dept. of Energy number DC-AC02-76SF00515
# sullivan@slac.stanford.edu

## HIGHLIGHTS

- The CEPC IR optics has been improved. The L* value has been lowered from 2.5 m to 1.5 m and the strength of the bend magnets in the chromaticity correction blocks on either side of the IP have been lowered. The Synchrotron Radiation (SR) power from the previous bends had been exceptionally large and now the values, though large, are looking manageable.
- The FCC-ee interaction region design is being studied. The design includes an 11 mrad crossing angle with two complete storage rings for the electrons and positrons. The overall design is quite ambitious with an energy range that goes from the $E_{cm}$: Z0 to the ttbar threshold from 92 GeV to 355 GeV
- A crab waist design was presented for the FCC-ee IR which looks quite promising.
- There was a very comprehensive presentation from the SuperKEKB background group. They have gone to great effort to model every detail of the detector hardware and the beam line components both inside and outside of the detector in order to get as accurate a simulation as possible. They have used this detailed simulation to study the effects of adding shielding in almost all possible remaining space inside the detector.
- There were two very interesting studies presented about beam-beam limits. One study collected all the available information about beam-beam limits from present and past machines and compared these numbers against some standard scaling laws and typical simulations. The other presentation showed a study of the CEPC IR design and concluded that a design $\beta_y$ of 2 mm gave more luminosity than the current $\beta_y^*$ of 1.5 mm.
- There was presentation on bunch trains and using pretzel orbits that revealed many of the difficulties of maintaining a good orbit and luminosity with such a design. This is the plan for the CEPC design. The issues of the pretzel design were difficult to handle even with a very flexible machine.
- There were three presentations on choices of L* values. The first presentation concentrated on the issues of SR coming from the final focus quadrupoles. Due to the very high strength of these quads, there is a very significant amount of SR

ISBN 978-3-95450-172-4

power generated by just the 4 final focus magnets. The background SR from these magnets mostly comes from the beam particles that populate the tails of the transverse beam distribution. This tail distribution and the number of beam sigmas used to track these particles are important design considerations. The second presentation concentrated on the effects of nonlinear fields in the IR. In the talk, three different sources of nonlinearities were investigated; *i.e.* the kinematic term mainly from the drift space from the IP to the final focus quadrupoles, the fringe fields mainly from the final focus quadrupoles and the paired sextupole magnets used in the local chromaticity correction blocks. To estimate the nonlinear features of the final focus system, the nonlinear detuning coefficients $\alpha$ (particularly the vertical value $\alpha_{yy}$), which have a tune dependence on the action variables, were taken as a figure of merit for the nonlinearities. The values of $\alpha_{yy}$ for the kinematic term, the fringe fields and the sextupoles for the chromaticity correction are proportional to L*, $L^{*3}$ and $L^{*2}$, respectively. It was shown that the nonlinearities from the paired sextupoles dominates in the case of the IR of the FCC. This nonlinearity is created by the finite length effect of the magnets and can be mitigated by additional (low-strength) sextupole correctors. The larger nonlinearities that correspond to the longer values of L* usually result in a reduction of the beam dynamic aperture. A tracking study has been done to check the dynamic aperture for the IR of the FCC with several values of L*, *i.e.* 0.7m, 1m, 2m and 3m. A preliminary result showed that an IR with an L* of 2m would give a sufficient dynamic aperture. The third presentation came from the detector group for the CEPC and there was expressed interest in a small radius central beam pipe. This desire will have to be balanced by the expected SR background level from the final focus quadrupoles. As for L*, it was shown that shorter L* brings several challenges for the detector. In the talk, mainly three challenges were discussed. The first possible problem is that the momentum resolution may get worse due to the leakage magnetic filed from the final focus quadrupoles (QD0). This problem may be overcome by optimizing the VXD/FTD and by a precise mapping of the fields. The second problem is that the jet flavour tag loses some efficiency and jet resolution may get worse due to the smaller coverage of the detector. However, the statistics is expected to compensate this. The third problem is that on accuracy of the luminosity measurement with a short distance from IP to the luminosity monitor for a precise measurement of the Bhabha event rate. This issue would be really a big challenge.

- There was a presentation on detector backgrounds from all manner of lost beam particles, Beam-gas interactions, Coulomb scattering, Inter-beam scattering, Touschek scattering, and beam-beam scattering especially beamstrahlung (bending of the beam particles due to the magnetic field of the other beam bunch during a collision). All of these backgrounds need to be calculated and simulated with collimators in various places. The LEP machine had ~100 collimators for four interaction regions to help control backgrounds from these sources.
- We had an interesting presentation on a detector that monitored infrared SR from the beam in real time to obtain information on the beam for diagnostic purposes.
- There was a presentation on initial studies of detector backgrounds for the CEPC design. The preliminary results looked encouraging but further work and more detailed simulations needed to follow.
- The last presentation was on SR power and vacuum chambers for the IR design of the PEP-II B-factory. The most important thing to remember was that all vacuum beam pipe components need to be cooled.

## SUMMARY

Below is a checklist of topics that came up during the Working Group 3 sessions that should be addressed by any accelerator design. There were many discussions during the workshop and we are sure we have forgotten some of the issues so here is, at best, a partial list of issues.

- The IR design is one of the more complicated sections of the accelerator with several overlapping and conflicting requirements.
- The value of L* is very important. A smaller number tends to help the accelerator design achieve the desired luminosity. It also lowers the chromaticity generated by the final focus quadrupoles. A larger value makes the IR easier to design and build as the quadrupoles are farther from the IP and this leaves more room for the detector.
- The SR power generated by local magnets near the IP must be managed and the backgrounds generated by SR must be carefully handled. The SR background studies include direct hits from SR sources but must also include one and possibly two bounces of SR photons from various local surfaces. In most cases, a suppression factor of on the order of $10^6$ (and sometimes higher) must be achieved in order to attain an acceptable level of background in the detector.
- The definition of the Beam-Stay-Clear (BSC) for the IR as well as for the rest of the accelerator is an important design consideration. It is also important that the IR area have a BSC definition that is larger than all other areas of the accelerator. Otherwise, all beam particles that are on the way of being lost from all around the ring will be lost in the IR area.
- With the BSC, is the definition of the non-gaussian beam tail distributions. These tail distributions will become the source of SR backgrounds in the IR area



ISBN 978-3-95450-172-4

and the particle density of these tails also will define the beam lifetime.

- The vacuum around the IR is very important. In most cases, it is desirable to have a much lower local vacuum pressure than the rest of the ring(s) in order to minimize local beam particle losses near the IP where one is unable to collimate because they occur too close to the IP.
- Beamstrahlung was an issue raised several times and this will need to be studied thoroughly. The effect on the beam core is one issue but, in addition, how it affects beam lifetime and whether or not there are background issues from the particles that are pushed into the beam tail distribution also needs to be looked at.
- Lost beam particles and even some of the SR in the IR area have enough energy to produce secondary backgrounds and in particular neutrons. Neutrons are very difficult to shield against and as a background in the detector can be very dangerous as they increase the total radiation doses for detector components.
- The issue of Higher-Order-Mode power (HOM power) came up several times. This will be an important consideration as vacuum chambers become more defined and beam pipe details are firmed up. HOM power is an issue for the entire ring but there are special considerations for the IR area. The detector components usually require special beam pipes that can be generating sources of HOM power that must be properly handled. This is especially true for short bunch length designs (like the CEPC) but it is an issue whenever the bunch charge is high, the beam current is high or the bunch length is short. Any one of these three conditions tend to increase luminosity and hence will be pushed to the limit. Planning in advance for HOM power handling and control will make an accelerator design much more robust.
- Vibration control of the final focus quadrupoles in particular is very important. The very small beam spots at the IP make controlling magnet vibrations an essential part of optimizing the luminosity and in maintaining the performance of the accelerator.
- It is also important to design a fast signal for luminosity performance. This signal will be crucial for machine optimization and allow operators to recognize running issues quickly when they happen as well as permit machine tuning for luminosity.

## CONCLUSION

The workshop overall was very interesting and informative. Working Group 3 had a very good list of speakers with quite interesting topics. A great many issues were discussed and brought to light. It was a very useful and helpful gathering of people to discuss the issues of a large e+e- collider.

## ACKNOWLEDGMENTS

We would like to thank the organizers of the workshop for bringing together a large number of people that are experts in many aspects of accelerator design. We especially thank Weiren Chou and Qing Qin as principle organizers for this great workshop. The support staff were always friendly and helpful and they kept the workshop running smoothly throughout the meeting. Many thanks to them as well.



ISBN 978-3-95450-172-4

# SUMMARY OF WORKING GROUP 4: SR AND SHIELDING

J. Seeman, SLAC, Stanford, CA 94025, USA
M. E. Biagini, LNF, INFN, Frascati, Italy

*Abstract*

In this paper a summary of the work done in Working Group 4, Synchrotron Radiation and Shielding, is presented. A short description of the topics discussed and future issues to be addressed in this field by high energy circular colliders designers is given.

## TALKS PRESENTED

The talks presented in WG4 two sessions and summarized in this paper are the following:

1. Monte Carlo Simulations of Synchrotron Radiation for CEPC Vacuum System, by Z. Ma (IHEP);
2. Vacuum System requirements for a HF e+e- Accelerator, by R. Kersevan (CERN);
3. Synchrotron Radiation Effects in the HF Injector, by Y. Papaphilippou (CERN)
4. Electronics shielding in the tunnel, by L. Esposito (CERN);
5. Infrared Synchrotron Methods and Systems for Monitoring and Controlling Particle Beam in Real Time, by M. Maltseva (TENZOR);
6. Lost Particles in the IR and Beam Induced Backgrounds in a Higgs Factory, by M. Boscolo (INFN);
7. Synchrotron Radiation Absorption and Vacuum Issues in the IR, by J. Seeman (SLAC).

## VACUUM AND SR

Talks 1 and 2 addressed the impact of the SR on the design of the vacuum system.

### *CEPC*

Radiation protection topics addressed were:

- synchrotron radiation shielding;
- thickness of the main tunnel;
- shielding for straight tunnel, beam dump, collimate station, injection section, maze, duct, shielding doors, RF station, etc…;
- induced radioactivity analysis: cooling water, ventilation air, accelerator component, local shielding concrete, ground water, environmental samples, etc…;
- personal safety interlock system;
- radiation dose monitoring system.

Since there are different radiation thresholds for different operational zones, like inner and outer tunnel, all areas should be clearly defined after the functional structures are determined.

A Monte Carlo simulation of the Synchrotron Radiation (SR) in the CEPC beam pipe has started. A model of the beam pipe similar to the LEP design was assumed for the first calculations (see Figure 1) with two material options: a few millimeters of Al covered by 3 or 8mm of Pb or only a few millimeters of Cu.

A comparison between LEP2 and CEPC SR parameters is shown in Table 1.

Table 1: SR Parameters for CEPC and LEP2

| Parameter | CEPC | LEP2 |
|---|---|---|
| Beam Energy (GeV) | 120. | 100. |
| Beam current (mA) | 16.6 | 5.5 |
| Bending radius (m) | 6094. | 3104. |
| Power/unit length (W/m) | 1305 | 805 |
| Critical energy (keV) | 629. | 709. |
| Bending angle (mrad) | 3.17 | 6.4 |
| Solid angle (μrad) | 4.3 | 5.1 |

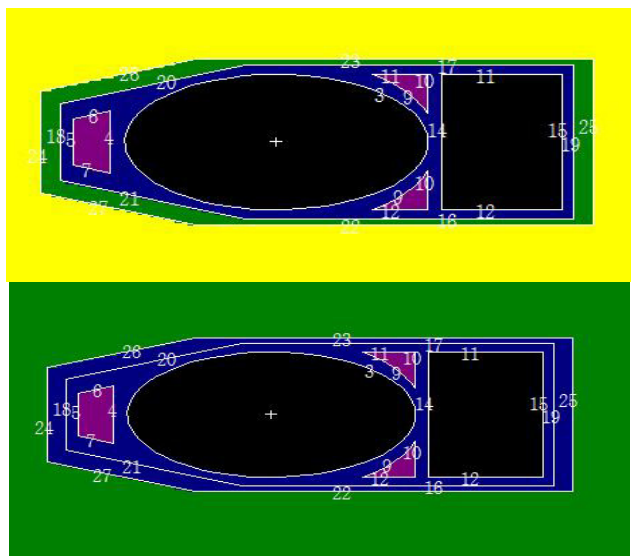

Figure 1: Cross section of the simulated beam pipe, Al&Pb (upper), Cu (lower).

The dose rate in the tunnel for CEPC is mainly dominated by synchrotron radiation. Copper seems to be a good material for beam pipe from the point of radiation protection, but manufacture/price and other points of view



ISBN 978-3-95450-172-4

have to be taken into account before making the final choice.

Detailed simulations have still to be done for reliability verification, actual structure, thermal analysis, etc.

### *FCC*

The requirements on the FCC vacuum systems were presented, such as:

- Beam Physics →Beam-gas lifetime specification
- Lattice →Gap (dipoles) or ID (quads/sextupoles) → cross-section of chambers → specific conductance → Effective pumping speed
- Lattice → Chamber vs. chamber-antechamber analysis
- Distributed vs. discrete SR absorbers
- Distributed vs. discrete pumping
- Outgassing: thermal and SR-induced
- Materials: Al, Cu, SS
- Heat dissipation (SR, Compton-scattered)

To start, for half FCC FODO cell distributed SR fan as a function of localized absorbers were computed (Ray-tracing with SYNRAD+). Photon fan profiles were converted into outgassing profiles via η(mol/ph) and a pressure profile calculation via 3D Monte Carlo code (Molflow+) was performed (see Figure 2).

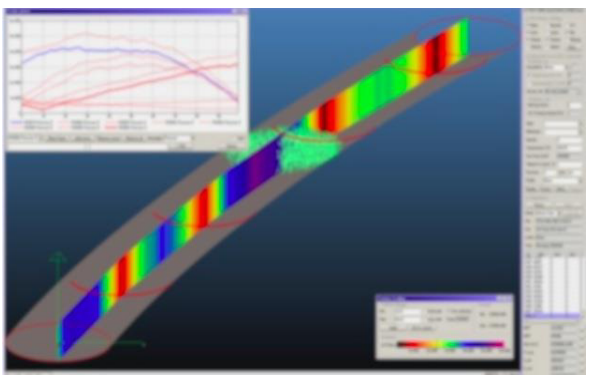

Figure 2: Example of Pressure profile calculation via 3D Monte Carlo code (Molflow+) for an FCCee half-FODO cell.

Some conclusions were presented.

1. Any design of a Higgs Factory with beam energies in the 45~175 GeV range inevitably makes a powerful source of SR.
2. A comprehensive ray-tracing analysis of SR fans is mandatory. Especially for delicate areas, such as IR, SRF, wigglers.
3. A careful choice of vacuum chamber material is needed.
4. The vacuum system geometry and pumping system must be carefully analysed and designed.
5. A special care has to be taken for any cross-sectional changes (tapers), and devices (BPMs, stripline kickers, RF cavities, gate-valves, etc…): proper shielding from SR and cooling for HOMs.
6. The operation of LEP and B-factories, and the design of low-emittance light sources can help a lot in the design of a HF's vacuum system.
7. The chamber vs. chamber/antechamber solutions must be carefully evaluated.
8. The distributed vs. discrete pumping solutions must be carefully evaluated.
9. Low-SEY coatings for e-cloud in the $e^+$ beam chamber are needed.
10. In-situ bake-out is recommended.

## HF INJECTION SYSTEM

A first look at the injector complex and SR losses for FCCee was given in Talk 3. A booster ring of the same size as the collider, hosted in the same tunnel, is needed to provide top-up injection at full energy in the ring/rings. Booster characteristics:

- same size of the RF system, with lower power (~MW),
- top-up frequency of ~0.1 Hz,
- injection energy ~20 GeV,
- long chicanes to bypass the experimental detectors.

A sketch of the injector complex for electron and positrons at 20 GeV is shown in Figure 3.

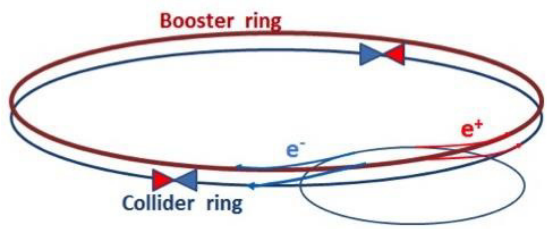


Figure 3: Sketch of the HF injector complex.

Target injector parameters for a Higgs factory, compared to LEP2, are listed in Table 2.

The SR power in the booster ring is much lower than in the collider, but the critical energy is similar: absorbers and shielding are also needed. The vacuum chamber design may become complex: needs for anti-chambers, coatings for SEY reduction and pumping, eddy currents. The pre-injector requirements are similar to a typical electron Linac, but the positron production system needs a careful design for the required yield and associated power deposition (damage) and shielding from radiation.



ISBN 978-3-95450-172-4

Table 2: Injector Parameters for HF Compared to LEP2

| Parameter | Z | W | H | tt | LEP2 |
|---|---|---|---|---|---|
| E (GeV) | 45.5 | 80 | 120 | 175 | 104 |
| I (mA) | 1442 | 151 | 30 | 7 | 1 |
| N. bunches | 16700 | 4490 | 1360 | 98 | 4 |
| Bunch population ($10^{11}$) | 1.8 | 0.7 | 0.46 | 1.4 | 4.2 |
| Lifetime (sec) | 298 | 73 | 29 | 21 | 434 |
| Time between injections (sec) | 361. | 88. | 35 | 25 | 263 |
| Injected top-up bunch population ($10^{11}$) | 601.2 | 62.9 | 12.5 | 2.7 | 0.34 |
| Required particle flux for top-up ($10^{11}$p/sec) | 2.1 | 0.89 | 0.44 | 0.13 | 0.001 |
| Required particle flux for full filling ($10^{11}$p/sec) | 31.3 | 3.3 | 0.7 | 0.1 | 0.02 |
| Booster injector ramp rate (GeV/sec) | 5.2 | 12.2 | 20.4 | 31.6 | 17.1 |

## TUNNEL SHIELDING

The need for shielding of the detector and accelerator electronics hosted in the tunnel was addressed in Talk 4.

As an example, in the CNGS 2007 run single event upsets in ventilation electronics caused ventilation control failure and interruption of communication (see Figure 4).

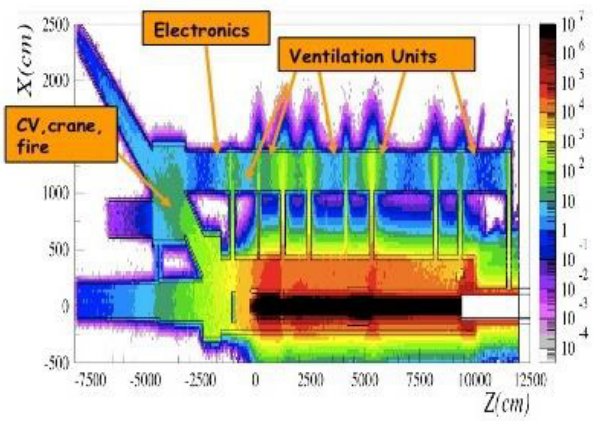


Figure 4: Example of ventilation control failure in CNGS 2007 run due to nuclear cascade.

Profiting of the LHC experience, a project called R2E was setup at CERN to estimate the radiation environment and sources, the effects of radiation on the electronics and the radiation levels for FCCee.

For LHC the sources of radiation are of a different kind:

- direct losses, such as collimators and collimator-like objects, injection, extraction and dump. Their levels scale with the beam intensity;
- collisions losses near the experiments, scale with the luminosity;
- beam-residual gas scattering losses, all around the ring. They scale with both intensity and residual gas density.

For a lepton collider losses are mainly due to the dipole emitted synchrotron radiation, which scales with both intensity and energy.

The total ionizing dose to the electronics has both stochastic (immediate effects such as rupture, bit flip…) and cumulative effects (integration over time, critical for injection lines), which start with performances worsening to finish with electronics and material damage.

The R2E project activities are:

- radiation monitoring,
- calculations,
- test facilities,
- developments,
- radiation tests,
- production and implementation.

As an example, for the LHC selected energy deposition studies were performed, and the agreement between the high energy hadrons flux simulation and the measured one was within 30%. The radiation field in the FCCee tunnel has been computed, including neutrons from photonuclear interactions, see Figure 5.

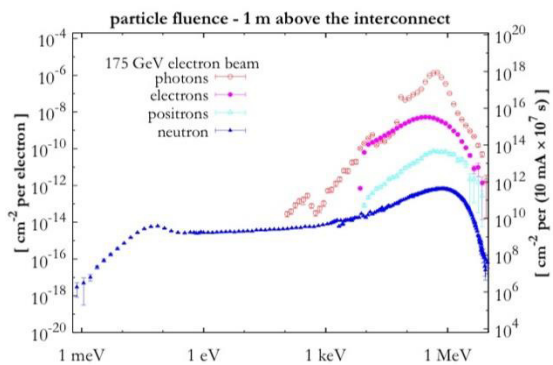


Figure 5: Radiation field in the FCC tunnel.



ISBN 978-3-95450-172-4

Figure 6 shows the total radiation levels in FCCee compared to those of LHC.

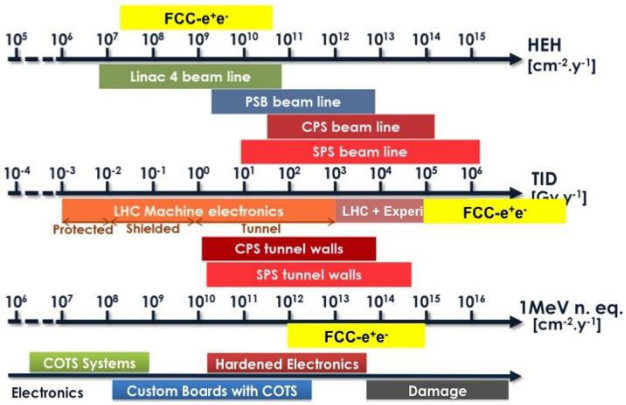


Figure 6: Radiation levels in FCCee compared to LHC.

The radiation to the electronics represents a crucial issue to be taken into account when designing any high energy and intensity machine. The Total Integrated Dose effect has to be mitigated through a carefully shielding design. The R2E project at CERN allowed creating a diffuse knowledge and expertise covering all the aspects of radiation hardening.

## DIAGNOSTICS

Talk 5 dealt with the synchrotron radiation diagnostics. It is very important to have:

- non-destructive monitors,
- high resolution IR optical devices,
- wide spectral range,
- distributions of SR power can be calculated,
- use modern devices for IR and ultraviolet,
- computerized opto-electronics (>100 μsec),
- spectrometric detection systems (0.4–40 μm),
- non-cryogenics systems.

Figure 7 shows a typical synchrotron radiation diagnostics device.

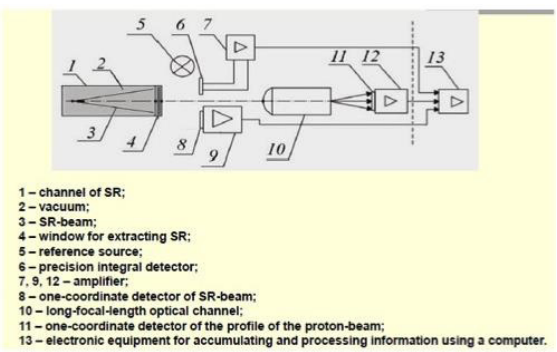


Figure 7: A typical synchrotron radiation diagnostics device.

## IR PARTICLE LOSSES AND BACKGROUNDS

The topics of main background sources, such as SR and beam particles effects (beam-beam, Touschek, beam-gas, etc…), were addressed in Talk 6. The design of the Interaction Region (IR) is a critical issue for the achievement of goal performances. This includes a trade-off of the machine and detector constraints, such as physical acceptance, smallest possible beam pipe radius, detector solenoid design with realistic field shaping and compensation, distance of the first quadrupole from the Interaction Point (IP). In this framework, a realistic simulation of all the effects inducing beam backgrounds is essential.

A Monte Carlo simulation tool, already tested at different colliders, is in place to estimate backgrounds from all these different sources, to compute the total beam lifetime and to find the appropriate masks and collimators location, with realistic IR physical aperture. For all estimations the ring energy acceptance is a very important parameter and should be included in lifetime calculations. A preliminary study of Touschek scattering simulation in CEPC IR was done, however the evolution of the IR design needs more iterations. Also radiative Bhabha trajectories in CEPC IR (old version) were computed, as shown in Figure 8. A constant 3cm aperture was assumed everywhere; losses are of course concentrated at high $\beta_x$ locations.

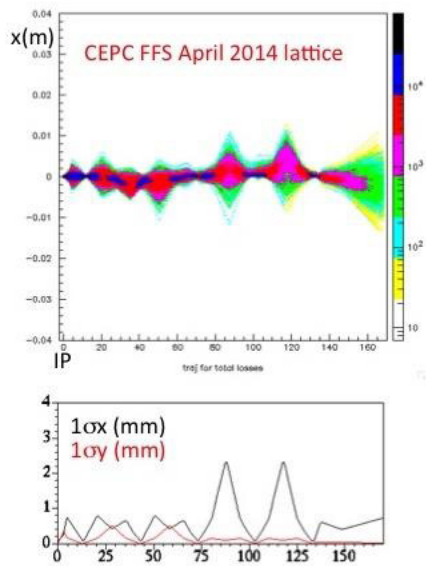


Figure 8: First estimate of CEPC radiative Bhabha trajectories (top) and beam size envelopes (bottom).

For the estimation of the SR in the IR care must be taken in evaluating: the compatibility of the stay clear apertures with an effective masking of the incoming SR, the edge scattering from the upstream SR masks, the backscattering from downstream aperture limitations.



ISBN 978-3-95450-172-4

## SR ABSORPTION AND VACUUM ISSUES IN THE IR

A discussion of how the SR photons absorption was done in the PEP-II IR vacuum chamber, with the deposited power taken away and the emitted gasses pumped away not to cause beam-gas backgrounds, together with implications for a Higgs Factory, were presented in Talk 7.

The PEP-II IR design was particularly complicated due to the head-on collision of two beams, of very different energies, coming from two rings vertically separated. A permanent magnet (B1) very close to the IP was used to provide early separation of the two beams, but was also producing unwanted SR in the IP region. The design of the beam pipe masking for power absorption, backgrounds and High Order Modes required special care. PEP-II masks are shown in Figure 9.


Figure 9: PEP-II IR masks near the Babar detector.

An example of the SR fans in the PEP-II IR of the High Energy Ring (HER) is shown in Figure 10.

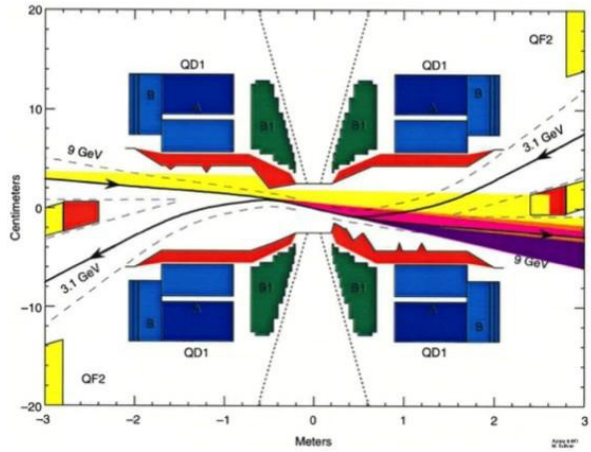


Figure 10: PEP-II IR HER X-rays fans.

## CONCLUSIONS

The key future topics for what concerns the SR and shielding in a Higgs Factory were identified:

A. Stabilize the storage ring parameters so that the injector parameters and power losses will stabilize.
B. Carryout the next layer of design of the injector chain.
C. Develop a tunnel design with shafts/cranes/CV etc, to study surrounding radiation effects and electronics shielding.
D. Design a vacuum system for the hard areas: SCRF, injection, IR, wigglers.
E. Need a next layer (realistic) of IR design.
F. Study in detail the SR power lost in the Interaction Region.
G. Develop a vacuum-pumping scheme for the IR.
H. Develop a masking scheme for the detector from x-rays and lost particles.
I. Develop non-destructive diagnostics with wide spectral range and high sensitivity.

## ACKNOWLEDGMENT

The authors warmly acknowledge all the speakers for their presentations and IHEP for hosting the ICFA beam dynamics workshop.



ISBN 978-3-95450-172-4

# HF2014 REPORT OF WORKING GROUP 5: SUPERCONDUCTING RF*

Sergey Belomestnykh[#,1,2] and Yoshiyuki Morita[§,3]
[1)]Brookhaven National Laboratory, Upton, NY 11973-5000, U.S.A.
[2)]Stony Brook University, Stony Brook, NY 11794, U.S.A.
[3)]KEK, Tsukuba, Ibaraki 305-0801, Japan

*Abstract*

This report summarizes presentations and discussions that took place during two sessions of the Working Group 5 (WG5) of the HF2014 workshop. In WG5 we reviewed Superconducting RF (SRF) systems of FCC-ee and CEPC and considered SRF structures, peripheral components and other issues relevant to the future circular colliders. In particular, we discussed the validity of cavity parameters and cavity design (frequency, voltage, input RF power, coupling, and HOM damping scheme), high power couplers, HOM dampers, frequency tuners, operating experience and other issues. As the result of WG5, we have come up with a list of important issues that have to be addressed in future studies.

## INTRODUCTION

The two proposed future high luminosity energy frontier $e^+e^-$ circular colliders, Circular Electron-Positron Collider (CEPC) in China and Future Circular Collider (FCC-ee) at CERN, would operate as Higgs Factories as well as at other energies of interest (Z, W, top quark) for precision measurements and search for rare processes. Circumference of these machines will be in the range of 50 to 100 km. Radio-frequency systems of these colliders will utilize superconducting RF structures and will have to compensate energy loss of several GeV due to synchrotron radiation with an RF power limit set to ~100 MW. As a result, these systems will have a large number of SRF cavities equipped with high-power RF input couplers and with strong damping of higher order modes (HOMs). Working Group 5 of the 55th ICFA Advanced Beam Dynamics Workshop on High Luminosity Circular $e^+e^-$ Colliders – Higgs Factory (HF2014) was dedicated to discuss topics relevant to the SRF systems. In this report we summarize the discussions and outline important R&D issues.

## SRF SYSTEM PARAMETERS AND REQUIREMENTS

Both CEPC and FCC-ee would use large superconducting RF systems as the energy loss to synchrotron radiation is very high and the systems would have to compensate power loss of ~50 MW per beam.

Table 1: Key Parameters of the CEPC and FCC-ee SRF Systems

| Parameter | CEPC | FCC-ee |
|---|---|---|
| Beam energy | 120 GeV | 120 GeV (175 GeV) |
| Energy loss per turn | 3.11 GeV | 1.67 GeV (7.5 GeV) |
| Synchrotron radiation power | 103.4 MW | 100 MW |
| Bunch charge | 60.56 nC | 59.2 nC (13 nC) |
| Bunch length | 2.65 mm | N/A |
| Beam current (two beams) | 33.2 mA | 60 mA (13.2 mA) |
| RF voltage | 6.87 GeV | 2.7 GeV (11.2 GeV) |
| RF frequency | 650 MHz | 400 MHz |
| Number of cavities | 384 | 568 |
| Number of cells per cavity | 5 | 5 |
| $E_{acc}$ | 15.5 MV/m | 2.53 MV/m (10.5 MV/m) |
| $Q_0$ | $2{\cdot}10^{10}$ at 2 K | $2{\cdot}10^{10}$ at 2 K |
| Number of cryomodules | 96 | 71 |
| RF power per cavity | 260 kW | 176 kW |
| HOM power per cavity | 3.5 kW | N/A |

As a result, requirements to the RF input power couplers are quite demanding. The systems need SRF cavities with strong HOM damping to avoid multi-bunch instabilities and reduce parasitic beam power loss to HOMs. These and some other considerations lead to selecting relatively low operating RF frequencies. Table 1 lists key parameters of the two colliders relevant to the SRF

*Work is partly supported by Brookhaven Science Associates, LLC under contract No. DE-AC02-98CH10886 with the US DOE.
[#]sbelomestnykh@bnl.gov
[§]yoshiyuki.morita@kek.jp



ISBN 978-3-95450-172-4

system considerations. To make the comparison easier, we list only the beam parameters at 120 GeV for both machines (Higgs Factory regime) and at 175 GeV for FCC-ee (Top Factory regime). More details can be found in references [1]-[2].

### *CEPC SRF System [1]*

The CEPC SRF system will be distributed through all eight straight sections of CEPC. In the baseline configuration, each cavity is driven by an individual RF power source. The total installed RF power will reach 124 MW. Eight 18-kW plants will comprise the CEPC cryogenic system, similar to LHC. The system design optimization led to choosing the SRF parameters listed in Table 1. The RF frequency, 650 MHz, has synergy with other projects, such as ADS and PIP-II.

Within a reasonable CW accelerating gradient range, the number of cavities in the collider ring is limited by an input coupler power of 260 kW. While in the future the project might benefit from alternative cavity materials (Nb/Cu or $Nb_3Sn$), the CEPC specifications are beyond the state-of-the-art of these materials at present. Therefore bulk niobium cavities operating at 2 K were chosen as the baseline design. The quality factor of $2 \cdot 10^{10}$ can be reached without advanced cavity treatment techniques. However, niobium doping and magnetic flux expulsion will be studied and might lead to a cost reduction.

Very dense beam frequency spectrum and short bunch length require strong HOM damping of the SRF structures with quality factors in a range from $10^3$ to $10^4$. An average HOM power loss is calculated to be 3.5 kW per five-cell SRF cavity with 80% of the power at frequencies above the cavity beam pipe cut-off, as illustrated in Figure 1. As a result, in addition to hook-type couplers, ferrite beam pipe absorbers will be installed to deal with the high-frequency portion of HOM spectrum. Waveguide HOM damping scheme is also under consideration.

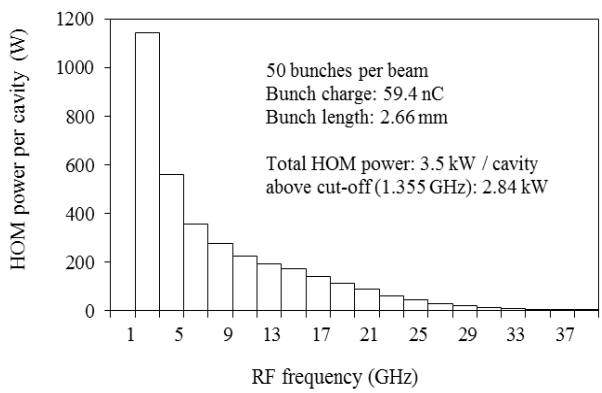


Figure 1: CEPC SRF cavity HOM power spectrum [1].

Large amount of HOM power traveling through the cryogenic environment will introduce an additional heat load. Careful evaluation and design optimisation will have to be carried out to minimize this parasitic heat load.

### *FCC-ee SRF System Considerations [2]*

An SRF frequency of 400 MHz was chosen for the FCC-ee as a staring point. Upon careful optimization it may change in a frequency range between 200 MHz and 800 MHz, but will have to be a harmonic of 40 MHz. As an accelerating gradient was chosen to be quite moderate at 10.5 MV/m, the preferred SRF cavity fabrication technology is thin film niobium on a copper substrate. In addition to cost savings, this would allow scaling to large cavity size (low frequency) if necessary. Three FCC RF R&D areas were identified with the following topics:

- Superconducting RF
  - Cavity technology
  - Power couplers
  - Cavity optimization
  - Cryomodules
- Large RF Systems
  - Availability
  - Reliability
  - Maintainability
  - Operational aspects
- Energy Efficiency
  - Efficient power sources
  - Lowering cryogenic load
  - Energy recovery?

In addition to pushing R&D of Nb/Cu coating techniques, $Nb_3Sn$ research recently produced promising results. New treatment techniques (nitrogen doping) will be looked at as well. The SRF R&D for FCC blends well into a wider R&D program at CERN, which includes developments for LHC, HL-LHC, HIE-ISOLDE, SPL and ERL-TF.

CERN is also pursuing a very high efficiency klystron development. Recent studies make an efficiency of 90% look possible. Another option would be a multi-beam IOT. ESS has revived this research recently in a joint effort with CERN.

## SRF CAVITY OPTIONS

There are no SRF structures developed specifically for either CEPC or FCC-ee yet. Both teams just starting this process and consider some existing structures as possible prototypes for their future designs. In particular, SRF cavities under development at BNL and JLab might be considered as such prototypes and were discussed at the workshop.

### *BNL3 Cavity as An Option for CEPC/FCC [3]*

A 704 MHz five-cell SRF cavity, BNL3, was designed at BNL for high current linacs (SPL, eRHIC). One of the cavity's salient features is a compact and efficient HOM damping scheme with three HOM coupler ports on each beam pipe of the cavity, as shown in Figure 2.



ISBN 978-3-95450-172-4

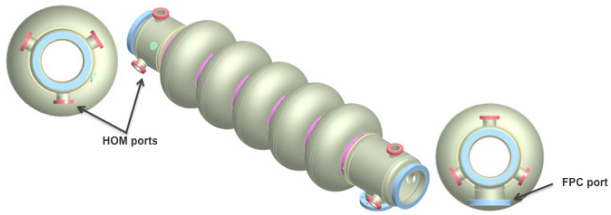


Figure 2: BNL3 cavity [3].

The strong HOM damping offered by this cavity makes it an attractive option as a prototype for future $e^+e^-$ colliders. Two versions of HOM couplers are under development. One version employs a high-pass lump-element filter; the other is based on a dual ridge waveguide. Each of the couplers will be capable of handling ~1 kW of the HOM power. Two Nb cavities have been fabricated with one of them reaching ~20 MV/m.

### *Alternative Structures at JLab [4]*

JLab is traditionally developing SRF structures with waveguide type HOM couplers. Recently, the focus of these efforts was directed toward the future electron-ion collider MEIC. The MEIC SRF systems face challenges similar to the future $e^+e^-$ colliders. The SRF structures will have to support high beam currents; deliver high accelerating voltage in a limited available space; provide large amount of RF power needed to compensate synchrotron radiation losses. The baseline design frequency is 750 MHz, while 1500 MHz is under consideration.

An "on-cell" damper concept, depicted in Figure 3, was shown to meet stringent HOM damping requirements of MEIC. However, there are still many technical challenges associated with this design.

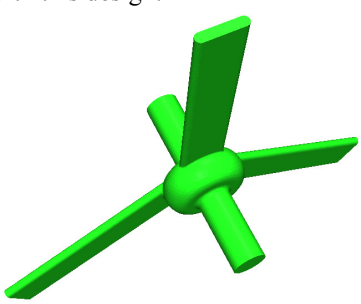

Figure 3: MEIC cavity concept with an "on-cell" HOM damper (courtesy of JLab).

Previously, two five-cell cavities were developed at JLab for high-current ERL applications: a 1500 MHz cavity for 100-mA beam current and an Ampere-class 750 MHz cavity. Both cavities feature waveguide HOM couplers attached to their beam pipes. Prototype cavities of both designs were built and tested, demonstrating very good performance. Figure 4 shows a photograph of the 750 MHz cavity.

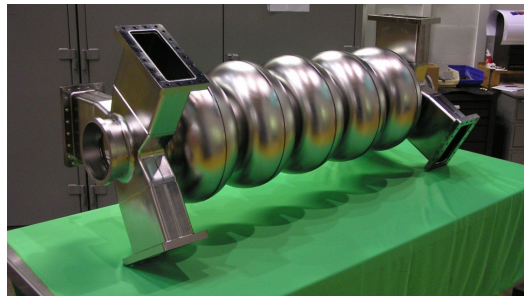

Figure 4: 750 MHz Ampere-class ERL cavity (courtesy of JLab).

## HOM DAMPER HARDWARE [5]

There are a large variety of HOM damper designs for SRF cavities. However, very few of those are designed to handle high average HOM power and even fewer demonstrated this in operation. Designs of the HOM dampers, existing and under development were reviewed in WG5 with an emphasis on applicability to future energy frontier circular colliders.

Three main design types were presented. Those types are beam pipe absorbers, rectangular waveguide HOM couplers and loop/antenna HOM couplers to a coaxial line. Then, pros and cons of different HOM damper types were discussed.

The beam pipe absorbers are arguably the most efficient in HOM damping and likely will be required to absorb very high frequency portion of the HOM power, which propagates along the beam pipe. Room temperature HOM loads demonstrated capacity to absorb several kW of HOM power at CESR and KEKB. Drawbacks of the beam pipe absorbers are: i) most absorber materials are brittle, can create particulates that contaminate SRF cavities; ii) parasitic beam-absorber interaction is significant and contributes to the overall HOM power; iii) the main disadvantage for large SRF systems is that the HOM loads occupy real estate along the beam axis and thus reduce the SRF system fill factor.

The waveguide couplers can provide very efficient damping in a broad frequency range and don't compromise the fill factor. In theory, these couplers should be able to handle high HOM power, but this has not been demonstrated in operation yet. The disadvantage of using waveguides is that their large size significantly complicates the cavity and cryomodule designs. This damping scheme is worked on at Jefferson Lab primarily.

The coaxial loop/antenna HOM couplers require means of rejecting the fundamental mode. Rejection filters can be very narrowband and difficult to tune. The LHC HOM couplers were designed for ~1 kW HOM power levels, but operate at lower HOM power levels so far. High-pass filters can be used instead of narrowband rejection filters. The high-pass filters, if properly designed, should be easy to tune. A couple of promising designs are under development at BNL for the BNL3 cavity as mentioned in the previous section. Yet another



ISBN 978-3-95450-172-4

~1 kW HOM coupler design, which might be suitable for the future colliders, is being worked on for the HL-LHC compact crab cavities.

## HIGH POWER COUPLERS [6]

A high power RF input coupler is one of the most critical components of an SRF system. Design of an input coupler strongly depends on a cryomodule structure. Essential considerations for input couplers are: RF power capability ( $P_{RF} = I_{beam} \cdot V_{acc} \cdot \cos\phi$ ); coupler type (coaxial or waveguide); ceramics window type (disk or cylindrical); number of windows (single or double); coupling with cavity (fixed or adjustable); cooling method (air, He-gas, $N_2$-gas or water); and bias voltage (useful or needless). Important technical issues are: ceramics window (material, purity); metalizing of ceramics; copper plating (thickness, RRR, adhesion, pits, uniformity); TiN coating (thickness, uniformity); joining by brazing; welding by TIG, laser or E-beam; RF properties; thermal characteristics; mechanical analysis; multipacting simulation; cleaning procedure; and assembly in clean room.

TRISTAN-type high power couplers were reviewed. The coupler was originally designed for TRISTAN 508 MHz SRF cavities by S. Noguchi, E. Kako, et al. It has a coaxial disk ceramic window with a choke structure. Couplers of this type are used for cavities at many laboratories around the world in a wide range of frequencies between 500 to 1300 MHz. An RF power up to 380 kW was demonstrated in CW operation and up to 2 MW in pulsed regime. High power couplers developed at CEA-Saclay, CERN and BNL were also reviewed.

At CEPC, the BEPC-II 500 MHz SRF cavity coupler is taken as the baseline for the CEPC main ring SRF cavities. The KEK cERL main linac power coupler is taken as the baseline for the CEPC booster SRF cavities.

Parameters of the input couplers in a frequency range between 650 and 802 MHz were summarized in a table [6]. Main RF parameters were considered for the input couplers of CEPC and FCC, such as the RF frequency, required RF power, range of external $Q$ factors, etc.

Coaxial CW high power input couplers with a single warm RF window have been developed in a frequency range of 500 to 1300 MHz at a power level higher than 100 kW in many laboratories around the world. Design studies of high power couplers at 400 MHz, 176 kW CW for FCC and at 650 MHz, 260 kW CW for CEPC should be started as soon as possible. Fabrication of the prototype high power couplers and RF conditioning at a test stand should be carried out at an early stage.

## OTHER ISSUES [7]

Three other issues were presented. Those are frequency tuners, operating experience and performance recovery.

### *Frequency Tuners*

A frequency tuner is an important system for cavity operation to tune the cavity to its operating frequency, detune to compensate the beam loading and help to stabilize its RF amplitude and phase. The frequency tuner designs have well advanced for a variety of requirements. Presently there are many excellent tuner designs from which one can select an appropriate design. Mass production and reliability issues have to be taken into considerations during the tuner design selection. In this talk several tuner design examples were presented.

Four tuner systems from an early stage of the SRF technology development were reviewed. The CESR tuner had a flex hinge system without backlash. The CEBAF tuner had a drive shaft system with a stepping motor driver exterior to the cryomodule. The LEP tuner utilized thermal expansion and contraction of three Ni bars for coarse tuning with a magnetostrictive effect utilized for a fine tuner. The TRISTAN tuner applied a lever system with a piezoactuator for fine tuning. This mechanism was also used for the KEKB 509 MHz, single cell cavity. Furthermore it will be used for the SuperKEKB operation.

The S1-Global cavity string test for the ILC at the superconducting RF test facility (STF) of KEK has three tuner systems. Those are a blade tuner developed by INFN Milan, a double lever system developed by DESY based on the Saclay tuner and a slide jack system developed by KEK. All components of the first two systems are located in a cold section while the driver of the KEK tuner is located in a warm section.

Other tuner examples are a double lever and eccentric shafts system recently developed by Saclay and a scissor jack system for the CEBAF upgrade cryomodule.

Among those tuner designs, the lever and piezoactuator system has been in service for a long time and proved to be a reliable system. The KEK 509 MHz tuner system has really long life. Location of the tuner driver is an important consideration. A cold location makes a tuner system compact, while a warm and exterior to the cryomodule location makes the maintenance easy.

### *Operating Experience*

Operating experience gained elsewhere provides very useful information for designing a new SRF system. As an example, operating experience at KEKB was presented. KEKB is a high luminosity, electron-positron double-ring asymmetric B-factory. Eight single cell SRF cavities, operating at 509 MHz, were operated in its high energy ring. Three main issues were presented. Those are cavity RF trip rate, cavity troubles, and performance degradation.

The cavity trips were mainly caused by high voltage breakdown in the cavity or in the high power coupler. The trip rate was 0.5 trips per day for eight cavities during the 1.4 A operation. In order to keep the trip rate low, maintenance work is important. RF processing of the input power coupler with voltage biasing was emphasized as an effective maintenance tool. There were several



ISBN 978-3-95450-172-4

vacuum leak troubles. Some of the leaked cavities were re-assembled at indium seal joints without further surface treatments.

KEKB cavities still provided an accelerating voltage of 2 MV after 10 years of operation. However the cavity's $Q$ factors degraded from $2{\cdot}10^9$ to several $10^8$ with strong field emission. Further degradation would make the operation difficult.

### *Performance Recovery*

Performance recovery methods are desired and needed for long-term operation. The recovery should be accomplished with a low risk, low cost and in a short period of time. KEK has developed a horizontal high pressure water rinsing that can be applied directly to a cavity in the cryomodule. Two KEKB cavities successfully recovered their $Q$ factors after horizontal high pressure rinsing.

## SUMMARY

In WG5, we have considered parameters of the SRF systems for CEPC and FCC-ee, requirements and challenges. Also, we discussed SRF cavity designs, HOM dampers, RF input couplers, frequency tuners and operational experience, performance degradation and recovery.

There are a number of important issues that have to be addressed in future studies. Among those are:

- HOM studies, including: trapped modes; efficient HOM coupler designs; propagation of the very high frequency portion of HOM power, its absorption, and associated parasitic heat load.
- SRF cavity design: frequency; number of cells per cavity; optimal operating temperature; nitrogen doping at low frequencies; new materials.
- Design of high power RF input couplers.
- Does FCC-ee at Higgs and Z energies require two different SRF systems? It appears that these are two very different regimes: LEP-like *vs.* B-factory-like.
- General SRF/cryogenic system optimization.
- Efficiency of RF power sources.

Ideally, these studies will be executed in collaborations, utilizing synergy with other projects and labs

## ACKNOWLEDGMENT

The authors would like to thank the WG5 presenters Frank Zimmermann (CERN), Jiyuan Zhai (IHEP), Wencan Xu (BNL) and Eiji Kako (KEK) for delivering talks and participating in the working group. Erk Jensen of CERN, Robert Rimmer and Haipeng Wang of Jefferson Lab are acknowledged for providing materials for the workshop.

## REFERENCES

[1] J. Zhai, "CEPC SRF system," these proceedings, HF2014, Beijing, China, (2014).
[2] F. Zimmermann and E. Jensen, " Future Circular Collider study: FCC-ee SC RF system," these proceedings, HF2014, Beijing, China, (2014).
[3] Wencan Xu, "704 MHz BNL3 cavity as an option for CEPC/FCC," these proceedings, HF2014, Beijing, China, (2014).
[4] R. Rimmer and H. Wang (Jefferson Lab), private communications.
[5] S. Belomestnykh, "HOM damper hardware considerations for future energy frontier circular colliders," these proceedings, HF2014, Beijing, China, (2014).
[6] E. Kako, "High power couplers for Higgs Factory," these proceedings, HF2014, Beijing, China, (2014).
[7] Y. Morita, "Other issues," these proceedings, HF2014, Beijing, China, (2014).



ISBN 978-3-95450-172-4

# SUMMARY OF WORKING GROUP 6 – INJECTORS AND INJECTION HF2014

Yannis Papaphilippou, CERN, Geneva, Switzerland
David Rice, Cornell University, Ithaca, U.S.A.

*Abstract*

We present a summary of presentations made in Working Group 6, *Injectors and Injection*, at the 55th ICFA Advanced Beam Dynamics Workshop on High Luminosity Circular e+e- Colliders – HF2014 in Beijing, China. The workshop was held October 9-12, 2014.

## PAPERS PRESENTED

Contributions covered planned injectors and injection for CEPC (Chuang Zhang) and FCC-ee (Yannis Papaphilippou), polarization preservation in synchrotrons (Ivan Koop), top-up injection (John Seeman and Richard Talman), and injection with pretzels (Dave Rice).

We cover the highlights from each presentation then offer our summary of injection highlights and challenges at the end of this paper.

## CEPC PLANS (IHEP)

Both CEPC and FCC-ee are planning on a full energy injector that is necessarily similar in size to the full ring, and thus sharing the same tunnel. Chuang Zhang presented a conceptual design for the CEPC full injector. Because the CEPC design anticipates building a newly constructed injector complex, the booster injection energy is 6 GeV from a linear accelerator, limited by cost considerations, though 10 GeV was mentioned as a possibility. The low energy of the injector is a primary issue for development.

An injection interval of 10 seconds, with intensity of 5% of the stored beam, simultaneously filling all 50 bunches in the collider ring will conservatively meet the needs of the predicted 25 minute collider beam lifetime, giving a factor of 3.75 combined margin for injection efficiency and beam lifetime.

A 6 GeV linac provides both electrons and positrons to the booster ring. A target at the 4 GeV point produces positrons that are accelerated to 200 MeV for return to the front end of the linac. Plans are to construct the linac on the surface with a sloped transfer line to the level of the booster.

The booster is filled with 50 bunches at 6 GeV by 50 linac pulses (operating at 100 Hz) then ramped to 120 GeV in 4 seconds. The plan presented did not include a positron damping ring, rather a booster dwell period at 120 GeV is expected to provide sufficient damping.

The beam is transferred from the booster to the storage ring 2 m below with horizontal bends and vertical Lambertson magnets. The beam is injected in the horizontal plane via a segmented septum magnet. Injection in the vertical plane is considered to ease concerns about the pretzel configuration, but this is complicated by the large $\beta_V^*$ needed for local chromaticity correction in the IR.

The booster employs a 1300 MHz RF system with details still in design process.

Primary concerns are stability of the net magnetic field (30 Gauss) at injection into the booster and beam stability (125 seconds damping time), and injection into the pretzel orbits. A "wiggling-bend" layout (Figure 1) with half of the bends being bipolar to decrease damping time at 6 GeV is being considered as is higher injection energy (longer linac) and a pre-booster ring.

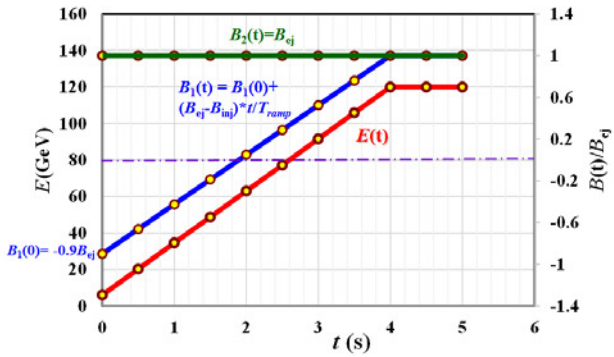


Figure 1: CEPC wiggling bend ramp program.

## FCC-ee PLANS (CERN)

Yannis Papaphilippou described the FCC-ee injector, which is being designed to provide e+/e- for Z, W, Higgs, and $t\bar{t}$ (45.5 – 175 GeV) compatible with the expected 20 minute lifetime at $t\bar{t}$ energy. (Table 1) The availability of the SPS as a 20 GeV pre-booster would allow higher energy injection into the booster compared to the 6-10 GeV CEPC plans.

Following the proposed CLIC design, a new linac operated at 50Hz would accelerate 1360 bunches (in the case of the Higgs production) in a 2GHz structure. Eight linac batches are injected into a 50MHz RF system in the SPS at 10GeV to be accelerated and injected into the booster ring at 20 GeV. Five SPS accelerating cycles of 1.2 s are used providing the total 1360 bunches in the Booster flat bottom. With the addition of wigglers, the SPS can also serve as a damping ring.

Both the linac injector and booster ring are designed to provide low emittance beams (~1 nm at 120 GeV) for improved injection efficiency (~ 80%). New RF systems are needed throughout the injector chain – linac (2000 MHz, SPS (50 MHz) and booster (50 MHz).

Alternative injection schemes were presented, including synchrotron injection (both Δp and Δt) and pulsed sextupole injection.



ISBN 978-3-95450-172-4

Primary concerns are the stability of the booster guide field at 20 GeV (60 g) including stray fields, finding the optimum pre-booster chain choosing from both new and existing systems, accommodating shared use, and meeting the needs of a wide range of collider energies, bunch patterns, and currents.

Table 1: FCC-ee Injector Tentative Parameters

| Accelerator | FCCee-Z | | FCCee-W | | FCCee-H | | FCCee-tt | |
|---|---|---|---|---|---|---|---|---|
| Energy [GeV] | 45.5 | | 80 | | 120 | | 175 | |
| Type of filling | Full | Top-up | Full | Top-up | Full | Top-up | Full | Top-up |
| LINAC # bunches | 3200 | | | | 1360 | | 280 | |
| LINAC repetition rate [Hz] | 50 | | | | | | | |
| LINAC RF freq [MHz] | 2000 | | | | | | | |
| LINAC bunch population [$10^8$] | 5.9 | 0.4 | 0.6 | 0.2 | 0.3 | 0.3 | 0.02 | 0.04 |
| # of LINAC injections | 8 | | | | | | 7 | |
| SPS/BR bunch spacing [MHz] | 50 | | | | | | | |
| SPS bunches/injection | 80 | | | | 34 | | 7 | |
| SPS bunch population [$10^{10}$] | 2.35 | 0.16 | 0.25 | 0.08 | 0.12 | 0.12 | 0.10 | 0.14 |
| SPS duty factor | 0.5 | | | | | | 0.29 | |
| SPS / BR # of bunches | 640/3200 | | | | 272/1360 | | 49/98 | |
| SPS / BR cycle time [s] | 1.2 / 12 | | | | | | 1.2 / 8.4 | |
| Number of BR cycles | 50 | 15 | 50 | 3 | 50 | 1 | 71 | 1 |
| Transfer efficiency | 0.8 | | | | | | | |
| Total number of bunches | 16700 | | 4490 | | 1360 | | 98 | |
| Filling time (both species) [sec] | 1200 | 360 | 1200 | 72 | 1200 | 24 | 1193 | 16.8 |
| Injected bunch population [$10^{10}$] | 18 | 0.36 | 7 | 0.14 | 0.46 | 0.092 | 14 | 0.28 |

## POLARIZATION

While physics with longitudinally polarized beams is desirable, the high luminosity and related IR configurations will be extremely challenging. The most likely use of polarization will be in energy calibration, especially at Z and WW energies where only a few percent polarization is required. A precision of $10^{-5}$ or better is desired. Maintaining polarization above 80 GeV beam energy becomes difficult as the depolarization time approaches the time the beam is in the booster.

Ivan Koop showed that polarization may be maintained throughout the acceleration cycle by having a spin tune of ½. This may be accomplished with an odd number of 180º snakes (Figure 2). With three snakes, depolarization time is 320 seconds at 45.5 GeV and 6.2 s at 80 GeV. Increasing the number of snakes to 7 or 9 would preserve polarization into the 80-100 GeV range, confirmed by spin tracking simulations.

Dynamic depolarization from orbit distortions and betatron oscillations appears minimal according to simulations performed to 86 GeV. Alternating signs of the solenoid field will substantially reduce spin tune chromaticity.

In summary, polarization should be maintainable in the booster synchrotron up to 80-100 GeV given sufficient care and installation of up to 9 180º snakes. Spin tracking, including radiative effects, is required for confidence in the design.

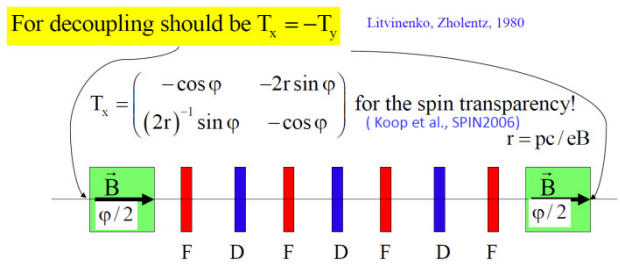


Figure 2: Spin transparent rotator for the solenoid partial snake. Two solenoids, each 40 m, 5T, provide 180º rotation at 45.5 GeV.

## TOP-UP INJECTION

Top-up injection has been used at PEP-II and KEK-B, producing impressive gains in performance. In addition to the expected 15-20% gain over periodic refilling, the nearly constant currents from topping up every one or two minutes permits more focused optimization of tuning, adding another 10-20% in luminosity.

John Seeman stated that, beyond an efficient injection strategy, top-up operation requires attention to individual storage ring bunch currents, injector bunch charges and timing relationships throughout the facility. In addition, the details of particle losses near the interaction region and the characteristics of the physics detectors' systems will determine need for masking, inhibiting of trigger systems, or protection of high voltage systems.

The PEP-II top-up ("trickle-charge") injection controller was able to track the bunches with lowest charge, tailor the gun charge to match what was needed to top up to nominal current, and time the gun pulse to fill the right storage ring bunch, even after positron generation and damping ring time. Each 3 to 15 Hz injection cycle carried 3-9x$10^9$ particles in one bunch.

Masking of the detector trigger was tailored around the lost particle pattern, covering the full azimuthal distribution of bunches for several turns, then limited to 100-200 bunches around the azimuth of the bunch just filled for over 1000 turns. (Figure 3)

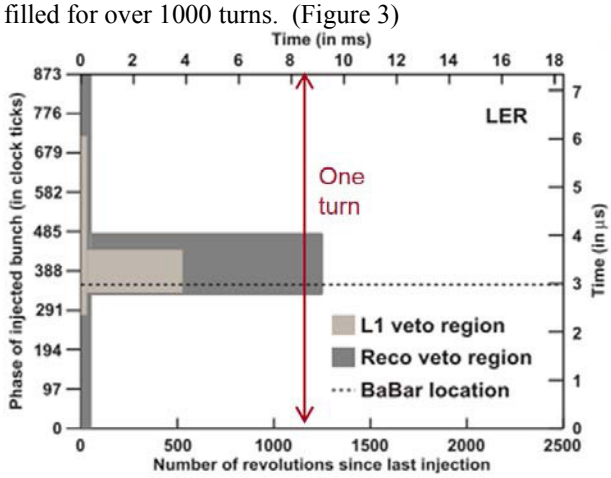


Figure 3: Regions of azimuth-time masked in BaBar detector at PEP-II for level-1 triggers and reconstruction triggers.

ISBN 978-3-95450-172-4

There should be no fundamental barriers for top-up operation in a Higgs factory, but attention will be required to control particle losses, background, and track bunch-by-bunch charges and timing. Close work with detector designers will be essential. A rapidly (2-4 seconds) ramped booster ring should be adequate to keep collider currents within a few percent of peak.

## INJECTION WITH PRETZELS

Dave Rice suggested that the major issue for injection with pretzels is the passage of the injected bunch near the core of the opposing beam. Economical design and optics considerations limit separation of the beams at parasitic crossing points to around 10 σ. (Figure 4) When stacking is done in betatron phase space, limiting the amplitude of the injected bunch core around the equilibrium orbit to much less than 10 σ (stored beam wall clearance, injected beam clearance, septum thickness) is challenging. If the pretzel and injection are in the same plane (typically horizontal) injection efficiency plummets. With flat beams, the beam dynamics at PC's impact vertical motion more than horizontal, placing a premium on good vertical apertures, physical and dynamic.

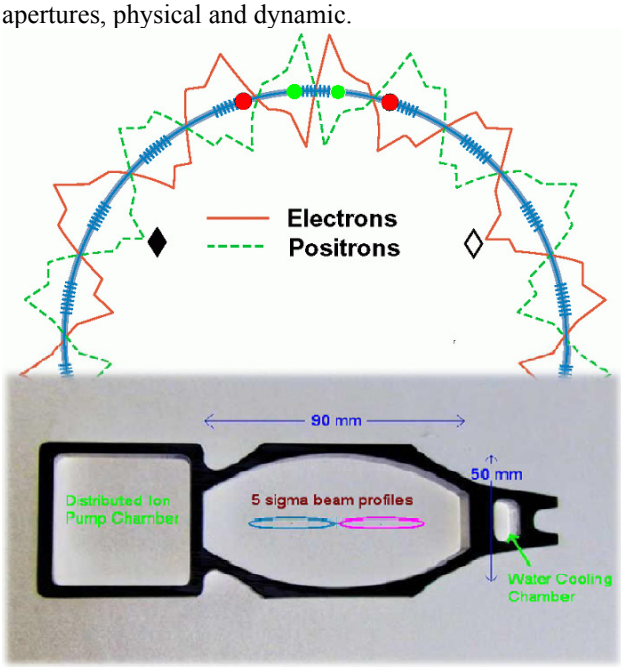


Figure 4: CESR pretzel orbits and beam profiles.

Beam-beam tune shift from parasitic crossings further complicate injection since, depending on distribution of bunch currents and optics functions at PC's, each bunch may have variation in betatron tunes.

These effects can bring the injection efficiency from a single-beam value of ~80% down to 10-30%. Simulations, either tracking or beam envelope analysis, can be useful to identify particularly bad crossing points.

Several mitigating steps used at CESR were presented, including: optics design for maximum separation at PC's; using special sextupole families to control the tunes of the two beams; increase the vertical emittance of the "strong" beam by coupling to reduce the vertical gradient for BBI;.a short kicker pulse may be used to decrease the amplitude of the injected bunch at the expense of small excitation of the previously stored bunch; keeping bunch populations even is usually beneficial.

The experience at LEP may offer guidance closer to the HF experience – in addition to the higher energy LEP had less (but still significant) flexibility in optics.

Other injection schemes such as vertical and longitudinal phase space stacking may be preferred if other factors are favorable (though the restriction of vertical acceptance by the IR configuration will challenge vertical injection designs). In determining an injection scheme, one may assume that any particles passing within 2 σ of the opposing beam are at risk. A program of detailed modelling and simulation must be part of any design effort where injection with pretzels is planned.

## LATTICE OPTIMIZATION FOR TOP-OFF INJECTION

Richard Talman stressed the critical role of efficient injection in a high-energy circular collider and presented several design strategies to meet this need.

Scaling parameters from LEP values, keeping dispersion constant will help in controlling chromaticity. This leads to cell length, $L_c$, scaling as $R^{1/2}$ as a reference point. Following through with the scaling of related parameters one reaches the conclusion that horizontal dynamic aperture $x_{d.a.}/\sigma_x \propto R^{1/2}$.

Designing the injector with smaller emittance than the storage ring would facilitate efficient injection and enable the kickerless injection described later. Talman suggests the cell length L to scale as $R^{1/4}$ for the injector and $R^{3/4}$ for the collider ring, varying about the central value mentioned above.

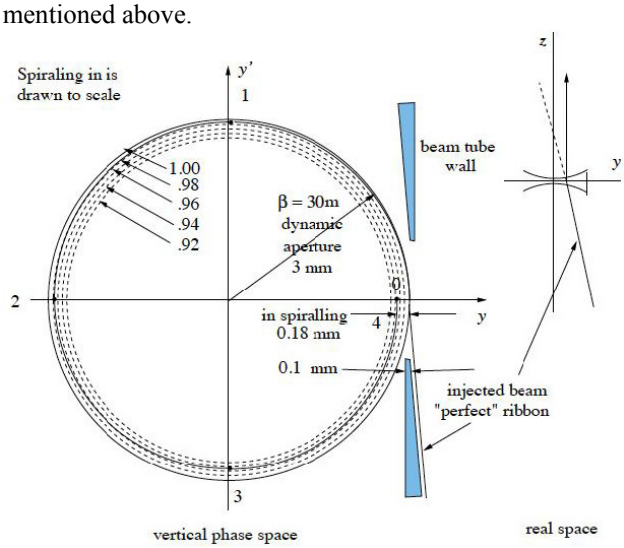


Figure 5: Schematic view of kicker-free vertical injection.

The fast damping in a Higgs factory might be exploited along with a thin (0.1 mm) septum and small vertical emittance to inject vertically without the need of kicker magnets. (Figure 5) Should this prove too challenging, a small pulsed closed-orbit bump would provide sufficient margin. As previously discussed, the IR designs to



ISBN 978-3-95450-172-4

implement a 1 mm $\beta_y^*$ will likely restrict vertical acceptance.

## SUMMARY

The short lifetimes and high energy inherent in high luminosity Higgs factories place new demands on the injector. Full energy, multiple-bunch topping off requires a booster ring similar in size to the collider ring, bringing the injector cost to a similar scale as the collider ring.

The relatively low B field of the booster ring at injection requires attention to power supply stability, stray currents from transient and ground capacitance effects, and shielding of ambient magnetic fields. Using ramped negative bends in a wiggler-ring configuration could mitigate some of these issues. Both projects consider low energy a primary booster ring design challenge.

Collective effects have not been studied in any depth. High frequency, multi-cell cavities exacerbate this concern, especially for the lower energy operation with optimum bunch numbers well over 1000. This concern ranks close to low B field in priority.

Maintaining polarization in the booster, at least up to 80 GeV, seems feasible with an odd number of 180º snakes. No design has yet made provision for these. Using polarization for energy calibration for Z and W operation is feasible, but beyond is more difficult. Longitudinal polarization for physics does not sound practical at this stage of machine design, nor does production of polarized positrons in sufficient quantity.

Proposals for reduction of positron emittance include adding damping wigglers to a pre-booster (SPS) and to the booster ring (CEPC), avoiding construction of a smaller, dedicated ring, although a dedicated ring may relax aperture requirements for the booster, thereby significantly reducing cost.

Top-up/trickle-charge operation is feasible with either 2 or 1 ring configuration. Careful thought must be given to instrumentation (bunch measurement and timing) and to detector backgrounds and having minimum dead-time from trigger masks and other detector protection measures.

Single ring / pretzel operation adds challenges to avoid "collisions" between injected bunches and opposing-beam bunches. CESR has had partial success mitigating these effects a variety of techniques. Pretzels and bunch trains were both used at LEP where the optics and beam energy were closer to the HF values. The critical issues with pretzel operation must be understood before finalizing a single-ring design.

Alternative injection schemes – vertical or longitudinal injection and optimization at every opportunity, such as reduction of emittance of the booster beam, will be key to successful operation of a Higgs factory.

## ACKNOWLEDGMENTS

The organizers of working group 6 were impressed by the enthusiastic participation and high level of presentations in this working group. We thank the workshop organizers for a stimulating week of interactions in a pleasant and well-organized meeting.



ISBN 978-3-95450-172-4

# SUMMARY FROM WORKING GROUP 9: INSTRUMENTATION AND CONTROL*

M. Minty#, Brookhaven National Laboratory
Upton, NY 11973, U.S.A

*Abstract*

Since the discovery of the Higgs particle at the Large Hadron Collider at CERN in 2012, feasibility studies for a very large future circular collider are ongoing for two designs in particular: the FCC in Europe and the CEPC-SppC in China. Both designs aim for initial operation as a Higgs factory. This workshop on High Luminosity Circular e+e- Colliders (HF2014), held in Beijing, China and hosted by the Institute of High Energy Physics (IHEP) and the Chinese Academy of Sciences (CAS), included a Working Group on Instrumentation and Control to consider important issues associated with these systems. While instrumentation and control designs are just starting, HF2014 provided the opportunity to discuss these systems and their challenges.

## INTRODUCTION

Instrumentation and Control are vital subsystems for a future e+e- collider operating for high luminosity Higgs boson production and beyond. The applied technologies must guarantee the challenging design parameters and collider luminosity. As the accelerator parameters are stabilizing, the diagnostic designs have recently started. These developments are expected to direct control system design, the technology for which is rapidly evolving and expected to continue so.

As instrumentation designs were anticipated by the working group conveners (M. Minty and H. Schmickler), prior to the workshop, as being quite similar to those demonstrated at existing accelerators with new challenges pertaining to the large-scale aspects of a future Higgs factory, presentations were solicited with the aim of understanding essential features, challenges and solutions based on experiences at existing accelerators most similar to those of a future e+e- collider.

## PRESENTATIONS

The working group activities consisted of invited talks and a discussion session starting with an additional talk on instrumentation in the CEPC design (instrumentation design for the FCC project has yet to start).

Y. Funakoshi (KEK) presented "Lessons learned from the B-Factories and implications for a high-luminosity circular e+e- Higgs factory" [1]. M. Wendt (CERN) presented "Challenges in beam instrumentation and diagnostics for large ring colliders – based on the LHC experience" [2]. The B-Factories have in common with the accelerator designs under consideration similar particle species while the LHC shares similarities in the context of the overall scale (many 10's of kilometre circumference). Concerning instrumentation and control (as well as many other aspects) both accelerators share certain similar challenges with technological developments of great importance for future large ring colliders ongoing.

M. Wendt's presentation contained an overview of instrumentation design challenges common to all future large ring colliders including:

(1) Large physical size of accelerator and correspondingly large number of instrumentation devices, impact on reliability and costs
(2) Issues associated with low temperatures in superconducting environments
(3) Higher-order modes and wakefields generated by the instrumentation
(4) For high power beams, the need for non-invasive beam detection methods
(5) Need for early observation and damping of beam instabilities
(6) Large dynamic range of instrumentation and compatibility with different particle species, need to anticipate changes as learned from operational experiences
(7) Damage potential from beams with high stored energy and impact on machine protection system (MPS) including all related components

Other challenges and motivations for requirements addressed by the presentations are given below.

Beam position monitors (BPMs) – The stringent tolerances on beam orbit stability, with rule-of-thumb scaling as ~ $1/10^{th}$ the beam size σ, imply the need for commensurately high accuracy beam position data. Real life experiences were presented showing susceptibility to ambient temperature variations which introduced significant systematic errors in the beam position

* Work supported by Brookhaven Science Associates, LLC under Contract No. DE-AC02-98CH10886 with the U.S. Department of Energy.
# minty@bnl.gov



ISBN 978-3-95450-172-4

measurements. Once identified these sensitivities were remedied.

- At KEKB, where BPM measurements are used for orbit feedback in the interactions regions (as well as for correction of the global orbit) up to 20% day-night variations in luminosity were essentially removed after application of thermal insulating sheets over the cables as diagnosed using an ingenious scheme involving signal processing using different combinations of signals from the BPM electrodes.
- At the LHC, the beam positions at an interaction point (IP) was reported to vary by up to 7 μm, a fraction of the beam size at the IP. Prototype tests with temperature controlled racks housing the BPM electronics virtually eliminated such variations in the reported beam positions.

For very large colliders other practical considerations for the BPMs and BPM electronics include the cumulative impedance of the large number of pickup electrodes, proximity of electronics for minimum cost and highest reliability and signal transport over long cables for which optical fibers were suggested to preserve signal quality. Signal-to-noise and dynamic range considerations will require special attention particularly in the single-ring collider scheme.

Ground motion effects – Sensitivity to slow orbit deviations depends on many factors including accelerator layout (single or double-ring collider), circumference scale (CEPC: ~ 50 km, FCC: 80-100 km, LHC: 27 km) and time scales of the variation. The effects of relatively slowly varying accelerator geometries were reported by both speakers.

- At KEKB slow vertical ground deformations of up to 25 mm were reported over the lifespan (construction to shutdown for SuperKEKB installations). Fortunately, almost no degradation of performance was observed provided the optics were corrected, which at KEKB were performed approximately every two weeks [1].
- At the LHC, orbit distortions due to gravitational forces (tidal forces) of ~ 200 μm peak-to-peak varying bi-diurnally were corrected by continuous operation of orbit feedback for which robust operation was of course essential.

Orbit stabilization in the presence of high power synchrotron radiation from high energy lepton beams – Orbit deviations caused by unexpected thermal heating (and cooling after a beam abort) of the vacuum chambers due to synchrotron radiation have been observed at KEKB (and PEP-II) despite elaborate vacuum chamber cooling designs. To address this, at KEKB, capacitive position sensors were installed to detect the relative position change between the BPMs and the adjacent sextupoles. The acquired data were then used to correct the BPM data. After implementation together with other cooling power reinforcements for the vacuum chambers in the interaction region and introduction of enormously beneficial continuous beam injection, orbit corrections performed as expected without any degradation to collider luminosity. Displacement sensors are planned for installation in SuperKEKB [3].

Electron clouds – Photoemission and secondary electron emission (electron cloud) formation was a limiting factor at both KEKB and the LHC.

- At KEKB, emittance dilution and degradation of the specific luminosity were observed due to electron clouds (in the positron ring). Several diagnostic tools have been developed to aid in their study including a sideband measurement sensitive to head-tail motion within a bunch, retarding field analysers and bunch-by-bunch position measurements. Counter-measures included solenoid windings around the drift spaces and a portion of the quadrupole magnets.
- At the LHC, electron clouds have included other adverse consequences such as particle loss and increased heat loads in the cryogenic systems. Instrumentation developments at the LHC have included a fast beam current transformer for measurement of the relative bunch intensities and gated cameras to allow measurement of the relative bunch sizes. In development also are a head-tail monitor and a multiband instability monitor to enable intra-bunch measurements.

Beam instabilities – Evaluation of electron cloud, fast-ion as well as impedance driven instabilities will need careful evaluation to ensure sufficiently high beam intensity thresholds. If instability thresholds appear marginal, fast feedback systems, both intrabunch and bunch-by-bunch may be applied to damp such instabilities. Careful engineering designs coupled with beam physics simulations should be performed. At SuperKEKB, for example, remediation efforts are planned with simulation results [3] showing a threshold electron density approximately 4-6 times higher than required.

Collision feedback – Y. Funakoshi presented a detailed overview of three algorithms used for maintaining collisions of e+e- beams in a double-ring collider: the beam-beam deflection method (as applied at the SLC and, in the vertical plane, at KEKB and planned for use at SuperKEKB), the luminosity dithering method (from PEP-II and planned for use at SuperKEKB) and beam size feedback (as applied in the horizontal plane of KEKB). At KEKB, special BPMs (OctoPos BPMs) were included close to the IP each with 8 electrodes used to measure the orbits of the two beams simultaneously. For routine beam operations however the orbit feedback systems used the set of four regular BPMs (each traversed by a single particle species). The orbit feedback was vital for maintaining luminosity and operated at a 0.25 Hz rate with a ~ 2 μm resolution. For single-ring colliders or anywhere where beams share a common vacuum

ISBN 978-3-95450-172-4

chamber, care must be taken to minimize coupling of BPM signals from different beams.

Luminosity tuning – Table 1 (from Ref. [1]) shows, the many tuning variables (knobs) used at KEKB and the measurements used to optimize these variables (observables). The frequency of corrections is also given. In addition to measurements of the beam position, the tuning algorithms require also measurements of the beam sizes from the synchrotron radiation interferometer (SRM) and of the luminosity. In addition to these corrections, it was found that linear optics corrections, performed approximately every two weeks, were essential for suppressing beam-beam blowup effects.

Beam orbit fluctuations due to triplet magnet vibrations will challenge measurement and correction schemes for future colliders with extremely small beam sizes at the interaction points.

Other developments in beam instrumentation – M. Wendt's talk included examples of instrumentation challenges from the LHC based on operating experiences. These include

- Beam loss monitoring (BLM) for the Machine Protection System (MPS) including high dynamic range, interplay with collimation system and measurements to detect unidentified falling objects (UFO)
- BLM R&D for close proximity of detector to beam including detectors (diamond, silicon, liquid-He ionization chambers) located within the cold cryostats
- Collimators with embedded BPMs to enable significantly faster collimator positioning
- High brightness, small beam size measurements including difficulties encountered using synchrotron light monitors (rf heating of mirror), possible use of interferometric methods and a new beam gas vertex detector (BGV) design
- R&D for mitigation of beam halo using a hollow electron lens
- More R&D on radiation tolerant chips and FPGAs

Several other instrumentation-related R&D efforts under consideration at the LHC were also presented including developments in non-invasive beam profile measurements such as gas jets, electron beam scanners and Schottky-based emittance measurements.

## DISCUSSION SESSION

J. Yue (IHEP) presented on "Beam instrumentation of CEPC" which included an overview of design principles and details on the types of diagnostics envisioned for the CEPC. The subsystems described largely followed conventional methods. In the short time remaining, an "Instrumentation Checklist" by H. Schmickler highlighting essential instrumentation subsystems and desirable features was presented and discussed. Flexibility in instrumentation design was considered absolutely necessary (design for all machine phases including commissioning, experiments and stable operation) with consensus that early written functional specifications should be made.

Questions were addressed on the effect of synchrotron radiation with high critical energy on the instrumentation and electronics. In addition, based on presentations during the plenary session and other working group sessions, it became clear that the physics programs for a future Higgs factory require precision measurements of the beam energy as needed also for determination of the beam's spin polarization and, to allow quantifying of various measurement errors, the beam energy spectrum. Such measurements are not only challenging but may even be needed on a single-bunch basis to determine differences in these properties between colliding and non-colliding bunches.

## SUMMARY

The accelerator designs for a future very large circular collider, with initial goal of operation as a Higgs factory, are now sufficiently advanced to allow development of the supporting instrumentation and control systems. At this conference, technological developments from accelerators sharing common features such as the high luminosity B-factories and the Large Hadron Collider were presented as relevant for the CEPC and FCC design. The instrumentation checklist presented during the discussion session could be extended and used as a basis for further definition of the specifications for instrumentation and control.

## REFERENCES

[1] Y. Funakoshi, "Lessons learned from the B-Factories and implications for a high-luminosity circular e+e- Higgs factory," these proceedings SUT1B1, HF2014, Beijing, China (2014).

[2] M. Wendt, R. Jones and J. Wenninger, "Challenges in beam instrumentation and diagnostics for large ring colliders – based on the LHC experience", these proceedings SUT1B2, HF2014, Beijing, China (2014).

[3] K. Ohmi and D. Zhou, "Study of Electron Cloud Effects in SuperKEKB," TUPRI020, IPAC2014, Dresden, Germany (2014).



ISBN 978-3-95450-172-4

Table 1: Tuning variables (knobs), input measurements (observables) and optimization frequency for luminosity optimization at KEKB.

| Knob | Observable | frequency: every |
|---|---|---|
| Relative beam offset IP | Beam-beam kick measured by BPMs around the IP | 1 sec |
| Relative beam angle IP | BPMs around the IP | 1 sec |
| Global closed orbit | All $\sim$ 450 BPMs | 15 sec |
| Beam offset at crab cavities[11] | BPMs around the crab cavity | 1 sec |
| Betatron tunes | tunes of non-colliding pilot bunches | $\sim$ 20 sec |
| Relative rf phase | center of gravity of the vertex | 10 min. |
| Global couplig, dispersion, beta-beat | orbit response to kicks & rf frequency | $\sim$ 14 days |
| LER to HER crab voltage ratio | response in the hor. beam-beam kick. vs. crab rf phase | $\sim$ 7 days |
| Rf phase of crab cavity | hor. kick vs. crab voltage response | $\sim$ 7 days |
| Vertical waist position | $\mathcal{L}$ and $\sigma_y$ at the SRM | $\sim$1 day |
| Local x-y couplings and dispersions at IP | $\mathcal{L}$ and $\sigma_y$ at the SRM | $\sim$1 day each |
| Sextupole settings | $\mathcal{L}$ and lifetime | $\sim$ 3 days |
| X-y coupling parameter at the crab cavities | $\mathcal{L}$ and $\sigma_y$ at the SRM | $\sim$ 3 days |
| Crab kick voltage | $\mathcal{L}$ and $\sigma_y$ at the SRM | $\sim$ 7 days |



ISBN 978-3-95450-172-4

ISBN 978-3-95450-172-4

# *List of Authors*

**Bold** papercodes indicate primary authors



ISBN 978-3-95450-172-4

ISBN 978-3-95450-172-4

# *Institutes List*

**BINP SB RAS**
Novosibirsk, Russia
- Bogomyagkov, A.V.
- Koop, I.
- Levichev, E.B.
- Muchnoi, N.Yu.
- Nikitin, S.A.
- Piminov, P.A.
- Shatilov, D.N.

**BNL**
Upton, Long Island, New York, USA
- Belomestnykh, S.A.
- Minty, M.G.
- Xu, W.

**CERN**
Geneva, Switzerland
- Bartmann, W.
- Benedikt, M.
- Brugger, M.
- Burkhardt, H.
- Cerutti, F.
- Esposito, L.S.
- Ferrari, A.
- Gutleber, J.
- Härer, B.
- Holzer, B.J.
- Jensen, E.
- Jones, O.R.
- Kersevan, R.
- Koratzinos, M.
- Lebrun, P.
- Losito, R.
- Martin, R.
- Medina Medrano, L.E.
- Mereghetti, A.
- Osborne, J.A.
- Papaphilippou, Y.
- Schulte, D.
- Tomás, R.
- Wendt, M.
- Wenninger, J.
- Zimmermann, F.

**Cornell University (CLASSE), Cornell Laboratory for Accelerator-Based Sciences and Education**
Ithaca, New York, USA
- Rice, D.H.
- Rubin, D. L.
- Talman, R.M.

**DPNC**
Genève, Switzerland
- Blondel, A.P.
- Koratzinos, M.

**ESRF**
Grenoble, France
- White, S.M.

**ESS**
Lund, Sweden
- Lari, L.
- Parker, T.I.

**Fermilab**
Batavia, Illinois, USA
- Chou, W.
- Gianfelice-Wendt, E.

**IHEP**
Beijing, People's Republic of China
- Bai, S.
- Bian, T.J.
- Cheng, J.
- Cui, X.
- Ding, Y.D.
- Dong, H.
- Dong, L.
- Duan, Z.
- Fu, S.
- Gao, J.
- Geng, H.
- Guo, Y.Y.
- Jin, D.P.
- Jin, S.
- Kang, W.
- Li, S.P.
- Li, X.P.
- Lin, G.P.
- Liu, Z.C.
- Lou, X.C.
- Ma, Z.J.
- Pei, G.
- Peng, Y.M.
- Qin, Q.
- Qu, H.
- Sun, Y.
- Wang, D.
- Wang, J.L.
- Wang, N.
- Wang, P.F.
- Wang, Q.B.
- Wang, Y.F.
- Wang, Y.
- Xiao, M.
- Xiu, Q.L.
- Xu, G.
- Yue, J.H.
- Yue, Y.
- Zhai, J.Y.
- Zhang, C.
- Zhang, Y.

ISBN 978-3-95450-172-4

- Zheng, H.J.
- Zhou, Z.S.
- Zhu, H.

**IIIEE**
Lund, Sweden
- Peck, P.C.

**INFN/LNF**
Frascati (Roma), Italy
- Biagini, M.E.
- Boscolo, M.

**Institute of High Energy Physics (IHEP)**
People's Republic of China
- Su, F.

**ITP-PKU**
Beijing, People's Republic of China
- Zhu, S.H.

**JINR/VBLHEP**
Dubna, Moscow region, Russia
- Gusakova, K.A.

**JINR**
Dubna, Moscow Region, Russia
- Maltsev, A.A.

**KEK**
Ibaraki, Japan
- Funakoshi, Y.
- Furukawa, K.
- Ishibashi, T.
- Kako, E.
- Kanazawa, K.
- Koiso, H.
- Morita, A.
- Morita, Y.
- Nakayama, H.
- Ohmi, K.
- Ohnishi, Y.
- Oide, K.
- Sugimoto, H.
- Zhou, D.

**KIT**
Karlsruhe, Germany
- Härer, B.

**MSU**
East Lansing, Michigan, USA
- Syphers, M.J.

**NSU**
Novosibirsk, Russia
- Muchnoi, N.Yu.

**SLAC**
Menlo Park, California, USA
- Cai, Y.
- Seeman, J.T.
- Sullivan, M.K.
- Wienands, U.

**Stony Brook University**
Stony Brook, USA
- Belomestnykh, S.A.

**TENZOR**
Dubna, Moscow region, Russia
- Golubev, V.A.
- Kaploukhiy, S.A.
- Maltseva, M.V.

**UGTO**
Leon, Mexico
- Medina, L.E.

**University of Pisa and INFN**
Pisa, Italy
- Paoloni, E.

ISBN 978-3-95450-172-4